Wave-Body Hydrodynamic Interactions

Selected Papers
from the Publications of

Masashi Kashiwagi
Osaka University, Japan

Department of Naval Architecture & Ocean Engineering
Osaka University

Wave-Body Hydrodynamic Interactions

Wave-Body
Hydrodynamic Interactions

Selected Papers
from the Publications of

Masashi Kashiwagi
Osaka University, Japan

Department of Naval Architecture & Ocean Engineering,
Osaka University / Osaka / Japan / 2021

The texts of the various papers contained in this book were set with $\LaTeX$ using the original manuscripts of the papers.

Printed by
Midori Printing Co., Ltd., Fukuoka, JAPAN
(TEL: +81-92-441-6747, FAX: +81-92-473-1275)

ISBN 978-4-907621-02-5

Printed in Japan

Contents

Masashi Kashiwagi

1955	Born in Imabari City, Ehime Prefecture
1978	Graduated from Osaka University (Naval Architecture)
1980	M.Eng. from Osaka University (Naval Architecture)
1984	Ph.D. from Osaka University (Naval Architecture)
1983	Assistant Professor of Kobe University of Mercantile Marine
1985	Associate Professor of Kyushu University, RIAM
2001	Professor of Kyushu University, RIAM
2008	Professor of Osaka University, NAOE
2021	Retired from Osaka University
2008	Professor Emeritus of Kyushu University
2021	Professor Emeritus of Osaka University

Preface

On the occasion of my retirement from Osaka University in March 2021, I prepared this book containing some selected papers from the publications made over the past 35 years of my research career. These selected papers were reproduced using a template of LaTeX and their original manuscripts kept in my computer, although no digital data exist for the manuscripts and figures before 1995. These selected papers are expected to be informative to those researchers who are interested in hydrodynamic interactions of water waves with floating bodies including ships with forward speed.

My research career started with working on unsteady lifting surfaces related to the prediction of maneuvering forces on a ship in following waves, when I was a PhD student of the late Professor Kensaku Nomoto of Osaka University. After moving to RIAM of Kyushu University, I started working in earnest on seakeeping problems in association with the late Professor Makoto Ohkusu, particularly by use of the slender ship theory. Research interests were gradually extended to other topics such as hydroelasticity related to a very large floating structure (VLFS) and wave interactions among a great number of floating columns. Further, I have been involved in research on hydrodynamics of a floating body in a two-layer fluid, strongly nonlinear violent flows using CFD techniques, the added resistance by means of the unsteady wave-pattern analysis and the unsteady pressure distribution measured on the whole ship surface, and so on. Looking at the selected papers, I can see that most of the works include the theory developed, numerical computations, and experimental results uniquely measured in towing tanks.

These works could be made possible through collaboration with colleagues and co-workers, particularly Professor Changhong Hu of RIAM, Kyushu University and Professor Hidetsugu Iwashita of Hiroshima University. I am very grateful for their support and long-standing relationship. Some papers are co-authored with my former students who finished master's or doctoral courses under my supervision at both Kyushu University and Osaka University. I can recall the pleasant times spent with students whose names appear in the complete list of all publications at the end of this book. The staff members in my laboratory have been supporting in many ways my activities in research and education, for which I am deeply thankful.

Looking back on the past 35 years, the International Workshop on Water Waves and Floating Bodies (IWWWFB), which was initiated by Professor J. N. Newman of MIT and Professor D. V. Evans of Bristol University and held annually, was very important for me to inspire good work of higher quality and to help get acquainted with friends around the world. I believe there are many friends in the community of IWWWFB, who would find this book useful because some papers might be difficult to find at present.

March 2021 Masashi Kashiwagi

Radiation and Diffraction Forces Acting on an Offshore-Structure Model in a Towing Tank*

Masashi KASHIWAGI
Research Institute for Applied Mechanics, Kyushu University
Kasuga, Fukuoka 816-8580, Japan

ABSTRACT

The integral-equation method is applied to calculate the effects of tank-wall reflections upon the hydrodynamic forces acting on a model of offshore structure. The Green function satisfying the tank-wall boundary condition is provided by first considering an infinite number of mirror images and then seeking a closed-form analytical expression for the resultant infinite series. By the analysis of energy and momentum conservation, the formulas are derived, giving damping coefficient, wave-exciting force, and drift force in terms of only the Kochin function. Numerical computations are performed for a structure, composed of four vertical circular cylinders with horizontal base, both in the open sea and in a towing tank. It is shown that the tank-wall effects on the second-order drift force are greater than those on the linear forces and resultant motions.

Keywords: Integral-equation method, tank-wall effects, offshore structure, added-mass and damping, wave-exciting force, drift force.

1. INTRODUCTION

Measurements of the hydrodynamic forces on models of offshore structures such as semisubmersibles and tension leg platforms are usually carried out in a towing tank with parallel side walls. If the tank width is not large enough, we must expect some degree of tank-wall effects to be included in the results of experiments.

In order to clarify the degree and nature of the effects of tank-wall interference, a number of theoretical studies have been made. Ohkusu (1975) considered first-order wave forces and second-order drift force on vertical circular cylinders arranged in multiple rows and an infinite number of piles. As Ohkusu's theory was confined only to the case where each cylinder extends to the sea bottom, there exist no evanescent-wave components. Masumoto et al. (1982) applied Ohkusu's idea to a floating structure composed of multiple columns with footing, neglecting the effects of evanescent waves. These two works were not done for the problem of tank-wall effects, but mathematical formulation is equivalent to that of tandem cylinders placed on the centerline of the wave tank.

Srokosz (1980) studied theoretically several hydrodynamic relations for the interaction of regular waves with a body in a canal. The obtained results can be regarded as an extension of Newman's (Newman, 1976) for the open-sea problem. Miles (1983) also analyzed theoretically the problem of a submerged circular duct that is centrally placed between parallel tank walls, with the limitation of tank width being small compared to the wavelength.

* *Reprinted from International Journal of Offshore and Polar Engineering, Vol. 1, No. 2, pp. 101-107, 1991 (June)*

Eatock Taylor and Hung (1985) provided an exact analytical representation for the velocity potential, which has no restrictions regarding the position of the cylinder in a wave tank. Computational results were also provided for first-order force and mean drift moment on an articulated column, and those were compared with corresponding experimental values. Matsui et al. (1986) made more detailed comparisons between experiments and numerical results based on their own theory. Recently, with a matching technique, Yeung and Sphaier (1989) and Çalişal and Sabuncu (1989) independently studied the effects of channel walls on the hydrodynamic properties of a vertical cylinder. The former gives reasonable behaviors of the hydrodynamic forces at transverse channel-resonant frequencies, but the latter shows physically unreasonable negative damping results at resonant frequencies.

In all of the cited works except for Eatock Taylor's and Hung's work, the body is assumed to be placed on the centerline of a tank and assumed to be of simple configuration such as a vertical circular cylinder. In principle, these limitations can be removed, if the interaction theory developed by Kagemoto and Yue (1985) is applied to the case of an infinite number of bodies. However, numerical results based on such idea have not been reported. It should be also emphasized that almost all the existing theories treating a vertical cylindrical body in a towing tank are described in cylindrical coordinates. Thus they include the infinite series of Bessel functions corresponding to an infinite number of image bodies: Efficient and accurate evaluation of this infinite series must be performed with caution.

In this paper, a three-dimensional (3-D) integral-equation method is applied to the problem of tank-wall effects. The integral-equation method offers, in principle, no restrictions on the geometry of the body. However, complications may exist in the derivation, and then in an efficient evaluation of the Green function satisfying the zero-flux condition on tank walls. In the present work, satisfaction of the zero-flux condition is achieved by considering an infinite number of image singularities, and then a closed-form expression for the resultant infinite series is analytically obtained; thus, unlike the existing studies, there is no need to worry about the convergence of the infinite series and its efficient and accurate evaluation.

A floating structure comprising four vertical circular cylinders with horizontal base is considered as a simple model of offshore structures; it is situated midway between two parallel tank walls and is responding to the incident wave. Computational results are presented of the added-mass and damping coefficients, wave-exciting force and moment, motion amplitude, and second-order drift force. Compact formulas for calculating the damping coefficient, wave-exciting force, and drift force are derived from the principle of energy and momentum conservations. It is analytically shown that the formulas reduce to the 2-D and 3-D results in the open sea in the low- and high-frequency limits, respectively.

2. FORMULATION OF PROBLEM

As shown in Fig. 1, we consider a structure in a towing tank of infinite depth and of width B_T between parallel and vertical walls. The x-axis of a coordinate system is horizontal and coincident with the centerline of a tank, and the z-axis is vertical and positive downward. The origin is placed at the center of a structure and on the undisturbed free surface. The structure consists of four equal circular cylinders with radius R and draft T, and spans of cylinders in the x-and y-directions are denoted by L and B, respectively. A regular incident wave of amplitude a and circular frequency ω propagates in the negative x-axis, and therefore the structure is supposed to oscillate sinusoidally in surge, heave and pitch.

Assuming the flow to be inviscid with irrotational motion, the flow field can be described by the velocity potential that satisfies the Laplace equation. Furthermore, we assume that the amplitudes of incident wave and oscillatory motions are small, which justifies to decompose the velocity potential in the form:

$$\Phi = \mathrm{Re}\left[\left\{\frac{ga}{i\omega}(\phi_0+\phi_7)+\sum_{j=1,3,5} i\omega\,\xi_j\,\phi_j\right\}e^{i\omega t}\right] \tag{1}$$

where ξ_j is the amplitude of j-th mode of motion, with $j=1$ for surge, $j=3$ for heave, and $j=5$ for pitch, and ϕ_j denotes the radiation potential of j-th mode. ϕ_0 and ϕ_7 are the normalized incident-wave and scattered potentials, respectively, and ϕ_0 is explicitly given by:

$$\phi_0 = e^{-Kz+iKx} \tag{2}$$

where K is the wavenumber equal to ω^2/g. In Eq. (1), Re means only the real part is to be taken, and in the analysis to follow we will proceed without this symbol and time dependence $e^{i\omega t}$.

The boundary conditions to be satisfied by the radiation and scattered potentials ϕ_j ($j = 1,3,5,7$) can be summarized as:

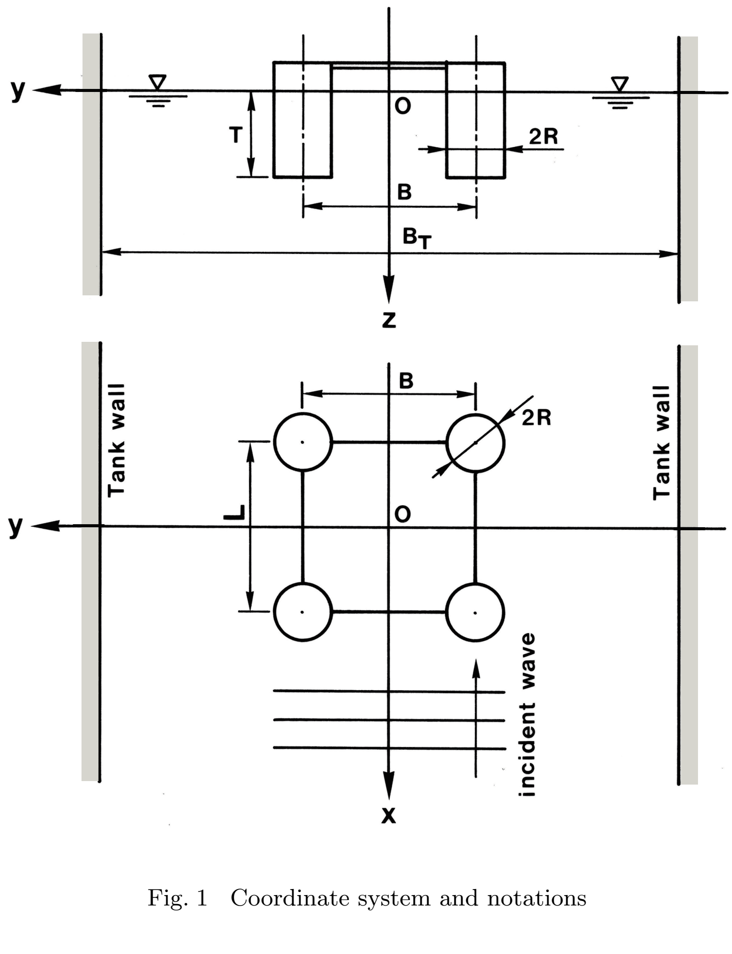

Fig. 1 Coordinate system and notations

$$[\,F\,] \quad \frac{\partial \phi_j}{\partial z} + \big(K - i\mu\big)\phi_j = 0 \qquad \text{on } z = 0 \tag{3}$$

$$[\,B\,] \quad \frac{\partial \phi_j}{\partial z} \to 0 \qquad \text{as } z \to \infty \tag{4}$$

$$[\,W\,] \quad \frac{\partial \phi_j}{\partial y} = 0 \qquad \text{on } y = \pm B_T/2 \tag{5}$$

$$[\,H\,] \quad \frac{\partial \phi_j}{\partial n} = \begin{cases} n_j & (j = 1,3,5) \\ -\dfrac{\partial \phi_0}{\partial n} & (j = 7) \end{cases} \qquad \text{on } S_H \tag{6}$$

Here μ in Eq. (3) is Rayleigh's artificial viscosity coefficient ensuring the radiation condition being satisfied; n_j in Eq. (6) denotes the components of unit normal vector with extended definition of $n_5 = zn_1 - xn_3$, and S_H denotes the submerged portion of the structure.

To determine the velocity potentials, we apply the integral-equation method. The idea of this method has been extensively tested in the open-sea problem, but in the present case complexity may exist in deriving and evaluating the so-called Green function. Discussion on an appropriate Green function will be given in the next section, but here let us assume this is already known.

Applying Green's theorem to the Green function and the velocity potential to be determined, one can obtain an integral equation for the velocity potential on the wetted surface of the structure, in the form:

$$\frac{1}{2}\phi_j(P) + \iint_{S_H} \phi_j(Q)\frac{\partial}{\partial n_Q} G(P;Q)\, dS(Q) = \iint_{S_H} \frac{\partial \phi_j(Q)}{\partial n_Q} G(P;Q)\, dS(Q) \tag{7}$$

where $P = (x, y, z)$ and $Q = (\xi, \eta, \zeta)$ are the field and source points, respectively. It should be noted that the normal differentiation is defined with respect to the source point, and $\partial \phi_j/\partial n$ on the right-hand side is prescribed by Eq. (6).

For the scattered potential ϕ_7, Eq. (7) is of course valid, but a more effective integral equation can be derived through the following procedures: 1) Apply Green's theorem to the Green function and the incident-wave potential ϕ_0 in the interior region of S_H; 2) combine the obtained equation with Eq. (7) and invoke the body boundary condition Eq. (6) for $j = 7$; 3) add ϕ_0 to both sides of the equation. The final result of this procedure is of the form:

$$\frac{1}{2}\phi_D(P) + \iint_{S_H} \phi_D(Q)\frac{\partial}{\partial n_Q} G(P;Q)\, dS(Q) = \phi_0(P) \tag{8}$$

where $\phi_D = \phi_0 + \phi_7$ is the total diffraction potential on the body surface. Eq. (8) may be advantageous to give a more accurate solution with less computing time, as the right-hand side is exactly given by Eq. (2, and there is no need to evaluate the Green function itself.

3. GREEN FUNCTION

The Green function appropriate to the present problem can be constructed by applying the method of mirror images, with the open-sea Green function used as a basis. Various expressions are known for the open-sea Green function, for which we use the notation $G_O(P;Q)$. For convenience in the derivation below, we adopt here the following, expressed in the Fourier-transformed domain:

$$G_O^*(k;y,z;\eta,\zeta) \equiv \int_{-\infty}^{\infty} G_O(P;Q)\,e^{-ikKx}\,dx \tag{9}$$

$$= -\frac{1}{2\pi}\,\mathrm{Re}\int_{-\infty}^{\infty} \frac{e^{-K|y-\eta|\sqrt{k^2+\ell^2}}}{\sqrt{k^2+\ell^2}}\left\{ e^{i\ell K(z-\zeta)} - \frac{1-i\ell}{1+i\ell}\,e^{i\ell K(z+\zeta)}\right\} d\ell$$

$$+\left[\begin{array}{l} \dfrac{i}{\sqrt{1-k^2}}\,e^{-K(z+\zeta)-iK|y-\eta|\sqrt{1-k^2}} \\ \dfrac{-1}{\sqrt{k^2-1}}\,e^{-K(z+\zeta)-K|y-\eta|\sqrt{k^2-1}} \end{array}\right] \tag{10}$$

where the upper and lower expressions in brackets are to be taken according as $|k| < 1$ and $|k| > 1$, respectively. We note that variable k in the Fourier transform is nondimensionalized in terms of K.

In order to satisfy the condition Eq. (5) on the tank walls, we consider an infinite number of mirror images. Taking into account the effects of all images under the condition $|y-\eta| < B_T/2$ and the symmetry of the flow with respect to $y = 0$, it can be understood that the exponential function of the form $e^{-|y-\eta|\ell}$ in Eq. (10) must be replaced by:

$$M(\ell) = e^{-|y-\eta|\ell} + \cosh(\ell y)\cosh(\ell\eta)\;2\sum_{p=1}^{\infty} e^{-p\ell B_T} \tag{11}$$

The first term on the right-hand side is the same one as in the open-sea case and therefore the second term represents the tank-wall effects. In relation to the infinite series in the second term, we can analytically obtain a closed-form expression in the form:

$$2\sum_{p=1}^{\infty} e^{-p\ell B_T} = -1 + \coth\bigl(\ell B_T/2\bigr) \tag{12}$$

For the case of $|k| < 1$ in Eq. (10), we must consider the case when the real ℓ is replaced by the pure imaginary $i\ell$; for this case, the expression corresponding to Eq. (12) can be given, with Dirac's delta function, in the form:

$$2\sum_{p=1}^{\infty} e^{-pi\ell B_T} = 2\pi\delta\bigl(\ell B_T, 2\pi\bigr) - 1 - i\cot\bigl(\ell B_T/2\bigr) \tag{13}$$

where

$$\delta\bigl(\ell, 2\pi\bigr) = \sum_{m=-\infty}^{\infty} \delta\bigl(\ell - 2\pi m\bigr) \tag{14}$$

Combining the above results and using the inverse Fourier transform, we can obtain the final result of the Green function, which can be expressed, as noted after Eq. 11, in addition form of the open-sea Green function plus the tank-wall-effect part. Namely:

$$G(P;Q) = G_O(P;Q) + G_T(P;Q) \tag{15}$$

where

$$
\begin{aligned}
G_T(P;Q) =& -\frac{K}{2\pi^2}\,\mathrm{Re}\int_0^{\pi/2} d\theta \int_0^{\infty} \cos(kX\cos\theta)\cosh(kKy)\cosh(kK\eta) \\
& \quad \times \left\{-1+\coth\left(k\frac{KB_T}{2}\right)\right\}\left[e^{iZ'k\sin\theta}-\frac{1-ik\sin\theta}{1+ik\sin\theta}\,e^{iZk\sin\theta}\right]dk \\
& +i\frac{K}{\pi}\,e^{-Z}\left(\frac{2\pi}{KB_T}\right)\sum_{m=0}^{M}\epsilon_m\frac{\cos\left(X\sqrt{1-u_m^2}\right)}{\sqrt{1-u_m^2}}\cos(Kyu_m)\cos(K\eta u_m) \\
& -i\frac{K}{\pi}\,e^{-Z}\oint_0^1\frac{\cos(kX)}{\sqrt{1-k^2}}\cos\left(Ky\sqrt{1-k^2}\right)\cos\left(K\eta\sqrt{1-k^2}\right) \\
& \quad \times\left\{1+i\cot\left(\frac{KB_T}{2}\sqrt{1-k^2}\right)\right\}dk \\
& -\frac{K}{\pi}\,e^{-Z}\oint_1^{\infty}\frac{\cos(kX)}{\sqrt{k^2-1}}\cosh\left(Ky\sqrt{k^2-1}\right)\cosh\left(K\eta\sqrt{k^2-1}\right) \\
& \quad \times\left\{-1+\coth\left(\frac{KB_T}{2}\sqrt{k^2-1}\right)\right\}dk
\end{aligned} \tag{16}
$$

and

$$
\left.\begin{aligned}
& X=K(x-\xi),\quad Z=K(z+\zeta),\quad Z'=K(z-\zeta) \\
& u_m=2\pi m/KB_T,\quad \epsilon_0=1/2,\quad \epsilon_m=1\ (m\geq 1) \\
& M:\ \text{max. of integer } m \text{ satisfying } m<KB_T/2\pi
\end{aligned}\right\} \tag{17}
$$

In this work, numerical computations of the open-sea Green function and its normal derivative were performed by a combination of Newman's series expansion (Newman, 1984) and Noblesse's asymptotic expansion (Noblesse, 1982).

The double integral appearing as the first term in Eq. (16) is well-behaved, as its integrand rapidly reduces to zero as the argument k increases. Therefore this integral was numerically evaluated by means of the Clenshaw and Curtis quadrature, with an absolute error below 10^{-4} required. When KB_T is large enough, we confirmed that the contribution from this term is almost negligible.

The last two integrals in Eq. (16) must be treated as Cauchy's principal-value integral at the points of k satisfying $k=\sqrt{1-(2\pi m/KB_T)^2}$ $(m=0,1,\ldots,M)$. In the numerical implementation of this integral, singular behaviors are subtracted from the integrand and analytically integrated. For this manipulation we have used the following relation:

$$
\int\frac{k\,dk}{\sqrt{1-k^2}\sin\left(\dfrac{KB_T}{2}\sqrt{1-k^2}\right)}=\frac{2}{KB_T}\ln\left|\tan\left(\frac{KB_T}{4}\sqrt{1-k^2}\right)\right| \tag{18}
$$

Resultant nonsingular integrals are evaluated, using the Clenshaw and Curtis quadrature with an absolute error below 10^{-4} required.

The normal derivative of Eq. (16) must be also computed in solving the integral Eqs. (7) and (8), which was done with almost the same procedure as for the Green function.

4. HYDRODYNAMIC FORCES

4.1 Pressure Integration

In the radiation problem, the hydrodynamic force acting in the j-th direction due to the k-th mode of motion can be expressed in terms of the added mass (A_{jk}) and damping (B_{jk}) coefficients; these can be calculated from:

$$A_{jk} + \frac{1}{i\omega} B_{jk} = -\rho \iint_{S_H} n_j \phi_k \, dS \tag{19}$$

where ρ is the fluid density and ϕ_k is the radiation potential on the body surface, which will be directly given after solving the integral Eq. (7).

Of most concern in the diffraction problem is the calculation of the wave-exciting force. The component in the j-th direction can be evaluated from:

$$E_j = \rho g a \iint_{S_H} n_j \phi_D \, dS \tag{20}$$

where ϕ_D is the total diffraction potential given as a solution of Eq. (8),

4.2 Damping Coefficient by Energy Conservation

The work done to oscillate the body is associated with the energy of outgoing waves at infinity. Therefore, by the analysis of energy conservation, we can obtain a formula giving the damping coefficient.

Ignoring the terms higher than $O(\phi_j^3)$ and taking the time average of the work, we have the relation of the form:

$$B_{jj} = \rho \frac{\omega}{K} \operatorname{Im} \int_0^{B_T/2} \left[\left(\phi_j \frac{\partial \phi_j^*}{\partial x} \right)_{z=0} \right]_{-\infty}^{\infty} dy \tag{21}$$

where ϕ_j^* designates the complex conjugate of ϕ_j. Im means only the imaginary part should be taken, and $[\quad]_{-\infty}^{\infty}$ indicates the difference between the values at $x = +\infty$ and at $x = -\infty$.

Further transformation of Eq. (21) requires an asymptotic expression of the velocity potential at $x = \pm\infty$. To obtain this, we consider first the behavior of the Green function as $x \to \pm\infty$, by the aid of Riemann-Lebesgue's lemma:

$$\lim_{X\to\infty} \int_a^b \frac{F(k)}{f(k)} \cos(kX) \, dk \sim -\pi \frac{F(\beta)}{f'(\beta)} \sin(\beta X) \tag{22}$$

Here β is the value of k satisfying $f(k) = 0$ in the range of integration. Applying Eq. (22) to the Green function in Eq. (15), we shall have the following result:

$$\begin{aligned} G(P;Q) \sim{}& i\frac{K}{\pi}\left(\frac{2\pi}{KB_T}\right) e^{-K(z+\zeta)} \\ &\times \sum_{m=0}^{M} \epsilon_m \frac{e^{\mp iK(x-\xi)\sqrt{1-u_m^2}}}{\sqrt{1-u_m^2}} \cos(Kyu_m)\cos(K\eta u_m) \\ &\qquad \text{as } (x-\xi) \to \pm\infty \end{aligned} \tag{23}$$

The velocity potential at arbitrary points in the fluid domain can be given by:

$$\phi_j(P) = \iint_{S_H} \left(\frac{\partial \phi_j}{\partial n_Q} - \phi_j \frac{\partial}{\partial n_Q} \right) G(P;Q)\, dS(Q) \tag{24}$$

Therefore, by substituting Eq. (23) in Eq. (24), the desired expression at $x = \pm\infty$ can be expressed in the form:

$$\phi_j(P) \sim i\frac{K}{\pi}\, e^{-Kz} \Big(\frac{2\pi}{KB_T} \Big) \sum_{m=0}^{M} \epsilon_m H_j^{\pm}(u_m) \frac{e^{\mp iKx\sqrt{1-u_m^2}}}{\sqrt{1-u_m^2}} \cos\big(Kyu_m\big) \tag{25}$$

where

$$H_j^{\pm}(u) = \iint_{S_H} \left(\frac{\partial \phi_j}{\partial n} - \phi_j \frac{\partial}{\partial n} \right) e^{-K\zeta \pm iK\xi\sqrt{1-u^2}} \cos\big(K\eta u\big)\, dS \tag{26}$$

is the Kochin function that is related to the complex amplitude of the radiation wave at $x = \pm\infty$.

Substituting Eq. (25) in Eq. (21) and performing the integral with respect to y, we shall get the following final result:

$$B_{jj} = \rho\omega \frac{K}{2\pi} \Big(\frac{2\pi}{KB_T} \Big) \sum_{m=0}^{M} \frac{\epsilon_m}{\sqrt{1-u_m^2}} \Big(\big|H_j^{+}(u_m)\big|^2 + \big|H_j^{-}(u_m)\big|^2 \Big) \tag{27}$$

Srokosz (1980) derived a similar expression to Eq. (27) by utilizing Green's theorem.

In the case of a narrow towing tank, only the case $m = 0$ contributes to Eq. (27), and the resulting formula is reminiscent of the 2-D result. On the other hand, if we consider the limiting case of $B_T \to \infty$, the open-sea result can be recovered. To show this, we note that the summation for $B_T \to \infty$ can be reduced to the finite integral by means of the following replacements:

$$u_m \to u, \quad \frac{2\pi}{KB_T} \to du, \quad \sum_{m=0}^{M} \epsilon_m \to \int_0^1 \tag{28}$$

Applying Eq. (28) to Eq. (27) and using the variable transformation of $u = \sin\theta$, we can show that the final result takes the form:

$$B_{jj} = \rho\omega \frac{K}{4\pi} \int_0^{2\pi} \big|H_j(\theta)\big|^2\, d\theta \tag{29}$$

where

$$H_j(\theta) = \iint_{S_H} \left(\frac{\partial \phi_j}{\partial n} - \phi_j \frac{\partial}{\partial n} \right) e^{-K\zeta + iK(\xi\cos\theta + \eta\sin\theta)}\, dS \tag{30}$$

Eq. (29) is a familiar expression in the open-sea case.

4.3 Drift Force by Momentum Conservation

A formula for the second-order drift force can be derived from momentum and energy conservation principles. Following the usual procedure, we neglect the terms higher than $O(\phi^3)$ and take the time average over one period. Then the calculation formula for the drift force is given as:

$$D = \frac{\rho}{4K}\, \mathrm{Re} \int_0^{B_T/2} \left[\left(\Big|\frac{\partial \phi}{\partial x}\Big|^2 - \Big|\frac{\partial \phi}{\partial y}\Big|^2 + K^2 \big|\phi\big|^2 \right)_{z=0} \right]_{-\infty}^{\infty} dy \tag{31}$$

Here the velocity potential ϕ includes all contributions from diffraction and radiation potentials. Namely:

$$\phi = \frac{ga}{i\omega}\left\{\phi_0 + \phi_7 - K\sum_{j=1,3,5}\left(\frac{\xi_j}{a}\right)\phi_j\right\} \tag{32}$$

The incident-wave potential ϕ_0 is given by Eq. (2), and the remaining potentials have the same asymptotic form as Eq. (25) at $x = \pm\infty$. With these taken into account, we can perform the evaluation of Eq. (31)1. After some lengthy reduction, it follows that:

$$\begin{aligned}\frac{D}{\rho g a^2} = \frac{K}{4\pi}\left(\frac{2\pi}{KB_T}\right)\sum_{m=0}^{M}\epsilon_m\Big(\big|H^+(u_m)\big|^2 - \big|H^-(u_m)\big|^2\Big)\\ +\frac{1}{2}\,\mathrm{Im}\Big[H^-(u_0)\Big]\end{aligned} \tag{33}$$

where

$$H^{\pm}(u) = H_7^{\pm}(u) - K\sum_{j=1,3,5}\left(\frac{\xi_j}{a}\right)H_j^{\pm}(u) \tag{34}$$

The last term can be transformed further if we apply the energy-conservation principle. As the structure is freely responding to the incident wave, the following relation must be satisfied:

$$\int_0^{B_T/2}\left[\left(\phi\frac{\partial\phi^*}{\partial x} - \phi^*\frac{\partial\phi}{\partial x}\right)_{z=0}\right]_{-\infty}^{\infty} dy = 0 \tag{35}$$

Transforming Eq. (35) in almost the same manner as in deriving the damping coefficient, we shall obtain:

$$\frac{1}{2}\,\mathrm{Im}\Big[H^-(u_0)\Big] = \frac{K}{4\pi}\left(\frac{2\pi}{KB_T}\right)\sum_{m=0}^{M}\frac{\epsilon_m}{\sqrt{1-u_m^2}}\Big(\big|H^+(u_m)\big|^2 + \big|H^-(u_m)\big|^2\Big) \tag{36}$$

Combining Eqs. (33) and (36), the final result for the drift force can be expressed as:

$$\begin{aligned}\frac{D}{\rho g a^2} = \frac{K}{4\pi}\left(\frac{2\pi}{KB_T}\right)\sum_{m=0}^{M}\frac{\epsilon_m}{\sqrt{1-u_m^2}}\\ \times\Big[\big|H^+(u_m)\big|^2\Big(1+\sqrt{1-u_m^2}\Big) + \big|H^-(u_m)\big|^2\Big(1-\sqrt{1-u_m^2}\Big)\Big]\end{aligned} \tag{37}$$

It is noteworthy that for the case of $m = 0$ only, Eq. (37) reduces to a similar form to the 2-D result, and that for the case of open sea ($B_T \to \infty$), Maruo's formula (Maruo, 1960) can be recovered by applying the replacement formula of Eq. (28).

4.4 Haskind-Newman's Relation

As shown by Eq. (20), the wave-exciting force can be calculated by the pressure integration. If Green's theorem is applied, Eq. (20) can be transformed further, and the relation between the exciting force and the Kochin function of the radiation problem may be found.

Applying Green's theorem and taking into account the body boundary condition for the scattered potential, it follows that:

$$\iint_{S_H}\phi_7\frac{\partial\phi_j}{\partial n}\,dS = -\iint_{S_H}\phi_j\frac{\partial\phi_0}{\partial n}\,dS \tag{38}$$

Then Eq. (20) can be transformed as follows:

$$
\begin{aligned}
E_j &= \rho g a \iint_{S_H} \left(\phi_0 \frac{\partial \phi_j}{\partial n} - \phi_j \frac{\partial \phi_0}{\partial n} \right) dS \\
&= \rho g a \, H_j^+(u_0)
\end{aligned}
\tag{39}
$$

where H_j^+ is the Kochin function defined by Eq. (26), and note that $u_0 = 0$. Eq. (39) can be regarded as Haskind-Newman's relation in the presence of tank-wall effects, and identical to the relation derived by Srokosz (1980).

In the analysis above, we found a number of relations that can be used for checking the validity and accuracy of the calculations. In the present paper, Haskind-Newman's relation and the energy-conservation principle associated with the damping coefficient were used for the check and found to be favorably satisfied.

5. NUMERICAL RESULTS AND DISCUSSION

Numerical computations were performed for the structure model shown in Fig. 1, which has two symmetry planes. Taking advantage of the symmetry of the flow, we analyzed only one quarter of the model. To solve the integral equation, the submerged surface of one cylinder was subdivided into several flat panels, and the velocity potential to be determined is assumed constant on each panel. Then the collocation method was used, enforcing the integral equation at the centroid of each panel; thereby the integral equation was replaced by a linear system of algebraic equations, and solved by the Gauss elimination method.

Discretization used for numerical computations is shown in Fig. 2, which contains 84 panels on one cylinder, thus

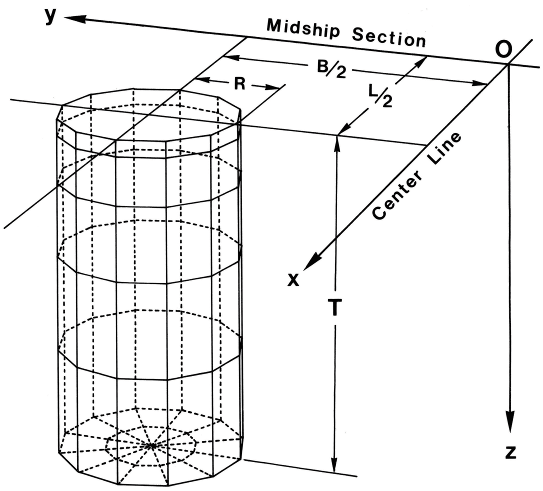

Fig. 2 Discretization with 84 panels on one quarter of the structure

Table 1 Principal parameters of the structure composed of four vertical circular cylinders

Span in y-direction	B/L	1
Draft	T/L	1/2
Radius of cylinder	R/L	1/6
Center of gravity	$\overline{OG}/T$	1/2
Waterplane area	A_W	$4\pi R^2$
Displacement volume	V	$A_W T$
Tank width	B_T/L	4

336 panels on the whole structure. Table 1 shows the ratios of dimensions for which numerical results are presented. These ratios correspond to the actual situation where a structure model of 1.0 m both in length and in breadth is tested in a towing tank of 4.0 m in width.

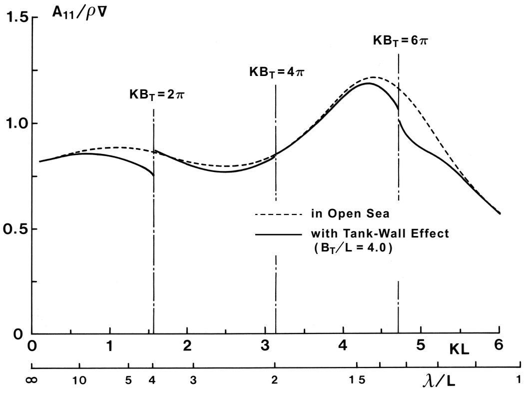

Fig. 3 Surge added-mass coefficient

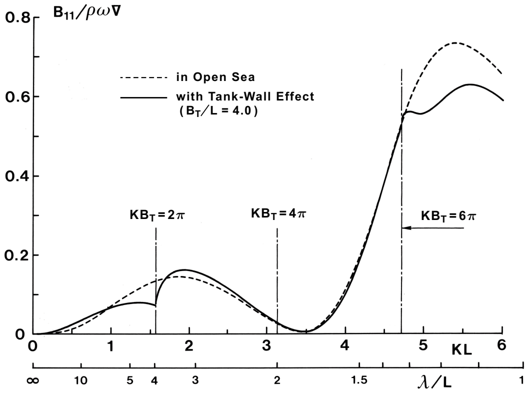

Fig. 4 Surge damping coefficient

Figures 3 and 4 show respectively the added-mass and damping coefficients of surge against the nondimensional wavenumber KL, which were obtained by the pressure integration Eq. (19). The results without tank-wall effects (that is, in open sea) are indicated by a dotted line, and the results with tank-wall effects are by solid line. Vertical dash-dotted lines in each figure show the wavenumbers at which a transverse tank resonance will occur, thus the ratio of wavelength to tank width is equal to the inverse of an integer. It can be seen from Figs. 3 and 4 that the tank-wall effects are not serious in surge mode except in the frequency range greater than the third tank-resonant frequency, where the wavelength becomes nearly equal to the span of columns; hence the free surface is expected to be seriously disturbed due to the interference effects between cylinders and tank walls.

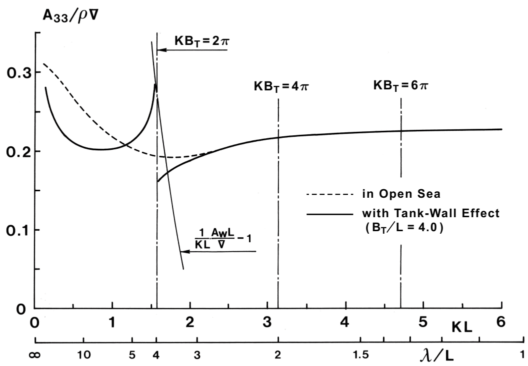

Fig. 5 Heave added-mass coefficient

The added mass of heave is shown in Fig. 5, but the damping force in heave is not shown because of its quite small magnitude. In contrast to the surge mode, the tank-wall effects are apparent only in the low frequency range. As the depth of vertical circular cylinder is three times the radius, there may be little influence of reflection waves on the heave mode when the wavelength is small.

The wave-exciting forces in surge and heave, computed by the pressure integration, are shown in Figs. 6 and 7, respectively. Only the modulus is presented, and notations are the same as before. The surge exciting force shows similar variation to that of surge damping coefficient, and the effects of tank-wall reflections are not great, except in the case of the wavelength being close to the span of columns. The tank-wall

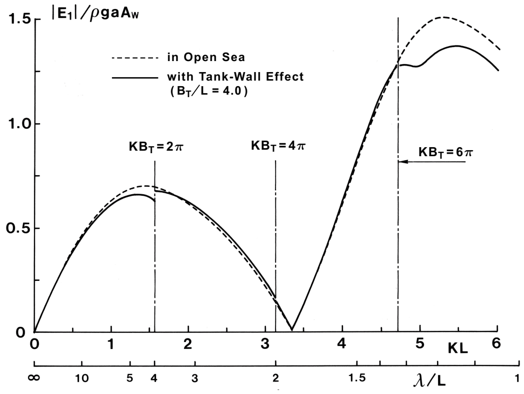

Fig. 6 Modulus of wave-exciting force in surge

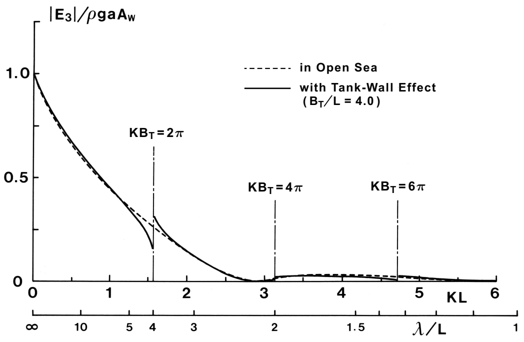

Fig. 7 Modulus of wave-exciting force in heave

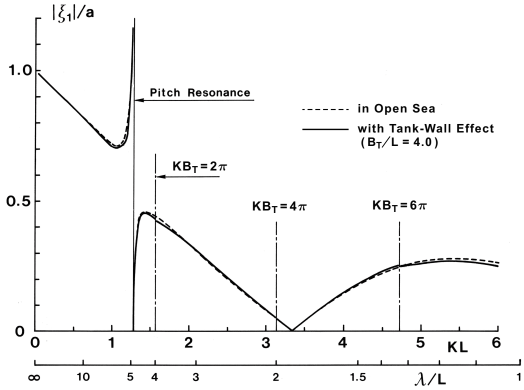

Fig. 8 Surge amplitude of four vertical cylinders in a towing tank

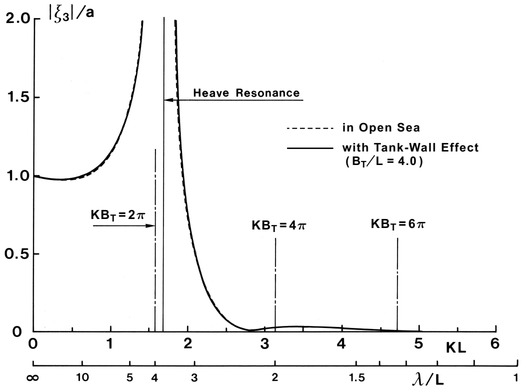

Fig. 9 Heave amplitude of four vertical cylinders in a towing tank

effects on the heave exciting force are also not serious, except near the first tank-resonant frequency.

The motions of surge, heave and pitch were calculated using theoretically computed first-order forces; only surge and heave amplitudes are displayed here in Figs. 8 and 9, respectively. Since surge and pitch are coupled, surge amplitude changes abruptly near the pitch resonance (Fig. 8). Nevertheless, the tank-wall effects are still negligible. Heave resonance occurs near $KL = 1.7$ regardless of whether the tank walls are present. This can be understood from Fig. 5, in which the intersection point between thin solid line and added-mass curve gives the resonant frequency. We can see that the tank-wall effects on heave motion are small even in the low frequency range, in contrast to the heave added mass in this range.

The second-order drift force is presented in Fig. 100, for the case of the structure being fixed in the incident wave. It can be seen that the drift force is considerably influenced by the tank-wall reflections, even in the frequency range where the wave-exciting force is not so affected. Fig. 11 shows the drift force on the structure freely responding to the action of incident wave. If we compare Fig. 11 with Fig. 10, the effects of motions can be made clear.

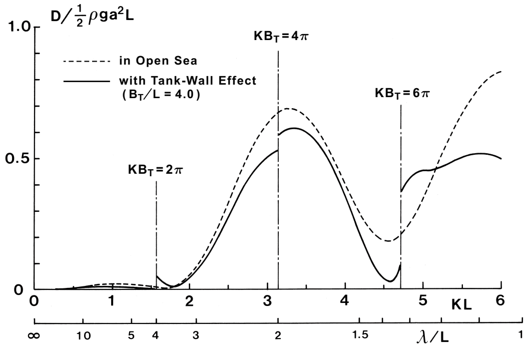

Fig. 10 Drift force on four vertical cylinders fixed in waves

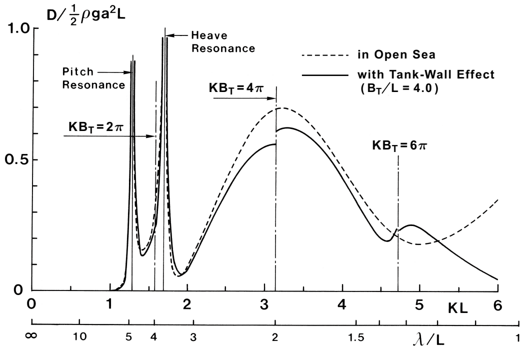

Fig. 11 Drift force on four vertical cylinders freely responding to waves

We can see that in the low frequency range, the effects of heave and pitch motions are great owing to their resonances. In the range between $KL = 2$ and 4, the motion amplitude in each mode is relatively small, as shown in Figs. 8 and 9, and thus the difference between Figs. 10 and 11 in this range is not large. On the other hand, as the wavelength approaches the span of cylinders, the effects of motion on the drift force become conspicuous; this is due mainly to the surge motion.

As seen above, the first-order forces and resultant responses are not seriously affected by the presence of tank walls, at least for the floating structure considered here. However, the effects on the second-order drift force are significant. This finding is consistent with the experiments shown by Matsui et al. (1986) for an articulated column.

6. CONCLUSIONS

A 3-D integral-equation method has been described for predicting linear hydrodynamic forces and second-order drift force on an offshore structure model in a parallel-sided towing tank. In order to derive the Green function satisfying the zero-flux condition on the tank walls, an infinite number of image singularities were considered, and a closed-form analytical expression was obtained for the resultant infinite series.

By applying the principle of energy and momentum conservation, compact formulas were derived for the damping coefficient, wave-exciting force, and drift force, which contain only the Kochin function associated with the amplitude of outgoing waves far away from the structure.

Computed results were presented for a floating structure composed of four columns of vertical circular cylinders, under the condition that the tank width is four times the span of columns. It was shown that the effects of tank-wall reflections are small on the linear forces and resultant motions, whereas on the second-order drift force the effects are remarkable and not to be neglected.

REFERENCES

1 Çalişal, S M, and Sabuncu, T (1989). "A Study of a Heaving Vertical Cylinder in a Towing Tank," *Journal of Ship Research*, Vol. 33, No. 2, pp. 107-114.

2 Eatock Taylor, R, and Hung, S M (1985). "Mean Drift Forces on an Articulated Column Oscillating in a Wave Tank," *Applied Ocean Research*, Vol. 7, No. 2, pp. 66-78.

3 Kagemoto, H, and Yue, D K P (1985). "Hydrodynamic Interactions among Multiple Three Dimensional Floating Bodies; An Exact Algebraic Method," *Journal of Fluid Mechanics*, Vol. 166, pp. 189-209.

4 Maruo, H (1960). "The Drift of a Body Floating on Waves," *Journal of Ship Research*, No. 4, pp. 1-10.

5 Masumoto, A, Yamagami, Y, and Sakata, R (1982). "Wave Forces on Cylinder Arrays," *Applied Ocean Research*, Vol. 4, No. 1, pp. 2-8.

6 Matsui, T, Ohmori, H, Shirai, T, Endo, M, Sugita, H, and Ohki, K (1986). "Slowly Varying Wave Drift Forces on an Articulated Column – 2nd Report, Experiment in Regular Waves," *Journal of the Society of Naval Architects of Japan*, No. 160, pp. 185-194.

7 Miles, J W (1983). "Surface Wave Diffraction by a Periodic Row of Submerged Ducts," *Journal of Fluid Mechanics*, Vol. 128, pp. 155-180.

8 Newman, J N (1976). "The interaction of Stationary Vessels with Regular Waves," *Proceedings of the 11th Symposium on Naval Hydrodynamics*, London, pp. 491-501.

9 Newman, J N (1984). "An Expansion of the Oscillatory Source Potential," *Applied Ocean Research*, Vol. 6, No. 2, pp. 116-117.

10 Noblesse, F (1982). "The Green Function in the Theory of Radiation and Diffraction of Regular Water Waves by a Body," *Journal of Engineering Mathematics*, Vol. 16, pp. 137-169.

11 Ohkusu, M (1975). "The Analysis of Wave Forces Acting upon Multi-Supported Platforms," *Transactions of the West Japan Society of Naval Architects*, Vol. 51, pp. 153-170.

12 Srokosz, M A. (1980). "Some Relations for Bodies in a Canal, with an Application to Wave-Power Absorption," *Journal of Fluid Mechanics*, Vol. 99, Part 1, pp. 145-162.

13 Yeung, R W, and Sphaier, S H (1989). "Wave-Interference Effects on a Truncated Cylinder in a Channel," *Journal of Engineering Mathematics*, Vol. 23, pp. 95-117.

A New Theory for Side-Wall Interference Effects on Forward-Speed Radiation and Diffraction Forces*

Masashi KASHIWAGI and Makoto OHKUSU

Research Institute for Applied Mechanics, Kyushu University
Kasuga, Fukuoka 816-8580, Japan

Abstract

A new rational theory predicts the effects of side-wall interference upon the hydrodynamic forces on a ship advancing in waves generated in a parallel-sided waterway. The radiation problem is solved by extending the forward-speed version of Newman's unified theory. Haskind-Newman's reciprocity relation gives wave-exciting forces and motions. Energy conservation gives a formula for the damping coefficients from the Kochin function associated with the far-field radiated waves. The theory is validated by experiments and independent numerical solutions by a 3-D panel method for simple bodies. New diagrams for checking the side-wall interference are provided.

Keywords: Tank wall interference, forward-speed effect, added mass, damping, wave excitation, ship motion, seakeeping, model experiments.

1. Introduction

The hydrodynamic forces and ship motions measured in a towing tank with finite width can exhibit experimental scatter around the expected results in open water. This phenomenon can be ascribed to the side-wall reflections of the waves generated by a tested ship model, and becomes prominent in the low frequency range when the ship has low or zero forward speed.

At zero forward speed, mathematical treatment for the side-wall interference is relatively simple. It is possible to predict the effects of side-wall interference with engineering accuracy, Cohen and Troesch (1988), Yeung and Sphaier (1989), Kashiwagi (1989,1990). With forward speed included, no satisfactory theory exists giving quantitatively good predictions.

Based on thin-ship theory, Hanaoka (1958) provided for the first time an analytical representation for the velocity potential describing the flow around a translating and oscillating ship in a restricted waterway. Hosoda (1976,1978) proposed a practical method of predicting the side-wall effects on ship motions in waves, using the strip-theory approach. Takaki's (1979) study was also based on the strip theory, in which the expressions were derived for the radiation and diffraction forces with the effects of bottom as well as side walls of the waterway taken into account. Despite several approximations associated with the strip theory, the obtained expressions appear to be complex and computed results are not in good agreement with experiments.

For unrestricted water, many studies based on the slender-body theory have been made. As a result, the unified slender-ship theory was developed by Newman (1978). The excellent performance of the unified theory is demonstrated in Newman and Sclavounos (1980)

∗ *Reprinted from Ship Technology Research (Schiffstechnik), Vol. 38, No. 1, pp. 17–47, 1991*

through a number of comparisons between computed and experimental results and the estimation of computation time required. We extend Newman's unified slender-ship theory to include side-wall effects.

2. Problem Formulation

A ship advances at constant forward speed U along the centerline of the waterway with vertical and parallel side walls. The depth of the waterway is assumed infinite and the breadth is denoted by B_T as shown in Fig. 1. Ship's length, breadth, and depth are denoted by L, B, and d, respectively. The x-axis of the coordinate system used is positive in the direction of ship's forward motion, the y-axis is horizontal, and the z-axis is vertical and positive downward, with the origin placed at midships and on the undisturbed free surface. A regular plane wave of amplitude a and circular frequency ω_0 is incident upon the ship as a head wave, and thus the ship is supposed to oscillate sinusoidally in symmetric modes around its mean position with the circular frequency of encounter ω and the amplitude ξ_j; the subscript j is the mode index, and in particular $j = 3$ for heave, $j = 5$ for pitch.

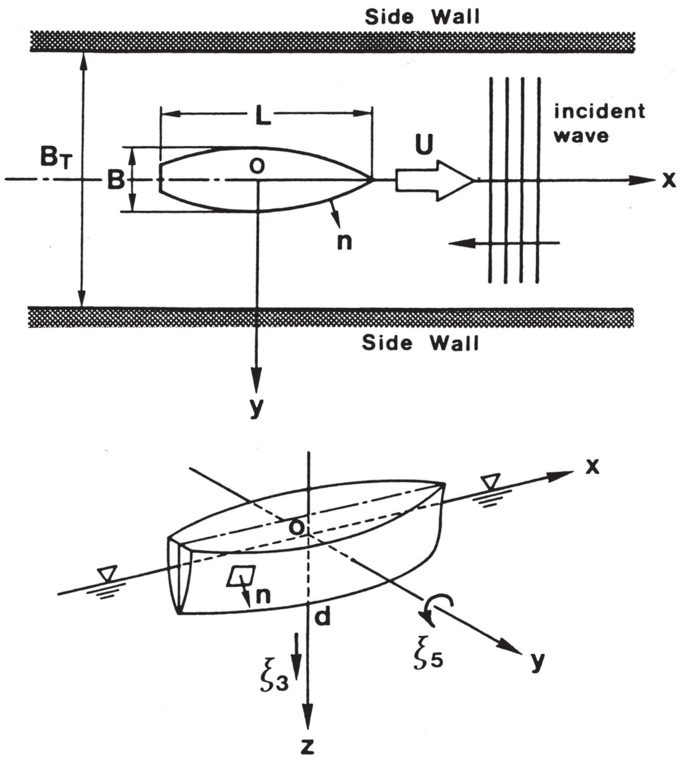

Fig. 1 Coordinate system and notations

Assuming that the flow is inviscid with irrotational motion and that the ship motion and incident-wave amplitudes are small, the velocity potential can be introduced and decomposed as

$$\varPhi = U\big[-x + \phi_S(x,y,z)\big] + \Re\Big[\psi(x,y,z)\,e^{i\omega t}\Big] \tag{1}$$

$$\psi = \frac{ga}{i\omega_0}\big\{\phi_0(x,z) + \phi_7(x,y,z)\big\} + i\omega \sum_{j=3,5} \xi_j\,\phi_j(x,y,z) \tag{2}$$

$$\phi_0 = e^{-k_0 K z + i k_0 K x} \tag{3}$$

where ϕ_S denotes the steady-state disturbance velocity potential, ϕ_0 the incident-wave velocity potential, k_0 the wavenumber of the incident wave nondimensionalized in terms of $K = \omega^2/g$, and g the acceleration of gravity. The symbol $\Re$ in (1) means only the real part should be taken, and hereafter the analysis will proceed without this symbol and time dependence $e^{i\omega t}$.

The governing equation and boundary conditions to be satisfied by the radiation potential ϕ_j $(j = 3, 5)$ and the scattered potential ϕ_7 may be given as follows:

$$[\,L\,] \quad \nabla^2\phi_j = 0 \qquad \text{in the fluid domain} \tag{4}$$

$$[\,F\,] \quad \frac{\partial\phi_j}{\partial z} + K\phi_j + i2\tau\frac{\partial\phi_j}{\partial x} - \frac{1}{K_0}\frac{\partial^2\phi_j}{\partial x^2} - i\mu\left(K\phi_j + i\tau\frac{\partial\phi_j}{\partial x}\right) = 0 \qquad \text{on } z = 0 \tag{5}$$

$$\text{where } K = \frac{\omega^2}{g},\ \tau = \frac{U\omega}{g},\ K_0 = \frac{g}{U^2} \tag{6}$$

$$[\,B\,] \quad \frac{\partial\phi_j}{\partial z} \to 0 \qquad \text{as } z \to \infty \tag{7}$$

$$[\,W\,] \quad \frac{\partial\phi_j}{\partial y} = 0 \qquad \text{on } y = \pm B_T/2 \tag{8}$$

$$[\,H\,] \quad \frac{\partial\phi_j}{\partial n} = n_j + \frac{U}{i\omega}m_j \quad (j = 3, 5) \tag{9}$$

$$\frac{\partial\phi_j}{\partial n} = -\frac{\partial\phi_0}{\partial n} \qquad (j = 7) \tag{10}$$

Here μ in (5) is Rayleigh's artificial viscosity coefficient, ensuring the appropriate radiation condition being satisfied. The components of unit normal vector along the x_j-axis ($x_1 = x$, $x_2 = y$, and $x_3 = z$) are denoted by n_j in (9), with extended definition of $n_5 = zn_1 - xn_3$. The forward-speed-effect part m_j in (9) is the so-called m-terms arising from ship's oscillation in the steady-state disturbance flow, which was originally derived in Timman and Newman (1962) and can be expressed as

$$\begin{aligned} (m_1,\, m_2,\, m_3) &= -(\boldsymbol{n}\cdot\nabla)\boldsymbol{W} \\ (m_4,\, m_5,\, m_6) &= -(\boldsymbol{n}\cdot\nabla)\big(\boldsymbol{r}\times\boldsymbol{W}\big) \\ \boldsymbol{W} &= \nabla\big[-x + \phi_S(x,y,z)\big] \end{aligned} \tag{11}$$

In order to solve the above three-dimensional boundary-value problem including side-wall effects, we adopt the approach of Newman's (1978) unified theory developed for the open-sea problem. A theoretical solution method based on this approach has been already provided by Kashiwagi and Ohkusu (1989) for the radiation problem, but for convenience in subsequent explanation for the wave-exciting forces, the outline of the theory will be given in the following subsections.

2.1 The outer solution

In the outer field far from the ship hull, the ship may be viewed as a segment on the x-axis. Therefore the outer solution can be approximated by a distribution of the 3-D Green function on the x-axis:

$$\phi_j^{(o)}(x, y, z) = \int_L q_j(\xi) G(x-\xi, y, z)\, d\xi \tag{12}$$

where $G(x, y, z)$ denotes the Green function, equivalent to the velocity potential of a translating and pulsating source, and $q_j(x)$ is its strength which is indeterminate in the outer problem because of the absence of the hull boundary conditions (9) and (10).

The Green function, satisfying eqs. (5) to (8), can be derived by the method of mirror images. Considering the Fourier transform with respect to x of the open-sea Green function located at the origin and of its mirror images reflected in the parallel side walls, the desired Green function is given in the Fourier space as

$$\begin{aligned}
\widetilde{G}(k; y, z) &= \int_{-\infty}^{\infty} G(x, y, z)\, e^{ikKx}\, dx \\
&= -\frac{1}{\pi}\int_0^{\infty} \frac{n\cos(nKz) - \nu\sin(nKz)}{n^2+\nu^2} \frac{n}{\sqrt{n^2+k^2}} \sum_{p=-\infty}^{\infty} e^{-K|y-pB_T|\sqrt{n^2+k^2}}\, dn \\
&\quad - \left[\begin{array}{l} \dfrac{-i\nu\,\mathrm{sgn}(1+k\tau)}{\sqrt{\nu^2-k^2}}\, e^{-\nu Kz} \displaystyle\sum_{p=-\infty}^{\infty} e^{-i\,\mathrm{sgn}(1+k\tau)K|y-pB_T|\sqrt{\nu^2-k^2}} \\ \dfrac{\nu}{\sqrt{k^2-\nu^2}}\, e^{-\nu Kz} \displaystyle\sum_{p=-\infty}^{\infty} e^{-K|y-pB_T|\sqrt{k^2-\nu^2}} \end{array} \right]
\end{aligned} \tag{13}$$

where

$$\nu = \big(1+k\tau\big)^2 \tag{14}$$

and the upper and lower expressions in brackets are to be taken according as $|k| < \nu$ and $|k| > \nu$, respectively.

The infinite series appearing in (13) can be expressed analytically in a closed form, under the condition $|y| < B_T/2$:

$$\sum_{p=-\infty}^{\infty} e^{-K|y-pB_T|\ell} = e^{-K|y|\ell} + \cosh(\ell Ky)\left[-1+\coth\Big(\frac{\ell KB_T}{2}\Big)\right] \tag{15}$$

$$\begin{aligned}
\sum_{p=-\infty}^{\infty} e^{\pm iK|y-pB_T|\ell} &= e^{\pm iK|y|\ell} \\
&\quad + \cos(\ell Ky)\left[\frac{2\pi}{KB_T}\,\delta\Big(\ell, \frac{2\pi}{KB_T}\Big) - 1 \pm i\cot\Big(\frac{\ell KB_T}{2}\Big)\right]
\end{aligned} \tag{16}$$

Here the first term in brackets of (16) denotes the series of Dirac's delta function, defined by

$$\delta\Big(\ell, \frac{2\pi}{KB_T}\Big) = \sum_{m=-\infty}^{\infty} \delta\Big(\ell - \frac{2\pi}{KB_T} m\Big) \tag{17}$$

In the limit of $B_T \to \infty$ in (15) and (16), the second term on the right-hand side of each equation vanishes and only the first term remains, implying that the Fourier transform of the Green function $\tilde{G}(k;y,z)$ can be expressed as a sum of the open-sea part $\tilde{G}_O(k;y,z)$ and the side-wall-effect part $\tilde{G}_T(k;y,z)$. The final expression for the Green function will be given by the inverse Fourier transform:

$$\begin{aligned} G(x,y,z) &= G_O(x,y,z) + G_T(x,y,z) \\ &= \frac{K}{2\pi}\int_{-\infty}^{\infty}\Big\{\tilde{G}_O(k;y,z) + \tilde{G}_T(k;y,z)\, e^{-ikKx}\, dk \end{aligned} \tag{18}$$

In the slender-ship theory, the unknown source strength $q_j(x)$ in (12) will be determined by requiring the inner expansion of (12) to be compatible with the outer expansion of an appropriate inner solution. For this matching procedure, the inner expansion of the above Green function must be sought; Kashiwagi and Ohkusu (1989) give details of this derivation. Only the final results will be summarized here.

The inner expansion of the open-sea Green function, which is the same as that in Newman's unified theory, can be expressed in the form

$$G_O(x,y,z) \sim \delta(x)G_{2D}(y,z) - \frac{1}{\pi}\big(1-Kz\big)\frac{d}{dx}F_O(Kx) \tag{19}$$

where $\delta(x)$ is Dirac's delta function and $G_{2D}(y,z)$ the 2-D Green function commonly used in the strip-theory solution. Newman and Sclavounos (1980) ingeniously derived an expression for $F_O(Kx)$, which in the nondimensional form is

$$F_O(Kx) = \begin{cases} F_1(Kx) + F_2(Kx) & \text{for } x < 0 \\ F_2(Kx) & \text{for } x > 0 \end{cases} \tag{20}$$

where

$$\begin{aligned} F_1(X) &= \left[-\int_{-\infty}^{k_1} + \int_{k_2}^{0}\right] e^{-ikX}\left\{\frac{\nu}{\sqrt{\nu^2-k^2}} - 1\right\}\frac{dk}{k} \\ &\quad + E_1\big(i|k_1X|\big) + E_1\big(i|k_2X|\big) \end{aligned} \tag{21}$$

$$\begin{aligned} F_2(X) &= \frac{1}{2}\left[\int_{0}^{k_3} + \int_{k_4}^{\infty}\right] e^{-ikX}\left\{\frac{\nu}{\sqrt{\nu^2-k^2}} - 1\right\}\frac{dk}{k} \\ &\quad + \frac{1}{2}\int_{k_3}^{k_4} e^{-ikX}\left\{\frac{i\nu}{\sqrt{k^2-\nu^2}} - 1\right\}\frac{dk}{k} \end{aligned} \tag{22}$$

$$\left.\begin{aligned} k_{1,2} &= -2/\big(1+2\tau \mp \sqrt{1+4\tau}\,\big) \\ k_{3,4} &= \ \ 2/\big(1-2\tau \pm \sqrt{1-4\tau}\,\big) \end{aligned}\right\} \tag{23}$$

$$E_1(z) = \int_{z}^{\infty}\frac{e^{-t}}{t}\, dt \tag{24}$$

The inner expansion of side-wall-effect part can be derived with relative ease, because no singularity exists in this near the x-axis. The result is of the form

$$G_T(x,y,z) \sim -\frac{1}{\pi}\big(1-Kz\big)\frac{d}{dx}F_T(Kx) \tag{25}$$

where

$$
\begin{aligned}
F_T(X) = {} & \frac{i}{2\pi}\int_{-\infty}^{\infty} e^{-ikX}\,\frac{dk}{k}\int_0^{\infty}\Big\{-1+\coth\Big(\frac{KB_T}{2}\sqrt{n^2+k^2}\Big)\Big\}\frac{n^2\,dn}{(n^2+\nu^2)\sqrt{n^2+k^2}} \\
& +\frac{1}{2}\Big(\frac{2\pi}{KB_T}\Big)\sum_{p=1}^{4}\sum_{m=0}^{\infty}\epsilon_m\left[e^{-ikX}\frac{\mathrm{sgn}(1+k\tau)}{k|d\nu/dk-k/\nu|}\right]_{k=k_{pm}} \\
& -\frac{1}{2}\left[\oint_{-\infty}^{k_1}+\oint_{k_2}^{k_3}+\oint_{k_4}^{\infty}\right]e^{-ikX}\frac{\nu}{\sqrt{\nu^2-k^2}} \\
& \times\Big\{\mathrm{sgn}(1+k\tau)+i\cot\Big(\frac{KB_T}{2}\sqrt{\nu^2-k^2}\Big)\Big\}\frac{dk}{k} \\
& +\frac{i}{2}\left[\int_{k_1}^{k_2}+\int_{k_3}^{k_4}\right]e^{-ikX}\frac{\nu}{\sqrt{k^2-\nu^2}}\Big\{-1+\coth\Big(\frac{KB_T}{2}\sqrt{k^2-\nu^2}\Big)\Big\}\frac{dk}{k}
\end{aligned}
\tag{26}
$$

In the second term of (26), notation $\epsilon_0 = 1/2$, $\epsilon_m = 1$ $(m \neq 0)$ has been used and the wavenumber k_{pm} denotes the values satisfying $KB_T\sqrt{\nu^2-k^2} = 2\pi m$ $(m = 0, 1, 2, \ldots)$, which exist at most four for each integer m and coincide with k_j $(j = 1 \sim 4)$ defined by (23) when $m = 0$. (A schematic explanation for k_{pm} is given in Fig. 2 for the case $\tau < 1/4$.) At these discrete wavenumbers, k_{pm}, the integrals in the third term of (26) must be treated as Cauchy's principal-value integral.

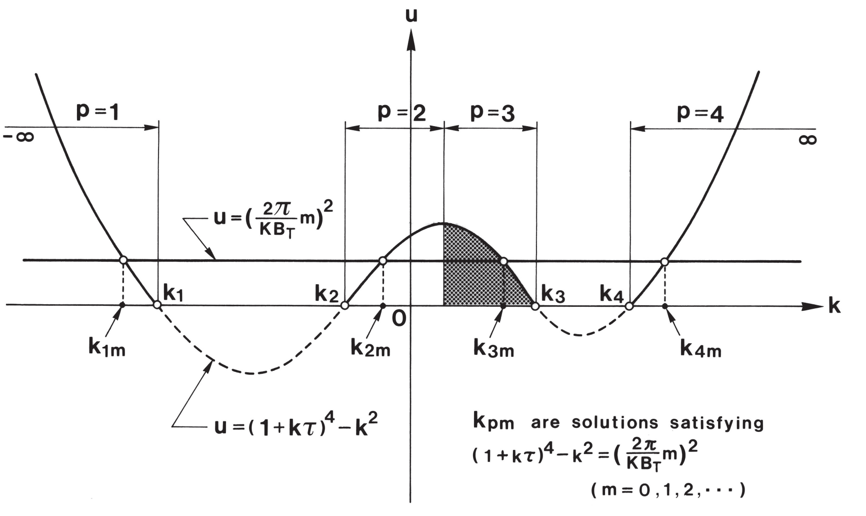

Fig. 2 Schematic explanation for discrete wavenumbers k_{pm} in the case of $\tau < 1/4$

Substituting into (12) the inner expansion of the Green function obtained above, we get the inner expansion of the outer solution:

$$
\begin{aligned}
\phi_j^{(o)}(x,y,z) \sim {} & q_j(x)G_{2D}(y,z)+\frac{1}{\pi}(1-Kz) \\
& \times\int_L q_j(\xi)\frac{d}{d\xi}\Big[F_O\big\{K(x-\xi)\big\}+F_T\big\{K(x-\xi)\big\}\Big]\,d\xi
\end{aligned}
\tag{27}
$$

2.2 The inner problem

In the inner field close to the ship hull, changes of the flow in the x-direction may be small compared to changes in the transverse plane, and the radiation condition and side-wall boundary condition can not be specified. Therefore the governing equation and boundary conditions for the present inner problem are identical to those in the open-sea problem considered by Newman (1978).

Following Newman's unified slender-ship theory, the inner solution can be constructed by the superposition of the particular solution commonly used in the strip theories and a homogeneous component; the latter is expected to account for the longitudinal flow interactions and the effects of side-wall interference. We write this inner solution as

$$\phi_j^{(i)}(x;y,z) = \varphi_j^P(y,z) + C_j(x)\varphi_j^H(y,z) \tag{28}$$

$$\varphi_j^P(y,z) = \varphi_j(y,z) + \frac{U}{i\omega}\widehat{\varphi}_j(y,z) \tag{29}$$

$$\varphi_j^H(y,z) = \varphi_j(y,z) - \varphi_j^*(y,z) \tag{30}$$

The particular solution (29), which consists of two parts, must satisfy the condition

$$[\ H\ ] \qquad \frac{\partial \varphi_j}{\partial N} = N_j\,, \quad \frac{\partial \widehat{\varphi}_j}{\partial N} = M_j \tag{31}$$

on the ship hull. Here N is the 2-D unit normal in the y-z plane, and N_jj and M_j are slender-body approximations of n_jj and m_j given in (9), respectively; in particular, N_5 and M_5 can be approximated as

$$N_5 = -x\,N_3\,, \quad M_5 = N_3 - x\,M_3 \tag{32}$$

The asterisk used as superscript in (30) denotes the complex conjugate, and hence from (31) the velocity potential φ_j^H satisfies the homogenous boundary condition. The coefficient of this homogeneous solution, $C_j(x)$, which is unknown at this stage, will be settled from the matching requirement between the inner and outer solutions.

The outer expansion of the inner solution necessary for this matching can be expressed as

$$\phi_j^{(i)}(x;y,z) \sim \Big[\sigma_j(x) + \frac{U}{i\omega}\widehat{\sigma}_j(x) + C_j(x)\Big\{\sigma_j(x) - \sigma_j^*(x)\Big\}\Big]\ G_{2D}(y,z) \\ +2iC_j(x)\sigma_j^*(x)\,e^{-Kz}\cos(Ky) \tag{33}$$

Here $\sigma_j(x)$ and $\widehat{\sigma}_j(x)$ are the 2-D effective source strengths and given numerically after solving the boundary-value problems for $\varphi_j(y,z)$ and $\widehat{\varphi}_j(y,z)$, respectively.

2.3 Matching

In the analysis described above, the unknowns are the 3-D source strength $q_j(x)$ in the outer solution and the coefficient $C_j(x)$ of a homogeneous component in the inner solution. These can be determined by matching the inner expansion of the outer solution (27) with the outer expansion of the inner solution (33) in an appropriate overlap region. The result of this matching procedure can be summarized as:

$$q_j(x) + \frac{i}{2\pi}\left\{\frac{\sigma_j(x)}{\sigma_j^*(x)} - 1\right\}\int_L q_j(\xi) \\ \times\frac{d}{d\xi}\Big[F_O\big\{K(x-\xi)\big\} + F_T\big\{K(x-\xi)\big\}\Big]\,d\xi = \sigma_j(x) + \frac{U}{i\omega}\widehat{\sigma}_j(x) \tag{34}$$

$$C_j(x) = \left[q_j(x) - \left\{ \sigma_j(x) + \frac{U}{i\omega} \widehat{\sigma}_j(x) \right\} \right] \Big/ \left\{ \sigma_j(x) - \sigma_j^*(x) \right\} \tag{35}$$

Eq. (34) is an integral equation for the outer source strength $q_j(x)$, and with a solution of this equation, the interaction coefficient $C_j(x)$ can be readily determined from (35). As mentioned earlier, the particular solution in the inner problem is not affected by the presence of side walls, and thus $\sigma_j(x)$ and $\widehat{\sigma}_j(x)$ on the right-hand side of (34) are the same as those in the open-sea case. Nevertheless, a numerical solution of (34) includes the effects of side-wall interference, because the kernel function $F_T\{K(x-\xi)\}$ contains the side-wall effects appropriately within the framework of the slender-ship theory. Therefore, from (35), the side-wall effects will be taken into account in the inner solution through the coefficient of a homogeneous component $C_j(x)$. In the limit of $B_T \to \infty$, the function $F_T\{K(x-\xi)\}$ becomes zero and the resulting equations reduce to the same ones as in Newman's unified theory for the open-sea problem.

2.4 Added-mass and damping coefficients

Of particular importance in the radiation problem is the prediction of hydrodynamic pressure force and moment acting on an oscillating ship. Substituting the inner velocity potential into Bernoulli's linearized pressure equation and integrating the pressure over the mean wetted surface of the ship, we obtain an expression for the added mass (A_{jk}) and damping (B_{jk}) coefficients in the j-th direction due to the k-th mode of motion:

$$A_{jk} + B_{jk}/i\omega = \int_L \left[a_{jk} + b_{jk}/i\omega \right] dx \tag{36}$$

where

$$\begin{aligned} a_{jk} + b_{jk}/i\omega = & -\rho \int_{C_H} N_j \varphi_k \, d\ell \\ & + i\rho \frac{U}{\omega} \int_{C_H} \left(N_j \widehat{\varphi}_k - M_j \varphi_k \right) d\ell - \rho \left(\frac{U}{\omega} \right)^2 \int_{C_H} M_j \widehat{\varphi}_k \, d\ell \\ & - \rho C_k(x) \int_{C_H} \left(N_j - \frac{U}{i\omega} M_j \right) \left(\varphi_k - \varphi_k^* \right) d\ell \end{aligned} \tag{37}$$

In (37), ρ is the fluid density and C_H denotes the sectional contour at station x.

The expression without the last term of (37), which has been used in conventional strip theories, includes no 3-D effects. Therefore, the last term in (37) plays an important role in accounting for the 3-D flow interactions among transverse sections and the effects of side-wall interference.

3. Energy Relation in the Radiation Problem

The work done to oscillate the ship is associated with the energy of far-field radiated waves. With this energy-conservation principle, Kashiwagi (1990) derived a formula giving the damping coefficient.

Following the usual procedure, we neglect the terms higher than $O(\phi_j^3)$ and take the time average of the work over one period. Then we have a calculation formula for the damping coefficient, in the form

$$
\begin{aligned}
B_{jj} = & -\rho\omega \, \Im \int_0^\infty dz \int_{-KB_T/2}^{KB_T/2} \left[\phi_j^* \frac{\partial \phi_j}{\partial x} \right]_{-\infty}^{\infty} dy \\
& -\rho\omega \, \Im \int_{-KB_T/2}^{KB_T/2} \left[\left\{ \phi_j^* \Big(i\tau\phi_j - \frac{1}{K_0} \frac{\partial \phi_j}{\partial x} \Big) \right\}_{z=0} \right]_{-\infty}^{\infty} dy
\end{aligned}
\tag{38}
$$

where ϕ_j^* denotes the complex conjugate of ϕ_j, $\Im$ the imaginary part, and $[\quad]_{-\infty}^{\infty}$ the difference between the values at $x = +\infty$ and $x = -\infty$.

Further transformation of (39) requires an asymptotic expression of the velocity potential at $x = \pm\infty$, which is derived in the Appendix. Substituting (58) and (59) shown in the Appendix into (38) and performing some lengthy reduction for the integrals with respect to y and z, we get:

$$
B_{jj} = \rho\omega \frac{K}{2\pi} \Big(\frac{2\pi}{KB_T} \Big) \sum_{p=1}^{4} \sum_{m=0}^{\infty} \epsilon_m \left[\big| H_j(k) \big|^2 \frac{\operatorname{sgn}(1+k\tau)}{|d\nu/dk - k/\nu|} \right]_{k=k_{pm}}
\tag{39}
$$

Here $H_j(k)$ is the Kochin function defined as

$$
H_j(k) = \iint_{S_H} \left(\frac{\partial \phi_j}{\partial n} - \phi_j \frac{\partial}{\partial n} \right) e^{-\nu Kz + ikKx} \cos\!\big(Ky\sqrt{\nu^2 - k^2} \big) \, dS
\tag{40}
$$

It should be noted that no slender-body approximations are involved in (39) and (40) and thus the velocity potential appearing in (40) must be uniformly valid throughout the fluid domain.

Since the Kochin function is related to the complex amplitude of the far-field radiating wave, it can be evaluated from the outer solution, with the result

$$
H_j(k) = \int_L q_j(x) \, e^{ikKx} \, dx
\tag{41}
$$

Although the inner solution is not valid in the field, substituting the inner velocity potential into (40) gives another representation for the Kochin function:

$$
\begin{aligned}
H_j(k) &= \int_L \alpha_j(x) \, e^{ikKx} \, dx \\
\alpha_j(x) &= \int_{C_H} \left(\frac{\partial \phi_j^{(i)}}{\partial N} - \phi_j^{(i)} \frac{\partial}{\partial N} \right) e^{-\nu Kz} \cos\!\big(Ky\sqrt{\nu^2 - k^2} \big) \, d\ell
\end{aligned}
\tag{42}
$$

Both (41) and (42) have been tested, and we refer to the former method as the outer-solution method and the latter as the inner-solution method.

4. Wave-Exciting Force and Moment

With the scattered velocity potential $\phi_7(x, y, z)$ assumed to be obtained, the wave-exciting force in the j-th direction can be calculated by integrating the linearized pressure over the ship hull S_H, with the result

$$
E_j = \rho g a \frac{\omega}{\omega_0} \iint_{S_H} n_j \left(1 + \frac{U}{i\omega} \boldsymbol{W} \cdot \nabla \right) (\phi_0 + \phi_7) \, dS
\tag{43}
$$

$$
= \rho g a \frac{\omega}{\omega_0} \iint_{S_H} \left(n_j - \frac{U}{i\omega} m_j \right) (\phi_0 + \phi_7) \, dS
\tag{44}
$$

where $\boldsymbol{W}$ is previously defined in (11), and in deriving (44), Tuck's theorem, Ogilvie and Tuck (1969), has been used.

If we apply further the Haskind-Newman reciprocity relation, Newman (1965), (44) can be reduced to a form in which there is no need to obtain the scattered velocity potential ϕ_7; this can be expressed as

$$E_j = \rho g a \frac{\omega}{\omega_0} \iint_{S_H} \left(\frac{\partial \phi_j^-}{\partial n} - \phi_j^- \frac{\partial}{\partial n} \right) e^{-k_0 K z + i k_0 K x} \, dS \tag{45}$$

Here ϕ_j^- denotes the reverse-flow radiation velocity potential, which describes the flow around the ship moving in the negative x-axis with the same velocity U as in the real-flow problem while oscillating in the j-th mode.

When deriving (45), two things should be noted: The first is that the so-called line-integral term arising from the intersection of the ship hull with the free surface has been neglected; which is of higher order in the context of slender-ship theory. The second is that the reverse-flow velocity potential ϕ_j^- must be found such that it satisfies the boundary condition

$$\frac{\partial \phi_j^-}{\partial n} = n_j - \frac{U}{i\omega} m_j \tag{46}$$

on the ship hull. Strictly speaking, unless the ship has fore-and-aft symmetry, the m_j-term in the reverse flow is different from that in the real flow, because the m-term will be calculated from the steady-disturbance velocity potential. The error due to this difference is, however, also considered small in the context of slender-ship theory.

When the body has indeed fore-and-aft symmetry like a prolate spheroid, the reverse-flow radiation problem need not be obtained and the evaluation of (45) can be accomplished with the real-flow velocity potential ϕ_j. More specifically, we can use in this case the following relations:

$$\begin{aligned} \phi_3^-(-x, y, z) &= \phi_3(x, y, z) \\ \phi_5^-(-x, y, z) &= -\phi_5(x, y, z) \end{aligned} \tag{47}$$

Substituting these relations into (45) and noting that $k_0 = -k_2 = \nu$, we get

$$E_j = \pm \rho g a \frac{\omega}{\omega_0} H_j(-k_0) \tag{48}$$

where $H_j(-k_0)$ is the Kochin function defined by (40) with the nondimensional wave number k replaced by $-k_0$, and the complex sign ($+$ or $-$) corresponds to heave ($j = 3$) or pitch ($j = 5$) respectively.

Sclavounos (1985) applied the forward-speed version of Haskind-Newman's reciprocity relation to the unified slender-ship theory for the open-sea problem and verified its good performance.

5. Numerical Solution Method

An important task in the numerical implementation is to solve the integral equation (34) for the outer source strength $q_j(x)$. After dividing ship's longitudinal axis equidistantly into N segments, the 2-D boundary-value problem for the inner solution must be solved at each transverse section; which gives the 2-D effective source strengths $\sigma_j(x)$ and $\widehat{\sigma}_j(x)$ appearing on the right-hand side of the integral equation. Haraguchi and Ohmatsu's (1983) method has been used for this purpose, which can easily get rid of irregular frequencies and gives an accurate solution.

With the assumption that the outer source strength $q_j(x)$ varies linearly within each segment, the integral equation (34) was transformed into a linear system of simultaneous equations for the discretized values of $q_j(x)$ at $N-1$ nodal points and solved numerically. (The source strengths at the ship ends have been postulated to vanish and thus treated as known.)

The Clenshaw-Curtis quadrature has been utilized for the numerical integration of the kernel function $F_O\{K(x-\xi)\}$ and $F_T\{K(x-\xi)\}$, with an absolute error less than 10^{-5} required. As shown in (26), the treatment with Cauchy's principal-value integral is needed in the side-wall-effect part $F_T\{K(x-\xi)\}$. The numerical implementation of this integral has been done by subtracting singular contributions from the integrand, integrating numerically the resultant non-singular part, and integrating analytically the subtracted part; for this analytical integration, the following formula has been effectively used:

$$\int \frac{d\nu/dk - k/\nu}{\sin\left(\frac{KB_T}{2}\sqrt{\nu^2-k^2}\right)} \frac{\nu}{\sqrt{\nu^2-k^2}}\, dk = \frac{2}{KB_T} \ln\left|\tan\left(\frac{KB_T}{4}\sqrt{\nu^2-k^2}\right)\right| \tag{49}$$

Once the solution of the outer source strength $q_j(x)$ is obtained, calculating the interference coefficient $C_j(x)$ in the inner solution is straightforward. Added-mass and damping coefficients and wave-exciting force and moment have been obtained by integrating their distribution along the x-axis with Simpson's rule. Numerical results presented in this paper were obtained by setting the number of division to $N = 40$; this number was based on the validation study in Kashiwagi and Ohkusu (1989).

6. Experiments

In the case of zero forward speed, the experiments using a ship model with fore-and-aft symmetry had been carried out in the narrow wave tank (60 m in length, 1.495 m in breadth, 1.5 m in depth) of the Research Institute for Applied Mechanics, Kyushu University. Transverse sections of the ship model used in that experiment can be represented as so-called Lewis forms. Therefore this model is referred to as the Lewis-form ship; its principal dimensions and body plan are shown in Table 1 and Fig. 3, respectively.

Experiments in the forward-speed case have been conducted in the towing tank (60 m in length, 4 m in breadth, 2.3 m in depth) of the Nagasaki Institute of Applied Science.

Tested models are

1. Half-immersed prolate spheroid ($L = 2.0$ m, $B/L = 1/5$)
2. Lewis-form ship, Fig. 3 ($L = 1.5$ m, $B/L = 1/6$)

Table 1 Principal particulars of Lewis-form ship

Length	L (m)	1.500
Breadth	B (m)	0.250
Draft	d (m)	0.125
Block coefficient	C_B	0.659
Midship section coefficient	C_M	0.942
Waterplane area coefficient	C_W	0.732

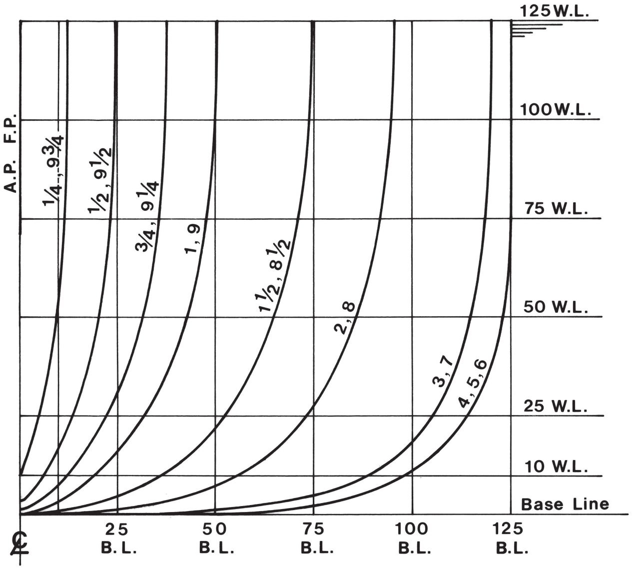

Fig. 3 Body plan of Lewis-form ship

Items and conditions of the experiment are

1. Forced heave oscillation test (amplitude 1.5 cm, Froude number 0.1)
2. Forced pitch oscillation test (amplitude 2.0 deg., Froude number 0.1)
3. Wave-exciting force measurement test (wave amplitude about 2.0 cm, Froude number 0.1)

7. Numerical Results and Comparison with Experiments

7.1 Radiation forces on prolate spheroid

A few numerical examples were already reported in Kashiwagi and Ohkusu (1989) for beam-length ratio 1/8 with zero and nonzero forward velocities. The results for zero forward velocity are in virtually perfect agreement with "exact" numerical solutions of a 3-D panel method.

Numerical computation at forward velocity requires the evaluation of the M_j-term appearing in (31) and (37), particularly of M_3 by (32); for which we have used an analytical expression

$$\begin{aligned}
&M_3 = \frac{1-\varepsilon^2}{D(\varepsilon)} \frac{\cos\theta\sin\theta}{\varDelta^3}\left(1+\frac{2\varepsilon^2}{\varDelta^2}\right)\cos\beta \\
&D(\varepsilon) = 1 - \frac{1-e^2}{2e}\ln\frac{1+e}{1-e}\,, \quad e = \sqrt{1-\varepsilon^2} \\
&\varDelta = \sqrt{\sin^2\theta + \varepsilon^2\cos^2\theta}\,, \quad \varepsilon = B/L \\
&x = \frac{L}{2}\cos\theta\,,\ z = \frac{B}{2}\sin\theta\cos\beta
\end{aligned} \tag{50}$$

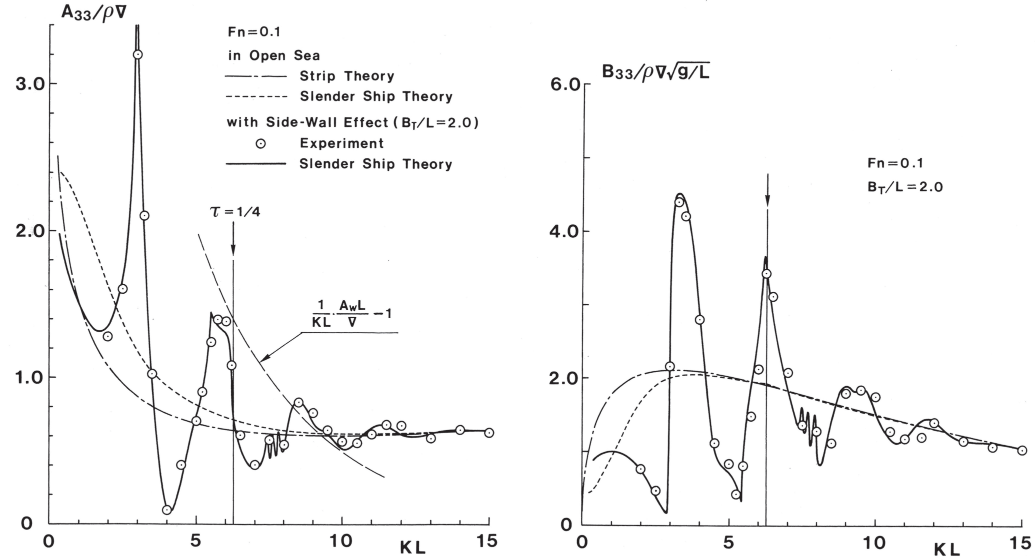

Fig. 4 Heave added-mass and damping coefficients of a floating spheroid of $B/L = 1/5$ in waterway of $B_T/L = 2$ ($F_n = 0.1$)

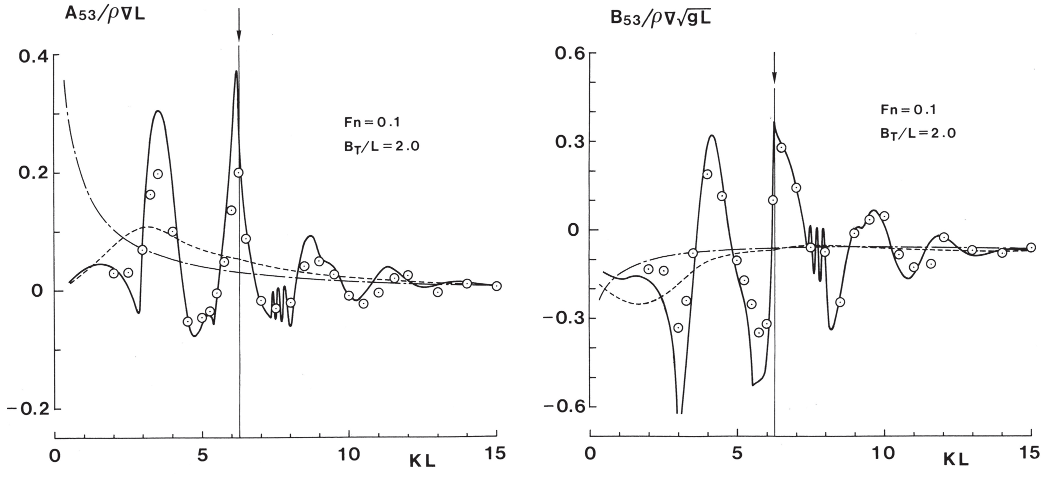

Fig. 5 Coupling added-mass and damping coefficients of heave into pitch of a floating spheroid of $B/L = 1/5$ in waterway of $B_T/L = 2$ ($F_n = 0.1$)

Results are shown in Figs. 4 to 7, for a floating spheroid of $B/L = 1/5$ advancing at a Froude number 0.1 in the waterway of $B_T/L = 2.0$; these rations are identical to the experiment conditions described earlier. For reference, the results in open sea, equal to Newman's unified-theory predictions, are demonstrated by the short-dashed line and the strip-theory results are by the dashed-dotted line. The experimental data shown in Figs. 4 and 5 were obtained from the forced heaving test, and the data in Figs. 6 and 7 were from the forced pitching test. The agreement between the experimental data and our results is

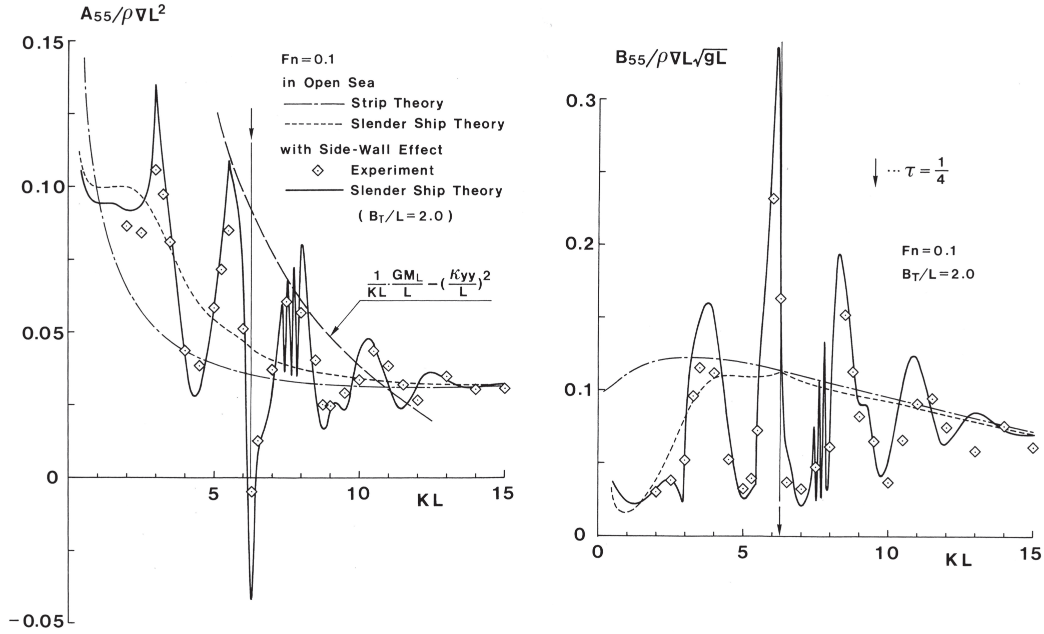

Fig. 6 Pitch added-mass and damping coefficients of a floating spheroid of $B/L = 1/5$ in waterway of $B_T/L = 2$ ($F_n = 0.1$)

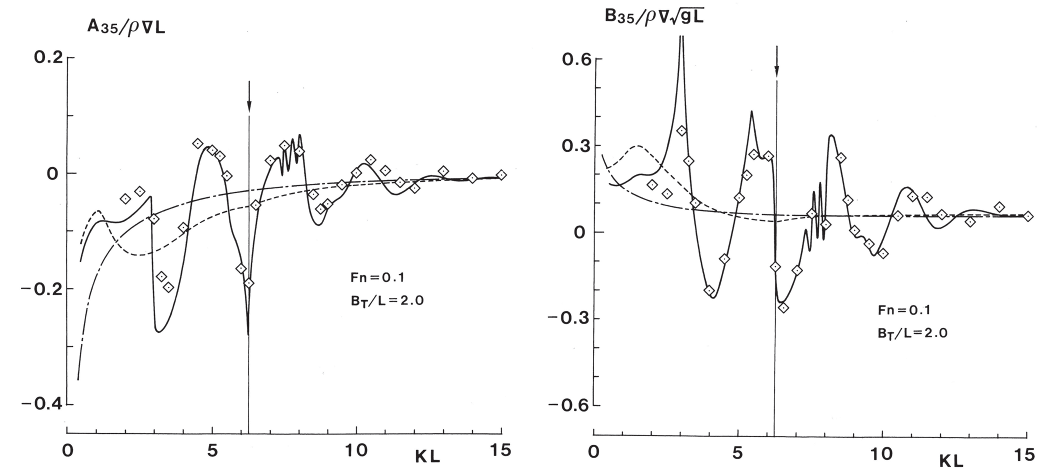

Fig. 7 Coupling added-mass and damping coefficients of pitch into heave of a floating spheroid of $B/L = 1/5$ in waterway of $B_T/L = 2$ ($F_n = 0.1$)

generally very good. The experiments show the tendency that as the wavenumber increases, the side-wall effects gradually diminish and the hydrodynamic coefficients approach the corresponding values in open sea. The theory accounts well for this tendency, though there are slight discrepancies around the wavenumber $KL = 11$.

Since the spheroid concerned is longitudinally symmetric, the cross-coupling coefficients

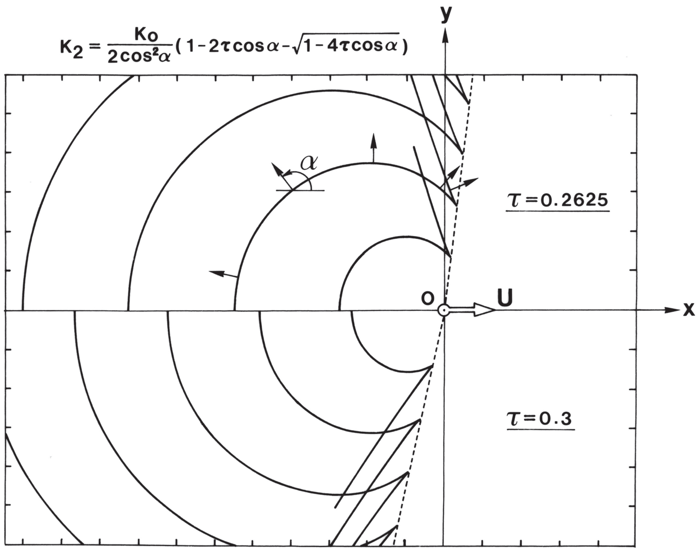

Fig. 8 Asymptotic wave contour calculated by stationary phase method ($\tau = 0.2625$ & 0.3)

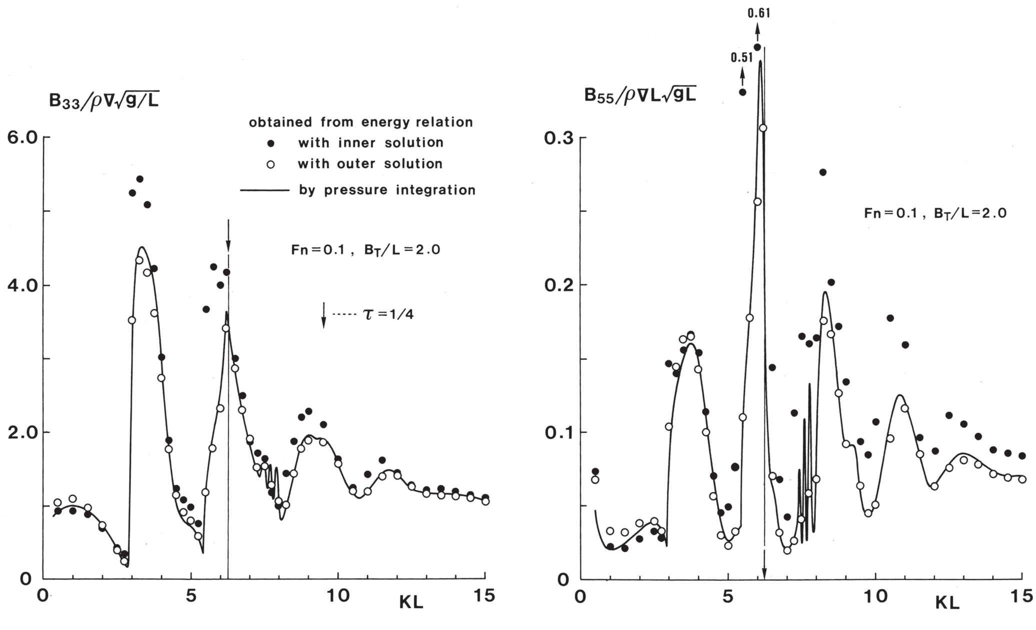

Fig. 9 Heave and pitch damping coefficients calculated from the principle of energy conservation for a floating spheroid of $B/L = 1/5$ in waterway of $B_T/L = 2$ ($F_n = 0.1$) Comparison with the results by pressure integration

shown in Figs. 5 and 7 exist only when the forward velocity is not zero. The experimental data for these cross-coupling coefficients agree well with computed results, and satisfy with good accuracy the Timman and Newman (1962) relation $A_{35} = -A_{53}$, $B_{35} = -B_{53}$.

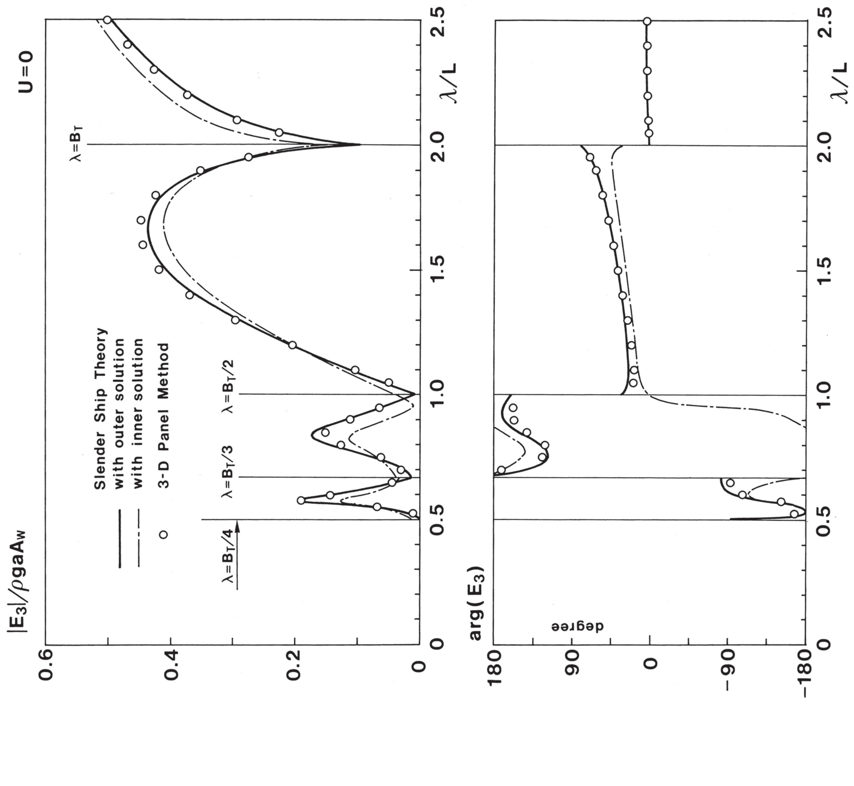

Fig. 10 Heave wave-exciting force of a floating spheroid of $B/L = 1/5$ in waterway of $B_T/L = 2$ $(U = 0)$

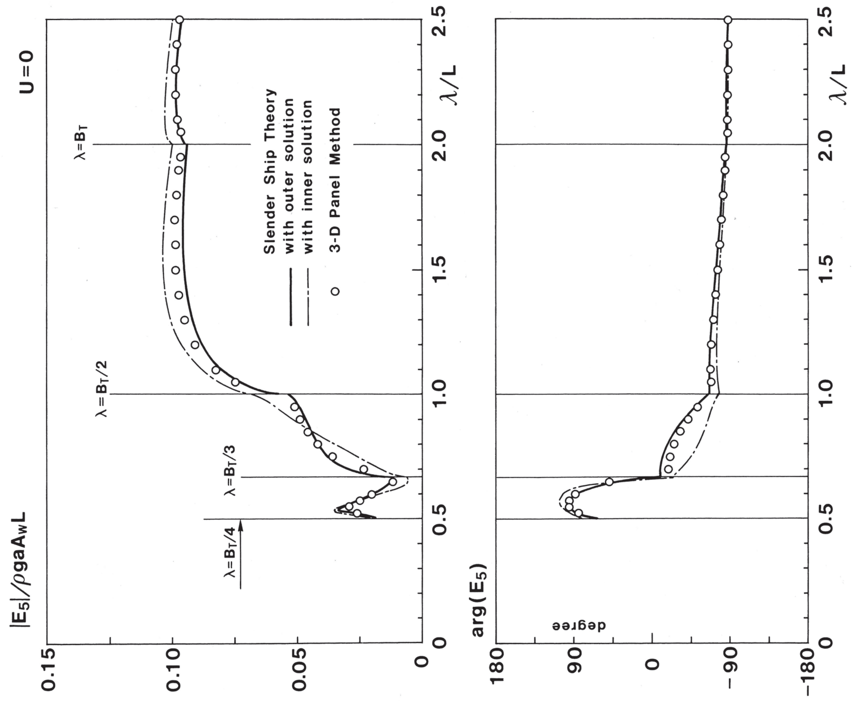

Fig. 11 Pitch wave-exciting moment of a floating spheroid of $B/L = 1/5$ in waterway of $B_T/L = 2$ $(U = 0)$

Incidentally, the computed results show a rapid variation at $KL = 7.5 \sim 8.0$, where the parameter τ takes the value ranging from 0.27 to 0.28 for the Froude number 0.1. To examine a physical reason for this, we calculated an asymptotic form of the open-sea wave contour for two values of τ, 0.2625 and 0.3, using the stationary phase method. The results are shown in Fig. 8, where only the component with longer wavelength, the so-called K_2-wave, is depicted. This wave component may propagate ahead of the ship and thus have close relations to the side-wall interference. (The definition of the wavenumber K_2 is also included in Fig. 8, and α denotes the propagation direction of an elementary wave, measured from the positive x-axis, as demonstrated on one of the contours.)

It can be expected from Fig. 8 that in the range between $\tau = 0.27$ and 0.28 the waves originating from the cusp part of the contour strike the ship model after being reflected by side walls of the waterway. Furthermore, elementary waves near the cusp are slightly different in value of α and consequently different in wavenumber. These lead to a conjecture that the rapid variation in the numerical results shown in Figs. 4 to 7 is due to the reflection waves emitted from the cusp part of the K_2-wave.

The damping coefficient can be also computed from the energy-conservation principle. Evaluating the Kochin function, which is necessary in the calculation formula (39), can be done with two different methods: the inner-solution method and the outer-solution method. The computed results by these two methods are shown for B_{33} and B_{55} in Fig. 9, together with the results by the pressure integration over the body surface. The outer-solution method (indicated by open circles) provides almost the same predictions as the pressure integration (solid line), whereas the inner-solution method (closed circles) does not, particularly for B_{55}, implying that the Kochin function in the slender-ship theory must be evaluated by the outer solution. This conclusion seems reasonable because the analysis of energy flux has been performed in the far field where the outer solution is more valid than the inner solution.

Figures 10 and 11 show heave and pitch exciting forces for a floating spheroid of $B/L = 1/5$ in a waterway of $B_T/L = 2$, computed by the inner- and outer-solution methods. Forces are nondimensionalized in terms of the waterplane area A_w, and λ denotes the wavelength of the incident wave. The outer-solution method provides closer results to the 3-D numerical solutions (indicated by open circles) than the inner-solution method. This result coincides with a conclusion derived earlier in relation to the energy-conservation principle. With these findings, only the results based on the outer-solution method will be presented hereafter.

For the case of $F_n = 0.1$, computed results are compared in Fig. 12 for the heave exciting force and in Fig. 13 for the pitch exciting moment to experimental values. The theory tends to underpredict the pitch exciting moment, but overall agreement is very good.

7.2 Wave-exciting forces on prolate spheroid

To confirm the utility of using Haskind-Newman's reciprocity relation, computations have been performed firstly for zero forward velocity and compared with "exact" numerical solutions by a 3-D panel method, Kashiwagi (1989).

The results are shown in Figs. 14 and 15 for zero forward speed, and in Figs. 16 and 17 for the Froude number 0.1. These are for a prolate spheroid of beam-length ratio 1/5. At zero speed, "exact" numerical solutions based on the 3-D panel method (in which the surge effect is correctly taken into consideration) are also shown for comparison. We can see that the present-theory calculations for zero forward speed are in good agreement with 3-D numerical solutions and that the effects of side-wall interference on motion amplitudes are very small, except for heave in the small wavelength region. The radiation and diffraction show quite

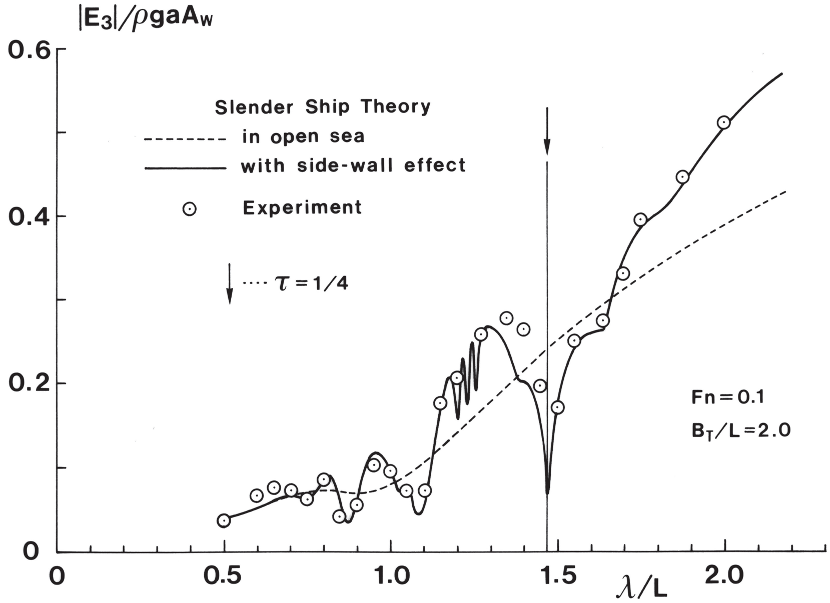

Fig. 12 Same as Fig. 10 with $F_n = 0.1$

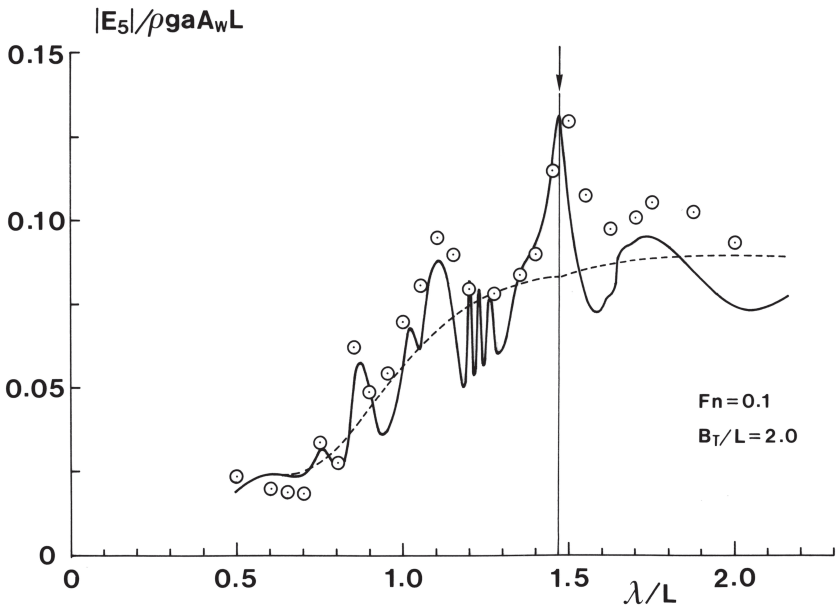

Fig. 13 Same as Fig. 11 with $F_n = 0.1$

large variation owing to the side-wall effects. So there must be precise cancellations between the right- and left-hand sides of the ship-motion equation.

At forward speed, on the other hand, the heave and pitch motions are greatly affected

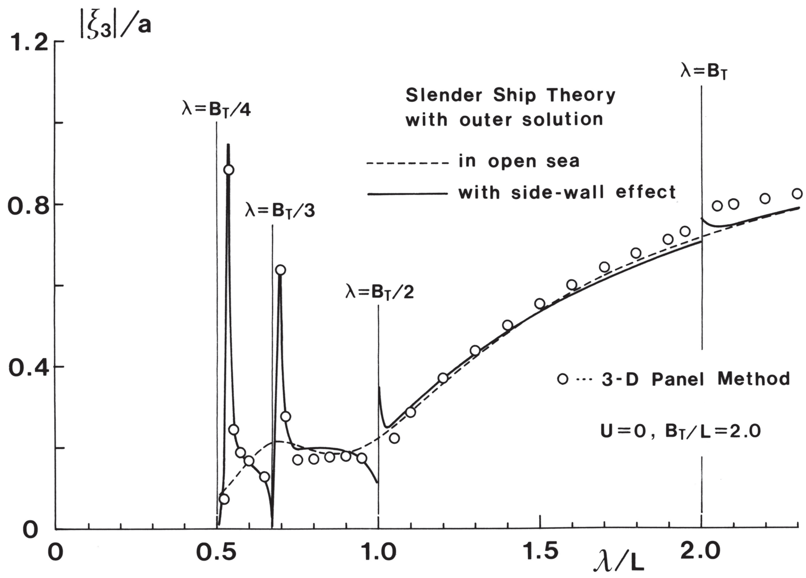

Fig. 14 Computed heave amplitude of a floating spheroid of $B/L = 1/5$ in waterway of $B_T/L = 2.0$ ($U = 0$)

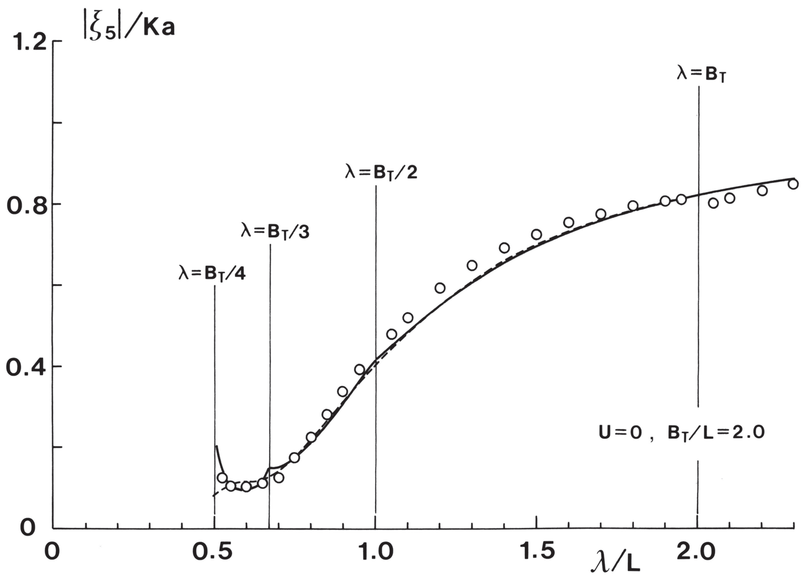

Fig. 15 Computed pitch amplitude of a floating spheroid of $B/L = 1/5$ in waterway of $B_T/L = 2.0$ ($U = 0$)

by the side-wall interference and thus different from corresponding results at zero speed. It should be emphasized that the presence of forward speed is the only difference in the calcula-

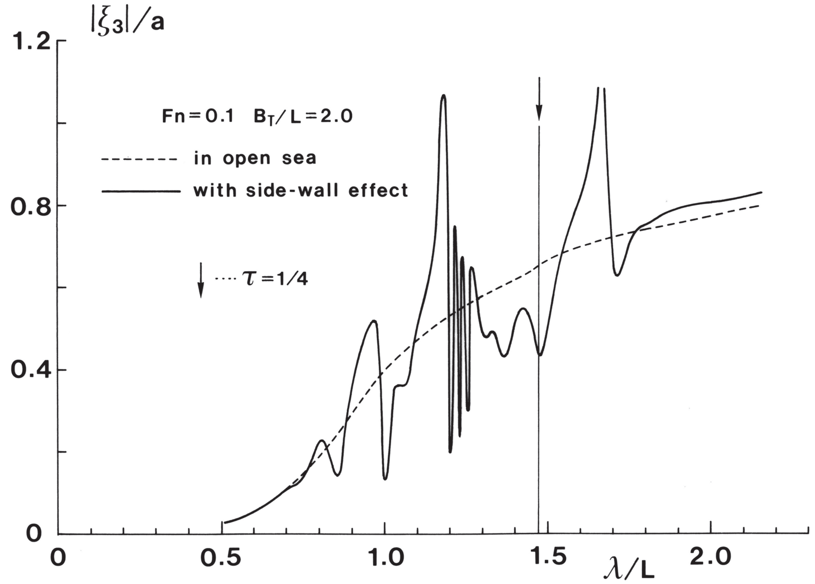

Fig. 16 Same as Fig. 14 with $F_n = 0.1$

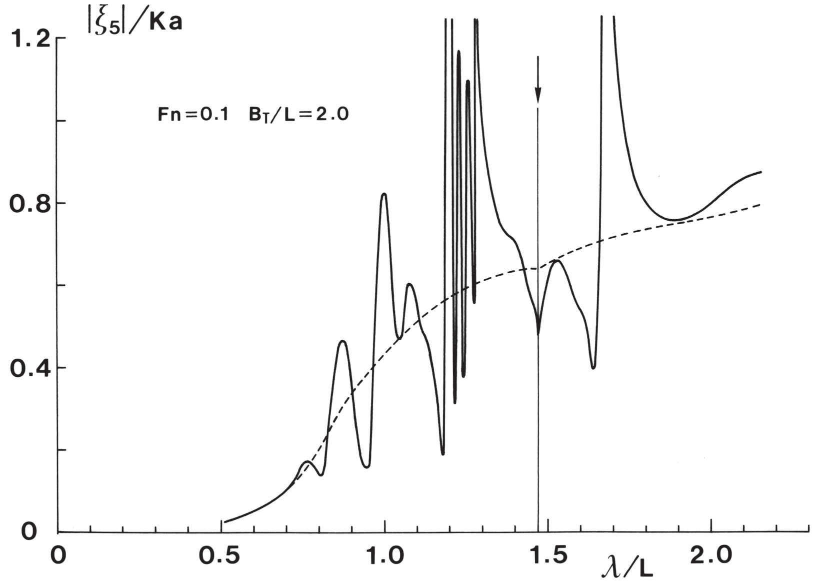

Fig. 17 Same as Fig. 15 with $F_n = 0.1$

tion conditions between Fig. 14 and Fig. 16, or Fig. 15 and Fig. 17. When the forward speed exists, there are no 3-D numerical solutions or experimental data with which to compare, and thus it is impossible to make a conclusive judgement on the validity of the computed results shown here. However the "beating" phenomena observed by Hosoda (1978) in the records of experiments seem to correspond to the rapid variation at $\lambda/L = 1.2 \sim 1.3$ in the numerical results. The magnitude of this variation is larger in pitch than in heave; this can be attributed to the plural number of pitch resonances in this frequency range, which is shown in the graph of A_{55} in Fig. 6, where the intersections between broken line and added-mass curve give the resonant frequencies.

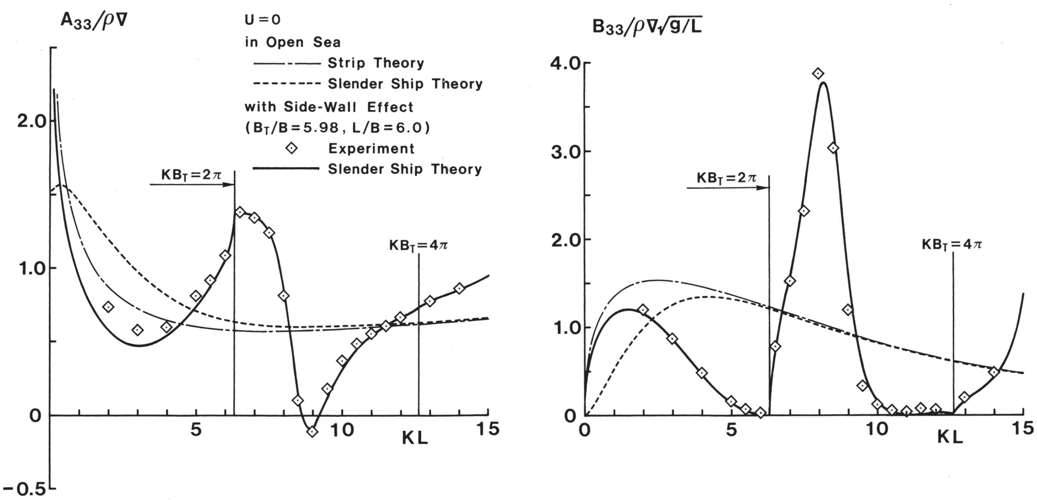

Fig. 18 Heave added-mass and damping coefficients of Lewis-form ship in waterway of $B_T/L = 0.997$ ($U = 0$)

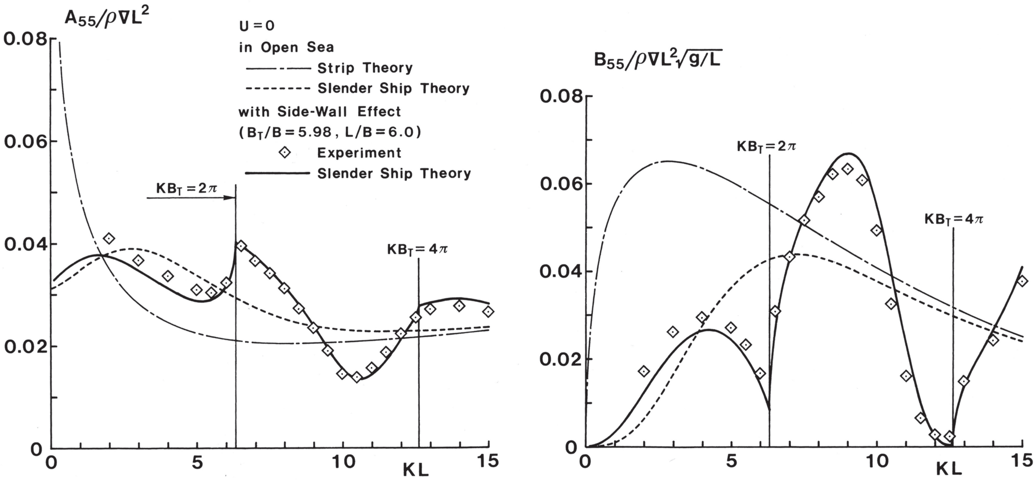

Fig. 19 Pitch added-mass and damping coefficients of Lewis-form ship in waterway of $B_T/L = 0.997$ ($U = 0$)

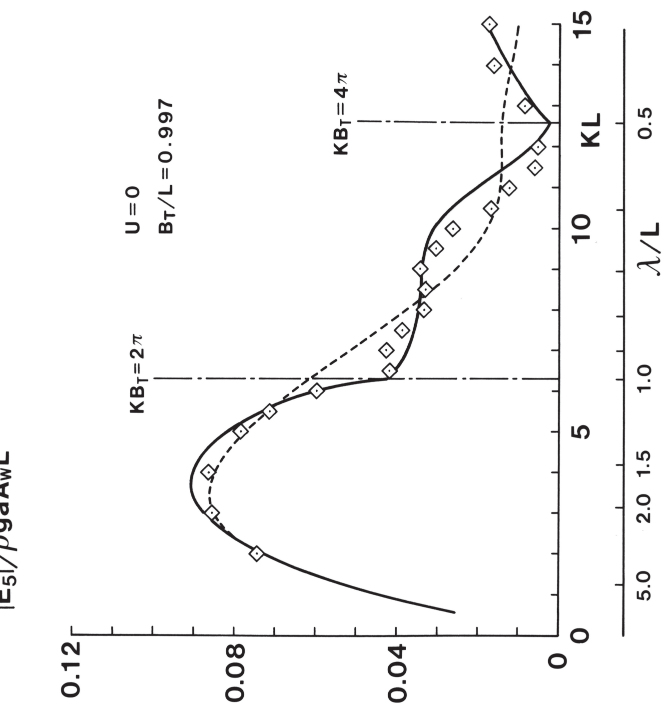

Fig. 21 Pitch wave-exciting moment of Lewis-form ship in waterway of $B_T/L = 0.997$ ($U = 0$)

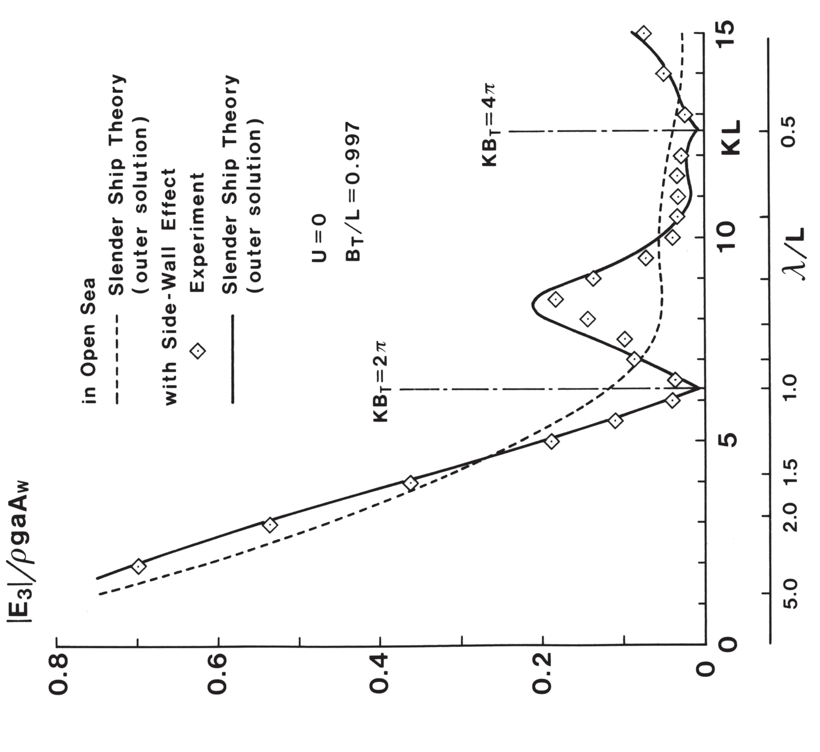

Fig. 20 Heave wave-exciting force of Lewis-form ship in waterway of $B_T/L = 0.997$ ($U = 0$)

7.3 Hydrodynamic forces at U=0 on Lewis-form ship

Usefulness of the present theory seems well demonstrated through the comparisons above for a floating spheroid. In those comparisons, however, only one ratio of tank width to ship length ($B_T/L = 2.0$) has been tested, and further the difference in shape of a ship model may cause new difficulties. To check these, we compare in this section numerical results with the zero-speed experiments for the Lewis-form ship shown in Kashiwagi (1989).

Figure 18 compares heave added-mass and damping coefficients with experiments, in which the ratio of tank width to model length is $B_T/L = 0.997$. Despite such a narrow tank-width case, the agreement is very good. This is because the present theory takes into account in a consistent manner the contributions of nonradiating local waves near the ship. Comparison of the added-moment of inertia and damping coefficients in pitch is demonstrated in Fig. 19. The degree of coincidence is slightly inferior to that in the heave mode, but it can be seen that the overall agreement is fairly good.

The computed results of heave exciting force and pitch exciting moment are compared with experiments in Fig. 20 and Fig. 21, respectively. Despite some discrepancies around $KL = 10$, it can be concluded that the calculation method accounts well for the effects of side-wall interference on the wave-exciting forces.

7.4 Hydrodynamic forces at U=0.1 on Lewis-form ship

For non-zero forward speed, the term M_3 must be evaluated. We have used an approximate representation for this term, derived by the following procedures: 1) neglect the contribution of steady-disturbance potential ϕ_S in the steady velocity vector $\boldsymbol{W}$; 2) perform the partial integration for (43) with respect to x; 3) compare the resulting equation with (44). The final result of this procedure is the expression

$$m_j = -\frac{\partial}{\partial x} n_j \tag{51}$$

As mentioned earlier, the model length used in experiments is 1.5 m and the towing tank is 4 m in width. Thus the ratio of these is $B_T/L = 2.667$, which is larger than that for a prolate spheroid.

The experimental values obtained from the forced heaving test are shown in Figs. 22 and 23 by the circle with dot. Computed results, shown by the solid line, agree very well.

Figures 24 and 25 compare experimental values obtained from the forced pitching test with our numerical results. Slight discrepancies can be seen in B_{55} and A_{35}, but the remaining coefficients show excellent agreement. The effects of side-wall interference on experimental results decrease with increasing wavenumber and vanish at the wavenumbers higher than approximately $KL = 12$. This experimental characteristic is also well accounted for by the theory.

Final comparisons are for the wave-exciting heave force and pitch moment, Fig. 26 and Fig. 27. There is good agreement for the heave exciting force, but the theory tends to underpredict the pitch exciting moment. This tendency is consistent with the spheroid case (Fig. 13). However, another possibility exists that the approximation (51) is not appropriate especially near the ship ends and thus the pitch moment depending on the forward speed is underpredicted.

In summary, our calculation method provides favorable predictions also for a ship-like form and irrespective of the breadth of a waterway.

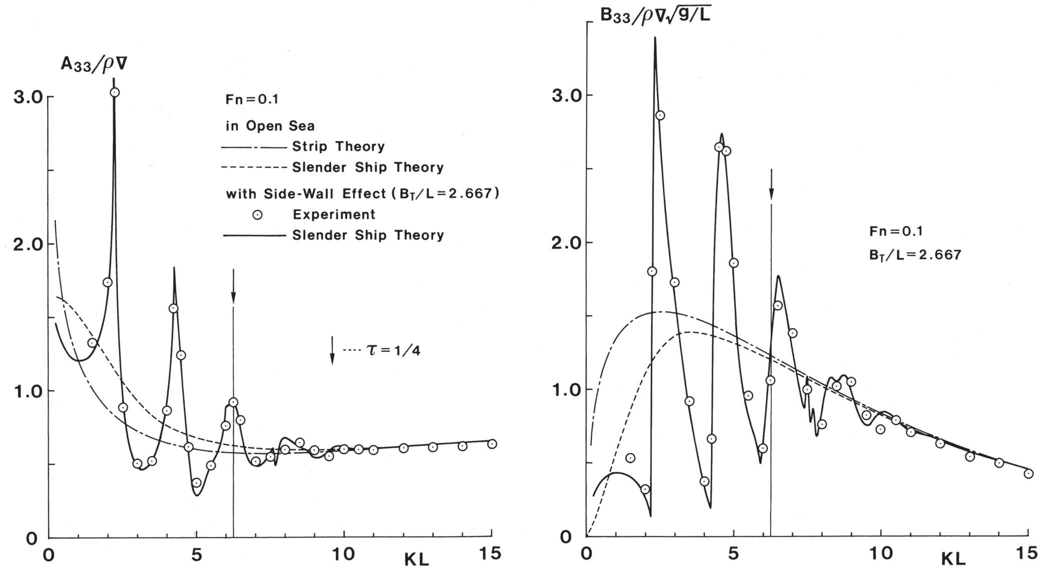

Fig. 22 Heave added-mass and damping coefficients of Lewis-form ship in waterway of $B_T/L = 2.667$ ($F_n = 0.1$)

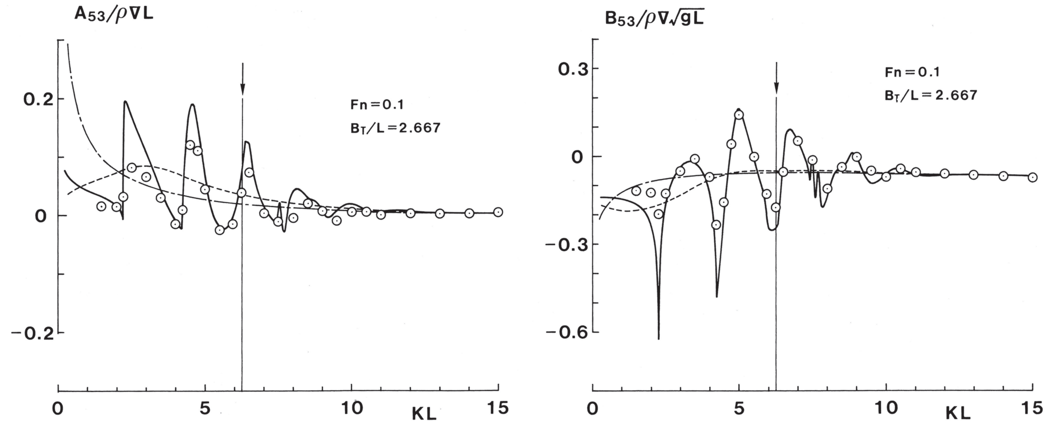

Fig. 23 Coupling added-mass and damping coefficients of heave into pitch of Lewis-form ship in waterway of $B_T/L = 2.667$ ($F_n = 0.1$)

8. Side-Wall Interference Diagram

Since the calculation method is based on slender-ship theory, the computation is not so time-consuming. This may be not true, however, when a minicomputer is used for the forward-speed case. Therefore it is desirable to prepare a diagram incorporating appropriately the information given by the theory. There exists already a diagram having been in conventional use, Vossers and Swaan (1960) and modified by Goodrich (1963). However, this diagram is not entirely correct because it was derived geometrically from asymptotic contours of the waves generated by hydrodynamic sink-source singularities, and thus this diagram gives no

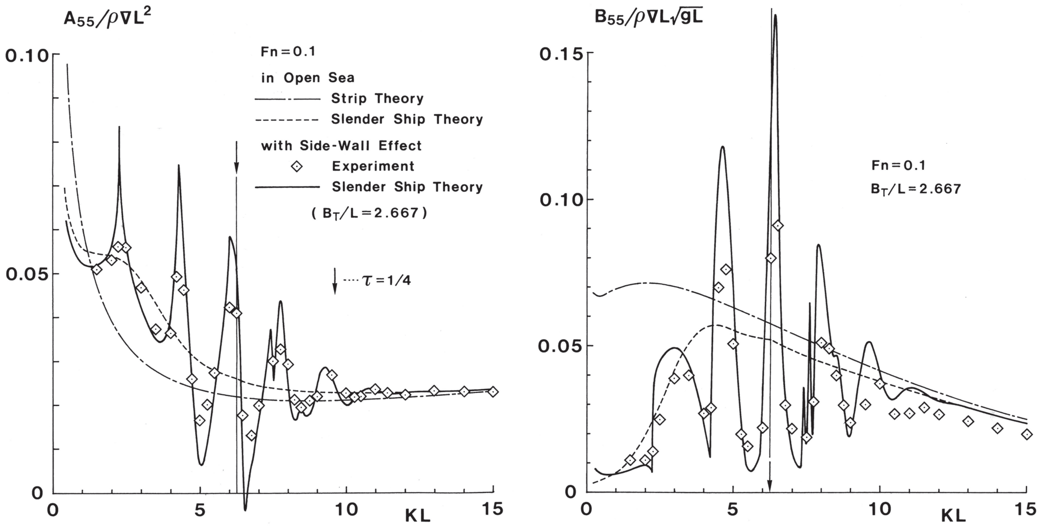

Fig. 24 Pitch added-mass and damping coefficients of Lewis-form ship in waterway of $B_T/L = 2.667$ ($F_n = 0.1$)

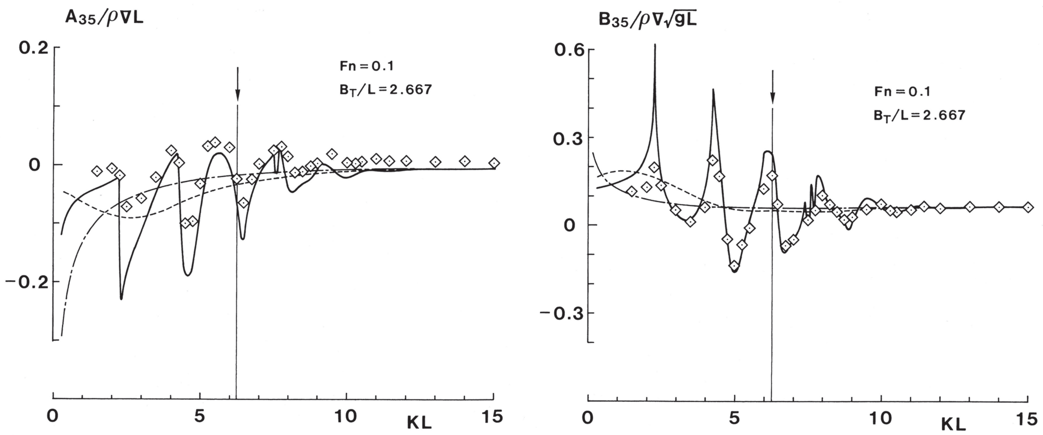

Fig. 25 Coupling added-mass and damping coefficients of pitch into heave of Lewis-form ship in waterway of $B_T/L = 2.667$ ($F_n = 0.1$)

information on the magnitude of side-wall effects.

For a new diagram, we performed a number of computations varying Froude number, frequency, and tank width. A prolate spheroid of beam-length ratio 1/8 was selected for these computations, because the present theory is considered to be accurate for a more slender body. Fig. 28 is an example of these computations. The solid line shows the predicted value with side-wall effects taken into account, and the dashed line the value in open sea. The difference between these two lines indicates the degree of side-wall interference. However, since the solid line fluctuates around the open-sea value, we regard the envelope as indicating

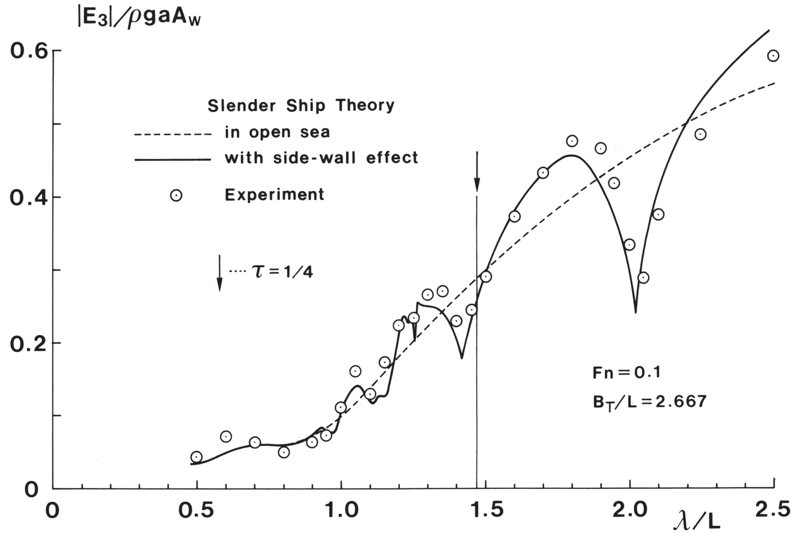

Fig. 26 Heave wave-exciting force of Lewis-form ship of $B/L = 1/6$ at $F_n = 0.1$

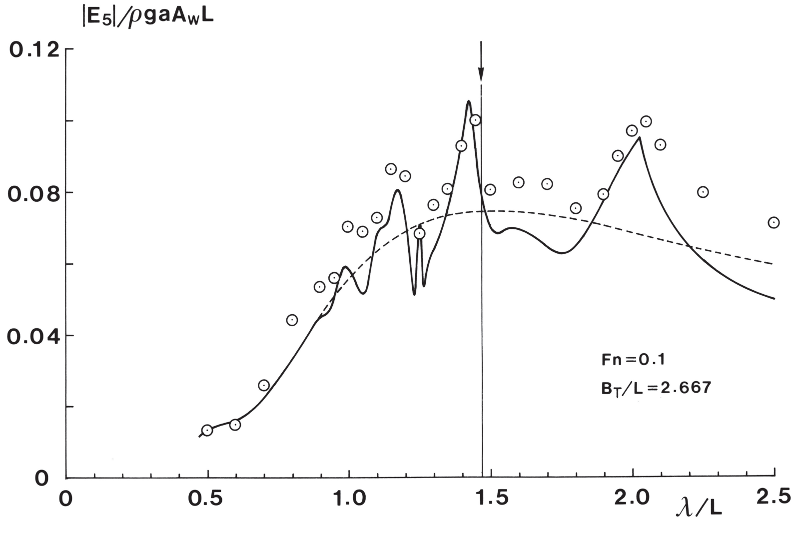

Fig. 27 Pitch wave-exciting moment of Lewis-form ship of $B/L = 1/6$ at $F_n = 0.1$

the actual side-wall interference. The expected envelope lines are shown in Fig. 28 as thin solid lines.

With this figure, one can estimate a critical wavenumber at which the side-wall interference will vanish. For Fig. 28, that wavenumber is $KL \approx 11.5$. On the other hand, as shown by the vertical solid line in Fig. 28, $KL = 6.8$ is the critical value estimated from asymptotic wave contours in open sea. The difference of these two values is due to the effect of nonradiating local waves in the vicinity of the ship; this local-wave effect becomes important when the tank width is narrow relative to the wavelength as for Fig. 28.

We determined critical lines showing the existence of the side-wall interference as a function of Froude number, wavenumber, and tank width. Results are shown by solid lines in Fig. 29. Dotted lines are obtained from asymptotic wave contours; these lines are linear because the characteristics of an asymptotic wave contour can be determined by only the parameter τ $(= F_n\sqrt{KL})$. The newly obtained lines approach the dotted lines at high frequencies, where the wavelength may be small relative to the tank width and an asymptotic approximation of the waves is valid.

From Fig. 28, we can also determine the frequency at which the side-wall effect is less than the permissible error to be included in the measured values. For instance, let 10% be the permissible error. Then, as shown in Fig. 28, we can draw two dotted lines above and

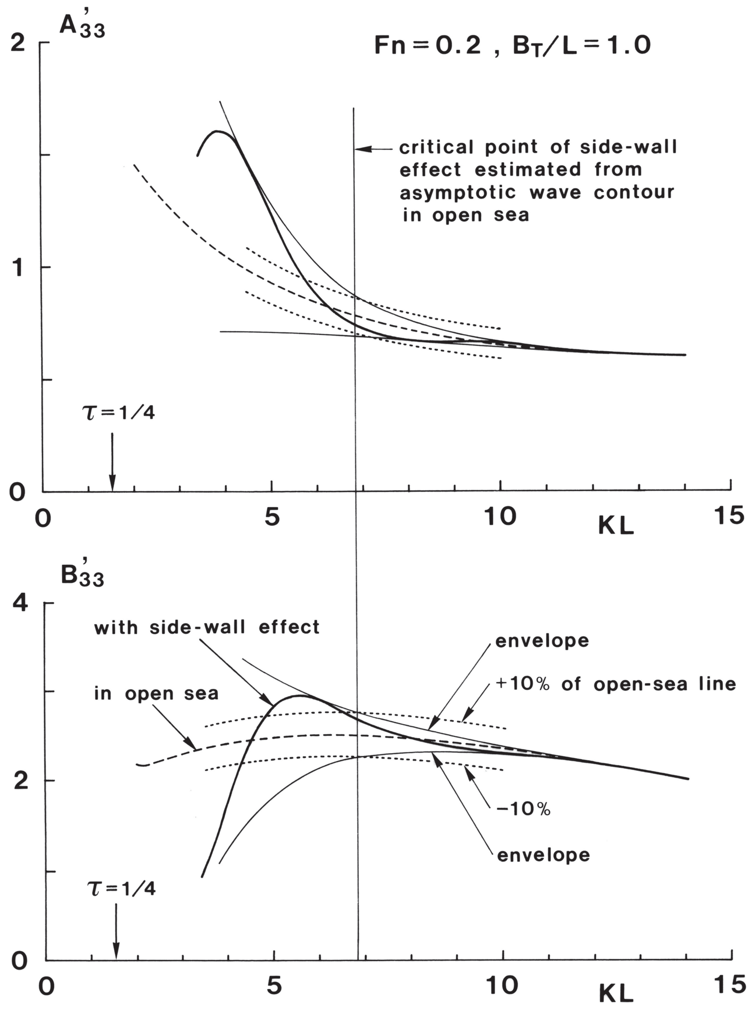

Fig. 28 Heave added-mass and damping coefficients of a floating spheroid of $B/L = 1/8$ $(B_T/L = 1.0,\ F_n = 0.2$

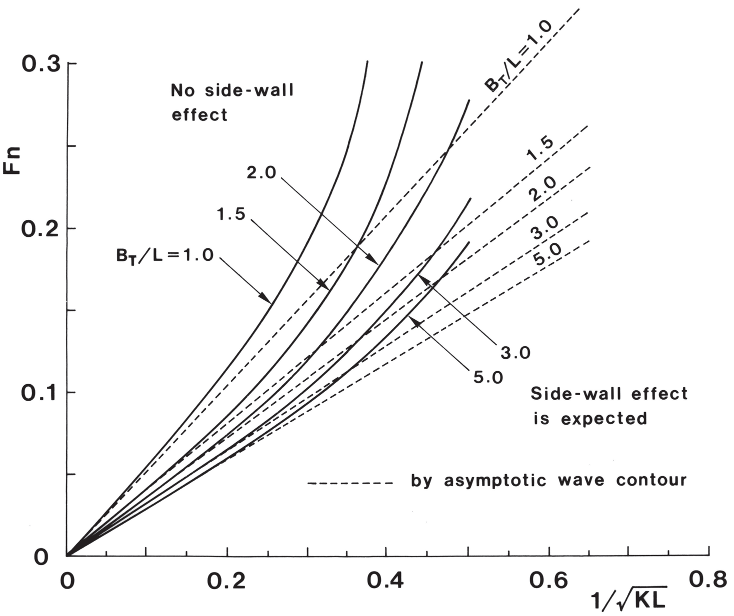

Fig. 29 Diagram showing whether tank-wall effects are expected. Comparison between present result (solid line) and asymptotic theory (dotted line)

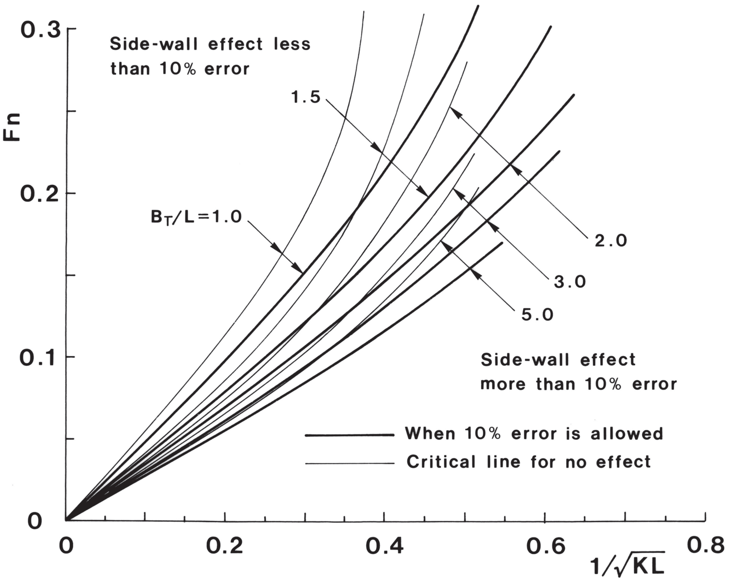

Fig. 30 Region where tank-wall effects are less than 10 %

below the open-sea line, and the critical frequency concerned can be given at intersections of these dotted lines with the envelope shown by thin solid lines. These can be for intersections (two are from A_{33}, other two are from B_{33}), but fortunately these four seem to give almost the same critical frequency; we confirmed this is the case for other computed results.

The results obtained in such a manner are shown by thick solid lines in Fig. 30. Thin solid lines are also included for comparison, which were reproduced from Fig. 29 and thus indicate the boundary of whether the side-wall interference exists or not. Therefore the region between the thick and thin solid lines for each tank width shows the area in which the side-wall interference less than 10% can be expected.

Strictly speaking, the newly obtained diagrams, Fig. 29 and Fig. 30, should be applied only to the radiation forces on a prolate spheroid of beam-length ratio 1/8, because basic computations were performed for that case. However, the critical frequency of vanishing the side-wall interference seems not to be very dependent on the hull form or the measured items (radiation forces, exciting forces, ship motions). Therefore at least Fig. 29 can be regarded as generally applicable. On the other hand, the magnitude of the side-wall interference is sensitive to the measured items and possibly to the hull form. This suggests that Fig. 30 should be used only for the forced heaving test with a slender body.

References

1 COHEN, S.B. and TROESCH, A.W. (1988), The interaction of a floating body with vertical walls, Int. Shipbuild. Progr. 35/401

2 GOODRICH, G.J. (1963), Proposed standards for seakeeping experiments in head and following seas, 10th I.T.T.C., Rep. of the Seakeeping Committee, Appendix I

3 HANAOKA, T. (1958), On the side-wall effects on the ship motions among waves in a canal, J. Soc. Nav. Arch. Japan 102

4 HARAGUCHI, T. and OHMATSU, S. (1983), On an improved solution of the oscillation problem on non-wall-sided floating bodies and a new method for eliminating the irregular frequencies, Trans. West-Japan Soc. Nav. Arch. 66

5 HOSODA, R. (1976), Side wall effects of towing tank on the results of experiments in waves (1), J. Soc. Nav. Arch. Japan 139

6 HOSODA, R. (1978), Effect of side-wall interference of towing tank on the results of experiments in waves (2), J. Soc. Nav. Arch. Japan 143

7 KASHIWAGI, M. (1989), 3-D integral-equation method for calculating the effects of tank-wall interference on hydrodynamic forces acting on a ship, J. Kansai Soc. Nav. Arch. Japan 212

8 KASHIWAGI, M. (1990), Radiation and diffraction forces acting on an offshore-structure model in a towing tank, Proc. 1st Pacific/ Asia Offshore Mech. Symp. Vol. 2

9 KASHIWAGI, M. and OHKUSU, M.(1989), Side-wall effects on hydrodynamic forces acting on a ship with forward and oscillatory motions, 5th Numerical Ship Hydrodyn., Hiroshima

10 NEWMAN, J.N. (1965), The exciting forces on a moving body in waves, J. Ship Res. 9/3

11 NEWMAN, J.N. (1978), The theory of ship motions, Adv. Appl. Mech. 18

12 NEWMAN, J.N. and SCLAVOUNOS, P.D. (1980), The unified theory of ship motions, 13th Symp. on Nav. Hydrodyn., Tokyo

13 OGILVIE T.F. and TUCK, E.O. (1969), A rational strip theory for ship motions, Dep. NAME, Univ. Michigan, Rep. No. 13

14 SCLAVOUNOS, P.D. (1985), Forward-speed vertical wave exciting forces on ships, J. Ship Res. 29/2

15 TAKAKI, M. (1979), Effects of breadth and depth of restricted waves on longitudinal motions in waves, J. Soc. Nav. Arch. Japan 146

16 TIMMAN, R. and NEWMAN, J.N. (1962), The coupled damping coefficients of symmetric ships, J. Ship Res. 5/4

17 VOSSERS, G. and SWAAN, W.A. (1960), Some seakeeping tests with a Victory model, Int. Shipbuild. Progr. 7/69

18 YEUNG, R.W. and SPHAIER, S.H. (1989), Wave interference effects on a truncated cylinder in a channel, J. Eng. Math. 23

Appendix

A1. An asymptotic form of the velocity potential

First, let us consider an asymptotic behavior of the Green function as $x \to \pm\infty$. In the analysis in subsection 2.1, the position of the source point $Q = (\xi, \eta, \zeta)$ is fixed at the origin of the coordinate system. Removing this restriction here and discarding the terms associated with the nonradiating local waves, we can get from eqs. (13) to (18) the following expression:

$$
\begin{aligned}
G(P;Q) \sim\ & i\frac{K}{2\pi}\left(\frac{2\pi}{KB_T}\right)\sum_{p=1}^{4}\sum_{m=0}^{\infty}\epsilon_m\left[\frac{\mathrm{sgn}(1+k\tau)}{|d\nu/dk - k/\nu|}\right.\\
&\left.\times e^{-\nu(z+\zeta)-ik(x-\xi)}\cos\big(y\sqrt{\nu^2-k^2}\big)\cos\big(\eta\sqrt{\nu^2-k^2}\big)\right]_{k=k_{pm}}\\
&+\frac{K}{2\pi}\left[\int_{-\infty}^{k_1}+\int_{k_2}^{k_3}+\int_{k_4}^{\infty}\right]\frac{\nu}{\sqrt{\nu^2-k^2}}\,e^{-\nu(z+\zeta)-ik(x-\xi)}\\
&\times\cos\big(y\sqrt{\nu^2-k^2}\big)\cos\big(\eta\sqrt{\nu^2-k^2}\big)\cot\Big(\frac{KB_T}{2}\sqrt{\nu^2-k^2}\Big)\,dk\\
&-\frac{K}{2\pi}\left[\int_{k_1}^{k_2}+\int_{k_3}^{k_4}\right]\frac{\nu}{\sqrt{k^2-\nu^2}}\,e^{-\nu(z+\zeta)-ik(x-\xi)}\\
&\times\cosh\big(y\sqrt{k^2-\nu^2}\big)\cosh\big(\eta\sqrt{k^2-\nu^2}\big)\coth\Big(\frac{KB_T}{2}\sqrt{k^2-\nu^2}\Big)\,dk\\
&\text{as } |x-\xi|\to\infty
\end{aligned}
\tag{52}
$$

Here, for brevity, the coordinates $P = (x, y, z)$ and $Q = (\xi, \eta, \zeta)$ are nondimensionalized in terms of the wavenumber K. The meanings of symbols ϵ_m and k_{pm} are already described in subsection 2.1. (Fig. 2 may be useful in understanding k_{pm}.) In order to transform (52) further, we exploit the Riemann-Lebesgue lemma:

$$\lim_{X\to\infty}\int_a^b \frac{F(k)}{f(k)}\, e^{-ikX}\, dk \sim -\pi i\,\frac{F(\beta)}{f'(\beta)}\, e^{-i\beta X} \tag{53}$$

where β is the value of k satisfying $f(k)=0$ in the range of integration $[a,\,b]$.

Now let us consider first the case of $(x-\xi)\to+\infty$, with the sum of the second and third terms of (52) denoted by J_{23}. Applying the above lemma to the integrals in (52), we shall have the following result:

$$\begin{aligned} J_{23} \sim -i\,\frac{K}{2\pi}\left(\frac{2\pi}{KB_T}\right)\sum_{p=1}^{4}\sum_{m=0}^{\infty}\epsilon_m\Bigg[&\frac{1}{d\nu/dk-k/\nu} \\ &\times e^{-\nu(z+\zeta)-ik(x-\xi)}\cos\big(y\sqrt{\nu^2-k^2}\big)\cos\big(\eta\sqrt{\nu^2-k^2}\big)\Bigg]_{k=k_{pm}} \\ &\text{as } (x-\xi)\to+\infty \end{aligned} \tag{54}$$

Note that, as can be understood from Fig. 2, $d\nu/dk-k/\nu$ is positive for $p=2$ and 4, and negative for $p=1$ and 3. Therefore the sum of (54) and the first term in (52) gives the final result of the form

$$\begin{aligned} G(P;Q) \sim i\,\frac{K}{\pi}\left(\frac{2\pi}{KB_T}\right)\sum_{m=0}^{M}\epsilon_m\Bigg[&\frac{1}{|d\nu/dk-k/\nu|} \\ &\times e^{-\nu(z+\zeta)-ik(x-\xi)}\cos\big(y\sqrt{\nu^2-k^2}\big)\cos\big(\eta\sqrt{\nu^2-k^2}\big)\Bigg]_{k=k_{3m}} \\ &\text{as } (x-\xi)\to+\infty \end{aligned} \tag{55}$$

where M is the maximum of integer m satisfying $KB_T\sqrt{\nu^2-k^2}=2\pi m$ when $k_2\le k\le k_3$, that is, for $p=3$ (see Fig. 2).

If we consider next the case of $(x-\xi)\to-\infty$, the asymptotic form of J_{23} can be shown to be equal in form but opposite in sign to (54). Therefore we shall have

$$\begin{aligned} G(P;Q) \sim i\,\frac{K}{\pi}\left(\frac{2\pi}{KB_T}\right)\sum_{p=1,2,4}\sum_{m=0}^{\infty}\epsilon_m\Bigg[&\frac{\mathrm{sgn}(1+k\tau)}{|d\nu/dk-k/\nu|} \\ &\times e^{-\nu(z+\zeta)-ik(x-\xi)}\cos\big(y\sqrt{\nu^2-k^2}\big)\cos\big(\eta\sqrt{\nu^2-k^2}\big)\Bigg]_{k=k_{pm}} \\ &\text{as } (x-\xi)\to-\infty \end{aligned} \tag{56}$$

The velocity potential at an arbitrary point in the fluid region can be given as

$$\phi_j(P)=\iint_{S_H}\left(\frac{\partial\phi_j}{\partial n}-\phi_j\,\frac{\partial}{\partial n}\right)G(P;Q)\,dS \tag{57}$$

where S_H is the ship hull.

Substituting the asymptotic form of the Green function given by (55) and (56) into (57), it follows that

$$\begin{aligned}\phi_j(P) &\sim i\,\frac{K}{\pi}\left(\frac{2\pi}{KB_T}\right)\sum_{m=0}^{M} \\ &\quad \epsilon_m\left[H_j(k)\,\frac{1}{|d\nu/dk-k/\nu|}\,e^{-\nu z-ikx}\cos\bigl(y\sqrt{\nu^2-k^2}\bigr)\right]_{k=k_{3m}} \\ &\quad \text{as } x\to+\infty \end{aligned}\tag{58}$$

$$\begin{aligned}\phi_j(P) &\sim i\,\frac{K}{\pi}\left(\frac{2\pi}{KB_T}\right)\sum_{p=1,2,4}\sum_{m=0}^{\infty} \\ &\quad \epsilon_m\left[H_j(k)\,\frac{\mathrm{sgn}(1+k\tau)}{|d\nu/dk-k/\nu|}\,e^{-\nu z-ikx}\cos\bigl(y\sqrt{\nu^2-k^2}\bigr)\right]_{k=k_{pm}} \\ &\quad \text{as } x\to-\infty \end{aligned}\tag{59}$$

where
$$H_j(k)=\iint_{S_H}\left(\frac{\partial\phi_j}{\partial n}-\phi_j\,\frac{\partial}{\partial n}\right)e^{-\nu\zeta+ik\xi}\cos\bigl(\eta\sqrt{\nu^2-k^2}\bigr)\,dS \tag{60}$$

Eqs. (58) and (59) are the asymptotic forms of the velocity potential at positive and negative infinities of a parallel-sided waterway. If we recall that the above analysis proceeded with the coordinates nondimensionalized in terms of K, we can confirm that eq. (60) is the same as (40) given in Chapter 3.

Calculation Formulas for the Wave-Induced Steady Horizontal Force and Yaw Moment on a Ship with Forward Speed*

Masashi KASHIWAGI
Research Institute for Applied Mechanics, Kyushu University
Kasuga, Fukuoka 816-8580, Japan

Abstract

A new analysis method based on the theory of Fourier transform is provided for the added resistance, steady sway force, and yaw moment acting on an advancing ship in oblique waves. The principle of linear and angular momentum conservation is used to relate the steady force and moment to far-field disturbance waves generated by the ship. Maruo's added-resistance formula is derived easily with the present method in which Parseval's theorem is effectively used in place of the stationary-phase method. The new method is extended to the analysis of the steady sway force and yaw moment. Calculation formulas for these force and moment are obtained in a form analogous to that for the added resistance, involving only the Kochin function as unknown. In the limit of vanishing forward speed, the obtained formulas reduce to Maruo's for the drift force and Newman's for the drift moment.

Keywords: Added resistance, Steady sway force, Steady yaw moment, Principle of momentum conservation, Kochin function, Forward-speed effects, Fourier transform, Parseval's theorem.

1. Introduction

When a ship is floating on the surface of waves, the mean drifting force and yawing moment will be exerted on the ship as a result of wave actions. These drift force and moment are of second order in the wave amplitude, but of engineering importance in designing the control system to maintain the position or heading of ships in waves. A rational theoretical analysis of this subject, based on the principle of momentum conservation, was provided first by Maruo[1)] for the drift force in the horizontal plane and later by Newman[2)] for the steady yawing moment. It has been common since these two papers to perform "exact" numerical computations of the drift force and moment when the ship's forward speed is zero.

When a ship is advancing at constant forward speed, the same kind of second-order steady force and moment will be also exerted on the ship. Maruo[3),4)] applied the momentum-principle analysis to the case of forward speed present, and provided a formula for the ship's longitudinal component of the steady horizontal force. This component is known as the added resistance in waves and has interested many researchers in the field of naval architecture, because the prediction of wave resistance is crucial in considering economical operations of ships in actual seaways. With this engineering reason, many studies on the

* *Reprinted from Reports of Research Institute for Applied Mechanics, Vol. 37, No. 107, pp. 1–18, 1991*

added resistance have been made so far; references of these are included in the proceeding of symposium[5)] held by the Society of Naval Architects of Japan.

In oblique waves, due to the wave-induced steady sway force and yaw moment, the ship will advance with drift angle and check helm to maintain a designated course and thus experience the increase of resistance arising from these secondary causes. Therefore in discussing the overall propulsive performance of a ship in waves, we need to focus more attention on the wave-induced sway force and yaw moment besides the added resistance. However no calculation formulas exist for these steady force and moment, involving only the Kochin function as does the added-resistance formula. It may be true that Maruo's added-resistance analysis can be directly applied to the lateral force component, but it seems difficult to derive a compact formula for the yaw moment, as long as we follow Maruo's procedure of analyzing the momentum relation. His procedure is complicated, because the stationary-phase method is skillfully used to lead to the final expression. Therefore, to succeed in obtaining a compact formula for the steady yaw moment, we must first develop a new analysis method with which Maruo's added-resistance formula can be easily derived, and next apply it to the principle of angular momentum conservation which relates the moment on a ship to the far-field ship-generated waves.

The present paper reports the work performed along the above lines. In the new analysis method, Parseval's theorem in the Fourier-transform theory is effectively utilized, and thereby complicated calculi seen in Maruo's analysis are avoided. The obtained formulas permit the prediction of the wave-induced steady sway force and yaw moment in terms only with the Kochin function equivalent to the complex amplitude of far-field disturbance waves. Of course Newman's zero-speed results are recovered from the present formulas in the limit of vanishing forward speed.

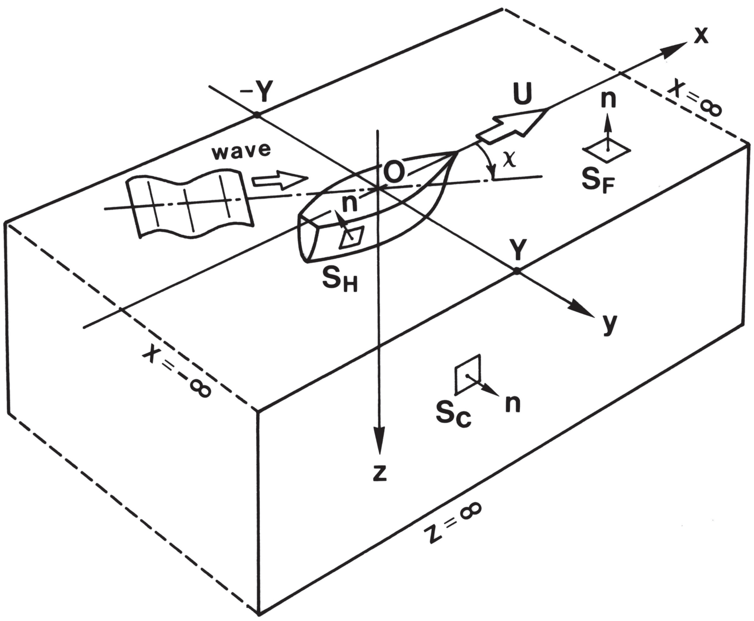

Fig. 1 Coordinate system and notations

2. Far-Field Asymptotic Form of the Velocity Potential

For the sake of subsequent analyses on the principle of momentum and energy conservation, we need to obtain the asymptotic form of the disturbance velocity potential at large distances from a ship. Let us consider a ship advancing at constant forward velocity U into a plane progressive wave of amplitude a, circular frequency ω_0, and wavenumber k_0. The water depth is assumed infinite and thus $k_0 = \omega_0^2/g$, with g the acceleration of gravity. The angle of wave incidence is denoted by χ and measured as in Fig. 1, with $\chi = 0$ corresponding to the following wave. Due to the effect of this incident wave, the ship performs sinusoidal oscillations about its mean position with the circular frequency of encounter ω, which is related to ω_0 by $\omega = \omega_0 - k_0 U \cos\chi$.

As shown in Fig. 1, we take a right-hand Cartesian coordinate system O-xyz, translating with the same velocity as that of the ship. The x-axis is positive in the direction of ship's forward motion, the y-axis positive starboard, and the z-axis positive downward, with the origin placed on the undisturbed free surface.

To justify the linearity, we assume the amplitudes of incident wave and ship's oscillations to be small. Further we assume the flow inviscid with irrotational motion. Then the velocity potential can be introduced and written by linear assumption as

$$\varPhi(x,y,z,t) = -Ux + \phi(x,y,z,t) \tag{1}$$

$$\phi(x,y,z,t) = \mathrm{Re}\left[\,\psi(x,y,z)\,e^{i\omega t}\right] \tag{2}$$

$$\psi(x,y,z) = \frac{g\,a}{i\omega_0}\left\{\varphi_0(x,y,z) + \varphi(x,y,z)\right\} \tag{3}$$

$$\varphi_0(x,y,z) = e^{-k_0 z - ik_0(x\cos\chi + y\sin\chi)} \tag{4}$$

$$\varphi(x,y,z) = \varphi_7(x,y,z) - \frac{\omega\omega_0}{g}\sum_{j=1}^{6}\frac{\xi_j}{a}\,\varphi_j(x,y,z) \tag{5}$$

In the above, φ_0 is the potential of the incident wave and φ the disturbance potential due to the presence of a ship. The latter is divided into the scattered potential φ_7 and the radiation potential φ_j $(j = 1, 2, \cdots, 6)$ due to forced motion of the ship in each mode of six degrees of freedom; ξ_j is the amplitude in the jth mode of motion. The symbol 'Re' in (2) means the real part to be taken.

The velocity potentials, φ_0 and φ, are governed by Laplace's equation and subject to the linearized free-surface boundary condition

$$\left(i\omega - U\frac{\partial}{\partial x}\right)^2 \psi - g\frac{\partial\psi}{\partial z} = 0 \tag{6}$$

on $z = 0$ and the condition of vanishing velocity as $z \to \infty$. In addition, the disturbance potential φ satisfies a suitable radiation condition.

From Green's theorem, the disturbance potential φ at any point $P = (x, y, z)$ in the fluid is given by

$$\varphi(P) = \iint_{S_H}\left(\frac{\partial\varphi(Q)}{\partial n} - \varphi(Q)\frac{\partial}{\partial n}\right) G(P;Q)\,dS(Q) \tag{7}$$

where $Q = (\xi, \eta, \zeta)$ denotes the integration point on the wetted portion of ship hull S_H; $\partial/\partial n$ is the normal differentiation with respect to the integration point, with the normal defined positive into the ship hull; and $G(P;Q)$ denotes the Green function or source potential which satisfies the same free-surface and radiation conditions as those to be satisfied by φ. With the Fourier-transform technique, this Green function can be written in the form[6)]

$$
\begin{aligned}
G(P;Q) = &-\frac{1}{4\pi}\left(\frac{1}{r}-\frac{1}{r'}\right) \\
&-\frac{1}{2\pi}\int_{-\infty}^{\infty} e^{-ik(x-\xi)}\,dk\cdot \mathrm{Re}\int_0^{\infty}\frac{e^{-in(z+\zeta)-|y-\eta|\sqrt{n^2+k^2}}}{(n+i\nu)\sqrt{n^2+k^2}}\,ndn \\
&-\frac{1}{2\pi}\left[\int_{k_1}^{k_2}+\int_{k_3}^{k_4}\right]\frac{\nu}{\sqrt{k^2-\nu^2}}\,e^{-\nu(z+\zeta)-|y-\eta|\sqrt{k^2-\nu^2}-ik(x-\xi)}\,dk \\
&+\frac{i}{2\pi}\left[-\int_{-\infty}^{k_1}+\int_{k_2}^{k_3}+\int_{k_4}^{\infty}\right]\frac{\nu}{\sqrt{\nu^2-k^2}} \\
&\qquad\qquad \times e^{-\nu(z+\zeta)-i\epsilon_k|y-\eta|\sqrt{\nu^2-k^2}-ik(x-\xi)}\,dk
\end{aligned}
\tag{8}
$$

where

$$
\left.\begin{matrix} r \\ r' \end{matrix}\right\} = \sqrt{(x-\xi)^2+(y-\eta)^2+(z\mp\zeta)^2}
\tag{9}
$$

$$
\nu = \frac{1}{g}(\omega+kU)^2 = K + 2k\tau + \frac{k^2}{K_0}
\tag{10}
$$

$$
K = \frac{\omega^2}{g}, \quad \tau = \frac{U\omega}{g}, \quad K_0 = \frac{g}{U^2}
\tag{11}
$$

$$
\left.\begin{matrix} k_1 \\ k_2 \end{matrix}\right\} = -\frac{K_0}{2}\left[1+2\tau\pm\sqrt{1+4\tau}\right]
\tag{12}
$$

$$
\left.\begin{matrix} k_3 \\ k_4 \end{matrix}\right\} = \frac{K_0}{2}\left[1-2\tau\mp\sqrt{1-4\tau}\right]
\tag{13}
$$

$$
\epsilon_k = \mathrm{sgn}(\omega+kU) = \left\{\begin{array}{rll} -1 & \text{for} & -\infty<k<k_1 \\ 1 & \text{for} & k_2<k<\infty \end{array}\right.
\tag{14}
$$

In the case of $\tau > 1/4$, wavenumbers k_3 and k_4 given by (13) is not real, and thus the limits of integration in (8) should be interpreted such that $k_3 = k_4$ for $\tau > 1/4$. (Hereafter this convention will be understood.)

To obtain a far-field approximation to the disturbance potential φ when the transverse distance $|y|$ is large, let us first consider the asymptotic approximation of the Green function itself. It is obvious that all the terms except the last one in (8) vanish for large values of $|y|$. (These terms represent the local disturbance in the vicinity of the x-axis.) Therefore, substituting only the last term of (8) into (7), we obtain the desired approximation of the velocity potential valid at large distances from the x-axis:

$$
\begin{aligned}
\varphi(x,y,z) \sim &\frac{i}{2\pi}\left[-\int_{-\infty}^{k_1}+\int_{k_2}^{k_3}+\int_{k_4}^{\infty}\right] H^{\pm}(k) \\
&\qquad \times \frac{\nu}{\sqrt{\nu^2-k^2}}\,e^{-\nu z\mp i\epsilon_k y\sqrt{\nu^2-k^2}-ikx}\,dk
\end{aligned}
\tag{15}
$$

where

$$
H^{\pm}(k) = \iint_{S_H}\left(\frac{\partial\varphi}{\partial n}-\varphi\frac{\partial}{\partial n}\right)e^{-\nu\zeta\pm i\epsilon_k\eta\sqrt{\nu^2-k^2}+ik\xi}\,dS
\tag{16}
$$

is the Kochin function equivalent to the complex amplitude of the far-field disturbance wave. The upper of lower of the complex signs in (15) and (16) is to be taken according as the sign of yy is positive or negative, respectively. With the convention that the Kochin function is zero outside of the integration range explicitly shown in (15), we shall write (15) in the form

$$\varphi(x,y,z) \sim \frac{1}{2\pi}\int_{-\infty}^{\infty} i\epsilon_k H^{\pm}(k)\frac{\nu}{\sqrt{\nu^2-k^2}}\, e^{-\nu z \mp i\epsilon_k y\sqrt{\nu^2-k^2}}\, e^{-ikx}\, dk \tag{17}$$

Here the notation (14) has been used.

From this equation, we can readily obtain the Fourier transform of the disturbance potential in the far field:

$$\mathcal{F}\{\varphi(x,y,z)\} \equiv \int_{-\infty}^{\infty} \varphi(x,y,z)\, e^{ikx}\, dx \tag{18}$$

$$= i\epsilon_k H^{\pm}(k)\frac{\nu}{\sqrt{\nu^2-k^2}}\, e^{-\nu z \mp i\epsilon_k y\sqrt{\nu^2-k^2}} \tag{19}$$

Note that neglected in (17) or (19) are only the local disturbances near the x-axis and that the momentum or the energy associated with these terms become infinitely small as the coordinate x tends to plus or minus infinity.

The Fourier transform of the incident-wave potential φ_0 will be derived by substituting (4) into the definition (18), with the result

$$\mathcal{F}\{\varphi_0(x,y,z)\} = 2\pi\,\delta(k-k_0\cos\chi)\, e^{-k_0 z - ik_0 y\sin\chi} \tag{20}$$

where $\delta(k-k_0\cos\chi)$ is Dirac's delta function, thus contributing only for $k=k_0\cos\chi$.

For convenience in subsequent derivations, we decompose the Kochin function in the form

$$H^{\pm}(k) = C(k) \pm i\epsilon_k S(k) \tag{21}$$

where

$$\left.\begin{aligned} C(k) &= \iint_{S_H}\left(\frac{\partial\varphi}{\partial n} - \varphi\frac{\partial}{\partial n}\right) e^{-\nu\zeta+ik\xi}\cos\bigl(\eta\sqrt{\nu^2-k^2}\bigr)\, dS \\ S(k) &= \iint_{S_H}\left(\frac{\partial\varphi}{\partial n} - \varphi\frac{\partial}{\partial n}\right) e^{-\nu\zeta+ik\xi}\sin\bigl(\eta\sqrt{\nu^2-k^2}\bigr)\, dS \end{aligned}\right\} \tag{22}$$

We note that $C(k)$ and $S(k)$ represent the symmetric and antisymmetric components, respectively, with respect to the center plane of a ship symmetrical about $y=0$.

3. Added Resistance

3.1 Principle of linear momentum conservation

In this section, we shall consider by use of the Fourier-transform technique the same problem as that analyzed by Maruo[4)] and show that Maruo's added-resistance formula can be derived with considerable ease. Following Maruo, we begin by considering the rate of change of linear momentum within the fluid domain bounded by ship's wetted surface S_H, free surface S_F, and control surface S_C at a large distance from the ship. Using Gauss' theorem and taking account of no flux across S_H and S_F and zero pressure on S_F, we get:

$$\frac{d\boldsymbol{M}}{dt} = -\iint_{S_H} p\,\boldsymbol{n}\, dS - \iint_{S_C}\Bigl[p\,\boldsymbol{n} + \rho\nabla\Phi\bigl(\boldsymbol{n}\cdot\nabla\Phi\bigr)\Bigr]\, dS \tag{23}$$

where p is the fluid pressure, ρ the fluid density, and $\boldsymbol{n}$ the normal vector.

As usual, we take time average of the above. Because of the periodicity of fluid motion, there can be no net increase of momentum in the control volume from one cycle no another. Therefore the steady force in the horizontal plane can be related to the far-field velocity potential, in the form

$$\overline{\boldsymbol{F}} = \overline{\iint_{S_H} p\,\boldsymbol{n}\, dS} = -\overline{\iint_{S_C} \Big[p\,\boldsymbol{n} + \rho \nabla\phi \Big(\frac{\partial \phi}{\partial n} - U n_x \Big) \Big]\, dS} \tag{24}$$

where, from Bernoulli's equation,

$$p = -\rho \Big\{ \frac{\partial \phi}{\partial t} - U \frac{\partial \phi}{\partial x} + \frac{1}{2} \nabla\phi \cdot \nabla\phi - g z \Big\} \tag{25}$$

and n_x is the x-component of the normal vector. In (24) and (25), eq.(1) has been substituted and the overbar in (24) means taking time average.

Since the resistance is defined as the force in the negative x-direction, we obtain from (24) an expression for the added resistance:

$$\overline{R} = \overline{\iint_{S_C} \Big[p\, n_x + \rho \frac{\partial \phi}{\partial x} \Big(\frac{\partial \phi}{\partial n} - U n_x \Big) \Big]\, dS} \tag{26}$$

In the present analysis, instead of the usual control surface of a circular cylinder of large radius about the z-axis, we take two flat plates as the control surface, which are, as shown in Fig. 1, located at $y = \pm Y$ and extend from $x = -\infty$ to $x = +\infty$ and from the instantaneous free surface down to $z = +\infty$. (The value of Y is assumed large such that the local waves near the x-axis can be neglected.) Careful readers might be anxious about the momentum flux from the vertical planes parallel to the y-axis at $x = \pm\infty$. However the control surface considered here is of infinite length in the x-direction and all the disturbance waves radiating away from the x-axis are precisely taken into account. Thus, neglected are only the contributions from the local waves which exist only near the x-axis; these will become zero at $x = \pm\infty$ in the three-dimensional case.

Note that the x-component of the normal vector is zero on the present control surface. Then, neglecting terms higher than $O(\phi^3)$ as in the usual procedure, we readily obtain from (26)

$$\overline{R} = \rho \int_0^\infty dz \int_{-\infty}^\infty \Big[\overline{\frac{\partial \phi}{\partial x} \frac{\partial \phi}{\partial y}} \Big]_{-Y}^{Y} dx \tag{27}$$

Here $\big[\quad \big]_{-Y}^{Y}$ means the difference between the values of the quantity in brackets at $y = Y$ and at $y = -Y$. Substituting (2) into (27) and performing the time-average calculation, it follows that

$$\overline{R} = \frac{1}{2} \rho \,\mathrm{Re} \int_0^\infty dz \int_{-\infty}^\infty \Big[\frac{\partial \psi}{\partial x} \frac{\partial \psi^*}{\partial y} \Big]_{-Y}^{Y} dx \tag{28}$$

where the asterisk denotes the complex conjugate.

Next we substitute the velocity potential (3) for ψ into the above. The result will involve terms which are quadratic in the disturbance potential φ and the incident-wave potential φ_0 separately, plus the cross terms of φ and φ_0. The contribution from φ_0 alone is zero, because there can be no force associated with the undisturbed incident wave system. Taking these into consideration, (28) can be written in the form

$$\overline{R} = \frac{\rho g a^2}{k_0}\left(\overline{R_1} + \overline{R_2}\right) \tag{29}$$

$$\overline{R_1} = \frac{1}{2}\,\mathrm{Re}\int_0^\infty dz \int_{-\infty}^\infty \left[\frac{\partial\varphi}{\partial x}\frac{\partial\varphi^*}{\partial y}\right]_{-Y}^{Y} dx \tag{30}$$

$$\overline{R_2} = \frac{1}{2}\,\mathrm{Re}\int_0^\infty dz \int_{-\infty}^\infty \left[\frac{\partial\varphi}{\partial x}\frac{\partial\varphi_0^*}{\partial y} + \frac{\partial\varphi_0^*}{\partial x}\frac{\partial\varphi}{\partial y}\right]_{-Y}^{Y} dx \tag{31}$$

We notice that the integrations with respect to x are of the form to which the following Fourier-transform theorem (Parseval's theorem) can be applied:

$$\int_{-\infty}^\infty f(x)g^*(x)\,dx = \frac{1}{2\pi}\int_{-\infty}^\infty F(k)G^*(k)\,dk \tag{32}$$

where $F(k)$ and $G(k)$ are Fourier transforms of $f(x)$ and $g(x)$, respectively, which may be calculated from the definition (18).

Let us consider first eq. (30). Since the potential φ has exponential dependence on the coordinate z as seen in (17), the z-integration in (30) can be carried out with the formula:

$$\int_0^\infty e^{-2\nu z}\,dz = \frac{1}{2\nu} \tag{33}$$

The x-integration in (30), on the other hand, can be performed by applying the Parseval's theorem (32) in terms of the Fourier transform of φ given by (19). After performing the x- and z-integrations in this manner, we get the following result with relative ease.

$$\begin{aligned}\overline{R_1} &= \frac{1}{8\pi}\int_{-\infty}^\infty \epsilon_k\Big\{|H^+(k)|^2 + |H^-(k)|^2\Big\}\frac{\nu}{\sqrt{\nu^2-k^2}}\,k\,dk\\ &= \frac{1}{8\pi}\left[-\int_{-\infty}^{k_1} + \int_{k_2}^{k_3} + \int_{k_4}^{\infty}\right]\Big\{|H^+(k)|^2 + |H^-(k)|^2\Big\}\frac{\nu}{\sqrt{\nu^2-k^2}}\,k\,dk\end{aligned} \tag{34}$$

Here we have used the convention concerning the integration range noted in deriving (17). In (34), it is understood that $k_3 = k_4$ in the case of $\tau > 1/4$.

We proceed to the second term $\overline{R_2}$ defined by (31). In the calculation of (31), it is sufficient to retain only the terms which are independent of the coordinate y, because according to the theory of hyperfunction[7)], sinusoidal terms will vanish when taking the limit of $Y \to \infty$ after performing the x- and z-integrations. Therefore only two cases should be considered here: $k_0 \sin\chi = \epsilon_k\sqrt{\nu^2-k^2}$ and $k_0\sin\chi = -\epsilon_k\sqrt{\nu^2-k^2}$.

We begin with the first case, $k_0\sin\chi = \epsilon_k\sqrt{\nu^2-k^2}$. Since we are going to apply the Parseval's theorem (32) to the x-integration in (31), we must consider the product of the Fourier transforms of φ and φ_0, given by (19) and (20), respectively. Thus due to Dirac's delta function appearing in (20), we can put $k = k_0\cos\chi$; from this and $k_0\sin\chi = \epsilon_k\sqrt{\nu^2-k^2}$, we have $\nu = k_0$. Therefore the z-integration in (31) takes the form

$$\int_0^\infty e^{-(\nu+k_0)z}\,dz = \frac{1}{(\nu+k_0)} = \frac{1}{2\nu} \tag{35}$$

Applying this result and Parseval's theorem, eq. (31) can be reduced to

$$\overline{R_2} = -\frac{1}{2} k_0 \cos\chi \,\mathrm{Im}\big[H(k_0,\chi)\big] \tag{36}$$

where 'Im' denotes the imaginary part, and $H(k_0,\chi)$ is the function obtained after substituting $k = k_0\cos\chi$ and $\epsilon_k\sqrt{\nu^2-k^2} = k_0\sin\chi$ into the Kochin function $H^+(k)$ and thus can be written as

$$H(k_0,\chi) = \iint_{S_H} \left(\frac{\partial\varphi}{\partial n} - \varphi\frac{\partial}{\partial n}\right) e^{-k_0\zeta + ik_0(\xi\cos\chi+\eta\sin\chi)}\, dS \tag{37}$$

In the second case of $k_0\sin\chi = -\epsilon_k\sqrt{\nu^2-k^2}$, we can easily confirm that the reductions analogous to the first case lead to the same final result as (36) and (37). Therefore we have completed all of the necessary integrations.

Substituting (34) and (36) into (29) gives the formula for the added resistance in waves:

$$\begin{aligned}\frac{\overline{R}}{\rho g a^2} = \frac{1}{8\pi k_0}&\left[-\int_{-\infty}^{k_1} + \int_{k_2}^{k_3} + \int_{k_4}^{\infty}\right]\Big\{|H^+(k)|^2 + |H^-(k)|^2\Big\} \\ &\times \frac{\nu}{\sqrt{\nu^2-k^2}}\,k\,dk - \frac{1}{2}\cos\chi\,\mathrm{Im}\big[H(k_0,\chi)\big]\end{aligned} \tag{38}$$

3.2 Principle of energy conservation

In Maruo's analysis, the last term of (38) is transformed further using the energy-conservation principle. Since no external force exists except the constant towing force and the gravitational force keeping the equilibrium position of the ship in space, there is no work done or no dissipation of energy. Thus, owing to the periodic nature of the fluid motion, we have the relation[4)]

$$\overline{\iint_{S_C} \frac{\partial\phi}{\partial t}\Big(\frac{\partial\phi}{\partial n} - Un_x\Big)\, dS} = 0 \tag{39}$$

Noting that $n_x = 0$ on the control surface shown in Fig. 1 and neglecting higher-order terms resulting from the free-surface elevation, the above equation can be transformed as

$$\int_0^\infty dz \int_{-\infty}^\infty \left[\overline{\frac{\partial\phi}{\partial t}\frac{\partial\phi}{\partial y}}\right]_{-Y}^{Y} dx = \frac{1}{2}\mathrm{Re}\int_0^\infty dz\int_{-\infty}^\infty \left[i\omega\psi\,\frac{\partial\psi^*}{\partial y}\right]_{-Y}^{Y} dx = 0 \tag{40}$$

Substituting (3) and decomposing the result into two parts like (29), we can write (40) in the form

$$\begin{aligned}&\frac{1}{2}\mathrm{Im}\int_0^\infty dz\int_{-\infty}^\infty\left[\varphi\,\frac{\partial\varphi^*}{\partial y}\right]_{-Y}^{Y} dx \\ &\quad = -\frac{1}{2}\mathrm{Im}\int_0^\infty dz\int_{-\infty}^\infty\left[\varphi\,\frac{\partial\varphi_0^*}{\partial y} - \varphi_0^*\frac{\partial\varphi}{\partial y}\right]_{-Y}^{Y} dx\end{aligned} \tag{41}$$

The procedure of performing these integrations with respect to x and z is the same as that for (30) and (31); that is, we apply Parseval's theorem (32) with the Fourier transforms of φ and φ_0. After straightforward reductions, we get the following result:

$$\begin{aligned}\frac{1}{8\pi}&\left[-\int_{-\infty}^{k_1} + \int_{k_2}^{k_3} + \int_{k_4}^{\infty}\right]\Big\{|H^+(k)|^2 + |H^-(k)|^2\Big\}\frac{\nu}{\sqrt{\nu^2-k^2}}\,dk \\ &= \frac{1}{2}\mathrm{Im}\big[H(k_0,\chi)\big]\end{aligned} \tag{42}$$

Here $H(k_0, \chi)$ is the Kochin function defined by (37).

With this energy relation, the added-resistance formula (38) can be recast in the form

$$\frac{\overline{R}}{\rho g a^2} = \frac{1}{8\pi k_0}\left[-\int_{-\infty}^{k_1} + \int_{k_2}^{k_3} + \int_{k_4}^{\infty}\right]\Big\{|H^+(k)|^2 + |H^-(k)|^2\Big\} \times \frac{\nu}{\sqrt{\nu^2 - k^2}}\,(k - k_0\cos\chi)\,dk \tag{43}$$

If the relation (21) is substituted for $H^{\pm}(k)$, the above equation can be expressed as

$$\frac{\overline{R}}{\rho g a^2} = \frac{1}{4\pi k_0}\left[-\int_{-\infty}^{k_1} + \int_{k_2}^{k_3} + \int_{k_4}^{\infty}\right]\Big\{|C(k)|^2 + |S(k)|^2\Big\} \times \frac{\nu}{\sqrt{\nu^2 - k^2}}\,(k - k_0\cos\chi)\,dk \tag{44}$$

Introducing Hanaoka's variable transformation[8)]

$$k = \frac{K_0}{2\cos\theta}\big\{1 - 2\tau\cos\theta \pm \sqrt{1 - 4\tau\cos\theta}\big\}, \tag{45}$$

we can confirm that (43) or (44) is identical to that derived by Maruo[4)]. However, a point to be emphasized here is that the derivation in this paper is quite simple in comparison to Maruo's, because the Fourier-transform technique is used in place of the stationary-phase method which was essential in Maruo's analysis. We can see form (44) that symmetric waves $C(k)$ and antisymmetric waves $S(k)$ contribute independently to the added resistance and no contribution exists from the interaction between them.

4. Steady Sway Force

The y-component of (24) gives the formula for the steady sway force:

$$\overline{F_y} = \overline{\iint_{S_H}\Big[p n_y + \rho\frac{\partial\phi}{\partial y}\Big(\frac{\partial\phi}{\partial n} - U n_x\Big)\Big]\,dS} \tag{46}$$

Evaluating this on the control surface shown in Fig. 1, (46) can be reduced to

$$\begin{aligned}\overline{F_y} &= -\overline{\int_{\zeta_w}^{\infty} dz \int_{-\infty}^{\infty}\Big[p + \rho\Big(\frac{\partial\phi}{\partial y}\Big)^2\Big]_{-Y}^{Y} dx} \\ &= \frac{1}{2}\rho\int_0^{\infty} dz\int_{-\infty}^{\infty}\overline{\Big[\Big(\frac{\partial\phi}{\partial x}\Big)^2 + \Big(\frac{\partial\phi}{\partial z}\Big)^2 - \Big(\frac{\partial\phi}{\partial y}\Big)^2\Big]}_{-Y}^{Y} dx \\ &\quad + \frac{1}{2}\rho g\int_{-\infty}^{\infty}\Big[\,\overline{\zeta_w^2}\,\Big]_{-Y}^{Y} dx \; + O(\phi^3)\end{aligned} \tag{47}$$

Here eq. (255) for the pressure p has been substituted and ζ_w is the unsteady elevation of the free surface, which is given by

$$\zeta_w = \frac{1}{g}\left(\frac{\partial\phi}{\partial t} - U\frac{\partial\phi}{\partial x}\right)_{z=0} + O(\phi^2) \tag{48}$$

Calculating the time average in (47) and substituting (3) for the velocity potential, we can write (47) in the following decomposed form

$$\overline{F_y} = -\frac{\rho g a^2}{k_0}\Big(\overline{Y_1} + \overline{Y_2}\Big) \tag{49}$$

where

$$\begin{aligned}\overline{Y_1} = &-\frac{1}{4}\int_0^\infty dz \int_{-\infty}^\infty \Big[\,\Big|\frac{\partial\varphi}{\partial x}\Big|^2 + \Big|\frac{\partial\varphi}{\partial z}\Big|^2 - \Big|\frac{\partial\varphi}{\partial y}\Big|^2\,\Big]_{-Y}^{Y} dx \\ &+\frac{1}{4}\,\mathrm{Re}\int_{-\infty}^\infty \Big[\Big\{K|\varphi|^2 + \frac{1}{K_0}\Big|\frac{\partial\varphi}{\partial x}\Big|^2 + i2\tau\varphi^*\frac{\partial\varphi}{\partial x}\Big\}_{z=0}\Big]_{-Y}^{Y} dx\end{aligned} \tag{50}$$

$$\begin{aligned}\overline{Y_2} = &-\frac{1}{2}\,\mathrm{Re}\int_0^\infty dz \int_{-\infty}^\infty \Big[\frac{\partial\varphi}{\partial x}\frac{\partial\varphi_0^*}{\partial x} + \frac{\partial\varphi}{\partial z}\frac{\partial\varphi_0^*}{\partial z} - \frac{\partial\varphi}{\partial y}\frac{\partial\varphi_0^*}{\partial y}\Big]_{-Y}^{Y} dx \\ &+\frac{1}{2}\,\mathrm{Re}\int_{-\infty}^\infty \Big[\Big\{K\varphi\varphi_0^* + \frac{1}{K_0}\frac{\partial\varphi}{\partial x}\frac{\partial\varphi_0^*}{\partial x} + i\tau\Big(\varphi_0^*\frac{\partial\varphi}{\partial x} - \varphi\frac{\partial\varphi_0^*}{\partial x}\Big)\Big\}_{z=0}\Big]_{-Y}^{Y} dx\end{aligned} \tag{51}$$

Note that $\overline{Y_1}$ represents the contributions from ship-generated disturbance waves and $\overline{Y_2}$ the contributions from the interactions of incident wave and ship-generated waves.

Let us first consider $\overline{Y_1}$. In order to apply the Parseval's theorem (32) to the x-integrations in (50), we need to obtain the Fourier transform of the derivatives with respect to x, y, z of the disturbance potential φ; which can be done easily using (19). The z-integration, which is necessary in the first term in (50), can be performed by use of (33). Summarizing these, we obtain the result

$$\begin{aligned}\overline{Y_1} &= -\frac{1}{8\pi}\int_{-\infty}^\infty \Big\{|H^+(k)|^2 - |H^-(k)|^2\Big\} \\ &\quad\times\Big\{\frac{k^2\nu}{2(\nu^2-k^2)} + \frac{\nu^3}{2(\nu^2-k^2)} - \frac{\nu}{2} - \frac{\nu^2}{\nu^2-k^2}\Big(K + \frac{k^2}{K_0} + 2\tau k\Big)\Big\}\,dk \\ &= \frac{1}{8\pi}\int_{-\infty}^\infty \Big\{|H^+(k)|^2 - |H^-(k)|^2\Big\}\nu\,dk\end{aligned} \tag{52}$$

From (21), the following relation holds:

$$|H^+(k)|^2 - |H^-(k)|^2 = 2\epsilon_k\,\mathrm{Im}\Big\{\,2C(k)S^*(k)\,\Big\} \tag{53}$$

Thus, recalling the convention about the range of integration with respect to k, eq.(52) can be written in the form

$$\overline{Y_1} = \frac{1}{4\pi}\Big[-\int_{-\infty}^{k_1} + \int_{k_2}^{k_3} + \int_{k_4}^{\infty}\Big]\,\mathrm{Im}\Big\{\,2C(k)S^*(k)\,\Big\}\nu\,dk \tag{54}$$

Next we consider the second term, $\overline{Y_2}$, defined by (51). Also here, we apply the Parseval's theorem with the Fourier transforms of φ and φ_0; these are given by (19) and (20), respectively. With the reasons stated in transforming the interaction terms between φ and φ_0 in the added-resistance formula, we can concentrate on the case of $k = k_0\cos\chi$,

$\pm\epsilon_k\sqrt{\nu^2-k^2}=k_0\sin\chi$, and thus $\nu=k_0$. Using these relations, eq. (51) can be transformed as

$$\begin{aligned}\overline{Y_2} &= -\frac{1}{2}\,\mathrm{Re}\left[\frac{i}{2}H(k_0,\chi)\left\{\frac{k_0\cos^2\chi}{\sin\chi}+\frac{k_0}{\sin\chi}-k_0\sin\chi\right.\right.\\&\qquad\left.\left.-\frac{2}{\sin\chi}\left(K+\frac{(k_0\cos\chi)^2}{K_0}+2\tau k_0\cos\chi\right)\right\}\right]\\&= -\frac{1}{2}k_0\sin\chi\,\mathrm{Im}\Big[\,H(k_0,\chi)\Big]\end{aligned}\tag{55}$$

where $H(k_0,\chi)$ is given by (37).

As in the added-resistance formula, the above result can be put in a different form by applying the principle of energy conservation. Substituting the relation (42) in (55) and expressing the resulting equation in terms of $C(k)$ and $S(k)$ defined by (21), we get:

$$\overline{Y_2}=-\frac{1}{4\pi}k_0\sin\chi\left[-\int_{-\infty}^{k_1}+\int_{k_2}^{k_3}+\int_{k_4}^{\infty}\right]\Big\{|C(k)|^2+|S(k)|^2\Big\}\frac{\nu}{\sqrt{\nu^2-k^2}}\,dk\tag{56}$$

Therefore, substitution of (54) and (56) into (49) gives the formula for the second-order steady sway force:

$$\begin{aligned}\frac{\overline{F_y}}{\rho g a^2} &= -\frac{1}{4\pi k_0}\left[-\int_{-\infty}^{k_1}+\int_{k_2}^{k_3}+\int_{k_4}^{\infty}\right]\mathrm{Im}\Big\{2C(k)S^*(k)\Big\}\nu\,dk\\&\quad+\frac{\sin\chi}{4\pi}\left[-\int_{-\infty}^{k_1}+\int_{k_2}^{k_3}+\int_{k_4}^{\infty}\right]\Big\{|C(k)|^2+|S(k)|^2\Big\}\frac{\nu}{\sqrt{\nu^2-k^2}}\,dk\end{aligned}\tag{57}$$

From this result, we can see that the first term comes from the interaction between symmetric and antisymmetric waves, whereas the second term comes from the independent contributions of symmetric and antisymmetric waves. Since the second term is multiplied by $\sin\chi$, both terms in (57) become zero in head and following waves for a ship with transverse symmetry.

5. Steady Yaw Moment

In order to relate the wave-induced steady yaw moment to the far-field velocity potential, we consider the principle of angular momentum about the z-axis. Newman[2)] gave an expression for the rate of change of the vertical component of angular momentum, which is general and thus applicable to the present problem. This can be expressed as

$$\begin{aligned}\frac{d\boldsymbol{K}_z}{dt} &= -\iint_{S_H}p\big(\boldsymbol{r}\times\boldsymbol{n}\big)_z\,dS\\&\quad-\iint_{S_C}\Big[p\big(\boldsymbol{r}\times\boldsymbol{n}\big)_z+\rho\big(\boldsymbol{r}\times\nabla\Phi\big)_z\big(\boldsymbol{n}\cdot\nabla\Phi\big)\Big]\,dS\end{aligned}\tag{58}$$

Here $\boldsymbol{r}$ is the position vector and the subscript z denotes the z-component of vector quantities. Note that the first term on the right-hand side of (58) is the minus yaw moment, because the unit normal is defined positive when pointing out of the fluid domain.

We take time average of (58). Since the fluid motion is periodic, there exists no net increase of angular momentum in the control volume. Therefore we get:

$$\overline{M_z} = \overline{\iint_{S_H} p\big(\boldsymbol{r}\times\boldsymbol{n}\big)_z\, dS}$$
$$= -\overline{\iint_{S_C} \Big[p\big(\boldsymbol{r}\times\boldsymbol{n}\big)_z + \rho\big(\boldsymbol{r}\times\nabla\Phi\big)_z\big(\boldsymbol{n}\cdot\nabla\Phi\big)\Big]\, dS} \tag{59}$$

Here the pressure of fluid p is given by (25), and it follows from (1) that

$$\left.\begin{aligned} &\big(\boldsymbol{r}\times\boldsymbol{n}\big)_z = xn_y - yn_x \\ &\big(\boldsymbol{r}\times\nabla\Phi\big)_z = x\frac{\partial\phi}{\partial y} - y\Big(\frac{\partial\phi}{\partial x} - U\Big) \\ &\boldsymbol{n}\cdot\nabla\Phi = n_x\Big(\frac{\partial\phi}{\partial x} - U\Big) + n_y\frac{\partial\phi}{\partial y} \end{aligned}\right\} \tag{60}$$

Evaluating the above equations on the control surface shown in Fig. 1 and discarding terms higher than $O(\phi^3)$, eq.(59) can be reduced to

$$\begin{aligned} \overline{M_z} =\ & \frac{1}{2}\rho\int_0^\infty dz\int_{-\infty}^{\infty}\left[\overline{x\Big\{\Big(\frac{\partial\phi}{\partial x}\Big)^2 + \Big(\frac{\partial\phi}{\partial z}\Big)^2 - \Big(\frac{\partial\phi}{\partial y}\Big)^2\Big\}}\right]_{-Y}^{Y} dx \\ & -\frac{1}{2}\rho g\int_{-\infty}^{\infty}\Big[\overline{x\,\zeta_w^2}\Big]_{-Y}^{Y} dx \\ & +\rho\int_0^\infty dz\int_{-\infty}^{\infty}\left[\overline{y\frac{\partial\phi}{\partial x}\frac{\partial\phi}{\partial y}}\right]_{-Y}^{Y} dx + \rho U\int_{-\infty}^{\infty}\left[\overline{y\zeta_w\frac{\partial\phi}{\partial y}}\right]_{-Y}^{Y} dx \end{aligned} \tag{61}$$

where ζ_w is given by (48).

As before, calculating the time average and substituting (3) gives the following expression:

$$\overline{M_z} = \frac{\rho g a^2}{k_0}\Big(\overline{N_1} + \overline{N_2}\Big) \tag{62}$$

where

$$\begin{aligned} \overline{N_1} =\ & \frac{1}{4}\,\mathrm{Re}\int_0^\infty dz\int_{-\infty}^{\infty}\left[x\bigg(\Big|\frac{\partial\varphi}{\partial x}\Big|^2 + \Big|\frac{\partial\varphi}{\partial z}\Big|^2 - \Big|\frac{\partial\varphi}{\partial y}\Big|^2\bigg) + 2y\frac{\partial\varphi}{\partial x}\frac{\partial\varphi^*}{\partial y}\right]_{-Y}^{Y} dx \\ & -\frac{1}{4}\,\mathrm{Re}\int_{-\infty}^{\infty}\Bigg[x\bigg\{K|\varphi|^2 + \frac{1}{K_0}\Big|\frac{\partial\varphi}{\partial x}\Big|^2 + i2\tau\varphi^*\frac{\partial\varphi}{\partial x}\bigg\}_{z=0} \\ & \qquad +2y\bigg\{\Big(i\tau\varphi^* + \frac{1}{K_0}\frac{\partial\varphi^*}{\partial x}\Big)\frac{\partial\varphi}{\partial y}\bigg\}_{z=0}\Bigg]_{-Y}^{Y} dx \end{aligned} \tag{63}$$

$$\begin{aligned} \overline{N_2} =\ & \frac{1}{2}\,\mathrm{Re}\int_0^\infty dz\int_{-\infty}^{\infty}\Bigg[x\Big(\frac{\partial\varphi}{\partial x}\frac{\partial\varphi_0^*}{\partial x} + \frac{\partial\varphi}{\partial z}\frac{\partial\varphi_0^*}{\partial z} - \frac{\partial\varphi}{\partial y}\frac{\partial\varphi_0^*}{\partial y}\Big) \\ & \qquad +y\Big(\frac{\partial\varphi}{\partial x}\frac{\partial\varphi_0^*}{\partial y} + \frac{\partial\varphi_0^*}{\partial x}\frac{\partial\varphi}{\partial y}\Big)\Bigg]_{-Y}^{Y} dx \\ & -\frac{1}{2}\,\mathrm{Re}\int_{-\infty}^{\infty}\Bigg[x\bigg\{K\varphi\varphi_0^* + \frac{1}{K_0}\frac{\partial\varphi}{\partial x}\frac{\partial\varphi_0^*}{\partial x} + i\tau\Big(\varphi_0^*\frac{\partial\varphi}{\partial x} - \varphi\frac{\partial\varphi_0^*}{\partial x}\Big)\bigg\}_{z=0} \\ & +y\bigg\{i\tau\Big(\varphi_0^*\frac{\partial\varphi}{\partial y} - \varphi\frac{\partial\varphi_0^*}{\partial y}\Big) + \frac{1}{K_0}\Big(\frac{\partial\varphi}{\partial x}\frac{\partial\varphi_0^*}{\partial y} + \frac{\partial\varphi_0^*}{\partial x}\frac{\partial\varphi}{\partial y}\Big)\bigg\}_{z=0}\Bigg]_{-Y}^{Y} dx \end{aligned} \tag{64}$$

In order to apply Parseval's theorem (32) to the x-integration in (63) and (64), the Fourier transform of the derivatives of φ times the coordinate x must be obtained. Considering $x(\partial\varphi/\partial x)$ as an example, it follows from (17) that

$$\begin{aligned} x\frac{\partial\varphi}{\partial x} &= \frac{1}{2\pi}\int_{-\infty}^{\infty}\epsilon_k H^{\pm}(k)\frac{\nu k}{\sqrt{\nu^2-k^2}}\, e^{-\nu z\mp i\epsilon_k y\sqrt{\nu^2-k^2}}\, x\, e^{-ikx}\, dk \\ &= -\frac{i}{2\pi}\int_{-\infty}^{\infty}\frac{d}{dk}\left[\epsilon_k H^{\pm}(k)\frac{\nu k}{\sqrt{\nu^2-k^2}}\, e^{-\nu z\mp i\epsilon_k y\sqrt{\nu^2-k^2}}\right] e^{-ikx}\, dk \end{aligned} \tag{65}$$

Therefore the Fourier transform of the above can be readily found:

$$\begin{aligned} \mathcal{F}\Big\{x\frac{\partial\varphi}{\partial x}\Big\} &= -i\frac{d}{dk}\left[\epsilon_k H^{\pm}(k)\frac{\nu k}{\sqrt{\nu^2-k^2}}\, e^{-\nu z\mp i\epsilon_k y\sqrt{\nu^2-k^2}}\right] \\ &= -i\frac{d}{dk}\Big\{H^{\pm}(k)\Big\}\frac{\epsilon_k\nu k}{\sqrt{\nu^2-k^2}}\, e^{-\nu z\mp i\epsilon_k y\sqrt{\nu^2-k^2}} \\ &\quad -iH^{\pm}(k)\frac{d}{dk}\left\{\frac{\epsilon_k\nu k}{\sqrt{\nu^2-k^2}}\, e^{-\nu z}\right\} e^{\mp i\epsilon_k y\sqrt{\nu^2-k^2}} \\ &\quad \mp H^{\pm}(k)\frac{\nu k(\nu\nu'-k)}{\nu^2-k^2}\, e^{-\nu z}\, y\, e^{\mp i\epsilon_k y\sqrt{\nu^2-k^2}} \end{aligned} \tag{66}$$

where

$$\nu' = \frac{d\nu}{dk} = 2\Big(\tau+\frac{k}{K_0}\Big) \tag{67}$$

Regarding the Fourier transform of $\partial\varphi^*/\partial x$, we have from (17)

$$\mathcal{F}\Big\{\frac{\partial\varphi^*}{\partial x}\Big\} = \big[H^{\pm}(k)\big]^*\frac{\epsilon_k\nu k}{\sqrt{\nu^2-k^2}}\, e^{-\nu z\pm i\epsilon_k y\sqrt{\nu^2-k^2}} \tag{68}$$

Similarly, we can obtain Fourier transforms which are necessary in carrying out the x-integration in (63). According to Parseval's theorem, we must consider the integration of the product of (66) and (68) with respect to k and similar integrations appearing in (63). In carrying out these integrations, we note that the integrand originating from the second term on the right-hand side of (66) is pure imaginary and thus does not contribute to the final result. Furthermore we can confirm that the summation of all the terms linearly proportional to y, including the contribution from the last term in (66), is precisely zero. Concerning the integration with respect to z in (63), eq.(33) can be used.

Summarizing these reductions, we shall get:

$$\overline{N_1} = -\frac{1}{8\pi}\,\mathrm{Im}\int_{-\infty}^{\infty}\left[\frac{d}{dk}\Big\{H^+(k)\Big\}\Big(H^+(k)\Big)^* - \frac{d}{dk}\Big\{H^-(k)\Big\}\Big(H^-(k)\Big)^*\right]\nu\, dk \tag{69}$$

Using (21), this equation can be rewritten in the form

$$\begin{aligned} \overline{N_1} &= \frac{1}{4\pi}\int_{-\infty}^{\infty}\epsilon_k\,\mathrm{Re}\Big\{C'(k)S^*(k)-C^*(k)S'(k)\Big\}\nu\, dk \\ &= \frac{1}{4\pi}\left[-\int_{-\infty}^{k_1}+\int_{k_2}^{k_3}+\int_{k_4}^{\infty}\right]\mathrm{Re}\Big\{C'(k)S^*(k)-C^*(k)S'(k)\Big\}\nu\, dk \end{aligned} \tag{70}$$

Here from (22), $C'(k)$ and $S'(k)$ are explicitly given as

$$\left.\begin{array}{l} C'(k) \\ S'(k) \end{array}\right\} = \iint_{S_H} \left(\frac{\partial \varphi}{\partial n} - \varphi \frac{\partial}{\partial n}\right) e^{-\nu\zeta + ik\xi} \times \left[\left(-\nu'\zeta + i\xi\right) \left\{ \begin{array}{l} \cos\left(\eta\sqrt{\nu^2 - k^2}\right) \\ \sin\left(\eta\sqrt{\nu^2 - k^2}\right) \end{array} \right\} \mp \frac{\nu\nu' - k}{\sqrt{\nu^2 - k^2}} \eta \left\{ \begin{array}{l} \sin\left(\eta\sqrt{\nu^2 - k^2}\right) \\ \cos\left(\eta\sqrt{\nu^2 - k^2}\right) \end{array} \right\} \right] dS \tag{71}$$

It is clear from (70) that only the interactions between symmetric and antisymmetric waves contribute to the $\overline{N_1}$ term, which is the same as the steady sway force.

Next, we consider the second term, $\overline{N_2}$, defined by (64), which originates from the interaction of the incident wave and ship-generated waves. Following the foregoing procedure, the Parseval's theorem (32) will be used in conjunction with the Fourier transforms (20) and (66). Then we can put $k = k_0 \cos\chi$ due to the property of Dirac's delta function in (20) and $k_0 \sin\chi = \epsilon_k \sqrt{\nu^2 - k^2}$ or $k_0 \sin\chi = -\epsilon_k \sqrt{\nu^2 - k^2}$ depending on the value of χ due to the reasons stated in transforming (31); thus the relation $\nu = k_0$ holds.

After the x-integration using Parseval's theorem and the z-integration using

$$\int_0^\infty z\, e^{-2\nu z}\, dz = \left(\frac{1}{2\nu}\right)^2 \tag{72}$$

and (33), the interim result will consist of three parts, just like (66): The first (denoted by $\overline{N_{21}}$) includes the derivative of the Kochin function, the second ($\overline{N_{22}}$) includes the terms linearly proportional to y, and the third ($\overline{N_{23}}$) is the remainder. After somewhat lengthy calculations, these three parts can be found to be:

$$\overline{N_{21}} = -\frac{1}{2} \sin\chi\, \mathrm{Re}\left\{ k_0 \frac{d}{dk}\left[H^{\pm}(k)\right] \right\} \tag{73}$$

$$\overline{N_{22}} = 0 \tag{74}$$

$$\overline{N_{23}} = -\frac{1}{2} \sin\chi\, \mathrm{Re}\left\{ \left(\tau + \frac{k_0 \cos\chi}{K_0}\right) H(k_0, \chi) \right\} \tag{75}$$

Here the quantity in braces in (73) should be evaluated at $k = k_0 \cos\chi$ and $\pm\epsilon_k \sqrt{\nu^2 - k^2} = k_0 \sin\chi$, with the complex sign taken according to $H^+(k)$ or $H^-(k)$, respectively. Therefore, using the relation $k_0 = \nu = (\omega + kU)^2/g$ and notation (21), the final result can be written as

$$\begin{aligned} \overline{N_2} &= \overline{N_{21}} + \overline{N_{22}} + \overline{N_{23}} \\ &= -\frac{1}{2g} \sin\chi\, \mathrm{Re}\left[\left(\omega + kU\right) \frac{d}{dk}\left\{ \left(\omega + kU\right) H^{\pm}(k) \right\} \right]_{\substack{k = k_0 \cos\chi \\ \pm\epsilon_k \sqrt{\nu^2 - k^2} = k_0 \sin\chi}} \qquad (76) \\ &= -\frac{1}{2} \sin\chi\, \mathrm{Re}\left[k_0 \left\{ C'(k_0, \chi) + iS'(k_0, \chi) \right\} + \left(\tau + \frac{k_0 \cos\chi}{K_0}\right) H(k_0, \chi) \right] \qquad (77) \end{aligned}$$

where $C'(k_0, \chi) + iS'(k_0, \chi)$ is to be interpreted as

$$C'(k_0, \chi) + iS'(k_0, \chi) = \left[\frac{d}{dk}\left\{ C(k) + iS(k) \right\} \right]_{\substack{k = k_0 \cos\chi \\ \sqrt{\nu^2 - k^2} = k_0 \sin\chi}}$$

Substituting (70) and (77) into (62), we obtain the formula for the steady yawing moment in waves:

$$\frac{\overline{M_z}}{\rho g a^2} = \frac{1}{4\pi k_0}\left[-\int_{-\infty}^{k_1} + \int_{k_2}^{k_3} + \int_{k_4}^{\infty}\right] \mathrm{Re}\Big\{C'(k)S^*(k) - C^*(k)S'(k)\Big\}\nu\, dk$$
$$-\frac{1}{2}\sin\chi\,\mathrm{Re}\left[C'(k_0,\chi) + iS'(k_0,\chi) + \frac{1}{k_0}\Big(\tau + \frac{k_0\cos\chi}{K_0}\Big)H(k_0,\chi)\right] \tag{78}$$

This is the result obtained for the first time by the present analysis. In the limit of vanishing forward speed, τ and $1/K_0$ are zero from (11), and $k_1 = -\infty$, $k_2 = -K$, $k_3 = K$, $k_4 = \infty$ from (12) and (13). Thus we can confirm that Newman's result[2)] at zero forward speed is recovered from the present result.

6. Concluding Remarks

The formulas obtained in this paper permit us to calculate the second-order sway force and yaw moment, provided that the Kochin function is determined from the velocity potential on the ship hull. Although there are still a number of problems to be resolved for a reliable solution by the three-dimensional panel method, some progress have been made recently in developing a fast algorithm of the Green function with forward speed and sinusoidal oscillation; for instance, Iwashita & Ohkusu[9)]. Therefore it will be possible in the near future to obtain the Kochin function from the "exact" solution of the entire boundary-value problem. However, from the viewpoint of economical computations with relatively good accuracy, the unified slender-ship theory developed by Newman[10)] and Sclavounos[11)] may be the first to be tested for the determination of the Kochin function. The computational work along this line is now in progress, and the results will be presented in the foreseeable future together with experiments to verify a part of them.

Acknowledgments

The author wishes to thank Prof. Makoto Ohkusu of Research Institute for Applied Mechanics, Kyushu University, and Dr. Matao Takagi of Technical Research Institute of Hitachi Shipbuilding & Engineering Co., Ltd., for their invaluable discussions and encouragement.

References

1) Maruo, H.: *The Drift of a Body Floating on Waves*, J. Ship Res., Vol. 4, No. 401, (1960) pp. 1-10

2) Newman, J. N.: *The Drift Force and Moment on Ships in Waves*, J. Ship Res., Vol. 11, No. 1, (1967) pp. 51-60

3) Maruo, H.: *Wave Resistance of a Ship in Regular Head Seas*, Bulletin of the Faculty of Engineering, Yokohama National Univ., Vol. 9, (1960) pp. 73-91

4) Maruo, H.: *Resistance in Waves*; Chapter 5 in Researches on Seakeeping Qualities of Ships in Japan, Soc. Nav. Arch. Japan 60th Anniv. Ser., Vol. 8, (1963) pp. 67-102

5) Proceeding of the 1st Marine Dynamics Symposium; *Ship Motions, Wave Load and Propulsive Performance in a Seaway* (in Japanese), Soc. Nav. Arch. Japan, (1984) pp. 1-189

6) Ogilvie, T. F. and Tuck. E. O.: *A Rational Strip Theory for Ship Motions*, Dep. Nav. Arch. Mar. Eng., Univ. Michigan, Rep. No. 13, (1969) pp. 1-92

7) Imai, I.: *The Theory of Hyperfunction and Its Applications*(in Japanese), Science Inc., Japan, (1981) Vol. 1, pp. 61

8) Hanaoka, T.: *Hydrodynamical Investigation Concerning Ship Motions in Regular Waves* (in Japanese), Doctoral Thesis, Kyushu Univ., (1957)

9) Iwashita, H. and Ohkusu, M.: *Hydrodynamic Forces on a Ship Moving with Forward Speed in Waves*, J. Soc. Nav. Arch. Japan, Vol. 166, (1989) pp. 187-205

10) Newman, J. N.: *The Theory of Ship Motions*, Adv. Appl. Mech., Vol. 18,(1978) pp. 221-283

11) Sclavounos, P. D.: *The Diffraction of Free Surface Waves*, J. Ship Res., Vol. 28, No. 1, (1984) pp. 29-47

Prediction of Surge and Its Effect on Added Resistance by Means of the Enhanced Unified Theory*

Masashi KASHIWAGI
Research Institute for Applied Mechanics, Kyushu University
Kasuga, Fukuoka 816-8580, Japan

Summary

The unified theory is enhanced to account for the wave diffraction in the direction of ship's longitudinal axis near the ship ends and to solve the surge-mode radiation problem. Three-dimensional and forward-speed effects are taken into account as in the original unified theory, by solving the integral equation for the outer source strength along the ship length. Numerical examples are shown for the surge added-mass and damping coefficients, pressure distributions, wave-exciting forces, and added resistance in head waves; these are compared with experimental data and corresponding results of other calculation methods.
It is confirmed that the effects of wave diffraction near the ship ends are properly accounted for in the present method, which is pronounced in the prediction of the added resistance. The importance of the cross-coupling effects between surge and pitch is also noted in the surge motion calculations.

1. Introduction

Because of numerical simplicity and relatively nice agreement with measurements, the strip theory has been used for predicting the wave-induced motions and the seakeeping performance of ships. However it is also recognized that the strip theory is unable to account for 3-D effects; such as the wave attenuation along the ship, the wave diffraction near the bow, and the change of wave patterns with increasing forward speed. In the 1970s, the slender-ship theories had been developed with the aim of overcoming these defects of the strip theory. As one of the excellent developments, we can name the unified theory which was proposed by Newman [1] and extended by Sclavounos [2] to the diffraction problem and by Kashiwagi & Ohkusu [3] to the tank-wall interference problem. The unified theory bring in a certain amount of 3-D corrections to the 2-D strip-theory solution. In fact, very impressive agreement with experimental values was found in the heave and pitch related problems [4, 5].

However, it is said that the surge motion and the wave diffraction in the ship's longitudinal axis cannot be analyzed by means of the slender-ship theory. From this reasoning, a number of correction methods in the short-wavelength region have been proposed in the prediction of the added resistance, by Takahashi [6], Faltinsen [7], Sakamoto & Baba [8], and Ohkusu [9]. In the context of strip theories, the analysis of surge motion has been made as an independent single mode, with only the Froude-Krylov force and ship's mass taken into account.

Of course if we use a fully 3-D calculation method, hydrodynamic forces associated with the surge mode can be computed in the same manner as other modes of motion. With

* *Reprinted from Transactions of West-Japan Society of Naval Architects, No. 89, pp. 77-89, 1995 (March)*

advance of the computer performance, 3-D calculation methods have been recently studied [10, 11, 12] as an alternative of the slender-ship theory. At present, however, these are still several difficulties to be resolved to enhance the reliability of the method, particularly when the forward speed is present.

Computations of the surge-mode radiation problem and of the wave diffraction near the bow and stern are related to the x-component of normal vector in the body boundary condition; which is regarded as higher order in the slender-ship theory and not easy to compute in comparison with the y- and z-components. In practice, once the x-component of the normal is given, the strip-theory concept can be applied to the surge radiation problem, and 3-D corrections must be computed by means of Newman's unified theory in the same fashion as for the heave and pitch modes. The same is true of the diffraction problem including the wave scattering in the direction of ship's longitudinal axis.

This paper demonstrates the applicability of the unified theory to the surge related problems, and numerical results are presented for the surge added-mass and damping coefficients, the pressure distribution, the wave-exciting force and moment, and the added resistance in head waves. Comparison with other calculation methods and experimental data confirms the validity and excellent performance of the present method.

2. Calculation Method

Consider a ship advancing with constant speed U and undergoing small-amplitude motions of angular frequency ω in deep water. A steady reference frame is chosen with the x-axis pointing in the direction of the forward motion and the z-axis pointing downward. As shown in Fig. 1, the plane progressive wave is incident upon the ship with angle of incidence χ.

Assuming inviscid flow with irrotational motion, the velocity potential is expressed as

$$\Phi = -Ux + \mathrm{Re}\left[\,\phi(x,y,z)\,e^{i\omega t}\right] \tag{1}$$

$$\phi = \frac{ga}{i\omega_0}\Big\{\phi_0(x,y,z) + \phi_7(x,y,z)\Big\} + i\omega\sum_{j=1}^{6} X_j\,\phi_j(x,y,z) \tag{2}$$

$$\varphi_0 = \exp\big\{-k_0 z - ik_0(x\cos\chi + y\sin\chi)\big\} \tag{3}$$

$$\omega = \omega_0 - k_0 U\cos\chi, \quad k_0 = \omega_0^2/g \tag{4}$$

Here ϕ_0 denotes the incident-wave potential, ϕ_7 the scattered potential, and ϕ_j the radiation potential of the j-th mode with complex amplitude X_j, where in particular $j=1$ for surge, $j=3$ for heave, and $j=5$ for pitch; a, ω_0, k_0 denote the amplitude, circular frequency, wavenumber of the incident wave; g the acceleration of gravity. For simplicity, the disturbance due to the steady forward motion is neglected in (1).

Hereafter we will consider only the symmetric modes, $j = 1, 3, 5$, in the radiation problem and the symmetric component of the diffraction problem. The theory used here is an extension of the unified theory;

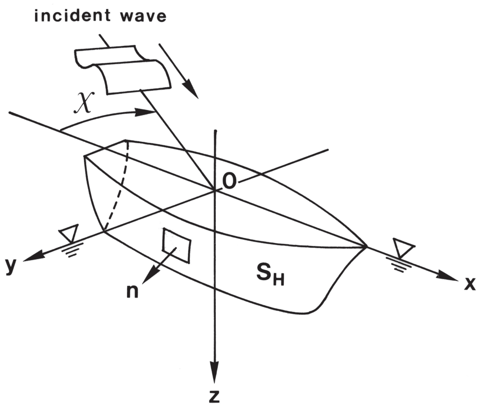

Fig. 1 Coordinate system

for the detailed description of the unified theory, the readers should refer to published references, e.g. [1]$\sim$[5].

2.1 The radiation problem

As in Newman's unified theory [1], the velocity potentials in the inner region satisfy

$$\frac{\partial^2 \phi_j}{\partial y^2} + \frac{\partial^2 \phi_j}{\partial z^2} = 0 \tag{5}$$

$$\frac{\partial \phi_j}{\partial z} + K\,\phi_j = 0 \quad \text{on } z = 0 \tag{6}$$

where $K = \omega^2/g$.

On the other hand, the body boundary condition takes the form

$$\frac{\partial \phi_j}{\partial n} = n_j + \frac{U}{i\omega} m_j \quad (j = 1, 3, 5) \quad \text{on } S_H \tag{7}$$

where S_H denotes the ship-hull surface, n_j denotes the j-th component of unit normal outward to the hull, and $m_1 = m_3 = 0$, $m_5 = n_3$, and $n_5 = -x n_3$.

With the slenderness assumption, (7) implies that the surge potential is of higher order. However, this should not be a reason to deduce that computations of the surge mode are impossible. In fact, the surge mode is of the same order as the roll mode whose computations are commonly in the strip method.

The general inner solution satisfying (5)$-$(7) can be given in the form

$$\phi_j(x; y, z) = \varphi_j(y, z) + \frac{U}{i\omega} \widehat{\varphi}_j(y, z) + C_j(x) \Big\{ \varphi_3(y, z) - \varphi_3^*(y, z) \Big\} \tag{8}$$

where the asterisk denotes the complex conjugate. Thus the function in braces is a homogeneous solution, and $C_j(x)$ is its unknown coefficient. In accordance with approximations for the m_j-term, we have $\widehat{\varphi}_1 = \widehat{\varphi}_3 = 0$, $\widehat{\varphi}_5 = \varphi_3$, and $\varphi_5 = -x\varphi_3$.

The unknown $C_j(x)$ can be determined by requiring (8) to be matched with the outer solution which includes another unknown $Q_j(x)$: the 3-D source strength along the x-axis. The matching procedure gives the following results:

$$Q_j(x) + \frac{i}{2\pi} \Big(\frac{\sigma_3}{\sigma_3^*} - 1 \Big) \int_L Q_j(\xi) \frac{d}{d\xi} F(x - \xi)\, d\xi = \sigma_j + \frac{U}{i\omega} \widehat{\sigma}_j \tag{9}$$

$$C_j(x) \big\{ \sigma_3 - \sigma_3^* \big\} = Q_j(x) - \Big\{ \sigma_j + \frac{U}{i\omega} \widehat{\sigma}_j \Big\} \tag{10}$$

where σ_j and $\widehat{\sigma}_j$ are 2-D Kochin function associated with the velocity potentials φ_j and $\widehat{\varphi}_j$, respectively. The kernel function $F(x - \xi)$ is identical to that used in Newman & Sclavounos [4], which includes the 3-D corrections and forward-speed effects.

After solving the integral equation (9) for $Q_j(x)$, the coefficient of inner homogeneous solution $C_j(x)$ can be readily obtained from (10), thereby completing the inner solution which will be used for computing the added-mass and damping coefficients.

2.2 The diffraction problem

The symmetric part of the body boundary condition on S_H, corresponding to (7) in the radiation problem, is written as

$$\frac{\partial \phi_7^S}{\partial n} = k_0\, e^{-k_0 z} \big\{ n_2 \sin\chi \sin(k_0 y \sin\chi) + (n_3 + i n_1 \cos\chi) \cos(k_0 y \sin\chi) \big\}\, e^{i\ell x} \tag{11}$$

where $\ell = -k_0 \cos\chi$.

In conventional slender-body theories, the x-component of the normal, n_1, may be discarded as higher order by comparison to n_2 and n_3. However once the values of n_1 along the sectional contour are given, no difficulty exists in solving the boundary-value problem with n_1 kept in (11). In fact, this n_1 term is expected to be more crucial than the n_2- and n_3-terms near the ship ends, contributing significantly to the surge exciting force and the added resistance in head waves.

Following the unified theory, we seek the inner solution in the form:

$$\phi_7^S = \psi_7(x; y, z)\, e^{i\ell x} \tag{12}$$

The governing equation and the free-surface and body boundary conditions for the slowly-varying part ψ_7 are given as

$$\frac{\partial^2 \psi_7}{\partial y^2} + \frac{\partial^2 \psi_7}{\partial z^2} - \ell^2 \psi_7 = 0 \tag{13}$$

$$\frac{\partial \psi_7}{\partial z} + k_0 \psi_7 = 0 \quad \text{on } z = 0 \tag{14}$$

$$\frac{\partial \psi_7}{\partial n} = k_0\, e^{-k_0 z}\big\{ n_2 \sin\chi \sin(k_0 y \sin\chi) + (n_3 + i n_1 \cos\chi)\cos(k_0 y \sin\chi)\big\} \tag{15}$$

The numerical procedure of solving the above problem can be identical to that described in Kashiwagi [13], with n_3 replaced by $n_3 + i n_1 \cos\chi$. Then the inner solution can be constructed in the form

$$\begin{aligned} \phi_7^S(x; y, z) = &- e^{-k_0 z + i\ell x} \cos(k_0 y \sin\chi) \\ &+ C_7(x) \Big\{ \psi_7^S(y, z) + e^{-k_0 z} \cos(k_0 y \sin\chi) \Big\}\, e^{i\ell x} \end{aligned} \tag{16}$$

Here the second line on the right-hand side is a homogeneous solution, in which $\psi_7^S(y, z)$ denotes a numerical solution satisfying (13)$-$(15); this solution may be obtained using 2-D boundary element method.

The coefficient $C_7(x)$ in (16) is unknown, which can be determined after solving the integral equation for the outer source strength $Q_7(x)$. The equations corresponding to (9) and (10) in the radiation problem are of the form

$$Q_7(x) + \frac{1}{\pi}\sigma_7 \Big\{ Q_7(x)\, h_1(\chi) - \int_L Q_7(\xi)\, \frac{d}{d\xi} F(x - \xi)\, d\xi \Big\} = \sigma_7\, e^{i\ell x} \tag{17}$$

$$C_7(x)\, \sigma_7\, e^{i\ell x} = Q_7(x) \tag{18}$$

where
$$h_1(\chi) = \csc\chi \cosh^{-1}(|\sec\chi|) - \ln(2|\sec\chi|) \tag{19}$$

The kernel function $F(x - \xi)$ in (17) is identical to that appearing in (9), and σ_7 is the 2-D Kochin function to be explicitly obtained from $\psi_7^S(y, z)$.

2.3 Hydrodynamic forces

Added-mass and damping coefficients

Substituting the completed inner solution (8) into the linearized Bernoulli's equation, integrating over the mean wetted surface of the ship, and using Tuck's theorem, the hydrodynamic force acting in the i-th direction can be expressed as

$$F_i = -(i\omega)^2 \sum_{j=1,3,5} \Big[A_{ij} + \frac{1}{i\omega} B_{ij} \Big] X_j \tag{20}$$

$$\begin{aligned} A_{ij} + \frac{1}{i\omega} B_{ij} = &- \rho \int_L dx \int_{C_H} \Big(n_i - \frac{U}{i\omega} m_i \Big) \Big\{ \varphi_j + \frac{U}{i\omega}\, \widehat{\varphi}_j \Big\}\, ds \\ &- \rho \int_L dx\, C_j(x) \int_{C_H} \Big(n_i - \frac{U}{i\omega} m_i \Big) \big\{ \varphi_3 - \varphi_3^* \big\}\, ds \end{aligned} \tag{21}$$

where A_{ij} and B_{ij} are the added-mass and damping coefficients in the i-th direction due to the j-th mode of motion, and C_H denotes the sectional contour below the free surface at station x. As noted before, neglecting the steady disturbances generated by the steady forward motion gives the following approximations:

$$\left. \begin{array}{lll} m_1 = m_3 = 0, & m_5 = n_3\,, & n_5 = -x n_3 \\ \widehat{\varphi}_1 = \widehat{\varphi}_3 = 0, & \widehat{\varphi}_5 = \varphi_3\,, & \varphi_5 = -x \varphi_3 \end{array} \right\} \tag{22}$$

It is noteworthy that the first line in (21) gives identical results to the strip theory except for the surge related coefficients, and that the cross-coupling coefficients between surge and pitch are nontrivial even for a longitudinally symmetric ship with zero forward speed. The second line in (21) contains the 3-D corrections and forward-speed effects, which is of great importance in the unified theory.

Diffraction pressure and wave-exciting forces

In the diffraction problem, the hydrodynamic pressure is given from the sum of the incident-wave and scattered potentials. Therefore, the symmetric part of the diffraction pressure can be expressed as

$$\begin{aligned} P_d &= -\rho g a \frac{\omega}{\omega_0} \Big(1 - \frac{U}{i\omega} \frac{\partial}{\partial x} \Big) \big\{ \phi_0^S + \phi_7^S \big\} \\ &= -\rho g a C_7(x) \Big\{ \psi_7^S(y,z) + e^{-k_0 z} \cos(k_0 y \sin\chi) \Big\}\, e^{i\ell x} \end{aligned} \tag{23}$$

Here the approximation has been used that the x-derivative of the slowly varying part of the diffraction potential is small relative to the x-derivative of $\exp(i\ell x)$.

Integrating (23) over the ship hull gives the expression of the wave-exciting force acting in the jj-th direction:

$$E_j = \rho g a \int_L dx\, C_7(x)\, e^{i\ell x} \int_{C_H} n_j \Big\{ \psi_7^S(y,z) + e^{-k_0 z} \cos(k_0 y \sin\chi) \Big\}\, ds \tag{24}$$

At this point, let us consider the corresponding expression of the pressure in strip theories. There are a number of slight differences among researchers [14] in the free-surface condition and in the treatment of the body boundary condition and the x-derivative of the velocity potential, which makes it difficult to write in a decisive form. In the so-called NSM (New Strip Method), the body boundary condition is approximated using the relative-motion hypothesis, with the result

$$\frac{\partial \phi_7^S}{\partial n} \simeq n_3 k_0\, e^{-k_0 Z_s + i\ell x} \tag{25}$$

where Z_s is called the sub-surface given by $A(x)/B(x)$, with $A(x)$ and $B(x)$ the sectional area and breadth, respectively.

Since the free-surface condition for the diffraction problem is not (14) but (6), the above body boundary condition (25) implies that ϕ_7^S can be expressed in terms of the heave radiation potential, $\varphi_3(y,z)$. Therefore the total diffraction pressure by NSM is given as

$$P_d = -\rho g a \Big\{ \varphi_3(y,z)\, k_0 e^{-k_0 Z_s} + e^{-k_0 z} \cos(k_0 y \sin\chi) \Big\}\, e^{i\ell x} \tag{26}$$

It should be noted that the x-derivative of the slowly-varying part is neglected as in the unified-theory expression (23), but in deriving the expression of the pitch exciting moment, NSM employs the partial differentiation to cope with the x-derivative of the velocity potential.

2.4 Ship motion equations

Having completed the hydrodynamic forces, the surge, heave, and pitch motions can be easily obtained as the solution of the following complex linear system:

$$\sum_{j=1,3,5} \Big[-\omega^2 \big(M_{ij} + A_{ij} \big) + i\omega B_{ij} + C_{ij} \Big] X_j = E_i \quad \text{for } i = 1,3,5 \tag{27}$$

where M_{ij} denotes the generalized mass matrix and C_{ij} the restoring coefficients; these are evaluated independent of the hydrodynamic analysis, and nonzero terms among these are

$$\left. \begin{aligned} & M_{11} = M_{22} = \rho\nabla,\ M_{55} = I_{yy} \\ & C_{33} = \rho g A_W,\ C_{35} = C_{53} = -\rho g A_W x_W,\ C_{55} = \rho g \nabla \overline{GM}_L \end{aligned} \right\} \tag{28}$$

Here ∇ is the displaced volume, I_{yy} the moment of inertia about the y-axis, A_W the waterplane area, x_W the center of the waterplane area, and $\overline{GM}_L$ the longitudinal metacentric height.

In the conventional strip theories, the surge mode is treated as independent single mode. However, as will be shown later, the cross-coupling terms between surge and pitch play an important role in the precise prediction of the surge motion, and likewise the pitch motion may be slightly influenced by these coupling terms.

2.5 Added resistance and Kochin function

The added resistance is calculated from Maruo's formula [15]:

$$\frac{R_{AW}}{\rho g a^2} = \frac{1}{4\pi k_0} \left[-\int_{-\infty}^{k_1} + \int_{k_2}^{k_3} + \int_{k_4}^{\infty} \right] \Big\{ \big| C(k) \big|^2 + \big| S(k) \big|^2 \Big\} \frac{\nu(k)\{k - k_0 \cos\chi\}}{\sqrt{\nu^2(k) - k^2}}\, dk \tag{29}$$

where

$$\nu(k) = \frac{(\omega + kU)^2}{g} = K + 2\tau k + \frac{k^2}{K_0} \tag{30}$$

$$\left. \begin{matrix} k_1 \\ k_2 \end{matrix} \right\} = -\frac{K_0}{2}\big(1 + 2\tau \pm \sqrt{1+4\tau}\big),\quad \left. \begin{matrix} k_3 \\ k_4 \end{matrix} \right\} = \frac{K_0}{2}\big(1 - 2\tau \mp \sqrt{1-4\tau}\big) \tag{31}$$

$$K = \frac{\omega^2}{g},\ \tau = \frac{U\omega}{g},\ K_0 = \frac{g}{U^2} \tag{32}$$

Here $C(k)$ and $S(k)$ denote the symmetric and antisymmetric parts of the Kochin function respectively, which are given in a form of the linear superposition:

$$\left.\begin{aligned} C(k) &= C_7(k) - \frac{\omega\omega_0}{g} \sum_{j=1,3,5} \frac{X_j}{a} C_j(k) \\ S(k) &= S_7(k) - \frac{\omega\omega_0}{g} \sum_{j=1,3,5} \frac{X_j}{a} S_j(k) \end{aligned}\right\} \tag{33}$$

The solution method for the antisymmetric velocity potentials are not described in this paper, but in principle similar techniques to the symmetric problem can be applied. Needless to say, the added resistance in head or following waves can be computed using the symmetric Kochin function only, which is given by means of the outer source strength in the theory, in the form

$$C_j(k) = \int_L Q_j(x)\, e^{ikx}\, dx \tag{34}$$

There are a couple of things to be noted here. First, unlike the conventional prediction methods based on the strip theory, the line distribution of outer sources is placed on $z = 0$. However no difficulty arises in evaluating the infinite integrals in (29), by use of the semi-analytical method described in Kashiwagi [13]. Second, an important difference between the present and original unified theories exists in the diffraction Kochin function $C_7(k)$. Namely, the present method contains the effects of wave diffraction in the x-direction near the bow; the absence of which has been pointed out as an essential defect of the slender-ship theory. Lastly, the present method also stands out in that it contains the surge motion and its indirect effects on the heave and pitch motions through the cross-coupling terms in the motion equations.

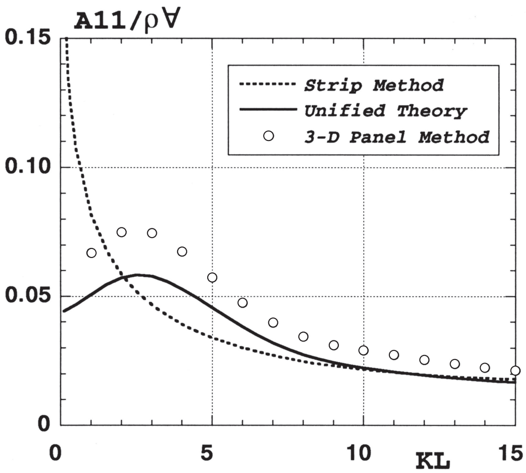

Fig. 2 Surge added-mass coefficient of a half-immersed spheroid of $B/L = 1/5$ at $U = 0$

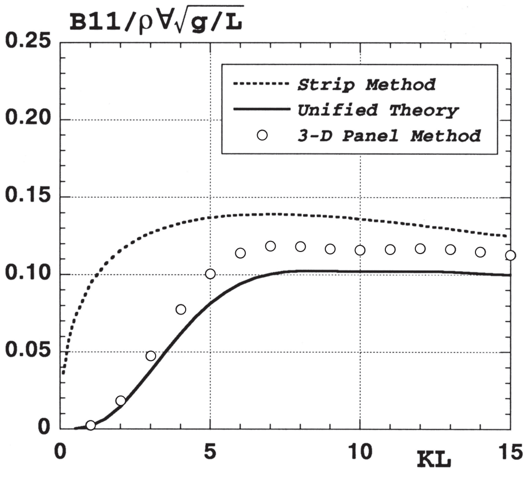

Fig. 3 Surge damping coefficient of a half-immersed spheroid of $B/L = 1/5$ at $U = 0$

3. Numerical Results and Discussion

3.1 Zero speed case

To confirm the performance of the present method, computations were firstly carried out for a half-immersed prolate spheroid of beam-length ratio 1/5 at zero forward speed.

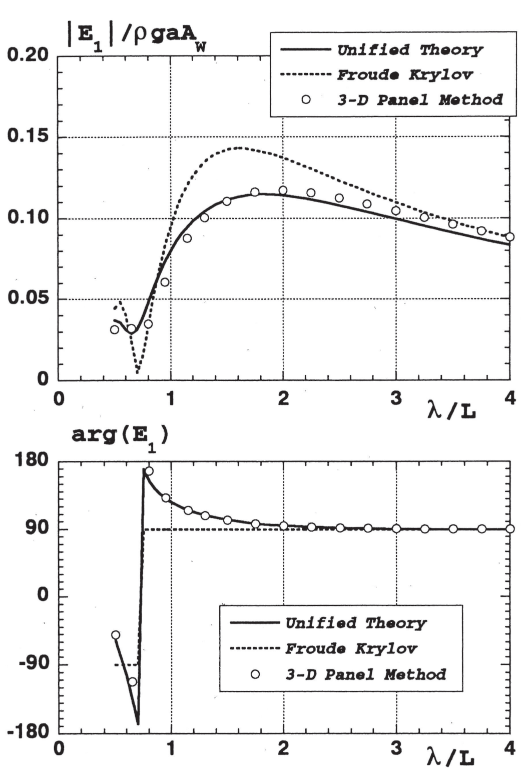

Fig. 4 Wave-exciting surge force on a half-immersed spheroid of $B/L = 1/5$ in head waves at $U = 0$

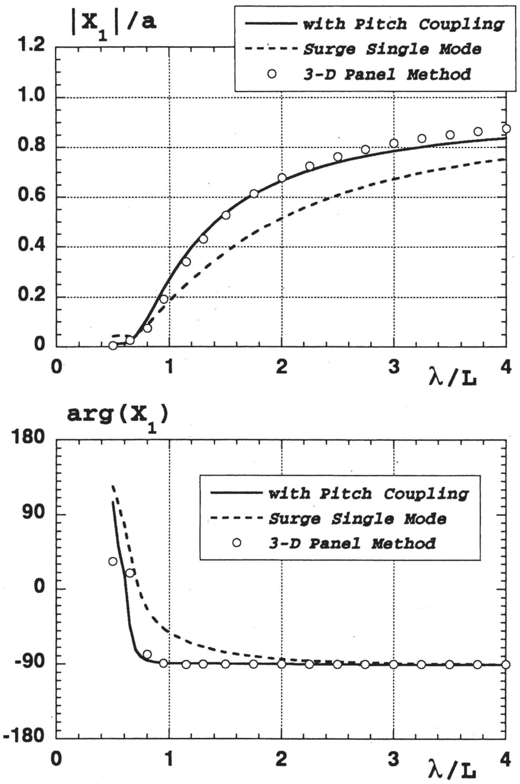

Fig. 5 Surge motion of a half-immersed spheroid of $B/L = 1/5$ in head waves at $U = 0$

Computed added-mass and damping coefficients in surge mode are shown in Figs. 2 and 3. The strip theory and more rigorous 3-D panel method were also applied for comparison. In general, surge related computations are not included in the strip method, but here 'the strip method' in the legend means the results computed with 2-D inner particular solution in the unified theory. Although the unified-theory results are slightly smaller than the results of the 3-D panel method, it appears that the 3-D effects in lower frequencies are properly accounted for.

Figure 4 shows the wave-exciting surge force in head wave ($\chi = 180°$). In this case, as shown in (13), the governing equation of the inner scattered potential is different from Laplace's equation in strip theories. Thus instead of the strip-theory results, the component of Froude-Krylov force is shown by the dotted line. The present method agrees excellently with the 3-D panel method, which must be attributed to the inclusion of n1 in the body boundary condition.

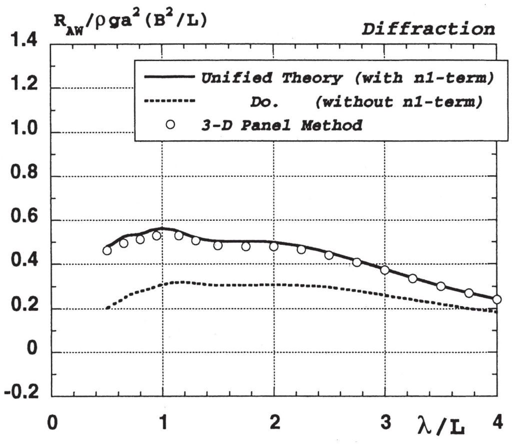

Fig. 6 Drift force on a fixed half-immersed spheroid of $B/L = 1/5$ in head waves at $U = 0$ (diffraction only)

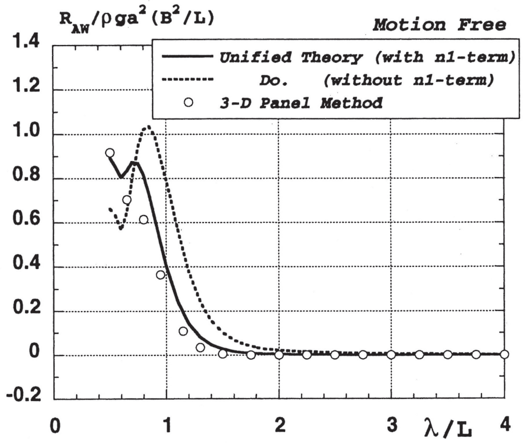

Fig. 7 Drift force on a freely oscillating half-immersed spheroid of $B/L = 1/5$ in head waves at $U = 0$

Computed results of the surge motion in head wave are shown in Fig. 5. The center of gravity is assumed at the origin of the coordinate system. The solid line indicates the present-theory results, obtained from the coupled motion equations expressed by (27); these are in good agreement with the results of 3-D panel method. On the other hand, the dashed line indicates the solution as the single mode of surge motion, using the numerical results shown in Fig. 4. The discrepancy between the dashed and solid lines implies that the cross coupling between surge and pitch must be taken into account. (In the present case the heave mode is not coupled, because of longitudinal symmetry of the body and zero forward speed.)

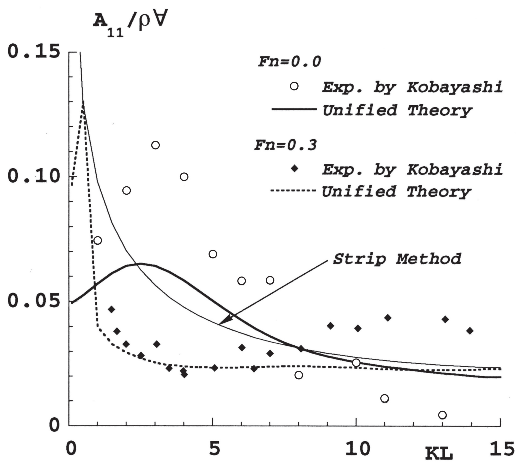

Fig. 8 Surge added-mass coefficient of a half-immersed ellipsoid ($B/L = 1/4$, $B/2d = 5/4$) at $Fn = 0$ and 0.3

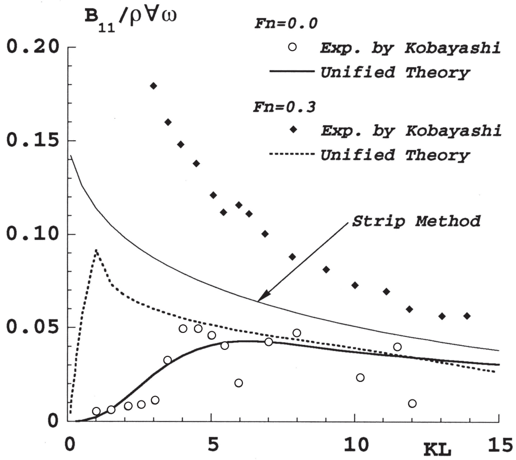

Fig. 9 Surge damping coefficient of a half-immersed ellipsoid ($B/L = 1/4$, $B/2d = 5/4$) at $Fn = 0$ and 0.3

We can expect that including n_1 in the body boundary condition will be pronounced in the drift force acting in the x-direction due to head waves. (At zero speed, the term 'drift force' is preferable to the added resistance.) Fig. 6 shows the results exerted by the wave diffraction only, and Fig. 7 is the results including all the ship motion effects. In Fig. 6, the solid line demonstrates the results in which the contribution of n_1 is taken into account when solving the diffraction problem. Compared with the 3-D panel method, the solid line is superior to the dotted line, confirming the usefulness of the present calculation method.

3.2 Forward speed case

In this case, predictions were compared with experimental data shown in published papers [12, 16]. Main comparisons are made for a half-immersed ellipsoid which was used in the extensive experiments by Kobayashi [16] and expressed mathematically as

$$\left(\frac{x}{L/2}\right)^2 + \left(\frac{y}{B/2}\right)^2 + \left(\frac{z}{d}\right)^2 = 1 \qquad (35)$$

where $L = 2.5\,\mathrm{m}$, $B = 0.625\,\mathrm{m}$, and $d = 0.25\,\mathrm{m}$. Note that the beam-length ratio of this model is $B/L = 1/4$; this is blunt considering the slenderness assumption of the present theory.

Figures 8 and 9 show the surge added-mass and damping coefficients, where both results of Froude number $Fn = 0.0$ and 0.3 are included. Experimental values at $Fn = 0.0$ are scattered owing to the tank-wall interference. Furthermore according to Koyabashi's remarks [16], measured values of the damping coefficient at $Fn = 0.3$ might be devoid of the quantitative precision. With these experimental problems taken into consideration, the present method is able to account for the forward-speed effects, providing much better results than the 3-D Rankine source method shown in Takagi [11]. The thin solid line, depicted as the strip theory, is the results of the inner particular solution, which is independent of the forward speed. Therefore it should be noted that all the forward-speed effects are introduced through the coefficient of homogeneous inner solution.

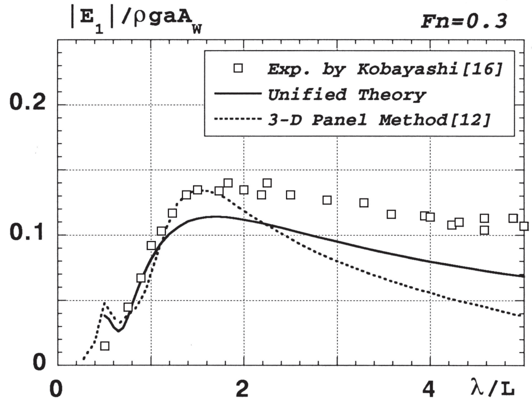

Fig. 10 Wave-exciting surge force of a half-immersed ellipsoid ($B/L = 1/4$, $B/2d = 5/4$) in head waves at $Fn = 0.3$

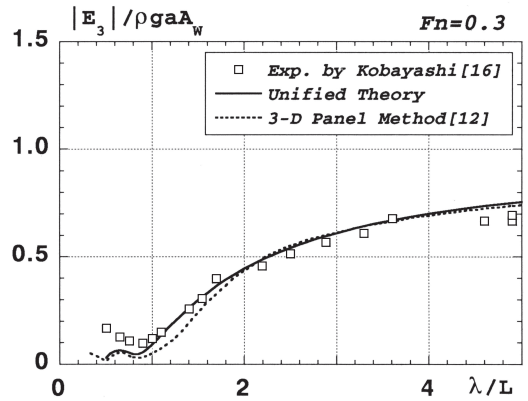

Fig. 11 Wave-exciting heave force of a half-immersed ellipsoid ($B/L = 1/4$, $B/2d = 5/4$) in head waves at $Fn = 0.3$

Figures 10, 11, and 12 compare the wave-exciting surge force, heave force, and pitch moment, respectively. Experimental data measured at $Fn = 0.3$ are used for comparison. Lin *et al.* [12] performed full 3-D computations for Kobayashi's ellipsoid model and compared with the same experimental data; hence their results shown as the 3-D panel method are reproduced in Figs. 10 to 12 with dotted lines. The present method underpredicts the surge exciting force, but accounts well for the qualitative tendency as compared to the 3-D panel method.

On the other hand, the heave exciting force and pitch exciting moment predicted by the present method are in excellent agreement with experiments. Since the scattered potential in the inner solution is determined with the n_1-term retained in the body boundary condition, the heave force and pitch moment are, to some extent, different from the results of the original unified theory.

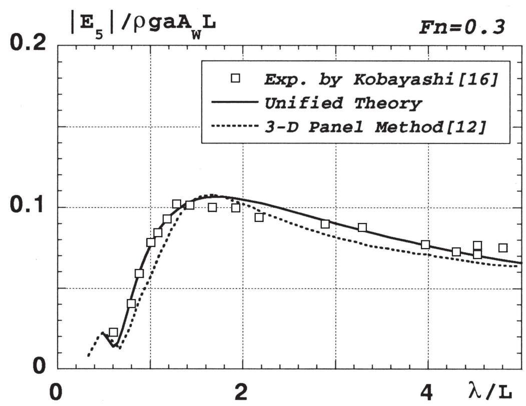

Fig. 12 Wave-exciting pitch moment of a half-immersed ellipsoid ($B/L = 1/4$, $B/2d = 5/4$) in head waves at $Fn = 0.3$

The effect of retaining the n_1-term will be made clear by Fig. 13, which shows hydrodynamic pressure distributions in the head-sea diffraction problem of $\lambda/L = 1.0$, measured at two Froude numbers ($Fn = 0.1$ and 0.3) and

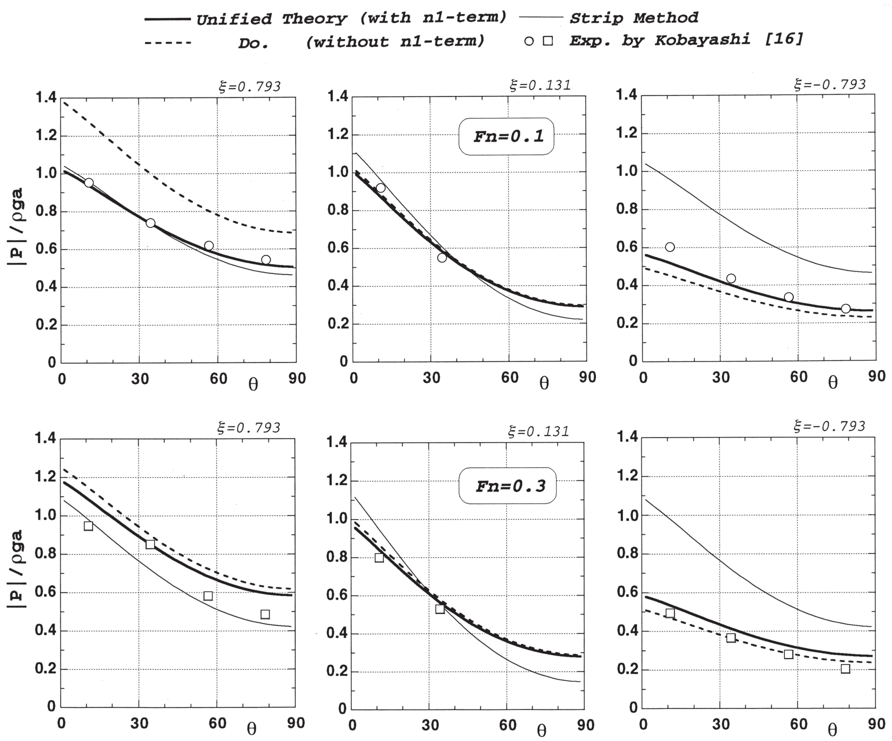

Fig. 13 Hydrodynamic pressure distributions on a half-immersed ellipsoid in head waves of $\lambda/L = 1.0$, measured at three sections ($x/(L/2) = 0.793, 0.131, -0.793$) and at $Fn = 0.1$ and 0.3 (diffraction problem)

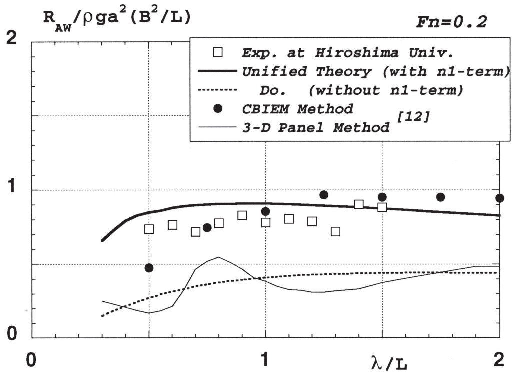

Fig. 14 Added resistance on a half-immersed spheroid of $B/L = 1/5$ in head waves at $Fn = 0.2$ (diffraction problem)

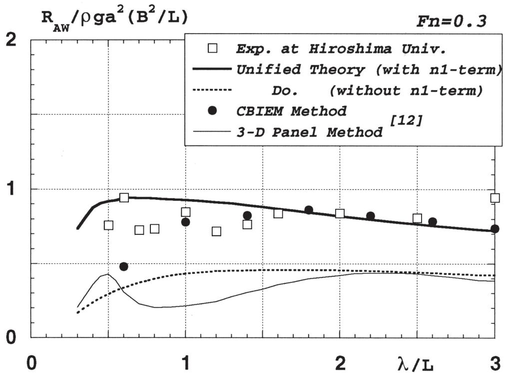

Fig. 15 Added resistance on a half-immersed spheroid of $B/L = 1/5$ in head waves at $Fn = 0.3$ (diffraction problem)

at three different transverse sections ($x/(L/2) \equiv \xi = 0.793$, 0.131, -0.793). The section at $\xi = 0.793$ is near the bow, and $\theta = 90°$ in the abscissa means the center of the section. The thick solid line shows the present results with n_1-term taken into account, and the dotted line the results of ordinary unified theory.

The strip theory does not contain the 3-D effects of wave attenuation along the ship, resulting in the same pressure distribution at $\xi = 0.793$ and $\xi = -0.793$. In contrast, the unified theory accounts for 3-D effects and the agreement with measured values is favorable. At $Fn = 0.1$ in particular, the results of taking the n_1-term into account show a sizable improvement over the results of not taking the n_1-term into account.

Comparison of the added resistance in the head-sea diffraction problem is shown in Figs. 14 and 15. The ship model is a prolate spheroid of beam-length ratio $B/L = 1/5$, and experimental data for this model were obtained at Hiroshima University using Ohkusu's theory of the unsteady wave-pattern analysis [17]. Lin *et al.* [12] computed the added resistance using the combined boundary integral equation method (CBIEM) and the 3-D panel method with forward speed; the results of which are reproduced in Figs. 14 and 15.

The present-method results are shown by the thick solid line, which include contributions of the n_1-term. The dotted line is the results of the ordinary unified theory neglecting the n_1 shorter wavelength region.

The difference between the dotted and thick solid lines implies that the wave diffraction in the x-axis near the bow is of great importance. The deficiency of slender-ship theories, unable to take account of the bow wave diffraction, has been pointed out so far and this is why we are using Takahashi's pragmatic correction method [6] or other theories to be applied in the range of short wavelengths. However we can say that by adopting the calculation method proposed in this paper, there is no need to employ a correction method in the prediction of the added resistance.

4. Concluding Remarks

It has been said so far that the slender-ship theory cannot cope with the wave diffraction in the x-axis from the bow and stern, and thus a reliable 3-D method should be awaited.

An important outcome in this paper is that the unified theory can be easily modified to include contributions of the x-component of normal vector, which explains physically the wave diffraction near the ship ends, and provides a remarkable improvement in the pressure distribution and the added resistance in head waves. One additional burden in the practical stage of numerical computations might be evaluating the x-component of normal vector. But with the level of recent computers, we believe that it is not that fatal.

Another outcome worth nothing is that the level of the surge-motion calculation was enhanced in the framework of the unified theory. It will be common that the symmetric motions are computed from the coupled motion equations of surge, heave, and pitch. In particular, the surge-pitch coupling effects are important and should be taken into account.

Finally, all the numerical computations in this paper have been carried out with the workstation of HP9000-735 in the Section of Ocean Systems Engineering, Research Institute for Applied Mechanics.

References

[1] Newman, J. N. : The theory of Ship Motions, Adv. Appl. Mech., Vol. 18, (1978), pp. 221-283

[2] Sclavounos, P.,D. : The Diffraction of Free-Surface Waves by a Slender Ship, J. Ship Res., Vol. 28, No. 1, (1984), pp. 29-47

[3] Kashiwagi, M. and Ohkusu, M. : A New Theory for Side-Wall Interference Effects on Forward-Speed Radiation and Diffraction Forces, Ship Technology Res., Vol. 38, No, 1, (1991), pp. 17-47

[4] Newman, J. N. and Sclavounos, P. D. : The Unified Theory of Ship Motions, Proc. 13th Symp. on Nav. Hydrodyn. Tokyo, (1980), pp. 373-394

[5] Sclavounos, P. D. : The Unified Slender-Body Theory: Ship Motions in Waves, Proc. 15th Symp. on Naval Hydrodyn. Hamburg, (1985), pp. 177-192

[6] Takahashi, T. : A Practical Prediction Method of Added Resistance of a Ship in Waves and the Direction of Its Application to Hull Form Design, Trans. of West-Japan Soc. Nav. Arch., No. 75, (1988), pp. 75-95

[7] Faltinsen, O. M., Minsaas, K. J., Liapis, N. and Skjordal, S. O. : Prediction of Resistance and Propulsion of a Ship in a Seaway, Proc. 13th Symp. on Nav. Hydrodyn. Tokyo, (1980), pp. 505-523

[8] Sakamoto, T. and Baba, E. : Minimization of Resistance of Slowly Moving Full Hull Forms in Short Waves, Proc. 16th Symp. on Nav. Hydrodyn. Berkeley, (1986)

[9] Ohkusu, M. : Added Resistance of Blunt Bow Ships in Very Short Waves, J. Kansai Soc. Nav. Arch. Japan, No. 202, pp. 39-42

[10] Iwashita, H., Ito, A. et al. : Wave Forces Acting on a Blunt Ship with Forward Speed in Oblique Sea, J. Soc. Nav. Arch. Japan, Vol. 171, (1992), pp. 109-123

[11] Takagi, K. : Calculation of Unsteady Pressure by Rankine Source Method, J. Kansai Soc. Nav. Arch. Japan, No. 219, (1993), pp. 47-56

[12] Lin, X., Takaki, M. and Iwashita, H. : Effects of the Steady Disturbance on the Unsteady Flow around a Ship in Waves, J. Soc. Nav. Arch. Japan, Vol. 174, (1993), pp. 151-162

[13] Kashiwagi, M.: Added Resistance, Wave-Induced Steady Sway Force and Yaw Moment on an Advancing Ship, Ship Technology Res., Vol. 39, No. 1, (1992), pp. 3-16

[14] Mizoguchi, S. and Hirayama, T.: Improved Calculation of Strip Theory –Vertical Ship Motions and Wave Loads–, 1st Marine Dynamics Symp., Soc. Nav. Arch. Japan, (1984), pp. 217-230

[15] Maruo, H.: Wave Resistance of a Ship in Regular Head Seas, Bulletin of the Faculty of Eng., Yokohama National Univ., Vol. 9, (1960), pp. 73-91

[16] Kobayashi, M.: On the Hydrodynamic Forces and Moments Acting on a Three-Dimensional Body with a Constant Forward Speed, J. Soc. Nav. Arch. Japan, Vol. 150, (1981), pp. 175-189

[17] Ohkusu, M.: Analysis of Waves Generated by a Ship Oscillating and Running on a Calm Water with Forward Velocity, J. Soc. Nav. Arch. Japan, Vol. 142, (1977), pp. 36-44

Heave and Pitch Motions of a Catamaran Advancing in Waves*

Masashi KASHIWAGI
Research Institute for Applied Mechanics, Kyushu University
Kasuga, Fukuoka 816-8580, Japan

ABSTRACT

A new linear theory is presented for computing the radiation and diffraction forces and the motions of a catamaran advancing with forward speed in waves. The radiation problem is solved with the concept of Newman's unified slender-ship theory. The wave-exciting forces and ship motions are calculated by use of Haskind-Newman's reciprocity relation without having to solve the diffraction problem. The validity of the theory is confirmed for the zero-speed case by comparison with more accurate results by a 3-D panel method. For the case of nonzero speed, comparisons are made with experimental values measured at Froude numbers 0.15 and 0.3 using a rather blunt catamaran model. The present-theory predictions agree well with experiments except for the pitch mode at higher Froude number and in the lower frequency range.

1. INTRODUCTION

Twin-hull motion problems have been studied so far by the strip theory (Ohkusu and Takaki, 1971) incorporating 2-D exact interaction solutions. This strip-theory approach allows the wave energy to flow only in the transverse direction, and therefore it can not account for the important 3-D effects such as the dissipation of the wave energy reflecting between twin hulls and the drastic change of 3-D wave characteristics with increasing forward speed.

Recently a 3-D Green function method was applied by Kobayashi *et al.* (1990) to the catamaran problem in order to account for the forward-speed effects. However the computation time is enormous at present and the numerical accuracy seems not reliable because of the limited number of discretized panels over the twin hulls.

On the other hand, some new approaches have also been applied with the limitation to the high speed problems, such as Chapman's type pseudo 3-D theory by Ohkusu *et al.* (1990), Rankine panel method by Kring and Sclavounos (1991), and Hanaoka's thin-ship theory by Watanabe (1992). However there exists no theory which can bridge a gap between zero and high speeds and can be computed with relative ease. A new theory in this paper is meant to serve that purpose.

The theory in this paper was inspired by Newman's unified theory for a monohull ship (Newman, 1978), and can be regarded as an extension of the tank-wall interference problem by Kashiwagi and Ohkusu (1991). Breit and Sclavounos (1986) developed a similar slender-ship theory for a catamaran, but their theory is limited to the zero-speed case and seems difficult to extend to the forward-speed case, because the radiation problem is viewed as a set of radiation-diffraction problems.

∗ *Reprinted from Proceedings of the 2nd International Conference on Fast Sea Transportation (Yokohama), pp. 643-655, 1993 (December)*

The present theory is different from Breit and Sclavounos' and featured in that not only symmetric but also antisymmetric homogeneous solutions are included in the inner solution, which plays an important role in accounting for the hydrodynamic interactions between twin hulls. The unknown coefficients of the inner homogeneous solutions are determined from the matching with the outer solution, giving the coupled integral equations for strengths of the source and doublet distributions comprising the outer solution.

With the completed inner solution, it is straightforward to compute the heave and pitch added-mass and damping coefficients. The wave-exciting force and moment are evaluated using the forward-speed version of Haskind-Newman's reciprocity relation (Newman, 1965); this makes it possible to compute the wave-induced heave and pitch motions without solving the diffraction problem.

The validity of the theory for the zero speed case is confirmed by comparison with independent numerical results by a more rigorous 3-D panel method. In the presence of forward speed, experiments are carried out using a rather blunt catamaran model, and comparisons of experimental values with corresponding numerical results lead to discussions on the validity of the present theory.

2. FORMULATION ON THE PROBLEM

As in Fig. 1, we consider a catamaran advancing at constant speed U in waves, and denote the separation distance between twin hulls by D, the length by L, the breadth of each demihull by B, and the wetted surfaces of the left and right hulls by S_L and S_R, respectively. For convenience in the analysis, two coordinate systems are taken; the first one is $\overline{o}$-$\overline{x}\,\overline{y}\,\overline{z}$, with the origin at the center of a catamaran and on the undisturbed free surface, and another one, o-xyz, is simply shifted parallel to the y-axis to the midship of the left hull. Thus no distinctions are needed between two coordinate systems except the only difference $\overline{y} = y - D/2$.

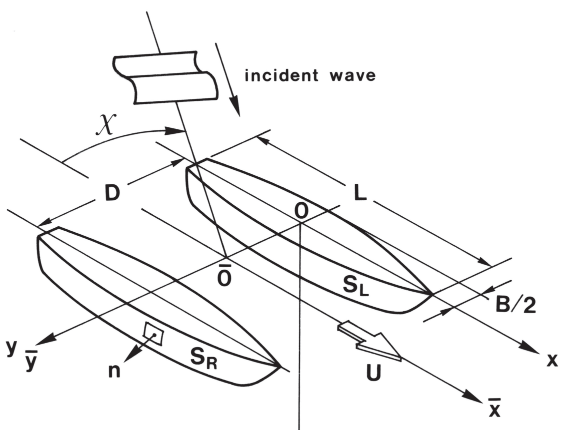

Fig. 1 Coordinate system and notations

For simplicity, only heave and pitch motions are considered here and each demihull is assumed transversely symmetric, although there exist no essential obstacles to extending the present theory to other modes of motion and to the case of antisymmetric demihulls. Assuming the flow inviscid with irrotational motion and the linearity of the phenomena, the velocity potential can be introduced and expressed as

$$\varPhi = U\big[-x + \phi_S(x,\overline{y},z)\big] + \Re\Big[\,\psi(x,\overline{y},z)\,e^{i\omega t}\Big] \tag{1}$$

$$\psi = \frac{ga}{i\omega_0}\big\{\phi_0(x,\overline{y},z) + \phi_7(x,\overline{y},z)\big\} + i\omega \sum_{j=3,5} X_j\,\phi_j(x,\overline{y},z) \tag{2}$$

$$\varphi_0 = \exp\{-k_0 z - ik_0(x\cos\chi + \overline{y}\sin\chi)\} \tag{3}$$

$$\omega = \omega_0 - k_0 U\cos\chi, \quad k_0 = \omega_0^2/g \tag{4}$$

Here ϕ_S denotes the steady perturbation potential and ψ the oscillatory velocity potential consisting of the incident-wave potential ϕ_0, the scattered potential ϕ_7, and the radiation potential ϕ_j of the j-th mode with complex amplitude X_j, where $j = 3$ for heave and $j = 5$ for pitch; a, ω_0, k_0, χ denote the amplitude, circular frequency, wavenumber, incident angle defined in Fig. 1, respectively, of the incident wave; g the acceleration of gravity and ω the circular encounter frequency.

The velocity potentials to be obtained, ϕ_j ($j = 3,5,7$), are governed by the three-dimensional Laplace equation and subject to the linear free-surface condition given by

$$\frac{\partial\phi_j}{\partial z} + K\phi_j + i2\tau\frac{\partial\phi_j}{\partial x} - \frac{1}{K_0}\frac{\partial^2\phi_j}{\partial x^2} = 0 \quad \text{on } z = 0 \tag{5}$$

with

$$K = \omega^2/g, \quad \tau = U\omega/g, \quad K_0 = g/U^2 \tag{6}$$

and the condition of outgoing waves at infinity and vanishing velocity at $z = \infty$. Furthermore the following boundary condition on the twin hulls must be satisfied:

$$\frac{\partial\phi_j}{\partial n} = n_j + \frac{U}{i\omega}m_j \quad (j = 3,5) \tag{7}$$

$$= -\frac{\partial\phi_0}{\partial n} \qquad (j = 7) \tag{8}$$

where n_j is the j-th component of normal vector $\boldsymbol{n}$ pointing out of the ship hull, with extended definition of $n_5 = zn_1 - xn_3$, and m_j represents the forward-speed effect which was originally derived in Timman and Newman (1962) and expressed in the form

$$\left.\begin{aligned} (m_1, m_2, m_3) &= -(\boldsymbol{n}\cdot\nabla)\boldsymbol{V} \\ (m_4, m_5, m_6) &= -(\boldsymbol{n}\cdot\nabla)(\boldsymbol{r}\times\boldsymbol{V}) \\ \boldsymbol{V} &= \nabla\left[-x + \phi_S(x,\overline{y},z)\right] \end{aligned}\right\} \tag{9}$$

The computation of ship motions, which is a main object of this paper, may be carried out after solving the above boundary-value problem and computing the hydrodynamic coefficients in the radiation problem and the wave-exciting forces in the diffraction problem.

For that purpose, the following section summarizes a proposed solution method, utilizing the basic concept of the unified slender-ship theory developed by Newman (1978). The details of the derivation may be found in Kashiwagi (1993a).

3. SOLUTION METHOD

3.1 Radiation Problem

The fact that each demihull of a catamaran is geometrically slender justifies applying the unified slender-ship theory to the analysis of the flow around each demihull. Therefore in the present theory the vicinity of the left hull is defined as the inner region and the influence of the right hull disturbance is taken into account in the outer solution, which implicitly assumes that the separation distance D is of order $O(1)$ relative to the ship length.

3.1.1 Outer solution

Far from the ship, the velocity potential due to disturbances of each demihull can be expressed by a line distribution of the 3-D source and doublet along the center line of each demihull:

$$\begin{aligned}\phi_j^{(o)}(x,\overline{y},z) = &\int_{S_L}\Big[Q_j(\xi)G\Big(x-\xi,\overline{y}+\frac{D}{2},z\Big)+D_j(\xi)H\Big(x-\xi,\overline{y}+\frac{D}{2},z\Big)\Big]\,d\xi\\ &+\int_{S_R}\Big[Q_j(\xi)G\Big(x-\xi,\overline{y}-\frac{D}{2},z\Big)-D_j(\xi)H\Big(x-\xi,\overline{y}-\frac{D}{2},z\Big)\Big]\,d\xi\end{aligned} \tag{10}$$

where $G(x,y,z)$ is the velocity potential due to a 3-D translating and oscillating source of unit strength; likewise $H(x,y,z)$ is the doublet of unit moment with transverse axis; $Q_j(\xi)$ and $D_j(\xi)$ are unknown strengths of source and doublet, respectively.

The reason of equal source strength and opposite sign in the doublet between the left and right hulls is that we consider a catamaran which is symmetric about $\overline{y}=0$ and oscillating in heave and pitch.

The unknowns in (10), $Q_j(x)$ and $D_j(x)$, will be determined by the matched asymptotic expansion method. For that purpose, the inner expansion of (10) must be sought; this can be achieved by first substituting $\overline{y}=y-D/2$ in (10) and then expanding the Green function for $y=O(\epsilon)$, $z=O\epsilon)$, and $D=O(1)$, where ϵ is a small quantity representing the slenderness of a demihull. The final result of this procedure can be written in the form

$$\begin{aligned}\phi_j^{(o)}(x,y,z) \sim\ & Q_j(x)G_{2D}(y,z)-\big(1-Kz\big)\mathcal{L}_S(Q_j,D_j;x)\\ &+D_j(x)H_{2D}(y,z)-Ky\cdot\mathcal{L}_A(Q_j,D_j;x)\end{aligned} \tag{11}$$

with

$$\mathcal{L}_S=\int_L Q_j(\xi)\Big\{g_L(x-\xi)+g_R(x-\xi)\Big\}\,d\xi+\int_L D_j(\xi)\,f_R(x-\xi)\,d\xi \tag{12}$$

$$\mathcal{L}_A=\int_L Q_j(\xi)\,f_R(x-\xi)\,d\xi+\int_L D_j(\xi)\Big\{h_L(x-\xi)+h_R(x-\xi)\Big\}\,d\xi \tag{13}$$

where $G_{2D}(y,z)$ and $H_{2D}(y,z)$ are the Green functions of 2-D source and doublet respectively, and other functions of x represent 3-D effects of forward speed and hydrodynamic interactions. The subscript L to the kernel functions in (12) and (13) stands for the contribution from the left hull and likewise the subscript R is from the right hull; the detailed expressions of these are given in the appendix of Kashiwagi (1993a). The lowest order neglected in (11) may be $O(K^2r^2,(\kappa-K)r)$, where $r=\sqrt{y^2+z^2}$ and κ is the 3-D wavenumber defined from (5), including the forward-speed effects.

It is noteworthy that the source distribution along the centerline of right hull gives not only the symmetric component, $g_R(x-\xi)$, but also the antisymmetric component, $f_R(x-\xi)$, and the latter is exactly the same as the symmetric component given from the doublet distribution. These terms, which are the influence of the right hull, play an important role in accounting for the interactions between twin hulls.

3.1.2 Inner solution

In the inner region, gradients of the flow in the x-direction may be neglected. Therefore the governing equation and boundary conditions to be satisfied are formally identical to those in the single-hull problem by Newman (1978). In line with the basic concept of Newman's unified theory, we write the solution as the superposition of the particular and homogeneous solutions:

$$\phi_j^{(i)}(x;y,z) = \varphi_j(x;y,z) + \frac{U}{i\omega}\widehat{\varphi}_j(x;y,z) + C_j^S(x)\Big\{\varphi_3(y,z) - \varphi_3^*(y,z)\Big\}$$
$$+ C_j^A(x)\Big\{\varphi_2(y,z) - \varphi_2^*(y,z)\Big\} \tag{14}$$

Here the first two terms on the right-hand side are the particular solution satisfying the following body boundary condition:

$$\frac{\partial \varphi_j}{\partial N} = N_j \quad (j = 2,3,5), \qquad \frac{\partial \widehat{\varphi}_j}{\partial N} = M_j \quad (j = 3,5) \tag{15}$$

where N is the 2-D unit normal, N_j and M_j are slender-body approximations of n_j and m_j given in (7) and (9); in particular N_5 and M_5 can be approximated by $N_5 = -xN_3$, $M_5 = N_3 - xM_3$. The mode index $j = 2$ designates the sway mode and the asterisk means the complex conjugate. Therefore the third and fourth terms in (14) are the symmetric and antisymmetric homogeneous solutions respectively with respect to the center plane of the left hull.

The inclusion of the antisymmetric homogeneous component is of great importance in the present analysis, because even when each demihull is transversely symmetric and oscillating in heave and pitch, the antisymmetric flow may be induced around the left hull due to the hydrodynamic influence from the right hull.

The coefficients of homogeneous solutions, $C_j^S(x)$ and $C_j^A(x)$, are unknown at this stage and expected to account for forward-speed effects and flow interactions between twin hulls. These will be determined by matching the outer expansion of (14) with (11).

The outer expansion of (14) takes the form

$$\phi_j^{(i)}(x;y,z) \sim \Big[\sigma_j(x) + \frac{U}{i\omega}\widehat{\sigma}_j(x) + C_j^S(x)\Big\{\sigma_3(x) - \sigma_3^*(x)\Big\}\Big]\, G_{2D}(y,z)$$
$$+ 2iC_j^S(x)\,\sigma_3^*(x)\,e^{-Kz}\cos Ky$$
$$+ C_j^A(x)\Big\{\sigma_2(x) - \sigma_2^*(x)\Big\}\, H_{2D}(y,z) + 2iC_j^A(x)\,\sigma_2^*(x)\,e^{-Kz}\sin Ky \tag{16}$$

where $\sigma_j(x)$ and $\widehat{\sigma}_j(x)$ are explicitly obtainable 2-D Kochin functions equivalent to the complex amplitude of outgoing waves.

3.1.3 Matching

Comparing (11) with (16) gives the following relations:

$$Q_j(x) = \sigma_j(x) + \frac{U}{i\omega}\widehat{\sigma}_j(x) + C_j^S(x)\Big\{\sigma_3(x) - \sigma_3^*(x)\Big\} \tag{17a}$$
$$\mathcal{L}_S(Q_j, D_j; x) = -2iC_j^S(x)\,\sigma_3^*(x) \tag{17b}$$
$$D_j(x) = C_j^A(x)\Big\{\sigma_2(x) - \sigma_2^*(x)\Big\} \tag{17c}$$
$$\mathcal{L}_A(Q_j, D_j; x) = -2iC_j^A(x)\,\sigma_2^*(x) \tag{17d}$$

Eliminating $C_j^S(x)$ from (17a)–(17b) and $C_j^A(x)$ from (17c)–(17d), we have a coupled integral equations for the outer source strength $Q_j(x)$ and the doublet strength $D_j(x)$, in the form

$$Q_j(x) - \frac{i}{2}\big(\sigma_3/\sigma_3^* - 1\big)\mathcal{L}_S(Q_j, D_j; x) = \sigma_j(x) + \frac{U}{i\omega}\widehat{\sigma}_j(x) \tag{18a}$$

$$D_j(x) - \frac{i}{2}\big(\sigma_2/\sigma_2^* - 1\big)\mathcal{L}_A(Q_j, D_j; x) = 0 \tag{18b}$$

With numerical solutions of Q_j and D_j, the coefficients of inner homogeneous component can be readily obtained from (17a) and (17c), thereby completing the inner solution which may be used for computing the added-mass and damping coefficients. It should be noted that with increasing forward speed or with increasing separation distance at a constant speed, $\mathcal{L}_A$ becomes independent of Q_j and $\mathcal{L}_S$ becomes independent of D_j; in this limiting case $D_j = 0$ from (18b) and $C_j^A = 0$ from (17c), therefore no hydrodynamic interactions exist between twin hulls and (18a) is identical to that of Newman's unified theory for a single-hull ship.

3.1.4 Added-mass and damping coefficients

Since the completed inner solution is the velocity potential near the left hull, we can compute the hydrodynamic force on the left hull, which can be summarized as follows:

$$F_j^L = -\big(i\omega\big)^2 \sum_{k=3,5} \Big[A_{jk}^L + B_{jk}^L/i\omega\Big] X_k \tag{19}$$

where for $j = 3$ (heave), 5 (pitch)

$$\begin{aligned} A_{jk}^L + B_{jk}^L/i\omega = &-\rho \int_L dx \int_{C_L} \Big(N_j - \frac{U}{i\omega}M_j\Big)\Big\{\varphi_k + \frac{U}{i\omega}\widehat{\varphi}_k\Big\}\, d\ell \\ &-\rho \int_L C_k^S(x)\, dx \int_{C_L} \Big(N_j - \frac{U}{i\omega}M_j\Big)\Big\{\varphi_3 - \varphi_3^*\Big\}\, d\ell \end{aligned} \tag{20}$$

and for $j = 2$ (sway), 4 (roll), 6 (yaw)

$$A_{jk}^L + B_{jk}^L/i\omega = -\rho \int_L C_k^A(x)\, dx \int_{C_L} \Big(N_j - \frac{U}{i\omega}M_j\Big)\Big\{\varphi_2 - \varphi_2^*\Big\}\, d\ell \tag{21}$$

We have taken into account that each demihull in the present analysis is transversely symmetric about its own center plane.

One thing to be emphasized here is that, as shown in (21), the horizontal side force or connecting moment will be exerted as inner forces and can be evaluated from the antisymmetric part of the homogeneous solution. It is needless to say that the hydrodynamic force on the right hull is the same as (20) in the symmetric mode (j = 3, 5) and opposite to (21) in the antisymmetric mode (j = 2, 4, 6).

3.2 Diffraction Problem

The analysis in the preceding section may be extended to the diffraction problem by referring to the unified theory established by Sclavounos (1984). However, as Sclavounos discussed in his paper (Sclavounos,1985a), if the integrated wave-exciting forces are main concern, it is advisable to use Haskind-Newman's reciprocity relation (Newman, 1965). With Haskind-Newman's relation, there is no need to obtain the scattered velocity potential, and then the wave-exciting force in the j-th direction can be computed from

$$E_j = \rho g a \frac{\omega}{\omega_0} H_j^-(k_0, \chi + \pi) \tag{22}$$

where

$$H_j^-(k_0,\beta) = \iint_{S_L+S_R} \left(\frac{\partial \phi_j^-}{\partial n} - \phi_j^- \frac{\partial}{\partial n} \right) e^{-k_0 z + i k_0 (x\cos\beta + \overline{y}\sin\beta)}\, dS \tag{23}$$

Here ϕ_j^- designates the reverse-flow radiation potential, which describes the flow around the ship moving in the negative x-axis at the same speed U as in the real-flow problem while oscillating in the j-th mode. We should note that applying Haskind-Newman's relation is exact in the zero-speed case, whereas in the presence of forward speed we have adopted a number of approximations:

1) When applying Tuck's theorem (Ogilvie and Tuck, 1969), the ship hull is assumed wall-sided near the free surface.

2) In deriving (22), Green's second identity has been used between the scattered potential ϕ_7 and the reverse-flow velocity potential ϕ_j^-. The resulting expression includes the so-called line-integral term along the intersection between the body and free surfaces, which is neglected.

3) In the reverse-flow problem, the m-term appearing in the body boundary condition is assumed the same as that in the real-flow problem except the opposite sign; this is not true, unless the ship has fore-and-aft symmetry.

In the context of slender-ship theory, however, the errors due to the above approximations may be small, which justifies the use of (22) even in the case of nonzero forward speed.

The function given by (23) is called the Kochin function, which can be calculated from the outer solution in the slender-ship theory. The details of the derivation may be found in Kashiwagi (1993b), and the final result is of the form

$$H_j^-(k_0,\beta) = 2\int_L e^{ik_0 x\cos\beta} \left\{ \cos\!\Big(k_0 \frac{D}{2}\sin\beta\Big) Q_j^-(x) + \sin\beta\cdot\sin\!\Big(k_0\frac{D}{2}\sin\beta\Big) D_j^-(x) \right\} dx \tag{24}$$

When the ship is longitudinally symmetric, (24) can be evaluated only in terms of the real-flow radiation solutions. More specifically,

$$\left. \begin{aligned} H_3^-(k_0,\chi+\pi) &= H_3(k_0,\chi) \\ H_5^-(k_0,\chi+\pi) &= -H_5(k_0,\chi) \end{aligned} \right\} \tag{25}$$

4. SHIP MOTIONS

The surge motion is regarded as higher order in the slender-ship theory and thus can be treated separately. Therefore, the heave and pitch motions of a catamaran can be obtained as a solution of the following complex linear system:

$$\sum_{j=3,5} \Big[-\omega^2 \big(M_{ij} + A_{ij}\big) + i\omega B_{ij} + C_{ij} \Big] X_j = E_i \quad \text{for } i = 3,5 \tag{26}$$

where A_{ij} and B_{ij} are the added-mass and damping coefficients in the i-th direction due to the j-th mode of motion, which are twice the values given by (20). Likewise M_{ij} is the generalized mass matrix and C_{ij} is the restoring coefficients; these are evaluated independent of the hydrodynamic analysis and we can refer to Newman (1977) for their detailed expressions. E_i on the right-hand side of (26) is the wave-exciting force to be evaluated from (22).

5. NUMERICAL CALCULATION METHOD

The first task in the numerical implementation is to obtain the particular solution in the inner problem and the 2-D Kochin functions, $\sigma_j(x)$ and $\widehat{\sigma}_j(x)$, necessary in solving (18); for which the 2-D integral-equation method was used with a remedy for getting rid of the irregular frequencies, but contributions of the steady perturbation potential ϕ_S were ignored in the evaluation of the M-terms, with the result

$$M_2 = M_3 = 0, \quad M_5 = N_3 \tag{27}$$

The numerical integration of the kernel functions in (18) was carried out by use of the Clenshaw-Curtis quadrature, with an absolute error less than 10^{-5} required. The solution method for the integral equation (18) is the same as that devised in Sclavounos (1985b), representing unknowns with Chebyshev polynomials and employing a Galerkin technique. Numerical tests confirmed that a sufficiently accurate solution was obtained by selecting 25–30 terms in the Chebyshev polynomials.

6. RESULTS AND COMPARISON WITH EXPERIMENTS

6.1 Zero Speed Case

To confirm the validity of the theory, computations were performed for the twin half-immersed spheroids with $B/L = 1/8$ and $D/B = 2$, and the results were compared with independent results by a 3-D panel method and a conventional strip theory incorporating 2-D interaction solutions.

As an example of the results in the radiation problem, the heave added-mass and damping coefficients are shown in Fig. 2. For reference, the results for a single hull are also

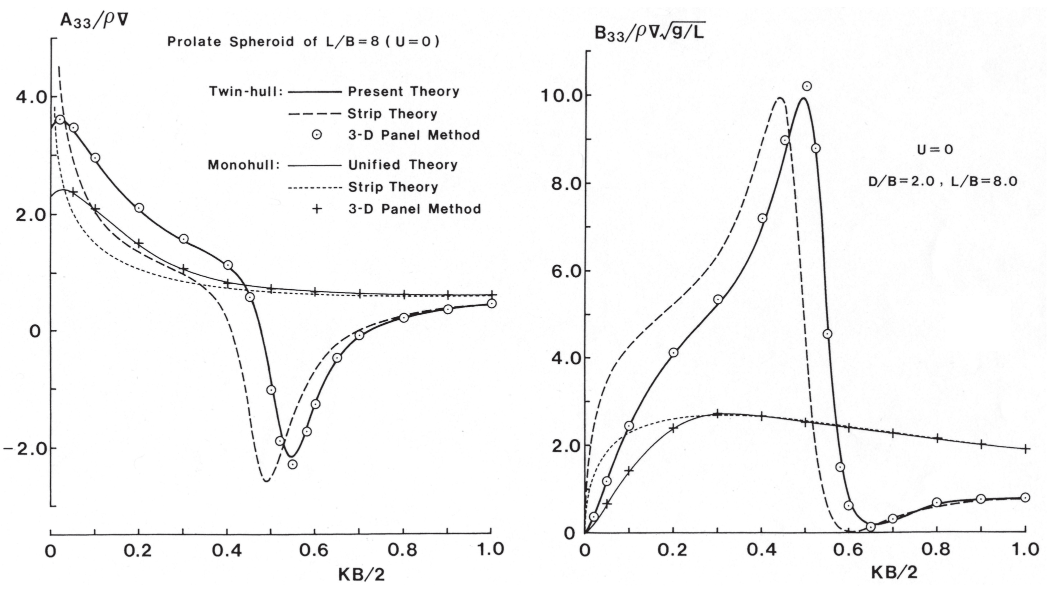

Fig. 2 Heave added-mass and damping coefficients of twin half-immersed spheroids with $B/L = 1/8$ and $D/B = 2$ at $U = 0$

included. The present-theory predictions are in excellent agreement with the 3-D panel method, although the separation distance $D/L = 1/4$ is small considering the assumption of the present theory i.e. $D/L = O(1)$. In the pitch mode, we found that the agreement between the present theory and the 3-D panel method was in almost the same degree as Fig. 2.

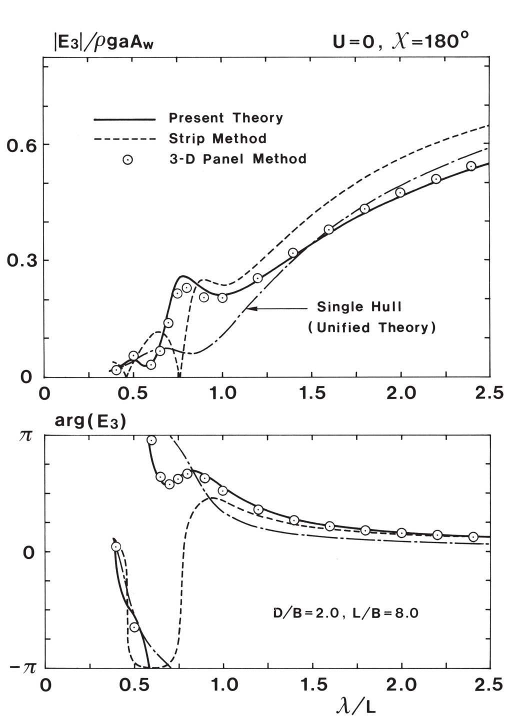

Fig. 3 Heave exciting force on twin half-immersed spheroids with $B/L = 1/8$ and $D/B = 2$ at $U = 0$, in head wave

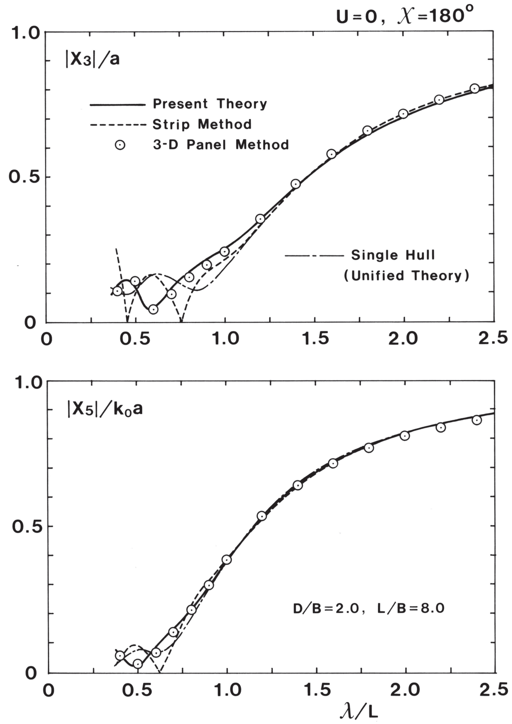

Fig. 4 Modulus of heave and pitch motions of twin half-immersed spheroids with $B/L = 1/8$ and $D/B = 2$ at $U = 0$, in head wave

Fig. 3 shows the wave-exciting heave force in head wave, and the present theory agrees well with the 3-D panel method which solves the diffraction problem directly. Good agreement was also confirmed in the pitch exciting moment and for other angles of wave incidence.

With the results of the radiation and wave-exciting forces shown above, the heave and pitch motions were calculated, with the center of gravity taken at the origin of the coordinate system. Examples are shown in Fig. 4 for the modulus of heave and pitch motions in head wave. Numerical results of the 3-D panel method and the strip theory are also shown for comparison. (It should be noted that the coupling effect of surge mode is correctly taken into account in the 3-D panel method.) By comparison, we can see that the interaction effects between twin hulls are unexpectedly small except in the short wavelength region, despite large effects in the radiation and diffraction forces as seen in Figs. 2 and 3. There must be cancellation between the right- and left-hand sides of the ship-motion equations.

6.2 Forward Speed Case

In the presence of forward speed, we carried out experiments at Froude number (Fn) 0.15 and 0.3, using twin Lewis-form ships with $B/L = 1/6$ and $D/B = 2$. The principal particulars and the body plan of the ship used as a demihull are shown in Table 1 and Fig. 5 respectively, which is symmetric not only longitudinally but also transversely. We should note that this Lewis-form ship is rather blunt as a demi hull and the separation distance is small contrary to the assumption of the theory.

For the comparison of radiation forces, forced oscillation tests in heave and pitch were carried out, an example of which is shown in Fig. 6 for the heave added-mass and damping coefficients at $Fn = 0.15$. Good agreement exists between the measured values and the present-theory predictions, except for slight discrepancies near the frequency at which the twin-hull interactions are reso-

Table 1 Principal particulars of Lewis-form ship

Length	L (m)	1.500
Breadth	B (m)	0.250
Draft	d (m)	0.125
Displacement	Δ (kgf)	30.91
Block coeff.	C_B	0.659
Midship section coeff.	C_M	0.942
Waterplane area coeff.	C_W	0.732

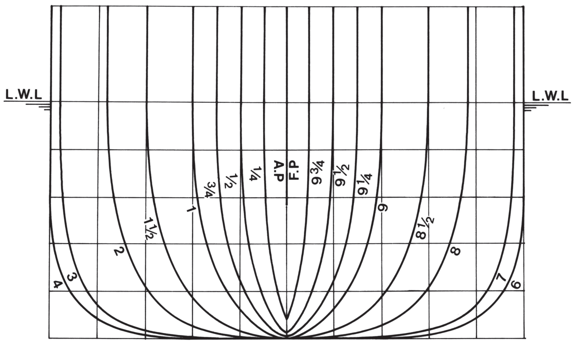

Fig. 5 Body plan of Lewis-form ship used as demihull of a catamaran

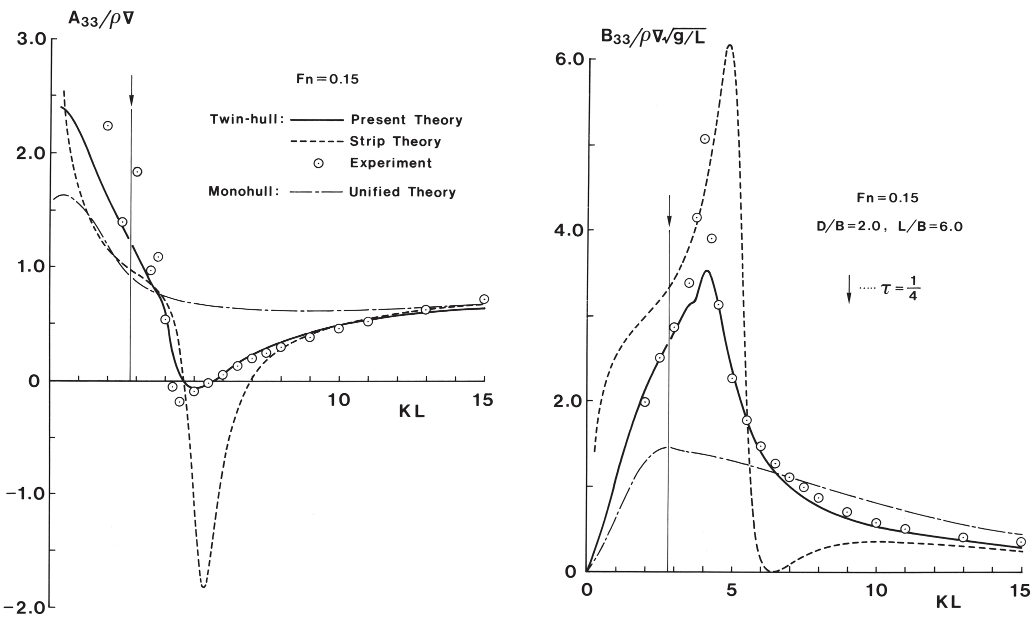

Fig. 6 Heave added-mass and damping coefficients of twin Lewis-form ships at $Fn = 0.15$

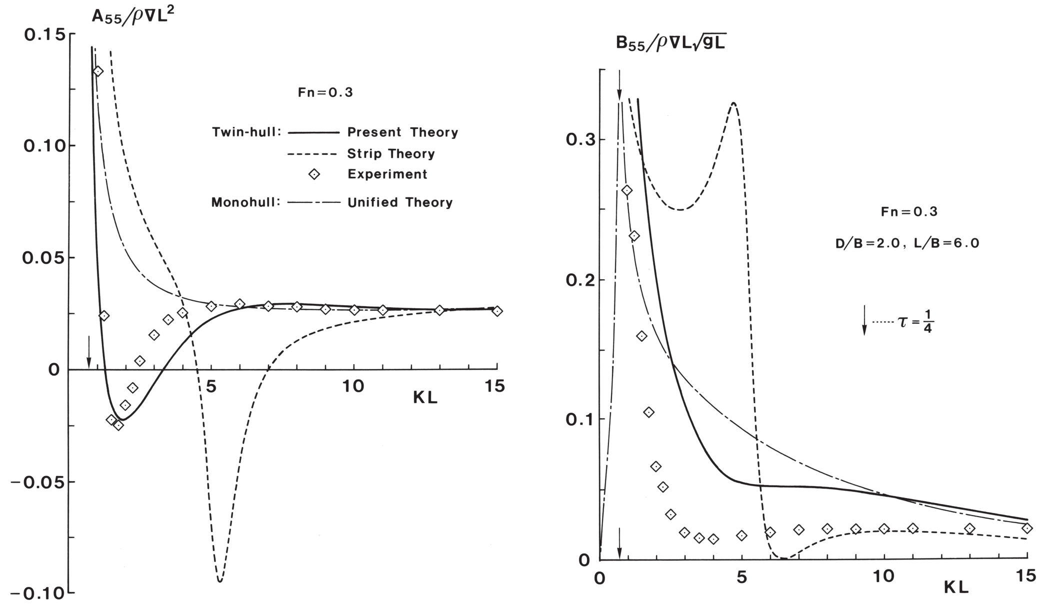

Fig. 7 Pitch added moment of inertia and damping coefficients of twin Lewis-form ships at $Fn = 0.3$

nant.

Likewise Fig. 7 is the comparison of the pitch added moment of inertia and damping coefficients at $Fn = 0.3$. The present theory overpredicts the damping coefficient (B_{55}, but in comparison with the strip theory and the unified theory for a monohull ship, the present theory accounts well for the qualitative tendency of experiments.

Next comparisons are for the wave-exciting heave force and pitch moment. The experiments were conducted at $Fn = 0.15$ and 0.3 in head wave. As a few examples, let us show Figs. 8 and 9, which are the wave-exciting heave force and pitch moment respectively at $Fn = 0.15$. The agreement between the measured and present-theory results is favorable in heave force, but in the pitch moment the quantitative differences can be seen in the region of longer wavelengths.

We confirmed that these differences were pronounced at $Fn = 0.3$ especially in the pitch moment. It should be understood from these facts that the forward-speed effects are not fully taken into account in the present theory and this deficiency is also the case in Newman's unified theory for a single-hull ship as discussed by Yeung (1985).

Final comparisons are for the heave and pitch motions in head wave, which are shown in Fig. 10 to Fig. 13. The setup of experiments were such that the radius of pitch gyration was equal to $0.225L$, the vertical position of gravity was 1 mm above the free surface, and the pitch angle was measured at the position of 195 mm above the free surface.

Figs. 10 and 11 show the results at $Fn = 0.15$. Although the agreement is not perfect, the present theory performs well in comparison with the strip theory and the unified theory without twinhull interactions. A reason of the underprediction in the pitch amplitude for $\lambda/L > 1.5$ may be related to the underprediction of the wave-exciting moment shown in Fig. 9.

The comparisons at $Fn = 0.3$ are shown in Figs. 12 and 13. Even in this case, predictions by the present theory are not that bad except the pitch motion in the region of longer

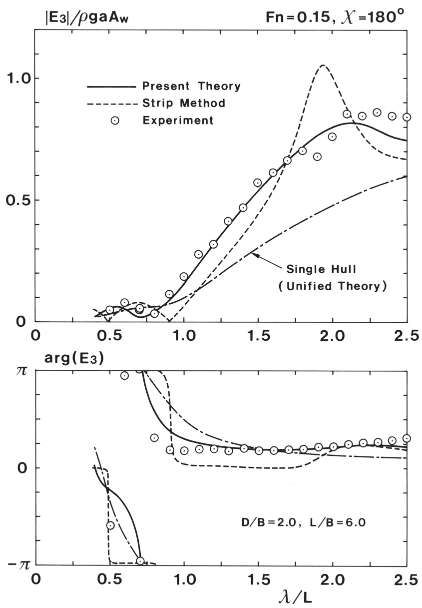

Fig. 8 Heave exciting force on twin Lewis-form ships at $Fn = 0.15$ in head wave

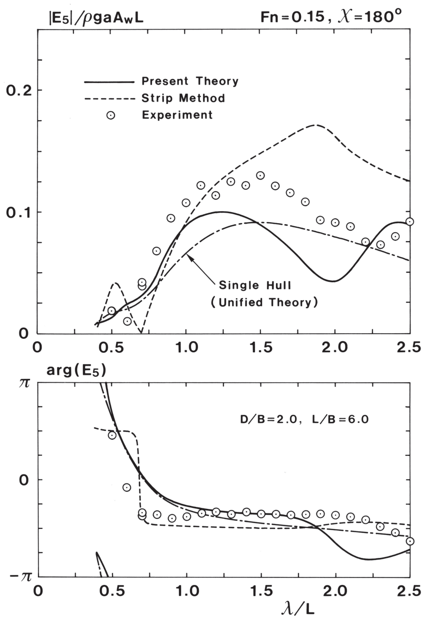

Fig. 9 Pitch exciting moment on twin Lewis-form ships at $Fn = 0.15$ in head wave

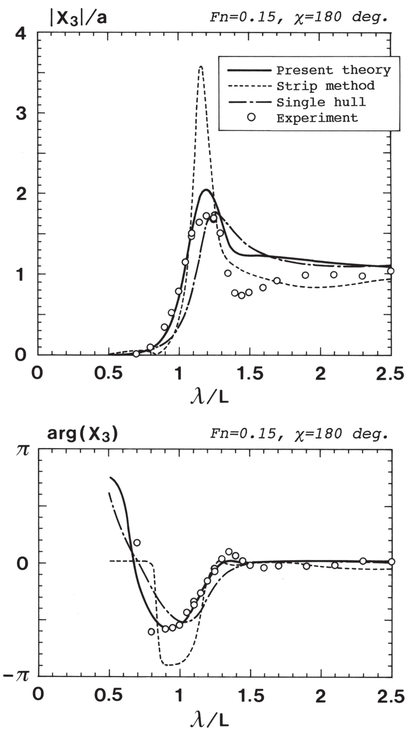

Fig. 10 Heave motion of twin Lewis-form ships at $Fn = 0.15$ in head wave

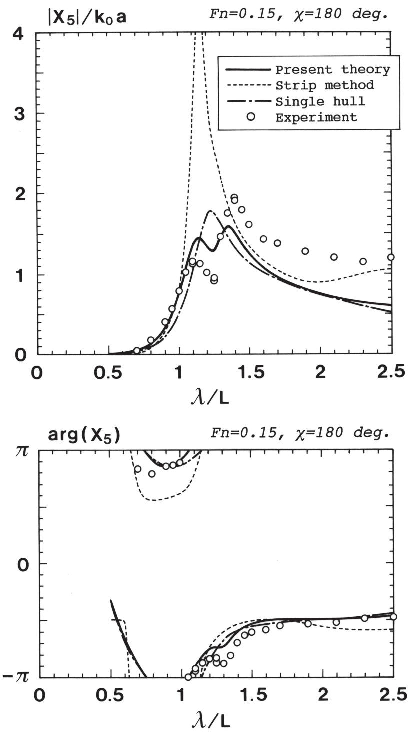

Fig. 11 Pitch motion of twin Lewis-form ships at $Fn = 0.15$ in head wave

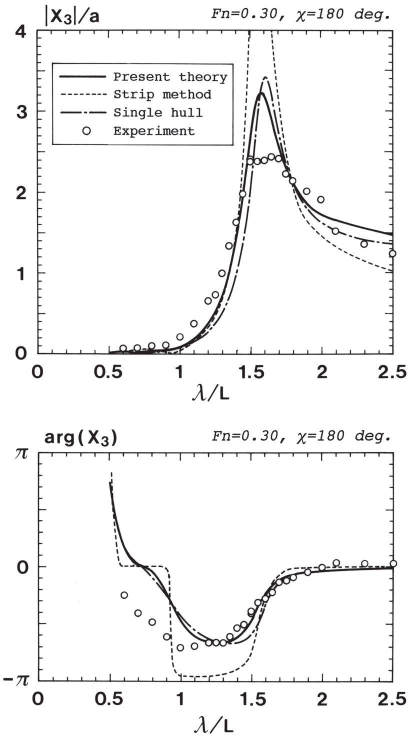

Fig. 12 Heave motion of twin Lewis-form ships at $Fn = 0.3$ in head wave

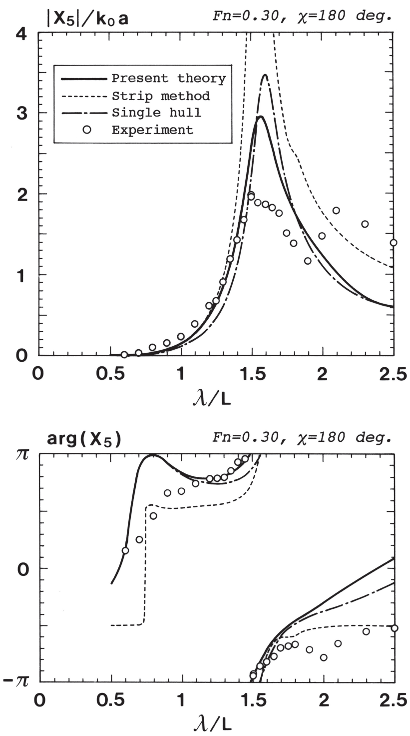

Fig. 13 Pitch motion of twin Lewis-form ships at $Fn = 0.3$ in head wave

wavelengths. The overprediction of the peak value at the resonance may be an inherent tendency in the unified theory (Sclavounos, 1985b). It has been pointed out so far that the strip theory taking account of the twin-hull interactions greatly overpredicts the peak value near the resonance; this tendency is also retrieved in the calculations here.

7. CONCLUDING REMARKS

By applying the concept of Newman's unified theory to the analysis of the flow around the demihull of a catamaran, we presented a new theory which predicts the radiation and diffraction forces and the wave-induced motions with relative ease.

As a validation of the theory, computations for the zero speed case were compared with independent results by a 3-D panel method, showing virtually perfect agreement. For the forward speed case, experiments were carried out at $Fn = 0.15$ and 0.3 to measure the heave and pitch added-mass and damping coefficients, the wave-exciting heave force and pitch moment, and the wave-induced ship motions in head waves, using a catamaran model with a Lewis-form ship as the demihull. The overall agreement between experimental results with present-theory predictions was favorable, except for the pitch mode at higher Froude number and in lower frequencies.

8. REFERENCES

Breit S. R. and Sclavounos P. D. (1986) Wave Interaction between Adjacent Slender Bodies, *Journal of Fluid Mechanics*, Vol. 165, pp. 273-296.

Kashiwagi, M. and Ohkusu, M. (1991) A New Theory for Side-Wall Interference Effects on Forward-Speed Radiation and Diffraction Forces, *Ship Technology Research*, Vol. 38, No. 1, pp. 17-47.

Kashiwagi, M. (1993a) Interaction Forces between Twin Hulls of a Catamaran Advancing in Waves (Part 1: Radiation Problem), *Journal of the Society of Naval Architects of Japan*, Vol. 173, pp. 119-131.

Kashiwagi, M. (1993b) Interaction Forces between Twin Hulls of a Catamaran Advancing in Waves (Part 2: Wave-Exciting Forces and Motions in Waves), *Journal of the Society of Naval Architects of Japan*, Vol. 174, pp. 181-191.

Kobayashi, M., Shimada, K. and Nishimura, K. (1990) Wave Loads on a Semi-Submerged Catamaran (SSC) with Forward Speed, *Journal of the Society of Naval Architects of Japan*, Vol. 168, pp. 159-170.

Kring, D. and Sclavounos, P. D. (1991) A New Method for Analyzing the Seakeeping of Multi-Hull Ships, *Proceedings of FAST'91 Symposium*, Trondheim.

Newman, J. N. (1965) The Exciting Forces on a Moving Body in Waves, *Journal of Ship Research*, Vol. 9, No. 3, pp. 190-199.

Newman, J. N. (1977) Marine Hydrodynamics, MIT Press, pp. 290-310.

Newman, J. N. (1978) The Theory of Ship Motions, Advances in Applied Mechanics, Vol. 18, pp. 221-283.

Ogilvie, T. F. and Tuck, E. O. (1969) A Rational Strip Theory for Ship Motions – Part 1, Report No. 013, Department of Naval Architecture and Marine Engineering, University of Michigan.

Ohkusu, M. and Takaki, M. (1971) On the Motion of Twin Hull Ship in Waves, *Journal of the Society of Naval Architects of Japan*, Vol. 129, pp. 29-40.

Ohkusu, M., Faltinsen, 0. M., Yasunaga, M. and lnada, M. (1991) Prediction of Hydrodynamic Forces on High-Speed Catamarans in a Seaway, *Journal of the Society of Naval Architects of Japan*, Vol. 170, pp. 153-161.

Sclavounos, P. D. (1984) The Diffraction of Free-Surface Waves by a Slender Ship, *Journal of Ship Research*, Vol. 28, No. 1, pp. 29-47.

Sclavounos, P. D. (1985a) Forward-Speed Vertical Wave Exciting Forces on Ships, *Journal of Ship Research*, Vol. 29, No. 2, pp. 105-111.

Sclavounos, P. D. (1985b) The Unified Slender-Body Theory: Ship Motions in Waves, *Proceedings of 15th Symposium on Naval Hydrodynamics*, Hamburg, pp. 177-193.

Timman, R. and Newman, J. N. (1962) The Coupled Damping Coefficients of Symmetric Ships, *Journal of Ship Research*, Vol. 5, No. 4, pp. 34-55.

Watanabe, I. (1992) A New Method of Calculating Unsteady Hydrodynamic Forces Acting upon High-Speed Catamaran Ships, *Proceedings of 19th Symposium on Naval Hydrodynamics*, Seoul.

Yeung, R. W. and Kim, S. H. (1985) A New Development in the Theory of Oscillating and Translating Slender Ships, *Proceedings of 15th Symposium on Naval Hydrodynamics*, Hamburg, pp. 33-50.

Numerical Seakeeping Calculations Based on the Slender Ship Theory*

Masashi KASHIWAGI
Research Institute for Applied Mechanics, Kyushu University
Kasuga, Fukuoka 816-8580, Japan

Abstract

The survey of recent developments in slender ship theory focuses on unified theory and high-speed slender-body theory. The unified theory is extended to include wave diffraction from the bow part near the free surface. The high-speed slender-body theory is extended to include a homogeneous component in the inner solution, accounting for the transverse wave system in addition to the longitudinal wave system dominant for high speeds. Several numerical examples demonstrate the usefulness of these extensions. These theories can be used as a practical calculation method, bridging the gap between the traditional strip theory and more involved 3-D panel method.

Keywords: Slender ship theory, seakeeping, radiation, diffraction, ship motion, added resistance, high speed.

1. Introduction

Because of numerical simplicity and relatively good agreement with measurements, the strip theory has been used for predicting the seakeeping performance of ships. However, the strip theory is deficient in accounting for the 3-D effects important for low frequencies and for some forward-speed effects. In the 1960s and 70s, slender-body theories were extensively studied to overcome the defects of strip theory. Many slender-ship theories were developed, assuming in several ways the order of the forward speed of a ship, U, and the frequency of oscillation, ω. *Maruo (1974)*, *Adachi and Ohmatsu (1977)*, *Takagi and Ohkusu (1977)* review these theories.

Early slender-ship theories could only validate the strip theory for high frequencies. However, since the late 1970s, a number of useful theories have been established, which account for some 3-D and forward-speed effects while still encompassing the strip theory as a special case, e.g. *Yeung and Kim (1985)*, *Maruo (1989)*. Among these theories, this review focuses on the 'unified theory', *Newman (1978)*, and the 'high-speed slender-body theory', *Chapman (1975, 1976)*. Both theories have been extended and enhanced and are recognized as practical calculation methods, bridging the gap between the strip theory and more complicated 3-D calculation methods. Other related theories, such as the 'rational strip theory', *Ogilvie and Tuck (1969)*, are also briefly reviewed.

∗ *Reprinted from Ship Technology Research (Schiffstechnik), Vol. 44, No. 4, pp. 167-192, 1997 (October)*

2. General Description of Slender-Ship Theory

We consider the linearized 3-D problem, assuming the inviscid fluid with irrotational motion. Then the flow can be described with the velocity potential, which is expressed as

$$\Phi = U\big[-x + \varphi_s(x,y,z)\big] + \Re\big[\phi(x,y,z)e^{i\omega t}\big] \tag{1}$$

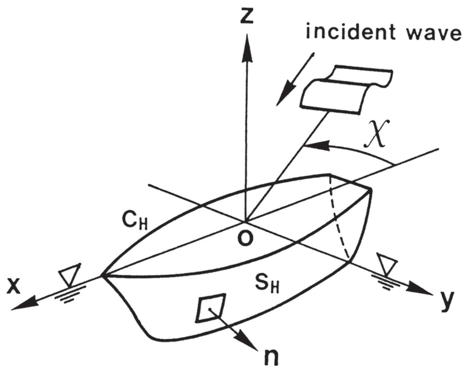

Fig. 1 Coordinate system

$$\phi = \frac{iga}{\omega_0}\Big\{\phi_0(x,y,z) + \phi_7(x,y,z)\Big\} + i\omega \sum_{j=1}^{6} \xi_j\, \phi_j(x,y,z) \tag{2}$$

$$\phi_0 = \exp\{k_0 z - ik_0(x\cos\chi + y\sin\chi)\} \tag{3}$$

U is the constant forward speed of a ship, $\omega = \omega_0 - k_0 U\cos\chi$ the circular frequency of oscillation, ω_0 the circular frequency of incident wave, $k_0 = \omega_0^2/g$ the wavenumber, and χ the incident wave angle, Fig. 1.

The amplitudes of incident wave, a, and of the j-th mode of oscillation, ξ_j ($j = 1 \sim 6$), are all assumed small. The unsteady potential ϕ is divided into the incident wave potential ϕ_0, the scattering potential ϕ_7, and the radiation potential ϕ_j. These potentials are subject to the free-surface condition of the form

$$\Big(i\omega - U\frac{\partial}{\partial x}\Big)^2\phi + g\frac{\partial\phi}{\partial z} + \mu\Big(i\omega - U\frac{\partial}{\partial x}\Big)\phi = 0 \qquad \text{on } z = 0 \tag{4}$$

where μ is Rayleigh's artificial viscosity coefficient ensuring the radiation condition to be satisfied at infinity.

The unknown potentials are ϕ_j ($j = 1 \sim 7$), which can be characterized by the body surface condition

$$\frac{\partial\phi_j}{\partial n} = n_j + \frac{U}{i\omega}m_j \qquad (j = 1 \sim 6) \tag{5}$$

$$= -\frac{\partial\phi_0}{\partial n} \qquad (j = 7) \tag{6}$$

where

$$\left.\begin{array}{ll} (n_1,\, n_2,\, n_3) = \boldsymbol{n} & (m_1,\, m_2,\, m_3) = -(\boldsymbol{n}\cdot\nabla)\boldsymbol{V} \\ (n_4,\, n_5,\, n_6) = \boldsymbol{r}\times\boldsymbol{n} & (m_4,\, m_5,\, m_6) = -(\boldsymbol{n}\cdot\nabla)(\boldsymbol{r}\times\boldsymbol{V}) \\ \boldsymbol{r} = (x,\, y,\, z) & \boldsymbol{V} = \nabla[-x + \varphi_s(x,y,z)] \end{array}\right\} \tag{7}$$

$\varphi_s(x,y,z)$ is the steady disturbance potential, which may be computed in advance, satisfying the rigid-wall free-surface condition on $z = 0$. The unit normal vector, $\boldsymbol{n}$, is positive when pointing into the fluid.

In the slender-ship theory, above equations may be simplified further by introducing the slenderness parameter ε as a guide, which is usually taken as B/L or T/L (B, T, L being ship's breadth, draft, and length, respectively). In the limit of $\varepsilon \to 0$, the ship will be viewed as a segment in the x-axis, and then the body boundary condition cannot be imposed (which is called *the outer problem*). To zoom in the body surface, the y- and z-axes may be stretched by the variable transformation of $y = \varepsilon Y$ and $z = \varepsilon Z$. Then, the body boundary condition can be satisfied in the magnified Y-Z plane. On the other hand, in this *inner problem* there is no radiation condition, because that holds for the flow at infinity.

Namely, both the outer and inner problems can be simplified to some extent, but includes unknowns. For a unique solution, the inner and outer problems have to be matched in an overlap region.

In the inner problem, besides the variable stretching in the y- and z-axes, it is customary to assume the order of U and ω, because the waves generated by the steady translation and the harmonic oscillation are different in nature and those wavelengths are related to U^2/g and g/ω^2, respectively. These assumptions have produced a number of variations in the slender-ship theory. Before proceeding to the details of those theories, the outer solution and its asymptotic and series expansions will be summarized first. In what follows, for clarity only the 'longitudinal problem', i.e. surge ($j = 1$), heave ($j = 3$), and pitch ($j = 5$) in the radiation problem and the symmetric component with respect to y of the diffraction problem ($j = 7$), will be discussed. Similar analyses are possible for the 'lateral problem' (see Appendix 1).

3. Outer Solution and Its Expansion

In the outer region far from the ship, the ship may be viewed as a segment along the x-axis. Then the disturbance due to the ship can be described by a line distribution of 3-D sources:

$$\phi_j^{(o)}(x, y, z) = \int_{-\infty}^{\infty} Q_j(\xi)\, G_{3D}(x - \xi, y, z)\, d\xi\,. \tag{8}$$

Here G_{3D} stands for the 3-D Green function, equivalent physically to the velocity potential of the source with unit strength. Q_j is its strength, which is unknown at this stage, because the body boundary condition is not considered.

The 3-D Green function, satisfying the 3-D Laplace equation and (4) together with the radiation condition, has been extensively studied; its Fourier transform with respect to x is

$$G_{3D}^{*}(k; y, z) = -\frac{1}{2\pi} \lim_{\mu \to 0} \int_{-\infty}^{\infty} \frac{e^{z\sqrt{k^2+m^2} - imy}}{\sqrt{k^2+m^2} - \frac{1}{g}(\omega + kU - i\mu)^2}\, dm \tag{9}$$

$$= -\frac{1}{\pi} K_0(|k|R) + \frac{\nu}{\pi} \int_{-\infty}^{0} e^{\nu\zeta}\, K_0\Big\{|k|\sqrt{y^2 + (z-\zeta)^2}\Big\}\, d\zeta + \left\{ \begin{array}{ll} \dfrac{i\epsilon_k}{\sqrt{1 - k^2/\nu^2}}\; e^{\nu z - i\epsilon_k \nu |y| \sqrt{1 - k^2/\nu^2}} & \text{for } \nu > |k| \\ \dfrac{-1}{\sqrt{k^2/\nu^2 - 1}}\; e^{\nu z - \nu |y| \sqrt{k^2/\nu^2 - 1}} & \text{for } \nu < |k| \end{array} \right. \tag{10}$$

where

$$\left. \begin{array}{l} \nu = (\omega + kU)^2/g = K + 2\tau k + k^2/K_0 \\ \epsilon_k = \mathrm{sgn}(\omega + kU) \\ R = \sqrt{y^2 + z^2}\ ,\ K = \omega^2/g\ ,\ \tau = U\omega/g\ ,\ K_0 = g/U^2 \end{array} \right\} \tag{11}$$

$K_0(x)$ in (10) is the modified Bessel function of second kind.

One important information to be obtained from the outer solution may be the Kochin function, which is physically the wave amplitude far from the ship. The Kochin function can be defined by considering the asymptotic expression of (10) and substituting it into (8):

$$C_j(k) = \int_{-\infty}^{\infty} Q_j(x)\, e^{ikx}\, dx \tag{12}$$

$$C(k) = C_7(k) + \frac{\omega\omega_0}{g} \sum_{j=1,3,5} \frac{\xi_j}{a}\, C_j(k)\,. \tag{13}$$

The amplitude of ship motion in the j-th mode, ξ_j/a, will be given after solving the motion equation. Further the source strength, $Q_j(x)$, will be determined by matching (8) with the inner solution in an overlap region.

For the matching procedure to follow, expansions of (10) must be sought. For $\nu R \gg 1$, the Taylor expansion for the integrand appearing in (10) gives readily the desired expansion. On the other hand, for $\nu R \ll 1$, we can use a method of *Kashiwagi and Ohkusu (1989)* or *Newman's (1978)* analysis extended from *Ursell's (1962)* analysis for $U = 0$. The results are:

$$\begin{aligned} G^*_{3D}(k;y,z) &= i\,\epsilon_k\, e^{\nu(z-i\epsilon_k|y|)} + \frac{\cos\theta}{\pi\nu R} \\ &\quad + O(\,(\nu R)^{-2},\ k^2/\nu^2,\ k^2 y/\nu\,) \quad \text{for } \nu R \gg 1 \end{aligned} \tag{14}$$

$$\begin{aligned} G^*_{3D}(k;y,z) &= \frac{1}{\pi}(1+\nu z)\Big(\ln\frac{|k|R}{2} + \gamma\Big) + \frac{1}{\pi}\nu R\,(\cos\theta + \theta\sin\theta) \\ &\quad + \frac{1}{\pi}(1+\nu z) \left[\begin{array}{l} \dfrac{1}{\sqrt{1-k^2/\nu^2}} \Big\{ \pi i\epsilon_k + \cosh^{-1}\Big(\dfrac{\nu}{|k|}\Big) \Big\} \\ \dfrac{1}{\sqrt{k^2/\nu^2-1}} \Big\{ -\pi + \cos^{-1}\Big(\dfrac{\nu}{|k|}\Big) \Big\} \end{array} \right] \\ &\quad + O(\nu^2 R^2,\ k^2 R^2\,) \qquad\qquad \text{for } \nu R \ll 1 \end{aligned} \tag{15}$$

where $z = -R\cos\theta$, $y = R\sin\theta$, γ is Euler's constant, and the upper and lower expressions in the brackets apply to $\nu > |k|$ and $\nu < |k|$, respectively.

Eq. (14) must be valid for the whole range of U, insofar as the frequency is high enough. However, further simplifications are possible for $U = O(1)$:

$$G^*_{3D}(k;y,z) \sim i\, e^{K(z-i|y|)-i2\tau k|y|}\,. \tag{16}$$

This is the expression of the rational strip theory of *Ogilvie and Tuck (1969)*, under the assumption of $\omega = O(\varepsilon^{-1/2})$ and $U = O(1)$.

4. 2-D Green Function and Its Expansion

The 2-D Green function considered here for the inner problem is the pseudo 3-D one, satisfying

$$\Big(\frac{\partial^2}{\partial y^2} + \frac{\partial^2}{\partial z^2}\Big) G^{(i)} = \delta(x-\xi)\,\delta(y-\eta)\,\delta(z-\zeta) \tag{17}$$

$$\Big[\, \Big(i\omega - U\frac{\partial}{\partial x}\Big)^2 + g\frac{\partial}{\partial z} + \mu\Big(i\omega - U\frac{\partial}{\partial x}\Big) \,\Big]\, G^{(i)} = 0 \quad \text{on } z = 0 \tag{18}$$

where $\delta(x)$ on the right-hand side of (17) denotes Dirac's delta function.

The explicit form of $G^{(i)}$ may be given by the Fourier transform, e.g. *Yeung and Kim (1985)*:

$$G^{(i)}(x,y,z;\xi,\eta,\zeta) = \frac{\delta(x-\xi)}{2\pi}\ln\frac{R}{R_1} + G_p(x-\xi,|y-\eta|,z+\zeta) \tag{19}$$

$$G_p(x,y,z) = \frac{1}{2\pi}\int_{-\infty}^{\infty} G_p^*(k;y,z)\,e^{-ikx}\,dk \tag{20}$$

$$G_p^*(k;y,z) = -\frac{1}{2\pi}\lim_{\mu\to 0}\int_{-\infty}^{\infty}\frac{e^{z|m|-imy}}{|m|-\frac{1}{g}(\omega+kU-i\mu)^2}\,dm \tag{21}$$

$$= -\frac{1}{\pi}\,\Re\Big[e^{\nu(z-i|y|)}E_1\{\nu(z-i|y|)\}\Big] + i\epsilon_k\,e^{\nu(z-i\epsilon_k|y|)}\,. \tag{22}$$

$E_1(u)$ is the exponential integral function with complex variable.

Eq. (20), which is the inverse Fourier transform of (22), can be written in the form

$$G_p(x,y,z) = u(-x)\,e^{i\frac{\omega}{U}x}\frac{\sqrt{K_0}}{\pi}\int_0^{\infty}\frac{d\ell}{\sqrt{\ell}}\,e^{\ell z}\cos(\ell y)\sin(\sqrt{K_0\ell}\,x) \tag{23}$$

$$= u(-x)\,e^{i\frac{\omega}{U}x}\frac{\sqrt{K_0}}{\pi}\,\Im\left[\sqrt{\frac{\pi}{|z|+i|y|}}\left\{w(\alpha)-e^{-\alpha^2}\right\}\right] \tag{24}$$

where

$$w(\alpha) = e^{-\alpha^2}\mathrm{Erfc}(-i\alpha)\,,\ \alpha = \frac{x}{2}\sqrt{\frac{K_0}{|z|+i|y|}}\,. \tag{25}$$

$\mathrm{Erfc}(-i\alpha)$ denotes the error function with complex variable, and $u(-x)$ the unit step function, equal to 0 for $x>0$ and 1 for $x<0$.

$G_p(x,y,z)$ represents physically the divergent (longitudinal) wave, existing far behind the source point. This fact can be explicitly shown either by using the expansion of (24) for $y,\,z = O(\varepsilon)$, in which $\exp(-\alpha^2)$ is the leading term, or by applying the stationary-phase method, *Faltinsen (1983)*, to the integral in (23).

By substituting into (22) the asymptotic and power-series expansions of the exponential integral function, the expansions of $G_p^*(k;y,z)$ for $\nu R \gg 1$ and $\nu R \ll 1$ can be obtained in the form

$$G_p^*(k;y,z) = i\,\epsilon_k\,e^{\nu(z-i\epsilon_k|y|)} + \frac{\cos\theta}{\pi\nu R} + O(\,(\nu R)^{-2})\quad \text{for } \nu R\gg 1 \tag{26}$$

$$G_p^*(k;y,z) = \frac{1}{\pi}(1+\nu z)\Big(\ln\nu R+\gamma+\pi i\epsilon_k\Big) + \frac{1}{\pi}\nu R\,(\cos\theta+\theta\sin\theta) + O(\nu^2R^2)\qquad \text{for } \nu R\ll 1\,. \tag{27}$$

Eq. (26) is identical to (14) in the leading term, implying that the pseudo 3-D Green function is equivalent to the 3-D Green function for all values of U for high frequencies. On the other hand, for low frequencies, comparison of (15) with (27) gives:

$$G_{3D}^*(k;y,z) = G_p^*(k;y,z) - \frac{1}{\pi}(1+\nu z)\,g^*(k) + O(\nu^2R^2,\,k^2R^2) \tag{28}$$

where

$$g^*(k) = \ln\frac{2\nu}{|k|} + \pi i\,\epsilon_k - \left[\begin{array}{c}\dfrac{1}{\sqrt{1-k^2/\nu^2}}\left\{\pi i\epsilon_k+\cosh^{-1}\Big(\dfrac{\nu}{|k|}\Big)\right\}\\ \dfrac{1}{\sqrt{k^2/\nu^2-1}}\left\{-\pi+\cos^{-1}\Big(\dfrac{\nu}{|k|}\Big)\right\}\end{array}\right]. \tag{29}$$

Since G_p represents only the divergent wave, $g^*(k)$ given by (29) can be understood as the correction term associated with the transverse wave which exists in the genuine 3-D wave field. $g^*(k)$ reduces to zero for $\nu \gg |k|$, giving automatically the relation $G_p(x;y,z) \approx G_{3D}(x,y,z)$.

Let the zero-speed 2-D Green function be denoted by $G_{2D}(y,z)$. Because the substitution of $U=0$ in (21) gives the same result as $k=0$, the following holds

$$G_{2D}(y,z) = G_p^*(0;y,z)\,. \tag{30}$$

Therefore, expansions of $G_{2D}(y,z)$ can be readily obtained from (26) and (27). The relation between G_{2D} and the 3-D Green function is also obtained from (28) and (29), by simply putting $k=0$, i.e. $\nu = K$ and $\epsilon_k = 1$.

5. Unified Theory

5.1 Radiation problem

In the inner problem, due to the coordinate stretching, differentiations with respect to y and z cause the change in order by $O(\varepsilon^{-1})$. This slender-body assumption allows us to use the 2-D Laplace equation as the governing equation. With the same argument, the leading term in the free-surface condition may be the rigid-wall condition, $\partial\phi_j/\partial z = 0$. This establishes the ordinary slender-body theory.

However, to seek a unified solution valid for the whole range of frequencies, *Newman (1978)* considered the following boundary-value problem:

$$\nabla^2_{2D}\,\phi_j^{(i)} = 0 \tag{31}$$

$$\frac{\partial \phi_j^{(i)}}{\partial z} - K\phi_j^{(i)} = 0 \qquad \text{on } z=0 \tag{32}$$

$$\frac{\partial \phi_j^{(i)}}{\partial N} = N_j + \frac{U}{i\omega}M_j \quad (j=1,3,5) \qquad \text{on } \mathcal{B}(x) \tag{33}$$

where N_j and M_j are slender-body approximations of n_j and m_j defined in (5), and $\mathcal{B}(x)$ denotes the contour of the transverse section at station x along the ship's length.

The surge mode ($j=1$) is retained in (33), although the surge mode is of higher order as compared to heave ($j=3$) and pitch ($j=5$) modes. In the conventional strip theories, the surge mode has been simply discarded as higher order. However, with slenderness assumption, the surge mode is of the same order as the roll mode which is commonly included in strip theories. We note that no radiation condition is specified in (32). Except for that, the computation method for solving (31)–(33) can be the same as that used in strip theories.

The unified theory considers a homogeneous solution plus the particular solution, i.e. the general inner solution takes the form:

$$\left.\begin{aligned} \phi_j^{(i)}(x;y,z) &= \varphi_j(y,z) + \frac{U}{i\omega}\widehat{\varphi}_j(y,z) + C_j(x)\,\varphi_H(y,z) \\ \varphi_H(y,z) &= \varphi_3(y,z) - \overline{\varphi_3(y,z)} \end{aligned}\right\} \tag{34}$$

where φ_j and $\widehat{\varphi}_j$ are the particular solutions, corresponding to the first and second terms on the r.h.s. of (33) respectively, and the overbar means the complex conjugate. Therefore, $\varphi_H(y,z)$ satisfies the homogeneous body boundary condition.

The complex conjugate of the velocity potential is physically equivalent to the situation in which the time is reversed, meaning the inward propagation of the wave, which must be allowed due to the absence of the radiation condition. Therefore $\varphi_H(y,z)$ represents the standing wave and its amplitude, $C_j(x)$, is related to the magnitude of 3-D interaction effects among transverse sections; which is unknown in the inner problem but will be determined in the matching procedure with the outer solution.

With (26) and (30) taken into account, the outer expansion of (34) can be obtained in the form

$$\phi_j^{(i)}(x;y,z) \sim \Big[\sigma_j + \frac{U}{i\omega}\widehat{\sigma}_j + C_j(x)\left\{\sigma_3 - \overline{\sigma}_3\right\}\Big]\, G_{2D}(y,z) + 2i\, C_j(x)\,\overline{\sigma}_3\, e^{Kz}\cos Ky \tag{35}$$

where σ_j and $\widehat{\sigma}_j$ denote the 2-D Kochin functions which can be computed from particular solutions of φ_j and $\widehat{\varphi}_j$, respectively.

The outer solution is given by (8) and the 3-D Green function has its inner expansion given as (28). However, in order to match with (35), further approximations may be needed concerning the order of forward speed. According to *Newman's (1978)* analysis, it takes the form

$$G^*_{3D}(k;y,z) = G_{2D}(y,z) - \frac{1}{\pi}(1+Kz)\,f^*(k) + O(K^2R^2,\,(\nu-K)R,\,k^2R^2) \tag{36}$$

where

$$f^*(k) = \ln\frac{2K}{|k|} + \pi i - \left[\begin{array}{c} \dfrac{1}{\sqrt{1-k^2/\nu^2}}\left\{\pi i\epsilon_k + \cosh^{-1}\Big(\dfrac{\nu}{|k|}\Big)\right\} \\ \dfrac{1}{\sqrt{k^2/\nu^2-1}}\left\{-\pi + \cos^{-1}\Big(\dfrac{\nu}{|k|}\Big)\right\} \end{array}\right]. \tag{37}$$

The upper and lower expressions in the brackets apply to $\nu > |k|$ and $\nu < |k|$, respectively.

The term $O((\nu-K)R)$ is neglected as a small quantity. This implies that the unified theory may be consistent for relatively low forward speeds. However, since the genuine 3-D wavenumber, $\nu(k)$, is retained in $f^*(k)$, forward-speed effects as well as 3-D interactions among transverse sections are to some extent expected to be accounted for; these will be made clear by comparison with experiments.

Substituting (36) in (8), the inner expansion of the outer solution can be expressed as

$$\phi_j^{(o)}(x,y,z) \sim Q_j(x)\,G_{2D}(y,z) - \frac{1}{\pi}(1+Kz)\int_{-\infty}^{\infty} Q_j(\xi)\,f(x-\xi)\,d\xi\,. \tag{38}$$

The expression for $f(x-\xi)$, suitable for numerical computations, can be found in *Newman and Sclavounos (1980)*, *Sclavounos (1984a)*, and *Sclavounos (1984b)*.

The inner and outer solutions may be matched by comparing (35) with (38). To leading order, the results are of the form

$$Q_j(x) = \sigma_j + \frac{U}{i\omega}\widehat{\sigma}_j + C_j(x)\left\{\sigma_3 - \overline{\sigma}_3\right\} \tag{39}$$

$$2i\,C_j(x)\,\overline{\sigma}_3 = -\frac{1}{\pi}\int_{-\infty}^{\infty} Q_j(\xi)\,f(x-\xi)\,d\xi\,. \tag{40}$$

Eliminating $C_j(x)$ from these two equations, the integral equation for $Q_j(x)$ can be obtained in the form

$$Q_j(x) + \frac{i}{2\pi}\Big(1-\sigma_3/\overline{\sigma}_3\Big)\int_{-\infty}^{\infty} Q_j(\xi)\,f(x-\xi)\,d\xi = \sigma_j + \frac{U}{i\omega}\widehat{\sigma}_j \quad (j=1,3,5)\,. \tag{41}$$

In numerical computations, the integration range with respect to ξ may be reduced over the ship's length. Once (41) is solved, it is straightforward to compute $C_j(x)$ from (39), thereby completing the inner and outer solutions.

5.2 Diffraction problem

The body boundary condition (6) can be written as

$$\frac{\partial \phi_7}{\partial n} = k_0\, e^{k_0 z - i k_0 y \sin\chi} \Big\{ i n_2 \sin\chi - (n_3 - i n_1 \cos\chi) \Big\} e^{i\ell x} \tag{42}$$

where the wavenumber in the x-axis is denoted by $\ell = -k_0 \cos\chi$, which will be used hereafter.

The rapidly varying part along ship's length is described by $\exp(i\ell x)$. In beam sea, $\ell = 0$. However, as in the radiation problem, no assumption should be made on the order of ℓ to obtain a unified solution applicable to all the wavelengths and incident-wave angles.

The inner solution may be sought in the form

$$\phi_7^{(i)}(x; y, z) = \Big\{ \psi_S(x; y, z) + \psi_A(x; y, z) \Big\} e^{i\ell x} \tag{43}$$

where ψ_S and ψ_A are symmetric and antisymmetric components with respect to $y = 0$, respectively, of the slowly-varying part of the solution.

For clarity, the explanations will be made only for ψ_S component. Similar analysis can be done for the ψ_A component, Appendix-1.

With the slender-ship assumption, the boundary-value problem for the inner solution can be formulated as follows:

$$\nabla_{2D}^2\, \psi_S - \ell^2 \psi_S = 0 \tag{44}$$

$$\frac{\partial \psi_S}{\partial z} - k_0\, \psi_S = 0 \qquad \text{on } z = 0 \tag{45}$$

$$\frac{\partial \psi_S}{\partial N} = k_0\, e^{k_0 z} \Big\{ N_2 \sin\chi\, \sin(k_0 y \sin\chi) - (N_3 - i N_1 \cos\chi)\, \cos(k_0 y \sin\chi) \Big\} \qquad \text{on } \mathcal{B}(x)\,. \tag{46}$$

The governing equation is not the Laplace equation but the 2-D modified Helmholtz equation, and the wavenumber appearing in the free-surface condition is not $K = \omega^2/g$ but $k_0 = \omega_0^2/g$.

The contribution from the N_1-component (the x-component of the normal vector) is retained in (46). In conventional slender-body theories, the N_1-term has been discarded as higher order by comparison to N_2 and N_3, implying that the effects of wave diffraction from the bow part near the water line cannot be taken into account in the context of slender-body theory. However, once the value of N_1 is given, no difficulty exists in solving (44)–(46) with N_1-term kept in (46). (The only thing to do in the program is replacing N_3 with $N_3 - i N_1 \cos\chi$.) In fact, the N_1-term is expected to be more crucial than the N_2- and N_3-terms near the ship ends, in predictions of the surge exciting force and the added resistance in head waves.

The inner solution can be constructed in the form of the particular solution ψ_S^P plus a homogeneous solution ψ_S^H:

$$\psi_S(x; y, z) = \psi_S^P(y, z) + C_{7S}(x)\, \psi_S^H(y, z) \tag{47}$$

$$\psi_S^P = -e^{k_0 z} \cos(k_0 y \sin\chi) \tag{48}$$

$$\psi_S^H = \psi_{2D}(y, z) + e^{k_0 z} \cos(k_0 y \sin\chi)\,. \tag{49}$$

Here the particular solution is taken as the incident wave with opposite sign, and $C_{7S}(x)$ is the unknown coefficient of homogeneous component. $\psi_{2D}(y,z)$ denotes a numerical solution for (44)–(46), which may be obtained using the integral-equation method. In that method, the Green function satisfying the 2-D modified Helmholtz equation is needed, for which *Kashiwagi (1992)* adopted the following:

$$G_H(\ell;y,z;\eta,\zeta) = -\frac{1}{2\pi}\Big\{K_0(|\ell|R) - K_0(|\ell|R_1)\Big\} + H_{2D}(\ell;|y-\eta|,z+\zeta) \tag{50}$$

$$H_{2D}(\ell;y,z) = \Re\Big[\,\mathcal{H}_{2D}(\ell;y,z)\,\Big] + i\,e^{k_0 z}\cos(k_0 y\sin\chi) \tag{51}$$

$$\mathcal{H}_{2D}(\ell;y,z) = -\frac{1}{2\pi}\lim_{\mu\to 0}\int_{-\infty}^{\infty}\frac{e^{z\sqrt{\ell^2+m^2}-imy}}{\sqrt{\ell^2+m^2}-(k_0-i\mu)}\,dm\,. \tag{52}$$

Here $\mathcal{H}_{2D}(\ell;y,z)$ is the exact expression satisfying the extraneous radiation condition, which can be given by substituting k_0 and $k_0|\cos\chi|$ instead of ν and $|k|$, respectively, into the Fourier transform of the 3-D Green function given in (9). Therefore, as is clear from (10), the imaginary part of $\mathcal{H}_{2D}$ takes the form

$$\Im\Big[\,\mathcal{H}_{2D}(\ell;y,z)\,\Big] = i\,\csc\chi\,e^{k_0 z}\cos(k_0 y\sin\chi)\,. \tag{53}$$

This function is singular at $\chi=\pi$ (head wave). The proper analysis for head wave was shown by *Ursell (1968)*, indicating that the imaginary part is proportional to $|y|$ and thus no progressive wave exists in the y-direction. This unrealistic property is inherent in the 2-D head-wave problem, and was surmounted by the matched asymptotic-expansion analyses of *Faltinsen (1971)*, *Maruo and Sasaki (1974)*, *Adachi (1977)*.

To seek a unified solution which is valid not only for head wave but also for all heading angles, *Sclavounos (1984a)* took only the real part of $\mathcal{H}_{2D}$ as the inner-problem Green function; this is one of the possible choices, because there is no need to satisfy the radiation condition in the inner problem. However, numerical computations based on the integral-equation method using the Green function of Sclavounos' choice showed the irregular-frequency phenomena at some frequencies. *Kashiwagi (1992)* resolved these defects by adopting a complex form, (51), as the inner-problem Green function, which is another possible choice and in fact regular for all heading angles.

An efficient calculation method for (52) is less popular than the radiation Green function, $G_{2D}(y,z)$. This seeming complexity might be a reason why the strip theory is still being used despite of its shortcomings. Appendix-2 provides a calculation method, with much attention paid on the calculation efficiency.

From (43) and (47)–(49), the outer expansion of the inner solution can be expressed as

$$\phi_{7S}^{(i)}(x;y,z) \sim C_{7S}(x)\,\sigma_7\,e^{i\ell x}\,H_{2D}(\ell;y,z) + \Big\{C_{7S}(x)-1\Big\}\,e^{k_0 z}\cos(k_0 y\sin\chi)\,e^{i\ell x} \tag{54}$$

where σ_7 denotes the 2-D Kochin function to be computed from $\psi_{2D}(y,z)$.

For obtaining the inner expansion of the outer solution, the relation between $H_{2D}(\ell;y,z)$ and $G_{3D}^*(k;y,z)$ must be known; which can be achieved by noting the similarity between (9) and (52), i.e. $\nu\to k_0$ and $|k|\to k_0|\cos\chi|$. The result can be expressed in the form

$$\phi_{7S}^{(o)}(x,y,z) \sim Q_7(x)\,H_{2D}(\ell;y,z) - \frac{1}{\pi}(1+k_0 z)\,\mathcal{L}_S(Q_7;x) \tag{55}$$

where

$$\mathcal{L}_S(Q_7; x) = Q_7(x)\, h_S(\chi) + \int_{-\infty}^{\infty} Q_7(\xi)\, f(x-\xi)\, d\xi \tag{56}$$

$$h_S(\chi) = \csc\chi\, \cosh^{-1}(|\sec\chi|) - \ln(2|\sec\chi|) \tag{57}$$

and the kernel function $f(x-\xi)$ in (56) is the same as that used in the radiation problem.

The matching requirement between (54) and (55) gives two equations for two unknowns, $C_{7S}(x)$ and $Q_7(x)$. Eliminating $C_{7S}(x)$ from those two equations, we can have the integral equation for $Q_7(x)$, in the form

$$Q_7(x) + \frac{1}{\pi}\, \sigma_7\, \mathcal{L}_S(Q_7; x) = \sigma_7\, e^{i\ell x}\,. \tag{58}$$

A numerical solution of $Q_7(x)$ determines readily $C_{7S}(x)$, completing the inner and outer solutions. The integral equation (58) may be solved with the same scheme as that for the corresponding equation, (41), in the radiation problem.

For $F_n < 0.15$, the x-axis may be divided into several segments of equal length and on each segment the unknown source strength be assumed to vary linearly, which can set up a linear system of simultaneous equations, giving stable solutions. However, as the Froude number increases, that scheme becomes unstable, probably because the integral equation will be of Vorterra type. To overcome this difficulty, *Sclavounos (1984b)* proposed a Chebyshev-polynomial representation for the unknown source distribution and the use of Galerkin's method to construct a well-conditioned matrix. This scheme seems to give a stable solution especially when the forward speed is relatively high.

6. Hydrodynamic Forces

Substituting the completed inner solution into the linearized Bernoulli equation, integrating over the mean wetted surface of the ship, and using Tuck's theorem, *Ogilvie and Tuck (1969)*, the hydrodynamic force acting in the i-th direction can be summarized as

$$F_i = -(i\omega)^2 \sum_{j=1,3,5} \Big[A_{ij} + B_{ij}/i\omega \Big]\, \xi_j \qquad (i = 1, 3, 5) \tag{59}$$

$$\begin{aligned} A_{ij} + B_{ij}/i\omega = &-\rho \int_L dx \int_{\mathcal{B}(x)} \Big(N_i - \frac{U}{i\omega} M_i \Big) \Big\{ \varphi_j(y,z) + \frac{U}{i\omega} \widehat{\varphi}_j(y,z) \Big\}\, ds \\ &-\rho \int_L dx\, C_j(x) \int_{\mathcal{B}(x)} \Big(N_i - \frac{U}{i\omega} M_i \Big)\, \varphi_H(y,z)\, ds \end{aligned} \tag{60}$$

where A_{ij} and B_{ij} are the added-mass and damping coefficients in the i-th direction due to the j-th mode of motion, and $\mathcal{B}(x)$ denotes the sectional contour below $z = 0$ at station x. M_i is the slender-body approximation of the m-term, defined in (7). If this is approximated further by neglecting the steady disturbance potential φ_s, it follows that $M_1 = M_3 = 0$, $M_5 = N_3$, and $N_5 = -x\, N_3$. Correspondingly, $\widehat{\varphi}_1 = \widehat{\varphi}_3 = 0$, $\widehat{\varphi}_5 = \varphi_3$, and $\varphi_5 = -x\, \varphi_3$.

The solutions to be obtained are φ_1 and φ_3. The calculation method for those can be the same as that commonly used in the strip theory, except that the surge mode ($j = 1$) is included in the present case.

The first line in (60) gives identical results to the strip theory except for surge-related coefficients, and the second line in (60) contains the 3-D and forward-speed effects through the coefficient of homogeneous solution, $C_j(x)$.

In the diffraction problem, not only the integrated value of exciting forces, but also the pressure distribution is required to predict local wave loads, e.g. *Mizoguchi et al. (1992).*

Neglecting the contribution of the steady disturbance potential and applying the differentiation with respect to x only to the rapidly-varying term, $\exp(i\ell x)$, the symmetric part of the diffraction pressure is

$$\begin{aligned} P_d &= -\rho g a \, \frac{\omega}{\omega_0} \Big(1 - \frac{U}{i\omega} \frac{\partial}{\partial x} \Big) \, C_{7S}(x) \, \psi_S^H(y,z) \, e^{i\ell x} \\ &\cong -\rho g a \, C_{7S}(x) \, \big\{ \, \psi_{2D}(y,z) + e^{k_0 z} \cos(k_0 y \sin\chi) \, \big\} \; e^{i\ell x} \, . \end{aligned} \tag{61}$$

Integrating (61) over the ship hull gives the exciting force in the j-th direction:

$$E_j = \rho g a \int_L dx \, C_{7S}(x) \, e^{i\ell x} \int_{\mathcal{B}(x)} \Big\{ \psi_{2D}(y,z) + e^{k_0 z} \cos(k_0 y \sin\chi) \Big\} n_j \, ds \, . \tag{62}$$

In seakeeping, the wave-induced steady force and moment are also important. The added resistance can be computed by *Maruo's (1960)* formula, using the Kochin function. Maruo's analysis is based on the stationary-phase method and thus rather complicated. *Kashiwagi (1991)* showed a simpler analysis by use of Parseval's theorem in the Fourier transform, and gave formulae for the steady lateral force ($\overline{Y}$) and yaw moment ($\overline{N}$) as well; those are summarized as follows:

$$\frac{R_{AW}}{\rho g a^2} = \frac{1}{4\pi k_0} \Big[- \int_{-\infty}^{k_1} + \int_{k_2}^{k_3} + \int_{k_4}^{\infty} \Big] \Big\{ \, |C(k)|^2 + |S(k)|^2 \Big\} \frac{\nu \, (k - k_0 \cos\chi)}{\sqrt{\nu^2 - k^2}} \, dk \tag{63}$$

$$\begin{aligned} \frac{\overline{Y}}{\rho g a^2} &= -\frac{1}{4\pi k_0} \Big[- \int_{-\infty}^{k_1} + \int_{k_2}^{k_3} + \int_{k_4}^{\infty} \Big] \, \Im \Big\{ 2 C(k) \overline{S(k)} \Big\} \, \nu \, dk \\ &\quad + \frac{1}{2} \sin\chi \; \Im \Big[\, C(k_0,\chi) + i S(k_0,\chi) \, \Big] \end{aligned} \tag{64}$$

$$\begin{aligned} \frac{\overline{N}}{\rho g a^2} &= \frac{1}{4\pi k_0} \Big[- \int_{-\infty}^{k_1} + \int_{k_2}^{k_3} + \int_{k_4}^{\infty} \Big] \, \Re \Big\{ C'(k) \overline{S(k)} - S'(k) \overline{C(k)} \Big\} \, \nu \, dk \\ &\quad - \frac{1}{2} \sin\chi \; \Re \Big[\, C'(k_0,\chi) + i S'(k_0,\chi) \\ &\qquad\qquad + \frac{1}{k_0} \Big(\tau + \frac{k_0 \cos\chi}{K_0} \Big) \Big\{ C(k_0,\chi) + i S(k_0,\chi) \Big\} \Big] \end{aligned} \tag{65}$$

where

$$\left. \begin{matrix} k_1 \\ k_2 \end{matrix} \right\} = -\frac{K_0}{2} \Big(1 + 2\tau \pm \sqrt{1 + 4\tau} \Big) \qquad \left. \begin{matrix} k_3 \\ k_4 \end{matrix} \right\} = \frac{K_0}{2} \Big(1 - 2\tau \mp \sqrt{1 - 4\tau} \Big) \, . \tag{66}$$

$C(k)$ is the symmetric part of the Kochin function, which, as shown in (12) and (13), can be evaluated with the source strength $Q_j(x)$ in the outer solution. In the unified theory, $Q_j(x)$ will be given as numerical solutions of integral equations (41) and (58). The antisymmetric part of the Kochin function, $S(k)$, may be evaluated in a similar manner from the doublet distribution along the ship's length, Appendix-1. $C'(k)$ and $S'(k)$ in (65) denote differentiations with respect to k, and $C(k_0,\chi)$ and $S(k_0,\chi)$ are the values evaluated at $k = k_0 \cos\chi$ and $\sqrt{\nu^2 - k^2} = k_0 \sin\chi$.

The effects of wave diffraction are rationally taken into account in $\psi_{2D}(y,z)$ by retaining the N_1-term in the body boundary condition. This means that the bow diffraction effects are implicitly included in σ_7 and therefore in $Q_7(x)$ as well, because σ_7 is computed from ψ_{2D} and $Q_7(x)$ is a solution of (58).

The present analysis also includes the surge motion and its indirect effects on the heave and pitch motions through the cross-coupling terms in the motion equations. This is also different from the original unified theory; thus the name 'enhanced' unified theory, *Kashiwagi (1995a)*, is used.

A few comments should be made on the numerical treatment of the infinite integrals in (63). Conventional methods based on the strip theory, e.g. *Takahashi (1987)*, usually multiply the integrand by a convergence acceleration factor, like $\exp(-\nu z_0)$ with small positive value for z_0, to ensure the convergence at infinity. This treatment is apparently inconsistent in the context of slender-ship theory. *Kashiwagi and Ohkusu (1993)* showed that no difficulty arises in the convergence, even if the sources are placed on $z = 0$. Their calculation method utilizes the Fourier-series representation for the line distribution of sources, and the resultant singular integral, similar to that appearing in the wing theory, is evaluated analytically.

7. High-Speed Slender-Body Theory (HSSBT)

The unified theory can account for the 3-D interactions among transverse sections for the whole range of frequencies. Particularly for zero speed, the unified theory gives satisfactory results. However, for rather high speed, the matching procedure shows a little constraint, because the inner solution satisfies the zero-speed free-surface condition. As is pointed out by *Yeung and Kim (1985)*, the 3-D flow is dictated by the inner flow in the unified theory. Reversely, the 3-D flow should dictate the inner flow.

In that respect, there is no ambiguity in the derivation of (28), the relation between the 2-D (pseudo 3-D) Green function, $G_p(x; y, z)$, and the 3-D Green function, $G_{3D}(x, y, z)$. Therefore we are tempted to consider (18) as the free-surface condition in the inner problem, implying the assumption of $\omega \leq O(\varepsilon^{-1/2})$ and $U \leq O(\varepsilon^{-1/2})$. Then we have

$$\nabla^2_{2D}\, \phi_j = 0 \tag{67}$$

$$\left(i\omega - U\frac{\partial}{\partial x}\right)^2 \phi_j + g\frac{\partial \phi_j}{\partial z} = 0 \qquad \text{on } z = 0 \tag{68}$$

$$\frac{\partial \phi_j}{\partial N} = N_j + \frac{U}{i\omega} M_j \quad (j = 2 \sim 6) \quad \text{on } \mathcal{B}(x)\,. \tag{69}$$

If the above equations are supplemented with the radiation condition, the resulting formulation will be the same as that considered by *Chapman (1975, 1976)*. Chapman solved the sway and yaw motions of a plate, applying the finite difference scheme to the above boundary-value problem.

Inspired by excellent agreement of Chapman's results with experiments, a number of studies have been made to extend to a general ship-like geometry; for lateral motion problems, by *Kashiwagi and Hatta (1984)*, *Kashiwagi (1984)*, and *Yamasaki and Fujino (1983, 1984, 1985)*. For heave and pitch problems, by *Saito and Takagi (1978)*, *Adachi (1980)*, *Yeung and Kim (1981)*, and *Faltinsen (1983)*. Recently, *Faltinsen and Zhao (1991)* and *Ohkusu et al.(1991)* applied the same formulation to the analysis of a high-speed catamaran.

However, calculation methods used in those studies are much more difficult than the strip theory or the unified theory. In fact several solution methods have been developed; such as Fourier-transform method, integral-equation method using the Green function of (19), boundary-element method with $\log R$ used as the Green function, and so on. Nevertheless, it seems that a reliable calculation method is still not established.

From the viewpoint of the matching with the outer solution, few studies have been done, except for *Adachi (1980)* and *Ohkusu and Faltinsen (1990)*. Thus a brief discussion will be made below on the matching at the level of outer and inner Green functions.

Firstly, in the range of high frequencies assuming $\omega = O(\varepsilon^{-1/2})$ and $U \leq O(\varepsilon^{-1/2})$, as is clear from comparison between (14) and (26), $G_p(x; y, z)$ can be smoothly matched with $G_{3D}(x, y, z)$, and thus there is no need to consider 3-D correction terms (homogeneous solutions). This conclusion is valid irrespective of the order of U. Therefore, as suggested in (16), HSSBT encompasses theoretically the rational strip theory of *Ogilvie and Tuck (1969)* assuming $U = O(1)$.

Next let us consider the case of low frequencies assuming $\omega = O(\varepsilon)$ and $U \leq O(\varepsilon^{-1/2})$. In this case, as explicitly shown in (28), the inner expansion of the 3-D Green function includes 3-D correction terms associated with the transverse wave in addition to the divergent wave represented by $G_p(x; y, z)$. Following the idea of the unified theory, the 3-D correction terms may be matched with the homogeneous component in the inner solution. However, unlike the unified theory, constructing the homogeneous solution is not so easy because of the convection term in the free-surface condition. Fig. 2 sums up the above discussion showing where existing slender-ship theories can be applied.

Theory	Applicable Region
Strip Theory	(2)
RST	(2) (3)
HSSBT	(2) (3) (4)
UT	(1) (2)

RST : Rational Strip Theory
HSSBT: High-Speed Slender-Body Theory
UT : Unified Theory

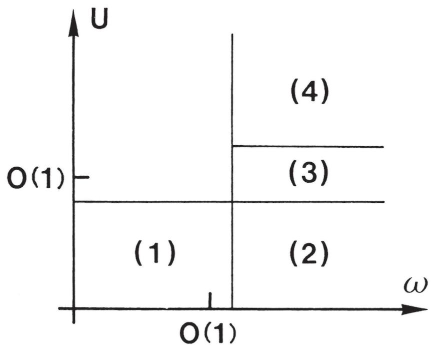

Fig. 2 Order of parameters valid for various theories

Returning to the homogeneous solution of HSSBT, *Kashiwagi (1995b)* recently showed an equation for that. Let us denote ϕ_j^+ for the solution satisfying (67)–(69) and the real-flow radiation condition, and likewise ϕ_j^- for the reverse-flow and reverse-time solution (with both signs of U and ω reversed).

Even when both U and ω are reversed in sign, (68) and (69) remain unchanged. Thus $\phi_j^+ - \phi_j^-$ gives a possible homogeneous solution. However, this solution is a function of x, affecting the downstream sections.

Therefore the homogeneous solution should have a form of convolution integral. Namely we can write

$$\phi_j^{(i)}(x; y, z) = \phi_j^+(x; y, z) + \int_{-\infty}^{\infty} C_j(\xi)\, \phi_H(x - \xi; y, z)\, d\xi \tag{70}$$

where

$$\phi_H(x; y, z) = \phi_j^+(x; y, z) - \phi_j^-(x; y, z)\,. \tag{71}$$

The weight function $C_j(\xi)$ is unknown in the above expression, which can be matched with the outer solution more easily by use of Fourier transform, *Kashiwagi (1995b)*.

Yeung and Kim (1985) also studied the 3-D corrections in the framework of HSSBT.

Instead of (70), they introduced a "generalized inner Green function", which is the same as the r.h.s. of (28), with $(1+\nu z)$ replaced by $\exp(\nu z)\cos(\nu y)$. They proposed a method using the generalized inner Green function in the 3-D panel method, but no numerical results were presented.

Lastly, let me refer to the popular transformation of the HSSBT formulation into an equivalent 2-D initial-value problem, which has been used in several published papers.

$$\begin{aligned} \phi_j(x;y,z) &= e^{i\frac{\omega}{U}(x-L/2)}\psi_j(x;y,z) \\ &= e^{-i\omega t^*}\psi_j(t^*;y,z)\ ,\ t^*=(L/2-x)/U\,. \end{aligned} \tag{72}$$

With this transformation, (67)–(69) can be rewritten as

$$\nabla_{2D}^2\,\psi_j = 0 \tag{73}$$

$$\frac{\partial^2\psi_j}{\partial t^{*2}} + g\frac{\partial\psi_j}{\partial z} = 0 \qquad \text{on } z=0 \tag{74}$$

$$\frac{\partial\psi_j}{\partial N} = \left(N_j + \frac{U}{i\omega}M_j\right)e^{i\omega t^*} \quad (j=2\sim 6) \quad \text{on } \mathcal{B}(x)\,. \tag{75}$$

If t^* is viewed as the time variable, the above is a 2-D time-domain problem and thus various existing solution methods may be used.

Equivalent initial condition can be given by

$$\psi_j = 0\ ,\quad \frac{\partial\psi_j}{\partial t^*} = 0 \qquad \text{at } t^*=0\ , \tag{76}$$

which means physically no disturbances at the bow.

Kashiwagi (1995b) showed numerical results based on this initial-value formulation, using the quadratic isoparametric elements in the boundary-element method and a numerical absorbing beach to satisfy the radiation condition.

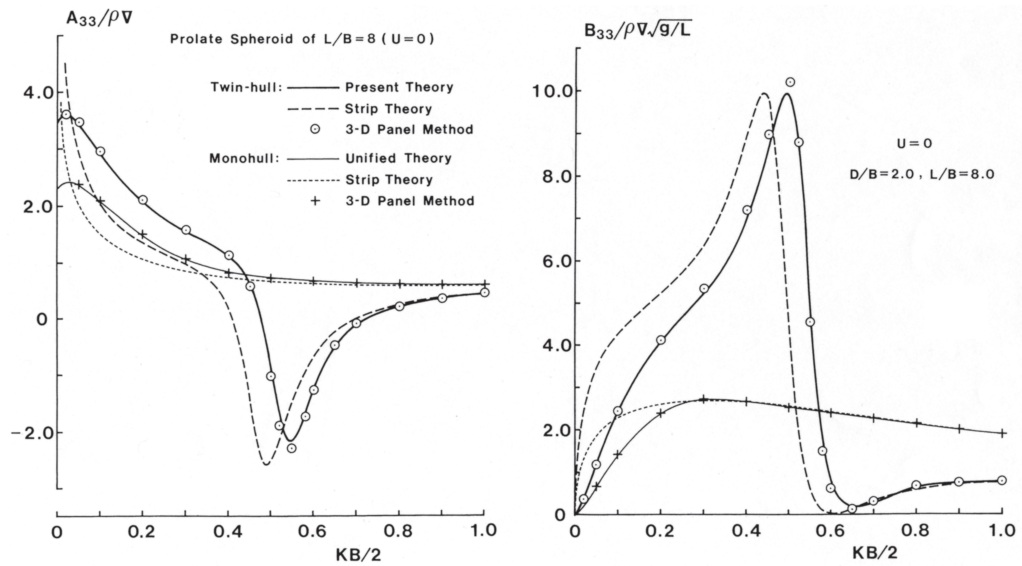

Fig. 3 Heave added-mass and damping coefficients of twin half-immersed spheroids with $L/B=8$ and $D/B=2$ at $U=0$ (D being the separation distance between twin hulls)

8. Comparison of Numerical Results with Experiments

Figure 3 shows the zero-speed results for the radiation problem of a catamaran with half-immersed spheroid of $L/B = 8$ used as a demihull, *Kashiwagi (1993)*. In this analysis, the inner region is defined as flow field near the right (or left) demihull, and the interaction effects from the other demihull are taken into account through the matching with the outer solution. The results for a monohull are also shown and compared with independent results by a more rigorous 3-D panel method. The agreement is very good for the whole range of frequencies.

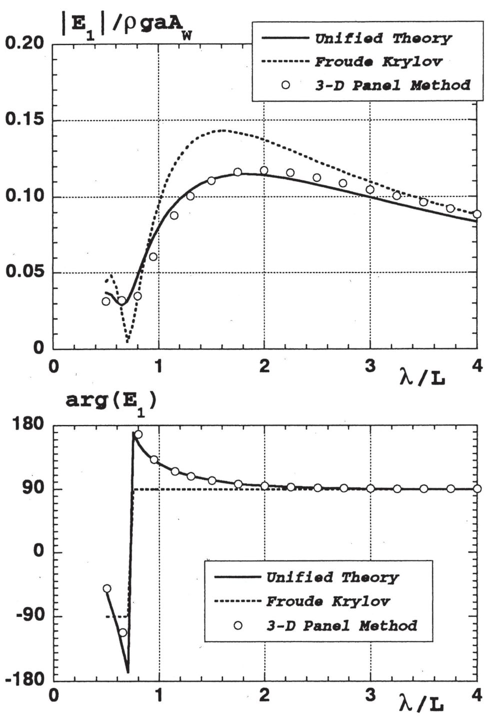

Fig. 4 Exciting surge force on a half immersed spheroid of $L/B = 5$ in head waves at $U = 0$

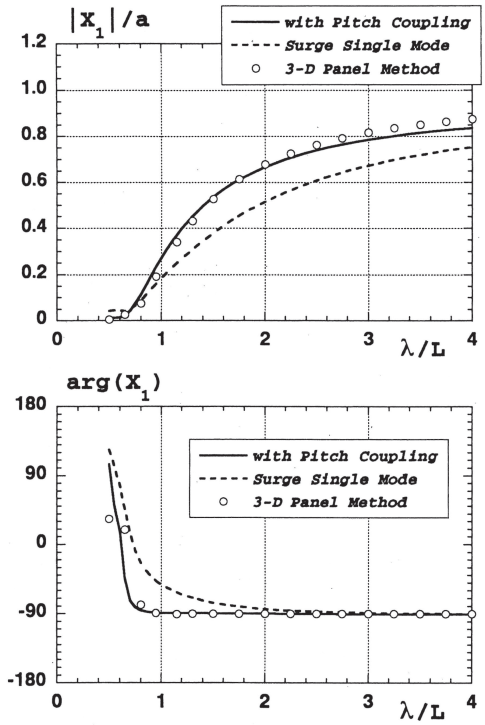

Fig. 5 Surge motion of a half immersed spheroid of $L/B = 5$ in head waves at $U = 0$

It has been said that the surge mode and the diffraction in the x-direction near the ship ends cannot be computed with the slender-ship theory. However, once the x-component of the normal vector is given, there are no fundamental difficulties in computations, as was shown by *Kashiwagi (1995a)* with various numerical examples. Fig. 4 shows the wave-exciting surge force on a rather blunt half-immersed spheroid of $L/B = 5$. The results agree well with the 3-D panel method, despite the small amplitude of the force. The dotted line is the result by the Froude-Krylov force only, which has been used in the strip theory but is obviously not enough.

With surge-related radiation forces and wave-exciting force, the surge motion was computed (Fig. 5). The solid line was obtained from the coupled motion equation between surge and pitch, and the dashed line is the solution as the single mode of surge. The noticeable

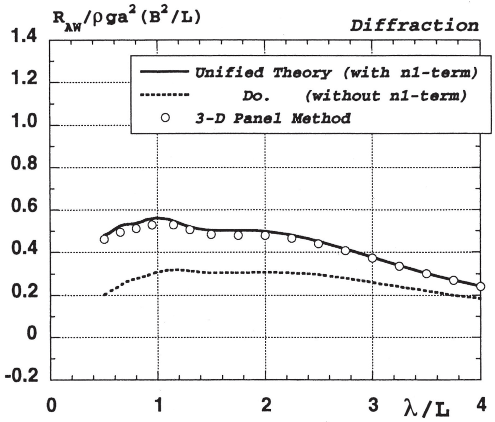

Fig. 6 Drift force on a fixed spheroid of $L/B = 5$ in head waves at $U = 0$ (diffraction only)

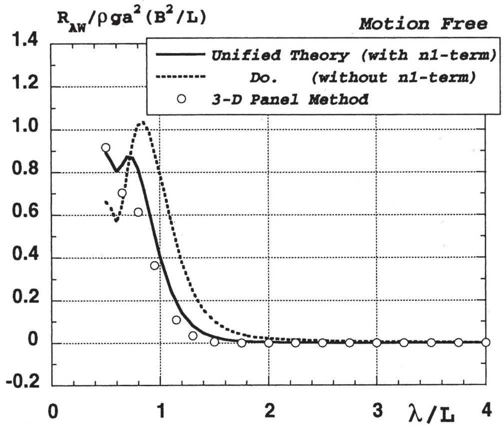

Fig. 7 Drift force on a freely oscillating spheroid of $L/B = 5$ in head waves at $U = 0$

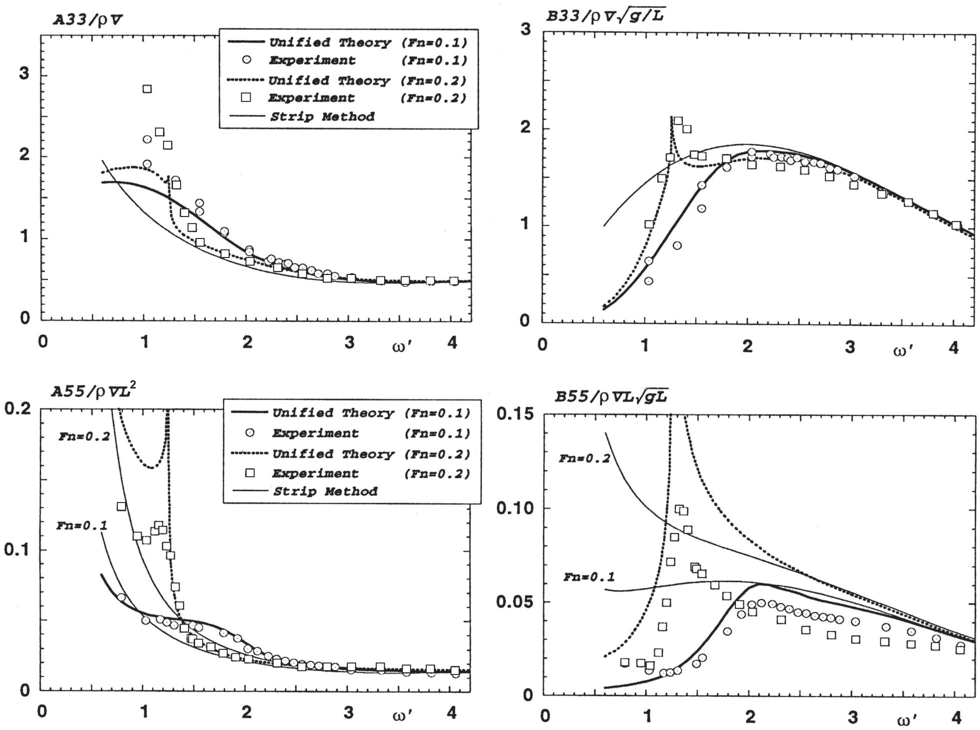

Fig. 8 Added-mass and damping coefficients in heave and pitch of a mathematical ship model at $F_n = 0.1$ and 0.2. Experiments are reproduced from *Matsunaga and Maruo (1981)*

discrepancy between the two and the good agreement between the solid line and the 3-D panel method implies that the coupling effects between surge and pitch must be taken into account.

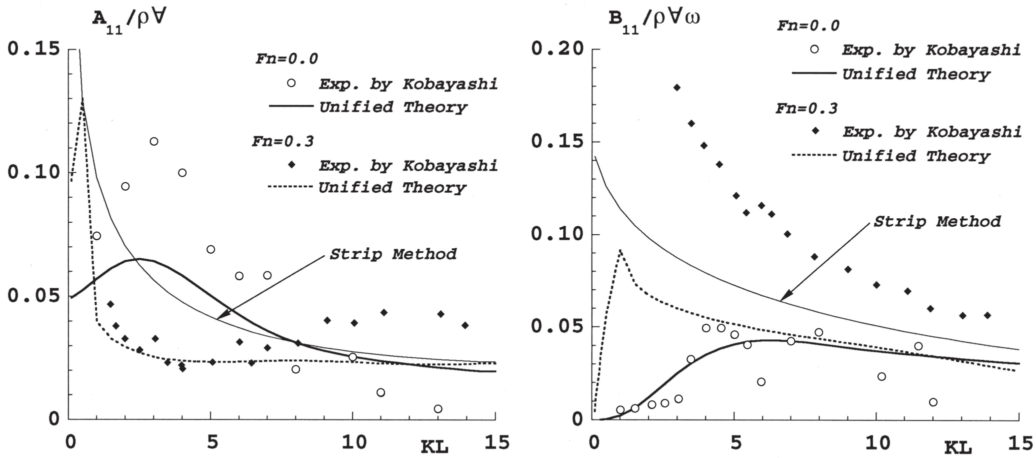

Fig. 9 Surge added-mass and damping coefficients of a half-immersed ellipsoid ($L/B = 4$, $B/2T = 1.25$) at $F_n = 0.0$ and 0.3

The effects of wave diffraction near the bow are expected to be pronounced in the drift force in head waves. Fig. 6 shows the results exerted by the wave diffraction only, and Fig. 7 the results including all effects of ship motions, demonstrating the importance of the N_1-term in the body-boundary condition.

Fig. 8 compares the diagonal coefficients in the heave and pitch motions of a mathematical ship model ($L/B = 8$) with transverse sections represented by the Lewis form to experiments of *Matsunaga and Maruo (1981)*. Except for the pitch damping coefficient at $F_n = 0.2$, the results of the unified theory agree well, including the rapid change near the critical frequency at $\tau = 1/4$. The unified theory is apparently superior to the interpolation theory developed by *Matsunaga and Maruo (1981, 1982)* and comparable to the 3-D Green function method of *Inoue and Makino (1989)*.

Experimental results for the surge added-mass and damping coefficients are published in very few papers. Comparisons are made here with experiments done by *Kobayashi (1981)*, using a half-immersed ellipsoid with length ratio $L/B = 4$ and $B/2T = 1.25$. $L/B =$

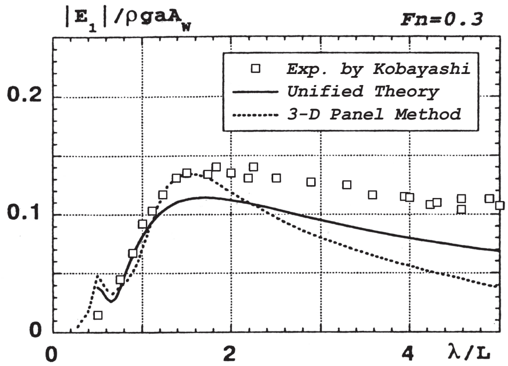

Fig. 10 Exciting surge force of a half-immersed ellipsoid in head waves at $Fn = 0.3$

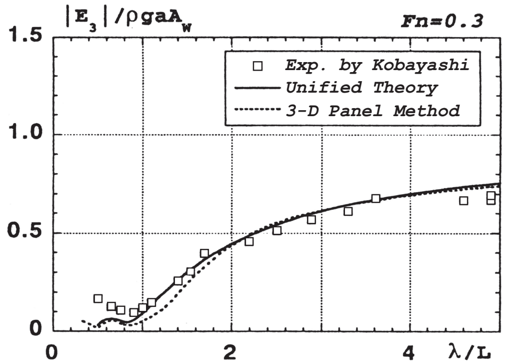

Fig. 11 Exciting heave force of a half-immersed ellipsoid in head waves at $Fn = 0.3$

4 is blunt considering the assumption of slender-ship theory.
Experimental values for $F_n = 0$ scatter due to the tank-wall interference, Fig. 9. Furthermore, the measurement of damping coefficient at $F_n = 0.3$ was not accurate, *Kobayashi (1981)* . With these taken into account, the 'enhanced' unified theory accounts well for the forward-speed effects.

Figs. 10, 11, and 12 compare the wave-exciting surge force, heave force, and pitch moment, respectively, at $F_n = 0.3$ with experiments of *Kobayashi (1981)* and 3-D panel method results of *Lin et al. (1993).* The unified theory underestimates the surge exciting force, but captures the tendency. Predictions in heave and pitch agree well with experiments. In the 'enhanced' unified theory, the effects of the bow diffraction are taken into account in the pressure level, and thus the heave force and pitch moment must, to some extent, differ from the results of original unified theory by *Sclavounos (1984a).*

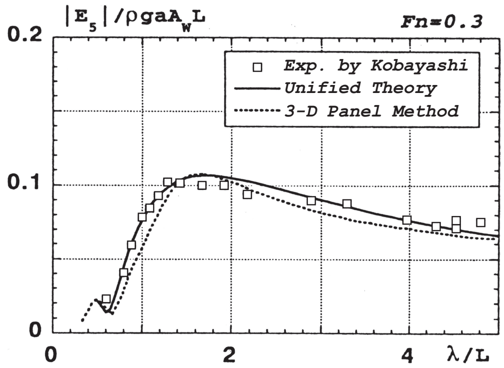

Fig. 12 Exciting pitch moment of a half-immersed ellipsoid in head waves at $Fn = 0.3$

The contribution of the N_1-term will be understood clearer by Fig. 13, which shows

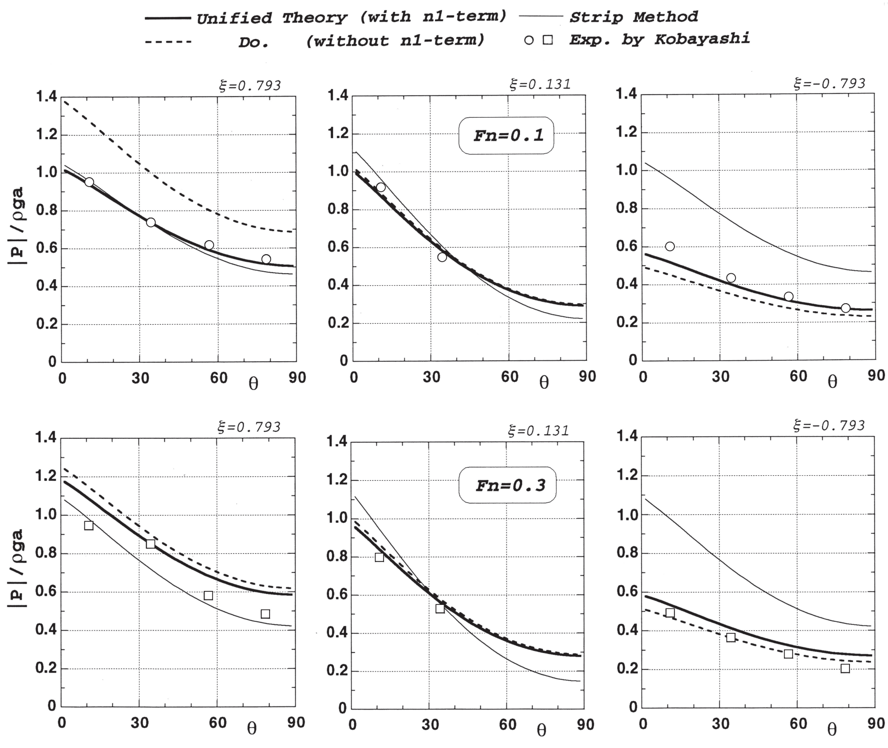

Fig. 13 Hydrodynamic pressure distributions on a half-immersed ellipsoid ($L/B = 4$, $B/2T = 1.25$) in head waves of $\lambda/L = 1.0$ (diffraction problem)

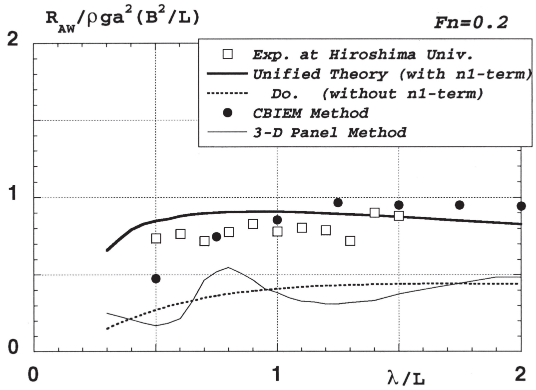

Fig. 14 Added resistance on a half-immersed spheroid of $B/L = 1/5$ in head waves at $Fn = 0.2$ (motions restrained)

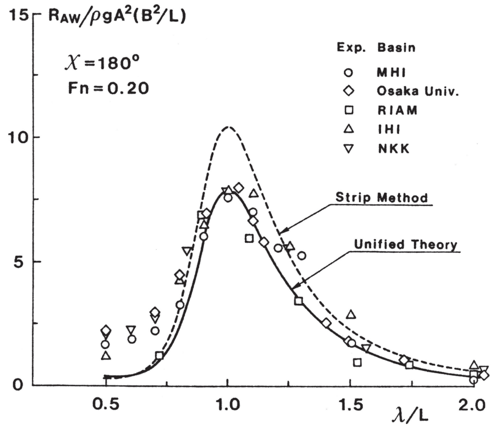

Fig. 15 Added resistance of SR108 container ship in head waves at $F_n = 0.2$ (free to surge, heave and pitch)

hydrodynamic pressure distributions in the head-sea diffraction problem of $\lambda/L = 1.0$, measured at $F_n = 0.1$ and 0.3 and at three different transverse sections ($x/(L/2) \equiv \xi = 0.793,\ 0.131,\ -0.793$). The section at $\xi = 0.793$ is near the bow and $\theta = 90°$ in the abscissa is the center of the section.

The strip theory does not contain the 3-D effects of wave attenuation along the ship, resulting in the same pressure at $\xi = 0.793$ and -0.793. In contrast, the unified theory accounts for the 3-D effects, and the agreement with measured values is remarkable. Particularly at $F_n = 0.1$, the results with the N_1-term show a sizable improvement over the results neglecting the N_1-term.

For precise predictions of the added resistance in short wavelengths it has been argued that the wave diffraction in x-direction near the bow should be taken into account but the slender-ship theory cannot, e.g. *Takahashi (1987)*. With this reasoning, *Fujii and Takahashi (1975)* proposed a semi-empirical formula, and other theoretical studies have been also made, *Faltinsen et al.(1980)*, *Nakamura et al.(1980)*, *Sakamoto and Baba (1986)*, *Ohkusu (1986)*. As expected from Fig. 13, the 'enhanced' unified theory provides a rational way of accounting for the wave diffraction near the bow. One example of that is shown in Fig. 14, which gives the added resistance on a half-immersed spheroid of $L/B = 5$ at $F_n = 0.2$. Experimental data were obtained at Hiroshima University, using the unsteady wave-pattern analysis proposed by *Ohkusu (1980)*. Other calculation by *Lin et al.(1993)*, using CBIEM (Combined Boundary Integral Equation Method) and the forward-speed version of the 3-D Green function method with flat-panel approximation, are also reproduced. The magnitude of wave diffraction effect in the x-direction is shown by the difference between the solid and dotted lines predicted by the unified theory. This difference is essential in the prediction of the added resistance in head waves.

Another example of the added resistance is shown in Fig. 15 for the SR108 container ship free to surge, heave and pitch, running at $F_n = 0.2$ in head waves. Due possibly to wave breaking or related phenomena, the prediction in short wavelengths is still smaller than measured forces, but the agreement becomes better as the wavelength increases. In head waves, the encounter frequency is relatively high at $F_n = 0.2$, which may be a good

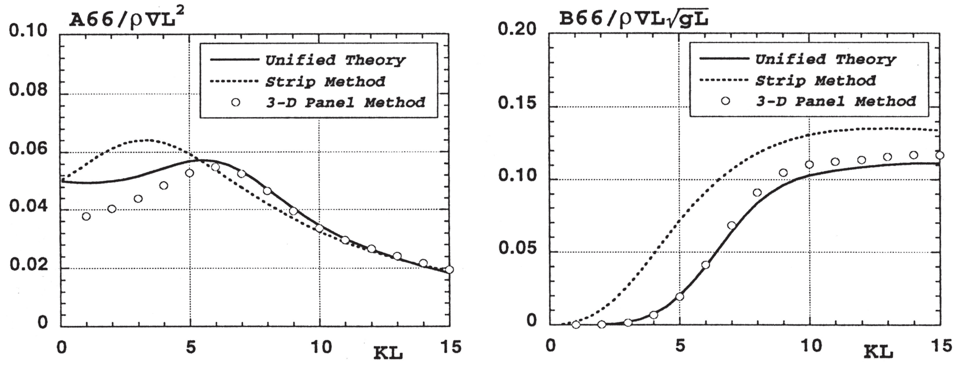

Fig. 16 Added-moment of inertia and damping coefficient in yaw of a half-immersed spheroid of $L/B = 5$ at $U = 0$

circumstance for the strip theory shown by the dashed line. However, the unified theory stands out in that it gives stable and favorable results for all heading angles, *Kashiwagi and Ohkusu (1993)*.

The results demonstrated above are all related to 'longitudinal' ship motions. As summarized in Appendix 1, the unified theory can be applied to the lateral ship-motion problems too, taking account of the 3-D and forward-speed effects. However, since the strip theory is valid at the limiting cases $\omega \to 0$ and $\omega \to \infty$, no correction terms are needed in the unified theory at those limiting cases. In fact, unlike 'longitudinal' motions, 3-D effects on the lateral motions are not so large, and forward-speed effects may be more prominent, *Kashiwagi (1985)*.

Fig. 16 shows the 3-D effects on the added moment of inertia and damping coefficient in yaw mode at $U = 0$ for a half-immersed spheroid of $L/B = 5$. In the limit $\omega \to 0$, the theory shown in Appendix 1 includes no 3-D corrections (the term $|k|^2 y \ln(|k|R)$ appearing in the first line on the r.h.s. of (A.3) is ignored). Therefore the unified theory is identical to the strip theory at $\omega \to 0$, which is different from the result of the 3-D panel method. Except for that point, the unified theory accounts for the 3-D effects over the wide range of frequencies. It is noteworthy that the 3-D effects on the sway mode are smaller than in Fig. 16, but qualitatively the same.

It is still difficult to make a definitive judgment on the Froude number range in which the unified theory is expected to give relatively good results. Judging from comparisons with experiments in the past published papers, it seems that $F_n = 0.25 \sim 0.3$ is a limiting value. For the Froude number higher than that, pseudo 3-D methods like HSSBT may be recommended. For comparison, Fig. 17 shows results of the unified theory, computed by *Newman and Sclavounos (1980)*, and Fig. 18 corresponding results of the HSSBT, computed by *Yeung and Kim (1981)*; both are compared with the same experiments at $F_n = 0.35$. Apparently cross-coupling terms between heave and pitch are well predicted by HSSBT, but the degree of agreement in the heave added-mass and damping coefficients is more or less the same.

The forward-speed term in the free-surface condition influences the cross coupling coefficients as a correction of $O(U)$ to the strip theory, whereas no corrections are necessary on the heave diagonal terms and $O(U^2)$ corrections on the pitch diagonal terms, *Ogilvie and Tuck (1969)*. These theoretical results are confirmed numerically by *Faltinsen (1974)*. Recalling that HSSBT encompasses the rational strip theory, we can expect that the cross-coupling coefficients predicted by HSSBT agree well with experiments.

Computations for sway and yaw motions using HSSBT were initiated by *Chapman (1975, 1976)*, and followed by *Kashiwagi and Hatta (1984)*, *Kashiwagi (1984)*, and *Yamasaki and Fujino (1983, 1984, 1985)*. In particular, Yamasaki and Fujino conducted extensive comparisons with experiments for a flat plate, Wigley ship, Series 60, and SR108 container ship models, showing encouraging agreement.

According to the comparison with experiments for the SR108 container ship by *Takaki and Tasai (1973)*, HSSBT accounts well for the forward-speed effects compared to the strip theory. However, at $F_n = 0.15$, the degree of agreement seems not enough in low frequencies. In that range, 3-D interaction effects among transverse sections become important, which are not taken into account in HSSBT.

Troesch (1981) extended the rational strip theory to the lateral motion problem and compared with the same experiments for SR108 container ship by *Takaki and Tasai (1973)*. Troesch's results are apparently superior to the strip theory but not so good as compared to the results of HSSBT.

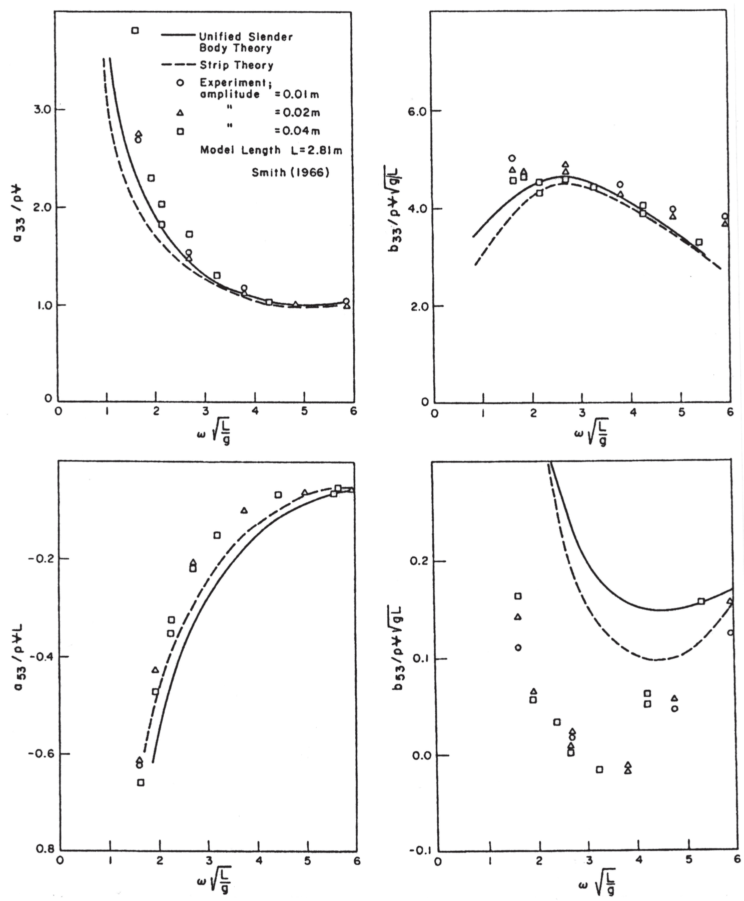

Fig. 17 Radiation force coefficients of a frigate hull ($C_B = 0.55$) due to heaving at $F_n = 0.35$ (computed by *Newman and Sclavounos (1980)* using the unified theory)

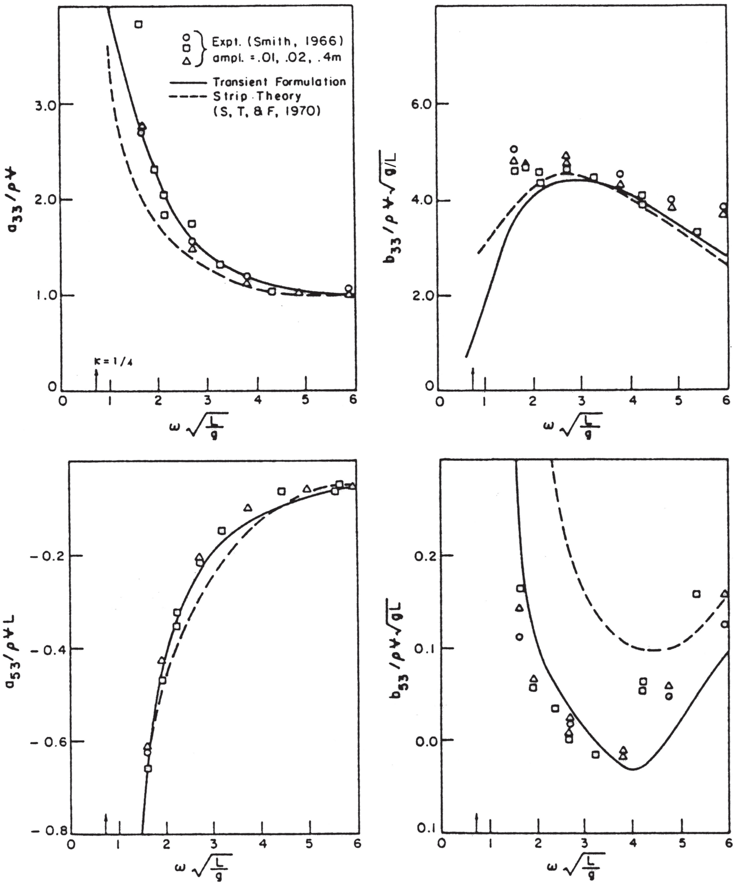

Fig. 18 Radiation force coefficients of a frigate hull ($C_B = 0.55$) due to heaving at $F_n = 0.35$ (computed by *Yeung and Kim (1981)* using high-speed slender-body theory)

9. Concluding Remarks

The unified theory encompasses the strip theory and includes the 3-D and forward-speed effects. However, for higher Froude numbers, we had better rely on a pseudo 3-D method like HSSBT, although its numerical calculation scheme is not fully validated. Furthermore, HSSBT must become faster to serve as a practical tool like strip theory.

It has been said that the slender-ship theory cannot account for the wave diffraction in x-direction near the ship ends and that the surge mode should be treated uncoupled using only the Froude-Krylov force. However, these defects are resolved by the 'enhanced' unified theory by retaining the x-component of the normal vector in the body boundary condition. Numerical examples showed that this theory can predict reasonably surge-related hydrodynamic forces and also remarkably improves the pressure distribution and the added resistance in head waves.

References

ADACHI, H. (1977), *On the interaction between head sea waves and slender ship (part 1* *and 2)*, Rep. of Ship Res. Inst. 14/4 and 14/6 (in Japanese)

ADACHI, H.; OHMATSU, S. (1977), *Ship motion analysis by slender-ship theory (part 1)*, Rep. of Ship Res. Inst. 14/5 (in Japanese)

ADACHI, H. (1980), *Ship motion analysis by slender-ship theory (part 3) – rational strip theory with forward-speed effects –*, Rep. of Ship Res. Inst. 17/3 (in Japanese)

CHAPMAN, R.B. (1975), *Numerical solution for hydrodynamic forces on a surface-piercing plate oscillating in yaw and sway*, 1st Int. Conf. Num. Ship Hydrodyn.

CHAPMAN, R.B. (1976), *Free-surface effects for yawed surface-piercing plates*, J. Ship Res. 20/3

FALTINSEN, O.M. (1971), *Wave forces on a restrained ship in head-sea waves*, Ph.D. Thesis, Univ. of Michigan

FALTINSEN, O.M. (1974), *A numerical investigation of the Ogilvie-Tuck formulas for added mass and damping coefficients*, J. Ship Res. 18/2

FALTINSEN, O.M.; MINSAAS, K.; LIAPIS, N.; SKJORDAL, S. (1980), *Prediction of resistance and propulsion of a ship in a seaway*, 13th Symp. Naval Hydrodyn., Tokyo

FALTINSEN, O.M. (1983), *Bow flow and added resistance of slender ships at high Froude number and low wave lengths*, J. Ship Res. 27/3

FALTINSEN, O.M.; Zhao, R. (1991), *Numerical predictions of ship motions at high forward speed*, Phil. Trans. Royal Soc., Series A

FUJII, H.; TAKAHASHI, T. (1975), *Experimental study on the resistance increase of a large full ship in regular oblique waves*, J. Soc. Nav. Arch. Japan 137 (in Japanese)

INOUE, Y.; MAKINO, Y. (1989), *The influence of forward speed upon three dimensional hydrodynamic forces*, J. Soc. Nav. Arch. Japan 166 (in Japanese)

KASHIWAGI, M.; HATTA, K. (1984), *On the hydrodynamic forces on high speed ships oscillating in sway and yaw*, J. Kansai Soc. Nav. Arch., Japan 194 (in Japanese)

KASHIWAGI, M. (1984), *On the hydrodynamic forces on high speed ships oscillating in sway and yaw (2nd report)*, J. Kansai Soc. Nav. Arch., Japan 195 (in Japanese)

KASHIWAGI, M. (1985), *The unified slender body theory for lateral motions of ships with forward speed*, J. Kansai Soc. Nav. Arch., Japan 197 (in Japanese)

KASHIWAGI, M.; OHKUSU, M. (1989), *Study on the effects of side-wall interference on added-mass and damping coefficients by means of slender-ship theory*, J. Soc. Nav. Arch. Japan 165 (in Japanese)

KASHIWAGI, M. (1991), *Calculation formulas for the wave-induced steady horizontal force and yaw moment on a ship with forward speed*, Rep. of RIAM, Kyushu Univ. 37/107

KASHIWAGI, M. (1992), *Added resistance, wave-induced steady sway force and moment on an advancing ship*, STR 39/1

KASHIWAGI, M.; OHKUSU, M. (1993), *Study on the wave-induced steady force and moment*, J. Soc. Nav. Arch. Japan 173 (in Japanese)

KASHIWAGI, M. (1993), *Interaction forces between twin hulls of a catamaran advancing in* *waves (part 1: radiation problem)*, J. Soc. Nav. Arch. Japan 173 (in Japanese)

KASHIWAGI, M. (1995a), *Prediction of surge and its effects on added resistance by means of the enhanced unified theory*, Trans. West-Japan Soc. Nav. Arch. 89

KASHIWAGI, M. (1995b), *A new theory for oscillating and translating slender ships*, J. Soc. Nav. Arch. Japan 178 (in Japanese)

KOBAYASHI, M. (1981), *On the hydrodynamic forces and moments acting on a three dimensional body with a constant forward speed*, J. Soc. Nav. Arch. Japan 150 (in Japanese)

LIN, X.; TAKAKI, M.; IWASHITA, H. (1993), *Effect of the steady disturbance on the unsteady flow around a ship in waves*, J. Soc. Nav. Arch. Japan 174

MARUO, H. (1960), *Wave resistance of a ship in regular head seas*, Bulletin of Faculty Eng., Yokohama National Univ. 9

MARUO, H. (1974), *Discussion of relative magnitude of governing parameters in the problem of slender ships in waves*, Bulletin of Faculty Eng., Yokohama National Univ. 23

MARUO, H.; SASAKI, N. (1974), *On the wave pressure acting on the surface of an elongated body fixed in head seas*, J. Soc. Nav. Arch. 136 (in Japanese)

MARUO, H. (1989), *Evolution of the theory of slender ships*, STR 36/3

MATSUNAGA, K.; MARUO, H. (1981), *On the radiation problem of slender ships with forward velocity*, J. Soc. Nav. Arch. Japan 150 (in Japanese)

MATSUNAGA, K.; MARUO, H. (1982), *On the diffraction problem of slender ships with forward velocity*, J. Soc. Nav. Arch. Japan 152 (in Japanese)

MIZOGUCHI, S.; KOBAYASHI, K; OKADA, T. (1992), *Ship motions and wave loads*, 9th Symp. Marine Dynamics Comm., Ch.2, Soc. Nav. Arch. Japan (in Japanese)

NAKAMURA, S.; TAKAGI, M.; HOSODA, R. (1980), *Diffraction problems of a slender ship with a blunt bow advancing in head seas*, 13th Symp. Naval Hydrodyn., Tokyo

NEWMAN, J.N. (1978), *The theory of ship motions*, Adv. Appl. Mech. 18

NEWMAN, J.N.; SCLAVOUNOS, P.D. (1980), *The unified theory of ship motions*, 13th Symp. on Naval Hydrodyn., Tokyo

OGILVIE, T.F.; TUCK, E.O. (1969), *A rational strip theory of ship motions*, NAME Rep. 013, Univ. of Michigan

OHKUSU, M. (1980), *Added resistance in waves in the light of unsteady wave pattern analysis*, 13th Symp. Naval Hydrodyn., Tokyo

OHKUSU, M. (1986), *Added resistance of blunt bow ships in very short waves*, J. Kansai Soc. Nav. Arch., Japan 202 (in Japanese)

OHKUSU, M.; FALTINSEN, O.M. (1990), *Prediction of radiation forces on a catamaran at high Froude number*, 18th Symp. Naval Hydrodyn., Ann Arbor

OHKUSU, M.; FALTINSEN, O.M.; YASUNAGA, M.; INADA, M. (1991), *Prediction of hydrodynamic forces on high-speed catamaran in a seaway*, J. Soc. Nav. Arch. Japan 170 (in

Japanese)

SAITO, K.; TAKAGI, M. (1978), *A solution for the oscillating slender-body with forward speed*, J. Soc. Nav. Arch. Japan 144

SAKAMOTO, T.; BABA, E. (1986), *Minimization of resistance of slowly moving full hull forms in short waves*, 16th Symp. Naval Hydrodyn., Berkeley

SCLAVOUNOS, P.D. (1984a), *The diffraction of free-surface waves by a slender ship*, J. Ship Res. 28/1

SCLAVOUNOS, P.D. (1984b), *The unified slender-body theory: Ship motions in waves*, 15th Symp. Naval Hydrodyn., Hamburg

TAKAGI, M.; OHKUSU, M. (1977), *State of the art of theories of ship motions in waves*, 2nd Symp. on Seakeeping, Ch.1, Soc. Nav. Arch. Japan (in Japanese)

TAKAHASHI, T. (1987), *A practical prediction method of added resistance of a ship in waves and the direction of its application to hull form design*, Trans. West-Japan Soc. Nav. Arch. 75 (in Japanese)

TAKAKI, M.; TASAI, F. (1973), *On the hydrodynamic derivative coefficients of the equations for lateral motions of ships*, Trans. West-Japan Soc. Nav. Arch. 46 (in Japanese)

TROESCH, A.W. (1981), *Sway, roll, and yaw motion coefficients based on a forward-speed slender-body theory; part 1 and 2*, J. Ship Res. 25/1

URSELL, F. (1962), *Slender oscillating ships at zero forward speed*, J. Fluid Mech. 14

URSELL, F. (1968), *On head seas travelling along a horizontal cylinder*, J. Inst. Math. Appl. 4

YAMASAKI, K.; FUJINO, M.; KAWAMURA, T. (1983), *Hydrodynamic forces acting on the three dimensional body advancing on the free surface (1st report)*, J. Soc. Nav. Arch. Japan 154 (in Japanese)

YAMASAKI, K.; FUJINO, M. (1984), *Hydrodynamic forces acting on the three dimensional body advancing on the free surface (2nd report)*, J. Soc. Nav. Arch. Japan 156 (in Japanese)

YAMASAKI, K.; FUJINO, M. (1985), *Hydrodynamic forces acting on the three dimensional body advancing on the free surface (3rd report)*, J. Soc. Nav. Arch. Japan 157 (in Japanese)

YEUNG, R. W.; KIM, S. H. (1981), *Radiation forces on a ship with forward speed*, 3rd Int. Conf. Num. Ship Hydrodyn., Paris

YEUNG, R.W.; KIM, S.H. (1985), *A new development in the theory of oscillating and translating slender ships*, 15th Symp. Naval Hydrodyn., Hamburg

Appendix

A1. Unified Theory for Lateral Modes

Kashiwagi (1985) extended the unified theory developed by *Newman (1978)* for longitudinal modes to the lateral modes in the radiation problem. Here, not only its summary but also a new analysis for the asymmetric component of the diffraction problem will be described. The Kutta condition must be imposed to determine the strength of circulation, crucial for computing the lift force. However, that condition is not accounted for in the present analysis.

The velocity potential in the outer region can be expressed by a doublet distribution along the x-axis:

$$\phi_j^{(o)}(x,y,z) = \int_{-\infty}^{\infty} M_j(\xi)\, G_{3D}^A(x-\xi,y,z)\,d\xi \tag{A.1}$$

M_j is the unknown strength of the doublet, and G_{3D}^A is the velocity potential due to the doublet with unit strength and axis parallel to the y-axis, satisfying the 3-D Laplace equation, linearized free-surface condition, and the radiation condition. Therefore G_{3D}^A can be computed from G_{3D} by differentiating with respect to y, and its expansion in the Fourier-transformed domain can be expressed as

$$G_{3D}^{A*}(k;y,z) \equiv -\frac{\partial}{\nu\partial y}\, G_{3D}^{*}(k;y,z) \tag{A.2}$$

$$\begin{aligned} &= -\frac{1}{\pi\nu}\left\{\frac{\sin\theta}{R} + \frac{1}{2}|k|^2 y\Big(\ln\frac{|k|R}{2}+\gamma-\frac{1}{2}\Big)+\cdots\right\} \\ &\quad + \frac{1}{\pi}\nu y\Big(\ln\frac{|k|R}{2}+\gamma-1\Big) - \frac{\theta}{\pi}(1+\nu z)+\cdots \\ &\quad + \frac{1}{\pi}\nu y\left[\begin{array}{c} \sqrt{1-k^2/\nu^2}\Big\{\pi i\epsilon_k + \cosh^{-1}\Big(\frac{\nu}{|k|}\Big)\Big\} \\ -\sqrt{k^2/\nu^2-1}\Big\{-\pi+\cos^{-1}\Big(\frac{\nu}{|k|}\Big)\Big\} \end{array}\right]. \end{aligned} \tag{A.3}$$

The Kochin function can be defined in the same manner as in the longitudinal mode, by substituting the asymptotic expansion of (A.2) as $|y|\to\infty$ into (A.1). The expressions corresponding to (12) and (13) are given in the form

$$S_j(k) = \sqrt{1-k^2/\nu^2}\int_{-\infty}^{\infty} M_j(x)\, e^{ikx}\,dx \tag{A.4}$$

$$S(k) = S_7(k) + \frac{\omega\omega_0}{g}\sum_{j=2,4,6}\frac{\xi_j}{a}\,S_j(k)\,. \tag{A.5}$$

(1) Radiation Problem (j =2, 4, 6)

The inner solution and its outer expansion, corresponding to (34) and (35), may be written as

$$\phi_j^{(i)}(x;y,z) = \varphi_j(y,z) + \frac{U}{i\omega}\widehat{\varphi}_j(y,z) + C_j(x)\Big\{\varphi_2(y,z) - \overline{\varphi_2(y,z)}\Big\} \tag{A.6}$$

$$\begin{aligned} &\sim \Big[\mu_j + \frac{U}{i\omega}\widehat{\mu}_j + C_j(x)\{\mu_2-\overline{\mu}_2\}\Big]\, G_{2D}^A(y,z) \\ &\qquad + 2i\, C_j(x)\,\overline{\mu}_2\, e^{Kz}\sin Ky \end{aligned} \tag{A.7}$$

where
$$G_{2D}^A(y,z) \equiv -\frac{\partial}{K\partial y}\,G_{2D}(y,z)$$

$$= -\frac{\sin\theta}{\pi KR} + \frac{1}{\pi}Ky\Big(\ln KR+\gamma-1\Big) - \frac{\theta}{\pi}(1+Kz) + iKy + \cdots \tag{A.8}$$

and μ_j and $\widehat{\mu}_j$ are the 2-D Kochin functions which can be computed from φ_j and $\widehat{\varphi}_j$ problems.

The inner expansion of the outer solution to be matched with (A.7) can be obtained with (A.3), in the form

$$\phi_j^{(o)}(x,y,z) \sim M_j(x)\, G_{2D}^A(y,z) - \frac{1}{\pi} K y \int_{-\infty}^{\infty} M_j(\xi)\, h(x-\xi)\, d\xi \tag{A.9}$$

where

$$h(x) = \frac{1}{2\pi}\int_{-\infty}^{\infty} h^*(k)\, e^{-ikx}\, dk \tag{A.10}$$

$$h^*(k) = \ln\frac{2K}{|k|} + \pi i - \left[\begin{array}{c} \sqrt{1-k^2/\nu^2}\Big\{\pi i\,\epsilon_k + \cosh^{-1}\Big(\dfrac{\nu}{|k|}\Big)\Big\} \\ -\sqrt{k^2/\nu^2-1}\,\Big\{-\pi + \cos^{-1}\Big(\dfrac{\nu}{|k|}\Big)\Big\} \end{array}\right]. \tag{A.11}$$

Two equations to be obtained by the matching between (A.7) and (A.9) are summarized as follows:

$$M_j(x) + \frac{i}{2\pi}\Big(1-\mu_2/\overline{\mu}_2\Big)\int_{-\infty}^{\infty} M_j(\xi)\, h(x-\xi)\, d\xi = \mu_j + \frac{U}{i\omega}\widehat{\mu}_j \tag{A.12}$$

$$C_j(x)\,\{\,\mu_2 - \overline{\mu}_2\,\} = M_j(x) - \Big\{\mu_j + \frac{U}{i\omega}\widehat{\mu}_j\Big\} \qquad (j=2,4,6)\,. \tag{A.13}$$

Solving the integral equation (A.12) and substituting its solution into (A.13), $C_j(x)$ can be determined, thereby completing the inner solution (A.6). On the other hand, substituting a numerical solution for $M_j(x)$ into (A.4) gives the asymmetric component of the Kochin function.

(2) Diffraction Problem (j =7)

The asymmetric component in (43), $\psi_A(x;y,z)$, can be constructed in the same fashion as (47)–(49):

$$\psi_A(x;y,z) = \psi_A^P(y,z) + C_{7A}(x)\,\psi_A^H(y,z) \tag{A.14}$$

$$\psi_A^P = i\,e^{k_0 z}\sin(k_0 y\sin\chi) \tag{A.15}$$

$$\psi_A^H = \psi_{2D}(y,z) - i\,e^{k_0 z}\sin(k_0 y\sin\chi)\,. \tag{A.16}$$

$\psi_{2D}(y,z)$ is a numerical solution for the asymmetric component, which can be computed by the 2-D integral-equation method using the Green function to be obtained from (50). In that computation, the body-boundary condition may be given by

$$\frac{\partial\psi_{2D}}{\partial N} = ik_0\, e^{k_0 z}\Big\{N_2\sin\chi\;\cos(k_0 y\sin\chi) + (N_3 - iN_1\cos\chi)\,\sin(k_0 y\sin\chi)\Big\}. \tag{A.17}$$

The contribution of N_1-term is retained here but expected to be small, because it is zero for both of $\chi=\pi/2$ (beam wave) and π (head wave).

The outer expression of (A.14) can be expressed as

$$\phi_{7A}^{(i)}(x;y,z) \sim C_{7A}(x)\,\mu_7\, e^{i\ell x}\, H_{2D}^A(\ell;y,z) - i\Big\{C_{7A}(x)-1\Big\}\, e^{k_0 z}\sin(k_0 y\sin\chi)\, e^{i\ell x} \tag{A.18}$$

where

$$\begin{aligned} H_{2D}^A(\ell;y,z) &\equiv -\frac{\partial}{k_0\partial y}H_{2D}(\ell;y,z) \\ &= -\frac{\sin\theta}{\pi k_0 R} + \frac{1}{\pi}k_0 y\Big(\ln\frac{|\ell|R}{2} + \gamma - 1\Big) - \frac{\theta}{\pi}(1+k_0 z) + \cdots \\ &\quad + \frac{1}{\pi}k_0 y\sin\chi\,\cosh^{-1}(|\sec\chi|) + i\,k_0 y\sin^2\chi \end{aligned} \tag{A.19}$$

and μ_7 denotes the 2-D Kochin function associated with ψ_{2D} problem.

The present Green function, H_{2D}^{A}, does not satisfy the radiation condition, because it is obtained from H_{2D} given in (51).

After establishing a relation between (A.3) and (A.19) and substituting the obtained relation into (A.1), the inner expansion of the outer solution can be obtained in the form

$$\phi_{7A}^{(o)}(x,y,z) \sim M_7(x)\, H_{2D}^{A}(\ell;y,z) - \frac{1}{\pi}\, k_0 y\, \mathcal{L}_A(M_7;x) \tag{A.20}$$

where

$$\mathcal{L}_A(M_7;x) = M_7(x)\, h_A(\chi) + \int_{-\infty}^{\infty} M_7(\xi)\, h(x-\xi)\, d\xi \tag{A.21}$$

$$h_A(\chi) = \sin\chi\, \cosh^{-1}(|\sec\chi|) - \ln(2|\sec\chi|) - \pi i\, \cos^2\chi\,. \tag{A.22}$$

The relations to be obtained by matching (A.18) with (A.20) can be summarized as follows:

$$M_7(x) + \frac{i\,\csc\chi}{\pi}\, \mu_7\, \mathcal{L}_A(M_7;x) = \mu_7\, e^{i\ell x} \tag{A.23}$$

$$C_{7A}(x) = M_7(x) \,/\, \mu_7\, e^{i\ell x}\,. \tag{A.24}$$

Eq. (A.23) is the integral equation for $M_7(x)$. With its solution, $C_{7A}(x)$ can be determined by (A.24), completing the inner solution expressed by (A.14). The 3-D Kochin function, $S_7(k)$, can be computed by substituting a solution of (A.23) into (A.4). With completed inner solutions of the radiation and diffraction problems, we can compute hydrodynamic forces and then the amplitude and phase of ship motions. Substituting those in ξ_j/a of (A.5) gives the Kochin function, with ship motion effects taken into account. Finally performing the integrations in (62)–(64) gives the wave-induced steady forces.

A2. Computation of the Diffraction Green Function

Let the real part of (50) times 2π be denoted by $\mathcal{G}_H$. Then $\mathcal{G}_H$ and its derivatives can be computed from the followings:

$$\begin{aligned}\mathcal{G}_H =\ & \ln R - \ln R_1 \\ & - \Big\{ K_0(|\ell|R) + \ln\frac{|\ell|R}{2} \Big\} + \Big\{ K_0(|\ell|R_1) + \ln\frac{|\ell|R_1}{2} \Big\} \\ & + G(k_0,\chi;y-\eta,z+\zeta)\end{aligned} \tag{A.25}$$

$$\begin{aligned}\frac{\partial\mathcal{G}_H}{\partial\eta} =& -(y-\eta)\Big\{\frac{1}{R^2} + \frac{1}{R_1^2}\Big\} \\ & - \frac{(y-\eta)}{R}\Big\{|\ell|\,K_1(|\ell|R) - \frac{1}{R}\Big\} - \frac{(y-\eta)}{R_1}\Big\{|\ell|\,K_1(|\ell|R_1) - \frac{1}{R_1}\Big\} \\ & + k_0\,\mathrm{sgn}(y-\eta)\, Y(k_0,\chi;y-\eta,z+\zeta)\end{aligned} \tag{A.26}$$

$$\begin{aligned}\frac{\partial\mathcal{G}_H}{\partial\zeta} =& -\frac{(z-\zeta)}{R^2} + \frac{(z+\zeta)}{R_1^2} \\ & - \frac{(z-\zeta)}{R}\Big\{|\ell|\,K_1(|\ell|R) - \frac{1}{R}\Big\} + \frac{(z+\zeta)}{R_1}\Big\{|\ell|\,K_1(|\ell|R_1) - \frac{1}{R_1}\Big\} \\ & + k_0\, G(k_0,\chi;y-\eta,z+\zeta)\end{aligned} \tag{A.27}$$

where $R\,,\; R_1 \;=\sqrt{(y-\eta)^2+(z\mp\zeta)^2}\,.$

1) For $k_0R_1 > 5.5$

$$G = 2\,\Re\Big[\mathcal{I}-\mathcal{F}\Big] + 2\pi\,\csc\chi\, e^{k_0(z+\zeta)}\sin(k_0|y-\eta|\sin\chi) \tag{A.28}$$

$$Y = 2\,\Im\Big[\mathcal{I}+\mathcal{F}\Big] - 2\pi\, e^{k_0(z+\zeta)}\cos(k_0|y-\eta|\sin\chi) \tag{A.29}$$

where

$$\mathcal{I} = \int_0^\infty e^{-k_0 v}\,(X+v)\left\{\frac{1}{|X+v|^2} - \frac{|\ell|\,K_1(|\ell||X+v|)}{|X+v|}\right\}dv \tag{A.30}$$

$$\mathcal{F} = e^{k_0 X}\,E_1(k_0X)\,, \qquad X=(z+\zeta)-i|y-\eta|\,. \tag{A.31}$$

2) For $k_0R_1 < 5.5$

$$\begin{aligned} G =& -2\,K_0(|\ell|R_1) + 2\,\csc\chi\;\beta\; e^{k_0(z+\zeta)}\cos(k_0|y-\eta|\sin\chi)\\ &+4\,\csc\chi\sum_{n=1}^{\infty}(-1)^n\sinh n\beta\left(\frac{|\ell|R_1}{2}\right)^n\\ &\times\sum_{m=0}^{\infty}\frac{\left(\frac{|\ell|R_1}{2}\right)^{2m}}{m!\,(n+m)!}\,\Re\left[\left(\ln\frac{|\ell|R_1}{2}+\gamma-\sum_{p=1}^{n+m}\frac{1}{p}+i\theta\right)e^{in\theta}\right] \end{aligned} \tag{A.32}$$

$$\begin{aligned} Y =\;& 2\beta\, e^{k_0(z+\zeta)}\sin(k_0|y-\eta|\sin\chi)\\ &+4\,\csc\chi\,\frac{1}{k_0R_1}\sum_{n=1}^{\infty}(-1)^n\sinh n\beta\left(\frac{|\ell|R_1}{2}\right)^n\sum_{m=0}^{\infty}\frac{\left(\frac{|\ell|R_1}{2}\right)^{2m}}{m!\,(n+m)!}\Bigg[\sin(n-1)\theta\\ &+\Im\left\{\left(\ln\frac{|\ell|R_1}{2}+\gamma-\sum_{p=1}^{n+m}\frac{1}{p}+i\theta\right)\left(ne^{i(n-1)\theta}-i\,2m\sin\theta\,e^{in\theta}\right)\right\}\Bigg] \end{aligned} \tag{A.33}$$

where

$$\left.\begin{aligned} &\beta=\cosh^{-1}(|\sec\chi|)=\ln\{|\sec\chi|(1+\sin\chi)\}\\ &z+\zeta=-R_1\cos\theta\,,\;\; |y-\eta|=R_1\sin\theta \end{aligned}\right\} \tag{A.34}$$

$K_n(x)$ is the modified Bessel function of second kind, and $E_1(u)$ the exponential integral function with complex variable; for these, numerical calculation methods are available in public libraries.

In summary, the Green function and its derivatives can be computed in terms of two functions only, G and Y, given by (A.28) and (A.29) for large k_0R_1 and (A.32) and (A.33) for small k_0R_1. The first line on the r.h.s in each of (A.25)–(A.27) is the singular part, which can be treated in the integral-equation method in the same way as in the corresponding 2-D radiation problem.

A B-Spline Galerkin Scheme for Calculating the Hydroelastic Response of a Very Large Floating Structure in Waves*

Masashi KASHIWAGI
Research Institute for Applied Mechanics, Kyushu University
Kasuga, Fukuoka 816-8580, Japan

Abstract

This paper presents an effective scheme for computing the wave-induced hydroelastic response of a very large floating structure, and a validation of its usefulness. The calculation scheme developed is based on the pressure-distribution method of expressing the disturbance caused by a structure, and on the mode-expansion method for hydroelastic deflection with the superposition of orthogonal mode functions. The scheme uses bi-cubic B-spline functions to represent unknown pressures and the Galerkin method to satisfy the body boundary conditions. Various numerical checks confirm that the computed results are extremely accurate, require relatively little computation time, and contain fewer unknowns, even in the region of very short wavelengths. Measurements of the vertical deflections in both head and oblique waves of relatively long wavelength are in good agreement with the computed results. Numerical examples using shorter wavelengths reveal that the hydroelastic deflection does not necessarily become negligible as the wavelength of incident waves decreases. The effects of finite water depth and incident wave angle are also discussed.

Keywords: Very large floating structure, hydroelastic response, B-spline function, Galerkin scheme.

1. Introduction

Very large floating structures (VLFS) will become increasingly necessary for airports, storage, and manufacturing facilities. This need comes from the lack of adequate land space and/or environmental concerns about such things as the pollution and noise associated with having such facilities near residential areas.

In Japan, a floating airport is being considered, and its safety and performance in waves are being intensively studied. The preferred configuration is a barge-type structure 5 km long, 1 km wide, and a few meters deep. This type of structure has two features: (1) the wavelengths of practical interest are small compared with the horizontal dimensions of the structure; and (2) hydroelastic responses are more important than the rigid-body motions owing to the relatively small flexural rigidity of the structure.

Several methods have been proposed to take account of these features (e.g., refs [1]–[5] and references therein). Among these, the most common is probably the mode-expansion method in the framework of linear potential theory, which represents the structural deflection by a set of "generalized" modes of hydroelastic responses, in addition to the conventional

∗ *Reprinted from Journal of Marine Science and Technology, Vol. 3, No 1, pp. 37–49, 1998 (May)*

components of the diffraction problem and the six separate radiation problems for rigid-body motions. One of the problems with this method is that accurate computations must be performed for very short wavelengths. Specifically, if realistic waves with wavelength of 50–100 m are considered, the length ratio to a VLFS 5 km long is 1/50–1/100.

The structure under consideration can be approximated by a zero-draft rectangular plate and thus hydrodynamically by the pressure distribution on the free surface. This approximation is known as the pressure distribution method. Several authors [6]–[8] have presented numerical results for a VLFS on the basis of this method. However their results are not accurate in the short-wavelength regime, because the integral equation used in this method is discretized with a limited number of panels, and on each panel the unknown pressure is represented by a constant value. If this traditional zero-th order panel method is used for wavelengths in this investigation, the number of unknowns would have to be $O(10^4)$, and thus the computational burden would be enormous. Recently, Wang et al. [9] proposed two computationally efficient techniques, but those are still not effective for very short wavelengths.

This paper presents a new calculation scheme to solve the integral equation in the pressure-distribution method. The scheme employs bi-cubic B-spline functions to represent the unknown pressure, and a Galerkin method to convert the integral equation into a linear system of simultaneous equations. The Galerkin method is effective in increasing the accuracy, but it also increases the computation time. In the present case, however, "relative similarity relations" can be used to evaluate the most influential coefficients in the matrix, which drastically reduces the computational time. Singular integrals originating from a Rankine-source part of the Green function multiplied by B-spline functions are evaluated analytically, which also contributes to the high accuracy with fewer unknowns.

Wave-induced hydroelastic responses are computed by a mode-expansion method, which represents the structural deflection by a superposition of normalized orthogonal functions. In this paper, the natural modes for the bending of a uniform beam with free ends are employed as a system of orthogonal functions both in both the x- and y-directions. The amplitude of each mode function is determined by solving the vibration equation of an elastic plate, with free-end boundary conditions along the periphery of the plate satisfied in the process of transforming the stiffness matrix by partial integrations.

The satisfactory performance of the present scheme is demonstrated by numerical checks of the energy-conservation principle, the Haskind-Hanaoka relation extended to elastic modes of motion [10], and the convergence of the numerical results as the number of panels increases. For routine use, accurate results up to $L/\lambda = 50$ (L, structure length; λ, wavelength) can be obtained with relatively short computation times and a small number of unknowns.

Computed hydroelastic responses were compared with the results of experiments conducted at Ship Research Institute [11] for relatively long wavelengths ($L/\lambda < 10$). The results are in virtually perfect agreement. For shorter wavelengths, experiments become difficult, and no reliable data are available in published papers. Therefore, the characteristic hydroelastic responses of a VLFS in short waves are discussed based only on the numerical results computed for several values of wavelength, incident wave angle, and water depth.

2. Mathematical Formulation

Cartesian coordinates are defined as shown in Fig. 1, with $z = 0$ as the plane of undisturbed free surface and $z = h$ as the horizontal sea bottom. The incident regular wave comes from the negative x-axis with incidence angle β.

Time-harmonic motions of small amplitude are considered, with the complex time dependence $e^{i\omega t}$ being applied to all first-order oscillatory quantities. The boundary conditions on the body and free surface are linearized, and the potential flow is assumed.

We then write the velocity potential ϕ, pressure p, and vertical displacement of the structure w, in the following decomposed form:

$$\phi = i\omega a\{\phi_I + \phi_S\} + \sum_{j=1}^{\infty} i\omega X_j\, \phi_j \tag{1}$$

$$p = \rho g a \left[p_I(x,y) + p_S(x,y) + \sum_{j=1}^{\infty} \left(\frac{X_j}{a} \right) p_j(x,y) \right] \tag{2}$$

$$w = a \left[\zeta_I(x,y) + \zeta_S(x,y) + \sum_{j=1}^{\infty} \left(\frac{X_j}{a} \right) \zeta_j(x,y) \right] \tag{3}$$

where a is the amplitude of an incident wave, ρ is the fluid density, and g is the gravitational acceleration.

Suffix I represents quantities related to the incident wave, suffix S refers to the scattering component, and suffix j refers to the radiation component of the j-th mode of motion. The definition of mode indices indicates that not only conventional rigid-body motions, but also a set of "generalized" modes to represent elastic deformations. X_j denotes the complex amplitude of the normalized mode function, ζ_j, which will be described later.

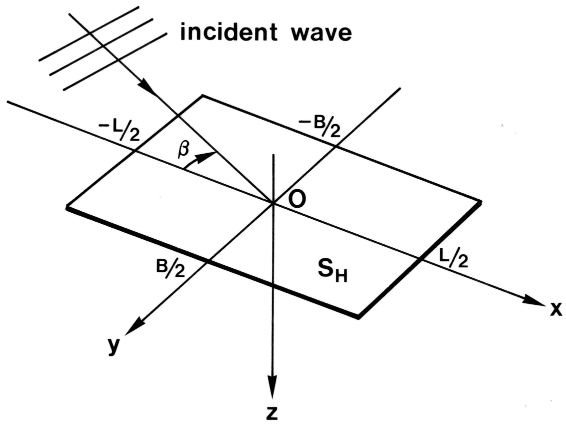

Fig. 1 Coordinate system and notation

The structure under consideration is rectangular in plan, with length L and width B. In linear theory, the draft is regarded as zero because of its very small value relative to L and B.

In what follows, the length dimensions are nondimensionalized in terms of $L/2$, and thus the structure exists in the region $|x| \le 1$ and $|y| \le b \equiv B/L$ on $z = 0$.

Hydrodynamically, the disturbance due to the presence of a structure can be expressed by the pressure applied on the free surface. Then the dynamic and kinematic free-surface boundary conditions are given by

$$p_j = K\phi_j + \zeta_j \ , \ \frac{\partial \phi_j}{\partial z} = \zeta_j \quad \text{on } z = 0 \tag{4}$$

where $K = \omega^2/g$ and $p_j = 0$ outside of the structure.

Since the velocity potential can be given by the convolution integral of the unknown pressure p_j and the Green function satisfying Eq. (4) with $p_j = 0$, it follows from the dynamic free-surface condition in Eq. (4) that the integral equation for the unknown pressure takes the form

$$p_j(x,y) - K \iint_{S_H} p_j(\xi,\eta) G(x-\xi, y-\eta, 0)\, d\xi d\eta = \zeta_j(x,y) \tag{5}$$

where S_H denotes the bottom of the structure situated on $z = 0$ and $G(x, y, z)$ is the Green function, which is given for the finite-depth case in the form

$$G(x,y,z) = \frac{1}{\pi}\sum_{n=1}^{\infty} C_n \frac{\cos k_n(z-h)}{\cos k_n h}\, K_0(k_n R) + \frac{i}{2}\, C_0 \frac{\cosh k_0(z-h)}{\cosh k_0 h}\, H_0^{(2)}(k_0 R) \tag{6}$$

where

$$\left.\begin{aligned} C_0 = \frac{k_0^2}{K + h(k_0^2 - K^2)}\ ,\ C_n = \frac{k_n^2}{K - h(k_n^2 + K^2)} \\ k_0 \tanh k_0 h = K\ ,\ k_n \tan k_n h = -K \end{aligned}\right\} \tag{7}$$

$K_0(k_n R)$ and $H_0^{(2)}(k_0 R)$ in Eq. (6) are the 2nd kind of modified Bessel function and Hankel function, respectively, with $R = \sqrt{x^2 + y^2}$. In numerical computations, the Green function is evaluated using the method developed by Seto [12, 13].

The right-hand side of Eq. (5) is the vertical displacement of the structure, which will be specified below.

In the diffraction problem ($j = S$), $\zeta_I + \zeta_S = 0$ and thus the vertical displacement due to scattering is given by

$$\zeta_S(x,y) = -\zeta_I(x,y) = -\exp\bigl\{-ik_0(x\cos\beta + y\sin\beta)\bigr\} \tag{8}$$

In the extended radiation problem ($j = 1, 2, \ldots$), the vertical displacement is expressed in terms of an appropriate set of mathematical mode functions. Here we write

$$\sum_{j=1}^{\infty} X_j\, \zeta_j(x,y) = \sum_{m=0}^{\infty}\sum_{n=0}^{\infty} X_{mn} u_m(x) v_n(y) \tag{9}$$

where the mode functions in the x- and y-axes, $u_m(x)$ and $v_n(y)$, respectively, are the natural modes for the bending of a uniform beam with free ends. Specifically $u_m(x)$ can be written as [14]

$$\left.\begin{aligned} u_0(x) &= \frac{1}{2} \\ u_{2m}(x) &= \frac{1}{2}\left[\frac{\cos\kappa_{2m}x}{\cos\kappa_{2m}} + \frac{\cosh\kappa_{2m}x}{\cosh\kappa_{2m}}\right] \end{aligned}\right\} \tag{10}$$

$$\left.\begin{aligned} u_1(x) &= \frac{\sqrt{3}}{2}\, x \\ u_{2m+1}(x) &= \frac{1}{2}\left[\frac{\sin\kappa_{2m+1}\, x}{\sin\kappa_{2m+1}} + \frac{\sinh\kappa_{2m+1}\, x}{\sinh\kappa_{2m+1}}\right] \end{aligned}\right\} \tag{11}$$

where the factors κ_m denote the positive real roots of the equation

$$(-1)^m \tan\kappa_m + \tanh\kappa_m = 0 \tag{12}$$

These functions are orthogonal, satisfying

$$\int_{-1}^{1} u_m(x) u_k(x)\, dx = \frac{1}{2}\,\delta_{mk} \tag{13}$$

for all m and k, where δ_{mk} is the Kronecker delta, equal to 1 when $m = k$ and zero otherwise.

$v_n(y)$ can be also written in a similar form, with x replaced by y/b on the right-hand sides of Eqs. (10) and (11).

Summing up the above, the right-hand side of Eq. (5) is given as $\zeta_j(x,y) = u_m(x)v_n(y)$. Depending on the combination of odd and even numbers of m and n, these are categorized into four types, as follows:

1. $\zeta_j(x,y) = u_{2m+1}(x)v_{2n}(y)$; which is odd in x and even in y, and referred to as the $F(X)$ type.
2. $\zeta_j(x,y) = u_{2m}(x)v_{2n+1}(y)$; which is even in x and odd in y, and referred to as the $F(Y)$ type.
3. $\zeta_j(x,y) = u_{2m}(x)v_{2n}(y)$; which is even in both x and y, and referred to as the $F(Z)$ type.
4. $\zeta_j(x,y) = u_{2m+1}(x)v_{2n+1}(y)$; which is odd in both x and y, and referred to as the $F(N)$ type.

Equation (8) for the diffraction problem can also be categorized into the same four types. Therefore, taking advantage of that the pressure has the same symmetries as those of the mode shapes, the unknowns in Eq. (5) can be confined to the first quadrant ($x > 0$ and $y > 0$) of the structure.

In numerical computations, the upper limits of summations in Eq. (9) are truncated to $MX-1$ for m and $MY-1$ for n. Note that only three modes correspond to the conventional rigid-body motions: u_1v_0 (pitch), u_0v_1 (roll), and u_0v_0 (heave).

3. Numerical Method

To solve Eq. (5) with fewer unknowns even for very short wavelengths, the unknown pressure is represented by use of bi-cubic B-spline functions, in the form

$$p(x,y) = \sum_{k=0}^{NX+2} \sum_{\ell=0}^{NY+2} \alpha_{k\ell}\, B_k(x) B_\ell(y) \tag{14}$$

Here $B_k(x)$ and $B_\ell(y)$ are normalized cubic B-spline functions, which can be obtained by Boor-Cox's recursion formula [15].

NX and NY are the number of panel divisions in the x- and y-directions, respectively. Since one cubic spline function extends its influence over four panels, the number of total unknowns, $\alpha_{k\ell}$ in Eq. (14), is $(NX+3)\times(NY+3)$.

To determine these unknowns with good accuracy, a Galerkin scheme is employed. That is, after substituting Eq. (14) in Eq. (5), both sides of Eq. (5) are multiplied by $B_p(x)B_q(y)$, where $p = 0 \sim NX+2$ and $q = 0 \sim NY+2$, and integrated over the plate S_H.

This procedure gives a linear system of simultaneous equations in the form

$$\sum_{k=0}^{NX+2} \sum_{\ell=0}^{NY+2} \alpha_{k\ell} \left[\mathcal{L}^{(1)}_{pq,k\ell} - K\, \mathcal{L}^{(2)}_{pq,k\ell} \right] = \mathcal{R}_{pq} \tag{15}$$

where $p = 0 \sim NX+2,\ q = 0 \sim NY+2$.

The influence coefficients in this matrix are defined as

$$\mathcal{L}^{(1)}_{pq,k\ell} = \iint_{S_H} B_p(x)B_q(y)\, B_k(x)B_\ell(y)\, dxdy \tag{16}$$

$$\mathcal{L}^{(2)}_{pq,k\ell} = \iint_{S_H} B_p(x)B_q(y) \Big[\iint_{S_H} B_k(\xi)B_\ell(\eta)\, G(x-\xi, y-\eta, 0)\, d\xi d\eta \Big]\, dxdy \tag{17}$$

$$\mathcal{R}_{pq} = \iint_{S_H} B_p(x) B_q(y)\, \zeta_j(x,y)\, dxdy \tag{18}$$

Among these, Eqs. (16) and (18) are relatively easy to evaluate, because these integrands are simple products of independent functions of x and y, respectively. For these integrals, a Clenshaw-Curtis quadrature is used in the x- and y-directions independently, with absolute error less than 10^{-7} specified.

The most time-consuming part of the computation is the integral in Eq. (17). However, when the discretization is made into panels of equal size, the amount of computations can be drastically diminished by taking advantage of "relative similarity relations" in the integral. For example, let us consider the case where the field point (x, y) is located at P_1 and the panel to be integrated is $j = 1$ (see Fig. 2). Since the Green function depends only on the relative distance, $x - \xi$ and $y - \eta$, the integral with respect to (ξ, η) in Eq. (17) is equivalent to the case where the field point (x, y) is at P_3 and the panel to be integrated is $j = 3$. (Some care must be paid to the order of B-spline functions, because there are 4×4 different patterns of $B_k(\xi)B_\ell(\eta)$ within one panel.) With these similarity relations, it is enough to consider only one panel for the integration with respect to (ξ, η), which can reduce the computational time to the order of $O(1/N)$, where N is the total number of panel divisions. For integrals with respect to (ξ, η) and (x, y) in Eq. (17), the Gauss quadrature is applied with $6 \times 6 = 36$ points used as integration points over one panel, which is intended to maintain a high degree of accuracy, although 36 points may be more than necessary.

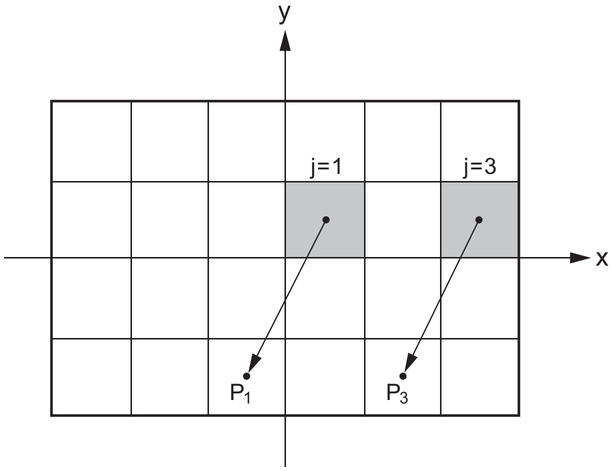

Fig. 2 Explanation of the relative similarity relation

The treatment described above is valid for the regular part of the integrand. When the field point is located near or within the integration panel, a special treatment is required for singularities due to $1/R$ and $\ln R$ included in the Green function.

In the present case, since the bi-cubic B-spline function is used as a weight function in the Galerkin scheme, the following singular integrals must be evaluated:

$$\psi_{mn} \equiv \iint_{\Delta S} \frac{(\xi - x)^m (\eta - y)^n}{R}\, d\xi d\eta \tag{19}$$

$$\varphi_{mn} \equiv \iint_{\Delta S} (\xi - x)^m (\eta - y)^n \, \ln R \, d\xi d\eta \tag{20}$$

where m and n are integers between 0 and 3, and ΔS denotes an elementary panel of the rectangle.

In this paper, these are analytically integrated by applying the idea described in Newman [16] for evaluating a higher-order polynomial distribution of sources.

4. First-Order Pressure Force

In the radiation problem that includes elastic modes, computation of the pressure force acting in the i-th direction due to the j-th mode of motion can be summarized as

$$\frac{F_i}{\rho g a (L/2)^2} = \sum_{j=1}^{\infty} \Big[K\{ A'_{ij} - i\, B'_{ij} \} - C'_{ij} \Big] \Big(\frac{X_j}{a} \Big) \tag{21}$$

where

$$A'_{ij} - i\, B'_{ij} = -\frac{1}{K} \iint_{S_H} (\, p_j - \zeta_j \,)\, \zeta_i \, dxdy \tag{22}$$

$$C'_{ij} = \iint_{S_H} \zeta_j \, \zeta_i \, dxdy = \frac{b}{4}\, \delta_{ij} \tag{23}$$

Here indices i and j can take on any values among not only rigid-body modes but also elastic modes. A'_{ij}, B'_{ij}, and C'_{ij} are "generalized" added mass, damping, and hydrostatic restoring force coefficients, respectively, given in nondimensional form. Equation (23) has been obtained by using Eqs. (9) and (13).

In the diffraction problem, $p_I = 0$ on $z = 0$ and thus the wave-exciting force in the i-th direction can be computed by

$$\frac{E_i}{\rho g a (L/2)^2} \equiv E'_i = - \iint_{S_H} p_S \, \zeta_i \, dxdy \tag{24}$$

The numerical accuracy of the above computations can be confirmed by checking various hydrodynamic relations which have been theoretically proven. In this paper, two different relations are considered: one is the energy-conservation principle associated with the damping force, and the other is the Haskind-Hanaoka relation between the radiation and diffraction problems. These relations can be derived by exploiting Green's second identity, e.g. Ertekin et al. [10], or the reciprocity theorem for a flat ship studied by Bessho [17].

Omitting derivations, final results are expressed in the form

$$B'_{ij} = \frac{C_0}{4\pi} \int_0^{2\pi} H_i^*(k_0, \theta)\, H_j(k_0, \theta)\, d\theta \tag{25}$$

$$E'_j = H_j(k_0, \beta + \pi) \tag{26}$$

where

$$H_j(k_0, \theta) = \iint_{S_H} p_j(\xi, \eta)\, e^{i k_0 (\xi \cos\theta + \eta \sin\theta)}\, d\xi d\eta \tag{27}$$

is defined as the Kochin function, and the asterisk in Eq. (25) means the complex conjugate.

As will be explained later, numerical satisfaction in the above relations does not necessarily mean the convergence of solutions when the number of discretized panels is increased.

5. Elastic Response in Waves

Using the pressure distribution obtained from Eqs. (14) and (15) as a forcing term, the amplitude of specified elastic modes can be determined from the vibration equation of a plate:

$$-m_B\, \omega^2 w(x, y) + D \Big\{ \frac{\partial^4}{\partial x^4} + 2 \frac{\partial^4}{\partial x^2 \partial y^2} + \frac{\partial^4}{\partial y^4} \Big\} w(x, y) = -p(x, y) \tag{28}$$

where m_B is the distribution of mass, which is equal to M/LB in the case of uniform distribution (M being the total mass), and D is the flexural rigidity given by $D = Et^3/12(1-\nu^2)$, with E, ν, and t being Young's modulus, Poisson's ratio, and the equivalent thickness of structure, respectively.

Since the structure is freely floating, the bending moment and the equivalent shear force must be zero along the periphery of the structure. That is,

$$\frac{\partial^2 w}{\partial n^2} + \nu \frac{\partial^2 w}{\partial s^2} = 0, \qquad \frac{\partial^3 w}{\partial n^3} + (2-\nu)\frac{\partial^3 w}{\partial n \partial s^2} = 0 \tag{29}$$

where n and s denote the normal and tangential directions, respectively.

In the case of a rectangular plate, a concentrated force, stemming from the replacement of the torsional moment with an equivalent shear force, acts at the four corners, and this must be also zero.

$$R = 2D(1-\nu)\frac{\partial^2 w}{\partial x \partial y} = 0 \qquad \text{at } x = \pm 1,\ y = \pm b \tag{30}$$

Substituting Eqs. (2) and (3) into Eq. (28) and writing the result in nondimensional form, we have

$$\begin{aligned} -KM'\Lambda \sum_{j=1}^{\infty} \Big(\frac{X_j}{a}\Big) \zeta_j(x,y) + D' \sum_{j=1}^{\infty} \Big(\frac{X_j}{a}\Big) \Big\{ \frac{\partial^4}{\partial x^4} + 2\frac{\partial^4}{\partial x^2 \partial y^2} + \frac{\partial^4}{\partial y^4} \Big\} \zeta_j(x,y) \\ = -p_S(x,y) - \sum_{j=1}^{\infty} \Big(\frac{X_j}{a}\Big) p_j(x,y) \end{aligned} \tag{31}$$

where $M' = M/\rho LBd$, $\Lambda = 2d/L$, and $D' = D/\rho g (L/2)^4$, with d being the draft of structure. In obtaining Eq. (31), the relations of $p_I = 0$ and $\zeta_I + \zeta_S = 0$ on $z = 0$ have been used.

Multiplying Eq. (31) by $\zeta_i(x,y) = u_k(x)v_\ell(y)$ (the relation of mode indices among k, ℓ and i is the same as that among m, n and j defined in Eq. (9)) and integrating over the bottom of the structure, we obtain a linear set of equations

$$\sum_{j=1}^{\infty} \Big(\frac{X_j}{a}\Big) \Big[-K\big(M_{ij} + A'_{ij} - i\, B'_{ij} \big) + C'_{ij} + D_{ij} \Big] = E'_i \tag{32}$$

where

$$M_{ij} = M'\Lambda \iint_{S_H} \zeta_i(x,y)\, \zeta_j(x,y)\, dxdy = M'\Lambda\, \frac{b}{4}\, \delta_{ij} \tag{33}$$

$$D_{ij} = D' \iint_{S_H} \zeta_i(x,y) \Big\{ \frac{\partial^4}{\partial x^4} + 2\frac{\partial^4}{\partial x^2 \partial y^2} + \frac{\partial^4}{\partial y^4} \Big\} \zeta_j(x,y)\, dxdy \tag{34}$$

Here M_{ij} is called the mass matrix and D_{ij} the stiffness matrix, which is the restoring force coefficient due to structural rigidity. A'_{ij}, B'_{ij}, C'_{ij}, and E'_i in Eq. (32) are defined in Eqs. (22)–(24).

It should be noted that the free-end conditions, Eqs. (29) and (30), are not explicitly imposed as constraints on the solution. In fact, the adopted mode functions, $\zeta_j(x,y) = u_m(x)v_n(y)$, does not satisfy the conditions of Eqs. (29) and (30). However, as suggested in Newman [14], the end conditions can be satisfied in the weaker context in the process of transforming the stiffness matrix by partial integrations.

Applying the Gauss theorem twice, the integral in Eq. (34) can be rewritten in the form

$$\begin{aligned}\mathcal{D}_{ij} &\equiv \iint_{S_H} \zeta_i(x,y)\, \nabla^4 \zeta_j(x,y)\, dS \\ &= \iint_{S_H} \nabla^2\zeta_i\, \nabla^2\zeta_j\, dS + \int_C \left\{ \zeta_i \frac{\partial}{\partial n}\left(\nabla^2\zeta_j\right) - \frac{\partial \zeta_i}{\partial n}\, \nabla^2\zeta_j \right\} ds \end{aligned} \tag{35}$$

The line integral in Eq. (35) is to be performed along the periphery where Eq. (29) must be satisfied, and Eq. (29) can be expressed as

$$\left.\begin{aligned} \frac{\partial}{\partial n}\left(\nabla^2\zeta_j\right) = \frac{\partial}{\partial n}\left(\frac{\partial^2\zeta_j}{\partial n^2} + \frac{\partial^2\zeta_j}{\partial s^2}\right) = -(1-\nu)\frac{\partial^3\zeta_j}{\partial n \partial s^2} \\ \nabla^2\zeta_j = \frac{\partial^2\zeta_j}{\partial n^2} + \frac{\partial^2\zeta_j}{\partial s^2} = (1-\nu)\frac{\partial^2\zeta_j}{\partial s^2} \end{aligned}\right\} \tag{36}$$

Therefore, we first substitute the above into Eq. (35) and then transform the resulting integrals further by partial integrations with respect to x and y to take account of the remaining condition Eq. (30). The stiffness matrix after these transformations can be expressed in the form

$$\begin{aligned} D_{ij} = D' \iint_{S_H} & \left\{ \frac{\partial^2\zeta_i}{\partial x^2}\frac{\partial^2\zeta_j}{\partial x^2} + \frac{\partial^2\zeta_i}{\partial x^2}\frac{\partial^2\zeta_j}{\partial y^2} + \frac{\partial^2\zeta_i}{\partial y^2}\frac{\partial^2\zeta_j}{\partial x^2} + \frac{\partial^2\zeta_i}{\partial y^2}\frac{\partial^2\zeta_j}{\partial y^2} \right\} dxdy \\ & + D'(1-\nu) \int_{-1}^{1} \left[\frac{\partial \zeta_i}{\partial x}\frac{\partial^2\zeta_j}{\partial x \partial y} - \frac{\partial \zeta_i}{\partial y}\frac{\partial^2\zeta_j}{\partial x^2} \right]_{-b}^{b} dx \\ & + D'(1-\nu) \int_{-b}^{b} \left[\frac{\partial \zeta_i}{\partial y}\frac{\partial^2\zeta_j}{\partial x \partial y} - \frac{\partial \zeta_i}{\partial x}\frac{\partial^2\zeta_j}{\partial y^2} \right]_{-1}^{1} dy \end{aligned} \tag{37}$$

All integrals shown above can be evaluated analytically with the orthogonality relation, Eq. (13), and the 4-th order differential equation satisfied by the mode functions ζ_i and ζ_j.

6. Results and Discussion

6.1 Numerical accuracy and computation time

Computations were performed for a rectangular plate of $L/B = 5$ in regular waves with an incidence angle of $\beta = 30°$. The discretization of the plate into panels was made such that the first quadrant ($x > 0$ and $y > 0$) is subdivided into NX in the x-axis and NY in the y-axis with the ratio $NX/NY = 5$, meaning that each panel is a square. The number of mode

Table 1 Computation time versus numbers of panels

(NX, NY)	Number of unknowns	Average CPU time*
(10, 2)	65	9 s
(20, 4)	161	38 s
(30, 6)	297	2 min 22 s
(40, 8)	473	5 min 10 s
(50, 10)	689	11 min 42 s

* By EWS HP 9000 series/model 735

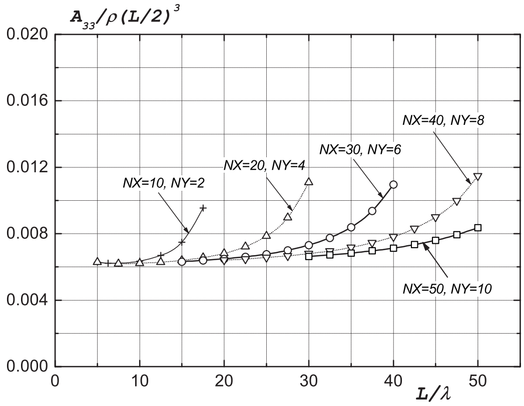

Fig. 3 Convergence of added mass in heave mode for the plate $L/B = 5$ in deep water

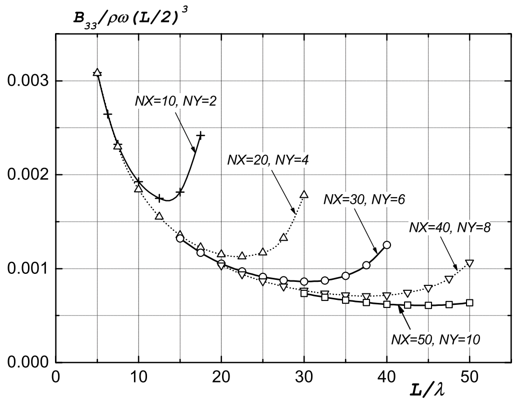

Fig. 4 Convergence of the heave damping coefficient for the plate $L/B = 5$ in deep water

functions was set to 25 for each of $F(X)$, $F(Y)$, $F(Z)$, and $F(N)$ types, and computations were implemented using an engineering workstation, HP 9000 series/model 735.

The computer program developed is not fully optimized. Nevertheless, as shown in Table 1, the average computation time per wavelength was found remarkably small, which is largely due to the exploitation of "relative similarity relations". In obtaining Table 1, the number of integration points for the Gauss quadrature over one panel was taken equal to $6 \times 6 = 36$, which may be more than necessary. In fact, it has been confirmed that 25 points are sufficient to obtain almost the same results, and that the computation time in that case is approximately 80% of that shown in Table 1.

Examples of numerical convergence with increasing numbers of panels are shown in Figs. 3 and 4, where Fig. 3 shows the added mass in heave mode ($\zeta_j = u_0(x)v_0(y)$ in Eq. (9)) and Fig. 4 shows the damping coefficient in the same heave

Table 2 Relative numerical error in the energy-conservation principle, shown as a percentage, for $L/\lambda = 45$ in deep water. The number of panels in the first quadrant is $NX = 40$ and $NY = 8$

Mode	BX(I, I)	BY(I, I)	BZ(I, I)	BN(I, I)
1	0.2227E-01	0.1363E-01	0.2505E-01	0.1330E-01
2	0.2189E-01	0.1239E-01	0.1886E-01	0.1301E-01
3	0.2784E-02	0.1170E-02	0.1010E-01	0.4330E-02
4	0.2280E-02	0.4132E-02	0.3198E-02	0.4178E-02
5	0.2068E-01	0.1342E-01	0.2298E-01	0.1263E-01
6	0.2018E-02	0.4629E-02	0.1112E-02	0.3293E-02
7	0.5100E-02	0.4719E-03	0.6977E-03	0.3421E-02
8	0.5151E-02	0.4239E-02	0.5964E-02	0.3460E-02
9	0.4536E-02	0.2332E-02	0.4328E-02	0.2234E-02
10	0.1985E-01	0.1177E-01	0.1827E-01	0.1227E-01
11	0.9950E-03	0.2454E-02	0.2263E-02	0.2821E-02
12	0.3865E-02	0.2049E-02	0.4611E-02	0.1258E-02
13	0.3102E-02	0.2718E-02	0.9917E-02	0.1117E-02
14	0.2565E-02	0.1865E-02	0.2021E-02	0.1467E-02
15	0.4295E-02	0.8927E-03	0.3059E-02	0.3270E-03
16	0.5915E-02	0.1047E-03	0.5317E-02	0.6188E-03
17	0.1833E-01	0.1245E-01	0.2014E-01	0.1180E-01
18	0.1058E-03	0.3354E-02	0.3817E-04	0.2941E-02
19	0.3582E-02	0.2958E-03	0.3300E-02	0.1900E-03
20	0.7494E-02	0.8798E-03	0.6425E-02	0.1233E-02
21	0.2638E-02	0.3325E-02	0.8399E-04	0.4133E-02
22	0.2698E-02	0.3287E-02	0.2854E-02	0.3404E-02
23	0.1430E-02	0.3313E-02	0.2055E-02	0.2427E-02
24	0.7174E-03	0.2087E-02	0.1323E-02	0.1779E-02
25	0.2679E-03	0.1618E-02	0.4669E-03	0.1239E-02

mode. The water depth is infinity and the abscissa is the length ratio, L/λ, between the structure length L and wavelength λ.

It can be seen that the results converge smoothly as the number of panels increases and reliable results are obtained provided $L/\lambda < 0.8 \times NX$ is satisfied.

It should be noted that all results plotted in Figs. 3 and 4 satisfy quite accurately the energy-conservation principle and the Haskind-Hanaoka relation, even when the results are a little different from the converged values. One typical example of that is shown in Table 2, which shows the relative error in the energy-conservation principle, checked for $L/\lambda = 45$ in deep water with $NX = 40$ and $NY = 8$. Surprisingly the error is within 0.03% for all specified mode shapes. Good agreement, of the same order, was also found in the Haskind-Hanaoka relation, and for different numbers of panels.

This fact implies that a numerical check based only on the energy-conservation principle and/or the Haskind-Hanaoka relation may be not sufficient to ensure the accuracy of

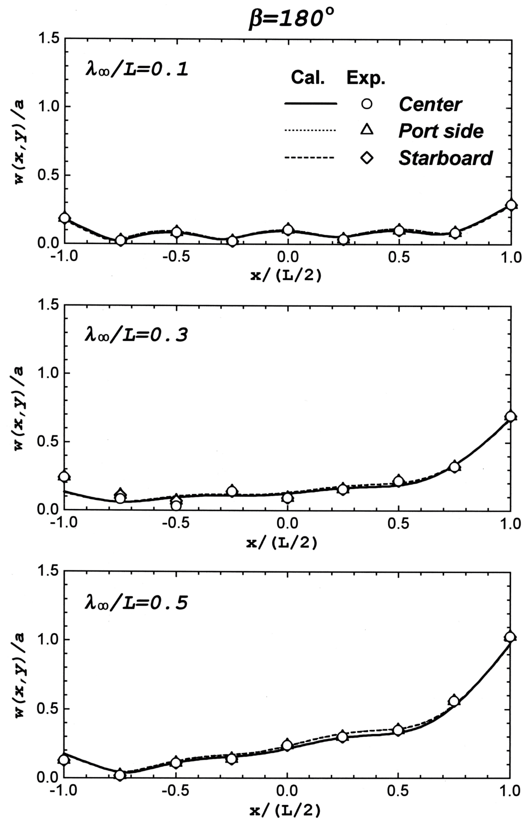

Fig. 5 Comparison of longitudinal distributions of the amplitude of vertical elastic displacement in head waves ($\beta = 180°$). The wavelength ratio is $\lambda_\infty/L = 0.1$, 0.3 and 0.5, where $\lambda_\infty = 2\pi g/\omega^2$, with ω being the circular frequency of the wavemaker

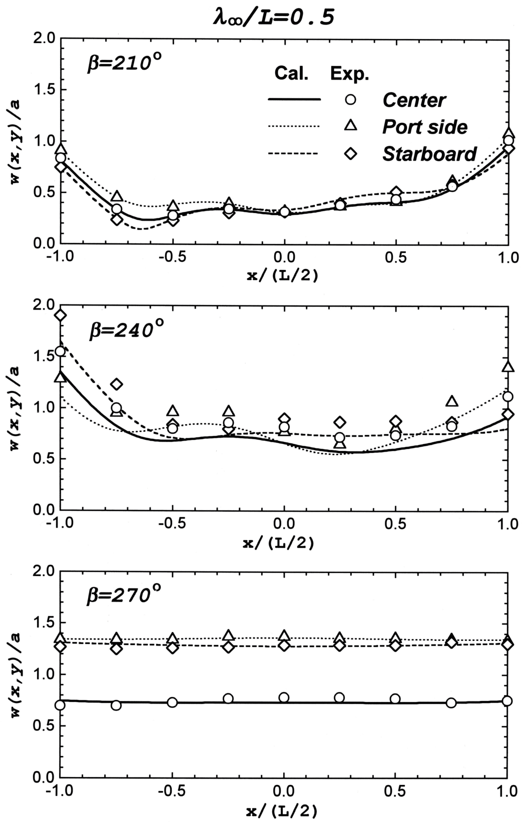

Fig. 6 Comparison of longitudinal distributions of the amplitude of vertical elastic displacement in oblique ($\beta = 210°$, 240°) and beam ($\beta = 270°$) waves. The wavelength ratio is $\lambda_\infty/L = 0.5$, where $\lambda_\infty = 2\pi g/\omega^2$, with ω being the circular frequency of the wavemaker

numerical results.

6.2 Comparison with experiments on elastic response

It is not easy to carry out model experiments of a VLFS, because the similarity of the bending rigidity as well as the geometrical dimensions must be satisfied at the same time. At the Ship Research Institute, the model experiments (assuming a floating structure of $L \times B = 300$ m $\times$ 60 m) were conducted using a 1/30.77 scale model ($L = 9.75$ m, $B = 1.95$ m, $d = 1.67$ cm, the bending rigidity $EI = 1.752 \times 10^4$ Nm^2) in a wave tank of $L \times B = 40\,\mathrm{m} \times 27.5\,\mathrm{m}$ with the water depth set to $h = 1.9$ m. Those results are reported by Yago and Endo [11]. The ratio of the wavelength in the experiments to the model length was in the range of $\lambda_\infty/L > 0.1$ (where λ_∞ is given by $2\pi g/\omega^2$, with ω being the circular frequency of the wavemaker). This ratio is not small enough considering real wavelengths for the VLFS problem, but the results may be used to confirm the validity of the numerical method in this paper.

Figure 5 shows the amplitude of vertical displacement of the model in head waves, incoming from the positive x-axis. The deflection is large at the bow, attenuates toward the lee side and then increases again near the tip of the lee side. As the wavelength decreases, especially for $\lambda_\infty/L = 0.1$, elastic deflections of a higher order becomes prominent. We can also observe that little difference in amplitude exists between the center line and the rim of the port or starboard sides. These measured properties of vertical deflection are precisely accounted for by the present computations.

Figure 6 shows the results in oblique ($\beta = 210°$ and $240°$) and beam ($\beta = 270°$) waves for the wavelength of $\lambda_\infty/L = 0.5$. Compared to the head-wave case, the amplitude is large and its variations along the center line, port, and starboard sides are different from each other. Computed results are in good agreement, confirming the validity of the present method.

6.3 Elastic response in a short-wavelength regime

For a study of a realistic floating airport, the relative wavelength must be much smaller than that in the experiments discussed above. However, experiments corresponding to a realistic situation are very difficult to design. Fortunately, the calculation method described in this paper has been validated for longer wavelengths, and confirmed numerically as being accurate enough for shorter wavelengths. Therefore, on the basis of numerical computations, the characteristics of the elastic response of a VLFS is discussed below.

As an illustration, computations were performed with the data shown in Table 3, which are for a floating airport of $L = 5000$ m, $B = 1000$ m, and $d = 5$ m. The bending rigidity was taken equal to $D = 1.96 \times 10^{11}$ Nm to give a realistic value.

Table 3 Numerical data for computations of elastic motions

$L \times B \times d = 5000\,(\mathrm{m}) \times 1000\,(\mathrm{m}) \times 5\,(\mathrm{m})$
$h = 50\,(\mathrm{m})$ or infinity
$D = 1.96 \times 10^{11}\,(\mathrm{Nm}), \quad \nu = 0.3$
$M' = M/\rho LBd = 1.0$
$D' = D/\rho g(L/2)^4 = 0.512 \times 10^{-6}$

There might be a problem about the convergence of elastic deflection with increasing the number of mode functions, because each individual mode function does not satisfy the free-end boundary conditions, Eqs. (29) and (30), as it is. Here, the free-end conditions are satisfied in the weaker context, with Eqs. (29) and (30) being taken into account in transforming the stiffness matrix by partial integrations. The validity of this technique was generally confirmed by Figs. 5 and 6. To provide a more rigorous numerical confirmation, Table 4 shows the amplitudes of elastic

Table 4 Convergence of the amplitude of the local elastic deflection and relative numerical error in the energy-conservation principle (as a percentage), computed for $L/\lambda = 20$ and $\beta = 0°$ in deep water, using $NX = 40$ and $NY = 8$

		On the center line			On the side line			
MX	MY	$(-1,0)$	$(0,0)$	$(+1,0)$	$(-1,0.2)$	$(0,0.2)$	$(+1,0.2)$	Error in Eq. 38
10	2	1.0815	0.0255	0.0846	0.8837	0.0197	0.0278	0.2477E-3
15	3	0.8050	0.2378	0.6125	0.8555	0.1527	0.4116	0.8208E-4
20	4	0.7594	0.2284	0.5932	0.8161	0.1456	0.3958	0.8112E-4
25	5	0.7551	0.2272	0.5878	0.8056	0.1517	0.3913	0.8236E-4
30	6	0.7550	0.2262	0.5856	0.8048	0.1530	0.3911	0.8308E-4
35	7	0.7552	0.2268	0.5846	0.8051	0.1539	0.3912	0.8347E-4
40	8	0.7560	0.2262	0.5834	0.8056	0.1545	0.3913	0.8285E-4

deflection at several selected positions. These are computed for $L/\lambda_\infty = 20$ and $\beta = 0°$ in deep water, using panel divisions of $NX = 40$ and $NY = 8$. The selected positions are $(x, y) = (-1, 0)$, $(0, 0)$, $(1, 0)$ on the center line and $(x, y) = (-1, 0.2)$, $(0, 0.2)$, $(1, 0.2)$ on the side line. Note that $x = -1$ is the weather side for $\beta = 0°$. As the number of elastic modes increases (with ratio $MX/MY = 5$ kept constant in the present case), the amplitudes at all computed positions converge within engineering accuracy.

The entry in the last column in Table 4 shows the numerical errors in the energy conservation principle for the case of a freely floating structure in an incident wave. The equation for that conservation principle can be written as

$$H(k_0, \beta) - H^*(k_0, \beta) = -iK\frac{C_0}{2\pi}\int_0^{2\pi} |\, H(k_0, \theta)\,|^2 \, d\theta \tag{38}$$

where

$$H(k_0, \theta) = H_S(k_0, \theta) + \sum_{j=1}^{\infty}\Big(\frac{X_j}{a}\Big)\, H_j(k_0, \theta) \tag{39}$$

Here $H_j(k_0, \theta)$ $(j = S, 1, 2, \cdots)$ is defined in Eq. (27) and X_j/a is the complex amplitude which can be computed from Eq. (32). It can be seen from Table 4 that the energy conservation principle is satisfied very accurately, even when the local elastic deflections are not converged.

The results of diffraction pressure and elastic deflection are shown in Fig. 7 and Fig. 8, respectively, at the frequency corresponding to $L/\lambda_\infty = 20$. Only the real part (i.e., a snapshot taken at $t = 0$) is shown. In both Figs. 7 and 8, the upper section is the result for head wave in deep water, the middle section is for head wave in shallow water of $h = 50$ m $(h/\lambda_\infty = 1/5)$, and the lower section is for oblique wave of $\beta = 30°$ in shallow water of $h = 50$ m. The number of panel divisions was set to $NX = 30$ and $NY = 6$ in the first quadrant and the mode functions in each of four motion types were taken as $MX = 30$ and $MY = 6$.

We can see that the diffraction pressure in head waves is almost zero inside the plate but increases sharply near the weather side, with small oscillations along the rim of both sides parallel to the direction of wave propagation.

However, the elastic deflection is large even inside the plate, and especially at the tip of the lee side. We can envisage that a thin elastic plate with free ends is excited near the tip

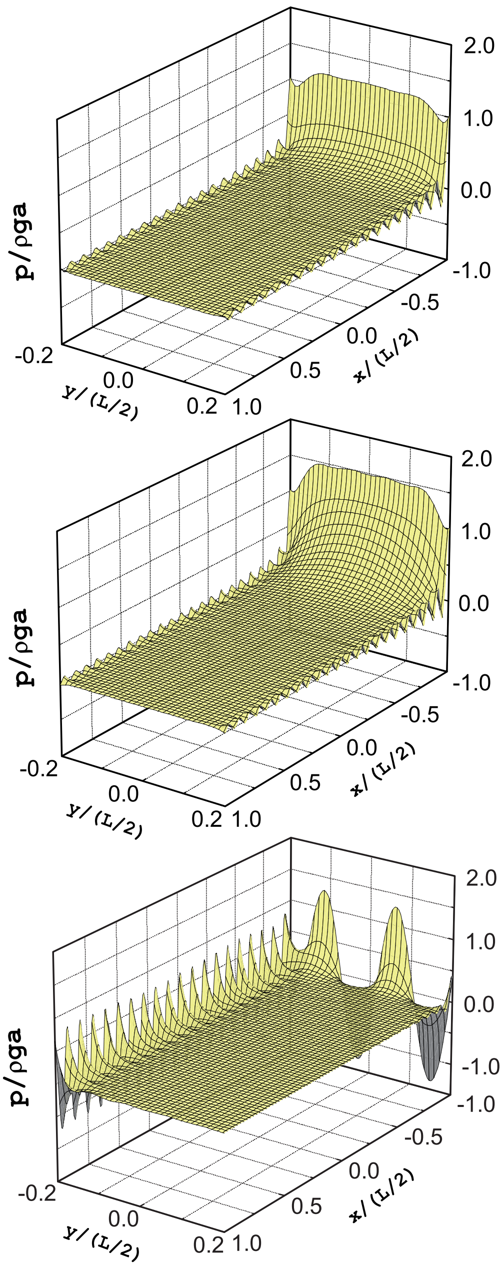

Fig. 7 Real parts of diffraction pressure distribution on the plate of $L/B = 5$. The upper section is for $\beta = 0°$ in deep water, the middle section is for $\beta = 0°$ in shallow water, and the lower section is for $\beta = 30°$ in shallow water. $L/\lambda_\infty = 20$ in all cases, and $h/\lambda_\infty = 1/5$ in shallow water

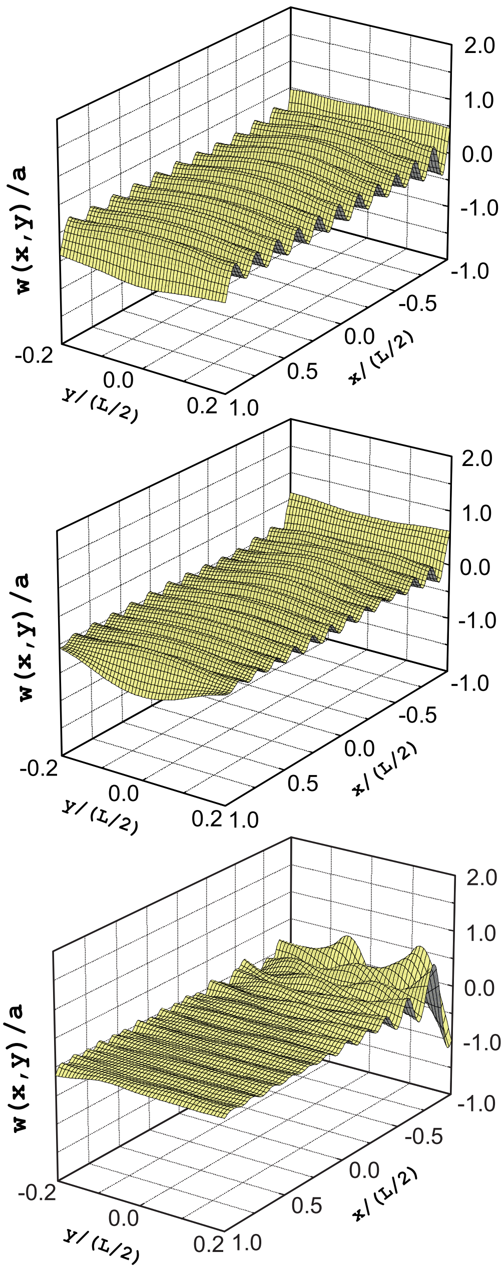

Fig. 8 Real parts of elastic deflection of the plate of $L/B = 5$. The upper section is for $\beta = 0°$ in deep water, the middle section is for $\beta = 0°$ in shallow water, and the lower section is for $\beta = 30°$ in shallow water. $L/\lambda_\infty = 20$ in all cases, and $h/\lambda_\infty = 1/5$ in shallow water

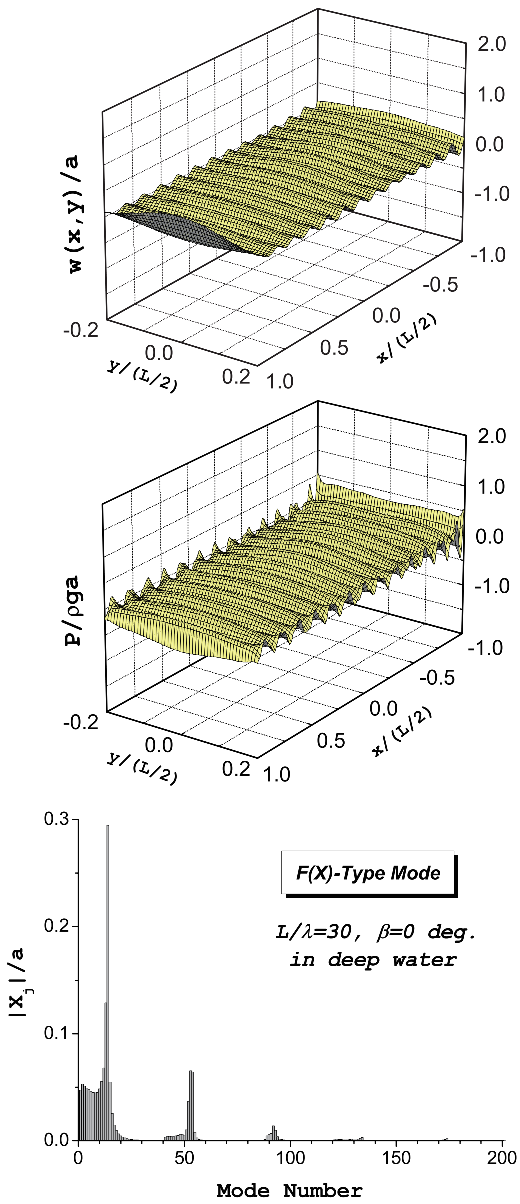

Fig. 9 The upper and the middle sections are the real parts of elastic deformation and the total pressure distribution, respectively, on the plate of $L = 5000$ m and $B = 1000$ m in deep water. The lower section shows the amplitude in each of elastic mode shapes. The wavelength ratio is $L/\lambda = 30$ in head wave ($\beta = 0°$)

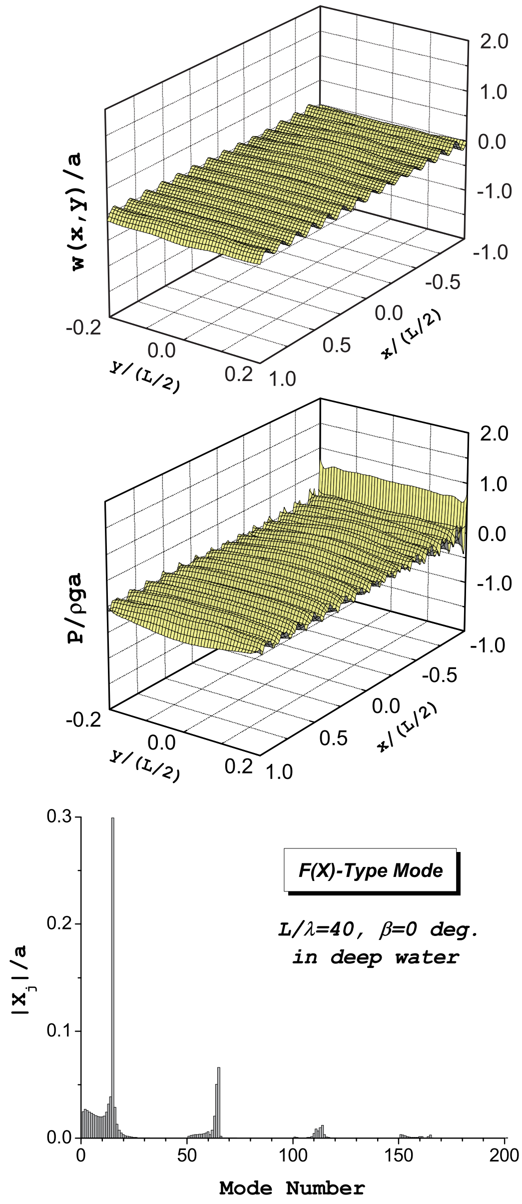

Fig. 10 As in Fig. 9 except that the wavelength ratio $L/\lambda = 40$

of the weather side by a wave force which is like a delta function, and that the disturbance is propagated towards the end of the plate. The dominant wavelength of elastic deflection is longer than that of the incident wave. In fact, as explained by Ohkusu and Nanba [18], the wavelength of elastic deflection is determined by the dispersion relation, in which the finite value of flexural rigidity is equivalent to a larger gravitational acceleration in water waves.

In shallow water, the wavelength of incoming wave becomes short relative to the infinite-depth case, which results in the shorter wavelength of the pressure oscillation. Another shallow water effect is that the flow under the plate is constrained horizontally, thus increasing the magnitude of the pressure and the depth of penetration of the dominant peak pressure. These shallow-water effects can be also observed in the elastic deflection, although the oscillation pattern looks similar to the infinite-depth case. It is noticeable that the amplitude is a little smaller than that in deep water.

In oblique waves, the diffraction pressure has several spikes along the up-wave side, in phase with the incident wave, which are negligible elsewhere. The elastic deflection, on the other hand, is not necessarily large along the up-wave side, and the amplitude is smaller than the head-wave case except near the fore end exposed to the incident wave.

Computations were also performed for $L/\lambda = 30$ and 40 in deep water to investigate the characteristics of hydroelastic deflection in the short wavelength region. The number of panels was $NX = 50$ and $NY = 10$, satisfying $L/\lambda < 0.8 \times NX$ which is a requirement for the numerical convergence suggested by Figs. 3 and 4. The number of mode functions was set to $MX = 50$ and $MY = 10$ in both $F(X)$ and $F(Z)$ types of motion.

The results for $L/\lambda = 30$ are shown in Fig. 9 and those for $L/\lambda = 40$ are shown in Fig. 10, where the upper part of the figure is the real part of the elastic deflection, the middle part is the total pressure distribution when the structure is freely oscillating in waves, and the lower part is the nondimensional amplitude of specified mode shapes. The serial mode number, j, is defined such that $j = n \times MX + m + 1,\ m = 0 \sim MX - 1$ for sequential integers of $n = 0 \sim MY - 1$.

We can see that the elastic deflection does not necessarily become negligible when the wavelength of incident waves decreases, and that a prominent wavelength exists in the elastic deflection. The latter can clearly be seen in the lower sections of Figs. 9 and 10, which show the contribution of each mode function.

Lastly, by comparing the distribution of total pressure with the diffraction pressure alone, as shown in Fig. 7, we can see that the pressure distribution is strongly influenced by the elastic motions and, except near the rim at both sides parallel to the x-axis, the fluctuation pattern of the total pressure looks similar to that of the elastic deflection.

7. Conclusions

A new method to solve the integral equation in the pressure-distribution method has been described. To maintain a high level of accuracy in the very short wavelength regime, with short computational times and few unknowns, the scheme uses bi-cubic B-spline functions to represent the unknown pressure, and a Galerkin method to satisfy the body boundary conditions. The good performance of the scheme was validated through numerical checks of various hydrodynamic relations, and a convergence test with an increasing number of panels.

The hydroelastic responses of a plate were computed by the mode-expansion method, using a superposition of one-dimensional free-free beam modes in both the x- and y-directions. The free-end boundary conditions along the periphery of each plate were satisfied as being the natural boundary conditions in the process of transforming the stiffness matrix by partial integrations. The validity of this technique was confirmed by observing the numerical convergence of the local elastic deflection at several positions as the number of elastic modes was increased.

The computed results of the amplitude of the elastic response were in good agreement with the results of experiments with wavelengths of $\lambda_\infty/L > 0.1$ conducted at the Ship Research Institute.

Assuming a realistic floating airport of 5000 m in length, computations were also performed for shorter wavelengths of $L/\lambda = 20$, 30 and 40. Those numerical results have shown that, as the wavelength of incident waves decreases, the elastic deflection does not necessarily become negligible and its amplitude becomes almost constant over the whole structure.

References

[1] Ertekin RC, Wang SQ, Riggs HR (1994) Hydroelastic response of a floating runway. Proceedings of the International Conference on Hydroelasticity in Marine Technology, Trondheim, 389–400

[2] Mamidipudi P, Webster WC (1994) The motions performance of a mat-like floating airport. Proceedings of the International Conference on Hydroelasticity in Marine Technology, Trondheim, 363–375

[3] Wang S, Ertekin RC, Stiphout ATFM et al (1995) Hydroelastic-response analysis of a box-like floating airport of shallow draft. Proceedings of the 5th International Offshore and Polar Eng Conference, The Hague, 145–152

[4] Yasuzawa Y, Kagawa K, Kawano D et al (1996) Wave response analysis of a flexible large floating structure. Proceedings of the International Workshop on Very Large Floating Structures, Hayama, 221–228

[5] Newman JN, Maniar HD, Lee CH (1996) Analysis of wave effects for very large floating structures. Proceedings of the International Workshop on Very Large Floating Structures, Hayama, 135–142

[6] Maeda H, Masuda K, Miyajima S et al (1995) Hydroelastic responses of pontoon type very large floating offshore structure (in Japanese). J Soc Nav Archit Jpn 178: 203–212

[7] Yago K (1995) Forced oscillation test of flexible floating structure and hydrodynamic pressure distributions (in Japanese). Proceedings of the13th Ocean Engineering Symposium, Soc Nav Archit Jpn, 313–320

[8] Takaki M, Gu X (1996) Motions of a floating elastic plate in waves. J Soc Nav Archit Jpn 180: 331–339

[9] Wang S, Ertekin RC, Riggs HR (1997) Computationally efficient techniques in the hydroelasticity analysis of very large floating structures. Computers and Structures 62 (4): 603–610

[10] Ertekin RC, Wang SQ, Che XL et al (1995) On the application of the Haskind-Hanaoka relations to hydroelasticity problems. Marine Structures 8: 617–629

[11] Yago K, Endo H (1996) On the hydroelastic response of box-shaped floating structure with shallow draft (in Japanese). J Soc Nav Archit Jpn 180: 341–352

[12] Seto H (1991) Efficient evaluation of some singular integrals appearing in multiple expansions in water of finite depth. Trans West-Japan Soc Nav Archit 83: 103–113

[13] Seto H (1992) Some expressions of pulsating source potentials in shallow water and their efficient algorithms. Trans West-Japan Soc Nav Archit 85: 25–36

[14] Newman JN (1994) Wave effects on deformable bodies. Applied Ocean Research 16: 47–59

[15] Sakurai A (1982) Spline function and applications (in Japanese). Tokyo Denki University Press, pp 88–118

[16] Newman JN (1986) Distributions of sources and normal dipoles over a quadrilateral panel. J Engineering Mathematics 20: 113–126

[17] Bessho M (1977) On the theory of hydrodynamic forces acting on a two-dimensional flat ship oscillating on a water surface (in Japanese). J Kansai Soc Nav Archit Jpn 165: 41–48

[18] Ohkusu M, Nanba Y (1996) Hydroelastic behavior of a large floating platform in waves. Proceedings of the 11th Workshop on Water Waves and Floating Bodies, Hamburg

A Time-Domain Nonlinear Simulation Method for Wave-Induced Motions of a Floating Body*

Masashi KASHIWAGI, Tetsushi MOMODA and Masaru INADA
Research Institute for Applied Mechanics, Kyushu University
Kasuga, Fukuoka 816-8580, Japan

Summary

A nonlinear calculation method based on the Mixed Eulerian Lagrangian method is presented for wave-induced motions of a 2-D floating body. Attention is placed on an effective calculation of the hydrodynamic force associated with the temporal derivative of the velocity potential in Bernoulli's pressure equation. Unlike other existing methods, the acceleration field can be computed simultaneously with the velocity field, which contributes greatly to the reduction of computation time. By use of Green's second identity, the new method is explained as an extension from the mode decomposition method, and close relations between the two methods are emphasized.

Computations are performed for a wall-sided model and a flared model, and numerical results of the waves at upwave and downwave positions and the body motions (sway, heave, and roll) are compared with corresponding experiments. The overall agreement is very good, confirming validity of the present method. Discussion is also made on the parametric oscillation in roll, observed for the flared model.

1. Introduction

Nonlinear calculation methods for the motion of a floating body in large-amplitude waves have been drawing attention in the seakeeping and ocean engineering research. Recently, great interest is placed on effects of the body geometry above the sea level, for which no information has been given by conventional linear theories. For this kind of research, the so-called Mixed Eulerian Lagrangian (MEL) method, initiated by Longuet-Higgins & Cokelet[1], is the most promising in the framework of the potential flow.

The MEL method has been studied by many researchers; recent references in this context are Cao et al.[2], Tanizawa[3),4], Kashiwagi[5], Wu & Eatock Taylor[6], and others cited therein. However, simulations of the wave-body interaction were not so successful, because of the difficulty in precise evaluation of the temporal derivative of the velocity potential, $\partial\phi/\partial t \equiv \phi_t$, appearing in Bernoulli's pressure equation.

The simplest way of evaluating ϕ_t is to use a backward finite-difference scheme in time. However, it is known that this scheme makes a solution inherently unstable, resulting in the breakdown of computations. An alternative is to solve the boundary-value problem for ϕ_t, which was initially proposed by Vinje & Brevig[7]. The difficulty in this case is that the body boundary condition for ϕ_t includes the acceleration of a body which is to be computed from the motion equation. The hydrodynamic force in the motion equation, in turn, requires the

* *Reprinted from Journal of the Society of Naval Architects of Japan, Vol.184, pp.139-148, 1998 (December)*

pressure integration and thus evaluation ϕ_t. To resolve this 'nested' situation, several ideas have been proposed. However, one common defect among those is that the boundary-value problem for ϕ_t must be solved after the velocity field is completely determined. That is, two boundary-value problems must be solved separately within one step of the time marching; this is a reason of large computation time in the wave-body interaction problem.

The present paper investigates a new indirect method, originally proposed by Wu & Eatock Taylor[6], in which the boundary-value problem is solved for an artificial function ψ_i (which is superficially similar to the radiation problem in the linear theory) instead of ϕ_t itself. In this method, the boundary-value problem for ψ_i is the same in form but independent of the velocity field. Thus it can be solved simultaneously with the boundary-value problem for the velocity field, which contributes greatly to the reduction of computation time. Mathematical transformations in the new method are based on Green's second identity. Close relations are noted between the new method and the mode decomposition method known as a conventional method for the present problem.

Computations are performed for two different profiles of a 2-D floating body: wall-sided and flared models. Results of waves and the sway, heave, and roll motions of a floating body are compared with corresponding experiments. Discussion is made on the validity and limitation of the present method and also on the parametric oscillation in roll observed for the flared model.

2. Formulation for the Velocity Potential

As shown in Fig. 1, we consider a freely floating body on the free surface, subjected to a wave generated by a plunger-type wavemaker. The x-axis of the coordinate system coincides with the plane of the undisturbed free surface and the positive y-axis is taken downward. The bottom of water is finite and horizontal, with its depth denoted by h.

The gravitational center of a floating body is initially located at the point (x_G, y_G), and subsequent displacement of that point due to wave-induced motions is denoted by $\xi_1(t)$, $\xi_2(t)$, and $\alpha(t)$ for sway, heave, and roll, respectively. The body is moored by a weak spring to prevent from a large excursion in the horizontal direction.

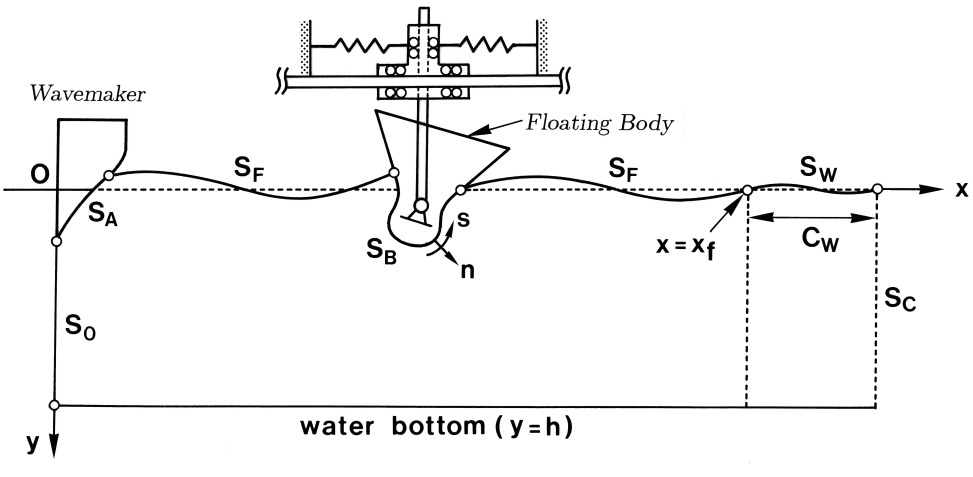

Fig. 1 Coordinate system and schematic view of experiment

The boundary of a fluid is denoted by S_0 on the y-axis, S_A on a wavemaker, S_F on the free surface, S_B on a floating body, S_W on a wave absorbing beach, and S_C on a control surface which is placed artificially at some distance from a body to make the fluid domain bounded.

In the analyses that follow, all quantities are nondimensionalized in terms of the half beam of a floating body, b, the gravitational acceleration, g, and the fluid density, ρ.

Assuming the fluid to be inviscid with irrotational motion, the velocity potential ϕ can be introduced, satisfying the Laplace equation:

$$\nabla^2\phi(x,y,t) = 0 \quad \text{in the fluid} \tag{1}$$

The boundary conditions to be satisfied by the velocity potential are written as follows:

$$\left.\begin{aligned} &\frac{Dx}{Dt} = \frac{\partial\phi}{\partial x}, \quad \frac{Dy}{Dt} = \frac{\partial\phi}{\partial y} \\ &\frac{D\phi}{Dt} = y + \frac{1}{2}\nabla\phi\nabla\phi \end{aligned}\right\} \text{on } S_F \tag{2}$$

$$\frac{\partial\phi}{\partial n} = \dot{y}_0(t)\, n_2 \qquad \text{on } S_A \tag{3}$$

$$\frac{\partial\phi}{\partial n} = \sum_{j=1}^{3} v_j\, n_j \qquad \text{on } S_B \tag{4}$$

$$\frac{\partial\phi}{\partial n} = \frac{\partial\phi}{\partial x} = 0 \qquad \text{on } S_0 \tag{5}$$

$$\frac{\partial\phi}{\partial n} = -\frac{\partial\phi}{\partial y} = 0 \qquad \text{at } y = h \tag{6}$$

where D/Dt in (2) denotes the substantial derivative; $\dot{y}_0(t)$ in (3) is the velocity of the wavemaker, and $\boldsymbol{n} = (n_1, n_2)$ is the unit normal vector; n_3 in (4) is defined as $n_3 = (x - x_G - \xi_1)\, n_2 - (y - y_G - \xi_2)\, n_1$, and $v_1 = \dot{\xi}_1(t)$, $v_2 = \dot{\xi}_2(t)$, and $v_3 = \dot{\alpha}(t)$. Note that the normal vector is defined in the spaced-fixed coordinate system and positive when directing from the body surface into the fluid.

The far-field condition of outgoing waves is satisfied by installing an artificial wave absorbing beach. Mathematically, as in the previous paper[5)] for the radiation problem, Newtonian cooling terms are introduced only in the kinematic free-surface condition in (2), in the form

$$\frac{Dx}{Dt} = \frac{\partial\phi}{\partial x}, \quad \frac{Dy}{Dt} = \frac{\partial\phi}{\partial y} - 2\nu y - \nu^2\phi \quad \text{on } S_W \tag{7}$$

Here ν is nonzero inside the beach and given by

$$\nu = 3\, C_S (x - x_f)^2 / C_W^3 \quad \text{for } x \geq x_f \tag{8}$$

with x_f being the starting point of the wave absorbing beach which extends over a length C_W (see Fig. 1). The value of coefficient C_S is taken equal to 1.2 for all computations in this paper.

3. Acceleration Field and Force

To compute the velocity field at some time instant, the displacement and velocity of a floating body must be known; these may be given by integrating in time the equations of the body motion expressed in the form

$$m\,a_1 = F_1\ , \quad m\,a_2 = F_2\ , \quad m\kappa^2 a_3 = F_3 \tag{9}$$

where m and κ are the body mass and the gyrational radius in roll, respectively, and $a_1 = \ddot{\xi}_1(t)$, $a_2 = \ddot{\xi}_2(t)$, and $a_3 = \ddot{\alpha}(t)$ are the components of the acceleration defined in the space-fixed reference frame.

The right-hand side of each equation in (9), F_i, is the force ($i = 1, 2$) and moment ($i = 3$) on a body, in which the components of hydrodynamic and hydrostatic forces may be obtained by integrating Bernoulli's pressure over the wetted surface of a body. Including the gravitational force and horizontal restoring force due to a weak spring, the total force in the i-th direction can be computed by

$$F_i = \int_{S_B} \Big\{ \phi_t + \frac{1}{2}\nabla\phi\nabla\phi - y \Big\} n_i \, d\ell - k\,\xi_1\,\delta_{i1} + W\,\delta_{i2} \tag{10}$$

where $\phi_t = \partial\phi/\partial t$ is the temporal derivative of the velocity potential, k is the linear spring constant, and W is the weight of the body, equal to mg. δ_{ij} denotes the Kronecker delta, equal to 1 when $i = j$, otherwise zero.

A numerical problem in (10) is evaluating ϕ_t. The simplest way for that may be to use a backward finite-difference scheme in time. However, it has been shown that the use of a backward finite-difference scheme makes a solution unstable, resulting in the breakdown of computations. Several recent works, e.g. Cointe et al.[8] and Tanizawa[3], recommend to solve the boundary-value problem for ϕ_t for stable and accurate simulations of motions of a freely oscillating body.

According to Tanizawa[3], the body boundary condition for ϕ_t can be written as

$$\frac{\partial\phi_t}{\partial n} = \sum_{j=1}^{3} a_j\,n_j + q_B \qquad \text{on } S_B \tag{11}$$

where

$$\begin{aligned} q_B = &- k_n\Big\{ \Big(\frac{\partial\phi}{\partial x} - \dot{\xi}_1 + \dot{\alpha}\big(y - y_G - \xi_2\big)\Big)^2 + \Big(\frac{\partial\phi}{\partial y} - \dot{\xi}_2 - \dot{\alpha}\big(x - x_G - \xi_1\big)\Big)^2 \Big\} \\ &+ n_1\Big\{ \dot{\alpha}^2(x - x_G - \xi_1) - 2\dot{\alpha}\Big(\frac{\partial\phi}{\partial y} - \dot{\xi}_2\Big)\Big\} \\ &+ n_2\Big\{ \dot{\alpha}^2(y - y_G - \xi_2) + 2\dot{\alpha}\Big(\frac{\partial\phi}{\partial x} - \dot{\xi}_1\Big)\Big\} \\ &+ k_n\Big\{ \Big(\frac{\partial\phi}{\partial x}\Big)^2 + \Big(\frac{\partial\phi}{\partial y}\Big)^2 \Big\} + \frac{\partial\phi}{\partial n}\frac{\partial}{\partial s}\Big(\frac{\partial\phi}{\partial s}\Big) - \frac{\partial\phi}{\partial s}\frac{\partial}{\partial s}\Big(\frac{\partial\phi}{\partial n}\Big) \end{aligned} \tag{12}$$

Here k_n is the curvature of body surface, and s is the tangential direction orthogonal to n (see Fig. 1).

It should be noted that q_B defined by (12) can be explicitly evaluated from solutions of the velocity field, whereas the components of the body acceleration, a_j, are unknown and to be given from (9) and (10). Namely, the calculation of the acceleration field is coupled with the body-motion equations.

The boundary condition on the wavemaker (S_A) can be obtained simply by substituting $\xi_1 = \alpha = 0$ and $\xi_2 = y_0(t)$ into (11), with the result

$$\frac{\partial\phi_t}{\partial n} = q_A \qquad \text{on } S_A \tag{13}$$

where
$$q_A = \ddot{y}_0\, n_2 - k_n\, \dot{y}_0 \Big(\dot{y}_0 - 2\frac{\partial \phi}{\partial y} \Big) + \frac{\partial \phi}{\partial n}\frac{\partial}{\partial s}\Big(\frac{\partial \phi}{\partial s}\Big) - \frac{\partial \phi}{\partial s}\frac{\partial}{\partial s}\Big(\frac{\partial \phi}{\partial n}\Big) \tag{14}$$

Since $y_0(t)$ may be given as an input, the right-hand side of (13), q_A, can be explicitly evaluated.

Other boundary conditions for ϕ_t are written as follows:

$$\phi_t = -\frac{1}{2}\nabla\phi\nabla\phi + y \quad \text{on } S_F \tag{15}$$

$$\frac{\partial \phi_t}{\partial n} = \frac{\partial \phi_t}{\partial x} = 0 \qquad \text{on } S_0 \tag{16}$$

$$\frac{\partial \phi_t}{\partial n} = -\frac{\partial \phi_t}{\partial y} = 0 \qquad \text{at } y = h \tag{17}$$

Eq. (15) has been obtained from the dynamic free-surface condition of $p = 0$.

The above boundary-value problem for ϕ_t is the same in the nature as that for ϕ itself. Therefore, as will be explained later, the velocity and acceleration fields can be calculated with the same numerical scheme based on the boundary-element method. However, it should be noted that the right-hand sides of (12)–(15) may not be evaluated unless the velocity field is completely determined. This implies that the boundary-value problem for ϕ and ϕ_t can not be solved at the same time.

4. Mode Decomposition Method

Several methods have been proposed for solving the acceleration field coupled with the motion equations of a floating-body; for instance, the iteration method by Cao et al.[2], the mode decomposition method by Vinje & Brevig[7] and Cointe et al.[8], and the implicit boundary-condition method by Tanizawa.[3] These are essentially the same in that the boundary-value problem for ϕ_t must be solved after the velocity field is completely determined. In this section, the mode decomposition method will be summarized as a typical conventional method.

Since the body boundary condition (11) is linear with respect to the acceleration, ϕ_t may be obtained in the form

$$\phi_t = \sum_{j=1}^{3} a_j\, \psi_j + \psi_4 \tag{18}$$

Then, ψ_j must be calculated so as to satisfy the followings:

$$\frac{\partial \psi_j}{\partial n} = \begin{cases} n_j & (j = 1 \sim 3) \\ q_B & (j = 4) \end{cases} \qquad \text{on } S_B \tag{19}$$

$$\frac{\partial \psi_j}{\partial n} = \begin{cases} 0 & (j = 1 \sim 3) \\ q_A & (j = 4) \end{cases} \qquad \text{on } S_A \tag{20}$$

$$\psi_j = \begin{cases} 0 & (j = 1 \sim 3) \\ -\dfrac{1}{2}\nabla\phi\nabla\phi + y & (j = 4) \end{cases} \qquad \text{on } S_F \tag{21}$$

$$\frac{\partial \psi_j}{\partial n} = 0 \qquad \text{on } S_0 \text{ and at } y = h \tag{22}$$

With this decomposition, ψ_j can be determined irrespective of the body acceleration, and the boundary-value problems for $j = 1 \sim 3$ are independent of the velocity field. It is noteworthy that (18) and (19) are reminiscent of the decomposition in the linear theory into the radiation and diffraction problems.

Once the boundary-value problems for ψ_j are solved, the total force in the i-th direction can be obtained in the form

$$F_i = -\sum_{j=1}^{3} a_j\, A_{ij} + Q_i \tag{23}$$

where

$$A_{ij} = -\int_{S_B} \psi_j\, n_i\, d\ell \tag{24}$$

$$Q_i = \int_{S_B} \Big\{ \psi_4 + \frac{1}{2}\nabla\phi\nabla\phi - y \Big\} n_i\, d\ell - k\,\xi_1\,\delta_{i1} + W\,\delta_{i2} \tag{25}$$

Here A_{ij} may be understood as the added mass and Q_i represents the other forces, dependent on the velocity, displacement, and incident waves.

Substituting (23) in (9), the components of the body acceleration can be explicitly given, which will give the velocity and displacement of the body in the next time step.

5. New Indirect Method

One defect in the above method is that the ψ_4-problem can not be solved unless the velocity field is completely determined. That is, after solving the boundary-value problems for ϕ and ψ_j $(i = 1 \sim 3)$, the boundary-value problem for ψ_4 must be solved separately in one time step; which is disadvantageous from a viewpoint of computation time, especially for long time simulations.

A favorable style in that respect is that the boundary-value problems for the velocity and acceleration fields can be solved at the same time. This requirement may be achieved by an idea proposed by Wu & Eatock Taylor[6]. Unfortunately, the body boundary condition for ϕ_t in their paper is different from (11) and no numerical results have been published. Therefore, necessary equations for computing the acceleration of a body, particularly the modification of Q_i given by (25), will be described below.

In Wu & Eatock Taylor[6], Green's second identity was applied to ϕ_t and ψ_i $(i = 1 \sim 3)$, but here we consider that identity for ψ_4 and ψ_i $(i = 1 \sim 3)$, which is written as

$$\int_{S_0+S_A+S_B+S_F+S_\infty} \Big\{ \psi_4 \frac{\partial \psi_i}{\partial n} - \psi_i \frac{\partial \psi_4}{\partial n} \Big\}\, d\ell = 0 \tag{26}$$

From the boundary conditions to be satisfied by ψ_4 and ψ_i, the integral along S_0 and S_∞ (which includes S_C and the water bottom) may be zero. Further, taking account of $\psi_i = 0$ on S_F, $\partial\psi_i/\partial n = 0$ on S_A, and $\partial\psi_i/\partial n = n_i$ on S_B, it follows that

$$\begin{aligned}\int_{S_B} \psi_4\, n_i\, d\ell &= \int_{S_A+S_B} \psi_i \frac{\partial \psi_4}{\partial n} d\ell - \int_{S_F} \psi_4 \frac{\partial \psi_i}{\partial n} d\ell \\ &= \int_{S_A} \psi_i\, q_A\, d\ell + \int_{S_B} \psi_i\, q_B\, d\ell + \int_{S_F} \Big\{ \frac{1}{2}\nabla\phi\nabla\phi - y \Big\} \frac{\partial \psi_i}{\partial n} d\ell \end{aligned} \tag{27}$$

In obtaining (27), conditions of (19)–(21) have been used.

With (27), the force term Q_i defined by (25), can be calculated as follows:

$$Q_i = \int_{S_A} \psi_i\, q_A\, d\ell + \int_{S_B} \psi_i\, q_B\, d\ell + \int_{S_B+S_F} \Big\{ \frac{1}{2}\nabla\phi\nabla\phi - y \Big\} \frac{\partial \psi_i}{\partial n} d\ell - k\,\xi_1\,\delta_{i1} + W\,\delta_{i2} \tag{28}$$

It should be emphasized that there is no need to solve the ψ_4-problem for computing (28) and that the boundary-value problems for ψ_i $(i = 1 \sim 3)$ and ϕ are independent and thus can be solved at the same time. With these facts, we can expect reduction of the computation time compared to the mode decomposition method.

We note that transformations in this new method are reminiscent of a proof of the Haskind relation in the linear theory, saying that the wave-exciting force can be computed in terms of only the radiation solutions. Another thing to be noted is that the pressure is not calculated in the new method and hence a solution of the ψ_4-problem is still needed if the pressure distribution is of concern.

6. Numerical Procedure

In the MEL method, the positions of fluid particles (x, y) on the free surface and the velocity potential ϕ on those points are pursued by integrating (2) in time. This means that the boundary condition for ϕ on S_F is of Dirichlet type, which is the same as that for ψ_j, (21).

Therefore, at each time step, the velocity field described by ϕ and the artificial flow described by ψ_j can be determined in the same manner. Let ϕ or ψ_j be denoted by ψ in general. Then a solution of ψ can be obtained by solving the boundary integral equation of the form

$$\begin{aligned} C(P)\psi(P) &+ \int_{S_0+S_A+S_B} \psi(Q)\frac{\partial G(P;Q)}{\partial n_Q}\,d\ell - \int_{S_F+S_W} \frac{\partial \psi(Q)}{\partial n_Q} G(P;Q)\,d\ell \\ &= \int_{S_A+S_B} \frac{\partial \psi(Q)}{\partial n_Q} G(P;Q)\,d\ell - \int_{S_F+S_W} \psi(Q)\frac{\partial G(P;Q)}{\partial n_Q}\,d\ell \end{aligned} \tag{29}$$

where

$$\left.\begin{aligned} G(P;Q) &= \frac{1}{2\pi}\big(\log r + \log r_h\big) \\ r &= \sqrt{(x-x')^2 + (y-y')^2} \\ r_h &= \sqrt{(x-x')^2 + \{y-(2h-y')\}^2} \end{aligned}\right\} \tag{30}$$

$P = (x, y)$ is a point on the boundary and $Q = (x', y')$ is an integration point. $C(P)$ is referred to as the solid angle, which is computed numerically from the equi-potential condition over the entire boundary.

As shown in (30), the Green function includes the mirror image reflected in the water bottom, so that the water bottom is excluded from the integration area in (29). Also excluded is a control surface S_C shown in Fig. 1, because $\psi = 0$ and $\partial\psi/\partial n = 0$ are expected by virtue of the absorbing beach.

To solve (29) accurately, a higher-order boundary-element method is applied using quadratic isoparametric elements, which is the same as in the previous paper[5)]. Once the values at nodes are determined, higher-order shape functions may be used for the interpolation; in this paper the Lagrangian interpolation function is used for that purpose.

In a higher-order boundary-element method, a double node is placed at the intersections between the free surface and a freely floating body. Then the potential ψ at a double node is assumed to be single-valued, but $\partial\psi/\partial n$ on S_F and S_B can be different. In the present case, ψ on S_F is given from the Dirichlet condition, (2) and (21), and $\partial\psi/\partial n$ on S_B is specified by the body boundary conditions, (4) and (19). Therefore the only unknown at the intersection is $\partial\psi/\partial n$ on S_F, which will be obtained as a solution of (29). The same numerical treatment is used at the intersection between the free surface and the wavemaker.

The 4-th order Runge-Kutta-Gill method is adopted as the time-marching scheme. At each time step, re-arranging the nodes on the free surface is conducted to avoid dense or sparse distribution of nodes, which is necessary for stable and accurate simulations for a long time.

7. Results and Discussion

7.1 Tested models and experiments

Experiments were carried out in the wave channel (length × breadth × depth = 14 m × 0.30 m × 0.45 m) at Osaka University. As shown schematically in Fig. 1, a plunger-type wavemaker is installed at the left end of the wave channel. The section shape and principal dimensions of a float of the wavemaker are shown in Fig. 2.

Two different floating bodies were used in experiments; one is a wall-sided model shown in Fig. 3, similar to the shape of midship section of a ship, and the other is a flared model shown in Fig. 4, similar to the shape of bow section of a ship. Other data associated with the equations of the body motion are listed in Table 1. Both models were initially placed at $x_G = 3.586$ m from the rear of the wavemaker, i.e. the origin of the coordinate system.

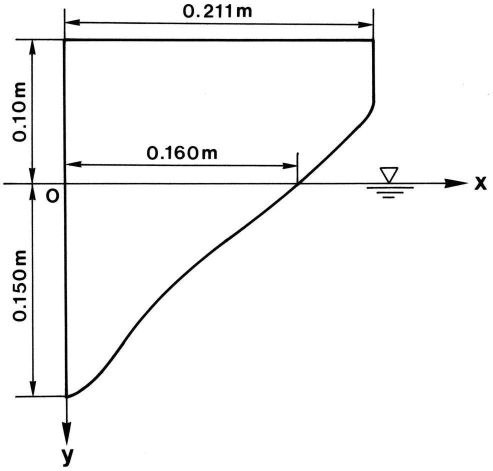

Fig. 2 Section shape and principal dimensions of the wavemaker

Measured items are the motions (sway, heave, and roll) of a floating body and the wave elevations at $x = 1.940$ m (between the wavemaker and a floating body) and at $x = 4.676$ m (the downwave side of a floating body). The movement of the wavemaker from the state of rest was also measured, which was found to include higher harmonic terms and thus approximated with a mathematical function of the form

$$\left.\begin{aligned} y_0(t) &= M(t)\big(a_0 + b_1 \sin\omega t + b_2 \sin 2\omega t + a_2 \cos 2\omega t\big) \\ M(t) &= 1 - e^{-\alpha t - \beta t^2} \end{aligned}\right\} \tag{31}$$

Coefficients $\alpha, \beta, a_0, b_1, b_2$ and a_2 were determined for each run of experiments by the least-square method using the iteration.

7.2 Waves generated by the wavemaker

When a floating body is absent, the present calculation scheme is the same as in the previous paper[5)], in which good agreement was confirmed between calculated and measured waves generated by a plunger-type wavemaker with wedge section. However, the experiments in this paper were carried out in a wave channel of small size and the section shape of the wavemaker was different from the previous one. Therefore, as a check of input waves impinging upon a floating body, simulations are performed first only for the waves generated by the wavemaker.

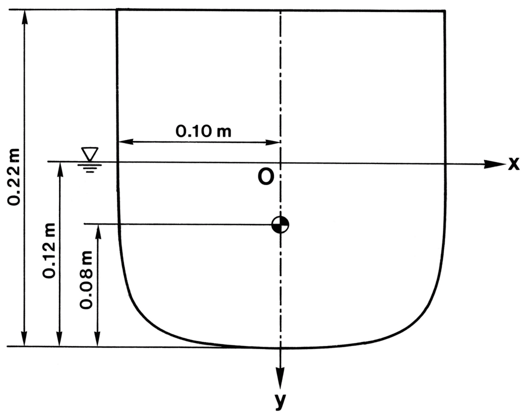

Fig. 3 Section shape and principal dimensions of a wall-sided model

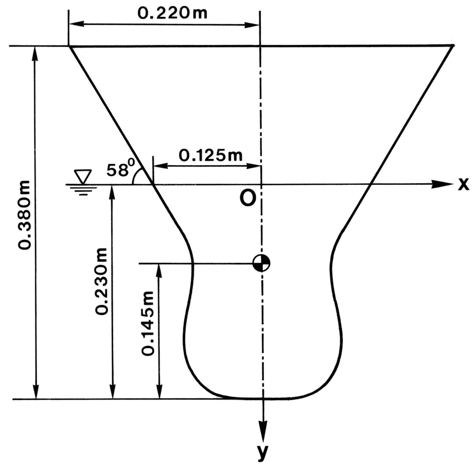

Fig. 4 Section shape and principal dimensions of a flared model

Table 1 Principal dimensions of tested models and constants in experiments

Kind of tested model		Wall-sided	Flared
Half breadth at W.L.	(b)	0.100 m	0.125 m
Draft	(d)	0.120 m	0.230 m
Length	(L)	0.297 m	0.297 m
Center of gravity	(y_G)	0.040 m	0.085 m
Radius of gyration	(κ)	0.067 m	0.123 m
Natural period of heave	(T_h)	0.82 sec	0.93 sec
Natural period of roll	(T_r)	1.07 sec	2.25 sec
Spring constant	(k)	42.44 N/m	
Weight of swaying carriage		6.272 N	

Two examples are shown here; Fig. 5 is the results for the oscillation period $T = 0.9$ sec and the wave steepness (the ratio of wave height to wavelength) $H/\lambda \approx 0.022$, and Fig. 6 is a case of longer wave with $T = 1.2$ sec and $H/\lambda \approx 0.019$. Results are shown in nondimensional form in terms of the oscillation amplitude of the wavemaker, Y. The abscissa is the nondimensional time $t\sqrt{g/a}$, with $a = 0.160$ m the breadth of the wavemaker at water line. Each figure is plotted such that the positive of the ordinate indicates the upward direction of movement.

In numerical computations, the length of the wave absorbing beach, C_W, is taken equal to 2λ, and the time-step size Δt is selected to be $T/20$, with T the oscillation period. The number of discretized elements is 30 on the wavemaker and 30 per wavelength on the free surface.

The overall agreement is very good, but we can point out two things. Firstly, measured waves include some disturbances, because the wave profile becomes distorted from that to be expected as a nonlinear wave, as the time elapses. Secondly, in a case of shorter wave, the wave amplitude is slightly attenuating with increasing the distance from the wavemaker; this

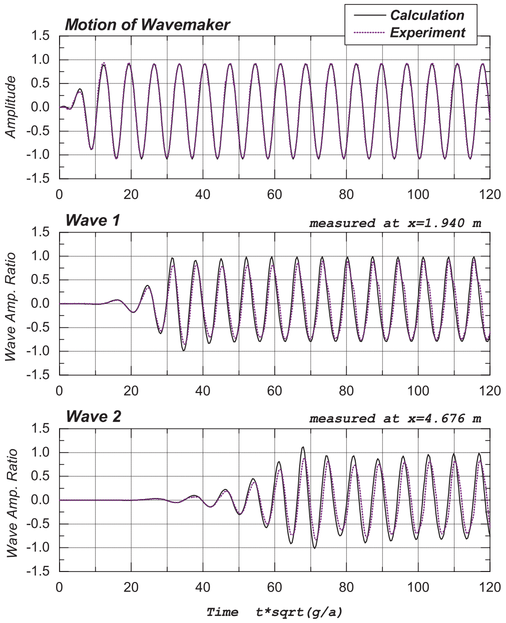

Fig. 5 Surface waves generated by the wavemaker shown in Fig. 2. The oscillation period is $T = 0.9\,\mathrm{sec}$ and the wave steepness is $H/\lambda \approx 0.022$

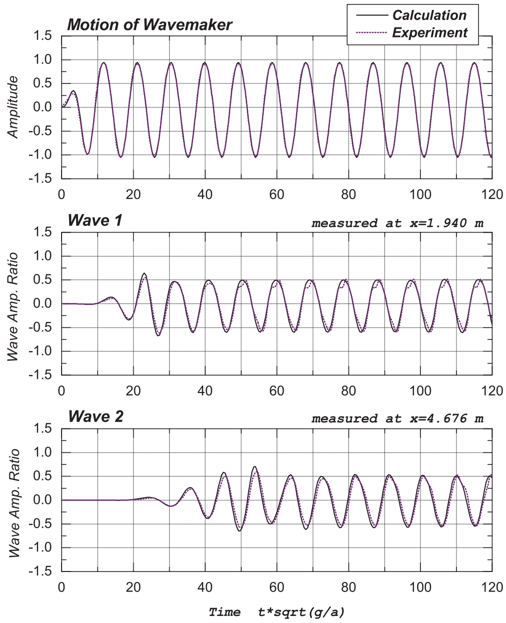

Fig. 6 Surface waves generated by the wavemaker shown in Fig. 2. The oscillation period is $T = 1.2\,\mathrm{sec}$ and the wave steepness is $H/\lambda \approx 0.0185$

may be due to a viscous effect from the boundary layer on side walls of the wave channel.

7.3 Floating-body motions in waves

When a floating body is placed on the free surface, the pursuit of the intersection between the body and free surfaces is crucial and the numerical accuracy of q_B expressed by (12) may influence subsequent results in the time marching. For these reasons, the number of discretized elements on the wetted surface of a floating body must be relatively large. In the present computations, 80 elements are used on S_B. The number of elements on other boundaries can be the same as in the preceding problem without a floating body. The length of the wave absorbing beach, C_W, and the time-stepping size, Δt, are also the same; that is, $C_W = 2\lambda$ and $\Delta t = T/20$.

It should be mentioned firstly that the numerical results by the new indirect method described in Section 5 are substantially the same as those by the mode decomposition method described in Section 4. The difference may not be distinguished in figures which will be shown below. This means that Eq. (26) is satisfied within a very small error, because the mathematical difference between the two methods stems from applying (26). However, we emphasize that the computation time in the new method is considerably reduced and roughly half of the computation time in the mode-decomposition method.

The results for the wall-sided model are shown in Figs. 7 and 8 in nondimensional form. The oscillation period of the wavemaker in Fig. 7 is 0.85 sec, which is close to the natural period of heave ($T_h = 0.82$ sec). Hence the heave amplitude is certainly large. However, measured results of heave are smaller than the calculated results. This difference can be partly explained from that the present calculation is based on the potential theory. Another

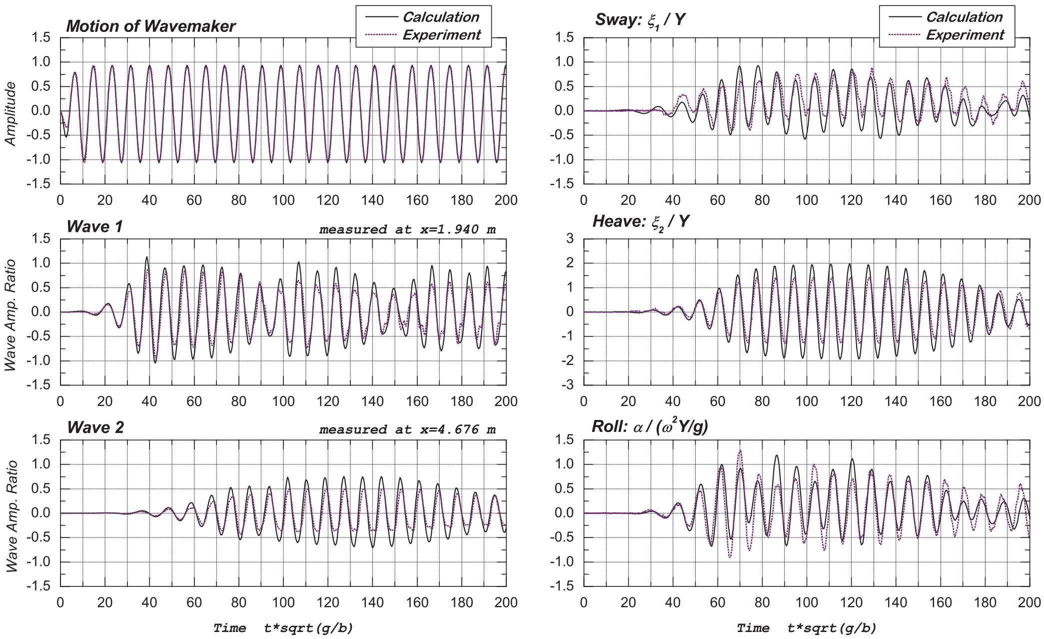

Fig. 7 Time histories of wave elevations, sway, heave, and roll of the wall-sided model shown in Fig. 3. The oscillation period is $T = 0.85$ sec and the wave steepness is $H/\lambda \approx 0.0129$

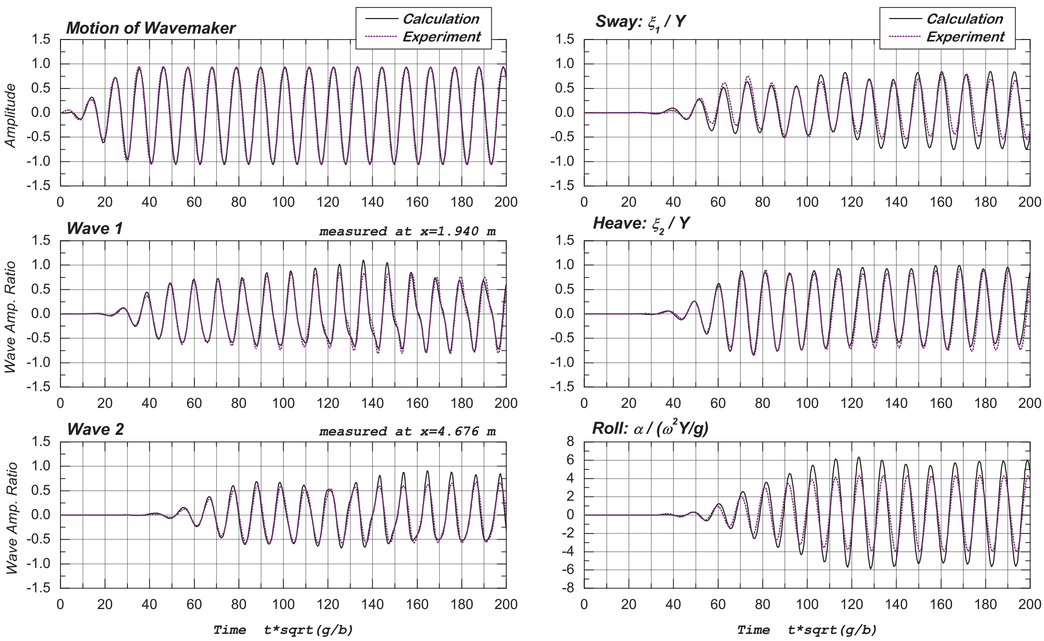

Fig. 8 Time histories of wave elevations, sway, heave, and roll of the wall-sided model shown in Fig. 3. The oscillation period is $T = 1.10$ sec and the wave steepness is $H/\lambda \approx 0.0235$

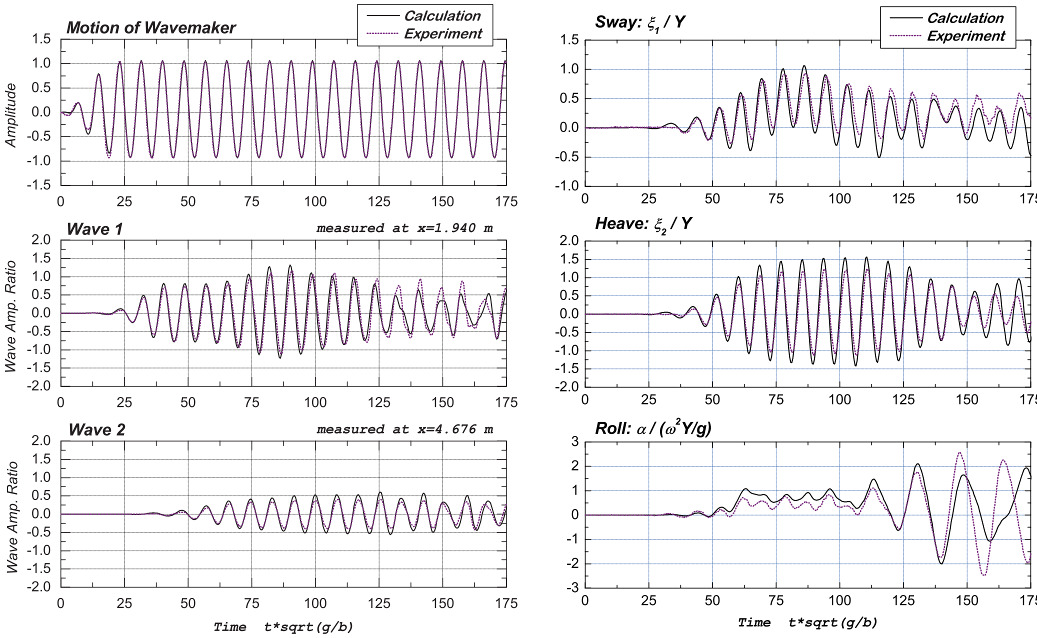

Fig. 9 Time histories of wave elevations, sway, heave, and roll of the flared model shown in Fig. 4. The oscillation period is $T = 0.95$ sec and the wave steepness is $H/\lambda \approx 0.0199$

reason is that the measured incident wave, the input, is slightly smaller that the calculated one, which has been already pointed out in relation to Fig. 5.

In the present computations and experiments, the reflection of waves is repeated between a floating body and the wavemaker. This is evident from the time history of the wave elevation labelled as Wave 1. Although there are some small differences in the amplitude, the overall agreement is very good.

Fig. 8 is an example of a longer-wave case and the oscillation period is $T = 1.1$ sec. Since this period is close to the natural period of roll ($T_r = 1.07$ sec), the amplitude of roll is much larger than that in Fig. 7. Here again measured results are smaller than the calculated results, which may be due to viscous effects. The waves are in good agreement, including a distorted profile after wave reflections. It can be seen for the wall-sided model that the oscillation period of roll is the same as that of the incident wave and the interaction between heave and roll is not large.

Next comparisons are for the flared model. Fig. 9 is the results for the oscillation period of $T = 0.95$ sec and the wave steepness of approximately $H/\lambda = 0.02$. This oscillation period is selected close to the natural period of heave ($T_h = 0.930$ sec).

Similar to the case of wall-sided model, the amplitudes of computed heave and sway are slightly larger than the measurements, but the phases are in good agreement. A big difference from the wall-sided model exists in the roll motion. We can see the steady inclination in the beginning of motion and then transition to a large amplitude of the parametric oscillation with the period of twice the heave oscillation period. This parametric oscillation may be induced by a reflected wave from the wavemaker (the amplitude of which is increased as seen from the time history of Wave 1). These transient and nonlinear phenomena are well accounted for by the present calculations.

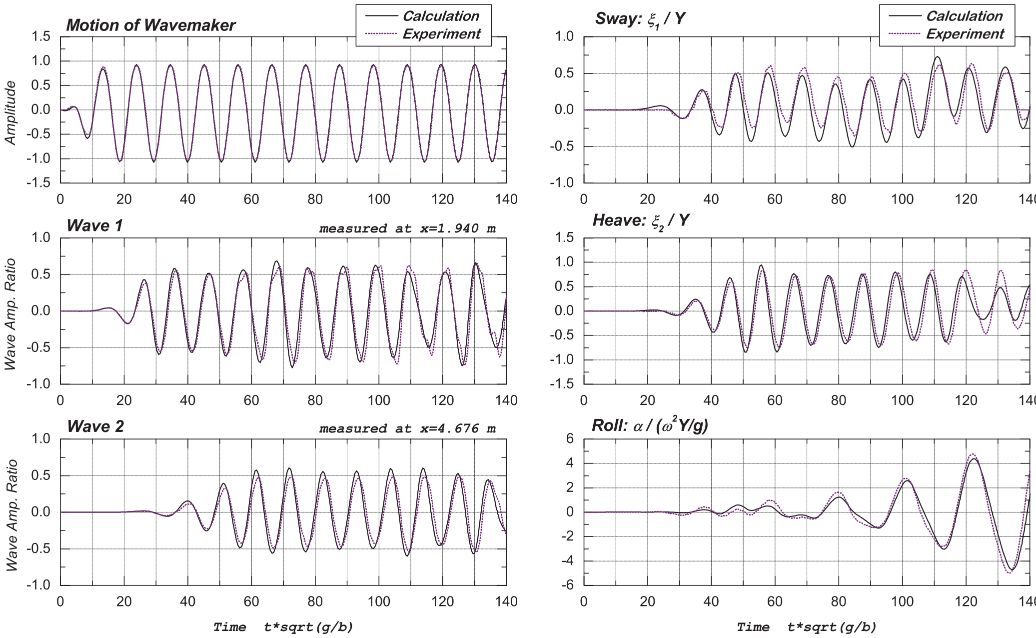

Fig. 10 Time histories of wave elevations, sway, heave, and roll of the flared model shown in Fig. 4. The oscillation period is $T = 1.20$ sec and the wave steepness is $H/\lambda \approx 0.0132$

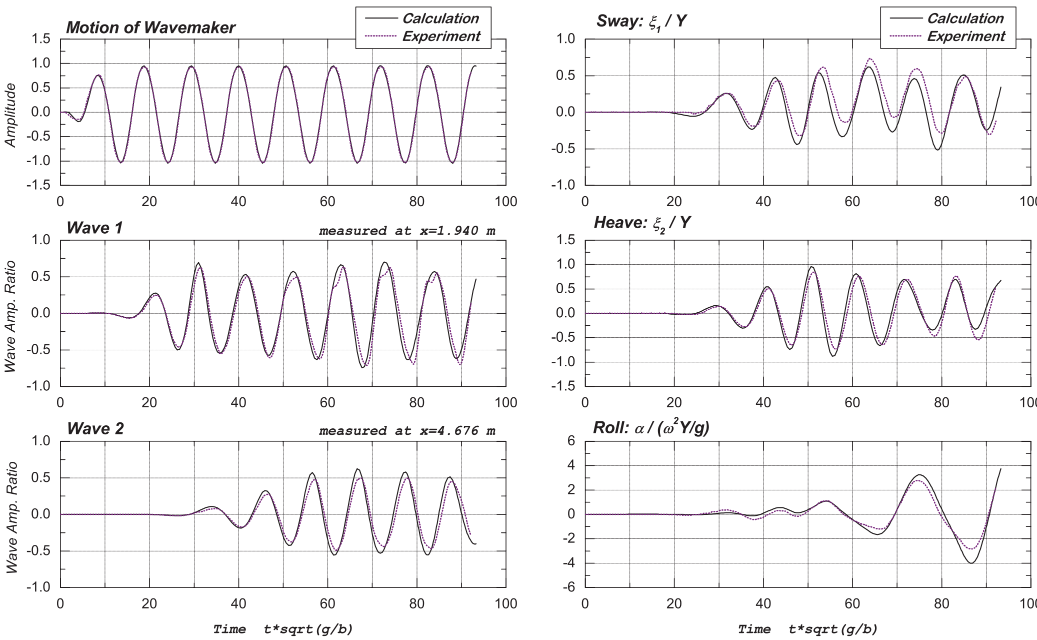

Fig. 11 Time histories of wave elevations, sway, heave, and roll of the flared model shown in Fig. 4. The oscillation period is $T = 1.20$ sec and the wave steepness is $H/\lambda \approx 0.0184$

It is known that the parametric oscillation in roll is most likely to occur when the period of the incident wave is close to half of the natural period of roll. Fig. 10 is the results for $T = 1.2$ sec and $H/\lambda \approx 0.013$, and as shown in Table 1, the roll natural period of the flared model is $T_r = 2.25$ sec.

Despite a small amplitude of the incident wave, the parametric oscillation is induced after transition for a certain period of time. Tanizawa et al.[9] studied the amplitude dependence on the parametric oscillation. According to that study, we can expect that the inception of the parametric oscillation becomes earlier as the amplitude of the incident wave increases. The correctness of this speculation is supported by Fig. 11, in which the oscillation period remains the same as Fig. 10, whereas the wave steepness is increased to $H/\lambda \approx 0.0184$. (In Fig. 11, the measurement was intentionally stopped at $t\sqrt{g/b} \approx 93$, because the roll amplitude approached the mechanical limit angle for measurement.) At any rate, in both cases of Figs. 10 and 11, calculated results are in excellent agreement with measured results.

8. Concluding Remarks

A nonlinear simulation method was presented for wave-induced transient motions of a floating body, using a new indirect method to compute the hydrodynamic force on and the acceleration of a body. With Green's second identity, the new method was explained as a further extension from the mode decomposition method. It is interesting to note that mathematical transformations in the new method are reminiscent of a derivation of the Haskind relation in the linear theory.

It was confirmed that the results by the new method are in virtually perfect agreement with the ones by the mode decomposition method. However, the new method is greatly advantageous in reducing the computation time, because there is no need to solve the boundary-value problem for ϕ_t itself. Conversely, the new method has a disadvantage, not capable of providing the pressure distribution.

Of course, the MEL method has a fatal defect that the computation can not proceed once the wave breaking occurs. However, as Tanizawa et al.[9),10)] has shown recently, we believe that the MEL method is still useful in studying nonlinear phenomena. Future work in this direction is the extension to 3-D problems, including a ship-motion problem with forward speed in severe waves.

Acknowledgment

The authors would like to thank Prof. Naito of Osaka University who allowed us to use the wave channel in his laboratory for carrying out the experiments shown in this paper.

References

1) Longuet-Higgins, M.S. and Cokelet, E.: The Deformation of Steep Surface Waves on Water, Proc. Roy. Soc. London, Series A 350 (1976), pp. 1-26.

2) Cao, Y., Beck, R. and Schultz, W. W.: Nonlinear Motions of Floating Bodies in Incident Waves, Proc. 9th Int. Workshop on Water Waves and Floating Bodies, Oita (1994), pp. 33-37.

3) Tanizawa, K.: A Nonlinear Simulation Method of 3-D Body Motions in Waves (1st Report), J. Soc. Nav. Arch. Japan, Vol. 178 (1995), pp. 179-191.

4) Tanizawa, K.: Long Time Fully Nonlinear Simulation of Floating Body Motions with Artificial Damping Zone, J. Soc. Nav. Arch. Japan, Vol. 180 (1996), pp. 311-319.

5) Kashiwagi, M.: Full-Nonlinear Simulations of Hydrodynamic Forces on a Heaving Two-Dimensional Body, J. Soc. Nav. Arch. Japan, Vol. 180 (1996), pp. 373-381.

6) Wu, G. X. and Eatock Taylor, R.: Transient Motion of a Floating Body in Steep Water Waves, Proc. 11th Int. Workshop on Water Waves and Floating Bodies, Hamburg (1996)

7) Vinje, T. and Brevig, P.: Nonlinear Ship Motions, Proc. 3rd Int. Conf. on Num. Ship hydrodyn., Paris (1981), pp. 257-268.

8) Cointe, R., Geyer, P., King, B., Molin, B. and Tramoni, M.: Nonlinear and Linear Motions of a Rectangular Barge in a Perfect Fluid, Proc. 18th Symp. on Nav. Hydrodyn., Ann Arbor (1990), pp. 85-99.

9) Tanizawa, K. and Naito, S.: A Study on Parametric Roll Motions by Fully Nonlinear Numerical Wave Tank, Proc. 11th ISOPE Conf., Honolulu, Vol. 3 (1997), pp. 69-75.

10) Tanizawa, K. and Naito, S.: An Application of Fully Nonlinear Numerical Wave Tank to the Study on Chaotic Roll Motions, Proc. 12th ISOPE Conf., Montreal, Vol. 3 (1998), pp. 280-287.

Hydrodynamic Interactions Among a Great Number of Columns Supporting a Very Large Flexible Structure*

Masashi KASHIWAGI
Research Institute for Applied Mechanics, Kyushu University
Kasuga, Fukuoka 816-8580, Japan

ABSTRACT

A hierarchical interaction theory is presented, which can treat hydrodynamic interactions among a great number of bodies rigorously in the framework of linear potential theory. After checking numerical accuracy and convergence for a square array of 64 half-immersed spheres, the theory is applied to column-supported structures with 1280, 2880, and 5120 equally spaced circular cylinders as supporting columns. With the computed hydrodynamic and hydrostatic forces, the motion equation of an upper deck is solved using the mode-expansion method. Trapped-wave phenomena among a large number of columns are observed at relatively short waves, and numerical examples of those effects on the elastic deflection of the upper deck and the wave pattern around column-supported structures are also shown.

1. INTRODUCTION

Very Large Floating Structures (VLFSs) are being considered for use as floating airports, storage, and manufacturing facilities. Those VLFSs are categorized according to the configuration under the sea level into: (i) a pontoon-type VLFS, having a box-shaped structure with very shallow draft, and (ii) a column-supported-type VLFS, consisting of a thin upper deck and a great number of buoyancy elements.

A number of studies have been made on the pontoon-type VLFS; e.g. Ohmatsu (1997), Kashiwagi (1998), Lin & Takaki (1998), and others cited therein. However, it may not be the case that pontoon-type structures are overwhelmingly advantageous. In fact, Kagemoto (1995) reported some engineering aspects in favor of a column-supported structure, under the assumption of the same flexural rigidity in both types of structure. His study was largely based on an approximate analysis, and therefore more careful study is needed using a rigorous but efficient numerical method.

In the case of column-supported-type VLFS, besides the upper deck being flexible due to its relatively small rigidity, hydrodynamic interactions among a great number of columns are important in evaluating the diffraction and radiation forces. It is said that the number of columns could exceed 10,000, and the conventional calculation methods cannot be used owing to the huge amount of computer memory and computation time required. In order to surmount this difficulty, a new hierarchical interaction theory is developed in this paper, which is regarded as an extension of Kagemoto & Yue's (1986) interaction theory. No matter

∗ *Reprinted from Journal of Fluids and Structures, Vol.14, No.7, pp.1013–1034, 2000 (October)*

how many columns are used, the present theory can be applied with reasonable computation time, and hydrodynamic interactions can be taken into account rigorously in the framework of linearized potential theory. In the hierarchical scheme, a great number of actual columns are grouped into several fictitious bodies and the fictitious bodies are grouped further into a certain number of larger fictitious bodies. This procedure can be repeated up to any hierarchical level, if necessary. The interactions are then considered at each level, and information on interactions can be transmitted upward or downward as required.

The elastic deflection of an upper deck is represented by a superposition of modal functions. Then, the hydrodynamic forces acting on supporting columns in response to specified modes of the deck are computed by the hierarchical interaction theory. With the computed hydrodynamic and hydrostatic forces, the amplitude of each modal function is determined by solving the motion equation of the deck by means of a Galerkin scheme.

Recently, Murai *et al.* (1998) independently developed almost the same theory and conducted some pilot computations. However, the contributions of evanescent wave components were ignored at the outset, and the motion equation of the deck was solved in a different way: that is, firstly the elastic deflection of the deck was represented by a succession of rigid-body vertical motions of small substructures; and then coupled equations of motion of the substructures were solved, with hydrodynamic and structural interactions taken into account. Their investigation seems not to extend to the effect of resonant interactions among many columns whose number is of a realistic order of several thousands.

In connection with hydrodynamic interactions, some researchers have recently studied trapped wave phenomena among a certain number of cylinders; e.g. Yoshida *et al.* (1994), Maniar & Newman (1997), Evans & Porter (1997), and Utsunomiya & Eatock Taylor (1998). According to these studies, trapped wave phenomena occur at some specific frequencies when the wavelength is of the same order as the distance between the centerlines of adjacent cylinders. This wavelength may be short for a realistic column-supported VLFS but must be studied, because these phenomena may cause detrimental effects on elastic responses of the upper deck. The present paper provides computations for these phenomena, including the wave pattern around column-supported-type structures with 1280 and 5120 equally spaced circular cylinders.

2. FORMULATION

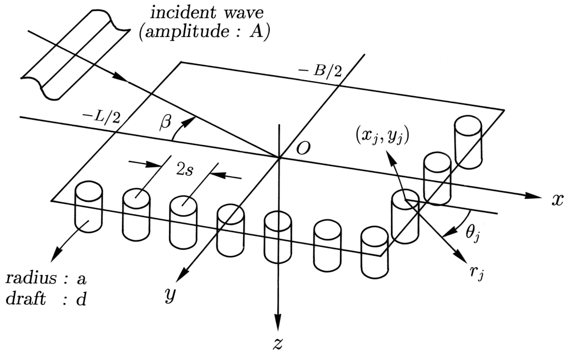

Fig. 1 Coordinate system and notations

We consider a column-supported VLFS, comprising of a thin deck and a great number of buoyancy columns. The deck is rectangular in plan, with length L and width B. Theoretically, the geometry and arrangement of elementary columns can be arbitrary, but in this paper identical and equally spaced columns are considered and each column is a truncated circular cylinder with radius a and draft d. The centerlines of adjacent cylinders are separated by a distance $2s$ in both x- and y-axis of a Cartesian coordinate system, where $z = 0$ is the plane of the undisturbed free surface and the water depth is constant at $z = h$ (see Figure 1). Incident plane waves propagate in the direction with angle β relative to the x-axis. In addition to the global coordinate system, we shall use a local cylindrical coordinate system (r_j, θ_j, z), with the origin placed at $(x_j, y_j, 0)$, i.e. the center of the jth cylinder. Time-harmonic motions of small amplitude are considered, with the complex time dependence $e^{i\omega t}$ applied to all first-order oscillatory quantities. The boundary conditions on the body and free surface are linearized, and potential flow is assumed. We then express the velocity potential, governed by Laplace's equation, in the form

$$\Phi = \frac{gA}{i\omega}\big(\Phi_I + \Phi_S\big) + \sum_{k=1}^{\infty} i\omega X_k\, \Phi_k \tag{1}$$

where A is the amplitude of an incident wave, ω is the circular frequency, and g is the gravitational acceleration.

Φ_I is the incident-wave velocity potential, which is given by

$$\Phi_I = Z_0(z)\, e^{-i\, k_0 (x\cos\beta + y \sin\beta)} \tag{2}$$

where

$$Z_0(z) = \frac{\cosh k_0(z-h)}{\cosh k_0 h}, \;\; k_0 \tanh k_0 h = \frac{\omega^2}{g} \equiv K \tag{3}$$

Φ_S in (1) represents the scattered potential and the sum, $\Phi_I + \Phi_S = \Phi_D$, is referred to as the total diffraction potential.

In the radiation component, suffix k refers to the kth mode of motion, which includes not only rigid-body motions but also a set of "generalized" modes to represent elastic deflections of a deck. X_k denotes the complex amplitude of each mode.

Since the deck is very thin compared with other dimensions of the structure, it is enough to consider only the vertical deflection. This is expressed in the form

$$w(x,y) = \sum_{k=1}^{\infty} X_k\, \zeta_k(x,y) = \sum_{m=0}^{\infty}\sum_{n=0}^{\infty} X_{mn}\, u_m(x)\, v_n(y) \tag{4}$$

where the modal functions in the x- and y-axes, $u_m(x)$ and $v_n(y)$, respectively, are the natural modes for the bending of a uniform beam with free ends. Specifically $u_m(x)$ can be written as

$$\left.\begin{aligned} u_0(x) &= \frac{1}{2} \\ u_{2m}(x) &= \frac{1}{2}\Big[\frac{\cos\kappa_{2m}x}{\cos\kappa_{2m}} + \frac{\cosh\kappa_{2m}x}{\cosh\kappa_{2m}}\Big] \end{aligned}\right\} \tag{5}$$

$$\left.\begin{aligned} u_1(x) &= \frac{\sqrt{3}}{2}\, x \\ u_{2m+1}(x) &= \frac{1}{2}\Big[\frac{\sin\kappa_{2m+1}\, x}{\sin\kappa_{2m+1}} + \frac{\sinh\kappa_{2m+1}\, x}{\sinh\kappa_{2m+1}}\Big] \end{aligned}\right\} \tag{6}$$

Here the coordinate x is normalized with $L/2$ and the same implication will be used hereafter. The factors κ_m are the positive roots of the equation

$$(-1)^m \tan\kappa_m + \tanh\kappa_m = 0 \tag{7}$$

$v_n(y)$ can also be written in a similar form, with x replaced by y/b, where $b = B/L$, on the right-hand sides of (5) and (6).

Following the notation of Newman (1994), the normal component of the kth modal function is defined as

$$n_k = \zeta_k(x, y)\, n_z \tag{8}$$

where n_z is the z-component of the unit normal vector pointing out of the body.

3. DIFFRACTION PROBLEM

3.1 Diffraction Characteristics of a Single Body

In the interaction theory among a large number of floating bodies, it is prerequisite to solve the diffraction problem of the jth body in a set of "generalized" incident waves, defined by

$$\{\, \psi_I^j \,\} = \left\{ \begin{array}{l} Z_0(z) J_p(k_0 r_j)\, e^{-ip\theta_j} \\ Z_n(z) I_p(k_n r_j)\, e^{-ip\theta_j} \end{array} \right\} \tag{9}$$

where $p = 0, \pm 1, \pm 2, \ldots, \pm\infty,\; n = 1, 2, \ldots, \infty$, and

$$Z_n(z) = \frac{\cos k_n(z-h)}{\cos k_n h},\;\; k_n \tan k_n h = -K \tag{10}$$

J_p and I_p in (9) denote the first kind of Bessel and modified Bessel functions, respectively.

The above diffraction problem can be solved with, for instance, the boundary-element method as shown in Appendix A, and the resulting scattered potentials can be written in the form

$$\{\, \varphi_S^j \,\} = \left[\, B_j \,\right]^T \{\, \psi_S^j \,\} \tag{11}$$

where

$$\{\, \psi_S^j \,\} = \left\{ \begin{array}{l} Z_0(z) H_m^{(2)}(k_0 r_j)\, e^{-im\theta_j} \\ Z_n(z) K_m(k_n r_j)\, e^{-im\theta_j} \end{array} \right\} \tag{12}$$

with $m = 0, \pm 1, \pm 2, \ldots, \pm\infty$, and $n = 1, 2, \ldots, \infty$. $H_m^{(2)}$ and K_m are the second kind of Hankel and modified Bessel functions, respectively. $\left[\, B_j \,\right]^T$ denotes the transpose of the matrix $\left[\, B_j \,\right]$. This coefficient matrix, $\left[\, B_j \,\right]$, is referred to as the diffraction characteristics matrix of the jth body.

Wave forces in response to the "generalized" incident waves may be computed at the same time, which are expressed in the form

$$\{\, E_z^j \,\} = \iint_{S_j} \{\psi_I^j + \varphi_S^j\} n_z\, dS = \iint_{S_j} \{\varphi_D^j\}\, n_z\, dS \tag{13}$$

where S_j denotes the surface of the jth body below $z = 0$.

3.2 Hierarchical Interaction Theory

We consider a rectangular array of identical and equally spaced columns, but for convenience of explanation, only a schematic arrangement of bodies is shown in Figure 2. The shaded bodies in Figure 2 are actual bodies, which are referred to as bodies at level one. A number of level-one bodies are grouped to form a fictitious body, which is at level two, and several fictitious bodies are grouped further to form a bigger fictitious body at level three. Repeating this hierarchical treatment makes it possible to view the interactions among a large number of bodies as a succession of simpler interactions due to smaller number of bodies. To explain

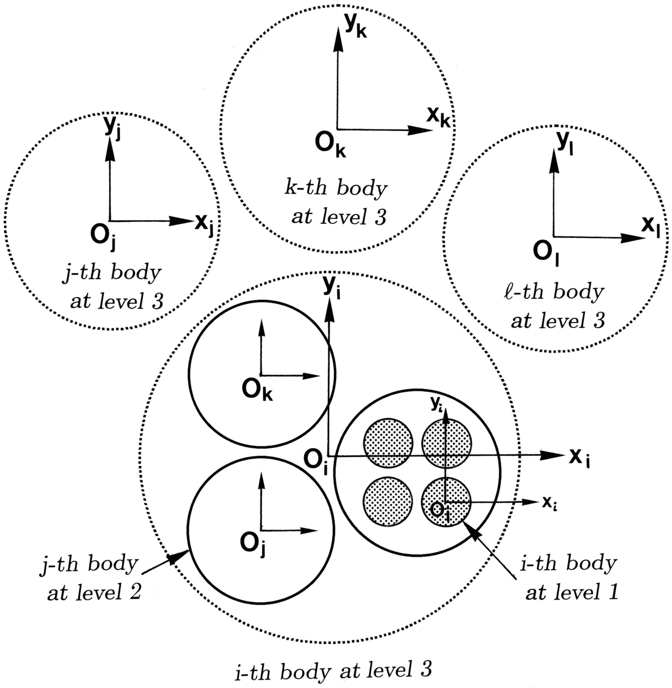

Fig. 2 Coordinate systems in hierarchical interaction theory

the theory, it may be enough to consider only two hierarchical levels, i.e. $\ell = 2$ would correspond to the highest level in this case.

Rewriting the incident-wave potential in terms of a polar coordinate system of a fictitious body i at level ℓ, we obtain the following:

$$\Phi_I = \alpha_i(k_0, \beta) \sum_{p=-\infty}^{\infty} e^{ip(\beta - \frac{\pi}{2})} \{ Z_0(z) J_p(k_0 r_i) \, e^{-ip\theta_i} \} \tag{14}$$

where

$$\alpha_i(k_0, \beta) = e^{-ik_0(x_i \cos\beta + y_i \sin\beta)} \tag{15}$$

With the vector of generalized incident waves defined by (9), (14) can be expressed in the form

$$\Phi_I = \{ a^i \}^T \{ \psi_I^i \} \tag{16}$$

where $\{a^i\}$ is the vector of coefficients defined by means of (14).

According to the Kagemoto & Yue (1986) interaction theory, scattered waves due to other bodies must be viewed as incident waves upon the body under consideration. Thus, utilizing the coordinate transformation matrix, $[T_{ij}]$ given in Appendix B, the total incident-wave potential on body i at level ℓ is written as

$$\phi_{I,\ell}^i = \left(\{a^i\}^T + \sum_{\substack{n=1 \\ n \neq i}}^{N_\ell} \{A_{S,\ell}^n\}^T [T_{ni}^\ell] \right) \{\psi_{I,\ell}^i\} \tag{17}$$

where N_ℓ is the number of fictitious bodies at level ℓ and $\{A^i_{S,\ell}\}$ is the vector of unknown coefficients of the scattered potential due to body i.

Assuming that the diffraction characteristics of a fictitious body i at level ℓ are obtained and expressed with the matrix $[\mathcal{B}_{i,\ell}]$, the following relation can be established:

$$\begin{aligned}\phi^i_{S,\ell} &= \left(\{a^i\}^T + \sum_{\substack{n=1\\n\neq i}}^{N_\ell}\{A^n_{S,\ell}\}^T[T^\ell_{ni}]\right)[\mathcal{B}_{i,\ell}]^T\{\psi^i_{S,\ell}\}\\ &= \{A^i_{S,\ell}\}^T\{\psi^i_{S,\ell}\}\end{aligned} \tag{18}$$

One can therefore obtain a linear set of equations for the unknown coefficients, $\{A^i_{S,\ell}\}$, in the form

$$\{A^i_{S,\ell}\} - [\mathcal{B}_{i,\ell}]\sum_{\substack{n=1\\n\neq i}}^{N_\ell}[T^\ell_{ni}]^T\{A^n_{S,\ell}\} = [\mathcal{B}_{i,\ell}]\{a^i\}, \quad \text{for } i = 1 \sim N_\ell \tag{19}$$

In reality, however, the matrix $[\mathcal{B}_{i,\ell}]$ is also unknown at this stage, because the level ℓ is fictitious. To determine this matrix, the diffraction problem of a fictitious body for the components of generalized incident waves, $\{\psi^i_{I,\ell}\}$, needs to be considered.

A fictitious body at level ℓ includes $N_{\ell-1}$ bodies at level $\ell-1$ (which are actual bodies here). Thus we must consider again the interactions among those bodies. The local (downward) expansion of $\{\psi^i_{I,\ell}\}$ about the origin of body j at level $\ell-1$ can be found in the Appendix B. Then, as in (17), the total incident-wave potential on body j at level $\ell-1$ is written in the following form

$$\{\varphi^j_{I,\ell-1}\} = \left([I^{\ell-1}_{ij}] + \sum_{\substack{n=1\\n\neq j}}^{N_{\ell-1}}[A^n_{S,\ell-1}]^T[T^{\ell-1}_{nj}]\right)\{\psi^j_{I,\ell-1}\} \tag{20}$$

Here, note that the unknown coefficients for the scattered potential, $[A^j_{S,\ell-1}]$, are given in a matrix form.

As shown in Subsection 3.1, the diffraction characteristics of a single body can be given by the matrix $[B_j]$, which is regarded as determinated, because the level $\ell-1$ is the lowest level. Therefore, in the same manner as in obtaining (19), the algebraic simultaneous equations for the coefficient matrix $[A^j_{S,\ell-1}]$ can be derived in the form

$$[A^j_{S,\ell-1}] - [B_{j,\ell-1}]\sum_{\substack{n=1\\n\neq j}}^{N_{\ell-1}}[T^{\ell-1}_{nj}]^T[A^n_{S,\ell-1}] = [B_{j,\ell-1}][I^{\ell-1}_{ij}]^T, \quad \text{for } j = 1 \sim N_{\ell-1} \tag{21}$$

Solving (21) means that the diffraction problem at level $\ell-1$ is completely solved. Thus, considering an outer-field expression of the corresponding scattered potentials of $N_{\ell-1}$ bodies, the diffraction characteristics of a fictitious body at level ℓ may be given. For that purpose, the multipole (upward) expansion of $\{\psi^j_{S,\ell-1}\}$ about the origin of body i at level ℓ must be considered, which is described also in the Appendix B. Then, collecting the contributions from all bodies inside a fictitious body, the vector of scattered potentials can be found as follows:

$$\sum_{j=1}^{N_{\ell-1}} \left[A^j_{S,\ell-1}\right]^T \left\{\psi^j_{S,\ell-1}\right\} = \sum_{j=1}^{N_{\ell-1}} \left[A^j_{S,\ell-1}\right]^T \left[M^\ell_{ji}\right] \left\{\psi^i_{S,\ell}\right\} \equiv \left[\mathcal{B}_{i,\ell}\right]^T \left\{\psi^i_{S,\ell}\right\} \tag{22}$$

Therefore we have

$$\left[\mathcal{B}_{i,\ell}\right] = \sum_{j=1}^{N_{\ell-1}} \left[M^\ell_{ji}\right]^T \left[A^j_{S,\ell-1}\right] \tag{23}$$

Substituting this diffraction characteristics matrix into (19) determines the coefficient vector of the scattered potential at level ℓ. This completes the description of the entire flow field.

3.3 Wave Exciting Force

Since fundamental wave forces due to each component of the generalized incident waves are already computed and given by (13), the only further requirement for computing the wave-exciting force is to find the amplitude of waves impinging upon the actual bodies at level $\ell - 1$. This can be done by simply combining (17) and (20), with the result

$$\phi^j_{I,\ell-1} = \left\{\mathcal{A}^j_D\right\}^T \left\{\psi^j_{I,\ell-1}\right\} \tag{24}$$

where

$$\left\{\mathcal{A}^j_D\right\}^T = \left(\left\{a^i\right\}^T + \sum_{\substack{n=1\\n\neq i}}^{N_\ell} \left\{A^n_{S,\ell}\right\}^T \left[T^\ell_{ni}\right] \right) \left(\left[I^{\ell-1}_{ij}\right] + \sum_{\substack{n=1\\n\neq j}}^{N_{\ell-1}} \left[A^n_{S,\ell-1}\right]^T \left[T^{\ell-1}_{nj}\right] \right) \tag{25}$$

With this notation, the linearized pressure on body j in the diffraction problem is given by $p_D = -\rho g A \left\{\mathcal{A}^j_D\right\}\left\{\varphi^j_D\right\}$. Therefore the total wave-exciting force in the mth mode can be computed as

$$\begin{aligned} -\iint_{S_H} p_D\, n_m\, dS &= \rho g A \sum_{j=1}^{N_B} \iint_{S_j} \left\{\mathcal{A}^j_D\right\}^T \left\{\varphi^j_D\right\} \zeta_m(x,y) n_z\, dS \\ &\simeq \rho g A \sum_{j=1}^{N_B} \zeta^j_m \left\{\mathcal{A}^j_D\right\}^T \left\{E^j_z\right\} \equiv \rho g A\, E_m \end{aligned} \tag{26}$$

where the definition of (8) has been used for n_m, and $\zeta^j_m = \zeta_\ell(x_j, y_j)$ is treated as constant on the bottom of an elementary cylinder. N_B is the total number of actual columns.

4. RADIATION PROBLEM

4.1 Radiation Characteristics of a Single Body

In the present study, since only the vertical deflection is considered, the basic solution necessary for considering hydrodynamic interactions is that of heave with unit velocity. The body boundary condition for that problem on the jth body is written as

$$\frac{\partial \Phi^j_R}{\partial n} = n_z \quad \text{on } S_j \tag{27}$$

Several methods exist for solving this radiation problem, and a solution can be written in terms of the vector of scattered potentials defined by (12), in the form

$$\Phi_R^j = \{R_j\}^T \{\psi_S^j\} \tag{28}$$

The coefficient vector, $\{R_j\}$, is referred to as the radiation characteristics vector of a single body, which is assumed to be known.

The hydrodynamic forces computed from the above solution are the added-mass and damping coefficients. The result of this computation is written as

$$-\iint_{S_j} \Phi_R^j \, n_z \, dS = A_{zz}^j - i\, B_{zz}^j \tag{29}$$

Here A_{zz}^j and B_{zz}^j are the added mass and damping coefficients in heave, respectively, for a single body j.

4.2 Hierarchical Interaction Theory

Basic concept of the hierarchical scheme is the same as in the diffraction problem. In the radiation problem, however, let us start by considering the interactions from the lowest level. Firstly, the body boundary condition for the kth mode of motion of body i at level $\ell - 1$ can be specified as

$$\frac{\partial \Phi_{R,k}^i}{\partial n} = n_k = \zeta_k(x,y)\, n_z \simeq \zeta_k^i \, n_z \tag{30}$$

Hence, by comparison with (27), the solution of $\Phi_{R,k}^i$ can be readily given by

$$\Phi_{R,k}^i = \zeta_k^i \, \Phi_R^i = \zeta_k^i \{R_i\}^T \{\psi_S^i\} \tag{31}$$

The radiated wave due to the above motion of body i may be regarded as an incident wave, when viewed from other bodies included in the same fictitious body. Taking account of interactions, the total incident-wave potential on the jth body at level $\ell - 1$ is expressed as

$$\varphi_{k,\ell-1}^j = \sum_{\substack{n=1 \\ n\neq j}}^{N_{\ell-1}} \left(\zeta_k^n \{R_n\}^T + \{A_{k,\ell-1}^n\}^T \right) \left[T_{nj}^{\ell-1} \right] \{\psi_{I,\ell-1}^j\} \tag{32}$$

Following the same argument as in obtaining (19), a linear set of equations for the unknown interaction coefficients, $\{A_{k,\ell-1}^j\}$, can be obtained in the form

$$\{A_{k,\ell-1}^j\} - \left[B_{j,\ell-1} \right] \sum_{\substack{n=1 \\ n\neq j}}^{N_{\ell-1}} \left[T_{nj}^{\ell-1} \right]^T \{A_{k,\ell-1}^n\} = \left[B_{j,\ell-1} \right] \sum_{\substack{n=1 \\ n\neq j}}^{N_{\ell-1}} \left[T_{nj}^{\ell-1} \right]^T \zeta_k^n \{R_n\}$$
$$\text{for } j = 1 \sim N_{\ell-1} \tag{33}$$

Then, by considering an outer-field expression of the sum of the forced radiation part plus the scattered interaction part, the radiation potential due to the kth mode of motion of a fictitious body i at level ℓ will be obtained. From this, the vector of radiation characteristics of a fictitious body can be derived, with the following result:

$$\{\mathcal{R}_{k,\ell}^i\} = \sum_{j=1}^{N_{\ell-1}} \left[M_{ji}^\ell \right]^T \left(\zeta_k^i \{R_j\} + \{A_{k,\ell-1}^j\} \right) \tag{34}$$

Next, let us proceed to the interactions at the upper level, ℓ. The analysis may be undertaken in the same way as that at level $\ell-1$, and the total incident-wave potential on body i at level ℓ can be written as

$$\varphi^i_{k,\ell} = \sum_{\substack{n=1\\n\neq i}}^{N_\ell} \Big(\{\mathcal{R}^n_{k,\ell}\}^T + \{A^n_{k,\ell}\}^T \Big) \big[T^\ell_{ni}\big]\{\psi^i_{I,\ell}\} \tag{35}$$

As shown in (23), the diffraction characteristics of body i at level ℓ are given by the matrix $\big[\mathcal{B}_{i,\ell}\big]$. Hence, simultaneous equations for the vector of interaction coefficients of the kth mode of motion can be obtained in the form

$$\{A^i_{k,\ell}\} - \big[\mathcal{B}_{i,\ell}\big] \sum_{\substack{n=1\\n\neq i}}^{N_\ell} \big[T^\ell_{ni}\big]^T \{A^n_{k,\ell}\} = \big[\mathcal{B}_{i,\ell}\big] \sum_{\substack{n=1\\n\neq i}}^{N_\ell} \big[T^\ell_{ni}\big]^T \{\mathcal{R}^n_{k,\ell}\}, \qquad \text{for } i = 1 \sim N_\ell \tag{36}$$

It is noteworthy that the matrices of influence coefficients on the left-hand side of (21) and (33) are of the same form, and thus can be solved at the same time. The same is true of the simultaneous equations at level ℓ, i.e. equations (19) and (36).

4.3 Hydrodynamic Pressure Force

The radiation potential can be divided into two parts: the first is due to the forced oscillation in the absence of other bodies, and the second one is due to radiated waves from other bodies and reflected waves. The first part is given by (31) and the second part may be obtained from (32) and combination of (35) and (20). This leads to

$$\Phi^j_k = \zeta^j_k \Phi^j_R + \{\mathcal{A}^j_k\}^T \{\varphi^j_D\} \tag{37}$$

where

$$\begin{aligned}\{\mathcal{A}^j_k\}^T = &\sum_{\substack{n=1\\n\neq j}}^{N_{\ell-1}} \Big(\zeta^n_k \{R_n\}^T + \{A^n_{k,\ell-1}\}^T \Big) \big[T^{\ell-1}_{nj}\big] \\ &+ \sum_{\substack{n=1\\n\neq i}}^{N_\ell} \Big(\{\mathcal{R}^n_{k,\ell}\}^T + \{A^n_{k,\ell}\}^T \Big) \big[T^\ell_{ni}\big] \left(\big[I^{\ell-1}_{ij}\big] + \sum_{\substack{n=1\\n\neq j}}^{N_{\ell-1}} \big[A^n_{S,\ell-1}\big]\big[T^{\ell-1}_{nj}\big] \right)\end{aligned} \tag{38}$$

Therefore, the hydrodynamic pressure force in the mth mode due to a superposition of all radiation modes can be computed as

$$\begin{aligned}-\iint_{S_H} p_R\, n_m\, dS &= -\rho g A\, K \sum_{k=1}^{\infty} \Big(\frac{X_k}{A}\Big) \sum_{j=1}^{N_B} \iint_{S_j} \Phi^j_k\, \zeta_m(x,y) n_z\, dS \\ &\equiv \rho g A\, K \sum_{k=1}^{\infty} \Big(\frac{X_k}{A}\Big) F_{mk}\end{aligned} \tag{39}$$

where F_{mk} can be given by substituting (37) and then using (13) and (29), with the result

$$F_{mk} = \sum_{j=1}^{N_B} \zeta^j_m \Big[\zeta^j_k \big(A^j_{zz} - i\, B^j_{zz}\big) - \{\mathcal{A}^j_k\}^T \{E^j_z\} \Big] \tag{40}$$

Here again $\zeta_m(x,y)$ has been assumed constant over the water-plane area of each cylinder, and represented by $\zeta_m(x_j,y_j)=\zeta_m^j$.

4.4 Hydrostatic Pressure Force

Variation of the static pressure due to the deck motion can be expressed by

$$p_S=\rho g w=\rho g A\sum_{k=1}^{\infty}\Big(\frac{X_k}{A}\Big)\,\zeta_k(x,y) \tag{41}$$

Thus, the resulting force in the mth mode can be analytically computed as

$$-\iint_{S_H} p_S\, n_m\, dS=-\rho g A\sum_{k=1}^{\infty}\Big(\frac{X_k}{A}\Big)\,C_{mk} \tag{42}$$

where

$$C_{mk}\simeq A_W\sum_{j=1}^{N_B}\zeta_m^j\,\zeta_k^j \tag{43}$$

and A_W denotes the water-plane area, which is given by πa^2 for a hemisphere or circular cylinder.

5. MOTIONS OF AN ELASTIC DECK

The equation of motion of a thin plate is given as

$$-m_B\,\omega^2 w(x,y)+D\nabla^4 w(x,y)=-p(x,y) \tag{44}$$

where m_B is the distribution of mass, which is equal to M/LB in the case of uniform distribution (M being the total mass); D is the flexural rigidity given by $D=EI/(1-\nu^2)$, with EI and ν being the equivalent stiffness factor and Poisson's ratio, respectively; and $\nabla=(\partial/\partial x,\partial/\partial y)$ is the 2-D differential operator. Despite a great number of columns being attached beneath the upper deck, it is assumed that the plate is isotropic and the flexural rigidity is constant; that is just for simplicity of the analysis.

Since the structure is freely floating, the bending moment and the equivalent shear force must be zero along the edge of the plate. That is,

$$\frac{\partial^2 w}{\partial n^2}+\nu\frac{\partial^2 w}{\partial s^2}=0,\ \ \frac{\partial^3 w}{\partial n^3}+(2-\nu)\frac{\partial^3 w}{\partial n\partial s^2}=0 \tag{45}$$

where n and s denote the normal and tangential directions, respectively. In the case of a rectangular plate, a concentrated force, stemming from replacement of the torsional moment with an equivalent shear force, acts at the four corners, and this must also be zero:

$$R_f=2D(1-\nu)\frac{\partial^2 w}{\partial x\partial y}=0 \quad \text{at } x=\pm 1, y=\pm b \tag{46}$$

Substituting (4) into (44), multiplying both sides by the normal component of the mth modal function, $n_m=\zeta_m(x,y)\,n_z; m=1,2,\ldots,\infty$, and integrating over the structure, we obtain a linear set of equations

$$\sum_{k=1}^{\infty}\Big(\frac{X_k}{A}\Big)\Big[-K\big(M'\delta_{mk}+F_{mk}\big)+C_{mk}+D'S_{mk}\Big]=E_m, \tag{47}$$

where $M' = M/2\rho L^3$ and $D' = D/\rho g(L/2)^4$; δ_{mk} denotes the Kroenecker delta, equal to 1 when $m = k$ and zero otherwise. F_{mk}, C_{mk}, and E_m are pressure forces, and these are given by (40), (43), and (26), respectively. S_{mk} is the stiffness matrix, corresponding to the restoring force due to the structural rigidity.

Up to this point, the free-end conditions, (45) and (46), have not been explicitly imposed as constraints on the solution. However, as shown in Kashiwagi (1998), these conditions can be satisfied as natural boundary conditions in the process of transforming S_{mk} by partial integrations. The final form of S_{mk} to be used in (47) is expressed as

$$
\begin{aligned}
S_{mk} = &\iint_{S_H} \nabla^2\zeta_m \nabla^2\zeta_k \, dxdy \\
&+(1-\nu)\int_{-1}^{1}\left[\frac{\partial\zeta_m}{\partial x}\frac{\partial^2\zeta_k}{\partial x\partial y} - \frac{\partial\zeta_m}{\partial y}\frac{\partial^2\zeta_k}{\partial x^2}\right]_{-b}^{b} dx \\
&+(1-\nu)\int_{-b}^{b}\left[\frac{\partial\zeta_m}{\partial y}\frac{\partial^2\zeta_k}{\partial x\partial y} - \frac{\partial\zeta_m}{\partial x}\frac{\partial^2\zeta_k}{\partial y^2}\right]_{-1}^{1} dy
\end{aligned}
\tag{48}
$$

Since the present modal functions are expressed in closed form, all integrals shown above can be evaluated analytically.

6. RESULTS AND DISCUSSION

6.1 Accuracy and Convergence Check

Numerical accuracy and convergence are checked for a square array of half-immersed spheres with 64 total elements. As shown in Figure 3, 16 bodies in each quadrant are periodically placed with a distance of $s/a = 2.0$, but each group of 16 bodies is separated on both sides

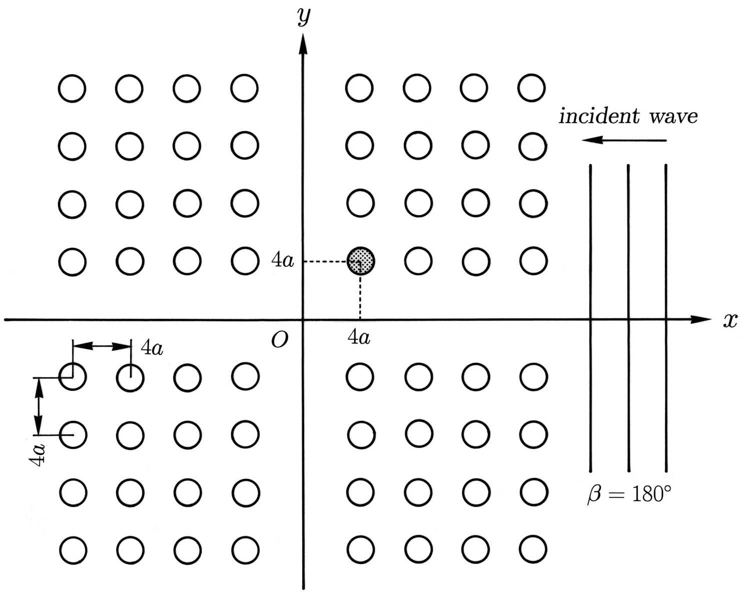

Fig. 3 Arrangement of 64 half-immersed spheres

Table 1 Amplitude of wave exciting forces in surge (E_x) and heave (E_z) on a body at $(x, y) = (4a, 4a)$, and the average of total heave force on 64 half-immersed spheres; $h/a = 3.0, Ka = 0.5, \beta = 180°, s/a = 2.0$

Hierarchical Interaction Theory (Level=3)				
No. of terms		$\|E_x\|$	$\|E_z\|$	$\|\sum E_z\|/N_B$
N=0	M=12	0.36597	0.70835	0.07340
	M=14	0.36579	0.70830	0.07339
	M=16	0.36576	0.70828	0.07339
N=1	M=12	0.36576	0.70923	0.07306
	M=14	0.36557	0.70918	0.07305
	M=16	0.36552	0.70916	0.07305
N=2	M=14	0.36558	0.70918	0.07305
Kagemoto & Yue's Theory (Level=1)				
No. of terms		$\|E_x\|$	$\|E_z\|$	$\|\sum E_z\|/N_B$
N=0	M=3	0.36574	0.70828	0.07339
	M=4	0.36574	0.70828	0.07339
N=1	M=4	0.36550	0.70916	0.07305
N=2	M=3	0.36552	0.70916	0.07305

Table 2 Added-mass and damping coefficients in heave of a body at $(x, y) = (4a, 4a)$, and the average of total heave added mass of 64 half-immersed spheres; $h/a = 3.0, Ka = 0.5, \beta = 180°, s/a = 2.0$

Hierarchical Interaction Theory (Level=3)				
No. of terms		A_{33}	B_{33}	$\sum A_{33}/N_B$
N=0	M=12	0.81751	0.29999	0.57249
	M=14	0.81769	0.30000	0.57249
	M=16	0.81764	0.30002	0.57246
N=1	M=12	0.82197	0.29881	0.59962
	M=14	0.82216	0.29882	0.59961
	M=16	0.82211	0.29884	0.59958
N=2	M=14	0.82216	0.29882	0.59961
Kagemoto & Yue's Theory (Level=1)				
No. of terms		A_{33}	B_{33}	$\sum A_{33}/N_B$
N=0	M=3	0.81763	0.30003	0.57244
	M=4	0.81764	0.30003	0.57246
N=1	M=4	0.82211	0.29885	0.59958
N=2	M=3	0.82211	0.29885	0.59963

of the x- and y-axis by double the distance between adjacent bodies inside the group. The water depth is taken as $h/a = 3.0$, and the head wave ($\beta = 180°$) with wavenumber $Ka = 0.5$ is selected as an example. Tables 1 and 2 show the results of the diffraction and radiation problems, respectively; listed are the forces on a body at $(x, y) = (4a, 4a)$ as depicted in Figure 3, and the average of the forces on all 64 bodies.

The hierarchical interaction theory is tested with the highest level set to $\ell = 3$, in which 2×2 bodies are grouped at each level. Computed results are compared with corresponding results based on Kagemoto and Yue's (1986) interaction theory. In both tables, N denotes the number of evanescent mode and M is the number of terms in azimuth angle in (9) and (12). The wave-exciting forces are nondimensionalized with $\rho g A(\pi a^2)$, and the added-mass and damping coefficients are nondimensionalized with $\rho\nabla$ and $\rho\nabla\omega$, respectively, where $\nabla = 2\pi a^3/3$.

By comparison with the results of Kagemoto and Yue's theory, the present hierarchical theory gives converged results of four decimal points with $M = 14$. Need for larger number of terms in M is caused by slow convergence of the multipole expansion, shown as (A.4) in the Appendix. Nevertheless, the computation time is little; for example, only 6 seconds are needed for the case of $N = 0$ and $M = 14$, by use of C200 model of HP workstation. Another thing to be noted is that the contributions of evanescent modes are small, and practically those effects may be ignored.

In the present computations, the diffraction and radiation characteristics of a single body are computed by means of a higher-order boundary element method with 9-point Lagrangian elements (Kashiwagi and Kohjoh, 1995). Furthermore, double symmetries with respect to the x- and y-axes are exploited, which can reduce the number of unknowns to 1/4.

6.2 Responses of a Column-Supported VLFS

Computations were performed for a practical number of columns, which are identical, equally-spaced, and attached beneath a thin rectangular deck of $L = 1200$ m and $B = 240$ m.

The principal particulars of this structure are shown in Table 3. The elementary column considered here is a truncated circular cylinder, and the number of columns are 1280, 2880, and 5120. In computations for these, 2×2 cylinders are grouped as one unit at the first and second levels in the hierarchical theory. At the highest level ($\ell = 3$), double symmetries with respect to the x- and y-axis are effectively used, which reduces the number of unknowns and thus the computation time. Despite the increase of column numbers, the displacement

Table 3 Principal particulars of column-supported structures used in calculations

	Model A	Model B	Model C
Length (L)		1200 m	
Width (B)		240 m	
Flexural rigidity		$D = 1.0 \times 10^{10}$ Nm	
Poisson's ratio		$\nu = 0.3$	
Number of columns (N_B)	$80 \times 16 = 1280$	$120 \times 24 = 2880$	$160 \times 32 = 5120$
Diameter of each column ($2a$)	7.5 m	5.0 m	3.75 m
Draft of each column (d)		3.75 m	
Separation ratio (s/a)		2.0	
Water depth (h)		18.75 m ($h/d = 5.0$)	

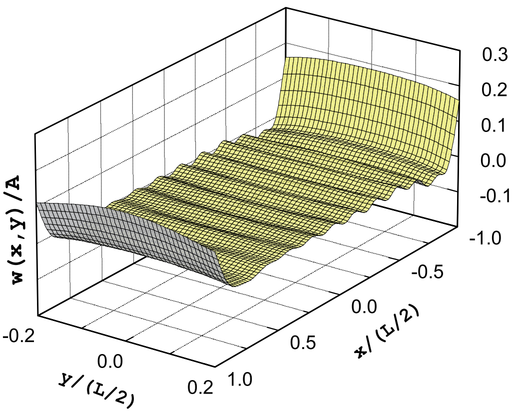

Fig. 4 Real part of the deflection of Model A ($N_B = 1280$) in head waves of $L/\lambda = 10$

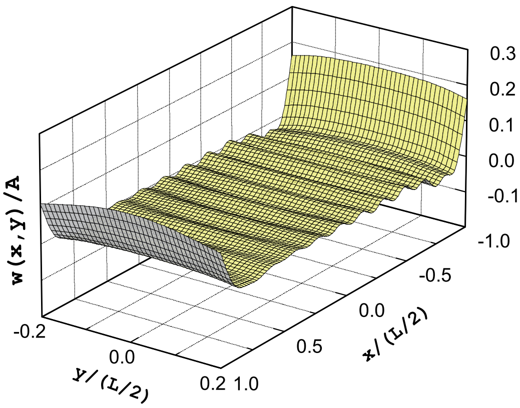

Fig. 5 Real part of the deflection of Model C ($N_B = 5120$) in head wave of $L/\lambda = 10$

volume is kept constant by decreasing only the diameter. (Thus the draft and the separation ratio are unchanged and the water-plane area is also the same.)

Figure 4 shows a snap shot taken at $t = 0$ (real part) of the deflection of Model A

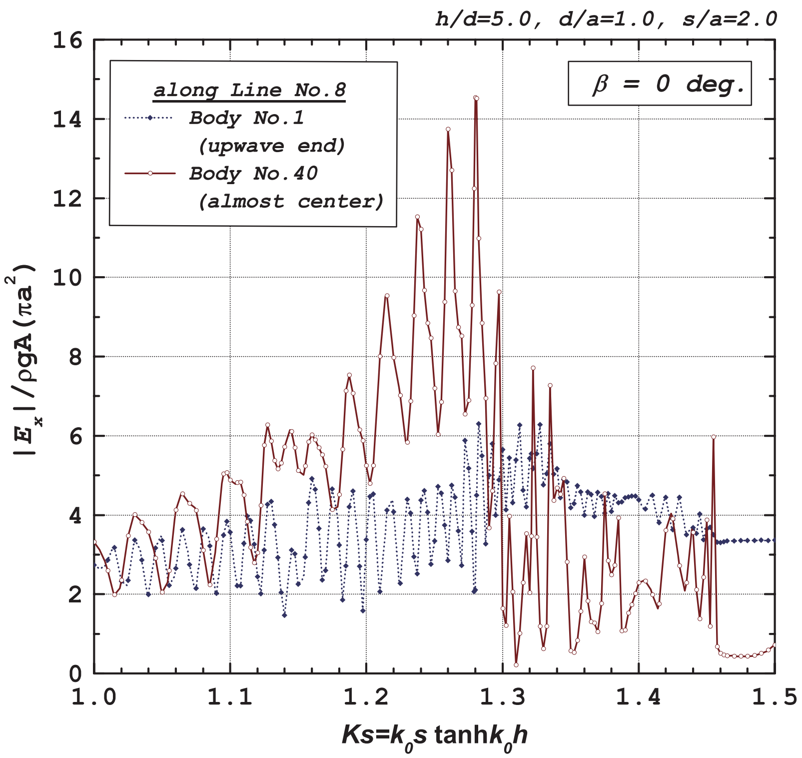

Fig. 6 Surge exciting force on bodies No. 1 and No. 40 along row No. 8 of Model A ($N_B = 1280$); $s/a = 2.0$, $h/d = 5.0$, $d/a = 1.0$

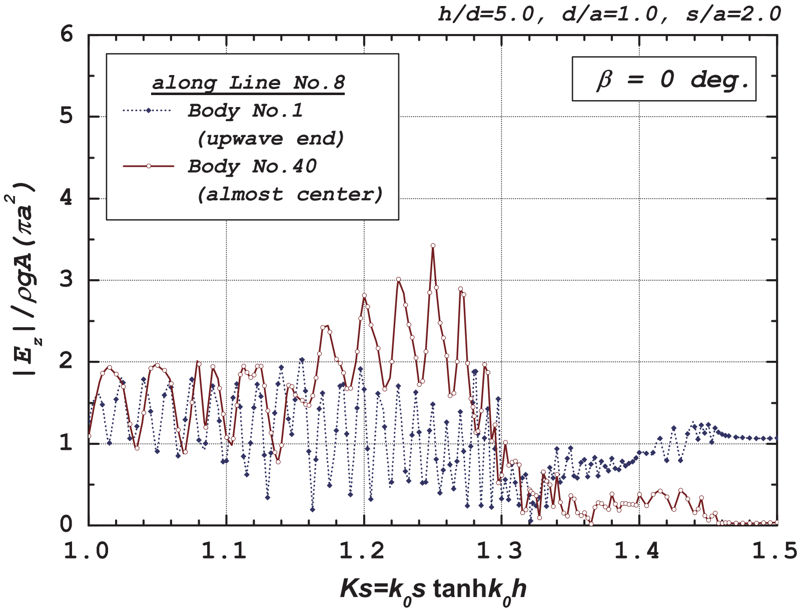

Fig. 7 Heave exciting force on bodies No. 1 and No. 40 along row No. 8 of Model A ($N_B = 1280$); $s/a = 2.0$, $h/d = 5.0$, $d/a = 1.0$

($N_B = 1280$) in a regular head wave ($\beta = 0°$) of $L/\lambda = 10$. (λ is the wavelength in deep water given by $2\pi g/\omega^2$.) The numbers of evanescent wave and progressive wave modes are taken as $N = 0$ and $M = 12$, respectively. It should be noted that perfect convergence as in Tables 1 and 2 is not achieved in the present case, probably because a fictitious cylinder at level 3 overlaps slightly with adjacent fictitious cylinders. However, the error caused by this is believed to be negligibly small; a similar problem was discussed by Yoshida *et al.* (1993). In fact, it is confirmed that the results including the first evanescent mode ($N = 1$) are

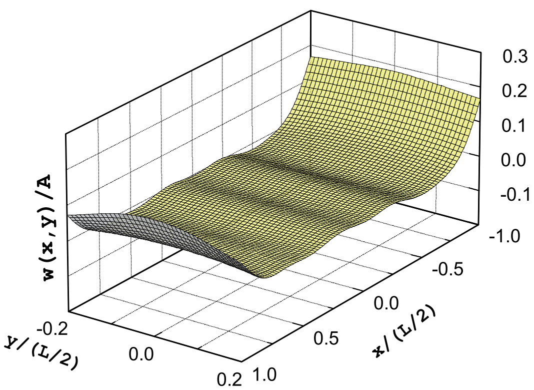

Fig. 8 Real part of the deflection of Model A ($N_B = 1280$) in head waves of $L/\lambda = 32.59$ ($Ks = 1.28$)

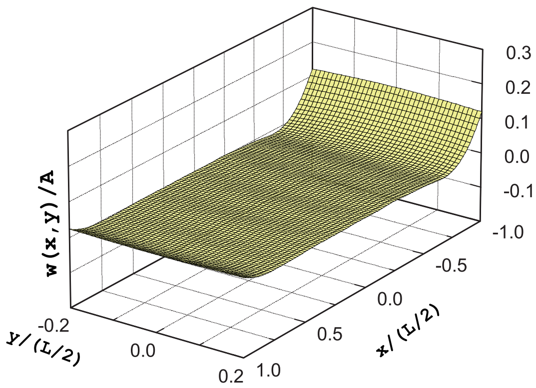

Fig. 9 Real part of the deflection of Model C ($N_B = 5120$) in head wave of $L/\lambda = 32.59$ ($Ks = 0.64$)

virtually the same as Figure 4 and the difference was not discernable in the figures.

Regarding the effect of increasing the number of modal functions, very good convergence is confirmed. To be on the safe side, modal functions in (4) are taken up to $m = 20$ and $n = 5$, which are much larger than necessary.

The deflection of a deck is strongly influenced by the rigidity, but compared to a pontoon-type VLFS studied by Kashiwagi (1998), the deflection looks small in the middle part and relatively large in the downwave end of a plate.

Figure 5 is the results of Model C ($N_B = 5120$) in the same wave as that for Figure 4; i.e. $L/\lambda = 10$ in head wave. Evanescent wave modes are not included, and the number of progressive wave modes is taken as $M = 12$, which is also the same as Figure 4.

Surprisingly, computed deflection patterns are very much the same irrespective of the number of columns. (Although the result for Model B is not shown here, it is confirmed to be almost the same as in Figures 4 and 5.) In these computations, the wavelength ($L/\lambda = 10$) is large relative to the size of each column, and the displacement volume, flexural rigidity, and water-plane area are exactly the same. Therefore, the deflection pattern may be determined predominantly by the restoring force. However, in short waves whose wavelength is of the same order as the separation distance between neighboring columns, hydrodynamic interactions will be intensified by the so-called trapped-wave phenomenon; this has been recently discussed by Maniar & Newman (1997), Evans & Porter (1997), and Utsunomiya & Eatock Taylor (1998).

To investigate this phenomenon, the wave exciting forces in surge and heave were computed for the two representative cylinders in an array of 1280 cylinders (Model A in Table 3). Figures 6 and 7 show the surge and heave forces, respectively. The dashed line denotes the results on body No. 1 (which is at the upwave end) and the solid line denotes the results on body No. 40 (which is at almost the center) along row No. 8.

We can see that there are many peaks even within a narrow range of the wavenumbers. One distinctive feature is that the surge force acting on a cylinder at almost the center becomes very large when the wavenumber is slightly less than $Ks \simeq 1.3$. The occurrence of these many peaks may be caused by a sequence of Neumann- and Dirichlet-trapped modes to be expected for a large number of equally spaced cylinders.

The wavenumber corresponding to $L/\lambda = 10$, adopted in Figure 4, is $Ks = 0.393$, which is far left of Figs. 6 and 7 and thus the interactions are expected to be small.

As an example for resonant hydrodynamic interactions, the deflection pattern of Model A was computed at $Ks = 1.28$ and the

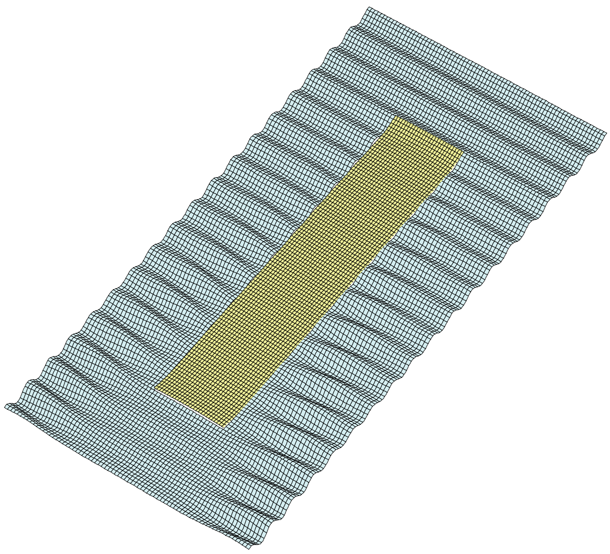

Fig. 10 Wave pattern around Model A in head wave of $L/\lambda = 10$, which is the same as those of Models B and C

result is shown in Figure 8. $Ks = 1.28$ corresponds to $L/\lambda = 32.59$, and the numbers of modal functions for this case are taken up to $m = 30$ and $n = 6$ in the x- and y-direction, respectively.

Compared to a longer-wave case of $L/\lambda = 10$ shown as Figure 4, the deflection amplitude remains small. However, the wavelength in the deflection pattern becomes long, in spite of shorter incident wave. A possible reason of this counter-intuitive phenomenon is as follows: in this particular short wave, the hydrodynamic interaction forces may be more dominant than the restoring force, and the spatial distribution of interaction forces is similar to the deflection pattern shown in Figure 8. It is noteworthy that the vertical deflection is caused by the vertical exciting force alone and not connected with the horizontal surge force. At $Ks = 1.28$, judging from Figure 7, the vertical exciting force may not be large and this is a reason for the small deflection.

To check the effect of resonant interactions, computations were also performed for Model C (5120 cylinders) at the same wavelength. Since the radius of an elementary cylinder in Model C is half the radius of that in Model A and s/a is unchanged, the nondimensional wavenumber is $Ks = 0.64$ for Model C. At this wavenumber, the variation of the wave field may be different from that in Model A. In fact, the deflection pattern of Model C shown in Figure 9 is different from that of Model A and almost zero except near the upwave end.

6.3 Wave Pattern Around Column-Supported VLFS

In connection with trapped waves, the wave pattern is one of the great interests for the case of a large number of cylinders. Waves outside of a structure can be computed in terms of the scattered and radiation potentials at the highest level, with the result

$$\frac{\zeta(x,y)}{A} = \Phi_I(x,y) + \sum_{j=1}^{N_\ell}\Bigg[\big\{A_{S,\ell}^j\big\}^T\big\{\psi_{S,\ell}^j\big\} - K\sum_{k=1}^{\infty}\Big(\frac{X_k}{A}\Big)\Big(\big\{\mathcal{R}_{k,\ell}^j\big\}^T + \big\{A_{k,\ell}^j\big\}^T\Big)\big\{\psi_{S,\ell}^j\big\}\Bigg], \tag{49}$$

where Φ_I is given by (2) and other coefficients and functions are already determined in Sections 3 and 4.

Firstly, the wave pattern at $L/\lambda = 10$ is shown in Figure 10. This pattern is the same irrespective of the number of columns and the effects of evanescent waves and structural deflection are also negligibly small. We can see in Figure 10 that the reflection from the bow is small and the wave amplitude along the side of the structure decreases.

Next, the wave pattern at $Ks = 1.28$ ($L/\lambda = 32.59$) around Model A, comprising 1280 cylinders, is shown in Figure 11. Likewise, Figure 12 shows the pattern around Model C (5120 cylinders) at the same wavenumber. In order to elucidate the wave height along the longitudinal side, the structural deflection on the deck is not shown.

Interestingly, the amplitude is increasing along the longitudinal side in Model A and there exist resonant waves whose crest line is perpendicular to that of the incident wave. These facts are connected with trapped waves among a great number of cylinders under the deck. In Model C, large amplitude waves still exist downstream of the structure, but the wave pattern is markedly different from that of Model A.

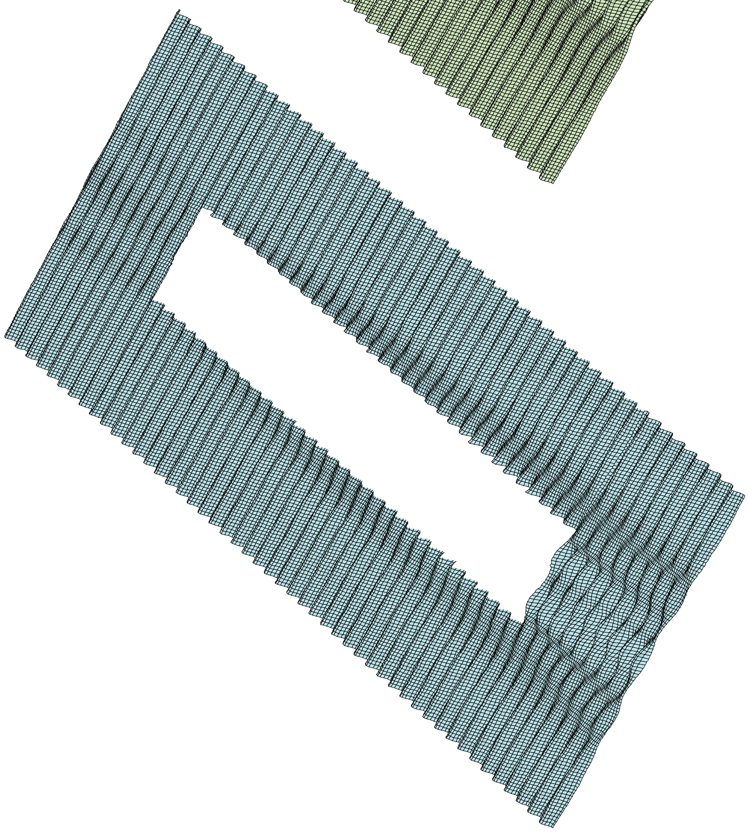

Fig. 11 Wave pattern around Model A ($N_B = 1280$) in a wave of $L/\lambda = 32.59$ coming from the right upper side

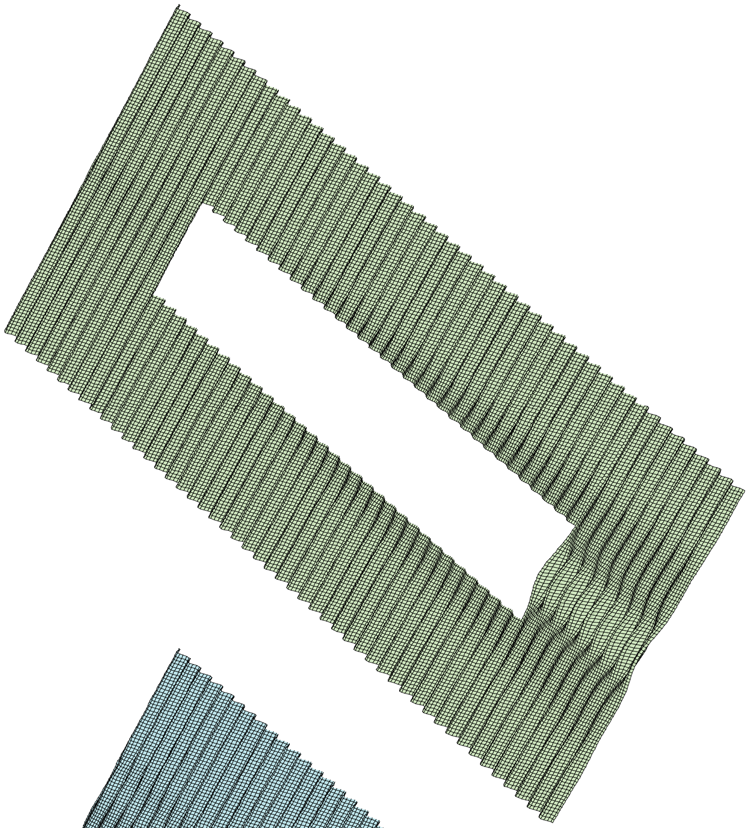

Fig. 12 Wave pattern around Model C ($N_B = 5120$) in a wave of $L/\lambda = 32.59$ coming from the right upper side

7. CONCLUSIONS

By using a newly developed hierarchical interaction theory, column-supported-type VLFSs were studied, with emphasis placed on hydrodynamic interactions among a large number of columns. Three different numbers of equally spaced circular cylinders were considered as supporting columns; these were 1280, 2880, and 5120 cylinders, but the total displacement volumes and water-plane areas were kept constant.

In the results for $L/\lambda = 10$, differences in the upper-deck deflection were very small among those three cases. This is probably because the interactions were small at this longer wavelength and the restoring force was dominant in the motion equation.

At shorter wavelengths, resonant phenomena were observed, which may be connected with trapped modes of Neumann and Dirichlet types, studied by Maniar & Newman (1997) for a single row of cylinders. In this wavelength region, the hydrodynamic interaction forces are more dominant than the restoring force, and the intensity and spatial distribution of the interaction forces vary depending on the ratio of the wavelength to the separation distance between adjacent cylinders. Therefore, as expected, the structural deflection was different between two structures supported by 1280 and 5120 cylinders.

The wave patterns around these two structures were also computed and their distinctive features associated with trapped-wave phenomena were shown in figures.

References

1. Evans, D.V. and Porter, R., 1997, Near-Trapping Waves by Circular Arrays of Vertical Cylinders, *Applied Ocean Research.* Vol. 19, pp. 83–99

2. Kagemoto, H. and Yue, D.K.P., 1986, Interactions among Multiple Three-Dimensional Bodies in Water Waves: An Exact Algebraic Method, *Journal of Fluid Mechanics*, Vol. 166, pp. 189–209

3. Kagemoto, H., 1995, On the Comparisons of Behaviors in Waves of Semisubmersible-Type and Pontoon-Type Very Large Floating Structures, *Proceedings of 13th Ocean Engineering Symposium*, Society of Naval Architects of Japan, pp. 231–238

4. Kashiwagi, M. and Kohjoh, T., 1995, A Method of Computing Hydrodynamic Interactions in Large Floating Structures Composed of Multiple Bodies, *Proceedings of 13th Ocean Engineering Symposium*, Society of Naval Architects of Japan, pp. 247–254

5. Kashiwagi, M., 1998, A B-Spline Galerkin Scheme for Calculating the Hydroelastic Response of a Very Large Floating Structure in Waves, *Journal of Marine Science and Technology*, Vol. 3, No. 1, pp. 37–49

6. Lin, X. and Takaki, M., 1998, A B-Spline Element Method for Predicting the Hydroelastic Responses of a Very Large Floating Structure in Waves, *Journal of the Society of Naval Architects of Japan*, Vol. 183, pp. 219–225

7. Maniar, H.D. and Newman, J.N., 1997, Wave Diffraction by a Long Array of Cylinders, *Journal of Fluid Mechanics*, Vol. 339, pp. 309–330

8. Murai, M., Kagemoto, H. and Fujino, M., 1998, On the Predictions of Hydroelastic Behaviors of a Huge Floating Structure in Waves, *Journal of the Society of Naval Architects of Japan*, Vol. 183, pp. 199–210

9. Newman, J.N., 1994, Wave Effects on Deformable Bodies, *Applied Ocean Research*, Vol. 16, pp. 47–59

10. Ohmatsu, S., 1997, Numerical Calculation of Hydroelastic Responses of Pontoon Type VLFS, *Journal of the Society of Naval Architects of Japan*, Vol. 182, pp. 329–340

11. Utsunomiya, T. and Eatock Taylor, R., 1998, Analogies for Resonances in Wave Diffraction Problems, *Proceedings of 13th International Workshop on Water Waves and Floating Bodies*, pp. 159–162

12. Yoshida, K. Suzuki, H., Oka, N., Iijima, K., Shimura, T. and Arima, T., 1993, Hydrodynamic Interaction Effects on Wave Exciting Force in Large Scale Floating Structures, *Journal of the Society of Naval Architects of Japan*, Vol. 174, pp. 243–251

13. Yoshida, K., Iijima, K., Suzuki, H. and Oka, T., 1994, Hydrodynamic Interaction Effects on Wave Exciting Force in Large Scale Floating Structures (2nd Report), *Journal of the Society of Naval Architects of Japan*, Vol. 176, pp. 185–192

Appendix A: Diffraction Characteristics

Let us consider the diffraction problem of the jth body in an elementary wave of "generalized" incident-wave vector defined by equation (9), and let the velocity potential of an elementary wave and the corresponding scattered potential be denoted by $\psi_I^j(x,y,z)$ and $\varphi_S^j(x,y,z)$, respectively.

We note that $\psi_I^j(x,y,z)$ satisfies Laplace's equation and the free-surface and bottom conditions. In addition, $\varphi_S^j(x,y,z)$ satisfies the radiation condition at infinity as well. Therefore, we can prove with Green's theorem that the total diffraction potential, $\varphi_D^j = \psi_I^j + \varphi_S^j$, is a solution of the integral equation:

$$C(P)\,\varphi_D^j(P) + \iint_{S_j} \varphi_D^j(Q)\frac{\partial}{\partial n_Q}G(P;Q)\,dS = \psi_I^j(P)\,, \tag{A.1}$$

where $C(P)$ is the solid angle, $P=(x,y,z)$ is the field point, $Q=(x',y',z')$ is the integration point, and $\partial/\partial n_Q$ denotes the normal derivative with the positive normal directed out of the body.

$G(P;Q)$ is the Green function, which can be expressed as

$$\begin{aligned} G(P;Q) &= \frac{i}{2}\,C_0 Z_0(z) Z_0(z')\,H_0^{(2)}\left\{k_0\sqrt{(x-x')^2+(y-y')^2}\right\} \\ &\quad + \frac{1}{\pi}\sum_{n=1}^{\infty} C_n Z_n(z) Z_n(z')\,K_0\left\{k_n\sqrt{(x-x')^2+(y-y')^2}\right\}\,, \end{aligned} \tag{A.2}$$

where
$$C_0 = \frac{k_0^2}{K + h(k_0^2 - K^2)}\,, \quad C_n = \frac{k_n^2}{K - h(k_n^2 + K^2)}\,, \tag{A.3}$$

and other notations are defined in equations (3) and (10).

$H_0^{(2)}$ and K_0 in (A.2) are the second kind of Hankel and modified Bessel functions, respectively. These functions can be recast in the series-expansion form by expressing $x + iy = r\exp(i\theta)$ and $x' + iy' = r'\exp(i\theta')$ and by utilizing the addition theorem of Bessel functions. Considering the case of field point P in the fluid, $C(P) = 1$ and $r > r'$. Therefore, from (A.1) and (A.2), we can obtain the following representation of the scattered potential:

$$\varphi_S^j(P) = \sum_{m=-\infty}^{\infty} \left[B_{m0}^j \left\{ Z_0(z) H_m^{(2)}(k_0 r)\, e^{-im\theta} \right\} + \sum_{n=1}^{\infty} B_{mn}^j \left\{ Z_n(z) K_m(k_n r)\, e^{-im\theta} \right\} \right], \quad \text{(A.4)}$$

where

$$\left. \begin{aligned} B_{m0}^j &= -\frac{i}{2}\, C_0 \iint_{S_j} \varphi_D^j(Q) \frac{\partial}{\partial n_Q} Z_0(z') J_m(k_0 r')\, e^{im\theta'}\, dS \\ B_{mn}^j &= -\frac{1}{\pi}\, C_n \iint_{S_j} \varphi_D^j(Q) \frac{\partial}{\partial n_Q} Z_n(z') I_m(k_n r')\, e^{im\theta'}\, dS \end{aligned} \right\} . \quad \text{(A.5)}$$

A set of coefficients $\{ B_{m0}^j,\ B_{mn}^j \}$ represents the diffraction characteristics corresponding to the elementary wave $\psi_I^j(P)$. By considering the diffraction problems for all elementary waves of $\{ \psi_I^j \}$ in the same manner, we can construct the matrix of the diffraction characteristics; which is denoted as $\left[B_j \right]^T$ in equation (11).

It should be noted that there is no need to compute the normal velocity of the incident wave in (A.1) and the solution of (A.1) is the total diffraction potential which can be directly used for computing (A.5) and the vector of elementary wave forces defined by equation (13).

Appendix B: Graf's Addition Theorem

Summaries are given below of Graf's addition theorems to be used in the hierarchical interaction theory.

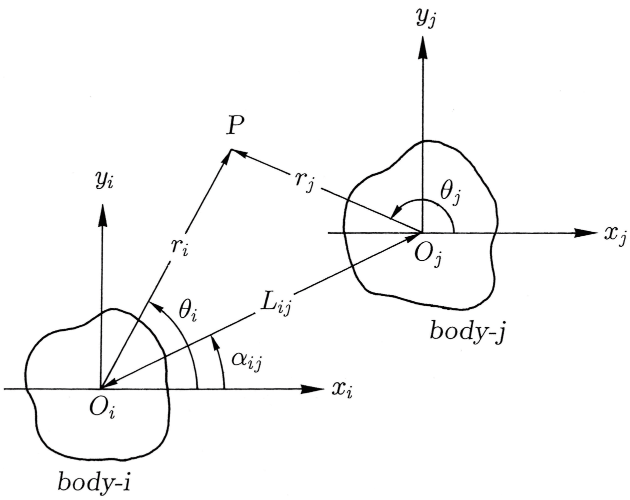

Fig. B1 Symbols used in the multiple scattering problem

In analyzing interactions at the same level, it is necessary to rewrite the scattered potential of body i with a coordinate system fixed at body j. In this case, as shown in Figure B1,

$r_j < L_{ij}$ and thus the following relations hold:

$$H_m^{(2)}(k_0 r_i)e^{-im\theta_i} = \sum_{p=-\infty}^{\infty} H_{m-p}^{(2)}(k_0 L_{ij})e^{-i(m-p)\alpha_{ij}} \Big\{ J_p(k_0 r_j)\, e^{-ip\theta_j} \Big\}, \tag{B.1}$$

$$K_m(k_n r_i)e^{-im\theta_i} = \sum_{p=-\infty}^{\infty} (-1)^p K_{m-p}(k_n L_{ij})e^{-i(m-p)\alpha_{ij}} \Big\{ I_p(k_n r_j)\, e^{-ip\theta_j} \Big\}, \tag{B.2}$$

where J_p and I_p denote the first kind of Bessel and modified Bessel functions, respectively, and $H_m^{(2)}$ and K_m are the second kind of Hankel and modified Bessel functions, respectively.

The above two equations can be expressed in a matrix form

$$\{\psi_S^i(r_i, \theta_i, z)\} = \big[\, T_{ij} \,\big] \Big\{\psi_I^j(r_j, \theta_j, z)\Big\}. \tag{B.3}$$

Here $\big[\, T_{ij} \,\big]$ is the coordinate transformation matrix, and the vectors on the left- and right-hand sides are defined in equations (12) and (9), respectively.

For the case of $r_j > L_{ij}$ in Figure B1, relations (B.1) and (B.2) must be modified, giving the followings:

$$H_m^{(2)}(k_0 r_i)e^{-im\theta_i} = \sum_{p=-\infty}^{\infty} J_{m-p}(k_0 L_{ij})e^{-i(m-p)\alpha_{ij}} \Big\{ H_p^{(2)}(k_0 r_j)\, e^{-ip\theta_j} \Big\}, \tag{B.4}$$

$$K_m(k_n r_i)e^{-im\theta_i} = \sum_{p=-\infty}^{\infty} (-1)^{m-p} I_{m-p}(k_n L_{ij})e^{-i(m-p)\alpha_{ij}} \Big\{ K_p(k_n r_j)\, e^{-ip\theta_j} \Big\}. \tag{B.5}$$

These equations can be expressed in the form

$$\{\psi_S^i(r_i, \theta_i, z)\} = \big[\, M_{ij} \,\big] \Big\{\psi_S^j(r_j, \theta_j, z)\Big\}. \tag{B.6}$$

This can be regarded as the multipole expansion of the scattered potential of body i around the origin of the jth coordinate system, and thus $\big[\, M_{ij} \,\big]$ is called the multipole expansion matrix.

Lastly, let us consider the local expansion of the vector of generalized incident waves around the origin of the jth coordinate system. In this case, the following relations hold for all values of r_j and L_{ij}:

$$J_m(k_0 r_i)e^{-im\theta_i} = \sum_{p=-\infty}^{\infty} J_{m-p}(k_0 L_{ij})e^{-i(m-p)\alpha_{ij}} \Big\{ J_p(k_0 r_j)\, e^{-ip\theta_j} \Big\}, \tag{B.7}$$

$$I_m(k_n r_i)e^{-im\theta_i} = \sum_{p=-\infty}^{\infty} I_{m-p}(k_n L_{ij})e^{-i(m-p)\alpha_{ij}} \Big\{ I_p(k_n r_j)\, e^{-ip\theta_j} \Big\}. \tag{B.8}$$

These can be written in the following form:

$$\{\psi_I^i(r_i, \theta_i, z)\} = \big[\, I_{ij} \,\big] \Big\{\psi_I^j(r_j, \theta_j, z)\Big\}. \tag{B.9}$$

Here $\big[\, I_{ij} \,\big]$ is the local expansion matrix, which is used in the downward transmission of the generalized incident-wave vector in the hierarchical diffraction problem.

A Time-Domain Mode-Expansion Method for Calculating Transient Elastic Responses of a Pontoon-Type VLFS*

Masashi KASHIWAGI
Research Institute for Applied Mechanics, Kyushu University
Kasuga, Fukuoka 816-8580, Japan

Abstract

A time-domain calculation method is described for elastic responses to arbitrary time-dependent external loads, on the basis of a general differential equation of second order including the convolution integral related to memory effects in the hydrodynamic forces. The time-dependent elastic deflection of a structure is represented by a superposition of mathematical modal functions, and a Galerkin scheme is employed to obtain a linear system of simultaneous differential equations for the amplitude of modal functions assumed. Special care is paid to numerical accuracy in computing the memory-effect function and the added mass at infinite frequency. The validity of the numerical results was confirmed through a comparison with time histories of the vertical deflection measured in an impulsive weight-drop test conducted at the Ship Research Institute and a comparison with existing numerical results for the same problem. To check the necessity of memory-effect terms, computations using a constant value for the hydrodynamic damping coefficient were also performed, and practical measures for reducing the computation time are discussed.

Keywords: Very large floating structure, Hydroelastic response, Time domain, Memory effect, Convolution integral.

1. Introduction

The safety and performance of a very large floating structure (VLFS) in various circumstances are being studied in Japan with the aim of using a VLFS as a floating airport. The configuration of the VLFS being considered is a pontoon type, 5 km long, 1 km wide, and only a few meters deep. In this type of structure, the flexural rigidity is relatively small, and the hydroelastic responses are more important than the rigid-body motions.

In a real situation, this "sheet-like" structure could be excited in various ways. The most probable and important one is wave excitation, and many studies have been carried out on wave-induced hydroelastic responses in regular waves (e.g., see a recent review by Kashiwagi [1]). The structure under consideration will also respond flexurally even under moving loads such as those imparted by an aircraft during landing or take-off. A huge mass impact would occur if an aircraft crashed onto the airport, or a VLFS might be used as a platform for a spacecraft launch. These transient phenomena must be studied to assess the safety of a floating airport.

∗ *Reprinted from Journal of Marine Science and Technology, Vol. 5, No. 2, pp. 89–100, 2000 (December)*

Only a few studies of transient problems have been reported to date. Using a FEM program, Watanabe and Utsunomiya [2] gave numerical results of the elastic responses when an aircraft lands on a circular VLFS. Kim and Webster [3] and Yeung and Kim [4] also studied transient phenomena on an infinite elastic runway by means of the double Fourier transform with respect to horizontal spatial variables.

Ohmatsu [5] presented a numerical method based on the Fourier transform, utilizing the frequency-domain responses of elastic deflection from the various excitations considered. In his method, the infinite integral with respect to the frequency was truncated at some finite frequency and contributions from higher frequencies were completely neglected.

In the meantime, Endo *et al.* [6, 7] had reported another method, in which the so-called memory-effect function for hydrodynamic forces was computed using frequency-domain results, and then the differential equations for elastic motions were solved directly in the time domain. Their calculation method for the structural deflection is based on a FEM, and thus the unknown deflections are defined at a large number of discrete nodes over an elastic plate. In the present problem, all elements in the resulting matrix are essentially nonzero, because of the effects of hydrodynamic interactions. However, Endo *et al.* neglected the cross terms in the hydrodynamic forces between the nodes located at a distance, and took advantage of the band characteristics to solve a sparse matrix common in the FEM. Moreover, the contributions of the damping coefficient at higher frequencies are approximated as zero when computing the memory-effect function.

The present study is also based on the time-domain differential equation, including the convolution integral which represents the memory effects in hydrodynamic forces, but the elastic motions of a plate are analyzed by the mode-expansion method. In this mode-expansion method, the structural deflection is expressed by a superposition of modal functions with time-dependent unknown amplitudes. By applying a Galerkin scheme, a linear system of simultaneous differential equations is obtained for the amplitudes of the modal functions assumed. An advantage of the mode-expansion method is that the number of unknowns (which is equal to the total number of modal functions) can be reduced in comparison with a discretized FEM, and that the contribution from each modal function can be obtained directly as a solution of simultaneous equations at each time step.

Good performance in the computation of the memory-effect function and the added mass at infinite frequency are confirmed first, and then numerical computations are carried out to simulate the weight drop test, which was conducted at the Ship Research Institute [7]. Great care is paid to accuracy in computing the memory-effect function, the convolution integral, and the added mass at infinite frequency for all possible combinations of modal functions assumed. The time marching for the differential equations is performed using the Runge-Kutta-Gill scheme with 4th-order accuracy in the time step size.

Convergence of the results with an increasing number of modal functions is checked, and the computed results are compared with independent numerical results by Endo and Yago [7]. The results were in good agreement with time histories measured at several points along the centerline of a tested model. Compared with the numerical results of Endo *et al.*, improvements were found in the variation pattern and amplitude of the deflection of higher modes, particularly as time elapses. However, a slight discrepancy was also found in the phase velocity of structural waves. Bird's-eye views of the structural deflection computed at several time instants were also taken to see the 3-D elastic response immediately after an impact load.

The present method is still too time-consuming for practical use. A large part of the computation is taken up in evaluating the convolution integral for the memory effects. To check the importance of memory-effect terms, complementary computations are performed by excluding the memory-effect terms. The trade-off between the computation time and prediction accuracy is briefly discussed.

2. Formulation

We consider a shallow-draft pontoon-type structure, which is rectangular in plan with length L and breadth B. Cartesian coordinates are used, with $z = 0$ defined as the plane of the undisturbed free surface and $z = h$ as the horizontal sea bottom. The boundary conditions on the body and free surfaces are linearized and the potential flow is assumed. Since the draft is very small relative to the dimensions in plan, it can be treated as zero in the linearized boundary-value problem.

All quantities will be described in nondimensional form, using the fluid density, ρ, the gravitational acceleration, g, and the half-length of the structure, $L/2$, as the characteristic length scale. $b = B/L$ may be used as the aspect ratio in plan.

With this convention, the dynamic and kinematic boundary conditions on the free surface are expressed as

$$p = -\frac{\partial \phi}{\partial t} + w\,, \quad \frac{\partial \phi}{\partial z} = \frac{\partial w}{\partial t} \quad \text{on } z = 0 \tag{1}$$

where $p(x, y, z, t)$ is the pressure, $\phi(x, y, z, t)$ is the velocity potential, and $w(x, y, t)$ is the elevation of the water surface or the deflection of the structure on $z = 0$. Note that $p = 0$ on the water surface, whereas $p \neq 0$ beneath the structure because of the disturbance exerted by the motion of the structure.

The motion equation of the VLFS under consideration can be described by the vibration equation of a thin plate, in the form

$$m\,\frac{\partial^2 w}{\partial t^2} + D\,\nabla^4 w = -\,p + p_E \tag{2}$$

where $m(x, y)$ is the mass per unit area, D is the flexural rigidity equal to $EI/(1-\nu^2)$ with EI the stiffness factor and ν Poisson's ratio, and $\nabla = (\partial/\partial x,\ \partial/\partial y)$ is the 2-D differential operator. $p_E(x, y, t)$ on the right-hand side denotes the external load distribution acting along the positive z-axis, which may be due to a landing and take-off of an airplane, or a huge mass impact onto the structure.

The boundary conditions along the edge of a plate also need to be satisfied. In the present case, the structure floats freely, and thus the bending moment and equivalent shear force must be zero, which can be expressed in the form

$$\frac{\partial^2 w}{\partial n^2} + \nu \frac{\partial^2 w}{\partial s^2} = 0\,, \quad \frac{\partial^3 w}{\partial n^3} + (2-\nu)\frac{\partial^3 w}{\partial n \partial s^2} = 0 \tag{3}$$

where n and s denote the normal and tangential directions, respectively.

In addition, a concentrated force stemming from replacement of the torsional moment with an equivalent shear force must also be zero at four corners of a rectangular plate. This condition can be expressed as

$$F_R = 2D(1-\nu)\frac{\partial^2 w}{\partial x \partial y} = 0 \quad \text{at } x = \pm 1,\ y = \pm b \tag{4}$$

3. Mode-Expansion Method

As in the analysis in the frequency domain (e.g. Kashiwagi [1]), we express the structural deflection by a superposition of modal functions in the form

$$w(x,y,t) = \sum_{j=1}^{\infty} X_j(t) w_j(x,y) \tag{5}$$

$$= \sum_{m=0}^{\infty}\sum_{n=0}^{\infty} X_{mn}(t) u_m(x) v_n(y) \tag{6}$$

where $w_j(x,y)$ is the j-th modal function, representing the modes not only of rigid-body motions, but also of elastic deformations.

As shown by (6), $w_j(x,y)$ is expressed by a simple product of one-dimensional modal functions in the x- and y-directions. In this paper, $u_m(x)$ and $v_n(y)$ are the natural modes for the bending of a uniform beam with free ends. Specifically, $u_m(x)$ can be written as

$$\left.\begin{aligned} u_0(x) &= \frac{1}{2} \\ u_{2m}(x) &= \frac{1}{2}\left[\frac{\cos \kappa_{2m} x}{\cos \kappa_{2m}} + \frac{\cosh \kappa_{2m} x}{\cosh \kappa_{2m}}\right] \end{aligned}\right\} \tag{7}$$

$$\left.\begin{aligned} u_1(x) &= \frac{\sqrt{3}}{2}\, x \\ u_{2m+1}(x) &= \frac{1}{2}\left[\frac{\sin \kappa_{2m+1} x}{\sin \kappa_{2m+1}} + \frac{\sinh \kappa_{2m+1} x}{\sinh \kappa_{2m+1}}\right] \end{aligned}\right\} \tag{8}$$

where the factors κ_m denote the positive real roots of the equation

$$(-1)^m \tan \kappa_m + \tanh \kappa_m = 0 \tag{9}$$

$v_n(y)$ can also be written in a similar form, with x replaced by y/b on the right-hand sides of (7) and (8).

These functions are orthogonal, and thus the following relation holds:

$$\iint_{S_H} w_i(x,y)\, w_j(x,y)\, dxdy = \frac{b}{4}\, \delta_{ij} \tag{10}$$

where S_H denotes the bottom of a rectangular plate, δ_{ij} is Kroenecker's delta, equal to 1 when $i = j$ and zero otherwise, and $b = B/L$ as defined before.

From (5) and (6), $w_j(x,y) = u_m(x)\, v_n(y)$. Hence, depending on the combination of odd and even numbers of m and n, the modal functions can be categorized into the following four types:

1. $w_j(x,y) = u_{2m+1}(x) v_{2n}(y)$, which is odd in x and even in y, and is referred to as FX type.
2. $w_j(x,y) = u_{2m}(x) v_{2n+1}(y)$, which is even in x and odd in y, and is referred to as FY type.
3. $w_j(x,y) = u_{2m}(x) v_{2n}(y)$, which is even in both x and y, and is referred to as FZ type.
4. $w_j(x,y) = u_{2m+1}(x) v_{2n+1}(y)$, which is odd in both x and y, and is referred to as FN type.

4. Motion Equation

The exact motion equation of a rigid body in the time domain has been known since the paper of Cummins [8]. However, the present problem is the transient elastic motion of a thin plate, and the analysis is based on the mode-expansion method, for which no comprehensive derivation of the motion equation has been given. Therefore, in what follows, we will consider the general expression for the time-dependent hydrodynamic pressure on a thin plate and the resulting equation of elastic motion in the time domain.

To avoid unnecessary complexity in the expression, let us consider only the j-th mode in (5) for the moment.

Considering the case of $X_j(-\infty) = 0$, the relation

$$X_j(t) = \int_{-\infty}^{\infty} X_j'(\tau)\, u(t-\tau)\, d\tau \tag{11}$$

holds in general, where $u(t)$ denotes the unit step function. Therefore we can write

$$X_j(t) w_j(x,y) = \int_{-\infty}^{\infty} X_j'(\tau) \Big\{ u(t-\tau) w_j(x,y) \Big\}\, d\tau \tag{12}$$

This implies that, if we can obtain the response (the pressure and resulting force) to the step-wise deflection given by $u(t)w_j(x,y)$, we can compute the response to arbitrary time-dependent input in terms of the convolution integral.

In the step-wise deflection problem, the body boundary condition for the velocity potential is given by (1) in the form

$$\frac{\partial \phi_j}{\partial z} = \delta(t)\, w_j(x,y) \tag{13}$$

where $\delta(t) = du(t)/dt$ is Dirac's delta function.

The velocity potential for this problem can be constructed in the form

$$\phi_j(x,y,z,t) = \delta(t)\psi_j(x,y,z) + \varphi_j(x,y,z,t) \tag{14}$$

Here $\psi_j(x,y,z)$ is the velocity potential at infinite frequency, satisfying the following conditions on $z = 0$:

$$\left.\begin{aligned} &\frac{\partial \psi_j}{\partial z} = w_j(x,y) \quad && \text{for } |x| < 1,\ |y| < b \\ &\psi_j = 0 && \text{for } |x| > 1,\ |y| > b \end{aligned}\right\} \tag{15}$$

The remaining part of (14) represents the fluid motion subsequent to the initial impulsive disturbance, and is therefore related to the so-called memory-effect part.

The pressure on $z = 0$ in the present case can be expressed as

$$p_j^S(x,y,t) = -\delta'(t)\, \psi_j(x,y,0) + \widehat{p}_j(x,y,t) + u(t) w_j(x,y) \tag{16}$$

where the second term is related to the memory effect, given explicitly by $\widehat{p}_j(x,y,t) = -\partial\varphi_j(x,y,0,t)/\partial t$, and the third term is the hydrostatic pressure due to the step-wise deflection.

The convolution integral using (16) gives the pressure caused by the general time-dependent motion of the j-th mode, in the form

$$\begin{aligned} p_j(x,y,t) &= \int_{-\infty}^{\infty} X_j'(\tau)\, p_j^S(x,y,t-\tau)\, d\tau \\ &= -X_j''(t)\, \psi_j(x,y,0) \\ &\quad + \int_{-\infty}^{t} X_j'(\tau)\, \widehat{p}_j(x,y,t-\tau)\, d\tau + X_j(t)\, w_j(x,y) \end{aligned} \tag{17}$$

With this result, let us consider next the motion equation expressed by (2). To get a linear system of simultaneous differential equations for all modes of elastic deflection, we substitute (5) into (2), multiply both sides of the equation by $w_i(x,y)$, and integrate the resultant equation over the bottom of the structure. The result of this transformation takes the form

$$\begin{aligned} \sum_{j=1}^{\infty} \Big[\Big\{ M_{ij} + A_{ij}(\infty) \Big\} X_j''(t) + \int_{-\infty}^{t} X_j'(\tau)\, K_{ij}(t-\tau)\, d\tau + \Big\{ C_{ij} + D\, S_{ij} \Big\} X_j(t) \Big] \\ = E_i(t), \quad \text{for } i = 1, 2, \cdots \end{aligned} \tag{18}$$

The matrix coefficients appearing above are defined by

$$M_{ij} = \iint_{S_H} m(x,y) w_i(x,y) w_j(x,y)\, dxdy \tag{19}$$

$$A_{ij}(\infty) = -\iint_{S_H} \psi_j(x,y,0) w_i(x,y)\, dxdy \tag{20}$$

$$K_{ij}(t) = \iint_{S_H} \widehat{p}_j(x,y,t) w_i(x,y)\, dxdy \tag{21}$$

$$C_{ij} = \iint_{S_H} w_i(x,y) w_j(x,y)\, dxdy = \frac{b}{4}\, \delta_{ij} \tag{22}$$

$$\begin{aligned} S_{ij} &= \iint_{S_H} \nabla^2 w_i(x,y) \nabla^2 w_j(x,y)\, dxdy \\ &\quad -(1-\nu) \iint_{S_H} \left\{ \frac{\partial^2 w_i}{\partial x^2} \frac{\partial^2 w_j}{\partial y^2} + \frac{\partial^2 w_i}{\partial y^2} \frac{\partial^2 w_j}{\partial x^2} - 2\, \frac{\partial^2 w_i}{\partial x \partial y} \frac{\partial^2 w_j}{\partial x \partial y} \right\} dxdy \end{aligned} \tag{23}$$

$$E_i(t) = \iint_{S_H} p_E(x,y,t) w_i(x,y)\, dxdy \tag{24}$$

Here the orthogonal relation shown by (10) has been used in (22). The same relation can be applied to M_{ij} in the case of uniform mass distribution.

The stiffness matrix S_{ij} shown by (23) has been obtained by taking account of the free-edge boundary conditions, (3) and (4); the detail of this transformation may be found in Kashiwagi [9]. Since modal functions are given in an analytical form in this paper, all integrals in (23) can be analytically performed.

If the distribution of external load, $p_E(x,y,t)$, is given, (18) can be solved in the time domain with appropriate initial conditions.

5. Added Mass at Infinity Frequency

$A_{ij}(\infty)$ defined by (20) is the added mass at infinite frequency. To compute this quantity, the velocity potential $\psi_j(x,y,z)$ must be determined as a solution of the boundary-value problem. Since the draft of the structure is regarded as zero and the boundary conditions are given by (15), $\psi_j(x,y,z)$ can be expressed in terms of the doublet distribution.

Taking the limit as $z \to 0$, the first equation in (15) gives the integral equation of the form

$$w_j(x,y) = \frac{1}{2\pi} \iint_{S_H} \psi_j(\xi,\eta,0) \frac{\partial^2}{\partial z \partial \zeta} \left(\frac{1}{r} \right) \Bigg|_{\substack{\zeta=0 \\ z=0}} d\xi d\eta \tag{25}$$

where $r = \sqrt{(\xi - x)^2 + (\eta - y)^2 + (\zeta - z)^2}$.

We note that the kernel function in (25) can be rewritten with notation of $R = \sqrt{(\xi - x)^2 + (\eta - y)^2}$, in the form

$$\frac{\partial^2}{\partial z \partial \zeta} \left(\frac{1}{r} \right) \Bigg|_{\substack{\zeta=0 \\ z=0}} = \frac{\partial}{\partial \eta} \left\{ \frac{\eta - y}{(\xi - x)^2 R} \right\} = \frac{1}{R^3} \tag{26}$$

As a solution method for (25), we express the unknown, $\psi_j(\xi,\eta,0)$, in terms of bi-cubic B-spline functions and employ a Galerkin method to determine the coefficients of B-spline functions. In this "B-spline Galerkin" scheme, singular integrals of the following form need to be evaluated:

$$\mathcal{A}_{mn} \equiv \iint_{\Delta S} \frac{\xi^m \eta^n}{R^3} d\xi d\eta \tag{27}$$

where m and n take integers among $0 \sim 3$, and ΔS denotes the area of each discretized panel.

Analytical results for all possible combinations of m and n in (27) are shown in the Appendix. As in Kashiwagi [9], the "relative similarity relation" can be used effectively when computing the elements in a matrix resulting from (25). Consequently, $\psi_j(x,y,0)$ can be determined precisely for all specified modes, and thus the added mass at infinite frequency, $A_{ij}(\infty)$, can be computed from (20) with high accuracy and less computation time.

6. Memory-Effect Function

$K_{ij}(t)$ defined by (21) is referred to as the memory-effect function, because $\widehat{p}_j(x,y,t)$ is related to the memory part of the velocity potential, as explained by (14)–(16). Kashiwagi [10] tried to compute $\widehat{p}_j(x,y,t)$ directly by solving the integral equation in the time domain. However, that attempt was unsuccessful because of highly-oscillatory behavior of the time-domain Green function for the zero-draft case.

Therefore in the present paper, $K_{ij}(t)$ is evaluated using the frequency-domain results. To show this relation, we start by considering the force in the i-th direction due to the pressure of the j-th mode. With (17), it follows that

$$\begin{aligned} F_{ij}(t) &= -\iint_{S_H} p_j(x,y,t)\, w_i(x,y)\, dxdy \\ &= -X_j''(t) A_{ij}(\infty) - \int_{-\infty}^{t} X_j'(\tau)\, K_{ij}(t-\tau)\, d\tau - X_j(t)\, C_{ij} \end{aligned} \tag{28}$$

Then, the Fourier transform of (28) takes the form

$$\mathcal{F}\{F_{ij}(t)\} = X_j(\omega) \left[\omega^2 A_{ij}(\infty) - i\omega \int_{-\infty}^{\infty} K_{ij}(t)\, e^{-i\omega t}\, dt - C_{ij} \right] \tag{29}$$

Comparing this with corresponding results in the frequency domain, we can obtain the following relations:

$$B_{ij}(\omega) = \int_0^\infty K_{ij}(t)\cos\omega t\,dt \tag{30}$$

$$\omega\Big\{A_{ij}(\omega) - A_{ij}(\infty)\Big\} = -\int_0^\infty K_{ij}(t)\sin\omega t\,dt \tag{31}$$

In the above expressions, the causality property of the memory-effect function, i.e. $K_{ij}(t) = 0$ for $t < 0$, has been taken into account.

The inverse Fourier transform of (30) gives the desired relation for computing the memory-effect function in the form

$$K_{ij}(t) = \frac{2}{\pi}\int_0^\infty B_{ij}(\omega)\cos\omega t\,d\omega \tag{32}$$

One problem in the numerical computation of (32) is how we estimate the values of $B_{ij}(\omega)$ at higher frequencies. Even though the B-spline Galerkin scheme developed by Kashiwagi [9] is employed, it is still difficult to compute $B_{ij}(\omega)$ up to very high frequencies where contributions to (32) are negligible.

In this paper, $B_{ij}(\omega)$ for higher frequencies is approximated by

$$B_{ij}(\omega) = \alpha\, e^{-\beta\,\omega} \tag{33}$$

where α and β are determined by a nonlinear version of the least-squares method using numerical values of $B_{ij}(\omega)$ computed in a relatively high-frequency region.

Substituting (33) into (32) and performing analytical integration, the final result is expressed as

$$K_{ij}(t) = \frac{2}{\pi}\int_0^{\omega_0} B_{ij}(\omega)\cos\omega t\,d\omega + \frac{2}{\pi}\frac{\alpha\, e^{-\beta\,\omega_0}}{\beta^2 + t^2}\Big\{\beta\cos\omega_0 t - t\sin\omega_0 t\Big\} \tag{34}$$

where ω_0 is the truncation frequency.

7. Numerical Calculation Method

The linear system of simultaneous differential equations shown in (18) is solved in uniform time steps using the Runge-Kutta-Gill scheme.

At each time instant, the acceleration $X_j''(t)$ is obtained by matrix inversion, with the convolution integral and restoring-force term transposed to the right-hand side of (18). The coefficients of acceleration are constant and independent of time, and therefore the inversion of the matrix is needed only once initially, which contributes greatly to a reduction of the computation time.

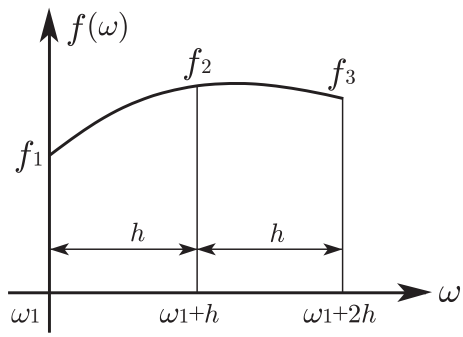

Fig. 1 Approximation of $f(\omega)$ by a quadratic function with equal frequency intervals

The first term on the right-hand side of (34) is evaluated numerically using the values of $B_{ij}(\omega)$ computed beforehand at discrete frequencies with equal interval. More specifically, as shown in Fig. 1, let us consider the following integral for $\omega_1 \leq \omega \leq \omega_1 + 2h$ (where $h = \Delta\omega$):

$$\mathcal{F}_C \equiv \int_{\omega_1}^{\omega_1+2h} f(\omega) \cos \omega t \, d\omega \tag{35}$$

Here $f(\omega)$ is approximated by a quadratic function in the form

$$f(\omega) = f_1 + \frac{1}{2h}(-3f_1 + 4f_2 - f_3)(\omega - \omega_1) + \frac{1}{2h^2}(f_1 - 2f_2 + f_3)(\omega - \omega_1)^2 \tag{36}$$

Integrating (35) after substituting (36) into it can be expressed as

$$\begin{aligned} \mathcal{F}_C = \frac{1}{t} \Bigg[& f_1 \Big\{ \frac{1}{\gamma}(3 + \cos\gamma) - \frac{4}{\gamma^2}\sin\gamma \Big\} + 4f_2 \Big\{ -\frac{1}{\gamma}(1 + \cos\gamma) + \frac{2}{\gamma^2}\sin\gamma \Big\} \\ & + f_3 \Big\{ \sin\gamma + \frac{1}{\gamma}(1 + 3\cos\gamma) - \frac{4}{\gamma^2}\sin\gamma \Big\} \Bigg] \end{aligned} \tag{37}$$

where $\gamma = t \cdot 2h$. In the case of $t = 0$, (37) can be reduced to the Simpson's rule using a quadratic approximation of the integrand. With this integration method, accurate results may be obtained irrespective of the value of t.

The most time-consuming part is the convolution integral. To keep numerical accuracy, the velocity and the memory-effect function are both approximated with linear variation within a constant time step.

To illustrate this in more detail, let us consider the following integral:

$$M(t) \equiv \int_0^t V(\tau) \, K(t - \tau) \, d\tau \tag{38}$$

Denoting a constant time-step size by Δt and the present time by $t = N\Delta t$, the above integral can be written as

$$M(N\Delta t) = \sum_{n=0}^{N-1} \int_{t_n}^{t_{n+1}} V(\tau) \, K(t - \tau) \, d\tau \tag{39}$$

where $t_n = n\Delta t$.

$V(t)$ and $K(t)$ are assumed to be obtained at each time instant in the past, and denoted by V_n and K_n ($n = 0, 1, 2, \cdots, N$). Then, $V(\tau)$ and $K(t - \tau)$ within $t_n \leq \tau \leq t_{n+1}$ are approximated as

$$\left. \begin{aligned} V(\tau) &= V_n + \frac{V_{n+1} - V_n}{\Delta t}(\tau - t_n) \\ K(t - \tau) &= K_{N-n} + \frac{K_{N-(n+1)} - K_{N-n}}{\Delta t}(\tau - t_n) \end{aligned} \right\} \tag{40}$$

Substituting these into (39), the integral with respect to τ can be performed analytically and the result takes the form

$$\begin{aligned} M(N\Delta t) = \sum_{n=0}^{N-1} \Delta t \Bigg[& \frac{1}{2} \Big\{ V_n K_{N-(n+1)} + V_{n+1} K_{N-n} \Big\} \\ & + \frac{1}{3}(V_{n+1} - V_n) \Big\{ K_{N-(n+1)} - K_{N-n} \Big\} \Bigg] \end{aligned} \tag{41}$$

8. Results and Discussion

8.1 Accuracy in the memory-effect function

Before starting numerical simulations, it is necessary to confirm good performance in the computation of the memory-effect function, $K_{ij}(t)$, and the added mass at infinite frequency, $A_{ij}(\infty)$.

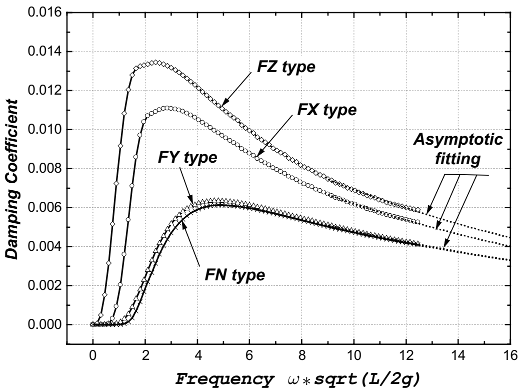

Fig. 2 Damping coefficients obtained by frequency-domain analysis for a rectangular plate of $L/B = 5$ in an infinite water depth

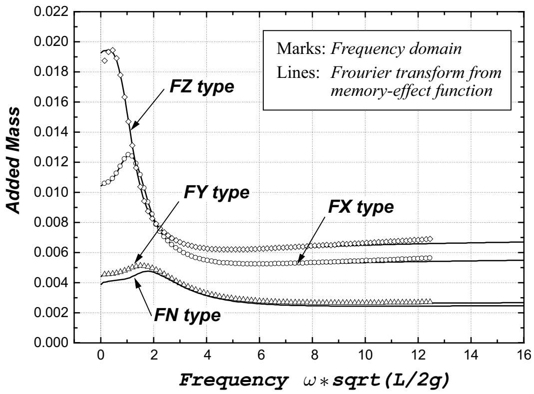

Fig. 3 Added mass obtained by frequency-domain analysis for a rectangular plate of $L/B = 5$ in an infinite water depth

One example of the damping coefficients is shown in Fig. 2, which is for $L/B = 5$ in infinite water depth ($h \to \infty$). The B-spline Galerkin scheme developed by Kashiwagi [9] was used to obtain Fig. 2. The modal shapes considered are the lowest one in (7) and (8); that is, $w_j = u_1 v_0 = \sqrt{3}x/4$ for FX type, $u_0 v_1 = \sqrt{3}y/4$ for FY type, $u_0 v_0 = 1/4$ for FZ type and $u_1 v_1 = 3xy/4$ for FN type.

The results in Fig. 2 are only for the case when $i = j$, and the highest frequency in computations is $\omega_0 = 12.53$, which corresponds to $L/\lambda = 50$ (where λ is the wavelength and thus $\omega = \sqrt{\pi L/\lambda}$). For wavelengths shorter than this value, a larger number of panels must be used and, although the B-spline Galerkin scheme is an efficient calculation method, this results in a drastic increase of the computation time. Therefore asymptotic fitting using (33) was applied. The results of asymptotic fitting are also included in Fig. 2, which seems to be reasonable.

In the present case of $\omega_0 = 12.53$, the contributions to $K_{ij}(t)$ from the first and second terms on the right-hand side of (34) are more or less of the same order, and thus the accuracy in $K_{ij}(t)$ may be influenced by the accuracy of approximation of (33). It should be emphasized that $\omega_0 = 12.53$, corresponding to $L/\lambda = 50$, is a very high frequency, at which the conventional zero-th order panel method cannot give reliable results, as shown in Endo and Yago [7].

To confirm indirectly the validity of the memory-effect function and the added mass at infinite frequency, the frequency-dependent added mass is computed from (31) and compared with corresponding values obtained from the frequency-domain solution. The results are shown in Fig. 3. Although slight differences can be seen in the low frequency range for FZ type, values computed by (31) are smooth and overall agreement is good.

8.2 Simulations for the weight drop test

As the next step, numerical simulations are implemented, corresponding to the experiments conducted at the Ship Research Institute (the results are reported in Endo and Yago [7]). The tested model is called VL-10, and its dimensions and bending rigidity are shown in Fig. 4. Although several kinds of experiments were made, the weight drop test (which is referred to as "Case FF1") is taken up as a typical impulsive experiment. In this experiment, the vertical deflections at points $Z1$–$Z9$ in Fig. 4 were measured.

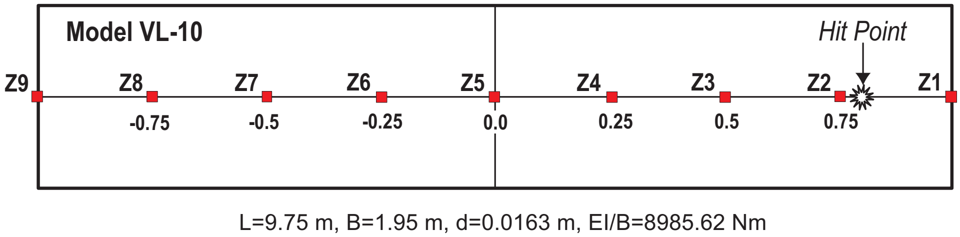

Fig. 4 Arrangement of Model VL-10 used in the weight drop test at the Ship Research Institute

In this weight drop test, a weight of 196 N was dropped from a height of 0.12 m onto the "hit point" indicated in Fig. 4. The acceleration of the weight during the impact was measured, and the result is shown in nondimensional form as the ratio to the gravitational acceleration g in Fig. 5. Therefore, this nondimensional acceleration multiplied by 196 N is regarded as the impact load. Denoting this impact load by $F_0(t)$ and the coordinates of the hit point by (x_p, y_p), the external pressure, $p_E(x, y, t)$, appearing in (24) can be expressed as follows:

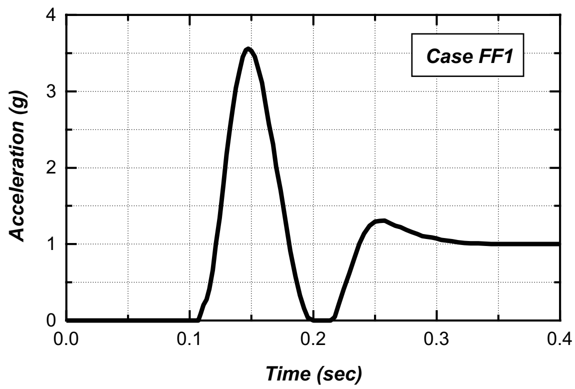

Fig. 5 Acceleration of the weight during impact onto VL-10

$$p_E(x, y, t) = F_0(t)\,\delta(x - x_p)\,\delta(y - y_p) \tag{42}$$

Since the present computations are based on the mode-expansion method, convergence must be checked by increasing the number of modes. The number of modes in the x- and y-directions are denoted by MX and MY, respectively. In the present case, FY and FN types of elastic deflection make no contribution, because the impulsive force acts on the longitudinal center line. The number of modes taken for FX and FZ types is equal. An example of a convergence study is shown in Fig. 6, for the deflection at the edge ($Z1$) and the center ($Z5$).

Good convergence is observed for the number of modes in the x-direction (with increasing MX), but more terms seem to be needed in the y-direction. Computationally, the time-step size, Δt, is determined by the highest mode, and thus if more terms in MY are adopted, the computation time will be prohibitive. In reality, the structural deflection of higher modes

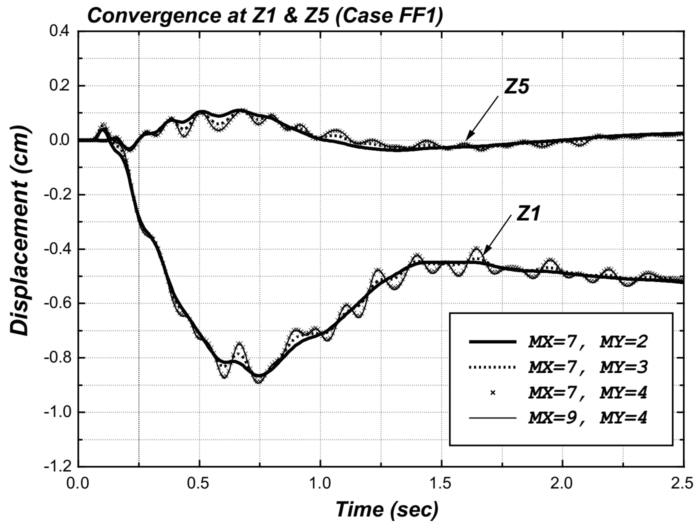

Fig. 6 Convergence check of computed results with increasing the number of elastic modes (structural deflection at $Z1$ and $Z5$)

includes a large structural damping, which reduces the variation amplitude as time elapses. With these reasons taken into account, the subsequent computations have been performed with $MX = 7$ and $MY = 4$. In this case, the time-step size is forced to be $\Delta t = 0.001$ s for stable computations.

The results of a comparison with measurements are shown in Fig. 7 for the vertical displacement at all measured points along the centerline indicated in Fig. 4. Computed results by Endo and Yago [7] using a FEM-BEM combined method are also reproduced by the

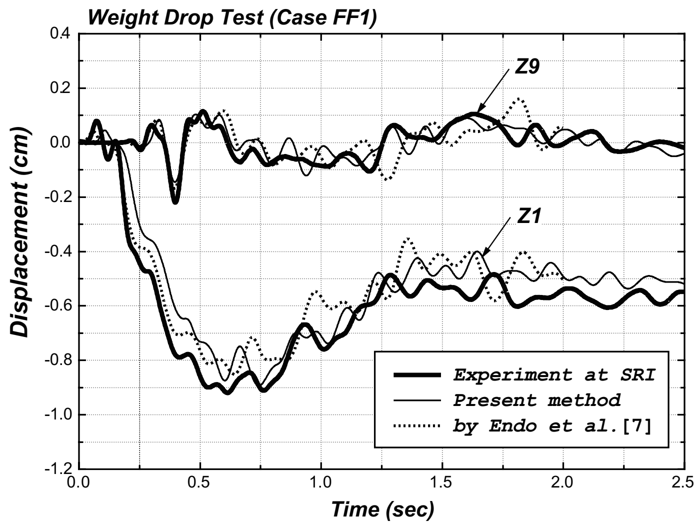

Fig. 7 a Comparison of the time histories of structural deflections at $Z1$ and $Z9$ due to weight drop impact

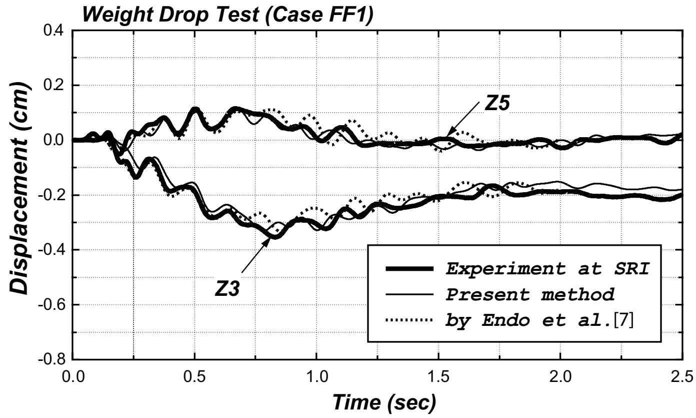

Fig. 7 b Comparison of the time histories of structural deflections at $Z3$ and $Z5$ due to weight drop impact

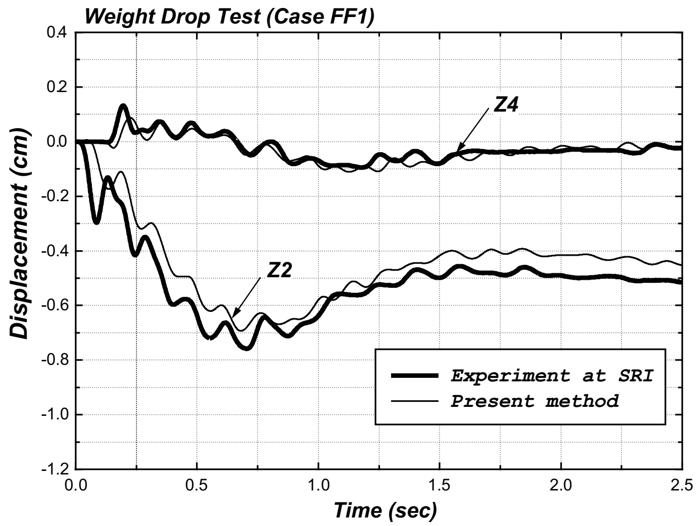

Fig. 7 c Comparison of the time histories of structural deflections at $Z2$ and $Z4$ due to weight drop impact

dashed lines in Fig. 7a and Fig. 7b. Their computations were terminated at 2.0 s and the results were shown for $Z1$, $Z3$, $Z5$, and $Z9$ only. (In the figures, a positive value of the displacement corresponds to vertically upward direction.)

First, by comparison with the measurements, we can see that the displacements near the hit point, $Z1$ in Fig. 7a and $Z2$ in Fig. 7c, are larger than the computed results. This may be attributed to the difference in the effective area of the impact load between the real situation (the size of a weight is finite) and the idealized computation (the load acts at just one point, as shown by (42)).

We can also see that the propagation velocity of structural waves by computation is slightly faster than the measurement. Possible reasons for this discrepancy are nonlinearity in the phenomenon, and the difference in the bending rigidity used in the computation from

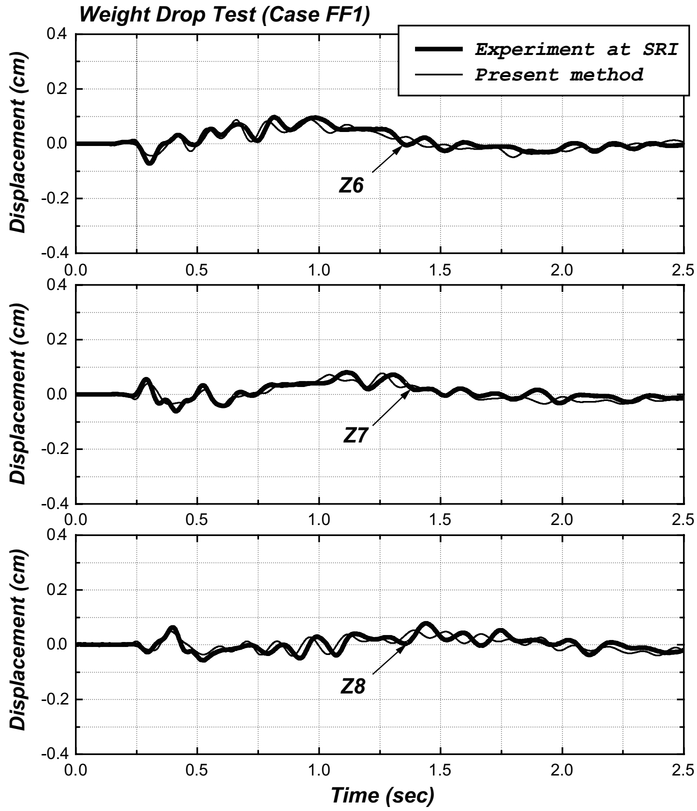

Fig. 7 d Comparison of the time histories of structural deflections at $Z6$, $Z7$, and $Z8$ due to weight drop impact

the value in the real experiment.

At any rate, the degree of agreement is favorable (particularly at the inside points of $Z3$–$Z8$) considering that the displacement is of the order of several millimeters, and the duration of the transient response is short.

Looking at closely the numerical results by Endo and Yago [7] shown in Figs. 7a and 7b, good agreement exists in the early stage of the phenomenon. However, as time proceeds, the variation pattern becomes different from the measurements, and the amplitude of higher-order variation seems to be large. In contrast, except for a slight difference in the propagation velocity of structural waves, the present results agree well with the measurements even in the vibration stage after the passing of the initial disturbance.

To indicate the 3-D responses of a structure, Fig. 8a shows snap shots of the deflection at $t = 0.20$, 0.35, and 0.50 s. Likewise, Fig. 8b shows bird's-eye view at $t = 0.70$, 0.95, and 1.95 s. It can be seen that the elastic deformation along the y-axis is noticeable in the early stage after the impact and at the edge of the plate in the longitudinal direction. A part of the structural wave is reflected at the longitudinal edge of the plate, and transient phenomena can be seen even at $t = 0.95$ s. However, the shape of deformation at $t = 1.95$ s is almost the same as that in the static equilibrium (which is also obvious from Fig. 7).

In the present computations, as already described, Δt was taken as equal to 0.001 s and thus the computation time for simulating the phenomena for a duration of 2.5 s was

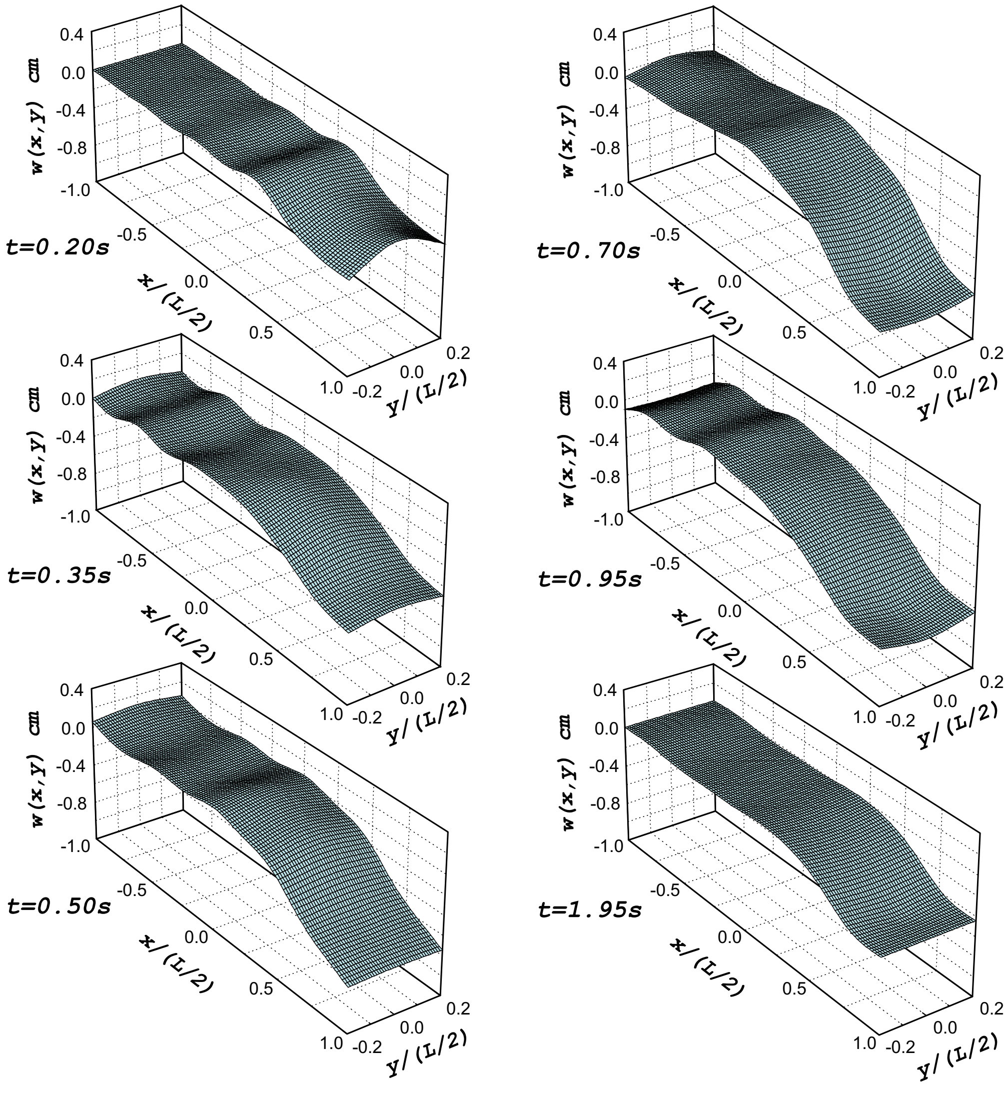

(a) ***Structural deflection at t=0.20, 0.35, 0.50 (s)*** **(b)** ***Structural deflection at t=0.70, 0.95, 1.95 (s)***

Fig. 8 Perspective view of structural deflection due to weight-drop impact, (a) at $t = 0.20$, 0.35 and 0.50 s, (b) at $t = 0.70$, 0.95 and 1.95 s

approximately 5 hours using a workstation of HP9000 series, model C200. As a measure of reducing the computation time for practical use, adopting only a slightly smaller number of lower modes can be recommended in the mode-expansion method. For example, the results of $MX = 7$ and $MY = 2$ shown in Fig. 6 could be obtained within 2 min computation time. Although small variations in the amplitude are filtered out, the overall tendency is well predicted with $MX = 7$ and $MY = 2$. Another alternative may be to neglect the memory effects in the hydrodynamic forces, because almost all the computation time is spent in computing the memory-effect function.

To check the necessity of memory-effect terms, the convolution integral in (18) was replaced by

$$\int_{-\infty}^{t} X_j'(\tau)\, K_{ij}(t-\tau)\, d\tau = B_{ij}(\omega_r)\, X_j'(t) \tag{43}$$

where ω_r denotes a representative frequency.

By doing this way, the damping coefficient can be treated as a constant value, and the computation time will only be a few seconds even when higher-order modes of deflection are included. The value of ω_r can be changed for each combination of mode indices, i and j, but it was taken as $\omega_r = 7.5$ for all modes just as a check (ω_r is nondimensional, as shown

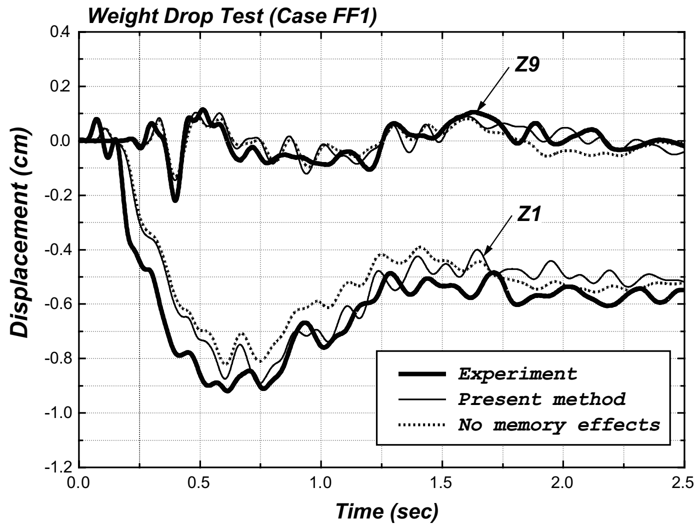

Fig. 9 a Time histories of structural deflections at $Z1$ and $Z9$ with and without memory-effect terms in the computation

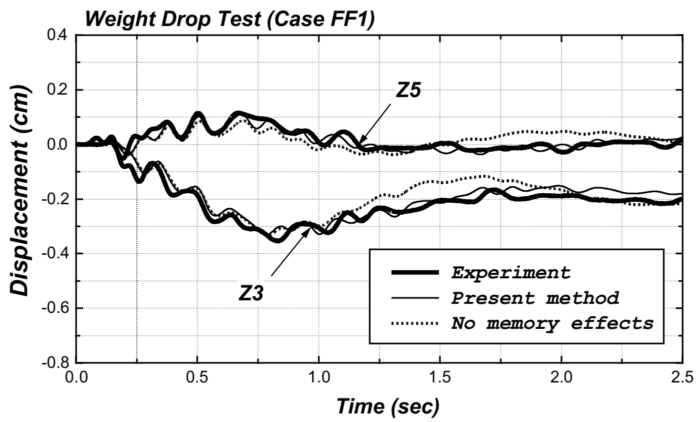

Fig. 9 b Time histories of structural deflection at $Z3$ and $Z5$ with and without memory-effect terms in the computation in Fig. 2).

The results of this approximation are shown by dashed lines in Fig. 9 for the case of $MX = 9$ and $MY = 4$. Surprisingly, the variation pattern in the early stage after the impact is close to more sophisticated computations including the memory effects. However, as time elapses, the detail of the variation becomes different (for example, the damping of the lowest mode seems to be small; see Fig. 9b for $Z3$ and $Z5$). This implies that the memory effects must be taken into account in the vibration stage after the passing of the impulsive disturbance. However, the selection of ω_r in (43) can be tuned up, depending on the combination of mode indices, which may improve the results. If this is the case, neglecting the memory-effect terms will greatly enhance the computational efficiency.

9. Conclusions

A time-domain calculation method has been presented which directly solves a linear system of general quadratic differential equations for the amplitude of specified modal functions representing the elastic deflection of a pontoon-type VLFS. Memory effects in the hydrodynamic forces are taken into account through the convolution integral over the previous history of the fluid motion. Special care was paid to numerical accuracy in evaluating the memory-effect function, the convolution integral, and the added mass at infinite frequency as they appeared in the differential equations.

Computed results were compared with measured data in the drop test conducted at the Ship Research Institute. The overall agreement was favorable, but a slight discrepancy was seen in the propagation velocity of the structural waves. This discrepancy might be caused by the nonlinearity of the problem.

A disadvantage of this calculation method is that the computation time becomes very large with increasing numbers of modal functions. As a practical measure to overcome this difficulty, computations neglecting the memory effects were performed. The results were in good agreement with more rigorous results which included the memory effects, particularly in the early stage of the phenomena. However, as time elapses, a difference in the variation pattern becomes prominent, implying the need to tune the damping coefficient for each component of the elastic modes.

Acknowledgment

The author would like to thank Dr. H. Endo at the Ship Research Institute, who provided invaluable experimental data and numerical results published [7] for comparison with our simulated results.

References

1. Kashiwagi M (1999) Research on hydroelastic responses of VLFS: recent progress and future work. Proceedings of the 9th International Offshore and Polar Engineering Conference, Brest, Vol 1, pp 17-26

2. Watanabe E and Utsunomiya T (1996) Transient response analysis of VLFS at airplane landing. Proceedings of the 2nd International Workshop on Very Large Floating Structure, Hayama, pp 243-247

3. Kim JW and Webster WC (1996) The drag of an airplane taking off from a floating runway. Proceedings of the 2nd International Workshop on Very Large Floating Structure, Hayama, pp 235-241

4. Yeung RW and Kim JW (1998) Structural drag and deformation of a moving load on a floating plate. Proceedings of the 2nd International Conference on Hydroelasticity in Marine Technology, Fukuoka, pp 77-88

5. Ohmatsu S (1998) Time domain analysis of hydroelastic behavior of VLFS. J Soc Naval Architect Japan 184, pp 223-230

6. Endo H, Yago K and Chiaki S (1998) Elastic responses of a floating platform stimulated by dynamic load. Proceedings of the 14th Ocean Engineering Symposium, Soc Naval Architect Japan, pp 411-416

7. Endo H and Yago K (1999) Time history response of a large floating structure subjected to dynamic load. J Soc Naval Architect Japan 186, pp 369-376

8. Cummins WE (1962) The impulse response function and ship motions. Schiffstechnik 9, pp 101-109

9. Kashiwagi M (1998) A B-spline Galerkin scheme for calculating the hydroelastic response of a very large floating structure in waves. J Marine Science and Technology, Vol 3, pp 37-49

10. Kashiwagi M (1999) A time-domain Green function method for transient problems of a pontoon-type VLFS. Proceedings of the 3rd International Workshop on Very Large Floating Structure, Honolulu, Vol 1, pp 97-104

Appendix: Evaluation of Singular Integrals

To get analytical expressions for singular integrals defined by (27), let us consider instead the following integral:

$$\mathcal{B}_{mn} = \iint \frac{(\xi - x)^m (\eta - y)^n}{R^3} \, d\xi d\eta \tag{A.1}$$

$$= \iint (\xi - x)^m (\eta - y)^n \frac{\partial}{\partial \eta} \left\{ \frac{\eta - y}{(\xi - x)^2 R} \right\} d\xi d\eta \tag{A.2}$$

Here (26) has been substituted to obtain (A.2).

It should be noted that $\mathcal{B}_{mn}$ may be easier to evaluate, because it can be expressed with only two arguments of $(\xi - x)$ and $(\eta - y)$. Furthermore, once an analytical expression of $\mathcal{B}_{mn}$ is obtained for $m \geq n$, $\mathcal{B}_{nm}$ can easily be obtained by simply exchanging $(\xi - x)$ for $(\eta - y)$ and $(\eta - y)$ for $(\xi - x)$. $\mathcal{A}_{mn}$ defined by (27) can be expressed in terms of $\mathcal{B}_{mn}$ by using a power-series expansion.

Since bi-cubic spline functions are considered, the values of m and n must be integers from 0 to 3. The final results of $\mathcal{B}_{mn}$ for necessary combinations of m and n can be summarized as follows:

$$
\begin{aligned}
\mathcal{B}_{00} &= -\,\frac{R}{(\xi - x)(\eta - y)} \\
\mathcal{B}_{10} &= -\,\log\Big|R + (\eta - y)\Big| \\
\mathcal{B}_{20} &= (\eta - y)\log\Big|R + (\xi - x)\Big| \\
\mathcal{B}_{30} &= (\eta - y)\,R \\
\mathcal{B}_{11} &= -\,R \\
\mathcal{B}_{21} &= \frac{1}{2}\left\{-(\xi - x)R + (\eta - y)^2\log\Big|R + (\xi - x)\Big|\right\} \\
\mathcal{B}_{31} &= \frac{1}{3}\left\{\,2(\eta - y)^2 - (\xi - x)^2\right\}R \\
\mathcal{B}_{22} &= \frac{1}{3}\left\{(\xi - x)^3\log\Big|R + (\eta - y)\Big| + (\eta - y)^3\log\Big|R + (\xi - x)\Big|\right. \\
&\qquad \left. -(\xi - x)(\eta - y)\,R\right\} \\
\mathcal{B}_{32} &= \frac{1}{4}\left[\,(\xi - x)^4\log\Big|R + (\eta - y)\Big| - (\eta - y)\Big\{(\xi - x)^2 - 2(\eta - y)^2\Big\}R\right] \\
\mathcal{B}_{33} &= \frac{1}{5}\left\{\,2(\xi - x)^4 + 2(\eta - y)^4 - (\xi - x)^2(\eta - y)^2\right\}R
\end{aligned}
$$

Transient Responses of a VLFS during Landing and Take-off of an Airplane*

Masashi KASHIWAGI
Research Institute for Applied Mechanics, Kyushu University
Kasuga, Fukuoka 816-8580, Japan

Abstract

The transient elastic deformation of a pontoon-type very large floating structure (VLFS) caused by the landing and take-off of an airplane is computed by the time-domain mode-expansion method. The memory effects in hydrodynamic forces are taken into account, and great care is paid to numerical accuracy in evaluating all the coefficients appearing in the simultaneous differential equations for the elastic motion of a VLFS. The time-histories of the imparted force and the position and velocity of an airplane during landing and take-off are modeled with data from a Boeing 747-400 jumbo jet. Simulation results are shown of 3-D structural waves on a VLFS and the associated unsteady drag force on an airplane, which is of engineering importance, particularly during takeoff. The results for landing show that the airplane moves faster than the structural waves generated in the early stage, and the waves overtake the airplane as its speed decreases to zero. The results for take-off are essentially the same as those for landing, except that the structural waves develop slowly in the early stage, and no obstacle exists on the runway after the take-off of airplane. The additional drag force on an airplane due to the elastic responses of the runway considered in this work was found to be small in magnitude.

Keywords: Very large floating structure (VLFS), hydroelastic response, time domain, landing, take-off.

1. Introduction

Because of relatively simple construction and ease of maintenance, pontoon-type very large floating structures (VLFS) are considered to be one of the most promising designs for a floating airport or runway, particularly in sheltered areas. Typical dimensions necessary as a floating airport could be 5 km long, 1 km wide, and only a few meters deep, so that the flexural rigidity is relatively small. Therefore, elastic responses are more important than rigid-body motions.

Since wave-induced motion and deflection can easily impose operational limits on the runway, the response of such a "sheet-like" structure to incoming waves has been the subject of many studies (e.g., see the review by Kashiwagi [1]). Even when no incoming waves exist, the structure under consideration will still respond flexurally to moving loads such as those imparted by an airplane during landing or take-off. In this case, structural waves generated on the runway and the associated additional drag may interfere with the safe operation of an aeroplane. Therefore, the transient responses of a VLFS to impulsive and moving loads must be studied by a reliable calculation method.

* *Reprinted from Journal of Marine Science and Technology, Vol. 9, No. 1, pp. 14–23, 2004 (April)*

Only a few studies of transient problems have been reported to date. Using a FEM program, Watanabe and Utsunomiya [2] presented numerical results for elastic responses due to impulsive loading on a circular VLFS. Kim and Webster [3] and Yeung and Kim [4] also studied transient phenomena on an infinite elastic runway in terms of the Fourier transform.

Ohmatsu [5] presented a numerical calculation method using the Fourier transform of the frequency-domain results of elastic deflection from the various excitations considered. In the meantime, Endo and Yago [6] proposed another method using the Fourier transform, in which the so-called memory-effect function for hydrodynamic forces was evaluated with frequency-domain results, and then the differential equations for elastic motions were solved directly in the time domain, with unknown structural deflections being defined by a FEM at a large number of discrete nodes over an elastic plate. However, these methods include several approximations, such as the truncation of high frequency components and the neglect of some cross-coupling terms in hydrodynamic forces. With these approximations included, Endo [7] applied his time-domain calculation method to a simulation of the landing and take-off of an aeroplane in waves, and similar work was reported by Shin *et al.* [8]

Kashiwagi [9] also studied a time-domain differential equation method, with elastic deflections being expressed by a superposition of mathematical modal functions and time-dependent unknown amplitudes. The numerical accuracy was much enhanced in an evaluation of the memory-effect function, the convolution integral, and the added mass at infinite frequency.

This article is concerned with numerical simulations of the transient responses of a pontoon-type VLFS during the landing or take-off of an airplane with realistic size and performance, and also with the increase in the drag force on an airplane due to the elastic deformation of the runway. For these simulations, the time-domain mode-expansion method developed by Kashiwagi [9] was used, because this method can be applied to any transient problem when the external force on the right side of the differential equation is modified in accordance with the problem concerned.

To know how much the drag force on an airplane will increase, particularly during take-off from a floating VLFS, is of great importance from an engineering viewpoint. Significant increases in the take-off drag could increase the length of runway needed (therefore increasing the construction cost of a floating runway), and increase the fuel usage during take-off (therefore increasing the operation costs of all flights from that runway).

In the first half of this article, the calculation method is summarized, with emphasis on special treatment to maintain numerical accuracy. In the second half, a modeling of the moving load during landing and take-off is described, with the assumption that a Boeing 747-400 jumbo jet lands on or takes off from a rectangular floating airport of about 5 km in length and 1 km in width. Simulation results for the transient responses of the airport are shown, together with some snapshots of the 3-D pattern of structural waves, and time histories of the vertical deflection at several points along the longitudinal centerline of the runway. We also present the time-histories of the additional drag force on an airplane induced by the dynamic response of a flexible runway. There is also a discussion of the characteristics of induced phenomena, the relation of the drag force to the structural waves generated, and the importance of the additional drag force.

2. Formulation

We first consider the time-domain transient problems for a shallow-draft pontoon-type floating airport, which is assumed for simplicity to be rectangular in plan with length L and breadth B. The z-axis of a Cartesian coordinate system is taken as positive vertically upward, with $z=0$ defined as the plane of the undisturbed free surface. The boundary conditions on the body and free surfaces are linearized, and the potential flow is assumed. Since the draft is very shallow relative to the dimensions in the plane, it can be treated as zero in the linearized boundary-value problem.

Except where otherwise noted, all quantities will be made nondimensional as follows:

$$\left.\begin{aligned} &p(x,y,z,t)=\rho g a\, p'(x',y',z',t') \\ &\phi(x,y,z,t)=a\sqrt{ga}\,\phi'(x',y',z',t') \\ &w(x,y,t)=a\, w'(x',y',t') \\ &t=\sqrt{a/g}\, t',\ (x,y,z)=a\,(x',y',z') \end{aligned}\right\} \tag{1}$$

where ρ is the fluid density, g is the gravitational acceleration, and a denotes the characteristic length scale, which is taken as equal to $L/2$ in this paper. $b=B/L$ may also be used as the aspect ratio in plan. $p(x,y,z,t)$ is the pressure, $\phi(x,y,z,t)$ is the velocity potential, and $w(x,y,t)$ denotes the elastic deflection of a floating airport (or the elevation of the water surface) on $z=0$.

The primed quantities in Eq. 1 are nondimensional, but for brevity the prime will be deleted hereafter. With this convention, the boundary conditions on $z=0$ are expressed as

$$p=-\frac{\partial\phi}{\partial t}-w,\quad \frac{\partial\phi}{\partial z}=\frac{\partial w}{\partial t}\quad \text{on } z=0 \tag{2}$$

Note that $p=0$ on the water surface, whereas $p\neq 0$ beneath the floating airport.

The motion equation of the structure under consideration can be described by the vibration equation of a thin plate in the form

$$m\,\frac{\partial^2 w}{\partial t^2}+D\,\nabla^4 w=p-p_E \tag{3}$$

where $m(x,y)$ is the mass per unit area, D is the flexural rigidity (and is equal to $Et^3/\{12(1-\nu^2)\}$, with t the equivalent plate thickness, E the elastic modulus, and ν Poisson's ratio), and $\nabla=(\partial/\partial x,\partial/\partial y)$ is the 2-D differential operator. Here, $p_E(x,y,t)$ on the right-hand side denotes the external time-dependent load distribution acting toward the negative z-axis (vertically downward), due to the landing or take-off of an airplane, whose modeling will be described subsequently.

The boundary conditions along the edge of a plate also need to be satisfied. In the present case, the structure floats freely, and thus the bending moment and equivalent shear force must be zero, which can be expressed in the form

$$\frac{\partial^2 w}{\partial n^2}+\nu\frac{\partial^2 w}{\partial s^2}=0,\ \frac{\partial^3 w}{\partial n^3}+(2-\nu)\frac{\partial^3 w}{\partial n\partial s^2}=0 \tag{4}$$

where n and s denote the normal and tangential directions, respectively. In addition, a concentrated force stemming from the replacement of the torsional moment with an equivalent shear force must also be zero at the four corners of a rectangular plate. This condition can be expressed as

$$\frac{\partial^2 w}{\partial x\partial y}=0\quad \text{at } x=\pm 1,\ y=\pm b \tag{5}$$

3. Mode Expansions

The elastic deflection of the structure is expressed by a superposition of mathematical modal functions in the form

$$w(x,y,t) = \sum_{j=1}^{\infty} X_j(t)\, w_j(x,y) \tag{6}$$

$$= \sum_{m=0}^{\infty}\sum_{n=0}^{\infty} X_{mn}(t)\, u_m(x) v_n(y) \tag{7}$$

where $X_j(t)$ is the unknown time-dependent amplitude of the j-th modal function $w_j(x,y)$, which is expressed, as shown in Eq. 7, by a simple product of one-dimensional modal functions in the x- and y-directions. Here, $u_m(x)$ and $v_n(y)$ are the natural modes for the bending of a uniform beam with free ends. Specifically, $u_m(x)$ can be written as

$$\left.\begin{aligned} u_0(x) &= \frac{1}{2} \\ u_{2m}(x) &= \frac{1}{2}\left[\frac{\cos\kappa_{2m}x}{\cos\kappa_{2m}} + \frac{\cosh\kappa_{2m}x}{\cosh\kappa_{2m}}\right] \end{aligned}\right\} \tag{8}$$

$$\left.\begin{aligned} u_1(x) &= \frac{\sqrt{3}}{2}\, x \\ u_{2m+1}(x) &= \frac{1}{2}\left[\frac{\sin\kappa_{2m+1}\, x}{\sin\kappa_{2m+1}} + \frac{\sinh\kappa_{2m+1}\, x}{\sinh\kappa_{2m+1}}\right] \end{aligned}\right\} \tag{9}$$

where the factors κ_m denote the positive real roots of the eigen-value equation

$$(-1)^m \tan\kappa_m + \tanh\kappa_m = 0 \tag{10}$$

and $v_n(y)$ can be written in the same form, with x replaced by y/b (where $b = B/L$) on the right-hand sides of Eqs. 8 and 9.

Note that these functions are orthogonal with the following orthogonality relation:

$$\iint_{S_H} w_i(x,y)\, w_j(x,y)\, dxdy = \frac{b}{4}\,\delta_{ij} \tag{11}$$

where S_H denotes the bottom of a rectangular plate, δ_{ij} is Kroenecker's delta, which is equal to 1 when $i = j$ and zero otherwise.

As shown in Eqs. 8 and 9, $u_{2m}(x)$ is even and $u_{2m+1}(x)$ is odd with respect to x, and similarly $v_{2n}(y)$ is even and $v_{2n+1}(y)$ is odd with respect to y. Thus, the modal functions $w_j(x,y) = u_m(x)v_n(y)$ can be categorized into the following four types:

1. $w_j(x,y) = u_{2m+1}(x)v_{2n}(y)$, which is odd in x and even in y, and is referred to as FX type;
2. $w_j(x,y) = u_{2m}(x)v_{2n+1}(y)$, which is even in x and odd in y, and is referred to as FY type;
3. $w_j(x,y) = u_{2m}(x)v_{2n}(y)$, which is even in both x and y, and is referred to as FZ type;
4. $w_j(x,y) = u_{2m+1}(x)v_{2n+1}(y)$, which is odd in both x and y, and is referred to as FN type.

In accordance with this type separation, hydrodynamic forces related to the pressure p and external loads related to p_E in Eq. 3 may be separated into four types, and then the resulting motion equation can be considered for each type separately.

4. Motion Equation

The exact motion equation of a rigid body in the time domain has been known since the paper by Cummins [10]. In the case of an elastic thin plate, a general expression for the motion equation in the time domain is given in Kashiwagi [9], which can be also applied to the present simulations.

To get a linear system of simultaneous differential equations for the time-dependent amplitude $X_j(t)$ for all modes of elastic deflection, we substitute Eq. 6 into Eq. 3, multiply both sides of the equation by $w_i(x,y)$, and integrate the resultant equation over the bottom of the structure. The result of this transformation takes the form

$$\sum_{j=1}^{\infty}\Big[\,\{\,M_{ij}+A_{ij}(\infty)\,\}X_j''(t)+\int_{-\infty}^{t}K_{ij}(t-\tau)X_j'(\tau)\,d\tau \\ +\{\,C_{ij}+D\,S_{ij}\,\}X_j(t)\Big]=E_i(t),\quad \text{for } i=1,2,\cdots \tag{12}$$

The matrix coefficients appearing in Eq. 12 are defined and given as follows:

$$M_{ij}=\iint_{S_H} m(x,y)w_i(x,y)w_j(x,y)\,dxdy \tag{13}$$

$$A_{ij}(\infty)=-\iint_{S_H}\psi_j(x,y,0)w_i(x,y)\,dxdy \tag{14}$$

$$K_{ij}(t)=\frac{2}{\pi}\int_0^{\infty}B_{ij}(\omega)\cos\omega t\,d\omega \tag{15}$$

$$C_{ij}=\iint_{S_H} w_i(x,y)w_j(x,y)\,dxdy=\frac{b}{4}\,\delta_{ij} \tag{16}$$

$$S_{ij}=\iint_{S_H}\nabla^2 w_i(x,y)\nabla^2 w_j(x,y)\,dxdy \\ -(1-\nu)\iint_{S_H}\left\{\frac{\partial^2 w_i}{\partial x^2}\frac{\partial^2 w_j}{\partial y^2}+\frac{\partial^2 w_i}{\partial y^2}\frac{\partial^2 w_j}{\partial x^2}-2\,\frac{\partial^2 w_i}{\partial x\partial y}\frac{\partial^2 w_j}{\partial x\partial y}\right\}dxdy \tag{17}$$

$$E_i(t)=-\iint_{S_H} p_E(x,y,t)w_i(x,y)\,dxdy \tag{18}$$

In this study, again for brevity, the mass distribution is assumed to be uniform with the total mass being $M=\rho LBd$ (d is the draft), and then the orthogonality relation Eq. 11 can be applied as in Eq. 16 for the hydrostatic restoring coefficients C_{ij}. Noting that the force is nondimensionalized with $\rho g a^3$, the mass matrix M_{ij} in the present case can be written as

$$M_{ij}=\frac{2d}{L}\,\frac{b}{4}\,\delta_{ij} \tag{19}$$

The stiffness matrix S_{ij} shown by Eq. 17 has been obtained by taking account of the free-edge boundary conditions (Eqs. 4–5). The details of this transformation may be found in Kashiwagi [11]. Since the modal functions are given in an analytical form here, all integrals in Eq. 17 can be evaluated analytically. Numerical calculation methods for other coefficients will be briefly explained in the subsequent sections.

5. Evaluation of $A_{ij}(\infty)$ and $K_{ij}(t)$

$A_{ij}(\infty)$, defined by Eq. 14, is the added mass at infinite frequency, which is calculated with $\psi_j(x, y, 0)$, the velocity potential at infinite frequency satisfying the following boundary conditions on $z = 0$:

$$\left.\begin{aligned} \frac{\partial \psi_j}{\partial z} &= w_j(x,y) \quad \text{for } |x| < 1,\ |y| < b \\ \psi_j &= 0 \qquad\qquad\ \ \text{for } |x| > 1,\ |y| > b \end{aligned}\right\} \tag{20}$$

The solution of ψ_j can be expressed in terms of the doublet distribution, the strength of which is determined by solving an integral equation by means of the so-called B-spline Galerkin scheme shown in Kashiwagi [9]. Therefore, the accuracy of $A_{ij}(\infty)$ is believed to be very high for all combinations of the mode indices i and j.

$K_{ij}(t)$ in Eq. 15 is referred to as the memory-effect (or retardation) function associated with time-dependent hydrodynamic forces. With the causality relation and the Fourier transform, it is known that the memory-effect function can be computed from the damping coefficients which are evaluated in the frequency-domain calculation, $B_{ij}(\omega)$, as specifically shown in Eq. 15.

In practice, it is difficult to compute $B_{ij}(\omega)$ up to very high frequencies where their contributions to Eq. 15 are negligible, especially for a zero-draft flat plate, even if the B-spline Galerkin scheme (Kashiwagi [11]) is employed. Therefore, $B_{ij}(\omega)$ for frequencies higher than the truncation frequency (denoted as ω_T) is approximated by

$$B_{ij}(\omega) = \alpha\, e^{-\beta\omega} \quad \text{for } \omega \geq \omega_T \tag{21}$$

where α and β are determined by the least-squares method using the numerical values of $B_{ij}(\omega)$ computed at some frequencies close to, but less than, ω_T.

Substituting Eq. 21 into Eq. 15 gives

$$K_{ij}(t) = \frac{2}{\pi}\int_0^{\omega_T} B_{ij}(\omega)\cos\omega t\, d\omega + \frac{2}{\pi}\,\frac{\alpha\, e^{-\beta\omega_T}}{\beta^2 + t^2}\Big\{\beta\cos\omega_T t - t\sin\omega_T t\Big\} \tag{22}$$

In this article, ω_T is taken as equal to 12.53, which corresponds to $L/\lambda = 50$ (where λ is the wavelength in the frequency domain).

The first term on the right-hand side of Eq. 22 is evaluated numerically using computed values of $B_{ij}(\omega)$ at discrete frequencies with equal intervals, say, $\Delta\omega$. To illustrate this, we write

$$\int_0^{\omega_T} f(\omega)\cos\omega t\, d\omega = \sum_{n=0,2,4,\cdots}^{N-2} \mathcal{F}_n, \quad \text{where } \mathcal{F}_n \equiv \int_{\omega_n}^{\omega_n + 2\Delta\omega} f(\omega)\cos\omega t\, d\omega \tag{23}$$

where $\omega_n = n\Delta\omega$ and the truncation frequency is given by $\omega_T = N\Delta\omega$. In the interval of $\omega_n \leq \omega \leq \omega_n + 2\Delta\omega$, the integrand $f(\omega)$ is approximated by a quadratic function, which makes it possible to integrate Eq. 23 analytically, with the following result

$$\begin{aligned} \mathcal{F}_n = \frac{1}{t}\bigg[& f_1\Big\{\frac{1}{\gamma}(3+\cos\gamma) - \frac{4}{\gamma^2}\sin\gamma\Big\} + 4 f_2\Big\{-\frac{1}{\gamma}(1+\cos\gamma) + \frac{2}{\gamma^2}\sin\gamma\Big\} \\ & + f_3\Big\{\sin\gamma + \frac{1}{\gamma}(1+3\cos\gamma) - \frac{4}{\gamma^2}\sin\gamma\Big\}\bigg] \end{aligned} \tag{24}$$

where $\gamma = t\,2\Delta\omega$, $f_1 = f(\omega_n)$, $f_2 = f(\omega_n + \Delta\omega)$, and $f_3 = f(\omega_n + 2\Delta\omega)$. Using this integration method, accurate results can be obtained irrespective of the value of t. Since there are no irregular frequencies in numerical solutions by the B-spline Galerkin scheme (the pressure distribution method) for a zero-draft plate, no fluctuation is observed in the asymptotic behavior of $K_{ij}(t)$ as $t \to \infty$. An analytical result on this asymptotic expression is described in Kashiwagi [12].

Related to the memory-effect function, the convolution integral in Eq. 12 must also be evaluated. To illustrate the calculation method, we consider the integral

$$\mathcal{M}(t) \equiv \int_0^t K(t-\tau)V(\tau)\,d\tau \tag{25}$$

where the integral from $\tau = -\infty$ to $\tau = 0$ is supposed to be zero because the VLFS is assumed to be at rest just before landing and take-off.

Denoting a constant time-step size by Δt and the present time by $t = N\Delta t$, the above integral can be written as

$$\mathcal{M}(t) = \sum_{n=0}^{N-1} \int_{t_n}^{t_{n+1}} K(t-\tau)V(\tau)\,d\tau \tag{26}$$

where $t_n = n\Delta t$.

$K(t-\tau)$ and $V(\tau)$ within $t_n \le \tau \le t_{n+1}$ are both approximated with linear variations, and then the integral with respect to τ in Eq. 26 can be performed analytically, giving

$$\begin{aligned}\mathcal{M}(N\Delta t) = \sum_{n=0}^{N-1} \Bigg[& \frac{1}{2}\Big\{K_{N-(n+1)}V_n + K_{N-n}V_{n+1}\Big\} \\ & + \frac{1}{3}\Big\{K_{N-(n+1)} - K_{N-n}\Big\}\Big(V_{n+1} - V_n\Big)\Bigg]\Delta t\end{aligned} \tag{27}$$

6. External Force

The motion equation Eq. 12 can be applied to any transient problem where the external force $E_i(t)$ is calculated for the problem concerned. Here, realistic landing and take-off of an airplane will be simulated, for which the external pressure distribution $p_E(x, y, t)$ in Eq. 18 must be modeled.

First, the position of the time-varying load is assumed to move with a constant acceleration α_0, and then the position of the load $\xi(t)$ and its velocity $V(t)$ are given by

$$\left.\begin{aligned}\xi(t) &= \xi_0 + V_0\,t + \frac{1}{2}\,\alpha_0\,t^2 \\ V(t) &= V_0 + \alpha_0\,t\end{aligned}\right\} \tag{28}$$

where ξ_0 and V_0 are the initial values of the position and velocity, respectively.

Second, for simplicity, the load distribution is assumed to be axisymmetric about the center of the moving load $(\xi(t), 0)$. In this case, in terms of a moving Cartesian coordinate system $\bar{o}$-$\bar{x}yz$ and a polar coordinate system $\bar{o}$-$\bar{r}\theta$, with the origin fixed to the center of loading, $p_E(x, y, t)$ can be written as

$$p_E(x, y, t) = p_E(\bar{r}, t) \equiv F_0(t)f(\bar{r}) \tag{29}$$

where $\bar{r} = \sqrt{\bar{x}^2 + y^2}$ and $\bar{x} = x - \xi(t)$.

As in Kim and Webster [3] and Yeung and Kim [4], the function of spatial distribution $f(\bar{r})$ in Eq. 29 is assumed to be a Gaussian distribution given by

$$f(\bar{r}) = \frac{1}{R^2}\, e^{-\pi(\bar{r}/R)^2} \tag{30}$$

with R being an effective radius of the loading.

Note that Eq. 30 is normalized such that

$$\iint_{-\infty}^{\infty} f(\bar{r})\, dxdy = \int_0^{\infty} f(\bar{r})\, 2\pi\bar{r}\, d\bar{r} = 1 \tag{31}$$

Therefore, $F_0(t)$ in Eq. 29 is the total force exerted by the landing or take-off of an airplane. With the assumption of a smooth transition, $F_0(t)$ may be given by the difference between the total weight W and the lift force $F_L(t)$ of an airplane. Supposing that W and $F_L(t)$ are provided with real physical unit, $F_0(t)$ can be given by

$$F_0(t) = \big\{W - F_L(t)\big\}/\rho g(L/2)^3 \tag{32}$$

The lift force during landing or take-off is calculated with the formula

$$F_L(t) = \frac{1}{2}\,\rho_a V^2(t) A_W\, C_L(t), \quad \text{where } C_L(t) = a_L\, e^{b_L t} \tag{33}$$

Here, $C_L(t)$ is the coefficient of the lift force, the parameters a_L and b_L are given as constant for the cases of landing and take-off, respectively. ρ_a is the density of air, $V(t)$ is the instantaneous speed to be given by Eq. 28, and A_W is the effective wing area of an airplane.

Substituting Eqs. 29 and 30 into Eq. 18, the external force in the i-th mode $E_i(t)$ can be computed as

$$\begin{aligned} E_i(t) &= \frac{F_0(t)}{R^2} \iint_{S_H} e^{-\pi(\bar{r}/R)^2} w_i(x,y)\, dxdy \\ &= \frac{F_0(t)}{R^2} \int_{-3R}^{3R} e^{-\pi(\bar{x}/R)^2} u_m\big(\bar{x} + \xi(t)\big)\, d\bar{x} \int_{-3R}^{3R} e^{-\pi(y/R)^2} v_n(y)\, dy \end{aligned} \tag{34}$$

Here, the range of integration is taken from $-3R$ to $3R$ with respect to both x and y, because the exponential function decays very rapidly, becoming

$$e^{-\pi(\bar{x}/R)^2} = e^{-9\pi} \simeq 5.26 \times 10^{-13} \tag{35}$$

at $\bar{x} = \pm 3R$.

The integrals in Eq. 34 with respect to x and y are numerically evaluated using Clenshaw-Curtis quadrature with the absolute error specified to be less than 10^{-8}.

7. Drag Force

The increase in the drag force on an airplane due to the elastic deformation of the runway is of particular engineering importance during take-off, since it will lengthen the running time and distance, which will eventually increase the fuel use of an airplane and the construction cost of a floating airport.

The drag force on the moving load, defined as positive in the negative x-direction, can be computed by

$$F_D = -\iint_{S_H} p_E(x,y,t) \frac{\partial}{\partial x} w(x,y,t)\, dxdy$$
$$= -\sum_{j=1}^{\infty} X_j(t) F_0(t) \iint_{S_H} f(\bar{r}) \frac{\partial}{\partial x} w_j(x,y)\, dxdy \tag{36}$$

Substituting Eq. 30 for $f(\bar{r})$ into Eq. 36, the resulting integral can be evaluated in the same manner as in Eq. 34. The derivative of the j-th modal function $w_j(x,y)$ with respect to x can readily be given by analytical differentiation of Eqs. 8 and 9.

It should be noted that the computation of the drag force based on Eq. 36 is similar to that of the wave-making resistance on a shallow-draft (flat) ship in water waves [13] under the potential-flow assumption, and thus Eq. 36 is associated with work equal to the energy dissipated in generating structural waves on a VLFS.

8. Modeling of an Airplane Landing and Take-off

We consider a realistic situation where a Boeing 747-400 airplane lands on or takes off from a floating VLFS with rectangular geometry in plan. The numerical data for these simulations are prepared as in Table 1 by referring to Takarada [14].

The initial positions of an airplane in landing and take-off are shown in Fig. 1 together with measurement points ($Z1$–$Z9$) for the elastic deflection. The time-histories of the airplane position $\xi(t)$, the velocity $V(t)$, and the external force (denoted as loading) $W - F_L(t)$ by the airplane are shown in Fig. 2 for both cases of the landing and take-off.

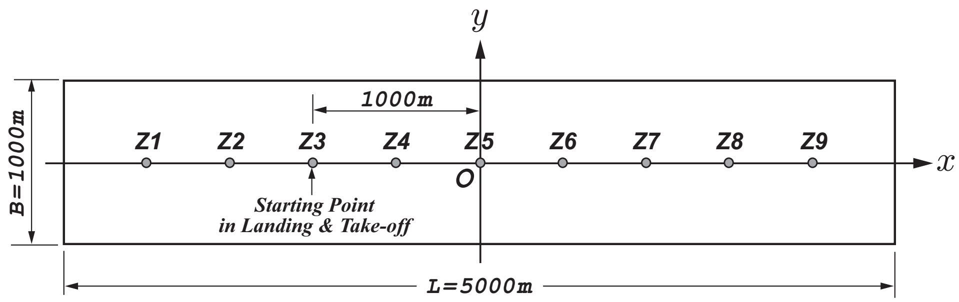

Fig. 1 Dimensions of VLFS and positions for measuring the elastic deflection

9. Results and Discussion

9.1 Numerical calculation method

The linear system of simultaneous differential equations shown in Eq. 12 is solved in uniform time steps using the 4-th order Runge-Kutta-Gill scheme.

At each time instant, the acceleration of the j-th mode $X_j''(t)$ is obtained by the matrix inversion, with the convolution integral and restoring-force term transposed to the right-hand side of Eq. 12. In this process, since the coefficients of the acceleration are constant and independent of time, the inversion of the matrix is performed only once initially and saved, which is used at all subsequent time steps.

Table 1 Numerical input data for simulations

Floating Airport		
Length (L)		5000 m
Breadth (B)		1000 m
Draft (d)		5.0 m
Flexural Rigidity (EI/B)		1.764×10^{11} Nm
Poisson's Ratio (ν)		0.3
Airplane (Boeing 747-400)		
Total Weight (W)		3867.08 kN
Effective Wing Area (A_W)		511.0 m^2
Density of Air (ρ_a)		1.2054 $\mathrm{Ns^2m^{-4}}$
Effective Radius of Landing (R)		10.0 m
Initial Position (ξ_0)		-1000 m
Initial Speed (V_0)	in Landing	69.35 $\mathrm{ms^{-1}}$
	in Take-off	0.00 $\mathrm{ms^{-1}}$
Acceleration (α_0)	in Landing	-1.263 $\mathrm{ms^{-2}}$
	in Take-off	1.026 $\mathrm{ms^{-2}}$
Parameters in Lift Coefficient: $C_L(t) = a_L\, e^{b_L t}$		
$a_L = \begin{cases} 2.61 & \text{in Landing} \\ 1.64\times 10^{-3} & \text{in Take-off} \end{cases}$		
$b_L = \begin{cases} -0.212 & \text{in Landing} \\ 0.125 & \text{in Take-off} \end{cases}$		

In actual computations, the number of modes in Eq. 12 must be finite. Since the modal functions in this paper are given as the product of $u_m(x)$ and $v_n(y)$, the number of modes in the x- and y-directions are truncated at different finite numbers. That is, $0 \le m \le MX$ and $0 \le n \le MY$, and thus $(MX + 1)$ terms in the x-direction and $(MY + 1)$ terms in the y-direction are used.

As already explained, calculations are carried out with modal functions categorized into four different types. In the present case, FY and FN types make no contribution, because the airplane is supposed to run along the longitudinal centerline of a rectangular floating airport. The number of modes taken for FX and FZ types is equal.

Convergence check for the present problem is not extensively performed, but referring to the results by Kashiwagi[9] for the impulsive weight drop test, $MX = 8$ and $MY = 3$ are adopted. When the same number of modes were used for the weight-drop simulation, the computed results could account for higher-order variation of the elastic deformation observed in measured results. In addition, the expected phenomena in the landing and take-off may be more modest than those in the impulsive weight drop, and thus $MX = 8$ and $MY = 3$ are expected to be enough for the present simulations. With these numbers of modes, stable and accurate results are obtained with the time-step size taken equal to $\Delta t = 0.025$ s. (In fact, when the number of modes in the y-direction is larger than $MY = 3$, stable results were not obtained unless the time-step size was taken equal to impractically very small.)

9.2 Landing

The touch-down onto the runway is assumed to take place at point $Z3$. Fig. 2 shows the subsequent time histories of the position, velocity, and loading of the airplane. The resultant

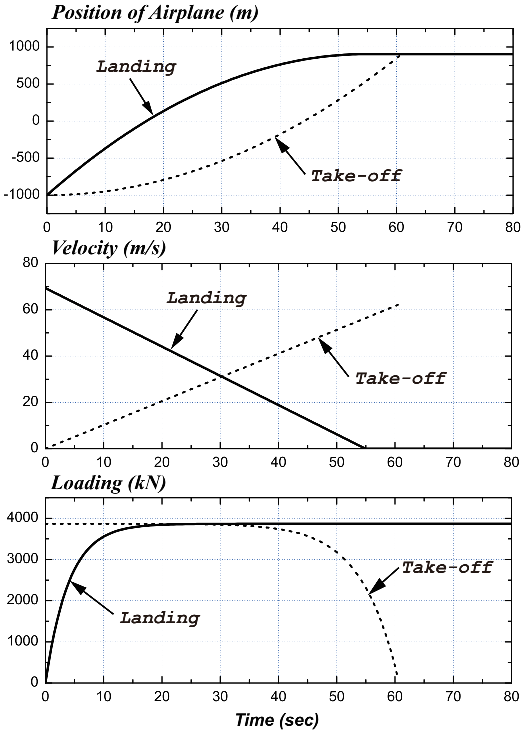

Fig. 2 Time histories of the airplane position, velocity and loading on the runway

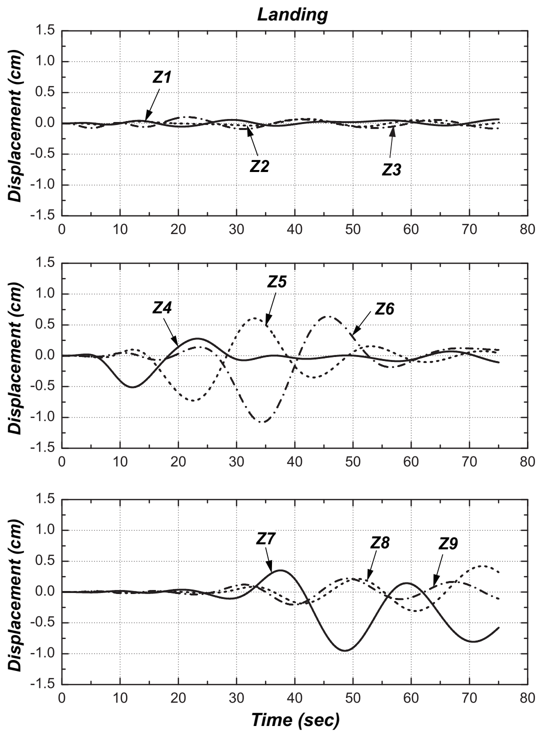

Fig. 3 Time histories of the elastic deflections obtained at $Z1 \sim Z9$ during landing

time histories of the vertical elastic deflections at $Z1 \sim Z9$ are shown in Fig. 3 with the unit of centimeter. (In Fig. 3 and subsequent figures, the vertically upward deflection is plotted as being positive.)

It can be seen that the vertical displacement is of the order of 1.0 cm at maximum in spite of a jumbo jet with the weight of approximately 4,000 kN. Unlike the impulsive weight drop onto the runway, the loading by the airplane landing increases smoothly from zero (which is in fact assumed as shown in Fig. 2). Therefore, no higher-order variation is observed in time histories of the deflection. Note that $Z4$, $Z5$, $Z6$ and $Z7$ are located at $x = -500$ m, 0 m, 500 m, and 1,000 m respectively. Looking at time histories of the position in Fig. 2 and the deflection in Fig. 3, it can be seen that the airplane runs faster than the trough of generated structural wave in the early stage (at least up to $t = 40$ s) and then the wave overtakes as the speed of airplane decreases to stop.

These can be observed more clearly in Fig. 4, showing snapshots of the elastic deflection along the longitudinal centerline and the position of airplane at various time instants. It is noted that the airplane completely stops at $t =$54.9 s and $x = 904$ m. Overtaking waves impinge upon the stopped airplane, and a part of them are scattered in various directions and the remainder transmit. This may explain why the amplitude of the deflection along the centerline is not so large at $t = 55$ s and retrieves after $t = 60$ s. This deformation of progressive waves is a 3-D phenomenon. To see this, bird's-eye views of the 3-D elastic deflection are shown in Fig. 6 at $t = 10$, 20, 30, 40, 50 and 60 s. It can be seen from the

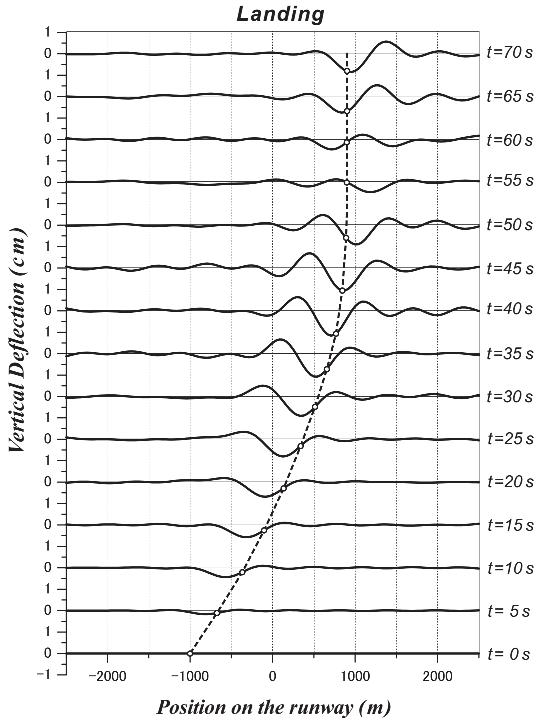

Fig. 4 Time histories of the spatial elastic deflections along the longitudinal centerline of the runway during landing. The *broken line* shows the trajectory of the airplane

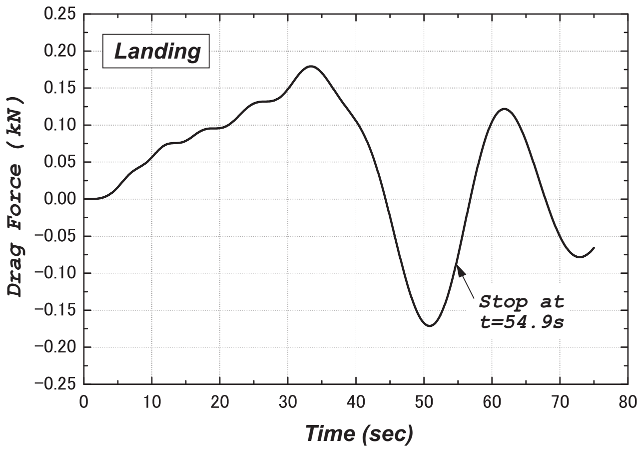

Fig. 5 Additional drag force on a landing airplane (The airplane stops at $t = 54.9\,\mathrm{s}$)

snapshots at $t = 50$ and $60\,\mathrm{s}$ that the generated wave overtakes the airplane and the wave is deformed due to the presence of the stopped airplane.

Fig. 5 shows the additional drag force computed from Eq. 36 during landing of the airplane. The drag force in the landing actually gives no unfavorable difficulties from a viewpoint of the additional fuel consumption. However, it may be informative to see variation of the

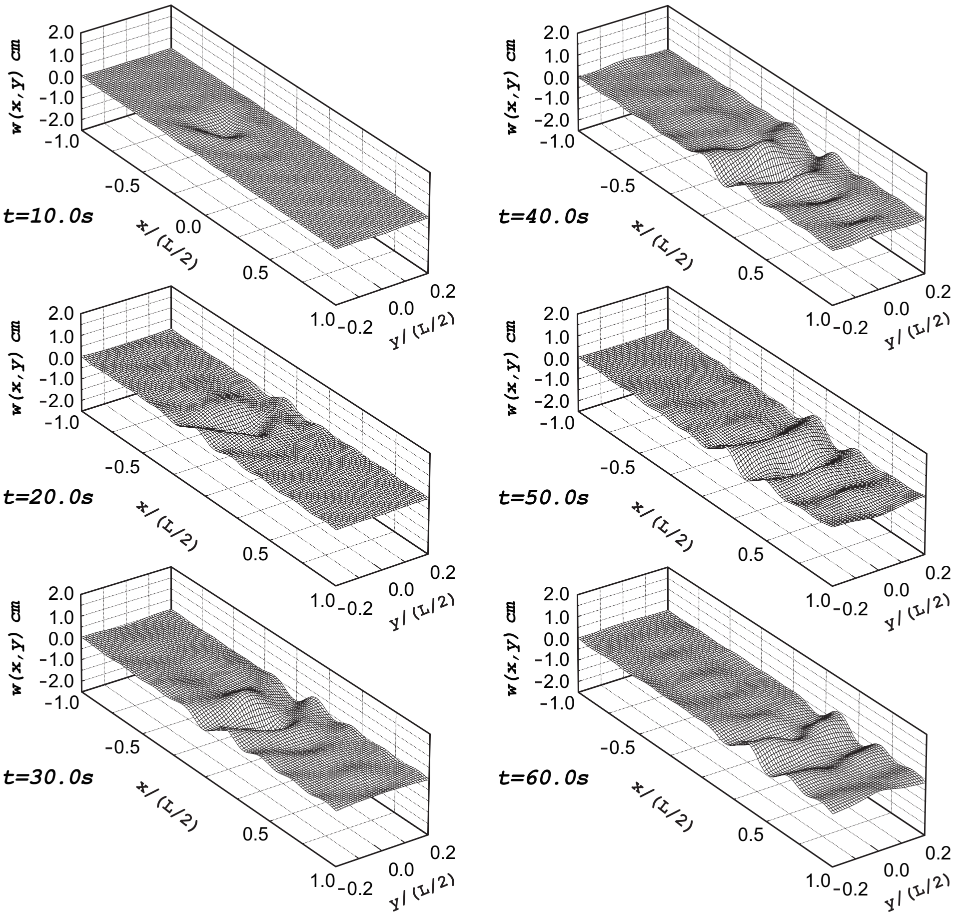

Fig. 6 Perspective view of the structural deflection during landing of a Boeing 747-400

drag force as a function of the position of a moving airplane relative to generated structural waves.

The drag force increases without changing the sign and takes the maximum at about $t = 33\,\mathrm{s}$. As can be understood from Fig. 4, the drag force becomes maximum when the airplane is located at the upslope of the dent (the maximum in slope). When the speed of airplane approaches zero, the waves pass the airplane and then variation of the drag force becomes simply oscillatory with the mean value being zero. The magnitude of the additional drag force is about 0.18 kN at maximum, which may be of negligible order for a jumbo jet. However, it should be noted that the drag force on an elastic runway varies depending on the flexural rigidity and thus definitive conclusions should not be made only from the present example.

9.3 Take-off

In the simulation of take-off, as the initial condition, the airplane (Boeing 747-400) is assumed to be at rest at $Z3$ ($x = -1000\,\mathrm{m}$). The initial static deflection is calculated from Eq. 12, with the velocity and acceleration set equal to zero. The time histories of the vertical deflections at $Z1 \sim Z9$ are shown in Fig. 7, from which one can see that the static deflection at $Z3$ is approximately 5.0 mm. The relative position of the airplane and the spatial profiles of the generated wave along the longitudinal centerline of the runway are shown in Fig. 8 at various time instants.

In the take-off, as compared to the landing, it takes much time for the airplane to move in the early stage, and thus the disturbance on the VLFS develops slowly. Looking at the positions of the airplane and the trough of generated wave (which may be understood from Figs. 2 and 7 or directly from Fig. 8), it can be seen that the airplane is ahead of the trough of generated wave.

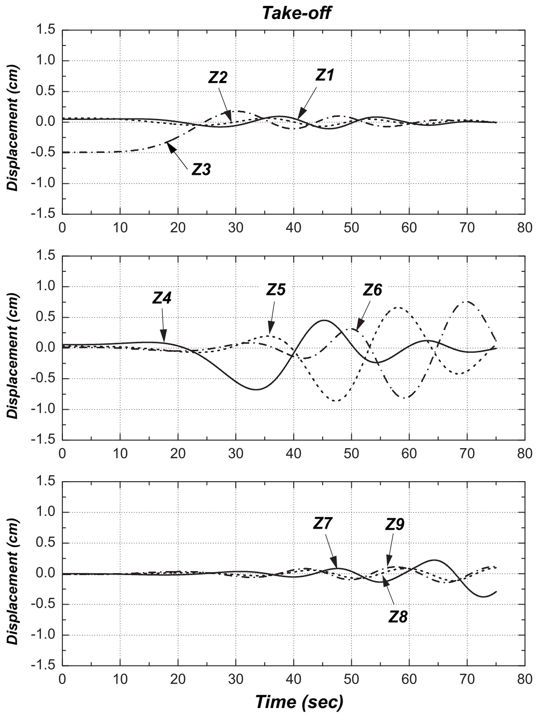

Fig. 7 Time histories of the elastic deflections obtained at $Z1 \sim Z9$ during take-off

As the time elapses, the speed of airplane and the dynamic disturbance increase. After the take-off at $t = 60.7$ s, no external force acts on the VLFS, but relatively large waves overtaking the airplane are still observed at $Z6$ and $Z7$ in Fig. 7. In the present simulations, the wavelength of the structural wave looks long due to relatively large value of the flexural rigidity, and thus the phase velocity is also relatively fast. In fact, it can be seen from Fig. 8 that the airplane overtakes only the first crest until the take-off at $t = 60.7$ s. Related to this fact, the additional drag force shown in Fig. 9 does not change in sign, although small variation can be seen until taking the maximum value at about $t = 50$ s. The time instant when the drag force takes its maximum corresponds to the location of the airplane at the maximum upslope of the dent, which can be confirmed from Fig. 8. Just before the take-off, the drag force becomes abruptly small. This is not because of the relative position of the airplane to the generated wave but because of sharply decreasing value of the imparted pressure, $F_0(t)$ in Eq. 36. Concerning the maximum value of the additional drag force during take-off, its magnitude is 0.15 kN, which may be negligible and give no serious problems for considering a VLFS as a floating airport.

Fig. 10 shows snapshots of the 3-D elastic deflection with time interval of 10.0 s. By comparison with the landing case, similar deflection pattern can be seen at certain time instant (e.g. the pattern at $t = 40$ s in landing is similar to that at $t = 60$ s in take-off). However the deflections in the beginning and last stages are different between landing and take-off, which is natural considering the behavior of an airplane.

10. Conclusions

Numerical simulations were carried out for the transient responses of a floating airport during landing and take-off by an airplane using realistic numerical data from a Boeing 747-400

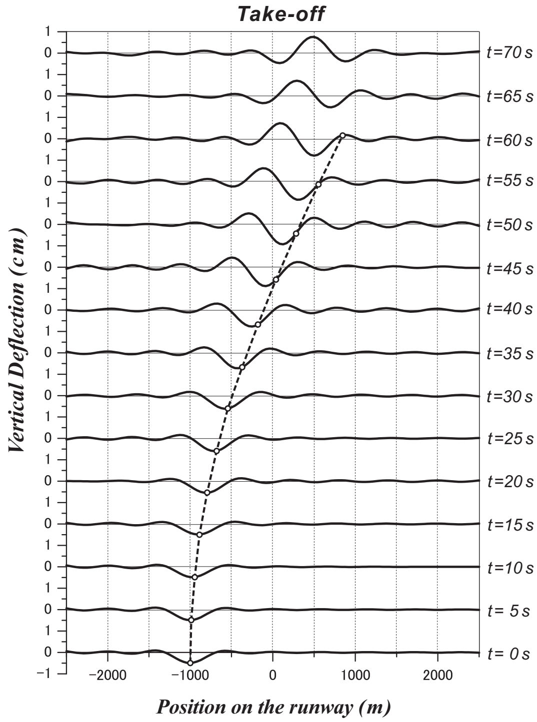

Fig. 8 Time histories of the spatial elastic deflections along the longitudinal centerline of the runway during take-off. The *broken line* shows the trajectory of the airplane

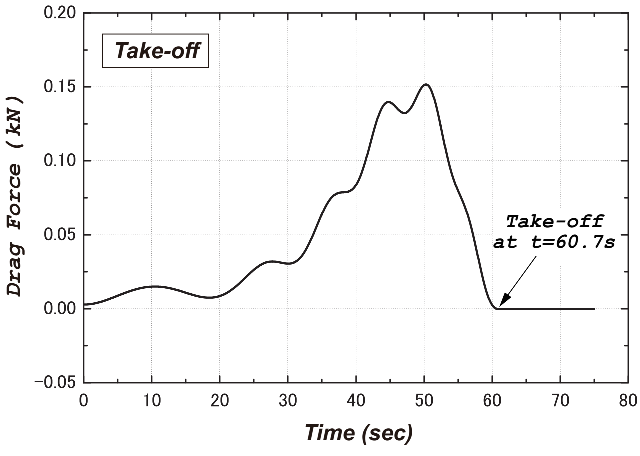

Fig. 9 Additional drag force on a taking-off airplane (The airplane takes off at $t = 60.7\,\mathrm{s}$)

jumbo jet. The calculation method is based on the time-domain mode-expansion method, taking account of memory effects in the hydrodynamic forces, which can be applied to any problem when the external force term on the right-hand side of the differential equation is modified in accordance with the problem being considered. Special care was paid to numerical accuracy in evaluating all the terms appearing in the differential equations.

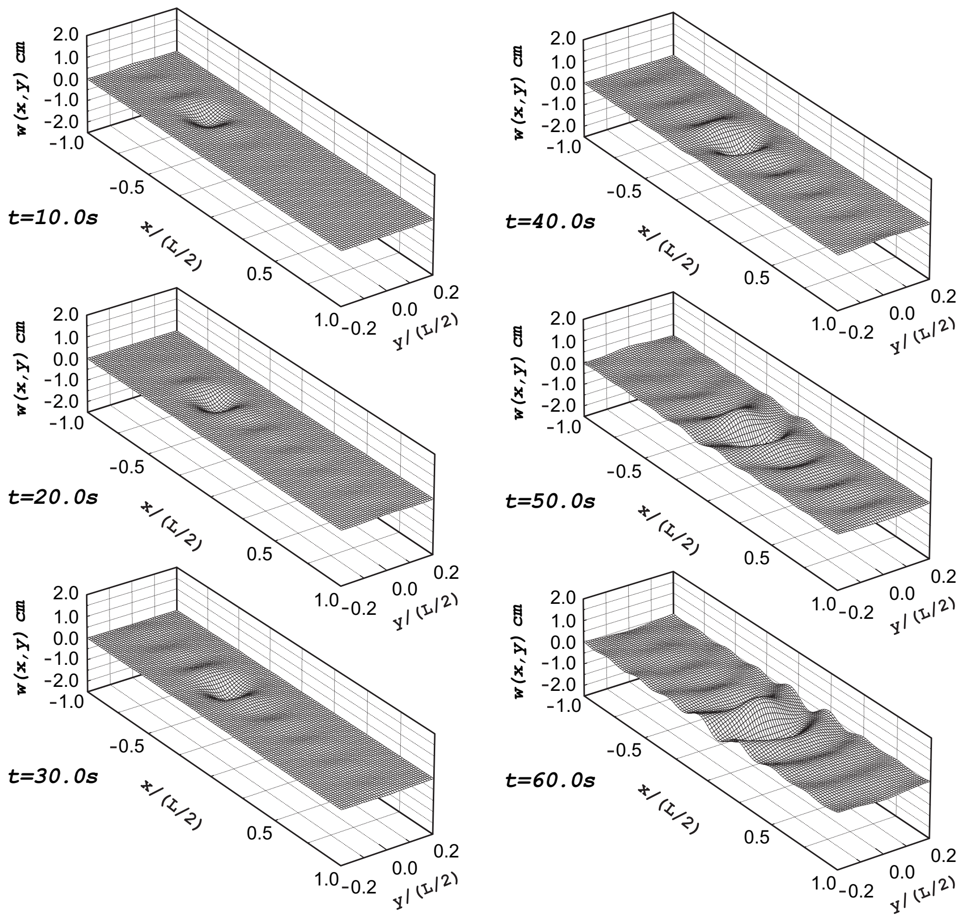

Fig. 10 Perspective view of the structural deflection during take-off of a Boeing 747-400

The computed results were shown, together with snapshots of the 3-D patterns of structural waves over the floating airport, the time-histories of the vertical deflection at several fixed positions, and the spatial deflection profiles along the longitudinal centerline of the structure at some time intervals. The additional drag forces on a moving load (as a model of the airplane) during landing and take-off due to the elastic deformation of the runway were also computed.

It was shown that the airplane moves faster than the generated waves in the early stage of landing, and that the waves overtake and are deformed due to the presence of the airplane as the speed of the airplane decreases to zero. In the case of take-off, the structural waves generated by the airplane develop slowly as the airplane accelerates in the early stages, and the propagation of generated waves is rather simple because there is no obstacle on the runway after the take-off of the airplane. It was confirmed that the drag force is at a maximum when the airplane is located on the up-slope of the dent made by the loading of airplane on an elastic runway, and that the magnitude of this drag force may be negligible for the VLFS considered in this study.

References

[1] Kashiwagi M (2000) Research on Hydrodynamic Responses of VLFS: Recent Progress and Future Work. J Offshore and Polar Engineering, Vol 10, No 2, pp 81-90

[2] Watanabe E and Utsunomiya T (1996) Transient Response Analysis of a VLFS at Airplane Landing. Proceedings of the 2nd International Workshop on Very Large Floating Structures, Hayama, pp 243-247

[3] Kim JW and Webster WC (1996) The Drag of an Airplane Taking-off from a Floating Runway. Proceedings of the 2nd International Workshop on Very Large Floating Structures, Hayama, pp 235-241

[4] Yeung RW and Kim JW (1998) Structural Drag and Deformation of a Moving Load on a Floating Plate. Proceedings of the 2nd International Conference on Hydroelasticity in Marine Technology, Fukuoka, pp 77-88

[5] Ohmatsu S (1998) Numerical Calculation of Hydroelastic Behavior of VLFS in Time Domain. Proceedings of the 2nd International Conference on Hydroelasticity in Marine Technology, Fukuoka, pp 89-97

[6] Endo H and Yago K (1999) Time History Response of a Large Floating Structure Subjected to Dynamic Load (in Japanese). J Soc Nav Archit Japan, Vol 186, pp 369-376

[7] Endo H (2000) The Behavior of a VLFS and Airplane During Takeoff/Landing Run in Wave Condition. Marine Structure, Vol 13, pp 477-491

[8] Shin H, *et al.* (2001) Hydroelastic Response Simulation of a VLFS in Irregular Waves Considering Taking-off and Landing Impact. Proceedings of the 20th International Conference on Offshore Mechanics and Arctic Engineering (OMAE), Rio de Janeiro

[9] Kashiwagi M (2000) A Time-Domain Mode-Expansion Method for Calculating Transient Elastic Responses of a Pontoon-Type VLFS. J Marine Science and Technology, Vol 5, pp 89-100

[10] Cummins WE (1962) The Impulse Response Function and Ship Motions. Schiffstechnik, Vol 9, pp 101-109

[11] Kashiwagi M (1998) A B-Spline Galerkin Scheme for Calculating the Hydroelastic Response of a Very Large Floating Structure in Waves. J Marine Science and Technology, Vol 3, pp 37-49

[12] Kashiwagi M (1999) A Time-Domain Green Function Method for Transient Problems of a Pontoon-Type VLFS. Proceedings of the 3rd International Workshop on Very Large Floating Structures, Honolulu, Vol 1, pp 97-104

[13] Bessho M (1992) Hydrodynamic Forces Acting on an Oscillating 2-D Shallow Draft Ship Advancing with a Constant Speed. Memories of National Defence Academy, Vol 30, No 1, pp 41-49

[14] Takarada N (1982) Technology Assessment of VLFS (Part 5) (in Japanese). Bulletin of Soc Nav Archit Japan, No 642, pp 20-37

Wave Drift Force and Moment on VLFS Supported by a Great Number of Floating Columns*

Masashi KASHIWAGI and Shogo YOSHIDA
Research Institute for Applied Mechanics, Kyushu University
Kasuga, Fukuoka 816-8580, Japan

ABSTRACT

A calculation method is presented of the wave-induced steady drift force and yaw moment on a very large floating structure (VLFS) comprising a multitude of floating columns. The theory is based on the momentum-conservation principle, and all necessary integrations are analytically implemented. Thus the resultant formulae include only the coefficients of the incident-wave and disturbance potentials at a large distance from the structure. A hierarchical interaction theory developed by Kashiwagi (1998) is applied to determine the disturbance potential due to hydrodynamic interactions among a great number of floating columns and elastic motions of a thin upper deck. Experiments in head waves were also conducted using 64 truncated vertical cylinders arranged periodically in 4 rows and 16 columns. Good agreement is found between computed and measured results. Furthermore, through numerical computations in oblique waves, discussions are made on variation characteristics of the steady force and yaw moment particularly around frequencies corresponding to the near-trapping.

Keywords: Drift force and moment, hydrodynamic interactions, momentum-conservation principle, elastic motion, near-trapped mode.

1. INTRODUCTION

Very large floating structures (VLFSs) are categorized with the configuration under the sea level into: (1) a pontoon type which looks like a simple plate with very shallow draft, and (2) a column-supported type in which a thin upper deck is supported by a large number of floating columns. It is said that the pontoon type is advantageous in low costs for construction and maintenance, but the wave-induced motions may be relatively large. On the other hand, the column-supported type has reverse features; that is, the motions in waves may be small relative to the pontoon type, because incident waves will transmit through a gap between columns.

The above position may not be the case, however. Recent study, including experiments (Kashiwagi *et al.*, 2000) on hydrodynamic interactions among many cylinders, reveals that near-resonant modes occur at some critical frequencies and cause large wave forces on each element of the array. According to Maniar and Newman (1997), these critical frequencies are eigen-frequencies in the diffraction problem, at which homogeneous solutions exist, and their existence depends on the number of cylinders and the ratio of cylinder diameter and separation distance between adjacent cylinders. Since the waves amplified at these frequencies have characteristics very similar to the trapped modes observed in a long wave channel

∗ *Reprinted from International Journal of Offshore and Polar Engineering, Vol. 11, No. 3, pp. 176–183, 2001 (September)*

containing cylinders along the centerline of the channel (e.g. Evans and Porter, 1997), these waves are called near-trapping waves.

It is known that the reflection and transmission of incident waves are related closely to the wave drift force through the momentum-conservation principle. In the limit of very short wavelength, the drift force will be of the same value irrespective of the pontoon or column-supported types of structure, because almost all of the wave will be reflected. Around frequencies of near-trapping, however, no information is given concerning how the wave drift force varies. Furthermore, few studies have been made on the drift yaw moment acting on a column-supported type VLFS.

The steady drift force and moment can be computed by either the near-field or far-field methods. The near-field method based on the direct pressure integration enables us to evaluate the forces on each column, but it is not effective for a VLFS consisting of a great number of columns. On the other hand, in the far-field method, it is doubtful that reliable results are given by a conventional method using numerical integrations with respect to the azimuth angle of the wave-amplitude function at a large distance from the structure.

Recently as an extension of existing interaction theories (e.g. Kagemoto and Yue, 1986; and Linton and Evans, 1990), a hierarchical interaction theory (Kashiwagi, 1998) was developed to compute hydrodynamic interactions among a great number of floating bodies. With this theory, the disturbance potential valid at a far field may be given in a simpler form in terms of a cylindrical coordinate system. In this case, all necessary integrations can be analytically performed, hence accurate results can be expected, provided that enough numbers of terms are retained in a series expansion.

In the present paper, the diffraction and radiation problems are solved by employing the hierarchical interaction theory, and an analytical expression is derived for the disturbance velocity potential valid at a far field. The effects of elastic motions of the upper deck are also taken into account as the generalized radiation problems. Applying orthogonal relations of the Fourier series to integrals in the circumferential direction and Wronskian formulae to some products of Bessel functions, simple calculation formulae are derived for the drift force in the horizontal plane and the drift yaw moment.

Experiments are also conducted in the present study using 64 truncated circular cylinders arranged in a rectangular array of 4 rows and 16 columns with equal-separation distance. Measured results in head waves are compared with corresponding results of the computation. In particular, cautious measurements and computations are conducted at frequencies around near-resonant modes, and discussions are made on variation characteristics of the wave drift force and moment.

2. FORMULATION

We consider a VLFS with a thin deck and a great number of identical and equally spaced buoyancy columns. As shown in Fig. 1, the deck is rectangular in plan, with length L and width B. The geometry of an elementary column considered here is a truncated circular cylinder with horizontal base, with radius a and draft d. The centerlines of adjacent cylinders are separated by a distance $2s$ in both x and y axes of a Cartesian coordinate system, where $z = 0$ is the plane of the undisturbed free surface and the water depth is constant at $z = h$.

Under the assumption of incompressible and inviscid flow with irrotational motion, we introduce the velocity potential satisfying the Laplace equation. The boundary conditions are linearized and all oscillatory quantities are assumed to be time-harmonic with circular

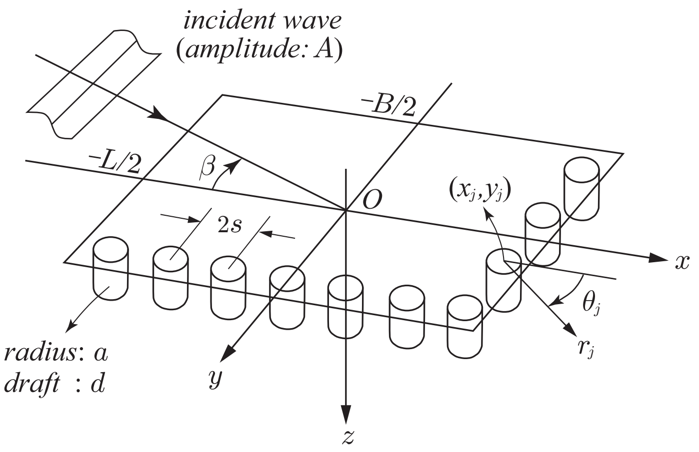

Fig. 1 Coordinate system and notations

frequency ω. Then, we express the velocity potential in the form:

$$\Phi = \mathrm{Re}\left[\, \phi(x, y, z)\, e^{i\omega t}\, \right] \tag{1}$$

$$\phi = \frac{gA}{i\omega}\left[\, \phi_I + \phi_S - K \sum_{k=1}^{\infty} \frac{X_k}{A} \left\{\, \phi_k + \varphi_k \,\right\} \right] \tag{2}$$

where g, A, and K are, respectively, the gravitational acceleration, the amplitude of an incident wave, and the wavenumber given by ω^2/g. ϕ_I and ϕ_S are the incident-wave and scattering potentials, respectively, and the sum $\phi_I + \phi_S \equiv \phi_D$ is referred to as the diffraction potential.

Incident plane waves propagate in the direction with angle β relative to the positive x-axis (see Fig. 1), and hence ϕ_I is given by:

$$\phi_I = \frac{\cosh k_0(z-h)}{\cosh k_0 h}\, e^{-ik_0(x\cos\beta + y\sin\beta)} \tag{3}$$

where $k_0 \tanh k_0 h = K$.

X_k in (2) denotes the complex amplitude of the k-th mode of motion in the radiation problem, which includes not only rigid-body motions but also a set of generalized modes to represent elastic deflections of a deck. ϕ_k is the velocity potential of a single body oscillating in the k-th mode (with no interactions) and φ_k represents the remaining part of the potential due to hydrodynamic interactions with radiated and scattered waves by the other cylinders.

3. HIERARCHICAL INTERACTION THEORY

The number of columns of a realistic VLFS will be in the order of more than several thousands. Hydrodynamic interactions among columns of this order may be taken into account by a hierarchical interaction theory developed recently by Kashiwagi (1998). In this hierarchical interaction theory, a number of actual bodies (labeled as level one) are grouped to form a fictitious body (level two), and several fictitious bodies are grouped further to form a bigger fictitious body (level three). This procedure can be repeated theoretically up to any hierarchical level. Then, the interactions are computed at each level, and information on interactions can be transmitted upward or downward as required.

At the highest level, the number of fictitious bodies may be in the order of several tens, to which existing interaction theories can be applied (e.g. Kagemoto and Yue, 1986, and Linton and Evans, 1990). Since the present paper is concerned with a general calculation method which can be applied to arbitrary-shaped columns with footing, the Kagemoto and Yue theory is adopted. It is a premise in their theory that the diffraction characteristics of a fictitious body in response to a set of generalized incident waves are known. For details of the analysis, we refer the reader to Kashiwagi (1998). In the present paper, with the assumption that the diffraction characteristics of a body at the highest level (denoted as ℓ) are already obtained, the calculation method of hydrodynamic interactions at the highest level is summarized.

In the analysis to follow, we will use a local cylindrical coordinate system (r_j, θ_j, z), with the origin placed at (x_j, y_j, 0), i.e. the center of the j-th fictitious body. The number of bodies at level ℓ is denoted as N_ℓ, which is, needless to say, identical to N_B (the number of actual columns) in the case of no hierarchical level.

3.1 Diffraction Problem

The incident waves impinging upon a fictitious body i consist not only of the wave expressed by (3) coming from the outside, but also of scattered waves due to other fictitious bodies. Thus we can write:

$$\begin{aligned}
\phi_{I,\ell}^{i} &= \{a^i\}^T \{\psi_{I,\ell}^{i}\} + \sum_{\substack{j=1 \\ j\neq i}}^{N_\ell} \{A_{S,\ell}^{j}\}^T \{\psi_{S,\ell}^{j}\} \\
&= \Big(\{a^i\}^T + \sum_{\substack{j=1 \\ j\neq i}}^{N_\ell} \{A_{S,\ell}^{j}\}^T \big[\, T_{ji}^{\ell} \,\big] \Big) \{\psi_{I,\ell}^{i}\}
\end{aligned} \tag{4}$$

Here $\{\psi_{I,\ell}^{i}\}$ and $\{\psi_{S,\ell}^{j}\}$ are the vectors of the generalized incident-wave and scattering potentials, respectively, which are expressed as:

$$\{\psi_I^i\} = \left\{ \begin{array}{l} Z_0(z)\, J_p(k_0 r_i)\, e^{-ip\theta_i} \\ Z_n(z)\, I_p(k_n r_i)\, e^{-ip\theta_i} \end{array} \right\} \tag{5}$$

$$\{\psi_S^j\} = \left\{ \begin{array}{l} Z_0(z)\, H_m^{(2)}(k_0 r_j)\, e^{-im\theta_j} \\ Z_n(z)\, K_m(k_n r_j)\, e^{-im\theta_j} \end{array} \right\} \tag{6}$$

where:

$$Z_0(z) = \frac{\cosh k_0(z-h)}{\cosh k_0 h}, \;\; Z_n(z) = \frac{\cos k_n(z-h)}{\cos k_n h} \tag{7}$$

and k_n is a solution of $k_n \tan k_n h = -K$ ($n = 1, 2, \cdots$), giving the wavenumber of evanescent wave modes. The number of terms in the θ-direction, p and m, must be taken as $0, \pm 1, \pm 2, \cdots$.

The coefficient vector of the incident wave, $\{\, a^i \,\}$, is known and may be explicitly given by expressing (3) in terms of a cylindrical coordinate system of the i-th body. Meanwhile, $[\, T_{ji}^{\ell} \,]$ is the coordinate transformation matrix, relating $\{\psi_{S,\ell}^{j}\}$ with $\{\psi_{I,\ell}^{i}\}$, a concrete expression of which can be given by Graf's addition theorem for Bessel functions.

Let the diffraction characteristics matrix corresponding to $\{\psi_{I,\ell}^i\}$ of a fictitious body be expressed as $[\,\mathcal{B}_{i,\ell}\,]$. Then the scattering potential due to (4) can be obtained in the form:

$$\begin{aligned}\phi_{S,\ell}^i &= \Big(\{a^i\}^T + \sum_{\substack{j=1\\j\neq i}}^{N_\ell}\{A_{S,\ell}^j\}^T[\,T_{ji}^\ell\,]\Big)[\,\mathcal{B}_{i,\ell}\,]^T\{\psi_{S,\ell}^i\}\\ &= \{A_{S,\ell}^i\}^T\{\psi_{S,\ell}^i\}\end{aligned} \tag{8}$$

From this relation, the unknown coefficient vector of the scattering potential, $\{A_{S,\ell}^i\}$, can be determined. Resulting simultaneous equations for all fictitious bodies are:

$$\{A_{S,\ell}^i\} - [\,\mathcal{B}_{i,\ell}\,]\sum_{\substack{j=1\\j\neq i}}^{N_\ell}[\,T_{ji}^\ell\,]^T\{A_{S,\ell}^j\} = [\,\mathcal{B}_{i,\ell}\,]\{a^i\}\,, \quad \text{for } \ i = 1 \sim N_\ell \tag{9}$$

Solving (9) completes the flow field at the highest level. By transmitting the information on hydrodynamic interactions down to lower levels, the flow field around actual bodies may be determined, hence the wave forces on floating columns of a VLFS can be computed.

3.2 Radiation Problem

The body boundary condition for the j-th actual body is given in the following form:

$$\frac{\partial\phi_k^j}{\partial n} = n_k^j\,, \quad \frac{\partial\varphi_k^j}{\partial n} = 0 \tag{10}$$

where n_k^j denotes the k-th component of normal vector on the j-th body.

As already described, then, ϕ_k is a solution of the radiation problem for a single body and φ_k is a solution of a sort of the diffraction problem due to radiated and scattered waves by the other bodies.

As a result of forced oscillations of each body and hydrodynamic interactions among other bodies at the same hierarchical level, the radiation potential of a fictitious body i at level ℓ can be given in the form:

$$\phi_{k,\ell}^j = \{\mathcal{R}_{k,\ell}^j\}^T\{\psi_{S,\ell}^j\} \tag{11}$$

where $\{\mathcal{R}_{k,\ell}^j\}$ may be explicitly given by transmitting the information on hydrodynamic interactions upward to a fictitious body at level ℓ.

On the other hand, a solution of $\varphi_{k,\ell}^j$ can be determined in the same way as the diffraction problem and given as:

$$\varphi_{k,\ell}^j = \{A_{k,\ell}^j\}^T\{\psi_{S,\ell}^j\} \tag{12}$$

where $\{A_{k,\ell}^j\}$ is the unknown coefficient vector.

When viewed from the i-th body, (11) and (12) may be regarded as incident waves, so contributions from all other bodies at level ℓ can be written as:

$$\varphi_{I,\ell}^i = \sum_{\substack{j=1\\j\neq i}}^{N_\ell}\Big(\{\mathcal{R}_{k,\ell}^j\}^T + \{A_{k,\ell}^j\}^T\Big)[\,T_{ji}^\ell\,]\{\psi_{I,\ell}^i\} \tag{13}$$

This velocity potential corresponds to (4) in the diffraction problem. Thus in the same way as in obtaining (9), one can obtain a linear system of simultaneous equations for $\{A^i_{k,\ell}\}$ in the following form:

$$\{A^i_{k,\ell}\} - \left[\mathcal{B}_{i,\ell}\right] \sum_{\substack{j=1 \\ j\neq i}}^{N_\ell} \left[T^\ell_{ji}\right]^T \{A^j_{k,\ell}\} = \left[\mathcal{B}_{i,\ell}\right] \sum_{\substack{j=1 \\ j\neq i}}^{N_\ell} \left[T^\ell_{ji}\right]^T \{\mathcal{R}^j_{k,\ell}\}, \quad \text{for} \quad i = 1 \sim N_\ell \tag{14}$$

It is noteworthy that the left-hand sides of (9) and (14) are exactly the same and can thus be solved at the same time.

Using the above results for the radiation problem, the added-mass and damping coefficients for all modes of motion will be computed. Then, by solving the motion equation of a thin upper deck, the complex amplitude X_k appearing in (2) will be determined.

3.3 Velocity Potential at Far Field

Substituting (8), (11) and (12) into (2), all but ϕ_I in brackets of (2) (which are denoted as ϕ_B) may be expressed in the form:

$$\left.\begin{aligned} \phi_B &= \sum_{j=1}^{N_\ell} \{\mathcal{A}^j_\ell\}^T \{\psi^j_{S,\ell}\} \\ \{\mathcal{A}^j_\ell\} &= \{A^j_{S,\ell}\} - K \sum_{k=1}^{\infty} \frac{X_k}{A} \Big(\{\mathcal{R}^j_{k,\ell}\} + \{A^j_{k,\ell}\} \Big) \end{aligned} \right\} \tag{15}$$

As a next step to obtain the wave drift force and moment by means of the momentum-conservation principle, we need to rewrite the above expression with the global coordinate system O-xyz (or equivalently O-$r\theta z$).

At a large distance from the structure, evanescent wave components decay, and thus we can consider only the progressive wave components (i.e. the Hankel function of the 2nd kind) in the vector expressed as $\{\psi^j_{S,\ell}\}$.

Equations expressed with a cylindrical coordinate system of the j-th body must be rewritten in terms of the global coordinate system O-$r\theta z$. For that purpose, using notations shown in Fig. 2 and noting that $r \gg L_{j0}$ at a far field from a structure, Graf's addition theorem gives the following:

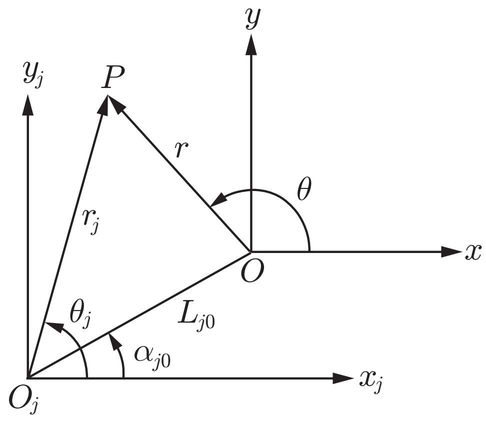

Fig. 2 Symbols in coordinate transformation

$$H^{(2)}_m(k_0 r_j)\, e^{-im\theta_j} = \sum_{p=-\infty}^{\infty} J_{m-p}(k_0 L_{j0})\, e^{-i(m-p)\alpha_{j0}} \left\{ H^{(2)}_p(k_0 r)\, e^{-ip\theta} \right\} \tag{16}$$

This relation can be expressed in a matrix form as follows:

$$\{\psi^j_{S,\ell}\} = \left[M^\ell_{j0}\right] \{\psi_S\} \tag{17}$$

Substituting the above into (15), one can obtain an expression for ϕ_B:

$$\phi_B = \sum_{j=1}^{N_\ell} \{\mathcal{A}_\ell^j\}^T \big[\, M_{j0}^\ell \,\big] \{\psi_S\} \equiv \{\mathcal{A}_\ell\}^T \{\psi_S\} \tag{18}$$

where:

$$\{\mathcal{A}_\ell\} = \sum_{j=1}^{N_\ell} \big[\, M_{j0} \,\big]^T \Big[\{A_{S,\ell}^j\} - K \sum_{k=1}^{\infty} \frac{X_k}{A} \Big(\{\mathcal{R}_{k,\ell}^j\} + \{A_{k,\ell}^j\} \Big) \Big] \tag{19}$$

Let us express the components of the above vector $\{\mathcal{A}_\ell\}$ as A_m ($m = 0, \pm 1, \pm 2, \cdots$). Then, as is clear from (16), the vector $\{\psi_S\}$ comprises only the Hankel function. Hence ϕ_B in (18) can be written in a simpler form:

$$\phi_B = \sum_{m=-\infty}^{\infty} A_m \big\{ Z_0(z)\, H_m^{(2)}(k_0 r)\, e^{-im\theta} \big\} \tag{20}$$

On the other hand, with the global cylindrical coordinate system, the incident-wave potential expressed by (3) may be written as:

$$\phi_I = \sum_{m=-\infty}^{\infty} \alpha_m \big\{ Z_0(z)\, J_m(k_0 r)\, e^{-im\theta} \big\} \tag{21}$$

where

$$\alpha_m = e^{im(\beta - \pi/2)} \tag{22}$$

Noting that the sum of (20) and (21) gives the total velocity potential in brackets of (2), we can write $\phi(x, y, z)$ as valid at a far field in the following form:

$$\phi = \frac{gA}{i\omega} \sum_{m=-\infty}^{\infty} Z_0(z) \Big\{ \alpha_m J_m(k_0 r) + A_m H_m^{(2)}(k_0 r) \Big\}\, e^{-im\theta} \tag{23}$$

In a special case of bottom-mounted vertical circular cylinders, Linton and Evans (1990) showed that (23) can be reduced further to a compact expression by use of Wronskian relations for Bessel functions.

4. WAVE DRIFT FORCE AND MOMENT

Following Maruo (1960) and Newman (1967), let us derive calculation formulae for the wave drift forces in the horizontal plane and the drift yaw moment on the basis of the conservation principle of linear and angular momenta. A notable feature in the present paper is to perform all necessary integrations analytically using (23).

Firstly, let us consider the time-averaged steady force acting in the x-axis. Retaining quadratic terms in the velocity potential and taking time average over one period, an expression for the steady force can be obtained in the form:

$$\begin{aligned} \overline{F}_x =& -\frac{\rho}{2} \int_0^h dz \int_0^{2\pi} \Big[\mathrm{Re}\Big\{ \frac{\partial \phi}{\partial x} \frac{\partial \phi^*}{\partial r} \Big\} - \frac{1}{2} \nabla\phi \nabla\phi^* \cos\theta \Big]\, r d\theta \\ & -\frac{\rho}{4} K \int_0^{2\pi} \phi\, \phi^* \Big|_{z=0} r \cos\theta\, d\theta \end{aligned} \tag{24}$$

where ϕ^* denotes the complex conjugate of ϕ.

Since the integrals in (24) are to be evaluated for large values of r, we can discard the terms decaying as $r \to \infty$. Taking this into account and performing the integral with respect to z, it follows that:

$$\overline{F}_x = -\frac{\rho}{8C_0} \int_0^{2\pi} \Big[\frac{\partial \phi}{\partial r} \frac{\partial \phi^*}{\partial r} + k_0^2 \, \phi \, \phi^* \Big]_{z=0} r \cos\theta \, d\theta \tag{25}$$

where

$$C_0 = \frac{k_0^2}{K + h(k_0^2 - K^2)} \tag{26}$$

The wave drift force in the y-axis can be analyzed in the same manner, and the expression corresponding to (25) is given by:

$$\overline{F}_y = -\frac{\rho}{8C_0} \int_0^{2\pi} \Big[\frac{\partial \phi}{\partial r} \frac{\partial \phi^*}{\partial r} + k_0^2 \, \phi \, \phi^* \Big]_{z=0} r \sin\theta \, d\theta \tag{27}$$

As shown by Newman (1967), the wave drift moment about the z-axis can be evaluated by applying the conservation principle of angular momentum. This gives the following expression:

$$\overline{M}_z = -\frac{\rho}{4C_0} \,\mathrm{Re} \int_0^{2\pi} \frac{\partial \phi}{\partial \theta} \frac{\partial \phi^*}{\partial r} \Big|_{z=0} r \, d\theta \tag{28}$$

To perform integrations with respect to θ in (25), (27) and (28), we substitute (23) and use orthogonal relations in trigonometric functions given as:

$$\left.\begin{aligned} &\int_0^{2\pi} e^{-im\theta} \, e^{in\theta} \, d\theta = 2\pi \, \delta_{m,n} \\ &\int_0^{2\pi} e^{-im\theta} \, e^{in\theta} \cos\theta \, d\theta = \pi \, \delta_{m,n\pm1} \\ &\int_0^{2\pi} e^{-im\theta} \, e^{in\theta} \sin\theta \, d\theta = \mp \pi i \, \delta_{m,n\pm1} \end{aligned}\right\} \tag{29}$$

Here $\delta_{m,n}$ is Kroenecker's delta, equal to 1 when $m = n$ and zero otherwise.

Noting that $Z_0(z) = 1$ at $z = 0$, the result after applying (29) to (25) takes the form:

$$\begin{aligned} \overline{F}_x = -\frac{\rho g A^2}{4} \frac{k_0}{C_0 K} \,\mathrm{Re} \sum_{m=-\infty}^{\infty} \pi k_0 r \\ \times \Big[\big\{ \alpha_m J_m' + A_m H_m^{(2)\prime} \big\} \big\{ \alpha_{m+1}^* J_{m+1}' + A_{m+1}^* H_{m+1}^{(1)\prime} \big\} \\ + \big\{ \alpha_m J_m + A_m H_m^{(2)} \big\} \big\{ \alpha_{m+1}^* J_{m+1} + A_{m+1}^* H_{m+1}^{(1)} \big\} \Big] \end{aligned} \tag{30}$$

The above equation can be transformed further using the formulae of Wronskians given by:

$$\left.\begin{aligned} &J_m' J_{m+1}' + J_m J_{m+1} = 0 \\ &J_m' H_{m+1}^{(1)\prime} + J_m H_{m+1}^{(1)} = -\frac{2i}{\pi k_0 r} \\ &H_m^{(2)\prime} H_{m+1}^{(1)\prime} + H_m^{(2)} H_{m+1}^{(1)} = -\frac{4i}{\pi k_0 r} \\ &H_m^{(2)\prime} J_{m+1}' + H_m^{(2)} J_{m+1} = -\frac{2i}{\pi k_0 r} \end{aligned}\right\} \tag{31}$$

Then the final result for the wave drift force along the x-axis can be obtained in the form:

$$\overline{F}_x = -\frac{\rho g A^2}{2} \frac{k_0}{C_0 K} \, \mathrm{Im} \sum_{m=-\infty}^{\infty} \left[2A_m A_{m+1}^* + \alpha_m A_{m+1}^* + A_m \alpha_{m+1}^* \right] \tag{32}$$

With almost the same transformation, the calculation formula for the drift force along the y-axis may be given in the form:

$$\overline{F}_y = -\frac{\rho g A^2}{2} \frac{k_0}{C_0 K} \, \mathrm{Re} \sum_{m=-\infty}^{\infty} \left[2A_m A_{m+1}^* + \alpha_m A_{m+1}^* + A_m \alpha_{m+1}^* \right] \tag{33}$$

Concerning the steady yaw moment given by (28), substitution of (23) and implementation of necessary calculations using (29) gives the following:

$$\overline{M}_z = -\frac{\rho g A^2}{2} \frac{\pi k_0 r}{C_0 K} \sum_{m=-\infty}^{\infty} m \Big[A_m A_m^* + \mathrm{Re}\big(\alpha_m A_m^*\big) \Big] \big(J_m Y_m' - J_m' Y_m \big) \tag{34}$$

Here Y_m denotes the second kind of Bessel function of order m, and the following formula of Wronskian exists:

$$J_m Y_m' - J_m' Y_m = \frac{2}{\pi k_0 r} \tag{35}$$

Substituting this formula in (34) gives the final expression for the steady yaw moment in the form:

$$\overline{M}_z = -\rho g A^2 \frac{1}{C_0 K} \sum_{m=-\infty}^{\infty} m \Big[A_m A_m^* + \mathrm{Re}\big(\alpha_m A_m^*\big) \Big] \tag{36}$$

It should be noted that (32), (33) and (36) include only the coefficients of the disturbance potential due to floating columns, A_m, and of the incident-wave potential, α_m, explicitly given by (22). These formulae are one of the important results in the present paper. We can see that the steady drift force and moment consist of quadratic terms in the disturbance and cross terms between the incident wave and the disturbance.

5. OUTLINE OF EXPERIMENTS

Although the calculation method above is intended for a VLFS supported by a great number of floating columns, experiments were conducted with 64 equally spaced cylinders because of limitations in the tank size and other facilities.

As shown in Fig. 3, an elementary body is a circular cylinder with a horizontal base and its diameter ($D = 2a$) is 114 mm. This cylinder was placed in a periodic array with 4 rows times 16 columns. The separation distance between the centerlines of adjacent cylinders is denoted as $2s$, and the experimental setting was such that $s = D$ in both x and y axes and $\beta = 0°$ (i.e. head waves only).

In this experiment, motions were completely fixed and, as shown in Fig. 3, the x and z components of the wave force were measured by dynamometers at two different positions. The draft of the cylinders was set to $d = 2D$, considering the capacity of the dynamometers used.

The experiments were carried out at the Ocean Engineering Model Basin (length 65 m, breadth 5 m, water depth 7 m) of the Research Institute for Applied Mechanics at Kyushu University. The steepness of regular waves (the ratio of wave height with wave length, H/λ)

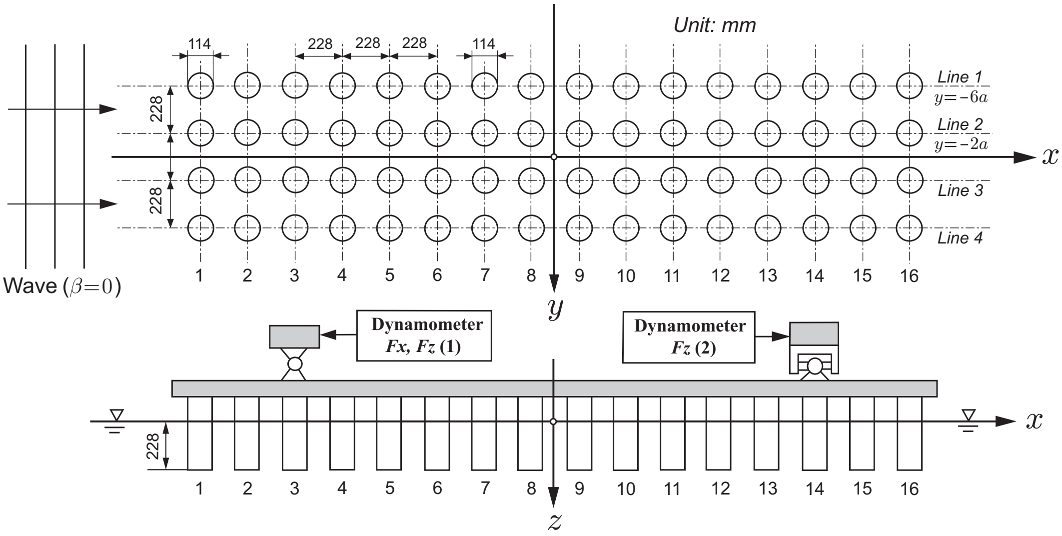

Fig. 3 Arrangement of 64 truncated cylinders fixed in head waves and measurement system

was set approximately equal to 1/50. The circular wave frequency ω $(=\sqrt{gK})$ was changed in the range of $Ks = 0.2\sim1.6$, considering that an important parameter in hydrodynamic interactions is Ks $(= 2\pi s/\lambda)$. Measured data were analyzed using an ordinary Fourier-analysis technique, from which the wave drift force in the x axis was obtained in addition to the linear wave-exciting forces in the x and z axes oscillating with circular frequency ω.

6. RESULTS AND DISCUSSION

6.1 Outline of Numerical Computations

Computations corresponding to the experiments with 64 columns can be performed without introducing hierarchical levels. That is, $\ell = 1$ and thus $N_\ell = N_B = 64$.

In actual computations, the number of Fourier series in the θ-direction (M) and of evanescent wave modes (N) must be finite. In the present paper, $M = 4$ and $N = 3$ are chosen after convergence checks for $Ks = 1.0$, $\beta = 0°$ and $h = 3d$, for which five decimal absolute accuracy has been achieved.

The number of total unknowns for $M = 4$, $N = 3$, and $N_B = 64$ is $(2M + 1) \times (N + 1) \times N_B = 2304$. Because the computation time in this case may be very long, if detailed computations must be carried out at many frequencies, double symmetries with respect to the x and y axes are exploited, which can reduce the number of unknowns to 1/4 (i.e. 2304/4=576).

When computing the coefficients of disturbance potential due to floating cylinders given by (19), we must compute the transformation matrix $[\,M_{j0}^{\ell}\,]$ defined by (17). As shown by (16), the elements in this matrix comprise Bessel functions. The convergence rate in the series expansion of (16) is very slow. It is found by pilot computations that the value of p (terms on the right-hand side) must be over 6 times the value of m (terms on the left-hand side) for obtaining sufficiently converged results. For example, in the case of $M = 4$ $(2M + 1 = 9)$, the number of terms in $\{\psi_S\}$ and thus $\{\mathcal{A}_\ell\}$ will be $P = 6M = 24$ $(2P + 1 = 49)$. In this paper, all computations have been performed with $P = 8M$, i.e. $2P + 1 = 65$, to ensure accurate results even in high frequencies.

6.2 Linear Wave-Exciting Force

To confirm validity of the present calculation method, the results of linear wave-exciting forces acting on 64 cylinders are shown in Figs. 4 and 5.

Figure 4 is concerned with the surge exciting force. In the frequency range less than $Ks \simeq 1.2$, we can see regular fluctuation due to hydrodynamic interactions. On the other hand, at frequencies higher than $Ks \simeq 1.2$, the variation pattern changes, which is also clear from the phase difference.

In fact, measurements of the wave elevation along the centerline of the present model reveals that approximately $Ks = 1.24$ corresponds to the frequency of the near-trapped mode of the Neumann type, discussed by Maniar and Newman (1997) (although the results supporting this fact are not shown here). Wave forces on each cylinder also change drastically near this critical frequency.

Figure 5 shows the heave exciting force. As the frequency increases, the amplitude of the force becomes very small, because variation in the pressure may be confined to the vicinity of the free surface, not contributing to the vertical force. However, variation in the phase tells us that a rapid change occurs near $Ks = 1.24$, corresponding to a near-trapped mode frequency.

At any rate, it can be said that the overall agreement is satisfactory between experiments and computations.

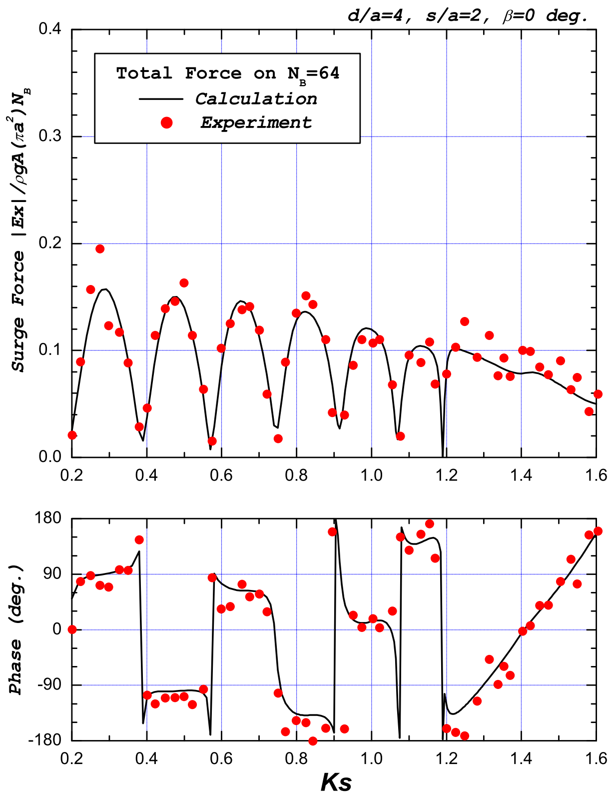

Fig. 4 Wave-exciting force in surge on 64 cylinders

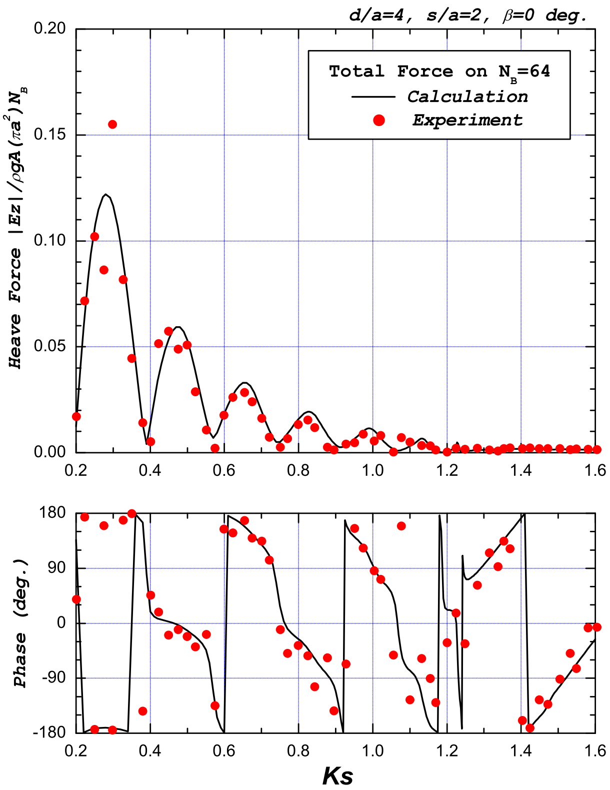

Fig. 5 Wave-exciting force in heave on 64 cylinders

6.3 Drift Force in Head Waves

Figure 6 shows the drift force in the x axis in head waves ($\beta = 0°$), which is nondimensionalized in terms of the wave-energy density of a regular wave ($0.5\rho g A^2$) and the projected length of cylinders along the y axis (the diameter times the number of cylinders in the y-axis $= D \times N_{BY} = 0.456$ m).

Measured results scatter somewhat, probably because of difficulty in measuring small physical quantities with the apparatus shown in Fig. 3. However, repeatability of the results in the Fourier analysis by changing the analyzing section was fairly good. In determining the analyzing section from the measured time histories, enough care was paid to the detection of the effect of reflection waves from the side walls of model basin. We can see from Fig. 6 that, at least in order and qualitatively, the results agree favorably with computed results.

In lower frequencies, measured results are obviously higher than the calculation, which may be attributed to viscous effects not included in the present theory. In the frequencies less than $Ks \simeq 1.24$ corresponding to the near-trapped mode, we can see regular variation of hump and hollow with increasing amplitude.

In contrast, for frequencies higher than $Ks \simeq 1.24$, the variation pattern changes and relatively large drift force can be seen. This is because the drift force is related closely to the reflection of incident waves, and the reflection in high frequencies becomes large due

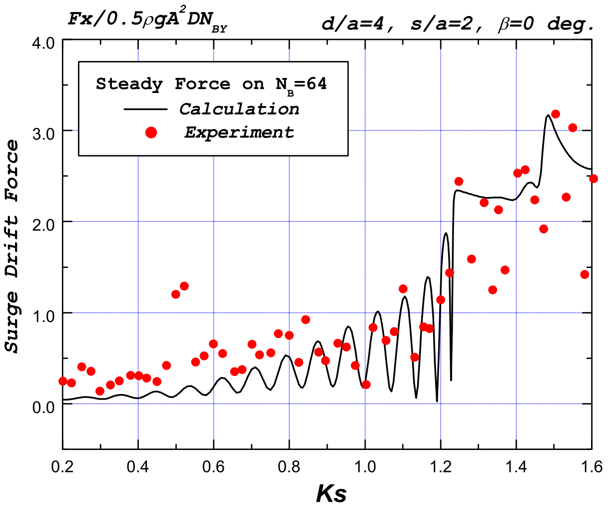

Fig. 6 Steady drift force in surge on 64 cylinders

to sheltering effects by a large number of cylinders, especially at frequencies higher than a trapped mode.

6.4 Drift Force and Moment in Oblique Waves

Although there are no measured results for comparison, numerical computations have been performed for oblique waves to understand variation tendency of the steady drift force and yaw moment as a function of incidence angle.

To increase the resolution, computations were made at 270 frequencies in the range of $Ks = 0.2 \sim 2.0$. Computed values are in fact shown by $\circ$ (open circle) for $\beta = 30°$, and by $\times$ (cross) for $\beta = 60°$ in Figs. 7∼9.

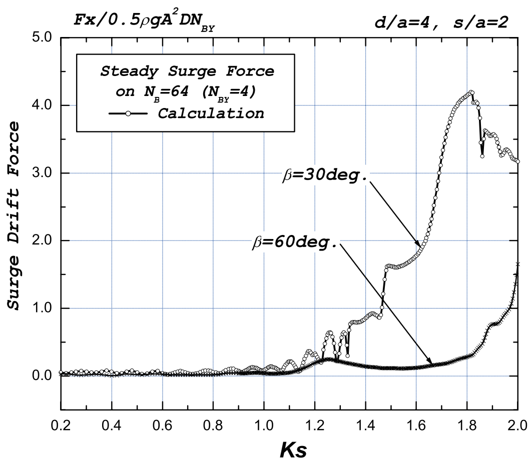

Fig. 7 Surge drift force on 64 cylinders in oblique waves

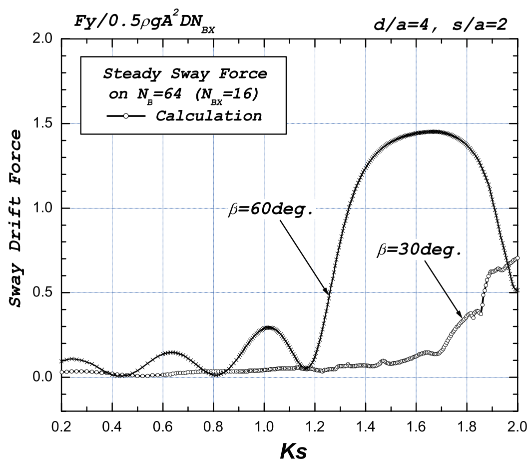

Fig. 8 Sway drift force on 64 cylinders in oblique waves

First, looking at the surge drift force ($\overline{F}_x$) for $\beta = 30°$, we can see that the amplitude of hump and hollow in lower frequencies decreases compared to the head-wave case, and a large drift force is predicted in higher frequencies. For $\beta = 60°$, occurrence of hump and hollow cannot be seen and the value itself is small; this is obviously because the waves reflected in the x axis are very small.

Second, looking at the sway drift force ($\overline{F}_y$), relatively slow variation can be seen for $\beta = 60°$ in lower frequencies. This is because the number of cylinders along the y axis is 1/4 of that along the x axis and thus the number of peaks due to hydrodynamic interactions may be small (approximately equal to 1/4). In higher frequencies, a large drift force is predicted over a somewhat wide range of the frequency around $Ks = 1.6$.

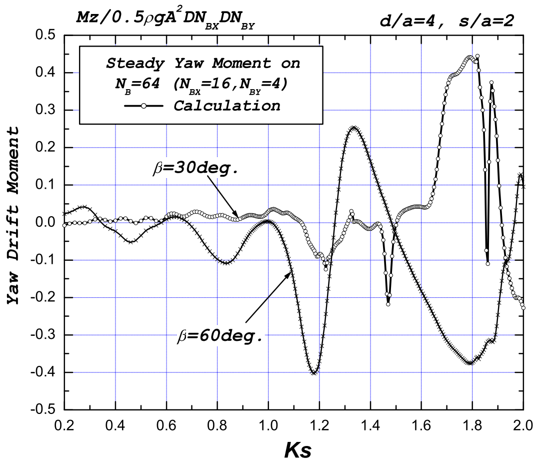

Fig. 9 Yaw drift moment on 64 cylinders in oblique waves

Finally, in the steady yaw moment ($\overline{M}_z$), we note that the moment becomes positive or negative for both $\beta = 30°$ and $60°$, depending on the value of Ks. Variation tendency for $\beta = 30°$ is similar to that of $\overline{F}_x$, and rapid changes are observed near $Ks = 1.47$ and 1.85. Meanwhile, for $\beta = 60°$, rapid variation is not observed, which is of the same feature as that of $\overline{F}_y$. These results may be understood by considering that the cylinders are arranged in 4 rows and 16 columns in the present case, hence hydrodynamic interactions along the x axis are more complicated than those along the y axis.

7. CONCLUDING REMARKS

A calculation method and numerical results have been demonstrated for the wave-induced steady drift force and moment on a great number of columns. The present theory is based on the conservation principle of linear and angular momenta. Thus, calculations of the force and moment can be made using the velocity potential valid at a far field and necessary integrations are analytically carried out. This greatly contributes to higher accuracy in numerical results.

A defect in the theory is that no information is given concerning the steady force on each column; that is, only the total force and moment can be computed. However, no matter how many columns are used, computation burden does not increase very much, because a hierarchical interaction theory can be applied and only the coefficients of disturbance potential at the highest hierarchical level are required in the calculation formulae derived in this paper.

Experiments were also conducted in head waves, using 64 circular cylinders arranged in equally separated 4 rows and 16 columns. Although somewhat experimental scatter exists, the overall agreement with computed results was good. Computations in oblique waves were performed, and the dependence of the wave incidence angle on the steady force and yaw moment was discussed.

Numerical results in this paper were just for the diffraction problem. However, it is easy to include the effects of motions of a structure, because necessary modification is to superimpose additional terms due to body motions onto the diffraction terms in evaluating the coefficient vector of the body disturbance potential.

ACKNOWLEDGMENT

The authors are indebted to Mr. Masaru Inada for his help in preparation of experiments shown in this paper.

REFERENCES

1 Evans, DV and Porter R (1997). "Trapped Modes about Multiple Cylinders in a Channel", *Journal of Fluid Mechanics*, Vol 339, pp 331–356.

2 Kashiwagi, M (1998). "Hydrodynamic Interactions among a Great Number of Columns Supporting a Very Large Flexible Structure", *Proc 2nd Intl Conf on Hydroelasticity*, Fukuoka, pp 165–176.

3 Kashiwagi, M and Yoshida, S (2000). "Hydrodynamic Interactions among Multiple Floating Cylinders in a Regular Arrangement", *Proc 15th Ocean Engineering Symp*, Soc of Nav Archit Japan, pp 231–238.

4 Linton, CM and Evans, DV (1990). "The Interaction of Waves with Arrays of Vertical Circular Cylinders", *Journal of Fluid Mechanics*, Vol 215, pp 549–569.

5 Maniar, HD and Newman, JN (1997). "Wave Diffraction by a Long Array of Cylinders", *Journal of Fluid Mechanics*, Vol 339, pp 309–330.

6 Maruo, H (1960). "The Drift of a Body Floating on Waves", *Journal of Ship Research*, Vol 4, pp 1–10.

7 Kagemoto, H and Yue, DKP (1986). "Interactions among Multiple Three-Dimensional Bodies in Water Waves: An Exact Algebraic Method", *Journal of Fluid Mechanics*, Vol 166, pp 189–209.

8 Newman, JN (1967). "The Drift Force and Moment on Ships in Waves", *Journal of Ship Research*, Vol 11, No 1, pp 51–60.

Wave-Induced Local Steady Forces on a Column-Supported Very Large Floating Structure*

Masashi KASHIWAGI
Research Institute for Applied Mechanics, Kyushu University
Kasuga, Fukuoka 816-8580, Japan

ABSTRACT

An accurate numerical calculation method is presented for the wave-induced steady forces and moments on each of the columns supporting a very large floating structure. The method is based on the direct integration of the pressure over the wetted surface of each column. First-order quantities needed in computing the pressure are determined by applying a higher-order boundary element method combined with the wave-interaction theory, taking into account the hydrodynamic interactions exactly within the linearized potential theory. The effects of motions of a structure are incorporated consistently up to the second-order in the wave amplitude. Experiments in head waves are also conducted using 64 truncated vertical cylinders arranged in a periodic array of 4 rows and 16 columns. Steady wave forces are measured at 6 different positions among 64 cylinders, and they are all in good agreement with computed results. Some characteristics in the variation tendency of the local steady forces are summarized.

Keywords: Drift force and moment, hydrodynamic interactions, pressure-integration method, trapped mode.

1. INTRODUCTION

A column-supported structure has been considered a possible type of very large floating structure (VLFS). This structure consists of a large number of floating columns which support a thin upper deck. By comparison with an alternative pontoon type which has been studied recently by many researchers (e.g. Kashiwagi, 1999, for a review), it is said that the column-supported type is advantageous in small motions in waves, because incident waves will transmit through a gap between columns. However, this recognition may not be true. For instance, according to Maniar and Newman (1997), near-trapped modes among many cylinders occur at some critical frequencies and exert large wave forces on each cylinder of the array. Their study is based on a simple geometry, where a large number of bottom-mounted circular cylinders are periodically placed along a single straight line. Hence no information is given on the near trapped-wave phenomena in a realistic array of columns and on the second-order wave drift force.

Recently, Kashiwagi (2000) presented a calculation method for the drift forces in the horizontal plane and the drift yaw moment on the basis of the momentum conservation principle. This method (referred to as the far-field method hereafter) is effective, because all necessary integrations over a control surface located far from the structure are analytically

∗ *Reprinted from International Journal of Offshore and Polar Engineering, Vol. 12, No. 2, pp.98–104, 2002 (June)*

performed using Graf ' s addition theorem and the Wronskian formulae for Bessel functions and the orthogonality of trigonometric functions to integrals in the circumferential direction. However, this method gives only the total force and moment acting on the structure.

Meanwhile, the steady drift forces can also be computed by integrating the pressure over the wetted surface of a structure and taking time average over a period. (Hereafter this method will be referred to as the pressure-integration method or the near-field method.) This pressure-integration method enables us to evaluate the local forces on each column, which is very useful in the analysis of structural strength and in the design of mooring systems. This paper is concerned with this pressure-integration method.

The wave drift force is a second-order steady force with respect to the wave amplitude, which can be obtained from quadratic products of first-order quantities. In this paper, the boundary-value problems for the first-order velocity potentials are solved using the Kagemoto and Yue wave-interaction theory (1986) combined with a higher-order boundary element method (HOBEM). Thus, hydrodynamic interactions among many columns are taken into account exactly in the framework of the potential theory. The resulting hydrodynamic forces and wave-induced motions of a structure are computed, with which the effects of body motions on the local steady forces are properly evaluated. In the pressure-integration method, spatial derivatives of the velocity potential and the wave elevation at the waterline must be computed. This is successfully performed with the 9-point isoparametric representation for the surface geometry and velocity potential. The validity and numerical accuracy of the present method are confirmed by comparing the sum of local steady forces with the drift force computed by the far-field method.

Experiments are also carried out using 64 identical circular cylinders with a horizontal base, arranged in a periodic array with 4 rows and 16 columns. Results of the steady wave forces measured at 6 selected positions are compared with corresponding numerical results. Good agreement is found between computed and measured results. Some characteristics of the local steady forces are noted, which are markedly different depending on the position of the cylinder in the array.

2. FORMULATION AND SECOND-ORDER FORCES

We consider the interactions of plane, regular incident waves with a VLFS. As shown in Fig. 1, the structure considered here comprises a thin upper deck and a large number of buoyancy columns which are identical and equally spaced. The geometry of an elementary column is a truncated circular cylinder with radius a and draft d. The centerlines of adjacent cylinders are separated by a distance $2s$ in both x- and y-axes of a Cartesian coordinate system. Here o-xyz is the body-fixed coordinate system with the origin placed at the center of gravity (G). In steady-state equilibrium, the position of G is supposed to be at $(0,\, 0,\, z_G)$ in a space-fixed coordinate system O-XYZ, where $Z = 0$ is taken as the undisturbed free surface and the Z-axis is positive vertically downward.

The structure is allowed to move with unsteady motions of 6 degrees of freedom in response to the wave excitation. The vectors of the translational and rotational motions are denoted by $\boldsymbol{\xi}(t)$ and $\boldsymbol{\alpha}(t)$, respectively, and the magnitudes of these motions are assumed to be small. The vector of local displacement at a point on the body surface can be expressed as:

$$\boldsymbol{\Xi}(t) = \boldsymbol{\xi}(t) + \boldsymbol{\alpha}(t) \times \boldsymbol{r}, \tag{1}$$

where $\boldsymbol{r} = (x,\, y,\, z)$ represents the position vector in the body-fixed reference frame.

Under the assumption of incompressible and inviscid flow with irrotational motion, we

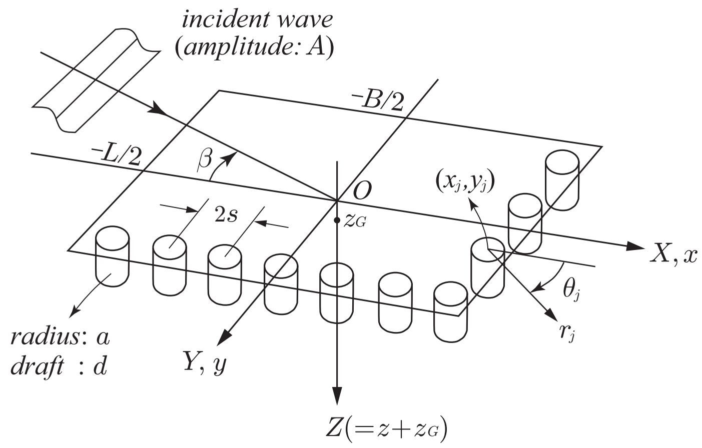

Fig. 1 Coordinate system and notations

introduce the velocity potential, Φ, satisfying the Laplace equation. Assuming weak non-linearities, the velocity potential and the motion vectors can be written as a perturbation series with respect to a small parameter ϵ, which is usually taken as the wave slope:

$$\left.\begin{aligned} \Phi &= \epsilon\,\Phi^{(1)} + \epsilon^2\Phi^{(2)} + O(\epsilon^3),\\ \boldsymbol{\xi} &= \epsilon\,\boldsymbol{\xi}^{(1)} + \epsilon^2\boldsymbol{\xi}^{(2)} + O(\epsilon^3),\\ \boldsymbol{\alpha} &= \epsilon\,\boldsymbol{\alpha}^{(1)} + \epsilon^2\boldsymbol{\alpha}^{(2)} + O(\epsilon^3). \end{aligned}\right\} \tag{2}$$

Given the above quantities, the hydrodynamic pressure will be computed. Then the wave force on a body can be obtained by integrating the pressure multiplied by unit normal vector over the instantaneous wetted body surface, say $S(t)$.

Using (2) and Taylor's expansion for both the pressure and unit normal vector on $S(t)$ with respect to the mean body surface, S_B, the wave forces on a body can be expressed in a perturbation series. Details of the derivation can be found, for example, in Ogilvie (1983) and Kim and Yue (1990). The result can be summarized as follows:

$$\boldsymbol{F} = \boldsymbol{F}^{(0)} + \epsilon\,\boldsymbol{F}^{(1)} + \epsilon^2\boldsymbol{F}^{(2)} + O(\epsilon^3), \tag{3}$$

where

$$\boldsymbol{F}^{(0)} = -\,\rho g V\boldsymbol{k}, \tag{4}$$

$$\boldsymbol{F}^{(1)} = \rho\iint_{S_B}\frac{\partial\Phi^{(1)}}{\partial t}\boldsymbol{n}\,dS - \rho g\iint_{S_B}\Xi_3^{(1)}n_3\boldsymbol{k}\,dS, \tag{5}$$

$$\boldsymbol{F}^{(2)} = \rho\iint_{S_B}\frac{\partial\Phi^{(2)}}{\partial t}\boldsymbol{n}\,dS - \rho g\iint_{S_B}\Xi_3^{(2)}n_3\boldsymbol{k}\,dS + \boldsymbol{F}_q^{(2)}, \tag{6}$$

$$\begin{aligned} \boldsymbol{F}_q^{(2)} = {}& \frac{1}{2}\rho\iint_{S_B}\left|\nabla\Phi^{(1)}\right|^2\boldsymbol{n}\,dS - \frac{1}{2}\rho g\oint_{C_B}\left\{\zeta_R^{(1)}\right\}^2\boldsymbol{n}\,d\ell\\ &+\rho\iint_{S_B}\boldsymbol{\Xi}^{(1)}\cdot\nabla\Big(\frac{\partial\Phi^{(1)}}{\partial t}\Big)\boldsymbol{n}\,dS + \boldsymbol{\alpha}^{(1)}\times\boldsymbol{F}^{(1)}\\ &-\rho g\iint_{S_B}\alpha_3^{(1)}\big(\alpha_1^{(1)}x + \alpha_2^{(1)}y\big)n_3\boldsymbol{k}\,dS. \end{aligned} \tag{7}$$

Here $\zeta_R^{(1)}$ in (7) denotes the first-order relative wave elevation given by:

$$\zeta_R^{(1)} = \frac{1}{g}\,\frac{\partial \varPhi^{(1)}}{\partial t}\bigg|_{Z=0} - \varXi_3^{(1)}, \tag{8}$$

which must be evaluated along the mean waterline C_B; ρ is the fluid density; g is the gravitational acceleration; V is the displacement volume; $\boldsymbol{n}$ is the unit normal vector directing into the fluid from the mean body surface S_B; $\boldsymbol{\varXi}^{(1)} = \boldsymbol{\xi}^{(1)} + \boldsymbol{\alpha}^{(1)} \times \boldsymbol{r}$ and thus $\varXi_3^{(1)} = \xi_3^{(1)} + \alpha_1^{(1)} y - \alpha_2^{(1)} x$; $\boldsymbol{k}$ is the unit vector in the z-direction of the space-fixed coordinate axes.

The present paper is concerned with time-averaged steady forces, which can be computed only from $\boldsymbol{F}_q^{(2)}$ containing only quadratic products of first-order quantities.

The corresponding expressions for the moment about the center of gravity can be obtained in a similar form. The second-order term to be computed from quadratic products of first-order quantities, which is denoted as $\boldsymbol{M}_q^{(2)}$, may be computed by:

$$\begin{aligned} \boldsymbol{M}_q^{(2)} = {} & \frac{1}{2}\,\rho \iint_{S_B} \big|\,\nabla \varPhi^{(1)}\big|^2 \boldsymbol{r} \times \boldsymbol{n}\, dS - \frac{1}{2}\rho g \oint_{C_B} \big\{\zeta_R^{(1)}\big\}^2 \boldsymbol{r} \times \boldsymbol{n}\, d\ell \\ & + \rho \iint_{S_B} \boldsymbol{\varXi}^{(1)} \cdot \nabla\Big(\frac{\partial \varPhi^{(1)}}{\partial t}\Big) \boldsymbol{r} \times \boldsymbol{n}\, dS + \boldsymbol{\alpha}^{(1)} \times \boldsymbol{M}^{(1)} \\ & - \rho g \iint_{S_B} \alpha_3^{(1)} \big(\alpha_1^{(1)} x + \alpha_2^{(1)} y\big) \boldsymbol{r} \times \boldsymbol{n}\, dS. \end{aligned} \tag{9}$$

The first-order motions, $\boldsymbol{\xi}^{(1)}$ and $\boldsymbol{\alpha}^{(1)}$, follow from the equations of motions based on Newton's second law, for which the first-order hydrodynamic force and moment must be computed.

3. SOLUTION OF FIRST-ORDER PROBLEM

The first-order quantities are assumed to be time-harmonic with the circular frequency of the incident wave, ω, and are expressed as:

$$\varPhi^{(1)} = \mathrm{Re}\Big[\,\frac{gA}{i\omega}\,\phi(x,y,z)\,e^{i\omega t}\,\Big], \tag{10}$$

$$\xi_k^{(1)} = \mathrm{Re}\Big[\,A X_k\, e^{i\omega t}\,\Big], \quad \alpha_k^{(1)} = \mathrm{Re}\Big[\,\frac{A}{a}\, X_{k+3}\, e^{i\omega t}\,\Big], \tag{11}$$

where A is the amplitude of the incident wave, and a is the radius of an elementary column which is used as the representative length scale for nondimensionalization. Note that $\phi(x,y,z)$ and X_j $(j = 1 \sim 6)$ are expressed as nondimensional quantities.

When solving the boundary-value problem with the free surface, it is convenient to use a space-fixed coordinate system. In the mean position of a body oscillating with a constant circular frequency, the body-fixed coordinate system coincides with one fixed in space except for the vertical shift of $z = z_G$. In the analysis to follow, then, (x,y,z) will be used as the space-fixed coordinates.

The spatial part of the velocity potential, $\phi(x,y,z)$, can be decomposed in the form:

$$\phi = \phi_I + \phi_S - K \sum_{k=1}^{6} X_k \big\{\, \phi_k + \varphi_k \,\big\}, \tag{12}$$

where $K = \omega^2 a/g$ is the nondimensional wavenumber.

ϕ_I and ϕ_S are the incident-wave and scattering potentials, respectively, and the sum, $\phi_I + \phi_S \equiv \phi_D$, is referred to as the diffraction potential. For plane waves propagating in the direction with angle β relative to the positive x-axis, ϕ_I is given by:

$$\phi_I = \frac{\cosh k_0(z-h)}{\cosh k_0 h}\, e^{-ik_0(x\cos\beta + y\sin\beta)}, \tag{13}$$

where k_0 is the solution of $k_0 \tanh k_0 h = K$, and h denotes the constant water depth, nondimensionalized in terms of a.

In the radiation problem, ϕ_k in (12) denotes the velocity potential of a single body oscillating in the k-th mode (with no interactions among cylinders) and φ_k represents the remaining part of the potential due to hydrodynamic interactions with radiated and scattered waves by the other cylinders.

Thus, the boundary conditions to be satisfied on the mean body surface, S_B, are given as

$$\frac{\partial \phi_D}{\partial n} = 0, \quad \frac{\partial \phi_k}{\partial n} = n_k, \quad \frac{\partial \varphi_k}{\partial n} = 0, \tag{14}$$

where $\boldsymbol{n} = (n_1, n_2, n_3)$ and $\boldsymbol{r} \times \boldsymbol{n} = (n_4, n_5, n_6)$.

Solutions satisfying (14) and other free-surface and radiation conditions may be obtained by using the Kagemoto and Yue interaction theory (1986). To obtain expressions valid near the j-th cylinder (see Fig. 1) using the interaction theory, we will use a local cylindrical coordinate system (r_j, θ_j, z), with the origin placed at the center of the j-th cylinder, $(x_j, y_j, 0)$. Namely, $x = x_j + r_j \cos\theta_j$ and $y = y_j + r_j \sin\theta_j$ will be substituted.

The expressions of the velocity potentials by the interaction theory, appropriate for the present analyses, may be found in Kashiwagi (1998), and the results are summarized as follows:

$$\phi_D^j = \left(\{a^j\}^T + \sum_{\substack{i=1 \\ i \neq j}}^{N_B} \{A_S^i\}^T [\,T_{ij}\,] \right) \{\psi_D^j\}, \tag{15}$$

$$\phi_k^j = \{\mathcal{R}_k^j\}^T \{\psi_S^j\}, \tag{16}$$

$$\varphi_k^j = \sum_{\substack{i=1 \\ i \neq j}}^{N_B} \left(\{\mathcal{R}_k^j\}^T + \{A_k^i\}^T \right) [\,T_{ij}\,] \{\psi_D^j\}, \tag{17}$$

where:

$$\{\psi_D^j\} = \{\psi_I^j\} + [\,B_j\,]\{\psi_S^j\}. \tag{18}$$

Here $\{\psi_I^j\}$ and $\{\psi_S^j\}$ in (18) are the vectors of the "generalized" incident-wave and scattering potentials, respectively, defined as:

$$\{\psi_I^j\} = \left\{ \begin{array}{c} Z_0(z)\, J_p(k_0 r_j)\, e^{-ip\theta_j} \\ Z_n(z)\, I_p(k_n r_j)\, e^{-ip\theta_j} \end{array} \right\}, \tag{19}$$

$$\{\psi_S^j\} = \left\{ \begin{array}{c} Z_0(z)\, H_m^{(2)}(k_0 r_j)\, e^{-im\theta_j} \\ Z_n(z)\, K_m(k_n r_j)\, e^{-im\theta_j} \end{array} \right\}, \tag{20}$$

where:

$$Z_0(z) = \frac{\cosh k_0(z-h)}{\cosh k_0 h}, \quad Z_n(z) = \frac{\cos k_n(z-h)}{\cos k_n h}, \tag{21}$$

and k_n $(n = 1, 2, \cdots)$ are solutions of $k_n \tan k_n h = -K$, giving the wavenumbers of evanescent wave modes. The number of terms in the θ-direction, p and m in (19) and (20), must be taken as 0, ± 1, ± 2, $\cdots$.

The coefficient vector of the incident wave, $\{a^j\}$, can be explicitly given by expressing (13) in terms of a local cylindrical coordinate system. Meanwhile, $[T_{ij}]$ is the coordinate transformation matrix, relating $\{\psi_I^i\}$ with $\{\psi_S^j\}$, which can be given by Graf's addition theorem for Bessel functions. N_B denotes the number of total cylinders.

The vector $\{\mathcal{R}_k^j\}$ in (16) can be numerically obtained by solving the radiation problem for a single body. Likewise, the matrix $[B_j]$ in (18) can be obtained by solving the diffraction problem for a single body, with each component of (19) regarded as an incident-wave velocity potential. For these numerical computations, a higher-order boundary element method using 9-point isoparametric elements is adopted in the present paper.

Other unknown vectors representing wave interactions, $\{A_S^i\}$ in (15) and $\{A_k^i\}$ in (17), are determined by the Kagemoto and Yue interaction theory.

Once the velocity potentials are determined, it is straightforward to compute the first-order forces acting in the k-th direction; those are expressed in a nondimensional form as follows:

$$\left.\begin{aligned} F_k^{(1)} &= \mathrm{Re}\big[\,\rho g A\, a^2\, \mathcal{F}_k\, e^{i\omega t}\,\big], \\ M_k^{(1)} &= \mathrm{Re}\big[\,\rho g A\, a^3\, \mathcal{F}_{k+3}\, e^{i\omega t}\,\big], \end{aligned}\right\} \tag{22}$$

where:

$$\mathcal{F}_k^j = E_k^j + \sum_{\ell=1}^{6} X_\ell \{\, K F_{k\ell}^j - C_{k\ell}^j \,\}, \tag{23}$$

$$E_k^j = \Big(\, \{a^j\}^T \sum_{\substack{i=1\\ i\neq j}}^{N_B} \{A_S^i\}^T [\,T_{ij}\,] \Big) \{e_k^j\}, \tag{24}$$

$$F_{k\ell}^j = f_{k\ell}^j - \sum_{\substack{i=1\\ i\neq j}}^{N_B} \Big(\{\mathcal{R}_k^i\}^T + \{A_k^i\}^T \Big) [\,T_{ij}\,] \{e_k^j\}. \tag{25}$$

Here $f_{k\ell}^j$ in the radiation force and $\{e_k^j\}$ in the diffraction and interaction forces are fundamental hydrodynamic forces of a single body, which can be computed by:

$$\left.\begin{aligned} f_{k\ell}^j &= -\iint_{S_B} \phi_\ell^j\, n_k^j\, dS, \\ \{e_k^j\} &= \iint_{S_B} \{\psi_D^j\}\, n_k^j\, dS, \end{aligned}\right\} \tag{26}$$

with n_k^j being the k-th component of unit normal vector on the j-th cylinder.

$C_{k\ell}^j$ appearing in (23) denotes the restoring force coefficients; nonzero values among these coefficients for a vertical circular cylinder are summarized as follows:

$$\left.\begin{aligned}
&C_{33}^{j}=\pi,\\
&C_{44}^{j}=\pi\Big\{\,y_j^2+\frac{1}{4}-d\left(\frac{d}{2}-z_G\right)\Big\},\\
&C_{55}^{j}=\pi\Big\{\,x_j^2+\frac{1}{4}-d\left(\frac{d}{2}-z_G\right)\Big\},\\
&C_{34}^{j}=C_{43}^{j}=\pi y_j,\quad C_{35}^{j}=C_{53}^{j}=-\pi x_j,\\
&C_{45}^{j}=C_{54}^{j}=-\pi x_j y_j.
\end{aligned}\right\} \tag{27}$$

Having determined the hydrodynamic and hydrostatic forces, the complex amplitude X_k defined in (11) will be determined by solving the motion equations of a structure with N_B buoyancy cylinders.

The steady wave forces and moments can be obtained by taking time average over one period of $\boldsymbol{F}_q^{(2)}$ given as (7) and $\boldsymbol{M}_q^{(2)}$ given as (9), respectively.

As shown in (10), (11) and (22), the time-dependent part of all first-order quantities are expressed as $e^{i\omega t}$. Thus, the time average can easily be computed by means of the following formula:

$$\overline{\mathrm{Re}\big[\,A\,e^{i\omega t}\,\big]\,\mathrm{Re}\big[\,B\,e^{i\omega t}\,\big]}=\frac{1}{2}\,\mathrm{Re}\big[\,A\,B^{*}\,\big], \tag{28}$$

where the overbar means the time average to be taken and the asterisk denotes the complex conjugate.

As a special case of (7) and (9), when the body motions are completely restrained, calculation formulae for the time-averaged steady forces and moments become much simpler, including only the diffraction components. For instance, the nondimensional expression for the steady force, $\overline{\boldsymbol{F}}$, can be given by:

$$\frac{\overline{\boldsymbol{F}}}{\frac{1}{2}\rho g A^2 a}=\frac{1}{2}\left[\,\frac{1}{K}\iint_{S_B}\Big|\,\nabla\phi_D\,\Big|^2\boldsymbol{n}\,dS-\oint_{C_B}\big|\,\phi_D\,\big|^2\,\boldsymbol{n}\,d\ell\,\right]. \tag{29}$$

4. OUTLINE OF EXPERIMENTS

With the calculation method described above, the effects of body motions on the steady forces can be taken into account. However, to check the validity and performance of the

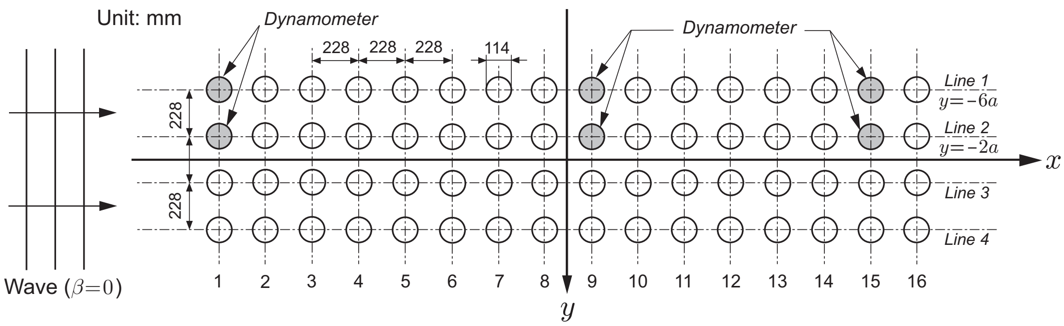

Fig. 2 Experimental model: arrangement of 64 truncated circular cylinders fixed in head waves

calculation method for the diffraction problem first, motions were completely fixed in experiments.

As shown in Fig. 2, experiments were conducted in head waves ($\beta = 0°$), using 64 equally spaced, truncated circular cylinders. The diameter ($D = 2a$) of an elementary cylinder is 114 mm. The separation distance between centerlines of adjacent cylinders, $2s$, was set equal to $2D$ in both x- and y-axes; that is, $s = D$. To see effects of the draft of cylinders on the wave interactions, 2 cases of $d = D$ and $d = 2D$ were tested, but only the results of $d = 2D$ will be presented in this paper, because there were no essential differences between them.

The wave forces were measured by dynamometers at 6 different positions. As shown in Fig. 2, 16 columns are numbered from the upwave side. By symmetry, the lines of $y = \pm 2a$ are called the inside and those of $y = \pm 6a$ are called the outside. Then the positions of measured cylinders are distinguished with the column number and the inside or outside line.

The steepness of regular waves (the ratio of wave height with wave length, H/λ) was set approximately equal to 1/50. The circular frequency ω of incident waves was varied in the range of $Ks = \omega^2 s/g = 0.2 \sim 1.6$. Measured data were analyzed using an ordinary Fourier analysis, from which the steady force in the x-axis was obtained.

5. RESULTS AND DISCUSSION

5.1 Outline of Numerical Computations

As the first step of numerical computations, the boundary-value problems for a single cylinder were solved by the boundary element method using 9-point quadratic representations for both the surface geometry and velocity potential. The number of panels over 1/4 of the submerged surface was 40, and in this case the number of total unknowns (velocity potentials at nodes) was 177.

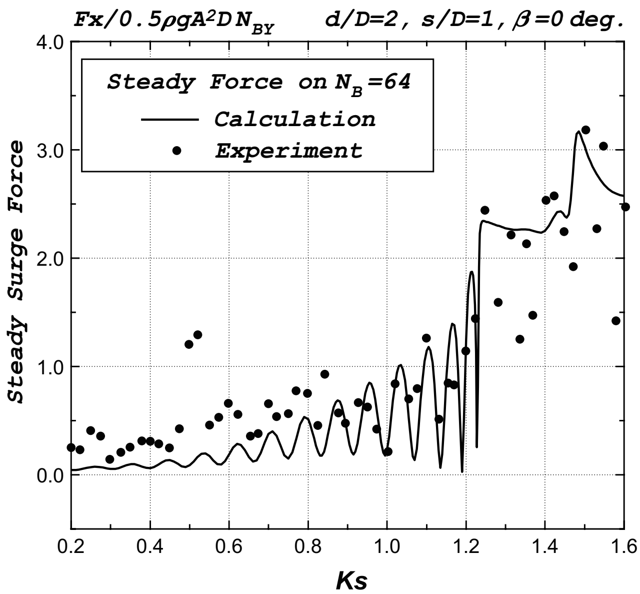

Fig. 3 Total wave drift force on 64 circular cylinders, computed by far-field method based on the momentum-conservation principle

In computing the wave interactions, the number of Fourier series in the θ-direction (M) and of evanescent wave mode (N) must be finite. In the present paper, $M = 5$ and $N = 3$ are chosen after a convergence check for $Ks = 1.0$, $\beta = 0°$, and $h = 3d$, for which 5 decimals' absolute accuracy has been achieved.

The number of total unknowns for $M = 5$, $N = 3$, and $N_B = 64$ is $(2M + 1) \times (N + 1) \times N_B = 2816$. The computation time in this case will be very long, if computations must be carried out at many frequencies for higher resolution. Thus, double symmetries with respect to x- and y-axes are exploited, which can reduce the number of unknowns to 1/4 (*i.e.* 2816/4=704).

The spatial derivatives of the velocity potential over the submerged surface, S_B, which are needed in computing the second-order steady forces by the present method, are evaluated using 2-D quadratic isoparametric representations for the velocity potential and coordinates (x, y, z). The line integral along the waterline, C_B, which is also needed in the pressure-integration method, is evaluated using 1-D quadratic isoparametric representations for the velocity potential at $z = 0$ and coordinates (x, y).

5.2 Total Drift Force on 64 Cylinders

Based on the momentum-conservation principle, Kashiwagi (2000) developed a calculation method (the so-called far-field method) for computing the drift forces in the horizontal plane and the drift yaw moment. Although this far-field method gives only the total force on the structure, accurate results can be expected, because all necessary integrations on a control surface located far from the structure are analytically performed. Hence, to check the numerical accuracy of the present method, the summation of the local steady forces on 64 cylinders was compared with independent results by the far-field method.

Figure 3 is taken from Kashiwagi (2000), showing the results computed by the

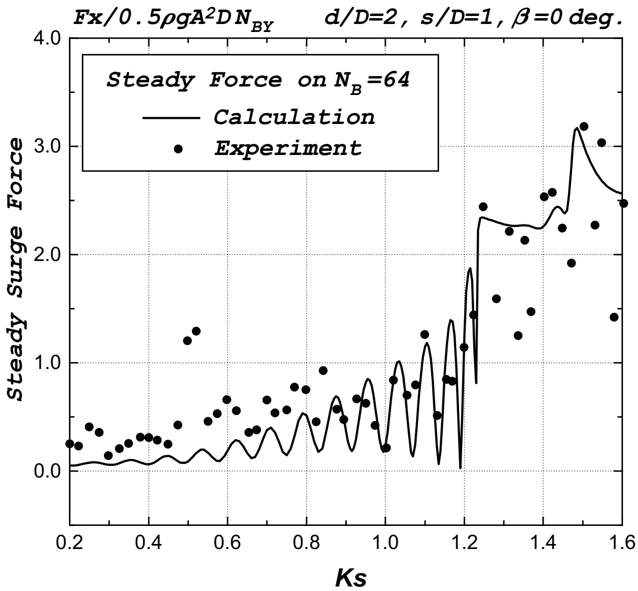

Fig. 4 Total wave drift force on 64 circular cylinders, computed by pressure-integration method

Table 1 Steady forces in surge, sway, and yaw on a structure with 64 circular cylinders arranged periodically in the array of 4 rows and 16 columns, computed by the far-field method and the pressure integration method. ($d = 2D$, $s = D$, $h = 7.5\,d$, $\beta = 30°$)

By Far-Field Method (Momentum-Conservation Principle)

	Diffraction Problem			Including Motion Effects		
Ks	FX	FY	MZ	FX	FY	MZ
0.50	0.05413	0.00876	0.00412	0.14638	0.01407	−0.10189
1.00	0.08821	0.04253	0.02977	0.08946	0.04258	0.03098
1.50	1.6217	0.08032	−0.00668	1.6218	0.08030	−0.00606
1.75	3.9364	0.27782	0.40703	3.9369	0.27766	0.40795
2.00	3.2052	0.70410	−0.26574	3.2048	0.70387	−0.26517
2.50	0.98615	0.50644	−0.37112	0.98633	0.50677	−0.37146

By Near-Field Method (Direct Pressure Integration)

	Diffraction Problem			Including Motion Effects		
Ks	FX	FY	MZ	FX	FY	MZ
0.50	0.05576	0.00874	0.00343	0.17035	0.01336	−0.10203
1.00	0.08868	0.04209	0.02975	0.08997	0.04213	0.03099
1.50	1.6222	0.08027	−0.00664	1.6223	0.08025	−0.00602
1.75	3.9368	0.27791	0.40708	3.9373	0.27775	0.40799
2.00	3.2056	0.70419	−0.26571	3.2052	0.70396	−0.26513
2.50	0.98646	0.50627	−0.37130	0.98664	0.50661	−0.37164

far-field method for the surge drift force in head waves. Fig. 4, which shows corresponding results computed by the present method, is in virtually perfect agreement with Fig. 3 except for a very small difference near $Ks = 1.24$.

For the case of free oscillation in response to wave excitation, Table 1 shows a comparison of the results at some wavenumbers. To show the results of the steady sway force (FY) and yaw moment (MZ), computations were performed for $\beta = 30°$, and other geometrical parameters are the same as Figs. 3 and 4. The center of gravity was assumed to be on the water plane, and the radii of gyration in roll, pitch, and yaw modes were set to $0.25B$, $0.25L$, and $0.25L$, respectively, with B and L being the breadth and length, respectively, of the structure composed of 64 cylinders.

We can see from Table 1 that very good agreement exists between the far-field method and the present method based on the direct pressure integration. For higher frequencies, the steady forces and moment become large, and the yaw moment changes the sign abruptly around $Ks = 1.7$, but major contributions stem from the diffraction component. This is because the structure considered here is large compared to the wavelength of the incident wave, and thus the wave-induced motions are relatively small for higher frequencies. Despite small values of motions, we can see that the effects of body motions are properly computed by the present method.

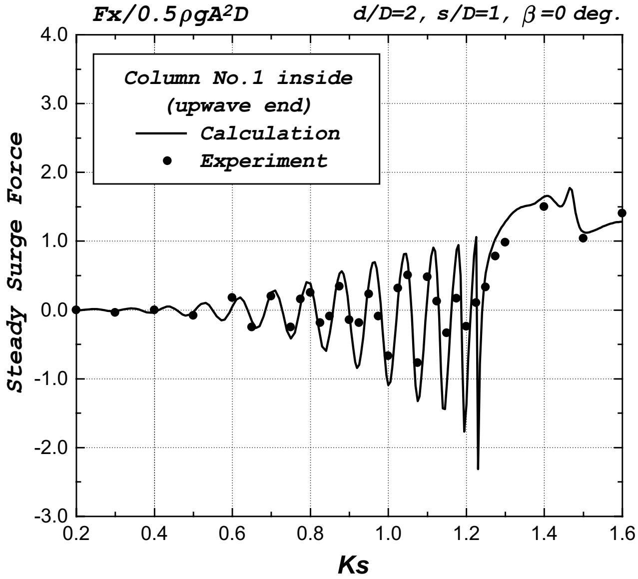

Fig. 5 Steady surge force on cylinder at Column No. 1 along inside line

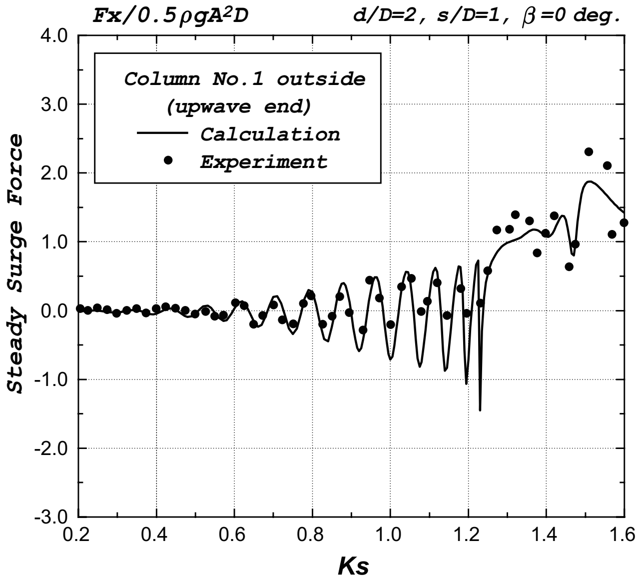

Fig. 6 Steady surge force on cylinder at Column No. 1 along outside line

5.3 Comparison with Experiments

Having confirmed the validity and accuracy of the present method, let us investigate the local steady forces on elementary cylinders by comparing with experimental measurements.

Figure 5 shows the steady surge force on the cylinder located at Column No. 1

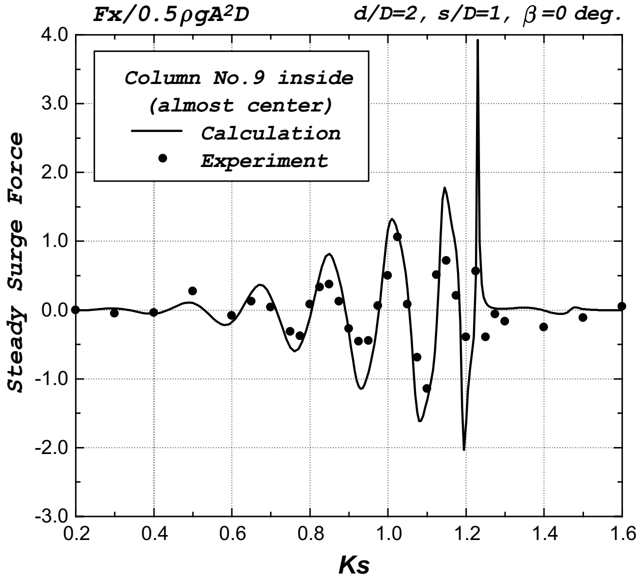

Fig. 7 Steady surge force on cylinder at Column No. 9 along inside line

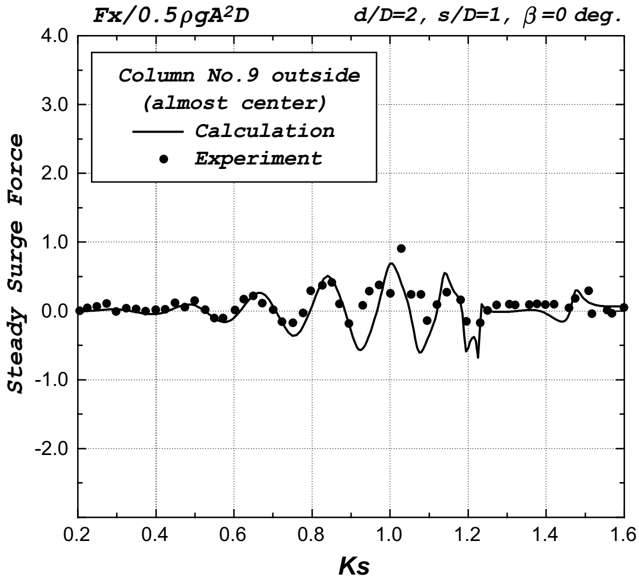

Fig. 8 Steady surge force on cylinder at Column No. 9 along outside line

along the inside line (see Fig. 2). Likewise, Fig. 6 shows the results on the cylinder at Column No. 1 along the outside line. In the frequency range less than $Ks \simeq 1.24$, we can see regular fluctuation with increasing amplitude, which may be due to the effects of wave reflection from downwave cylinders. On the other hand, at frequencies higher than $Ks \simeq 1.24$, the variation pattern changes and the steady force becomes positive. This implies that a large part of the incident wave is reflected by the cylinders placed

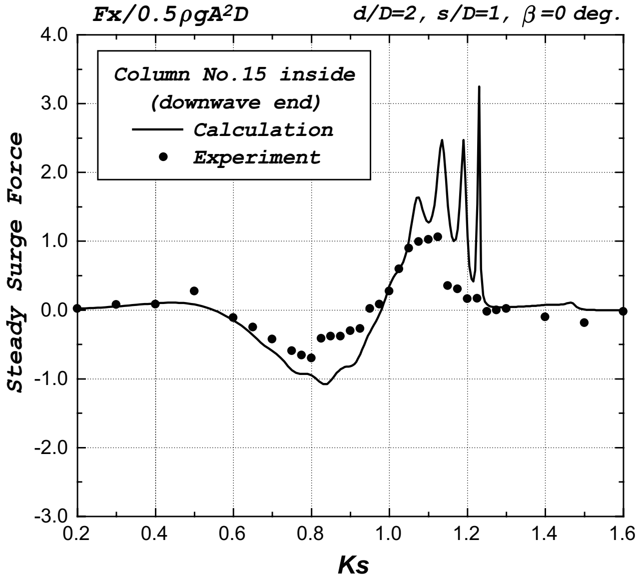

Fig. 9 Steady surge force on cylinder at Column No. 15 along inside line

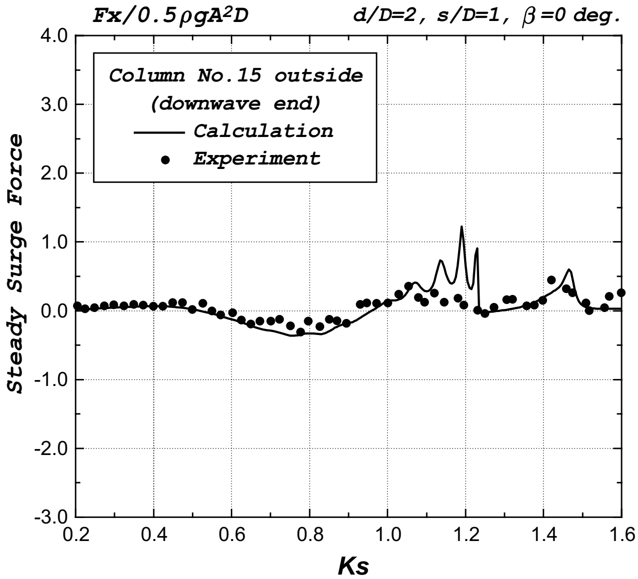

Fig. 10 Steady surge force on cylinder at Column No. 15 along outside line

near the upwave end, and that the total drift force (shown in Figs. 3 and 4) is determined almost by the local steady forces acting on upwave cylinders. (The latter conjecture will be endorsed by observing the results on downwave cylinders, shown in Figs. 7–10.) According to Maniar and Newman (1997), $Ks = 1.24$ corresponds approximately to a near trapped-mode frequency of Neumann type, around which linear wave forces become large and change drastically.

Comparison between Fig. 5 and Fig. 6 reveals that the amplitude of fluctuation at lower frequencies is larger at the inside than that at the outside. Although the fluctuation amplitude just below the near trapped-mode frequency is not so large in measured results, the overall agreement between computed and measured results is satisfactory.

Figures 7 and 8 are the results of the steady surge force on the cylinders at Column No. 9. It is clearly shown that the steady force at the inside (Fig. 7) is much larger in amplitude than that at the outside (Fig. 8). This implies that the wave interactions are intensified inside the array of a large number of cylinders. By comparison with Figs. 5 and 6, we can see that variation of the steady force with respect to Ks becomes mild for lower frequencies. On the other hand, at frequencies higher than $Ks \simeq 1.24$, the steady forces at Column No. 9 are almost zero. Including these characteristics, computed results are in good agreement with measured results.

Figures 9 and 10 show the steady surge force on cylinders at Column No. 15 (the second column from the most downwave side). We can see again that the steady force at the inside is larger than that at the outside, and the variation with respect to Ks becomes further milder. The present computations predict a spike-like rapid change just below the near trapped-mode frequency, but that is not clear in measured results; which may be attributed to a decay due to viscous effects.

6. CONCLUDING REMARKS

A calculation method based on the direct pressure integration was presented for computing the steady force and moment on a column-supported large floating structure. This method enables us to compute the local steady forces on each of a large number of columns. Although the steady forces are dominated by the diffraction component for practical frequencies because of the large scale of the structure, the effects of the structure's wave-induced motions are also taken into account. The pressure on the wetted surface of each column was computed by the wave-interaction theory, which is exact in the framework of the linear potential theory.

The validity and numerical accuracy of the present method were confirmed by comparing the sum of local steady forces on 64 vertical cylinders with the wave drift force computed by the far-field method based on the momentum-conservation principle.

Concerning the characteristics of the local steady forces on each cylinder, computed results were compared with measured ones using 64 vertical cylinders arranged in 4 rows and 16 columns, through which we observed the followings:

1) The overall agreement is very good, considering that the steady forces are second-order small quantities in the wave amplitude.

2) The steady force on each column can be negative, though the total force summing up the local forces of all columns is definitely positive.

3) At the upwave side, the variation of the steady force is rapid in the range of frequencies lower than the near trapped-mode frequency, but this variation becomes mild as the position of a cylinder goes downstream.

4) For frequencies higher than the near trapped-mode frequency, the local steady forces on upwave cylinders become positive and large, dominating the total

drift force on the whole structure.

5) The steady force on a cylinder along the inside line in the array is larger than that on a cylinder along the outside line in the variation amplitude with respect to the frequency.

ACKNOWLEDGMENTS

Experiments in this study have been conducted as a part of the master thesis of Mr. S. Yoshida, in the Interdisciplinary Graduate School of Engineering Sciences, Kyushu University. The author is thankful for his contribution. Thanks are also extended to Mr. M. Inada for his help in preparation of the experiments.

REFERENCES

1 Kagemoto, H and Yue, DKP (1986). "Interactions among Multiple Three-Dimensional Bodies in Water Waves: An Exact Algebraic Method", *Journal of Fluid Mechanics*, Vol 166, pp 189–209.

2 Kashiwagi, M (1998). "Hydrodynamic Interactions among a Great Number of Columns Supporting a Very Large Flexible Structure", *Proc 2nd Intl Conf on Hydroelasticity*, Fukuoka, pp 165–176.

3 Kashiwagi, M (1999). "Research on Hydroelastic Responses of VLFS: Recent Progress and Future Work", *Proc 9th Intl Offshore and Polar Engineering Conf*, Brest, Vol 1, pp 17–26.

4 Kashiwagi, M (2000). "Wave Drift Force and Moment on a VLFS Supported by a Great Number of Floating Columns", *Proc 10th Intl Offshore and Polar Engineering Conf*, Seattle, Vol 1, pp 49–56.

5 Kim, MH and Yue, DKP (1990). "The Complete Second Order Diffraction Solution for an Axisymmetric Body, Part 2. Bichromatic Incident Waves and Body Motions", *Journal of Fluid Mechanics*, Vol 211, pp 557–593.

6 Maniar, HD and Newman, JN (1997). "Wave Diffraction by a Long Array of Cylinders", *Journal of Fluid Mechanics*, Vol 339, pp 309–330.

7 Ogilvie, TF (1983). "Second Order Hydrodynamic Effects on Ocean Platforms", *Intl Workshop on Ship and Platform Motion*, Berkeley, pp 205–265.

Wave Scattering Among a Large Number of Floating Cylinders*

Masashi KASHIWAGI
Research Institute for Applied Mechanics, Kyushu University
Kasuga, Fukuoka 816-8580, Japan

Abstract

When a large number of identical cylinders are placed in an array with equal separation distance, near-resonant phenomena may occur between cylinders at critical frequencies, and cause large wave forces on each element of the array. In this paper, 64 truncated circular cylinders arranged in 4 rows and 16 columns are considered to check the occurrence of near-resonant phenomena and performance of theoretical predictions based on the potential flow. Experiments are conducted in head waves to measure the wave elevation along the longitudinal centerline of the model, and measured results are compared with numerical ones. Attention is focused on the spatial variation of the wave amplitude around the first near-trapped-mode frequency.

Keywords: Hydrodynamic interaction, trapped mode, wave transmission, spatial distribution, truncated circular cylinders.

1. Introduction

For the development of column-supported very large floating structures to be used as a floating airport or an artificial island, wave interactions among a great number of cylinders must be understood and predicted accurately. With the linear potential-flow assumption, several versions of the wave interaction theory are available at the present time (for a recent review, the reader is referred to Newman, 2001).

The author has developed a computer code that combines a quadratic isoparametric boundary-element method for computing the diffraction characteristics of an elementary body of general geometry and the Kagemoto and Yue (1986) theory of wave interactions among many bodies. This code has also been extended to the hierarchical scheme (Kashiwagi, 2000), which enables us to treat the wave interactions among a great number of columns with the order of several thousands. Using these calculation methods, we can predict the wave field around and resulting wave forces on individual floating bodies. A number of papers have been published (e. g. Kagemoto *et al.*, 1998), showing comparisons of the wave amplitude between measured and computed results. However those comparisons are made at certain limited points of a simple arrangement of bodies, and thus it is rather difficult to imagine the overall spatial distribution of a complicated wave field.

Another topic related to the present paper is the phenomena of near-trapped waves to be observed for periodically-arranged many cylinders, discussed by Maniar and Newman (1997).

∗ *Reprinted from Journal of Structural Engineering and Mechanics, Vol. 21, No. 1, pp. 53–66, 2005 (September)*

It is pointed out that the wave amplitude will be very large at near-trapped-mode frequencies and the linear potential-flow predictions are rather poor around these frequencies (Kagemoto et al., 2002). However, this should be checked more thoroughly through comparison between reliable measurements and accurate numerical computations.

In this paper, experiments are conducted using a model consisting of 64 equally-spaced vertical circular cylinders (an array of 4 rows times 16 columns), and waves are measured at a large number of frequencies including the first near-trapped-mode frequency of Neumann type and at 32 positions separated equally along the centerline of the tested model. Then the measured results are compared with corresponding numerical results by the wave interaction theory. It is shown that the overall quantitative agreement is very good, However, when the wave amplitude becomes large due to wave resonant phenomena, numerical results obviously tend to be larger than measured ones.

2. Calculation Method

2.1 Formulation

As shown in Fig. 1, a structure supported by a large number of columns is considered. The geometry of an elementary column considered here is a truncated circular cylinder with radius a (diameter $D = 2a$) and draft d. The centerlines of adjacent cylinders are separated by a distance $2s$ in both x- and y-axes of a Cartesian coordinate system, where $z = 0$ is the plane of the undisturbed free surface and the water depth is constant at $z = h$.

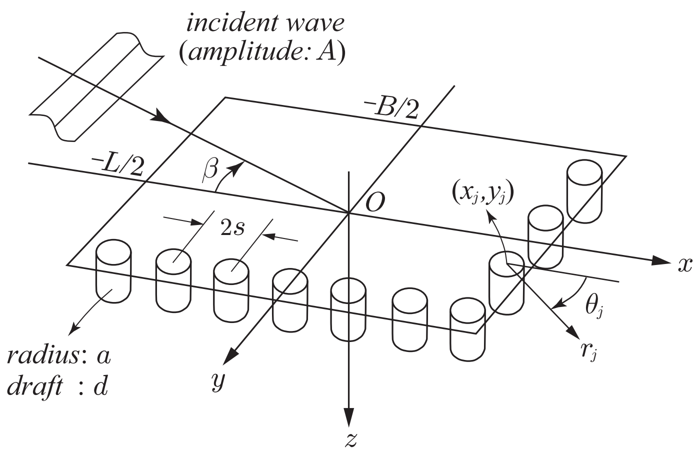

Fig. 1 Coordinate system and notations

Under the assumption of incompressible and inviscid flow with irrotational motion, the velocity potential is introduced, satisfying Laplace's equation. The boundary conditions are linearized and all oscillatory quantities are assumed to be time-harmonic with circular frequency ω. In accordance with the experiment which will be explained later, only the diffraction problem is considered in this paper. For the radiation problem including generalized elastic motions, the reader is referred to Kashiwagi (2000).

The velocity potential for the diffraction problem is expressed in the form

$$\Phi = \mathrm{Re}\left[\frac{gA}{i\omega} \left\{ \phi_I(x,y,z) + \phi_S(x,y,z) \right\} e^{i\omega t} \right], \tag{1}$$

where g and A are the gravitational acceleration and the amplitude of an incident wave, respectively. ϕ_I and ϕ_S are the incident-wave and scattering potentials, respectively, and the sum $\phi_I + \phi_S \equiv \phi_D$ is referred to as the diffraction potential.

2.2 Diffraction characteristics of elementary body

In the wave interaction theory for a large number of bodies, ϕ_I is not necessarily a plane progressive wave but the vector comprising a set of "generalized" incident waves defined in terms of a local cylindrical coordinate system $(r_j,\, \theta_j,\, z)$ of the j-th body (see Fig. 1):

$$\{\psi_I^j\} = \left\{ \begin{array}{l} Z_0(z)\, J_p(k_0 r_j)\, e^{-ip\theta_j} \\ Z_n(z)\, I_p(k_n r_j)\, e^{-ip\theta_j} \end{array} \right\}, \tag{2}$$

where $p = 0,\, \pm 1,\, \pm 2,\, \cdots,\, \pm\infty$, $n = 1,\, 2,\, \cdots,\, \infty$, and

$$\left.\begin{array}{l} Z_0(z) = \dfrac{\cosh k_0(z-h)}{\cosh k_0 h},\ Z_n(z) = \dfrac{\cos k_n(z-h)}{\cos k_n h}, \\ \dfrac{\omega^2}{g} \equiv K = k_0 \tanh k_0 h = -k_n \tan k_n h\,. \end{array}\right\} \tag{3}$$

J_p and I_p in Eq. (2) denote the first kind of Bessel function and modified Bessel function, respectively.

Let the velocity potential of an elementary wave in Eq. (2) and the corresponding scattering potential be denoted by $\psi_I^j(x,y,z)$ and $\varphi_S^j(x,y,z)$, respectively. These potentials satisfy Laplace's equation and the free-surface and sea-bottom conditions. In addition, $\varphi_S^j(x,y,z)$ satisfies the radiation condition at infinity. In this case, Green's theorem gives an integral equation for the diffraction potential, $\varphi_D^j = \psi_I^j + \varphi_S^j$, of the form

$$C(\mathrm{P})\varphi_D^j(\mathrm{P}) + \iint_{S_j} \varphi_D^j(\mathrm{Q}) \frac{\partial}{\partial n_{\mathrm{Q}}} G(\mathrm{P};\mathrm{Q})\, dS = \psi_I^j(\mathrm{P}), \tag{4}$$

where $C(\mathrm{P})$ is the solid angle, $\mathrm{P} = (x,y,z)$ is the field point, $\mathrm{Q} = (x',y',z')$ is the integration point on the wetted surface of the j-th body S_j, and $\partial/\partial n_{\mathrm{Q}}$ denotes the normal derivative with the normal vector defined as positive when directing out of the body. $G(\mathrm{P};\mathrm{Q})$ is the free-surface Green function, which can be expressed as

$$G(\mathrm{P};\mathrm{Q}) = \frac{i}{2} C_0 Z_0(z) Z_0(z') H_0^{(2)}\big(k_0 R\big) + \frac{1}{\pi} \sum_{n=1}^{\infty} C_n Z_n(z) Z_n(z') K_0\big(k_n R\big), \tag{5}$$

where

$$R = \sqrt{(x-x')^2 + (y-y')^2}, \tag{6}$$

$$C_0 = \frac{k_0^2}{K + h(k_0^2 - K^2)},\ C_n = \frac{k_n^2}{K - h(k_n^2 + K^2)}. \tag{7}$$

$H_0^{(2)}$ and K_0 in Eq. (5) are the second kind of Hankel function and modified Bessel function, respectively. These functions can be recast in the series-expansion form by expressing $x + iy = r\exp(i\theta)$ and $x' + iy' = r'\exp(i\theta')$ and by using the addition theorem of Bessel functions. Considering the case of field point P in a fluid, $C(\mathrm{P}) = 1$ and $r > r'$. In this case, from

Eq. (4) and Eq. (5), the following expression of the scattering potential may be obtained:

$$\varphi_S^j(\mathrm{P}) = \sum_{m=-\infty}^{\infty} \Big[B_{m0}^j \Big\{ Z_0(z) H_m^{(2)}(k_0 r)\, e^{-im\theta} \Big\} + \sum_{n=1}^{\infty} B_{mn}^j \Big\{ Z_n(z) K_m(k_n r)\, e^{-im\theta} \Big\} \Big], \tag{8}$$

where

$$\left. \begin{aligned} B_{m0}^j &= -\frac{i}{2} C_0 \iint_{S_j} \varphi_D^j(Q) \frac{\partial}{\partial n_Q} Z_0(z') J_m(k_0 r') e^{im\theta'}\, dS, \\ B_{mn}^j &= -\frac{1}{\pi} C_n \iint_{S_j} \varphi_D^j(Q) \frac{\partial}{\partial n_Q} Z_n(z') I_m(k_n r') e^{im\theta'}\, dS. \end{aligned} \right\} \tag{9}$$

These coefficients $\{B_{m0}^j,\, B_{mn}^j\}$ represent the diffraction characteristics corresponding to each component in the elementary-wave vector, $\psi_I^j(\mathrm{P})$. By considering the diffraction problems for all elementary waves in $\{\, \psi_I^j \,\}$ defined by Eq. (2) in the same manner, we can construct the matrix of the diffraction characteristics, the transpose of which is denoted as $[\, B_j \,]^T$. Then, the scattering potentials of the j-th elementary body corresponding to the generalized incident waves $\{\, \psi_I^j \,\}$ can be written in the vector form

$$\{\varphi_S^j\} = [\, B_j \,]^T \{\psi_S^j\}, \tag{10}$$

where

$$\{\psi_S^j\} = \left\{ \begin{aligned} & Z_0(z)\, H_m^{(2)}(k_0 r_j)\, e^{-im\theta_j} \\ & Z_n(z)\, K_m(k_n r_j)\, e^{-im\theta_j} \end{aligned} \right\} \tag{11}$$

with $m = 0,\, \pm1,\, \pm2,\, \cdots,\, \pm\infty$, and $n = 1,\, 2,\, \cdots,\, \infty$.

2.3 Wave-body interaction theory

When the number of columns is in the order more than several hundreds, the hierarchical interaction theory developed by Kashiwagi (2000) must be applied. However, for a comparison with the experiments of 64 vertical cylinders conducted in this paper, using the ordinary wave interaction theory (Kagemoto and Yue, 1986) is sufficient.

Let us consider the flow around the i-th body among N_B elementary columns. First the incident-wave potential incoming from the outside is expressed with a cylindrical coordinate system of the i-th body as follows:

$$\phi_I = Z_0(z)\, e^{-ik_0(x\cos\beta + y\sin\beta)} \tag{12}$$

$$= \alpha_i(k_0, \beta) \sum_{p=-\infty}^{\infty} e^{ip(\beta-\pi/2)} \big\{ Z_0(z) J_p(k_0 r_i) e^{-ip\theta_i} \big\}$$

$$\equiv \big\{a^i\big\}^T \big\{\psi_I^i\big\}, \tag{13}$$

where

$$\alpha_i(k_0, \beta) = e^{-ik_0(x_i\cos\beta + y_i\sin\beta)}, \tag{14}$$

with β the angle of incident wave relative to the positive x-axis and (x_i, y_i) the center of the i-th body in the global coordinate system. Note that the coefficient vector $\big\{a^i\big\}$ can be explicitly given from Eq. (13).

Incident waves impinging upon the i-th body consist not only of the incident wave given by Eq. (13) but also of the scattered waves from other bodies. Thus it can be written as

$$\begin{aligned}\phi_I^i &= \{a^i\}^T\{\psi_I^i\} + \sum_{\substack{j=1\\ j\neq i}}^{N_B}\{A_S^j\}^T\{\psi_S^j\}\\ &= \left(\{a^i\}^T + \sum_{\substack{j=1\\ j\neq i}}^{N_B}\{A_S^j\}^T[\,T_{ji}\,]\right)\{\psi_I^i\}.\end{aligned} \tag{15}$$

Here $\{A_S^j\}$ is the vector of unknown coefficients of the scattering potential due to the j-th body. $[\,T_{ji}\,]$ is the coordinate transformation matrix, relating $\{\psi_S^j\}$ with $\{\psi_I^i\}$; a concrete expression of which can be given by Graf's addition theorem for Bessel functions.

The quantity in parentheses in Eq. (15) can be regarded as the amplitude vector and $\{\psi_I^i\}$ is, as defined in Eq. (2), the vector of generalized incident waves. The scattering potentials in response to $\{\psi_I^i\}$ are already obtained in the form of Eq. (10). Therefore, the scattering potential of the i-th body due to the incident wave of Eq. (15) can be expressed as

$$\begin{aligned}\phi_S^i &= \left(\{a^i\}^T + \sum_{\substack{j=1\\ j\neq i}}^{N_B}\{A_S^j\}^T[\,T_{ji}\,]\right)[\,B_i\,]^T\{\psi_S^i\}\\ &= \{A_S^i\}^T\{\psi_S^i\}.\end{aligned} \tag{16}$$

One can therefore obtain a linear set of equations for determining the vector of unknown coefficients, $\{A_S^i\}$, in the form

$$\{A_S^i\} - [\,B_i\,]\sum_{\substack{j=1\\ j\neq i}}^{N_B}[\,T_{ji}\,]^T\{A_S^j\} = [\,B_i\,]\{a^i\}, \quad i = 1 \sim N_B. \tag{17}$$

Solving Eq. (17) completes the flow field, and then the wave elevation on the free surface ($z = 0$) can be computed from Eq. (12) and Eq. (16) as follows:

$$\frac{\zeta(x,y)}{A} = \phi_I(x,y,0) + \sum_{j=1}^{N_B}\{A_S^j\}^T\{\psi_S^j(r_j,\theta_j,0)\}. \tag{18}$$

2.4 Numerical computations

First we need to solve the integral equation Eq. (4) for an elementary body (which is a vertical circular cylinder in the present case) and to determine the diffraction characteristics matrix $[\,B_i\,]$. For this purpose, a higher-order boundary-element method using isoparametric 9-point quadratic elements is utilized. Since a vertical circular cylinder has double symmetries with respect to the x- and y-axes, only the first quadrant of a body is discretized into panels, and symmetry relations for the geometry and velocity potential are exploited. To assure high numerical accuracy, 320 panels over one quadrant were used, which was found to give completely converged results.

In computations of the interaction part, the numbers of Fourier series in the θ-direction (M) and of evanescent wave modes (N) must be finite, which depend on the arrangement

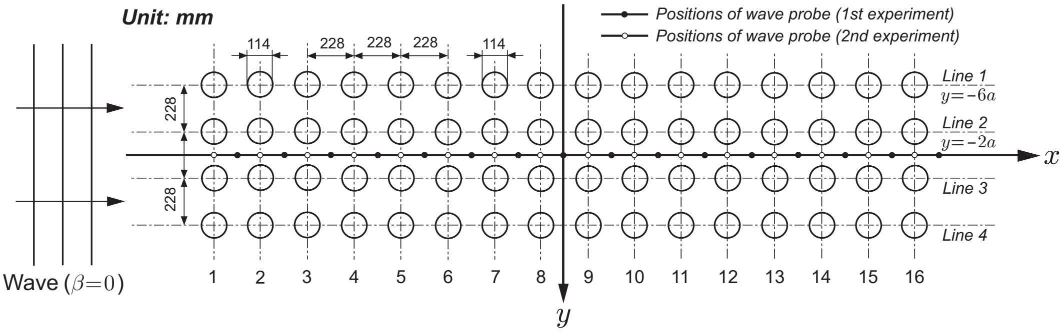

Fig. 2 Experimental model: arrangement of 64 truncated circular cylinders fixed in head waves

of columns, the frequency, and the water depth. In the present paper, computations are performed for a model used in the experiments; that is, as shown in Fig. 2, 64 circular cylinders arranged in 4 rows and 16 columns. For this model, $M = 4$ and $N = 3$ are chosen after convergence check for $Ks = 1.0$, $\beta = 0°$ and $h = 3d$, which achieved five decimals absolute accuracy. Even in this case, the number of total unknowns for $N_B = 64$ is $(2M + 1) \times (N + 1) \times N_B = 2304$. To reduce the number of unknowns and thus the computation time, double symmetry relations with respect to the x- and y-axes for the whole structure were exploited.

3. Outline of Experiments

Figure 2 shows a model used in the experiments, consisting of 64 equally-spaced truncated circular cylinders. The diameter of an elementary cylinder is $D = 114$ mm. The separation distance between centerlines of adjacent cylinders, $2s$, was set equal to $2D$ in both x- and y-axes. To see effects of the draft of cylinders on the wave interactions, two cases of $d = D$ and $d = 2D$ were tested. The wave elevation inside the structure was measured at 32 positions along the longitudinal centerline (x-axis) using wave probes of capacitance type. In reality, as shown in Fig. 2, an apparatus with 16 wave probes with equal separation distance of $2s$ was used and the measurement was performed twice by shifting the positions of wave probes by half of the separation distance, s.

The experiments were conducted in head waves generated in the Ocean Engineering Model Basin (length 65 m, breadth 5 m, water depth 7 m) of the Research Institute for Applied Mechanics at Kyushu University. The steepness of regular waves (the ratio of wave height with wave length, H/λ) was set approximately equal to 1/50. The circular frequency ω of incident wave was varied in the range of $Ks = \omega^2 s/g = 0.2 \sim 1.6$. Measured data were analyzed using an ordinary Fourier-analysis technique, from which the first-order term oscillating with circular frequency ω was extracted and stored as the complex amplitude, including both amplitude and phase difference. The phase lead is defined as positive and measured from the time instant when the trough of incident wave comes at $x = 0$.

4. Results and Discussion

4.1 Frequency dependence on wave elevation

To see the variation tendency of the wave elevation due to hydrodynamic interactions, measurements have been made for many different values of Ks. Because of shortage of space,

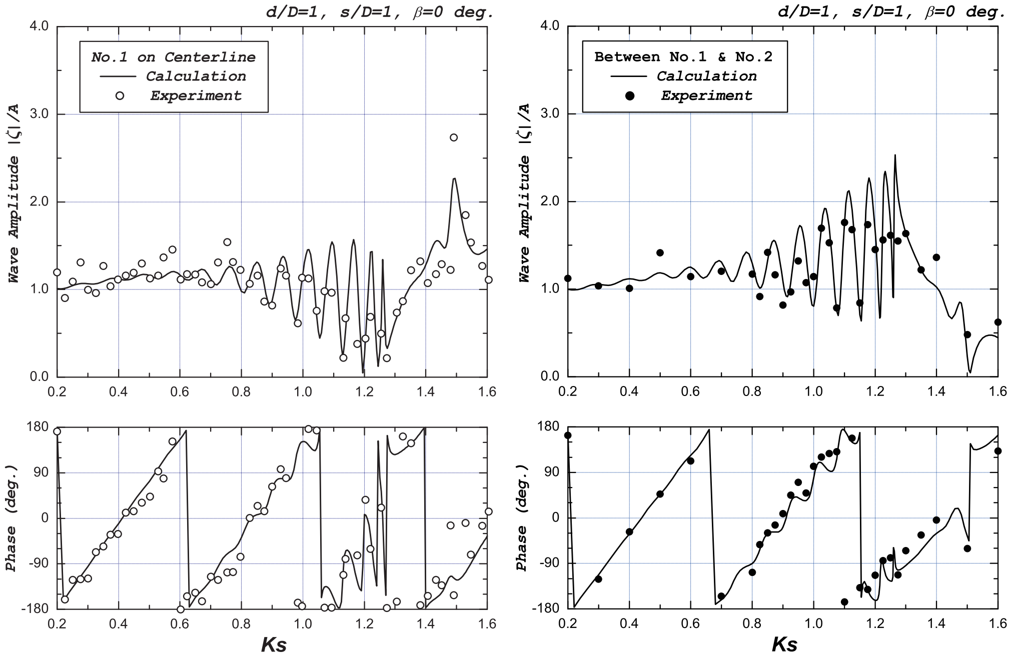

Fig. 3 Wave elevation along the centerline of the model shown in Fig. 2 at $x/a = -30$ (left figure) and at $x/a = -28$ (right figure), for the case of $d/D = 1$

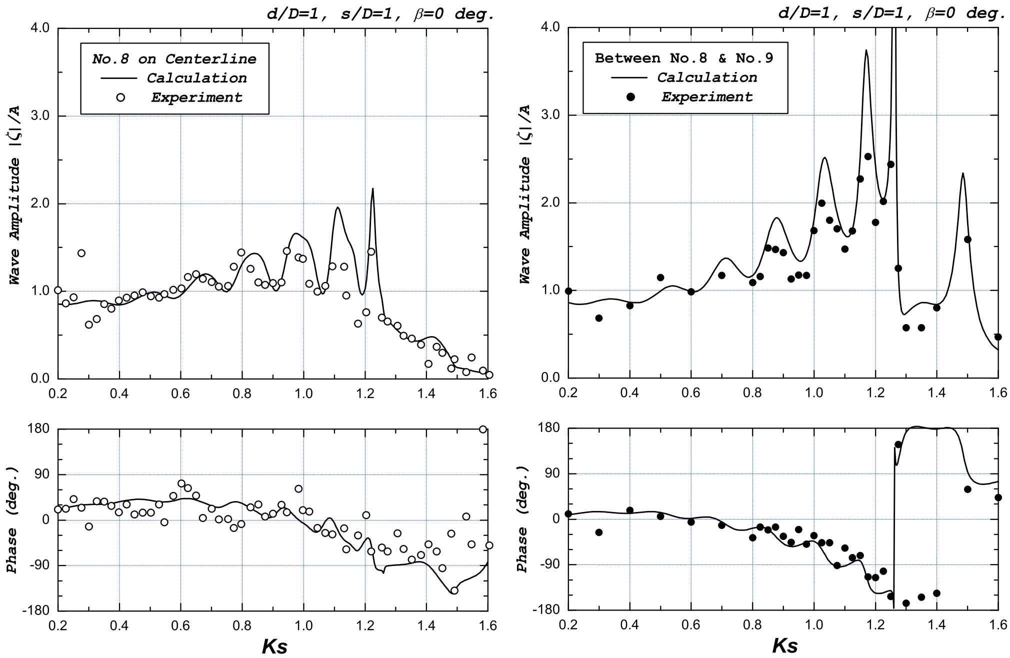

Fig. 4 Wave elevation along the centerline of the model shown in Fig. 2 at $x/a = -2$ (left figure) and at $x/a = 0$ (right figure), for the case of $d/D = 1$

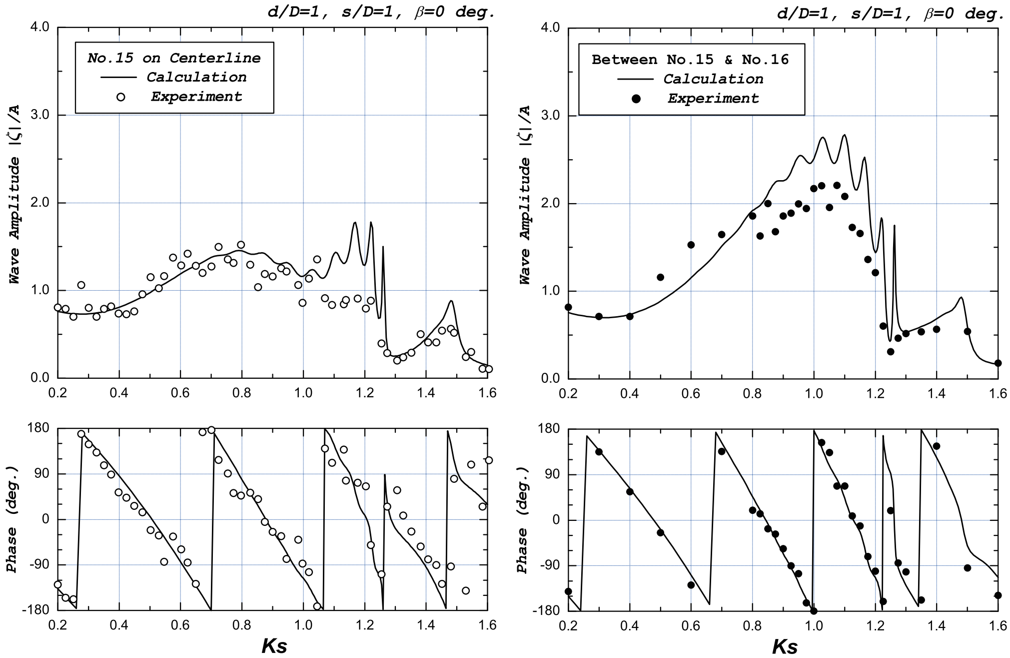

Fig. 5 Wave elevation along the centerline of the model shown in Fig. 2 at $x/a = 26$ (left figure) and at $x/a = 28$ (right figure), for the case of $d/D = 1$

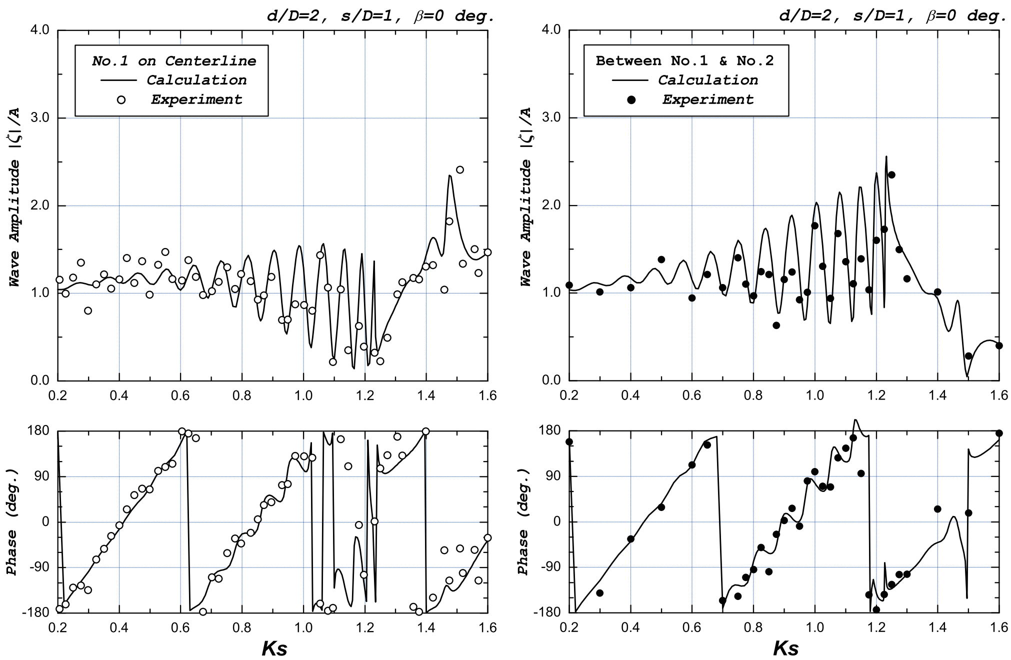

Fig. 6 Wave elevation along the centerline of the model shown in Fig. 2 at $x/a = -30$ (left figure) and at $x/a = -28$ (right figure), for the case of $d/D = 2$

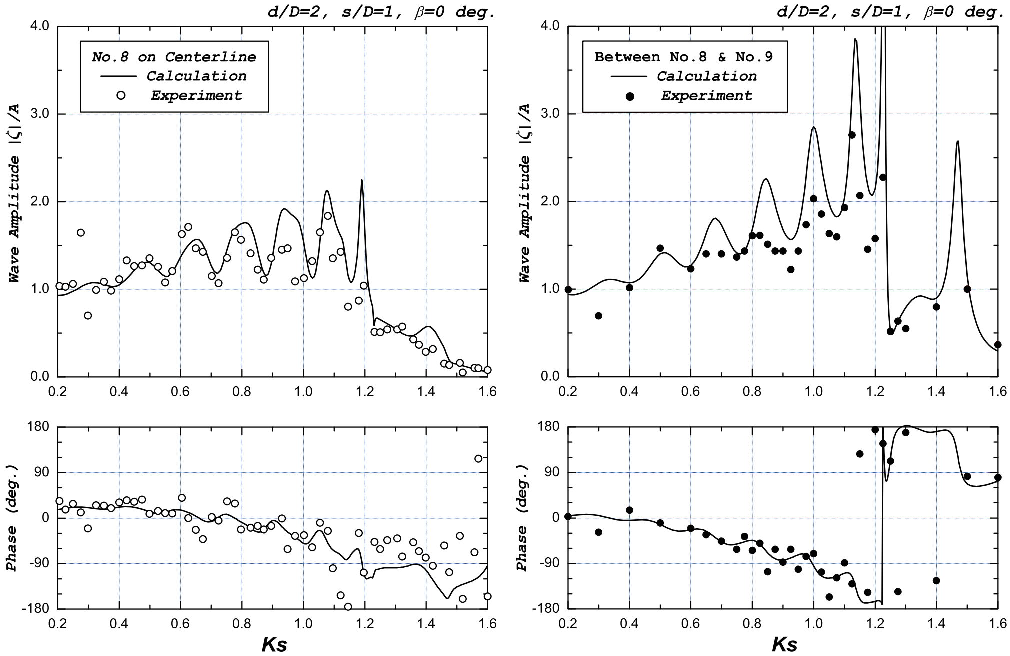

Fig. 7 Wave elevation along the centerline of the model shown in Fig. 2 at $x/a = -2$ (left figure) and at $x/a = 0$ (right figure), for the case of $d/D = 2$

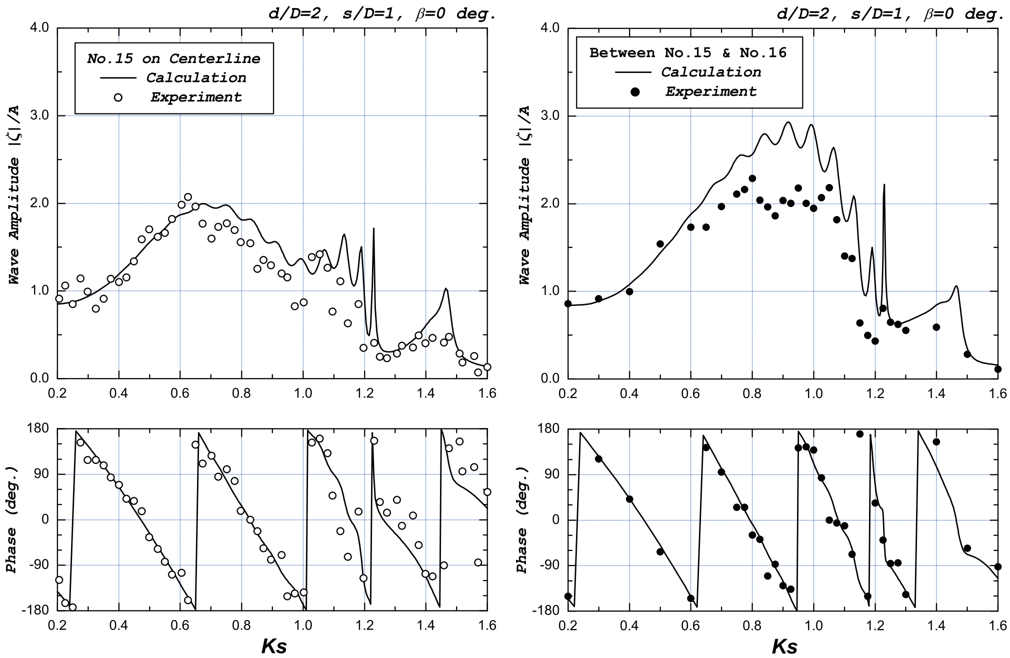

Fig. 8 Wave elevation along the centerline of the model shown in Fig. 2 at $x/a = 26$ (left figure) and at $x/a = 28$ (right figure), for the case of $d/D = 2$

only the results at 6 representative points are shown in Figs. 3–5, with Ks taken as the abscissa, for the case of $d = D$. The first two positions (just beside Column No. 1 and exactly between No. 1 and No. 2) shown as Fig. 3 are on the upwave side. Rapid and regular variation can be seen in the frequency range lower than $Ks \simeq 1.26$, which are due to hydrodynamic interactions with the waves diffracted from downstream cylinders. Although the separation distance between the first two positions is just s, the wave amplitude becomes much different as the frequency increases.

The second two positions shown as Fig. 4 are just beside Column No. 8 and exactly between No. 8 and No. 9; these are near the midst of the structure (the real midst is exactly between No. 8 and No. 9). Compared to the variation pattern at upwave positions, the amplitude variation with respect to Ks becomes mild for lower frequencies. However, at the midst (i. e. exactly between No. 8 and No. 9), the amplitude becomes very large especially when the frequency approaches $Ks \simeq 1.26$ from lower frequencies. According to Maniar and Newman (1997), $Ks = 1.26$ corresponds approximately to a near-trapped mode of Neumann type. Computed results are generally in good agreement with measured values. However, at frequencies slightly lower than the near-trapped-mode frequency, computations apparently overpredict, which may be attributed to the potential-flow assumption in the theory. It can be seen that nondimensional values of the measured wave amplitude are all less than 3.0. Considering that the wave steepness of incident wave was $H/\lambda \simeq 1/50$, we can envisage that the wave steepness of scattered wave is $H/\lambda \simeq 3/50 = 1/16.7$, which is close to the limit of wave breaking.

The last two positions shown as Fig. 5 are just beside Column No. 15 and exactly between No. 15 and No. 16, which are on the downwave side. The variation in amplitude with respect to Ks becomes further mild. In the frequency range slightly lower than the near-trapped-mode frequency, computations predict spike-like variation, but this is not clear in the measured results. Furthermore, in this frequency range, measured values are obviously lower than the computations, which may be due to effects of viscosity originating from the boundary layers of upwave cylinders. It can also be observed that the wave amplitude is much different between the two positions shown in Fig. 5, although the separation distance between these two positions is just s.

Figures 6–8 show the results for the case of deeper draft, $d = 2D$, at the same 6 representative positions along the centerline. By comparison with Figs. 3–5, variation tendency and the degree of agreement between experiments and computations are almost the same. One noticeable and important difference is that the value of Ks corresponding to the near-trapped-mode frequency is slightly lower than that for $d = D$; that is, $Ks \simeq 1.24$ for the case of $d = 2D$ whereas $Ks \simeq 1.26$ for the case of $d = D$.

4.2 Spatial variation at some fixed frequencies

It has been shown that the wave amplitude varies depending on the measurement position and the wave frequency. To see the spatial variation in the wave elevation, the wave amplitudes along the centerline are shown in Figs. 9 and 10, with positions along the centerline taken as the abscissa. Fig. 9 is the case of $d = D$ and includes the results for eight cases of $Ks = 0.8$, 1.0, 1.1, 1.15, 1.2, 1.3, 1.4 and 1.5. On the other hand, Fig. 10 is for the case of $d = 2D$ and the results are shown at $Ks = 0.8$, 1.0, 1.05, 1.1, 1.15, 1.2, 1.25 and 1.3.

First it can be seen that variation characteristics for two cases of $d = D$ and $d = 2D$ are very similar except that the near-trapped-mode frequency is slightly different. Computations have been performed at regular intervals of 201 points along the centerline and shown by a continuous solid line. The results in the first measurements are shown with closed circles (•),

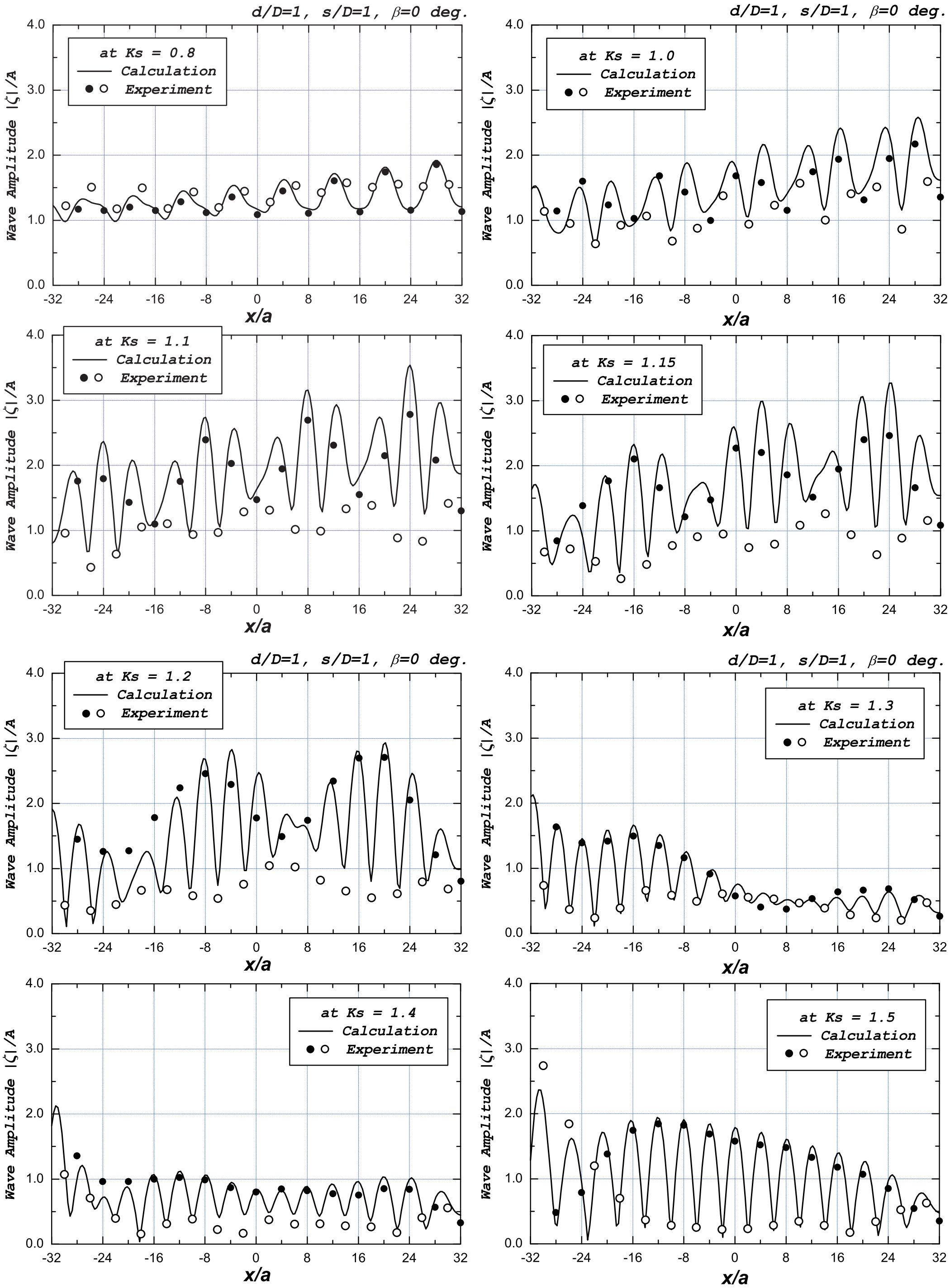

Fig. 9 Spatial variation of the wave amplitude along the centerline of the model shown in Fig. 2, for the case of $d/D = 1$

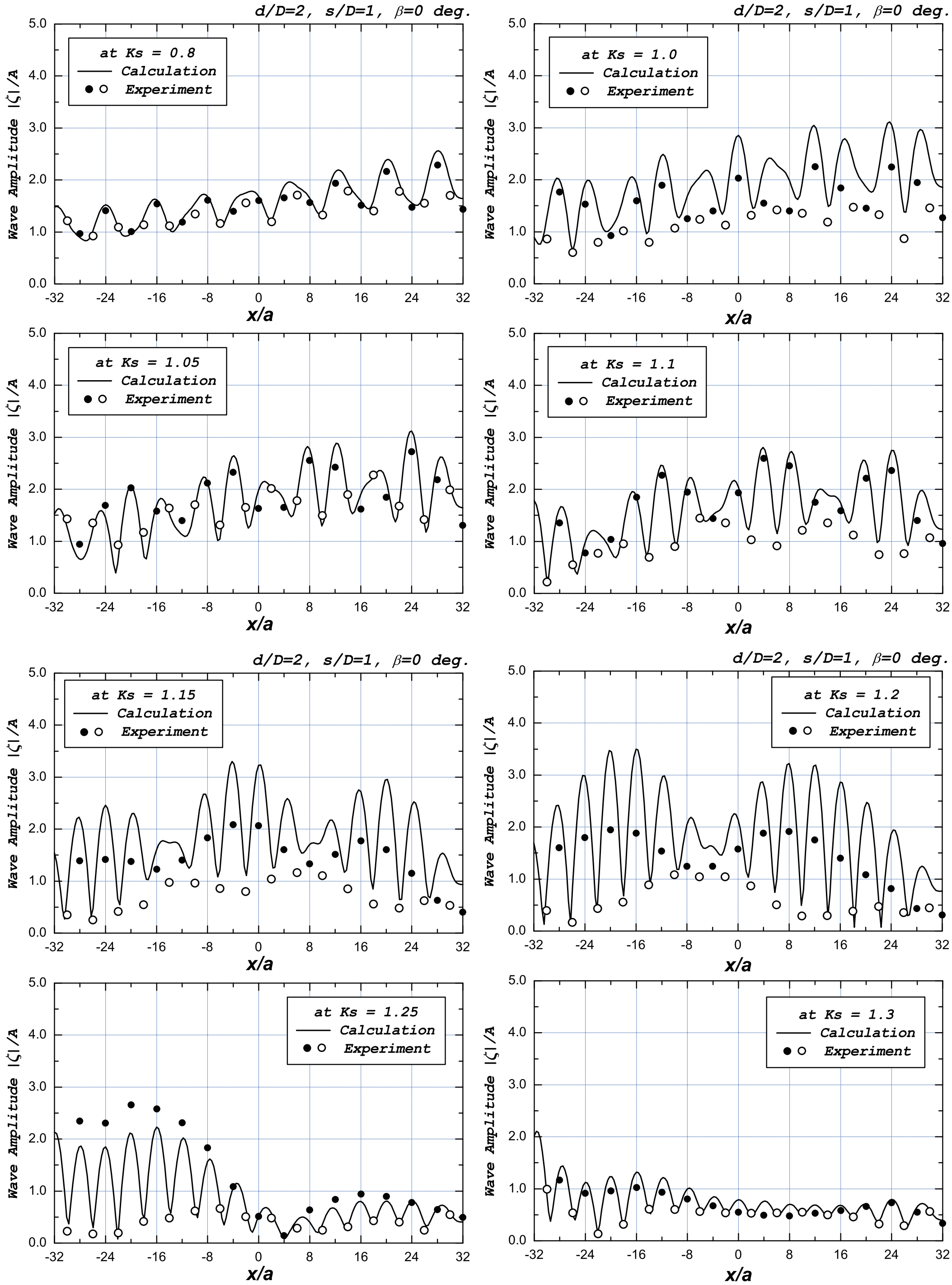

Fig. 10 Spatial variation of the wave amplitude along the centerline of the model shown in Fig. 2, for the case of $d/D = 2$

which correspond to the values measured at middle positions between the cylinders shown in Fig. 2. Shown by open circles (○) are the results in the second measurements at positions just beside the cylinders.

As the position goes downstream, the maximum of wave amplitude increases at lower frequencies, e. g. $Ks = 0.8$ to 1.1. Furthermore, the envelope of wave amplitude begins to fluctuate, as the frequency increases up to the near-trapped-mode frequency ($Ks \simeq 1.26$ for $d = D$ and $Ks \simeq 1.24$ for $d = 2D$). In fact, the number of crests in the envelope of amplitude variation decreases as the frequency approaches the near-trapped-mode frequency. The variation tendency changes drastically when the frequency becomes higher than the near-trapped-mode frequency. When the amplitude variation is large, the wave amplitudes at points just beside cylinders are relatively small, and on the contrary the values at middle points between cylinders are large. This is actually a typical wave pattern at near-trapped modes.

Regarding the degree of agreement between experiments and numerical computations, the overall agreement is good and variation tendency is well predicted by the present computations. However, when the amplitude variation is large due to strong hydrodynamic interactions, numerical results obviously overpredict, which may be attributed, as already discussed regarding Figs. 3 to 8, to viscous effects, not included in the present computations.

5. Conclusions

To have clear understanding on the wave interactions among a great number of columns, wave measurements have been conducted at a large number of frequencies and at 32 positions along the longitudinal centerline of a model composed of 64 vertical circular cylinders periodically placed in 4 rows and 16 columns. The results were compared with numerical computations made by a combination of the quadratic boundary-element method for evaluating the diffraction characteristics of an elementary body and the Kagemoto and Yue wave-interaction theory for multiple bodies.

The occurrence of the near-trapped mode was confirmed for the 64-column model used in the present study, and the near-trapped-mode frequency was found to be slightly different depending on the draft of columns. Around this near-trapped-mode frequency, the variation in wave amplitude is very large, and the amplitude tends to be maximal at positions exactly between adjacent cylinders and minimal at positions just beside cylinders; which is a typical wave pattern at near-trapped modes of Neumann type.

The overall quantitative agreement was favorable between measured and computed results, and the variation tendency in the wave amplitude with respect to the frequency and the spatial position was also well predicted by the present calculation method. However, when the wave amplitude becomes large due to near-trapped-wave phenomena, numerical results were obviously larger than measured ones.

References

1. Kagemoto, H. and Yue, D. K. P. (1985) "Interactions among Multiple Three-Dimensional Bodies in Water Waves: An Exact Algebraic Method", *J. of Fluid Mechanics*, **166**, 189–209.

2. Kagemoto, H., Fujino, M. et al. (1998) "On the Wave Decay around a Very Large Semisubmersible Type Floating Structure (2nd Report)", *J. of the Society of Naval Architects of Japan*, **184**, 271–282.

3. Kagemoto, H., Murai, M., Saito, M., Molin, B. and Malenica, S. (2002), "Experimental and theoretical analysis of the wave decay along a long array of vertical cylinders", *J. of Fluid Mechanics*, **456**, 113–135.

4. Kashiwagi, M. (2000) "Hydrodynamic Interactions among a Great Number of Columns Supporting a Very Large Flexible Structure", *J. of Fluids and Structures*, **14**, 1013–1034.

5. Maniar, H. D. and Newman, J. N. (1997) "Wave Diffraction by a Long Array of Cylinders", *J. of Fluid Mechanics*, **339**, 309–330.

6. Newman, J. N. (2001) "Wave Effects on Multiple Bodies", *Hydrodynamics in Ship and Ocean Engineering*, edited by M. Kashiwagi, RIAM, Kyushu Univ., 3–26.

Hydrodynamics of a Body Floating in a Two-Layer Fluid of Finite Depth. Part 2: Diffraction Problem and Wave-Induced Motions*

Masashi KASHIWAGI, Igor TEN and Makoto YASUNAGA
Research Institute for Applied Mechanics, Kyushu University
Kasuga, Fukuoka 816-8580, Japan

Abstract

A linearized two-dimensional diffraction problem in a two-layer fluid of finite depth was solved for a general floating body and relevant wave-induced motions were studied. In a two-layer fluid, for a prescribed frequency, incident waves propagate with two different wave modes. Thus the wave-exciting forces and resulting motions must be computed separately for each mode of the incident wave. The boundary integral equation method developed by the authors in the Part-1 article was applied to directly obtain the diffraction potential (pressure) on the body surface. With the computed results, an investigation was carried out on the effects of the fluid density ratio and the interface position on the wave-exciting forces on the body and the motions of the body, including the case in which the body intersects the interface. By a systematic derivation using Green's theorem, all the possible reciprocity relations were derived theoretically in explicit forms for a system of finite depth; these relations were confirmed to be satisfied numerically with very good accuracy. Experiments were also carried out using water and isoparaffin oil as the two fluids and a Lewis-form body. Measured results for the sway- and heave-exciting forces and the heave motion were compared with the computed results, and a favorable agreement was found.

Keywords: Two-layer fluid, surface-wave mode, internal wave mode, diffraction problem, wave-induced motions, finite water depth.

1. Introduction

This article is a sequel to the previous work by the authors [1] and is concerned with the wave diffraction and wave-induced motions of a general body floating in a two-layer fluid of finite depth. In the previous article (Part 1), the radiation problem was considered and a boundary integral equation method was developed to accommodate any shape of floating body, which may penetrate the interface between the upper and lower layers. It was shown that, for a given frequency of forced oscillation, two different waves with different wavenumbers are generated and these waves are referred to as the surface-wave mode (with longer wavelength) and the internal-wave mode (with shorter wavelength). Irrespective of the body shape and the mode of motion, a simple relation for the amplitude ratio between the waves on the free surface and on the interface holds for each wave mode. However, the amplitude ratio between the waves of surface- and internal-wave modes on the free surface or the interface is dependent on the shape of the floating body, and the wave elevation at a fixed position

∗ *Reprinted from Journal of Marine Science and Technology, Vol. 11, No. 3, pp. 150–164, 2006 (September)*

varies depending on the phase difference between the waves of surface- and internal-wave modes.

This wave radiation from a body can be regarded as wave generation by a wavemaker, and thus it is obvious that the incident wave to be considered in the diffraction problem has the same characteristics in the two different wave modes. Thus, in a two-layer fluid, the diffraction problem must be solved for two different incident waves at a given frequency. What makes the problem more complicated is that each incident wave will be diffracted by the body into two different wave modes, and hence some of the energy of the incident wave may be transferred from one mode to the other. This kind of somewhat complicated diffraction problem is solved in this article using the calculation method developed in Part 1, and the diffraction potential (which is the sum of the incident-wave and scattering potentials and is equivalent to the diffraction pressure) on the wetted surface of a general body is directly obtained.

In linear water wave theory, particularly in a single-layer fluid, a number of reciprocity relations are known and a systematic derivation of these relations was established by Newman [2] using Green's theorem. The same idea was applied in the previous article to derive some hydrodynamic relations satisfied in the radiation problem, and again is applied to the diffraction problem in this article. As a result, the Haskind-Hanaoka-Newman relation, which relates the wave-exciting force to the radiation wave by forced oscillation of a body, is derived in an explicit form and all the possible relations among transmitted and reflected waves observed in a two-layer fluid are derived. Yeung and Nguyen [3] described the idea of the far-field method for deriving the Haskind-Hanaoka-Newman relation in a two-layer fluid of finite depth, but no explicit expression was presented. Linton and McIver [4] and Cadby and Linton [5] also derived various reciprocity relations for the diffraction problem in a two-layer fluid, but in their work, the lower layer was of infinite depth.

Besides the works cited above, some studies have been done on the solution method for radiation and diffraction problems, for instance the work of Sturova [6]. However, no results have been presented for the wave-induced motions of a floating body in two-layer fluids. In this article, using hydrodynamic radiation and diffraction forces and hydrostatic restoring forces, the wave-induced motions of a body in various two-layer fluids of finite depth are computed. In addition, the ways in which differences in the ratio of the fluid density and the vertical position of the interface may influence the motions of a body are discussed.

Experiments were also conducted to measure the wave-exciting forces and the motions of a body in regular waves with a 2-D Lewis-form body. As in the previous article, the two-layer fluid was realized using Isozole 300 (a type of isoparaffin oil, manufactured by Nisseki Mitsubishi, Tokyo) as the upper-layer fluid and water as the lower-layer fluid, and two different conditions were tested for the depth ratio between the upper layer and lower layer. The measured results for the sway- and heave-exciting forces and the heave-motion in waves were compared with corresponding numerical computations, and the reasons for discrepancies and the effects of two-layer flow on the results are discussed.

2. Mathematical Formulation

We consider a 2-D floating body of general shape in a two-layer fluid with finite depth. The body may intersect the interface and is assumed to oscillate harmonically in response to an incident wave with circular frequency ω. The Cartesian coordinate system and notations used in the analyses below are shown in Fig. 1, with the origin on the undisturbed free surface and the z-axis positive in the downward direction. The free surface, the interface,

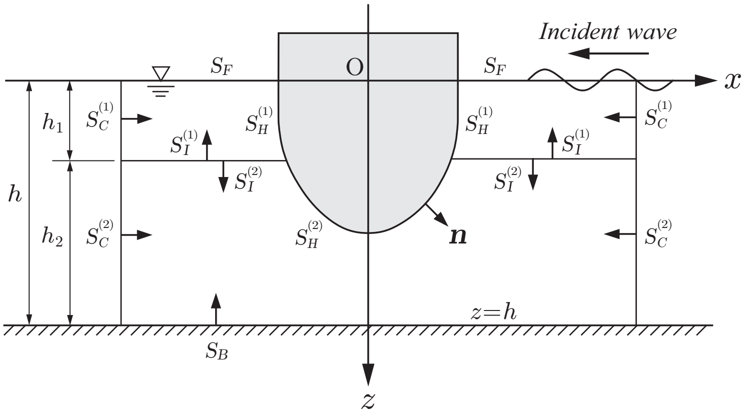

Fig. 1 Coordinate system and notations

and the flat rigid bottom of the water are located at $z = 0$, $z = h_1$, and $z = h\,(= h_1 + h_2)$, respectively.

With the linearized potential flow assumption, the velocity potential is introduced and written in the form:

$$\Phi^{(m)}(x, z, t) = \mathrm{Re}\Big[\,\phi^{(m)}(x, z)\,e^{i\omega t}\Big], \quad m = 1, 2 \tag{1}$$

$$\phi^{(m)}(x, z) = \phi_D^{(m)}(x, z) + \sum_{j=1}^{3} i\omega X_j\,\phi_j^{(m)}(x, z) \tag{2}$$

$$\phi_D^{(m)}(x, z) = \phi_0^{(m)}(x, z) + \phi_4^{(m)}(x, z) \tag{3}$$

Here the superscript (m) denotes the fluid layer, with $m = 1$ and 2 corresponding to the upper and lower layers, respectively. $\phi_0^{(m)}$ denotes the velocity potential of the incident wave (details of which will be described later), $\phi_4^{(m)}$ denotes the velocity potential associated with the scattering the incident wave, and the sum of these, $\phi_D^{(m)}$, is referred to as the diffraction potential. The second term on the right-hand side of Eq. 2 is, as described in the Part-1 article, associated with the radiation problem and X_j denotes the complex amplitude of the j-th mode of motion ($j = 1$ for sway, $j = 2$ for heave, and $j = 3$ for roll), which may be determined by solving the motion equations of a body in waves.

The governing equation for the diffraction and radiation velocity potentials ($j = D$ and $1{\sim}3$) is the Laplace equation:

$$\nabla^2\phi_j^{(m)} = 0 \tag{4}$$

The linearized boundary conditions to be satisfied are expressed as follows:

$$\frac{\partial\phi_j^{(1)}}{\partial z} + K\phi_j^{(1)} = 0 \quad \text{on } z = 0 \tag{5}$$

$$\left.\begin{aligned} &\frac{\partial\phi_j^{(1)}}{\partial z} = \frac{\partial\phi_j^{(2)}}{\partial z} \\ &\gamma\left(\frac{\partial\phi_j^{(1)}}{\partial z} + K\phi_j^{(1)}\right) = \frac{\partial\phi_j^{(2)}}{\partial z} + K\phi_j^{(2)} \end{aligned}\right\} \text{ on } z = h_1 \tag{6}$$

$$\frac{\partial \phi_j^{(2)}}{\partial z} = 0 \quad \text{on } z = h\,(= h_1 + h_2) \tag{7}$$

$$\left.\begin{aligned} \frac{\partial \phi_D^{(m)}}{\partial n} &= 0 \\ \frac{\partial \phi_j^{(m)}}{\partial n} &= n_j \;\; (j = 1 \sim 3) \end{aligned}\right\} \text{ on } S_H^{(m)} \tag{8}$$

where $K = \omega^2/g$, with g being the gravitational acceleration; $\gamma = \rho_1/\rho_2 \leq 1$, with ρ_m being the density of the upper ($m = 1$) and lower ($m = 2$) fluids; and n_j denotes the j-th component ($n_1 = n_x$, $n_2 = n_z$, and $n_3 = xn_z - zn_x$) of the normal vector, which is defined as positive when directed into the fluid domain from the boundaries (see Fig. 1). The parameter $\varepsilon = 1 - \gamma$, which is associated with the density ratio, will also be used hereafter.

The boundary-value problem may be completed by imposing the radiation condition of generated waves radiating away from the body, which is the case for the velocity potentials of the wave scattering and radiation, but is not the case for the velocity potential of the incident wave.

3. Incident Wave Potential

Let the incident wave propagate from the positive x-axis. The velocity potential of this incident wave can be determined from Eqs. 4–7 irrespective of the presence of a body, and is expressed in the form:

$$\phi_0^{(m)}(x, z) = \frac{gA}{i\omega}\, Z^{(m)}(k; z)\, e^{ikx} \tag{9}$$

where

$$\left.\begin{aligned} Z^{(1)}(k; z) &= \frac{k\,\mathrm{ch}kz - K\,\mathrm{sh}kz}{k} \\ Z^{(2)}(k; z) &= \frac{K\,\mathrm{ch}kh_1 - k\,\mathrm{sh}kh_1}{k\,\mathrm{sh}kh_2}\;\mathrm{ch}k(z-h) \end{aligned}\right\} \tag{10}$$

and A in Eq. 9 is unknown at this stage. For brevity, the hyperbolic functions of $\cosh(x)$ and $\sinh(x)$ will be written as $\mathrm{ch}(x)$ and $\mathrm{sh}(x)$, respectively, throughout this article.

The variable k in Eqs. 9 and 10 satisfies the dispersion relation, given by the boundary conditions in Eq. 6 on the interface, which can be expressed as:

$$D(k) = K(k\,\mathrm{sh}kh - K\,\mathrm{ch}kh) + \varepsilon(K^2 - k^2)\,\mathrm{sh}kh_1\,\mathrm{sh}kh_2 = 0 \tag{11}$$

For a given frequency, $K = \omega^2/g$, there exist two different solutions satisfying Eq. 11. These solutions are denoted as k_1 and k_2, which are the wavenumbers of progressive waves present on both the free surface and the interface. The smaller wavenumber k_1 is referred to as the surface-wave mode and the larger wavenumber k_2 is referred to as the internal-wave mode. In view of these two wave modes, we write the velocity potential of the incident wave as follows:

$$\phi_0^{(m)}(x, z) = \sum_{p=1}^{2} \frac{gA_p}{i\omega}\, \phi_{0p}^{(m)}(x, z) \tag{12}$$

$$\phi_{0p}^{(m)}(x, z) = Z^{(m)}(k_p; z)\, e^{ik_p x} \tag{13}$$

The unknown coefficient A_p in Eq. 12 may be determined by specifying the amplitude of the incident wave on the free surface ($z = 0$) or the interface ($z = h_1$). The relations between the velocity potential $\phi_{0p}^{(m)}$ and the associated wave elevation are given by the kinematic boundary condition as follows:

$$\frac{\partial \phi_{0p}^{(1)}}{\partial z} = i\omega\, a_p^{(1)}\, e^{ik_p x} \qquad \text{on } z = 0 \tag{14}$$

$$\frac{\partial \phi_{0p}^{(1)}}{\partial z} = \frac{\partial \phi_{0p}^{(2)}}{\partial z} = i\omega\, a_p^{(2)}\, e^{ik_p x} \qquad \text{on } z = h_1 \tag{15}$$

where $a_p^{(1)}$ and $a_p^{(2)}$ $(p = 1, 2)$ denote the amplitudes of the k_p-wave mode on the free surface and the interface, respectively.

Substituting Eq. 13 in Eq. 14, it follows that $A_p = a_p^{(1)}$. Likewise it follows from Eq. 15 that $A_p = \alpha(k_p)a_p^{(2)}$ with:

$$\alpha(k_p) = \frac{a_p^{(1)}}{a_p^{(2)}} = \frac{K}{K\,\mathrm{ch}k_p h_1 - k_p\,\mathrm{sh}k_p h_1} \tag{16}$$

Given that $A_p = a_p^{(1)} = \alpha(k_p)a_p^{(2)}$, amplitude $a_p^{(1)}$ or $a_p^{(2)}$ may be taken at each wave mode $(p = 1, 2)$ as the incident-wave amplitude for normalizing $\phi_0^{(m)}$. In the theory, using $a_p^{(1)}$ may be simpler for both wave modes. However, in the numerical computations for the incident wave of internal-wave mode ($p = 2$), using $a_2^{(2)}$ for normalization may be better for numerical accuracy because $|\, a_2^{(2)} \,| > |\, a_2^{(1)} \,|$ as was shown on Fig. 4 of the previous article. We note that no general relation exists between $a_1^{(1)}$ and $a_2^{(2)}$ and hence two different diffraction problems corresponding to the incident waves in surface-wave and internal-wave modes must be solved separately at a given frequency.

The scattering potential associated with $\phi_{0p}^{(m)}$ is represented by $\phi_{4p}^{(m)}$ and their sum, $\phi_{Dp}^{(m)} = \phi_{0p}^{(m)} + \phi_{4p}^{(m)}$, is defined as the diffraction potential for each wave mode. It should be noted that, even when the incident wave contains only one wave mode, the incident wave will be diffracted in two different wave modes with wavenumbers k_1 and k_2.

4. Boundary Integral Equation

As in the radiation problem, the integral equation for the diffraction potential on the wetted surface of a body will be derived for a general case in where the body penetrates the interface of a two-layer fluid.

With the notations shown in Fig. 1 for the boundaries, we invoke Green's theorem for the velocity potential $\phi^{(m)}(\mathrm{Q})$ to be obtained and an appropriate Green's function $G_n^{(m)}(\mathrm{Q};\mathrm{P})$ over the closed surfaces $S^{(1)} = S_H^{(1)} + S_C^{(1)} + S_I^{(1)} + S_F$ and $S^{(2)} = S_H^{(2)} + S_C^{(2)} + S_I^{(2)} + S_B$. (Here $\mathrm{Q} = (\xi, \zeta)$ is the integration point on the boundaries and $\mathrm{P} = (x, z)$ is the field point under consideration; for the definition of the Green function in a two-layer fluid, the reader is referred to the previous article [1].)

We note that both $\phi^{(m)}(\mathrm{Q})$ and $G_n^{(m)}(\mathrm{Q};\mathrm{P})$ satisfy the same boundary conditions on S_F, S_B and S_I, but the diffraction potential does not satisfy the radiation condition at $S_C^{(1)}$ and $S_C^{(2)}$. With these facts taken into consideration, the same analysis as that in the previous article gives the following result:

$$C(\mathrm{P})\phi^{(m)}(\mathrm{P}) = \sum_{n=1}^{2}\int_{S_H^{(n)}}\left\{\frac{\partial\phi^{(n)}}{\partial n}G_n^{(m)}(\mathrm{P};\mathrm{Q}) - \phi^{(n)}\frac{\partial G_n^{(m)}(\mathrm{P};\mathrm{Q})}{\partial n}\right\}d\ell$$
$$+\sum_{n=1}^{2}\int_{S_C^{(n)}}\left\{\frac{\partial\phi^{(n)}}{\partial n}G_n^{(m)}(\mathrm{P};\mathrm{Q}) - \phi^{(n)}\frac{\partial G_n^{(m)}(\mathrm{P};\mathrm{Q})}{\partial n}\right\}d\ell \tag{17}$$

where $C(\mathrm{P})$ is the solid angle which is taken as equal to 0.5 when P is on the boundary surface and 1.0 when P is in the fluid. The integrals and normal derivatives in Eq. 17 are to be performed with respect to $\mathrm{Q}(\xi,\zeta)$, but for brevity, the argument of the velocity potential is not displayed.

Let us consider $\phi_{Dp}^{(m)} = \phi_{0p}^{(m)} + \phi_{4p}^{(m)}$ for $\phi^{(m)}$ in Eq. 17. Then, taking account of the condition of zero normal velocity on $S_H^{(n)}$, shown in Eq. 8, and the fact that $\phi_{4p}^{(m)}$ satisfies the radiation condition but $\phi_{0p}^{(m)}$ does not, Eq. 17 can be reduced to the following:

$$C(\mathrm{P})\phi_{Dp}^{(m)}(\mathrm{P}) = -\sum_{n=1}^{2}\int_{S_H^{(n)}}\phi_{Dp}^{(n)}\frac{\partial G_n^{(m)}(\mathrm{P};\mathrm{Q})}{\partial n}\,d\ell$$
$$+\sum_{n=1}^{2}\int_{S_C^{(n)}}\left\{\frac{\partial\phi_{0p}^{(n)}}{\partial n}G_n^{(m)}(\mathrm{P};\mathrm{Q}) - \phi_{0p}^{(n)}\frac{\partial G_n^{(m)}(\mathrm{P};\mathrm{Q})}{\partial n}\right\}d\ell \tag{18}$$

To understand the second line of Eq. 18, let us apply Green's theorem to $\phi_{0p}^{(n)}(\mathrm{Q})$ and $G_m^{(n)}(\mathrm{Q};\mathrm{P})$. In this case, we need not consider the presence of a floating body, and hence the second line of Eq. 18 turns out to be $\phi_{0p}^{(m)}$ itself. Therefore, as a conclusion of the analysis, the integral equation for the diffraction potential on the body surface takes the form:

$$C(\mathrm{P})\phi_{Dp}^{(m)}(\mathrm{P}) + \sum_{n=1}^{2}\int_{S_H^{(n)}}\phi_{Dp}^{(n)}(\mathrm{Q})\frac{\partial G_n^{(m)}(\mathrm{P};\mathrm{Q})}{\partial n_{\mathrm{Q}}}\,d\ell = \phi_{0p}^{(m)}(\mathrm{P}) \quad (p=1,2) \tag{19}$$

The numerical solution method for Eq. 19 is the same as that employed for the radiation problem. In fact, the left-hand side of Eq. 19 is the same form of the integral equation as that for the radiation problem. Thus, simultaneous equations obtained from Eq. 19 using the constant-panel and collocation method can be solved at the same time with the radiation problem. We note again that the cases of $p = 1$ and 2 in Eq. 19 are to be solved as different problems and the term on the right-hand side for each case can directly be given by Eq. 13.

For a body with port-and-starboard symmetry, the unknowns can be limited to half of the body surface by considering the symmetry relation; that is, $\phi_{0p}^{(m)}$ in Eq. 13 can be separated into even and odd functions in x, and correspondingly $\phi_{Dp}^{(m)}$ can be decomposed into the symmetric and antisymmetric components.

5. Wave-Exciting Forces

Once the velocity potential on the wetted surface of the body is determined, the wave-exciting forces in sway and heave and the moment in roll can be readily calculated. The calculation formula for the nondimensional form of these quantities is given by:

$$E'_{jp} = \frac{E_{jp}}{\rho_1 g a_p b \epsilon_j} = \int_{S_H^{(1)}}\phi_{Dp}^{(1)}n_j\,d\ell + \frac{1}{\gamma}\int_{S_H^{(2)}}\phi_{Dp}^{(2)}n_j\,d\ell \tag{20}$$

where E_{jp} is the wave-exciting force in the j-th direction caused by the incident wave of k_p-wave mode. In the nondimensional form, a_p denotes the amplitude of the incident wave, $b = B/2$ denotes half the breadth at $z = 0$, and ϵ_j is defined as $\epsilon_1 = \epsilon_2 = 1$ and $\epsilon_3 = b$.

For nondimension in Eq. 20, the density of the upper fluid ρ_1 is used, but if the density of the lower fluid ρ_2 is used instead (this is the case in the experiments shown later), Eq. 20 must be multiplied by $\gamma = \rho_1/\rho_2$. In numerical computations, $a_p = a_p^{(p)}$ is adopted as the normalizing factor; that is, the amplitude on the free surface is used for the surface-wave mode ($p = 1$) and the amplitude on the interface is used for the internal-wave mode ($p = 2$). Therefore, the numerical solution for the internal-wave mode is multiplied by $\alpha(k_2)$, as defined by Eq. 16.

6. Asymptotic Expression in the Far Field

Let us consider the asymptotic form of the velocity potential as $|x - \xi| \to \infty$ and define the Kochin function, which will be used subsequently.

The asymptotic form of Green's function is shown in the previous article and is written as:

$$G_n^{(m)}(\mathrm{P};\mathrm{Q}) \sim i \sum_{q=1}^{2} \frac{W_n(k_q;\zeta)}{D'(k_q)}\, Z^{(m)}(k_q;z)\, e^{-ik_q|x-\xi|} \tag{21}$$

where

$$\left.\begin{aligned} W_1(k;\zeta) &= \gamma\, \alpha(k)\, k \,\mathrm{sh}\, kh_2\, Z^{(1)}(k;\zeta) \\ W_2(k;\zeta) &= \alpha(k)\, k \,\mathrm{sh}\, kh_2\, Z^{(2)}(k;\zeta) \end{aligned}\right\} \tag{22}$$

and $D'(k)$ denotes the derivative of $D(k)$, as defined by Eq. 11, which can be given as

$$\begin{aligned} D'(k) = {} & K\big(\mathrm{sh}\, kh + kh\, \mathrm{ch}\, kh - Kh\, \mathrm{sh}\, kh\big) \\ & + \varepsilon\Big\{-2k\, \mathrm{sh}\, kh_1\, \mathrm{sh}\, kh_2 + (K^2 - k^2)(h_1\, \mathrm{ch}\, kh_1\, \mathrm{sh}\, kh_2 + h_2\, \mathrm{sh}\, kh_1\, \mathrm{ch}\, kh_2)\Big\} \end{aligned} \tag{23}$$

Substituting Eq. 21 into Eq. 19 with $C(\mathrm{P}) = 1$, the desired result for the diffraction potential valid in the far field can be expressed in the form:

$$\phi_{Dp}^{(m)}(\mathrm{P}) \sim \phi_{0p}^{(m)} + i \sum_{q=1}^{2} H_{4p}^{\pm}(k_q)\, Z^{(m)}(k_q;z)\, e^{\mp ik_q x} \tag{24}$$

as $x \to \pm\infty$, where

$$H_{4p}^{\pm}(k) = -\sum_{n=1}^{2} \int_{S_H^{(n)}} \phi_{Dp}^{(m)} \frac{\partial}{\partial n} \frac{W_n(k;\zeta)}{D'(k)}\, e^{\pm ik\xi}\, d\ell \tag{25}$$

In the diffraction problem, the wave elevations on the free surface $\eta_{Dp}^{(1)}$ and on the interface $\eta_{Dp}^{(2)}$, nondimensionalized in terms of the incident-wave amplitude, may be obtained as:

$$\eta_{Dp}^{(1)} = \phi_{Dp}^{(1)}(x,0) \sim e^{ik_p x} + i \sum_{q=1}^{2} H_{4p}^{\pm}(k_q)\, e^{\mp ik_q x} \tag{26}$$

$$\eta_{Dp}^{(2)} = \frac{1}{1-\gamma}\Big\{\phi_{Dp}^{(2)} - \gamma \phi_{Dp}^{(1)}\Big\}_{z=h_1} \sim e^{ik_p x} + i \sum_{q=1}^{2} H_{4p}^{\pm}(k_q) \frac{1}{\alpha(k_q)}\, e^{\mp ik_q x} \tag{27}$$

We can see from these equations that the amplitude ratio between the scattered waves on the free surface and the interface for surface-wave ($q = 1$) and internal-wave ($q = 2$) modes can be given in the same form as Eq. 16.

For later convenience, let us define the coefficients of the transmitted and reflected waves. From Eq. 26, the diffraction wave on the free surface caused by the incident wave of k_p-wave mode incoming from the positive x-axis may be written as:

$$\eta_{Dp}^{(1)} \sim \begin{cases} e^{ik_p x} + \displaystyle\sum_{q=1}^{2} R_{pq}\, e^{-ik_q x} & \text{as } x \to +\infty \\ \displaystyle\sum_{q=1}^{2} T_{pq}\, e^{ik_q x} & \text{as } x \to -\infty \end{cases} \tag{28}$$

where

$$\left. \begin{aligned} T_{pq} &= \delta_{pq} + i\, H_{4p}^{-}(k_q) \\ R_{pq} &= i\, H_{4p}^{+}(k_q) \end{aligned} \right\} \tag{29}$$

with δ_{pq} being Kronecker's delta.

T_{pq} and R_{pq} in Eq. 29 are defined respectively as the coefficients of transmitted and reflected waves of the k_q-wave mode when the incident wave is of the k_p-wave mode.

7. Hydrodynamic Relations

In an analogous manner to that for the radiation problem, some reciprocity relations may be derived also for the diffraction problem, which can deepen our understanding of associated phenomena and may be used to check the accuracy in numerical computations.

Let us assume that $\phi^{(m)}$ and $\psi^{(m)}$ are two different solutions, both satisfying Eqs. 4–7 but not necessarily satisfying the same boundary conditions on the body surface (S_H) and the radiation surface (S_C) far from the body. Then, the use of Green's theorem and some mathematical transformations provide the following equation:

$$\begin{aligned} &\int_{S_H} w(z) \left\{ \frac{\partial \phi^{(m)}}{\partial n} \psi^{(m)} - \phi^{(m)} \frac{\partial \psi^{(m)}}{\partial n} \right\} d\ell \\ &= \left[\int_0^h w(z) \left\{ \frac{\partial \phi^{(m)}}{\partial x} \psi^{(m)} - \phi^{(m)} \frac{\partial \psi^{(m)}}{\partial x} \right\} dz \right]_{x=-\infty}^{x=+\infty} \end{aligned} \tag{30}$$

where

$$w(z) = \begin{cases} 1 & 0 \le z \le h_1 \\ 1/\gamma & h_1 \le z \le h = h_1 + h_2 \end{cases} \tag{31}$$

and the square brackets on the right-hand side of Eq. 30 means the difference between the quantities in brackets evaluated at $x = +\infty$ and $x = -\infty$.

First, we take the radiation potential of the j-th mode $\phi_j^{(m)}$ for $\phi^{(m)}$ and the diffraction potential $\phi_{Dp}^{(m)}$ for $\psi^{(m)}$. Note that these potentials satisfy the body boundary condition given by Eq. 8 and $\phi_j^{(m)}$ is expressed as:

$$\phi_j^{(m)} \sim i \sum_{q=1}^{2} H_j^{\pm}(k_q)\, Z^{(m)}(k_q; z)\, e^{\mp i k_q x} \tag{32}$$

at $x = \pm\infty$, with the Kochin function in the radiation problem defined by:

$$H_j^{\pm}(k) = \sum_{n=1}^{2} \int_{S_H^{(n)}} \left\{ \frac{\partial \phi_j^{(n)}}{\partial n} - \phi_j^{(n)} \frac{\partial}{\partial n} \right\} \frac{W_n(k;\zeta)}{D'(k)}\, e^{\pm ik\xi}\, d\ell \tag{33}$$

In this case, the left-hand side of Eq. 30 gives the wave-exciting force E'_{jp} from Eq. 20, and in terms of Eqs. 24 and 32 the right-hand side of Eq. 30 can be evaluated explicitly. The result takes the following form:

$$E'_{jp} = \mathcal{F}(k_p)\, H_j^{+}(k_p) \tag{34}$$

where

$$\begin{aligned}\mathcal{F}(k) &= \frac{2k}{\gamma}\left[\gamma \int_0^{h_1} \left\{Z^{(1)}(k;z)\right\}^2 dz + \int_{h_1}^{h_2} \left\{Z^{(2)}(k;z)\right\}^2 dz\right] \\ &= \frac{K}{k} + kh\frac{(K\,\mathrm{ch}\,kh_1 - k\,\mathrm{sh}\,kh_1)^2}{\gamma k^2\,\mathrm{sh}^2 kh_2} + \frac{\varepsilon}{\gamma}\frac{h_1}{k} \\ &\quad \times \left[\left(1 - \frac{k^2}{K^2} + \frac{1}{Kh_1}\right)\left(K\,\mathrm{ch}\,kh_1 - k\,\mathrm{sh}\,kh_1\right)^2 + \gamma\frac{(K^2-k^2)^2}{K^2}\,\mathrm{sh}^2 kh_1\right]\end{aligned} \tag{35}$$

Eq. 34 is the so-called Haskind-Hanaoka-Newman relation for the two-layer fluid, connecting the wave-exciting force with the wave-amplitude function in the radiation problem. $\mathcal{F}(k)$ given by Eq. 35 may be regarded as an influence coefficient associated with the two-layer and finite-depth effects.

Concerning this influence coefficient, let us transform directly the left-hand side of Eq. 30 by using Green's theorem and the body boundary condition. The result may be expressed as:

$$E'_{jp} = \int_{S_H^{(1)}} \left\{ \frac{\partial \phi_j^{(1)}}{\partial n} - \phi_j^{(1)} \frac{\partial}{\partial n} \right\} \phi_{0p}^{(1)}\, d\ell + \frac{1}{\gamma} \int_{S_H^{(2)}} \left\{ \frac{\partial \phi_j^{(2)}}{\partial n} - \phi_j^{(2)} \frac{\partial}{\partial n} \right\} \phi_{0p}^{(2)}\, d\ell \tag{36}$$

Here, from Eqs. 13 and 22, $\phi_{0p}^{(m)}$ can be written as:

$$\left.\begin{aligned} \phi_{0p}^{(m)} &= Z^{(m)}(k_p;z)\, e^{ik_p x} \\ Z^{(1)}(k;z) &= \frac{D'(k)}{\gamma\alpha(k)k\,\mathrm{sh}\,kh_2}\frac{W_1(k;z)}{D'(k)} \\ Z^{(2)}(k;z) &= \frac{D'(k)}{\gamma\alpha(k)k\,\mathrm{sh}\,kh_2}\,\gamma\,\frac{W_2(k;z)}{D'(k)} \end{aligned}\right\} \tag{37}$$

Therefore, substituting Eq. 37 in Eq. 36 and referring to Eq. 33, we can obtain an alternative expression for the Haskind-Hanaoka-Newman relation in the form

$$E'_{jp} = \mathcal{D}(k_p)\, H_j^{+}(k_p) \tag{38}$$

where

$$\mathcal{D}(k) \equiv \frac{D'(k)}{\gamma\alpha(k)k\,\mathrm{sh}\,kh_2} \tag{39}$$

$\mathcal{F}(k)$ must be identical to $\mathcal{D}(k)$ defined by Eq. 39. In fact this is the case, which can be proven analytically in terms of the dispersion relation Eq. 11, although necessary mathematical transformation is rather lengthy.

Next, as possible candidates for $\phi^{(m)}$ and $\psi^{(m)}$ in Eq. 30, we consider $\phi_{D1}^{(m)}$ and $\phi_{D2}^{(m)}$, their complex conjugates $\overline{\phi}_{D1}^{(m)}$ and $\overline{\phi}_{D2}^{(m)}$, or corresponding expressions for the case in where the direction of the incoming wave is opposite. In all of these cases, the left-hand side of Eq. 30 is zero from the body boundary condition, and several relations between the transmitted-wave and reflected-wave coefficients defined in Eq. 28 will be obtained. All possible relations to be obtained are of the form:

$$|R_{11}|^2 + |T_{11}|^2 - 1 + \mathcal{J}\big\{|R_{12}|^2 + |T_{12}|^2\big\} = 0 \tag{40}$$

$$|R_{21}|^2 + |T_{21}|^2 + \mathcal{J}\big\{|R_{22}|^2 + |T_{22}|^2 - 1\big\} = 0 \tag{41}$$

$$\mathrm{Re}\big\{R_{11}\overline{T}_{11}\big\} + \mathcal{J}\mathrm{Re}\big\{R_{12}\overline{T}_{12}\big\} = 0 \tag{42}$$

$$\mathrm{Re}\big\{R_{21}\overline{T}_{21}\big\} + \mathcal{J}\mathrm{Re}\big\{R_{22}\overline{T}_{22}\big\} = 0 \tag{43}$$

$$R_{21} = \mathcal{J}\, R_{12} \tag{44}$$

$$T_{21} = \mathcal{J}\, T_{12} \tag{45}$$

$$R_{11}\overline{R}_{21} + T_{11}\overline{T}_{21} + \mathcal{J}\big\{R_{12}\overline{R}_{22} + T_{12}\overline{T}_{22}\big\} = 0 \tag{46}$$

$$R_{11}\overline{T}_{21} + T_{11}\overline{R}_{21} + \mathcal{J}\big\{R_{12}\overline{T}_{22} + T_{12}\overline{R}_{22}\big\} = 0 \tag{47}$$

where

$$\mathcal{J} \equiv \mathcal{F}(k_2)/\mathcal{F}(k_1) \tag{48}$$

The corresponding relations for a case where the lower layer is of infinite depth are shown by Linton and McIver [4]. The present results are an extension of their results to the case of finite water depth.

All of the above relations were found to be satisfied with excellent accuracy (the error was in the order of 0.01% with 60 segments on the body surface) by the present numerical computation.

8. Hydrostatic Restoring Forces

The static restoring forces are unrelated to the velocity potentials described above, but they are critical in computing the motions of a body in waves. In the coordinate system fixed to a body that is oscillating with amplitude X_j ($j = 1 \sim 3$), the hydrostatic pressure in a two-layer fluid can be written as:

$$p_S = \begin{cases} \rho_1 g z' + \rho_1 g\,(X_2 + x' X_3) & \text{for } 0 \le z \le h_1 \\ \rho_2 g z' + (\rho_1 - \rho_2) g h_1 + \rho_2 g\,(X_2 + x' X_3) & \text{for } h_1 \le z \le h \end{cases} \tag{49}$$

where the body-fixed coordinates are denoted as (x', z').

The hydrostatic force in the j-th direction, F_j, can be obtained by integrating Eq. 49 over the wetted surface of a body. Namely

$$F_j = -\sum_{n=1}^{2} \int_{S_H^{(n)}} p_S(x', z')\, n_j\, d\ell \tag{50}$$

Noting that the hydrostatic force acts only in the vertical direction, it is sufficient to consider only for $j = 2$ and 3, and $n_3 = x' n_z - (z' - \overline{\mathrm{OG}}) n_x$ must be substituted for $j = 3$, because the body motions will be considered with respect to the center of gravity G.

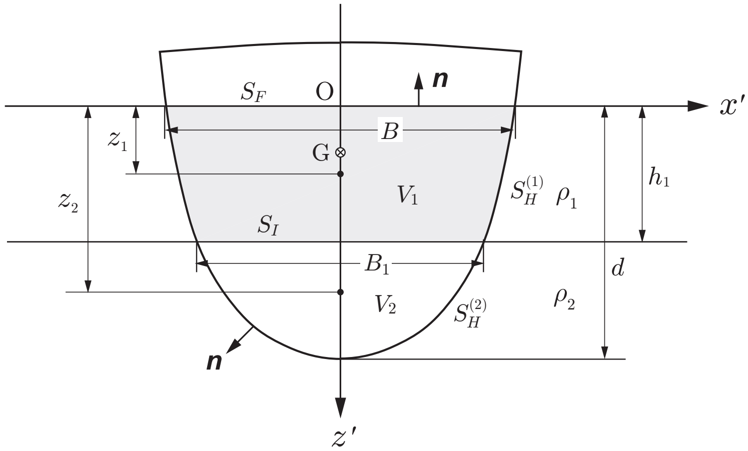

Fig. 2 Notations for computing restoring forces

It may be easier to apply Gauss' theorem to both the upper and lower layers of the mean submerged portion (see Fig. 2). In this way, the vertical force for $j = 2$ can be evaluated as follows:

$$\begin{aligned} F_2 &= -\rho_1 g V_1 - \rho_1 g (B - B_1) X_2 - \rho_2 g V_2 - \rho_2 g B_1 X_2 \\ &\equiv -\rho_1 g \mathcal{V} - C_{22} X_2 \end{aligned} \tag{51}$$

where

$$\mathcal{V} = V_1 \left(1 + \frac{1}{\gamma} \frac{V_2}{V_1} \right) \tag{52}$$

$$C_{22} = \rho_1 g B \left(1 + \frac{\varepsilon}{\gamma} \frac{B_1}{B} \right) \equiv \rho_1 g b \, C'_{22} \tag{53}$$

with V_1 and V_2 being the submerged areas of the body in the upper and lower layers, respectively, and $B\,(= 2b)$ and B_1 being the breadths at $z = 0$ and $z = h_1$, respectively. It is obvious from Eq. 51 that the coefficient of the restoring force in heave, C_{22}, can be computed from Eq. 53.

In the same way by applying Gauss' theorem, the roll moment for $j = 3$ can be evaluated and the result is expressed as

$$\begin{aligned} F_3 &= \rho_1 g X_3 (V_1 z_1 - V_1 \overline{\mathrm{OG}}) - \rho_1 g X_3 \left[\int_{S_F} - \int_{S_I} \right] x^2 \, dx \\ &\quad + \rho_2 g X_3 (V_2 z_2 - V_2 \overline{\mathrm{OG}}) - \rho_2 g X_3 \int_{S_I} x^2 \, dx \\ &\equiv - C_{33} \, X_3 \end{aligned} \tag{54}$$

where

$$\begin{aligned} C_{33} &= \rho_1 g \mathcal{V} \, (-\overline{\mathrm{OB}} + \overline{\mathrm{OG}} + \overline{\mathrm{BM}}) \\ &= \rho_1 g \mathcal{V} \, \overline{\mathrm{GM}} \equiv \rho_1 g b^3 \, C'_{33} \end{aligned} \tag{55}$$

and

$$\mathcal{V} \, \overline{\mathrm{OB}} = V_1 z_1 + \frac{1}{\gamma} V_2 z_2, \quad \mathcal{V} \, \overline{\mathrm{BM}} = \frac{B^3}{12} \left(1 + \frac{\varepsilon}{\gamma} \frac{B_1^3}{B^3} \right) \tag{56}$$

Here, as shown in Fig. 2, z_1 and z_2 denote the centers of submerged areas in the upper and lower layers, respectively. Thus $\overline{\mathrm{OB}}$ is the distance between the origin and the center of buoyancy, and $\overline{\mathrm{BM}}$ is the metacentric height in a two-layer fluid. As a consequence, the coefficient of the restoring moment in roll, C_{33}, can be computed from Eqs. 55 and 56.

9. Motion Equations in Waves

Since the motions of the body are considered with respect to the center of gravity G, the complex motion amplitude X_j and hydrodynamic radiation and diffraction forces must be transformed into corresponding quantities evaluated with respect to G. (Those are expressed with superscript G.) Their relationships for a symmetrical body are given as follows:

$$X_1 = X_1^G + \overline{\mathrm{OG}}\, X_3^G, \;\; X_2 = X_2^G, \;\; X_3 = X_3^G \tag{57}$$

$$\left.\begin{aligned} E_{3p}^G &= E_{3p} + \overline{\mathrm{OG}}\, E_{1p} \\ T_{13}^G &= T_{13} + \overline{\mathrm{OG}}\, T_{11}, \;\; T_{31}^G = T_{31} + \overline{\mathrm{OG}}\, T_{11} \\ T_{33}^G &= T_{33} + \overline{\mathrm{OG}}\,(T_{13}+T_{31}) + \overline{\mathrm{OG}}^2\, T_{11} \end{aligned}\right\} \tag{58}$$

where

$$T_{ij} = A_{ij} + \frac{B_{ij}}{i\omega} \tag{59}$$

and A_{ij} and B_{ij} represent the added mass and the damping coefficient, respectively, studied in the previous article.

With the hydrodynamic forces in Eq. 58 and the hydrostatic restoring forces considered in the preceding section, the equations of heave, sway, and roll of a symmetrical body may be written as follows:

Heave :

$$\Big[-K(m' + T_{22}') + C_{22}' \Big] \frac{X_2}{a_p} = E_{2p}' \quad (p=1,2) \tag{60}$$

Sway and Roll :

$$\Big[-K(m' + T_{11}') \Big] \frac{X_1^G}{a_p} + \Big[-K\, T_{13}^{G\prime} \Big] \frac{X_3 b}{a_p} = E_{1p}' \qquad (p=1,2) \tag{61}$$

$$\Big[-K\, T_{31}^{G\prime} \Big] \frac{X_1^G}{a_p} + \Big[-K(m'\kappa_{xx}^2 + T_{33}^{G\prime}) + C_{33}' \Big] \frac{X_3 b}{a_p} = E_{3p}^{G\prime} \quad (p=1,2) \tag{62}$$

Here $K = \omega^2 b/g$, m' is the mass of the body nondimensionalized with $\rho_1 b^2$, κ_{xx} is the gyrational radius in roll nondimensionalized with b, and all other quantities with prime are supposed to be nondimensional.

It should be noted that these motion equations are solved separately for the incident waves in surface-wave ($p=1$) and in internal-wave ($p=2$) modes.

10. Experiments

The experiments for measuring the wave-exciting forces and the wave-induced motions were conducted with a 2-D Lewis-form body, which has a half-breadth to draft ratio $H_0 = b/d = 0.833$ and a sectional area ratio $\sigma = A/Bd = 0.9$ (where half the breadth $b = B/2 = 0.1\,\mathrm{m}$ and the draft $d = 0.12\,\mathrm{m}$). As in the experiment for the radiation problem, the two-layer fluid was realized using isozole 300 for the lighter upper-layer fluid and water for the denser lower-layer fluid. Although the density of isozole 300 is written in the catalogue as $\rho_1 = 0.764\,\mathrm{g/cm^3}$ at 15°C, we concluded from the check of the static buoyancy and restoring force that $\rho_1 = 0.750\,\mathrm{g/cm^3}$ would be more plausible. Thus, this corrected value for ρ_1 has been used in our study.

The size of the wave channel used in the experiments was 10 m in length and 0.3 m in breadth, and the depth of fluid was set at $h = 0.40$ m. The depth ratios between the upper and lower fluids were set in two different conditions as follows:

— Measurement of wave-exciting forces
  (a) $h_1 = 0.075\,\mathrm{m}$, $h_2 = 0.325\,\mathrm{m}$
  (b) $h_1 = 0.155\,\mathrm{m}$, $h_2 = 0.245\,\mathrm{m}$

— Measurement of wave-induced motions
  (a) $h_1 = 0.060\,\mathrm{m}$, $h_2 = 0.340\,\mathrm{m}$
  (b) $h_1 = 0.150\,\mathrm{m}$, $h_2 = 0.250\,\mathrm{m}$

Given that the draft of the body is $d = 0.12$ m, (a) corresponds to the case in which the body intersects the interface, and (b) corresponds to the case in which the body floats in the upper-layer fluid only. For consistency, the setting of the depth of the upper and lower fluid layers should have been the same for the two different measurements, but each measurement was performed at very different times and there was no special reason to change the setting.

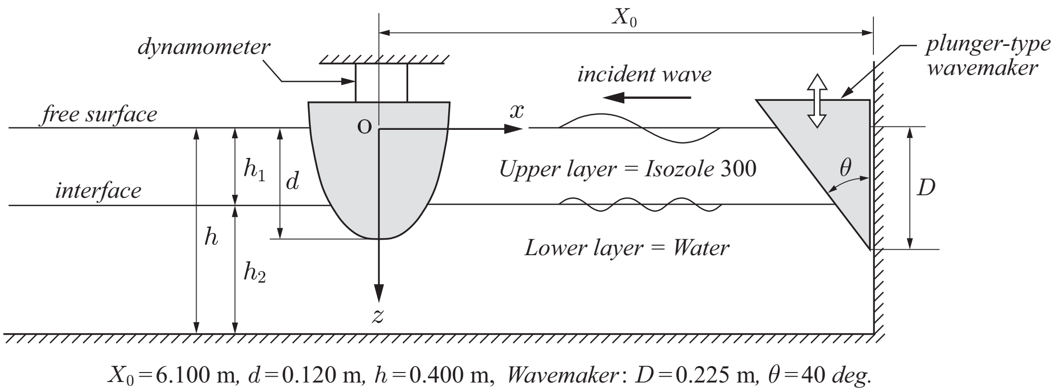

Fig. 3 Experimental setup for measuring wave-exciting forces

The section shape of the wavemaker installed in the wave channel is a triangle with a bottom angle equal to 40 degrees. The wave-exciting forces were measured directly with a dynamometer. A schematic view of the setup in the diffraction experiment is shown in Fig. 3, in which the distance from the wavemaker to the center line of the body was set to $X_0 = 6.1$ m. The wave elevation on the free surface (between air and isozole 300) was measured with a capacitance-type wave probe, the sensitivity of which was increased by using four sensors connected as a sequential string. The body motions were measured with potentiometers.

In the experiments with these measuring instruments, the amplitude of the incident wave generated by a wavemaker was measured first without the body at the position where the body was supposed to be set. Then the measurements of forces acting on the body and the motions of the body were performed, and the measured data were Fourier-analyzed. In the measurement of the body motions in waves, the sway motion was fixed to avoid wave drifting, and only the heave and roll motions were free to oscillate. Fig. 4 is a snap shot at the measurement of wave-induced motions of the Lewis-form body. The incident wave is incoming from the left and shorter waves seen at the interface are those scattered by the body.

In a two-layer fluid, a wavemaker generates two different waves simultaneously at a prescribed frequency: a longer wave of surface-wave mode and a shorter wave of internal-wave mode. However, it should be noted that the shorter wave tends to attenuate as it propagates, and in fact it does not reach the position of the body for high frequencies (approximately $Kb > 1.0$). On the other hand, in the low frequency region, the shorter wave may reach the position of the body, but before it does so, the longer wave reflects many times between the wavemaker and the body because of its faster celerity, and thus measured data is largely scatted. From the calculated celerity of a wave and the distance between the wavemaker and the body, the time in which there may be no effects caused by reflected waves can be estimated. With this estimation and from the time history of measured data displayed on the monitor screen of a computer, the length of the data to be used for the Fourier analysis was determined. In the process of this data analysis, the effects of the incident wave of internal-wave mode may not be included in Fourier-analyzed results.

We calibrated the measuring instruments frequently and confirmed that the possible error originating from variation in the calibration factor was much smaller than the order of the scatter in obtained results due to reflected waves. Measurements were repeated several times at the same frequency, particularly for measuring the wave-exciting forces, and all the results will be shown later; the scatter in the results may indicate the range of the error in the experiments.

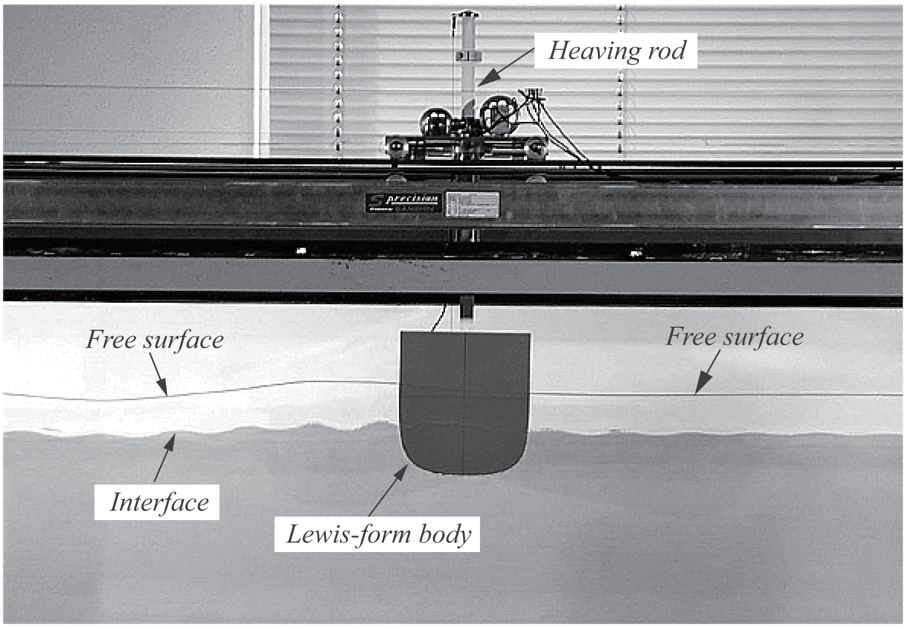

Fig. 4 A snap shot at the measurement of wave-induced motions in wave; the wave period is 0.7 sec and the sway motion is fixed

11. Results and Discussion

Numerical computations were performed for the Lewis-form body used in the experiment. Because this body is symmetrical with respect to the z-axis, only half the body surface was discretized into 30 segments for all computations in this article. With this number of segments, the error in the Haskind-Hanaoka-Newman relation was very small at less than 0.1% for all computed cases.

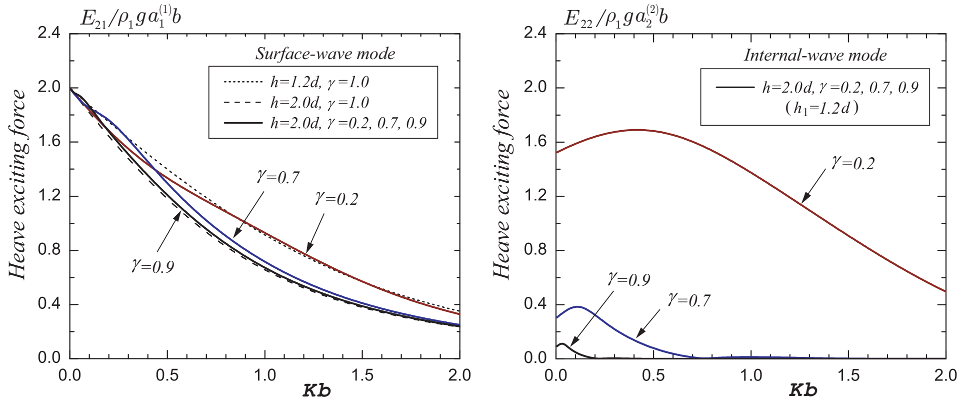

Fig. 5 Effects of the density ratio on the heave exciting force on a Lewis-form body of $H_0 = 0.833$ and $\sigma = 0.9$

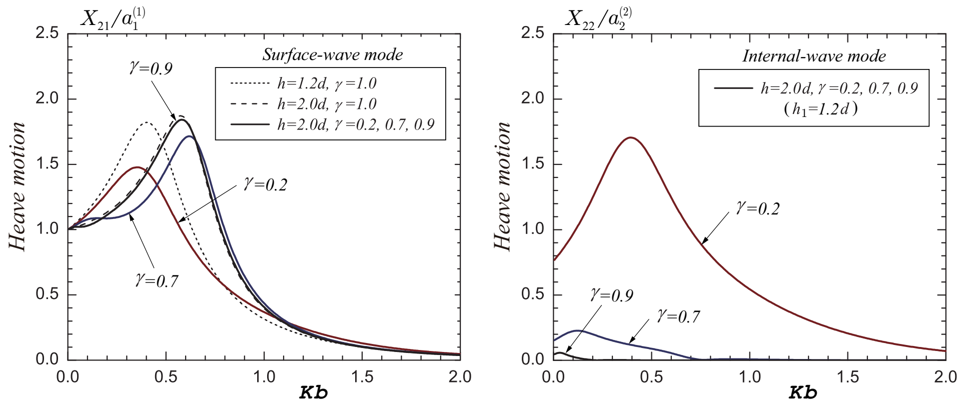

Fig. 6 Effects of the density ratio on the wave-induced heave motion of a Lewis-form body of $H_0 = 0.833$ and $\sigma = 0.9$

11.1 Effects of the density ratio

To see the effects of the density ratio on the wave-exciting forces on the body and resultant motions of the body, computations were implemented for $\gamma = 1.0$, 0.9, 0.7 and 0.2. For these runs, the depths of the fluid layers were fixed at $h_1 = 1.2d$ and $h = 2.0d$. As $\gamma \to 1$, the fluid reduces to a single layer of $h = 2.0d$. Conversely as $\gamma \to 0$, the lower fluid behaves more like a rigid block, and the results are expected to approach those for a single-layer fluid with a depth equal to that of upper layer. To illustrate this behavior, computations were also carried out for single-layer fluids of $h = 1.2d$ and $2.0d$.

Figure 5 shows the amplitude of heave exciting force, in which the left-hand and right-hand sides are for the surface-wave and internal-wave modes of the incident wave, respectively. In the surface-wave mode, as expected, the results for $\gamma = 0.2$ approach those for a single-layer fluid of $h = 1.2d$, and the results for $\gamma = 0.9$ are close to those for a single-layer fluid of $h = 2.0d$. At high frequencies, the results for $\gamma = 0.7$ are almost the same as those for $\gamma = 0.9$, which indicates that the presence of the interface at a deeper position is unimportant as long as the density difference is not so large.

When the incident wave is of internal-wave mode, the exciting forces for $\gamma = 0.7$ and 0.9 are negligibly small except at low frequencies. For $\gamma = 0.2$, however, the wavelength of the k_2 wave becomes comparable to that of the k_1 wave, and thus the heave exciting force becomes large and its nondimensional amplitude is larger than that for the surface-wave mode over a wide range of frequencies.

Computed amplitudes of the heave motion are shown in Fig. 6 in the same fashion as those for the heave exciting force. For the incident wave in surface-wave mode, the results

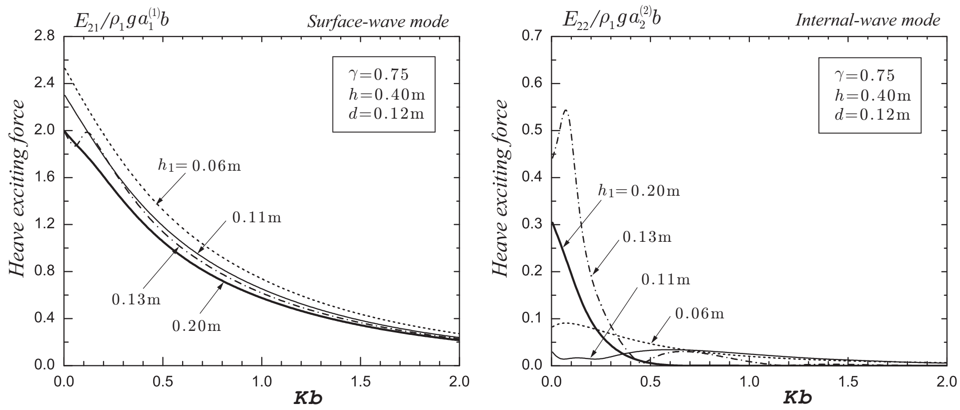

Fig. 7 Effects of the interface position on the heave exciting force on a Lewis-form body of $H_0 = 0.833$ and $\sigma = 0.9$

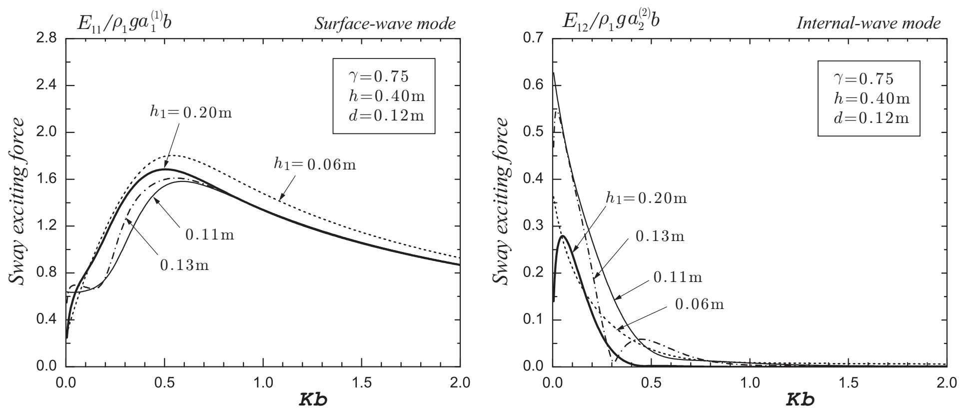

Fig. 8 Effects of the interface position on the sway exciting force on a Lewis-form body of $H_0 = 0.833$ and $\sigma = 0.9$

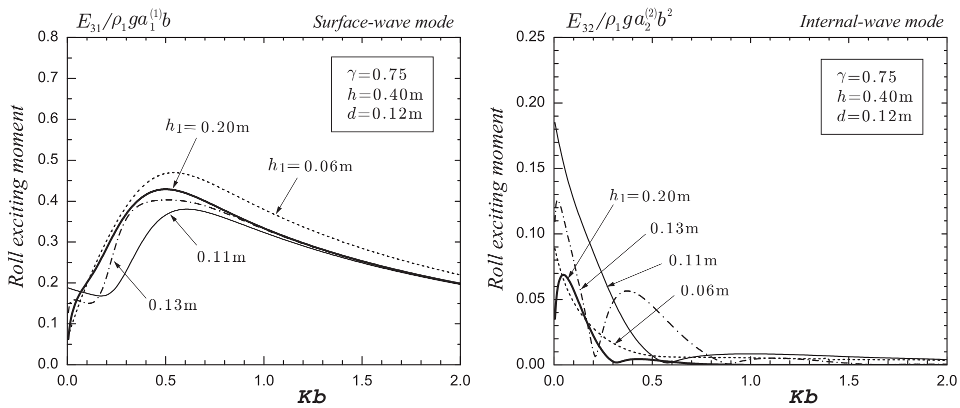

Fig. 9 Effects of the interface position on the roll exciting moment on a Lewis-form body of $H_0 = 0.833$ and $\sigma = 0.9$

for $\gamma = 0.9$ are almost the same as those in a single-layer fluid, and even the results for $\gamma = 0.7$ are almost the same at frequencies of $Kb > 0.65$. The reason of the smaller amplitude when $Kb < 0.65$ at $\gamma = 0.7$ is that, as was shown on Fig. 9 in the previous article, the damping force at $\gamma = 0.7$ is large compared to that at $\gamma = 0.9$ in $Kb < 0.65$. For $\gamma = 0.2$ or for a single-layer fluid of $h = 1.2d$, the heave resonant frequency moves to a lower frequency, which can be attributed to the fact that the heave added mass becomes large in shallow water. When the incident wave is of internal-wave mode, the relative magnitude of the heave motion for three different values of γ is consistent with that of the heave exciting force shown in Fig. 5, and the motion amplitude at $\gamma = 0.9$ is very small.

11.2 Effects of the interface position

Hydrodynamic characteristics may change significantly depending on whether the body intersects the interface. To see this, for the same Lewis-form body and fixed values of $h = 0.4$ m and $\gamma = 0.75$, only the vertical position of the interface was changed from $h_1 = 0.06$ m to 0.20 m, including the case where the body intersects the interface.

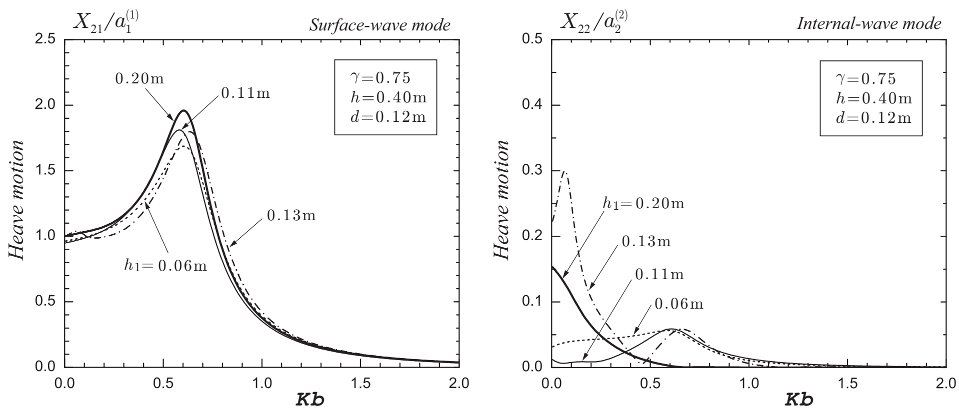

Fig. 10 Effects of the interface position on the wave-induced heave motion of a Lewis-form body of $H_0 = 0.833$ and $\sigma = 0.9$

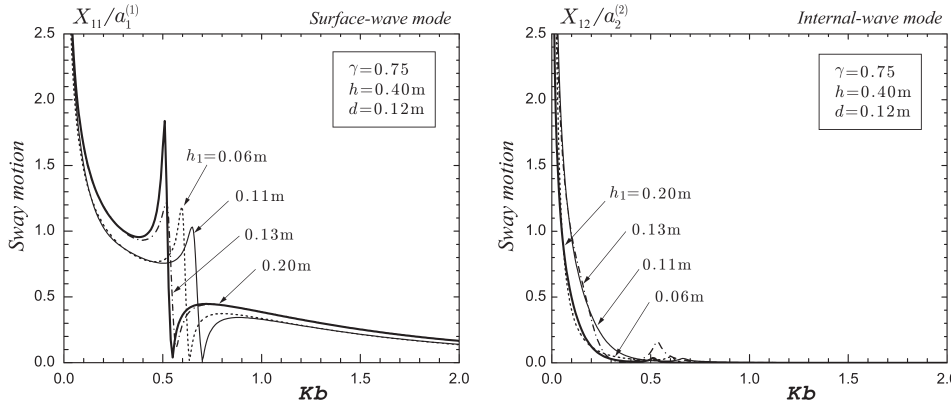

Fig. 11 Effects of the interface position on the wave-induced sway motion of a Lewis-form body of $H_0 = 0.833$ and $\sigma = 0.9$

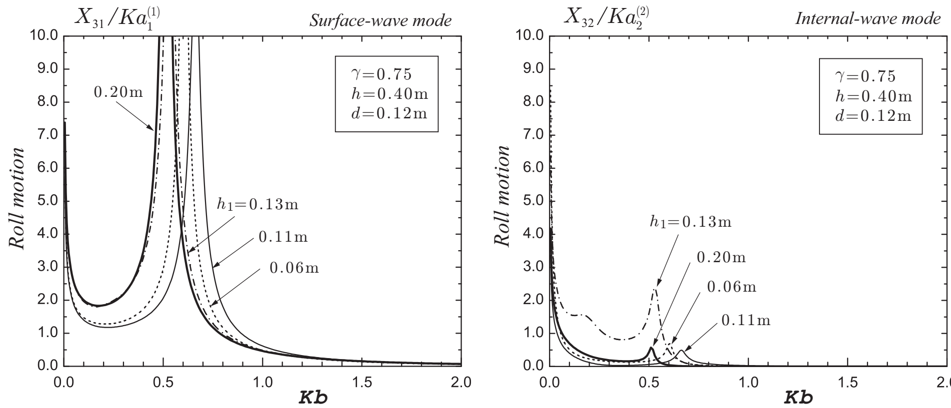

Fig. 12 Effects of the interface position on the wave-induced roll motion of a Lewis-form body of $H_0 = 0.833$ and $\sigma = 0.9$

Figures 7, 8 and 9 show computed results of the wave-exciting forces in heave, sway, and roll, respectively. For incident waves in surface-wave mode, no prominent difference exist in the heave exciting force among the results for different interface positions, except that undulatory variation can be seen at $Kb < 0.2$ when $h_1 = 0.13\,\mathrm{m}$ and the interface is located just below the bottom of the body ($d = 0.12\,\mathrm{m}$). For incident waves in internal-wave mode, the heave exciting force is very small, particularly when the body intersects the interface, whereas when the interface is just below the bottom of the body, the wave-exciting force becomes large at low frequencies.

On the other hand, for the sway exciting force, there is no distinctive difference depending on whether the body intersects the interface. It is noteworthy that a waveless frequency (where the wave-exciting force becomes zero) exists around $Kb = 0.3$ for the case of $h_1 = 0.13\,\mathrm{m}$.

Variation of the roll exciting moment shown in Fig. 9 is similar to that of the sway exciting force shown in Fig. 8; this similarity is because both modes of motion are antisymmetric and the hydrodynamic pressure on the side wall of the body contributes mainly to these antisymmetric modes.

Computed motions of the body are shown in Figs. 10, 11 and 12 for heave, sway, and roll, respectively. For heave with incident waves in surface-wave mode, no distinctive difference exists depending on the position of the interface, a feature that conforms to the heave exciting force shown in Fig. 6. For incident waves in internal-wave mode, the heave motions for all computed cases are negligibly small, which is also consistent with the results for the heave exciting force.

The effects of the vertical position of the interface appear more clearly as a shift of the roll resonant frequency, as seen in Fig. 12. (In the present computations, $\kappa_{xx} = 0.6b$ and $\overline{\mathrm{OG}} = 0.45b$.) Because the sway motion is coupled with the roll motion, the sway amplitude changes abruptly near the corresponding resonant frequency for roll, as seen in Fig. 11. We can see that the roll resonant frequency for the case of a body intersecting the interface ($h_1 = 0.06\,\mathrm{m}$ and $0.11\,\mathrm{m}$) is higher than that for the non-intersecting case ($h_1 = 0.13\,\mathrm{m}$ and $0.20\,\mathrm{m}$). This tendency may be explained by a fact that the value of $\overline{\mathrm{GM}}$ increases when a body intersects the interface, as can be understood from Eq. 56. The roll amplitude near the resonant frequency is very large, particularly for incident waves of surface-wave mode, which is unrealistic because the fluid viscosity is neglected in the present computations.

11.3 Comparison with experiments

Figure 13 shows a comparison of the wave-exciting forces in sway and heave for $h_1 = 0.075\,\mathrm{m}$, and likewise Fig. 14 shows the same kind of comparison for $h_1 = 0.155\,\mathrm{m}$. The abscissa is Kb, the nondimensional oscillation frequency of the wavemaker installed at the end of the wave channel.

The wave-exciting forces are nondimensionalized using ρ_2, the density of the lower-layer fluid (i.e. water), in the form:

$$E_j' = \frac{E_j}{\rho_2 g a_1^{(1)} b} \quad (j = 1, 2) \tag{63}$$

where $a_1^{(1)}$ denotes the amplitude of the incident wave with longer wavelength measured on the free surface. The incident wave was generated with a target wave steepness (ratio of the wave height to the wavelength) of 1/25, which means that the amplitude $a_1^{(1)}$ is about 1.25 cm at $Kb = 1.0$. For lower frequencies, the amplitude was made smaller than the target because of limitation in the performance of the wavemaker.

We should note that computed results are the results for just the incident wave in surface-wave mode, because as already explained, the measured results may not include the effects from the internal-wave-mode incident wave. (In fact, there is no information on the amplitude ratio and the phase difference between the waves in surface-wave and internal-wave modes.) For reference, computed results for a single-layer fluid ($h = 0.40\,\mathrm{m}$) are also shown as thin solid lines.

The overall agreement between the measured and computed results seems to be good, although the measured values of the sway force tend to be smaller than the computed ones. The sway force is dominated by the pressure near the free surface, which easily scatters because of the effect of reflected waves from the longitudinal ends of the wave channel. On the other hand, the heave force is dominated by the pressure near the bottom of the body, which is stabler than the pressure near the free surface. Looking at Fig. 13, the heave force is more or less the same as that in a single-layer fluid; this is because the bottom part of the body is in the lower-layer fluid and the effects of the waves of internal-wave mode are small.

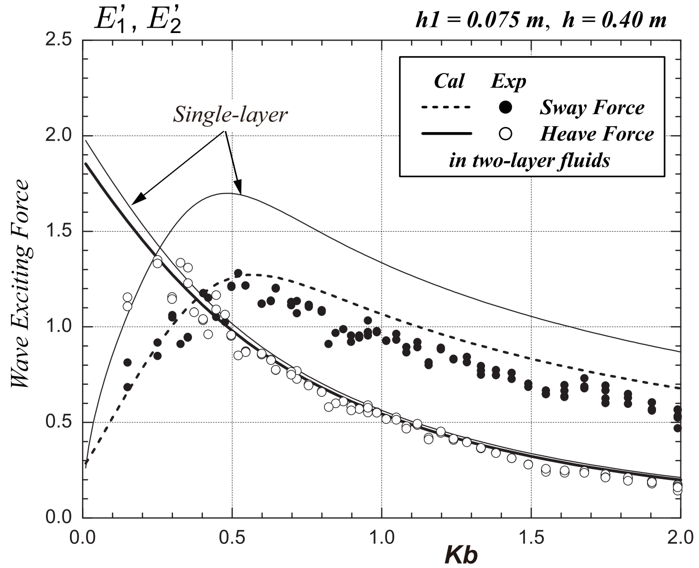

Fig. 13 Wave-exciting sway and heave forces on a Lewis-form body of $H_0 = 0.833$ and $\sigma = 0.9$, for the case of $h_1 = 0.075\,\mathrm{m}$ and $h = 0.40\,\mathrm{m}$

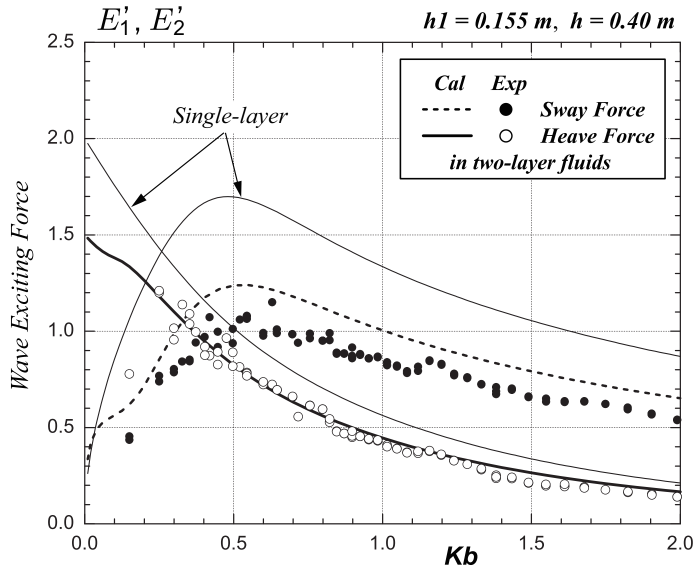

Fig. 14 Wave-exciting sway and heave forces on a Lewis-form body of $H_0 = 0.833$ and $\sigma = 0.9$, for the case of $h_1 = 0.155\,\mathrm{m}$ and $h = 0.40\,\mathrm{m}$

For the case of a deeper upper layer, shown in Fig. 14, at first glance the differences from the single-layer case look large in both sway and heave. However, if the density of the upper-layer fluid, ρ_1, is used for the nondimensional form (i.e., $\rho_2/\rho_1 = 1/\gamma \simeq 1.33$ is multiplied), it turns out that both sway and heave forces are very close to the results for a single-layer

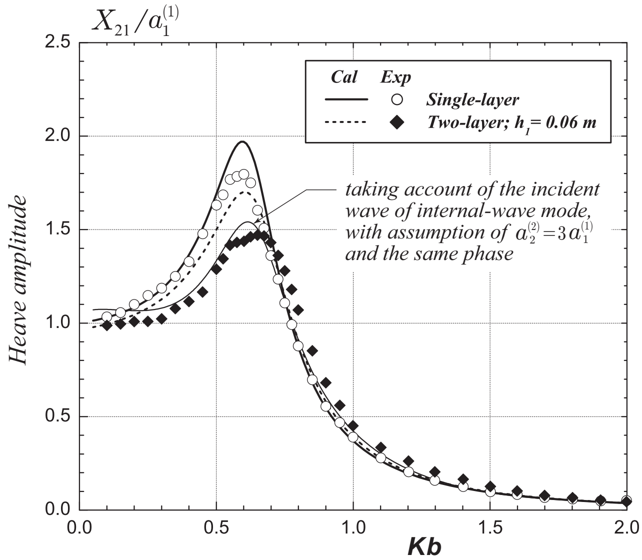

Fig. 15 Wave-induced heave motion of a Lewis-form body of $H_0 = 0.833$ and $\sigma = 0.9$, for the case of $h_1 = 0.06\,\mathrm{m}$ and $h = 0.40\,\mathrm{m}$

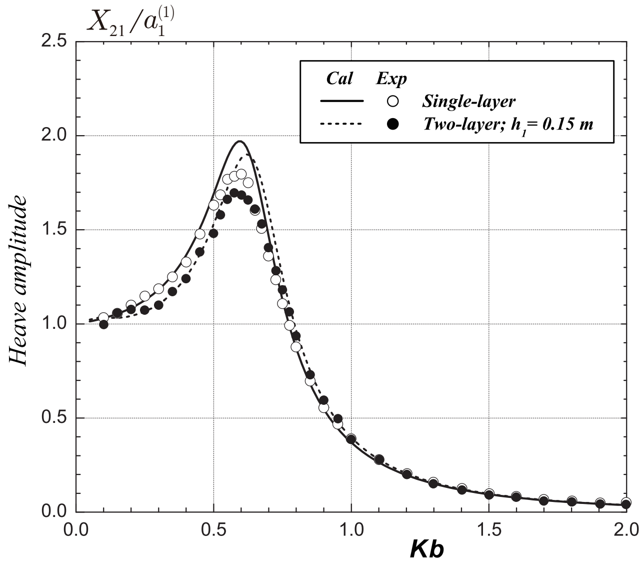

Fig. 16 Wave-induced heave motion of a Lewis-form body of $H_0 = 0.833$ and $\sigma = 0.9$, for the case of $h_1 = 0.15\,\mathrm{m}$ and $h = 0.40\,\mathrm{m}$

fluid. This is natural, considering that the body is floating only in the upper-layer fluid for the case of $h_1 = 0.155\,\mathrm{m}$.

Figures 15 and 16 show the amplitude of the wave-induced heave motion for $h_1 = 0.06\,\mathrm{m}$ and $0.15\,\mathrm{m}$, respectively. The experiments were performed also in a single layer of water to confirm the validity of the potential-flow calculation; these results are plotted with open circles and corresponding results from the numerical computation are shown by a thick solid line. We can see that the agreement in the single-layer fluid is very good, except for the peak value near the resonance.

In Fig. 15, computed results for the two-layer fluid shown by the broken line (in which the incident wave in surface-wave mode only is taken into account) are obviously different from the measured results, particularly for $Kb < 0.7$. When the upper layer is shallow and the frequency is relatively low, the incident wave in internal-wave mode may become prominent and affect the measured results. To support this conjecture, artificial computations were performed by assuming that the amplitude of the incident wave in internal-wave mode on the interface $a_2^{(2)}$ is equal to $3\,a_1^{(1)}$ and the phase is the same between the incident waves in surface-wave mode and internal-wave mode. (Note that these were not measured in the experiments.) Computed results are shown by a thin solid line, and obviously the heave amplitude tends to decrease for $Kb < 0.7$ and slightly increase at frequencies around $Kb = 1.0$ as compared to the broken line. This tendency agrees with measured results and thus we may conclude that measured results in Fig. 15 are affected by the incident wave in internal-wave mode.

For a deeper upper layer (shown in Fig. 16), the difference between the results in the single-layer and two-layer fluids is small, and computed results for the two-layer fluid are also in good agreement with the measured values, except near the resonant frequency. Therefore in this case, the effect of the incident wave in internal-wave mode is negligibly small.

12. Conclusions

In this second article, we have studied the diffraction problem of a body of general shape floating in a two-layer fluid of finite depth, including the case in which the body intersects the interface between the upper and lower fluids.

Some important hydrodynamic relations were also studied theoretically, and a reasonable extension from the single-layer case was derived for the Haskind-Hanaoka-Newman relation and for the energy-conservation relations to be satisfied between the transmitted and reflected waves. In addition, the boundary integral-equation method developed in the previous article was applied to compute directly the diffraction potential (pressure) on the body surface.

Computed results were presented for the wave-exciting forces on the body and for the resultant motions of the body in regular incident waves. In two-layer fluids, for a prescribed frequency, the incident wave has two different wave modes with different wavenumbers. Therefore numerical computations were implemented for each mode of the incident wave for a Lewis-form body. The effects of the density ratio and the interface position on the wave-exciting forces and wave-induced motions were discussed.

Furthermore, experiments were conducted to measure the wave-exciting forces in sway and heave and the wave-induced motions of heave and roll using a Lewis-form body in a two-layer fluid with water for the lower layer and isozole 300 (isoparaffin oil) for the upper layer. Measured results were compared with corresponding results from the numerical computation.

The results obtained through the present study may be summarized as follows:

1. As the density ratio γ becomes small (lower layer becomes more rigid), the resonant frequency for heave moves to a lower frequency as a result of the large added mass in shallow water.
2. The body motions are generally small in incident waves in internal-wave mode, but for $\gamma = 0.2$, the effect of the internal wave becomes large and the nondimensional amplitude

is of the same order as that for incident waves in surface-wave mode.

3. The position of the interface has no marked effect on the heave response; however, the roll resonant frequency clearly changes, depending on whether the body intersects the interface, which is mainly a result of the change in the restoring moment.
4. The degree of agreement between the measured and computed results is generally good. However, the measured values of the sway exciting force tend to be smaller than the computed values. The agreement for the heave motion is also generally good, but a noticeable difference exists for lower frequencies for the case where the body intersects the interface, and this difference may be a result of the effect of incident waves in internal-wave mode, which are not included in the numerical computations.

Acknowledgments

We are indebted to Mr. M. Inada for his constant support in the experiments. This work was partially supported by a Grant-in-Aid for Exploratory Research from the Ministry of Education, Culture, Sports, Science and Technology in Japan, for which we are also grateful.

References

[1] Ten, I and Kashiwagi, M (2004) Hydrodynamics of a body floating in a two-layer fluid of finite depth, Part 1: Radiation problem, J Marine Science and Technology 9 (3): 127–141

[2] Newman, J N (1976) The interaction of stationary vessels with regular waves. In: Proceedings of the 11th Symp on Naval Hydrodynamics, London, pp 491–501

[3] Yeung, R W and Nguyen T (1999) Radiation and diffraction of waves in a two-layer fluid. In: Proceedings of the 22nd Symp on Naval Hydrodynamics, Washington, D.C., pp 875–891

[4] Linton, C M and McIver, M (1995) The interaction of waves with horizontal cylinders in two-layer fluids. J Fluid Mech 304: 213–229

[5] Cadby, J R and Linton, C M (2000) Three dimensional water wave scattering in two-layer fluids. J Fluid Mech 423: 155–173

[6] Sturova, I V (2003) Radiation loads on interface piercing cylinder in a two-layer fluid of finite depth by a coupled element technique. In: Proceedings of the 8th International Conference on Numerical Ship Hydrodynamics, Busan, Vol 2, pp 80–91

Wave Drift Force in a Two-Layer Fluid of Finite Depth*

Masashi KASHIWAGI
Research Institute for Applied Mechanics, Kyushu University
Kasuga, Fukuoka 816-8580, Japan

Abstract

Based on the momentum and energy conservation principles, a compact calculation formula is analytically derived for the wave-drift force on a 2-D body floating in a two-layer fluid of finite depth. In a two-layer fluid, two different wave modes (the surface-wave mode with longer wavelength and the internal-wave mode with shorter wavelength) exist not only in the incident wave but also in the body-scattered wave, and these wave characteristics are properly incorporated in the obtained formula. It is noted that, unlike the single-layer case, the wave-drift force can be negative in the incident wave of surface-wave mode, if the transmitted wave with internal-wave mode is large. Numerical computations are implemented for a Lewis-form body by means of the boundary-integral-equation method with Green's function for the two-layer fluid problem. The effects of density ratio, interface position, and body motions on the wave-drift force are studied, and some important features are found for two-layer fluids.

Keywords: Two-layer fluid, wave drift force, surface-wave mode, internal-wave mode, finite water depth.

1. Introduction

Hydrodynamic studies of a body floating in a two-layer fluid of finite depth have been conducted for the radiation and diffraction problems which are of first order with respect to the incident-wave amplitude ([1, 2] and the references therein). However, to the author's knowledge, no study has been made on the second-order wave-drift force in a two-layer fluid. For the case of a single-layer fluid, it is well known that the coefficient of the reflection wave is directly connected with the wave-drift force and its calculation formula is established by the far-field method based on the momentum and energy-conservation principles.

For a two-layer fluid, however, the analyses look complicated, even for first-order problems. For example, in the diffraction problem, two different incident waves of surface-wave mode (with longer wavelength) and internal-wave mode (with shorter wavelength) must be considered separately for a prescribed frequency, and each incident wave will be scattered by a body into two different wave modes. Thus, the energy of the incident wave may be transferred from one mode to the other. Furthermore, when the body is oscillating in response to the incident wave, the body motion may change the reflected and transmitted waves. For this complicated wave field in a two-layer fluid, it is crucial to understand analytically what is the correct form of the calculation formula for the wave drift force, in what way two-layer

∗ *Reprinted from Journal of Engineering Mathematics, Vol. 58, pp. 51–66, 2007 (August)*

effects are incorporated in the formula, and what are distinctive differences with respect to the single-layer case.

In this article, after the definition and formulation of the problem, the asymptotic expression of the velocity potential valid in the far field is obtained, in which the coefficients of reflected and transmitted waves are defined in terms of the Kochin functions for the radiation and diffraction problems in a two-layer fluid. Then on the basis of the momentum and energy conservation principles, analytical integrations in the far field and some mathematical transformations are performed to derive the desired calculation formula for the wave-drift force. The key to success in this procedure is to apply the orthogonality properties to the eigenfunctions in the two-layer fluid of finite depth.

Numerical computations are performed for a Lewis-form body, using the boundary-integral-equation method developed by Ten and Kashiwagi [1]. The density ratio and the interface position between the upper and lower layers are varied and those effects on the wave-drift force are studied. Furthermore, by showing the results for three cases where the body is completely fixed, only the heave motion is free, and all modes of body motion are free in response to incident waves, the effects of body motions on the wave drift force are also discussed. Lastly, some findings from the theoretical and numerical studies in this article are discussed in the Conclusions.

2. Mathematical Formulation

We consider a 2-D floating body of general shape in a two-layer fluid with finite depth. The body may intersect the interface between the upper and lower layers and is assumed to oscillate sinusoidally in response to an incident wave with circular frequency ω. Figure 1 shows a Cartesian coordinate system and notations used in the analyses below, with the origin on the undisturbed free surface and the z-axis positive in the downward direction. The free surface, the interface, and the flat rigid bottom of the water are located at $z = 0$, $z = h_1$, and $z = h$, respectively.

Assuming both of the upper and lower fluids to be incompressible and inviscid with irrotational motion, we introduce the velocity potential in the form

$$\Phi^{(m)}(x,z,t) = \mathrm{Re}\big[\,\phi^{(m)}(x,z)\,e^{i\omega t}\,\big],\ m = 1,2 \tag{1}$$

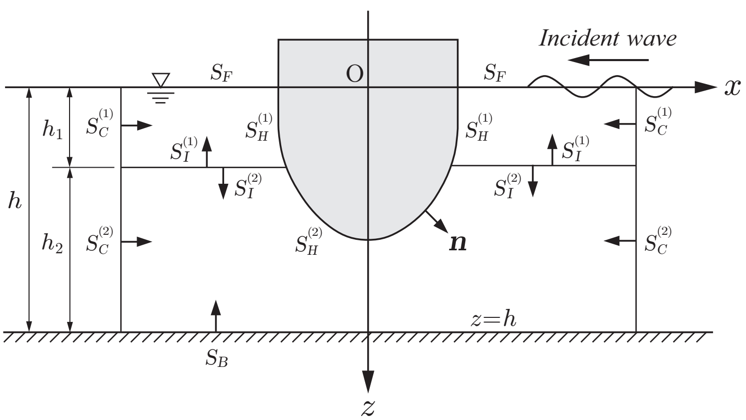

Fig. 1 Coordinate system and notations

$$\phi^{(m)}(x,z) = \sum_{p=1}^{2} \frac{gA_p}{i\omega}\,\phi_{Dp}^{(m)}(x,z) + \sum_{j=1}^{3} i\omega X_j\,\phi_{Rj}^{(m)}(x,z) \equiv \sum_{p=1}^{2} \frac{gA_p}{i\omega}\,\varphi_p^{(m)}(x,z), \tag{2}$$

where

$$\varphi_p^{(m)}(x,z) = \phi_{Dp}^{(m)}(x,z) - K\sum_{j=1}^{3}\frac{X_j}{A_p}\,\phi_{Rj}^{(m)}(x,z), \tag{3}$$

$$\phi_{Dp}^{(m)}(x,z) = \phi_{Ip}^{(m)}(x,z) + \phi_{Sp}^{(m)}(x,z), \tag{4}$$

with $K = \omega^2/g$, and g being the gravitational acceleration.

Here the superscript (m) denotes the fluid layer, with $m = 1$ and 2 corresponding to the upper and lower layers, respectively. As described in Yeung and Nguyen [3], there can be two different wave modes in the incident wave in two-layer fluids for a prescribed frequency. Those modes are differentiated with subscript (p), and specifically $p = 1$ is referred to as the surface-wave mode and $p = 2$ as the internal-wave mode.

A_p is (2) denotes the amplitude of incident wave at each mode. It is known that a simple relation holds at each mode on the amplitude ratio between the waves on the free surface and on the interface. However, the ratio between the waves of surface-wave and internal-wave modes on the free surface or the interface is not known a priori. Therefore, the diffraction problem must be solved for two different incident waves at a given frequency. In this article, A_p at each mode is defined in the theory as the incident wave on the free surface, whereas in numerical computations a larger amplitude is adopted as A_p at each wave mode (i.e., A_1 is the amplitude on the free surface and A_2 is the amplitude on the interface).

$\phi_{Dp}^{(m)}$ denotes the diffraction potential, which includes the incident-wave potential $\phi_{Ip}^{(m)}$ to be given as the input (explicit expressions of which will be shown below) and the scattering potential $\phi_{Sp}^{(m)}$. $\phi_{Rj}^{(m)}$ in (3) is the radiation potential with unit velocity in the jth direction ($j = 1$ for sway, $j = 2$ for heave, and $j = 3$ for roll) and the amplitude of the jth mode of motion, X_j/A_p, must be obtained by solving the equations of motions of a body, for which hydrodynamic forces must be computed with the solution of the boundary-value problem.

The governing equation for the velocity potentials is the 2-D Laplace equation

$$\frac{\partial^2\phi^{(m)}}{\partial x^2} + \frac{\partial^2\phi^{(m)}}{\partial z^2} = 0 \tag{5}$$

and the linearized boundary conditions to be satisfied on the free surface, the interface, and the rigid bottom of the lower layer are expressed as follows:

$$\frac{\partial\phi^{(1)}}{\partial z} + K\phi^{(1)} = 0 \quad \text{on } z = 0, \tag{6}$$

$$\left.\begin{aligned} &\frac{\partial\phi^{(1)}}{\partial z} = \frac{\partial\phi^{(2)}}{\partial z} \\ &\gamma\left(\frac{\partial\phi^{(1)}}{\partial z} + K\phi^{(1)}\right) = \frac{\partial\phi^{(2)}}{\partial z} + K\phi^{(2)} \end{aligned}\right\} \text{ on } z = h_1, \tag{7}$$

$$\frac{\partial\phi^{(2)}}{\partial z} = 0 \quad \text{on } z = h\,(= h_1 + h_2). \tag{8}$$

Here, by linearity, $\phi^{(m)}$ in the above can be any of the velocity potentials appearing in (1)–(4), and $\gamma = \rho_1/\rho_2 \leq 1$ is the density ratio, with ρ_m being the density of the upper ($m = 1$) and lower ($m = 2$) fluids.

Since the incident wave is independent of the presence of a body, the velocity potential of the incident wave, $\phi_{Ip}^{(m)}$, can be obtained from (5)–(8) and by specifying the amplitude of the incident wave on the free surface ($z=0$) or the interface ($z=h_1$). As shown in Fig. 1, the incident wave is assumed to propagate from the positive x-axis. Then the velocity potential of the incident wave is expressed in the form

$$\phi_{Ip}^{(m)}(x,z) = Z^{(m)}(k_p;z)\,e^{ik_p x} \tag{9}$$

where

$$\left.\begin{aligned} Z^{(1)}(k;z) &= \frac{k\,\mathrm{ch}\,kz - K\,\mathrm{sh}\,kz}{k} \\ Z^{(2)}(k;z) &= \frac{K\,\mathrm{ch}\,kh_1 - k\,\mathrm{sh}\,kh_1}{k\,\mathrm{sh}\,kh_2}\,\mathrm{ch}\,k(z-h) \end{aligned}\right\} \tag{10}$$

and the variable k in (9) and (10) is the wavenumber satisfying the dispersion relation for a two-layer fluid given by

$$D(k) = K\big(k\,\mathrm{sh}\,kh - K\,\mathrm{ch}\,kh\big) + \varepsilon\big(K^2-k^2\big)\,\mathrm{sh}\,kh_1\,\mathrm{sh}\,kh_2 = 0. \tag{11}$$

For brevity, $\cosh(x)$ and $\sinh(x)$ have been written as $\mathrm{ch}\,(x)$ and $\mathrm{sh}\,(x)$, respectively, and $\varepsilon = 1-\gamma$ in (11); these notations will be used throughout this article.

To determine the other velocity potentials associated with the disturbance by a body, the boundary condition on the body surface must be imposed, which can be given in the form

$$\left.\begin{aligned} \frac{\partial\phi_{Dp}^{(m)}}{\partial n} &= 0 \qquad (p=1,2) \\ \frac{\partial\phi_{Rj}^{(m)}}{\partial n} &= n_j \quad\; (j=1\sim 3) \end{aligned}\right\} \text{ on } S_H^{(m)} \tag{12}$$

where n_j denotes the jth component ($n_1=n_x$, $n_2=n_z$, $n_3=xn_z-zn_x$) of the normal vector, which is defined as positive when directed into the fluid domain from boundaries (see Fig. 1).

The boundary-value problems for the disturbance velocity potentials may be completed by imposing the radiation condition of generated waves radiating from the body.

3. Numerical Solution Method

The diffraction and radiation potentials formulated above are determined directly by the integral-equation method in terms of the Green function satisfying all homogeneous boundary conditions. This solution method can be applied to a general case where an arbitrary body intersects the interface between the upper and lower layers, and the derivation of the integral equation based on Green's theorem is shown in [1, 2]. The results may be summarized in the form

$$\begin{aligned} C(\mathrm{P})\phi_\ell^{(m)}(\mathrm{P}) &+ \sum_{n=1}^{2}\int_{S_H^{(n)}} \phi_\ell^{(m)}(\mathrm{Q})\frac{\partial}{\partial n_\mathrm{Q}}G_n^{(m)}(\mathrm{P};\mathrm{Q})\,ds \\ &= \begin{cases} \phi_{Ip}^{(m)}(\mathrm{P}) & (\,\ell = Dp;\ p=1,2\,) \\ \displaystyle\sum_{n=1}^{2}\int_{S_H^{(n)}} n_j(\mathrm{Q})G_n^{(m)}(\mathrm{P};\mathrm{Q})\,ds & (\,\ell=Rj;\ j=1\sim 3\,) \end{cases} \end{aligned} \tag{13}$$

where P $= (x, z)$ and Q $= (\xi, \zeta)$ denote the field and integration points, respectively, located on the body surface and $C(\mathrm{P})$ denotes the solid angle. $G_n^{(m)}(\mathrm{P};\mathrm{Q})$ represents the Green function, which has different forms depending on whether P and Q are in the upper or lower layer; details are shown in [1].

The so-called constant-panel collocation method is adopted for solving (13); that is, the body surface of $z > 0$ is divided into N segments and on each segment the unknown velocity potential is assumed to be constant. Then, considering N different points for P(x, z), we can recast (13) in a linear system of simultaneous equations for N unknowns.

In actual numerical computations, some additional field points are considered on both $z = 0$ and $z = h_1$ inside the body to remove the irregular frequencies. The resultant over-constrained simultaneous equations are solved using the least-squares method.

Once the velocity potentials on the body surface have been determined, it is straightforward to compute the hydrodynamic forces that must be used in solving the motion equations of a body in each of the incident waves of surface-wave mode ($p = 1$) and internal-wave mode ($p = 2$). The calculation method for the motions of a body in waves is described in [2].

4. Velocity Potentials in the Far Field

The analyses necessary for obtaining asymptotic expressions of the velocity potentials for $x \to \pm\infty$ may also be found also in [1], and the results are summarized as follows:

$$\phi_{Dp}^{(m)} \sim \phi_{Ip}^{(m)} + i \sum_{q=1}^{2} H_{Sp}^{\pm}(k_q)\, Z^{(m)}(k_q; z)\, e^{\mp i k_q x}, \tag{14}$$

$$\phi_{Rj}^{(m)} \sim i \sum_{q=1}^{2} H_{Rj}^{\pm}(k_q)\, Z^{(m)}(k_q; z)\, e^{\mp i k_q x}, \tag{15}$$

where

$$H_{Sp}^{\pm}(k) = -\sum_{n=1}^{2} \int_{S_H^{(n)}} \phi_{Dp}^{(n)} \frac{\partial}{\partial n} \frac{W_n(k;\zeta)}{D'(k)}\, e^{\pm i k \xi}\, ds, \tag{16}$$

$$H_{Rj}^{\pm}(k) = \sum_{n=1}^{2} \int_{S_H^{(n)}} \left\{ \frac{\partial \phi_{Rj}^{(n)}}{\partial n} - \phi_{Rj}^{(n)} \frac{\partial}{\partial n} \right\} \frac{W_n(k;\zeta)}{D'(k)}\, e^{\pm i k \xi}\, ds, \tag{17}$$

$$\left.\begin{aligned} W_1(k;\zeta) &= \gamma\, \alpha(k) k \,\mathrm{sh}\, k h_2\, Z^{(1)}(k;\zeta) \\ W_2(k;\zeta) &= \alpha(k) k \,\mathrm{sh}\, k h_2\, Z^{(2)}(k;\zeta) \end{aligned}\right\} \tag{18}$$

$$\alpha(k) = \frac{K}{K \,\mathrm{ch}\, k h_1 - k \,\mathrm{sh}\, k h_1}, \tag{19}$$

$$\begin{aligned} D'(k) = {}& K\bigl(\mathrm{sh}\, kh + kh \,\mathrm{ch}\, kh - Kh \,\mathrm{sh}\, kh\bigr) \\ &+ \varepsilon\Bigl\{-2k \,\mathrm{sh}\, kh_1 \,\mathrm{sh}\, kh_2 + (K^2 - k^2)(h_1 \,\mathrm{ch}\, kh_1 \,\mathrm{sh}\, kh_2 + h_2 \,\mathrm{sh}\, kh_1 \,\mathrm{ch}\, kh_2)\Bigr\}. \end{aligned} \tag{20}$$

Eqs. (16) and (17) are the Kochin functions (complex amplitude functions of the body-disturbance waves) computed from canonical velocity potentials in the diffraction and radiation problems. In terms of these Kochin functions and the complex amplitude of the jth mode of motion, X_j/A_p, to be obtained by solving the equations of motion of a body in the incident wave of the k_p-wave mode, the Kochin function representing the whole disturbance wave with wavenumber k_q can be obtained by linear superposition as follows:

$$H_p^{\pm}(k_q) \equiv H_{Sp}^{\pm}(k_q) - K\sum_{j=1}^{3} \frac{X_j}{A_p} H_{Rj}^{\pm}(k_q). \tag{21}$$

With this definition and taking the summation of both components of the surface-wave ($q=1$) and internal-wave ($q=2$) modes, the asymptotic expression of the velocity potential defined by (3) can be expressed in the following form:

$$\varphi_p^{(m)}(x,z) \sim Z^{(m)}(k_p;z)\,e^{ik_px} + \sum_{q=1}^{2} R_{pq}\,Z^{(m)}(k_q;z)\,e^{-ik_qx} \quad \text{as } x \to +\infty, \tag{22}$$

$$\varphi_p^{(m)}(x,z) \sim \sum_{q=1}^{2} T_{pq}\,Z^{(m)}(k_q;z)\,e^{ik_qx} \quad \text{as } x \to -\infty, \tag{23}$$

where

$$\left.\begin{aligned} R_{pq} &= i H_p^{+}(k_q) \\ T_{pq} &= \delta_{pq} + i H_p^{-}(k_q) \end{aligned}\right\} \tag{24}$$

with δ_{pq} being Kroenecker's delta.

R_{pq} and T_{pq} defined in (24) can be understood as the coefficients of reflected and transmitted waves, respectively, of the k_q-wave mode when the incident wave is of the k_p-wave mode.

5. Momentum-Conservation Principle

Following Maruo [4], a calculation formula for the wave drift force in the horizontal direction can be derived on the basis of the momentum- and energy-conservation principles. Let us consider first the momentum-conservation principle in the x-axis in a two-layer fluid. With the same transformation as that for a single layer fluid, the following equation may be obtained as a basis:

$$\overline{\sum_{m=1}^{2} \int_{S^{(m)}} \left\{ p^{(m)} n_x + \rho_m \frac{\partial \Phi^{(m)}}{\partial x} \left(\frac{\partial \Phi^{(m)}}{\partial n} - U_n \right) \right\} ds} = 0, \tag{25}$$

where

$$\left.\begin{aligned} S^{(1)} &= S_H^{(1)} + S_C^{(1)} + S_I^{(1)} + S_F \\ S^{(2)} &= S_H^{(2)} + S_C^{(2)} + S_I^{(2)} + S_B \end{aligned}\right\} \tag{26}$$

$$p^{(m)} = -\rho_m \Big\{ \frac{\partial \Phi^{(m)}}{\partial t} + \frac{1}{2} \nabla \Phi^{(m)} \cdot \nabla \Phi^{(m)} \Big\} + p_S^{(m)}, \tag{27}$$

$$\Phi^{(m)} = \mathrm{Re}\left[\frac{gA_p}{i\omega}\, \varphi_p^{(m)}(x,z)\, e^{i\omega t} \right]. \tag{28}$$

The overbar in (25) means the time average over one period and U_n in (25) represents the normal velocity of the boundaries surrounding the fluid under consideration. $p_S^{(m)}$ in (27) denotes the static pressure independent of the disturbance velocity potential. As explicitly written in (28), only the incident wave of the k_p-wave mode ($p=1$ or 2) is considered here.

As shown in Fig. 1, the control surface $S_C^{(m)}$ in the present study is parallel to the z-axis and in the linear theory the free surface S_F, the interface $S_I^{(m)}$, and the bottom of fluid S_B are parallel to the x-axis; these are fixed in space and thus $U_n = 0$ on these boundaries. On the other hand, the normal velocity of the body boundary must be equal to the normal velocity of the fluid and thus

$$U_n = \frac{\partial \Phi^{(m)}}{\partial n} \quad \text{on } S_H^{(m)}. \tag{29}$$

Taking these into consideration and retaining only quadratic terms in the velocity potential, we may write an expression for the wave drift force acting in the negative direction of the x-axis as follows:

$$\begin{aligned} F_D \equiv & \sum_{m=1}^{2} \overline{\int_{S_H^{(m)}} p^{(m)} n_x \, ds} \\ = & \ \frac{1}{2}\rho_1 \left[\int_0^{h_1} \left\{ \overline{\frac{\partial \Phi^{(1)}}{\partial x}\frac{\partial \Phi^{(1)}}{\partial x} - \frac{\partial \Phi^{(1)}}{\partial z}\frac{\partial \Phi^{(1)}}{\partial z}} \right\} dz \right]_{-\infty}^{+\infty} \\ & + \frac{1}{2}\rho_2 \left[\int_{h_1}^{h} \left\{ \overline{\frac{\partial \Phi^{(2)}}{\partial x}\frac{\partial \Phi^{(2)}}{\partial x} - \frac{\partial \Phi^{(2)}}{\partial z}\frac{\partial \Phi^{(2)}}{\partial z}} \right\} dz \right]_{-\infty}^{+\infty} \\ & - \rho_1 \int_{S_F} \overline{\frac{\partial \Phi^{(1)}}{\partial x}\frac{\partial \Phi^{(1)}}{\partial z}} \, dx + \rho_1 \int_{S_I^{(1)}} \overline{\frac{\partial \Phi^{(1)}}{\partial x}\frac{\partial \Phi^{(1)}}{\partial z}} \, dx - \rho_2 \int_{S_I^{(2)}} \overline{\frac{\partial \Phi^{(2)}}{\partial x}\frac{\partial \Phi^{(2)}}{\partial z}} \, dx. \end{aligned} \tag{30}$$

Here the square brackets with superscript $+\infty$ and subscript $-\infty$ in (30) means the difference between the quantities in the brackets evaluated at $x = +\infty$ and $x = -\infty$. The integrand in the integrals on S_F and S_I may be transformed in terms of the boundary conditions given by (6) and (7) as follows:

on S_F

$$\frac{\partial \Phi^{(1)}}{\partial x}\frac{\partial \Phi^{(1)}}{\partial z} = -K\Phi^{(1)}\frac{\partial \Phi^{(1)}}{\partial x} = -\frac{1}{2}K\frac{\partial}{\partial x}\left\{\Phi^{(1)}\Phi^{(1)}\right\}, \tag{31}$$

on S_I

$$\begin{aligned} \rho_1 \frac{\partial \Phi^{(1)}}{\partial x}\frac{\partial \Phi^{(1)}}{\partial z} - \rho_2 \frac{\partial \Phi^{(2)}}{\partial x}\frac{\partial \Phi^{(2)}}{\partial z} &= \frac{\rho_1}{\gamma}\frac{\partial \Phi^{(1)}}{\partial z}\frac{\partial}{\partial x}\left\{\gamma\Phi^{(1)} - \Phi^{(2)}\right\} \\ &= \frac{\rho_1}{\gamma}\frac{\partial \Phi^{(1)}}{\partial z}\frac{1-\gamma}{K}\frac{\partial}{\partial x}\frac{\partial \Phi^{(1)}}{\partial z} = \frac{1}{2}\rho_1\frac{1-\gamma}{\gamma K}\frac{\partial}{\partial x}\left\{\frac{\partial \Phi^{(1)}}{\partial z}\frac{\partial \Phi^{(1)}}{\partial z}\right\}. \end{aligned} \tag{32}$$

For taking time average, the following formula may be useful

$$\overline{\mathrm{Re}\big[\, A\, e^{i\omega t} \,\big]\, \mathrm{Re}\big[\, B\, e^{i\omega t} \,\big]} = \frac{1}{2}\,\mathrm{Re}\big[\, A\, B^* \,\big], \tag{33}$$

where A and B are complex in general and the asterisk means the complex conjugate.

Substituting (31) and (32) in (30) and applying (33) with (28) gives the following result:

$$
\begin{aligned}
F'_{Dp} &\equiv \frac{F_D}{\frac{1}{2}\rho_1 g A_p^2} \\
&= \frac{1}{2K}\left[\int_0^{h_1}\left\{\left|\frac{\partial\varphi_p^{(1)}}{\partial x}\right|^2 - \left|\frac{\partial\varphi_p^{(1)}}{\partial z}\right|^2\right\}dz + \frac{1}{\gamma}\int_{h_1}^{h}\left\{\left|\frac{\partial\varphi_p^{(2)}}{\partial x}\right|^2 - \left|\frac{\partial\varphi_p^{(2)}}{\partial z}\right|^2\right\}dz\right]_{-\infty}^{+\infty} \\
&\quad + \frac{1}{2}\left[\left|\varphi_p^{(1)}\right|^2_{z=0}\right]_{-\infty}^{+\infty} + \frac{1-\gamma}{2\gamma K^2}\left[\left|\frac{\partial\varphi_p^{(1)}}{\partial z}\right|^2_{z=h_1}\right]_{-\infty}^{+\infty}
\end{aligned} \tag{34}
$$

This may be regarded as an extension of the expression for a single-layer fluid to the case of a two-layer fluid, and in fact the last line in (34) can be understood as contributions from the square of wave height at the free surface ($z = 0$) and the interface ($z = h_1$). However, this form is not convenient for analytical integration with respect to z, because the derivatives with respect to z are included. Thus it is not straightforward to utilize the orthogonality properties of the eigenfunctions for a two-layer fluid summarized in the Appendix.

To overcome this inconvenience, we consider further transformation for the integrals including the derivatives with respect to z using the Laplace equation and the boundary conditions on $z = 0$, $z = h_1$, and $z = h$. Performing partial integrations and substituting (5)–(8), the following result can be justified:

$$
\begin{aligned}
\mathcal{I} &\equiv \int_0^{h_1}\frac{\partial\varphi^{(1)}}{\partial z}\frac{\partial\varphi^{(1)*}}{\partial z}\,dz + \frac{1}{\gamma}\int_{h_1}^{h}\frac{\partial\varphi^{(2)}}{\partial z}\frac{\partial\varphi^{(2)*}}{\partial z}\,dz \\
&= K\left\{\left|\varphi^{(1)}\right|^2_{z=0} + \frac{1-\gamma}{\gamma K^2}\left|\frac{\partial\varphi^{(1)}}{\partial z}\right|^2_{z=h_1}\right\} \\
&\quad + \int_0^{h_1}\frac{\partial^2\varphi^{(1)}}{\partial x^2}\,\varphi^{(1)*}\,dz + \frac{1}{\gamma}\int_{h_1}^{h}\frac{\partial^2\varphi^{(2)}}{\partial x^2}\,\varphi^{(2)*}\,dz.
\end{aligned} \tag{35}
$$

Substituting this result in (34), we can see that the first line on the right-hand side of (35) cancels exactly the last terms in (34) to be evaluated at $z = 0$ and $z = h_1$.

Therefore, as a final result convenient for analytical integrations with respect to z, the following expression can be obtained:

$$
F'_{Dp} = \frac{1}{2\gamma K}\left[\int_0^{h} w(z)\left\{\left|\frac{\partial\varphi_p}{\partial x}\right|^2 - \frac{\partial^2\varphi_p}{\partial x^2}\,\varphi_p^*\right\}dz\right]_{-\infty}^{+\infty} \tag{36}
$$

where $w(z)$ and φ_p are defined as

$$
\left\{
\begin{array}{lll}
w(z) = \gamma, & \varphi_p = \varphi_p^{(1)} & \text{for } \ 0 \le z \le h_1, \\
w(z) = 1, & \varphi_p = \varphi_p^{(2)} & \text{for } \ h_1 \le z \le h.
\end{array}
\right. \tag{37}
$$

6. Energy-Conservation Principle

A relation to be obtained from the energy conservation principle is usually used to derive a compact formula for the wave drift force and also to check the accuracy of computed results. With the same notations as for (25)–(28), a basis equation for the two-layer fluid may be given in the form

$$
\overline{\sum_{m=1}^{2}\int_{S^{(m)}}\left\{\rho_m\frac{\partial\Phi^{(m)}}{\partial t}\frac{\partial\Phi^{(m)}}{\partial n} - \left(p^{(m)} + \rho_m\frac{\partial\Phi^{(m)}}{\partial t}\right)U_n\right\}ds} = 0. \tag{38}
$$

With this equation, considering the normal velocity U_n of the boundaries, the work done by a body onto the fluid may be evaluated as follows:

$$
\begin{aligned}
W \equiv & \sum_{m=1}^{2} \overline{\int_{S_H^{(m)}} p^{(m)} U_n \, ds} \\
= & -\rho_1 \left[\int_0^{h_1} \overline{\frac{\partial \Phi^{(1)}}{\partial t} \frac{\partial \Phi^{(1)}}{\partial x}} \, dz \right]_{-\infty}^{+\infty} - \rho_2 \left[\int_{h_1}^{h} \overline{\frac{\partial \Phi^{(2)}}{\partial t} \frac{\partial \Phi^{(2)}}{\partial x}} \, dz \right]_{-\infty}^{+\infty} \\
& + \rho_1 \int_{S_F} \overline{\frac{\partial \Phi^{(1)}}{\partial t} \frac{\partial \Phi^{(1)}}{\partial z}} \, dx - \rho_1 \int_{S_I^{(1)}} \overline{\frac{\partial \Phi^{(1)}}{\partial t} \frac{\partial \Phi^{(1)}}{\partial z}} \, dx + \rho_2 \int_{S_I^{(2)}} \overline{\frac{\partial \Phi^{(2)}}{\partial t} \frac{\partial \Phi^{(2)}}{\partial z}} \, dx. \quad (39)
\end{aligned}
$$

Substituting (28) and taking the time-average over one period using the formula (33), we may obtain the following result:

$$
\begin{aligned}
W_p' \equiv & \frac{W}{\frac{1}{2}\rho_1 g A_p^2 \left(\frac{\omega}{K}\right)} \\
= & -\,\mathrm{Im}\left[\int_0^{h_1} \frac{\partial \varphi_p^{(1)}}{\partial x} \, \varphi_p^{(1)*} \, dz + \frac{1}{\gamma} \int_{h_1}^{h} \frac{\partial \varphi_p^{(2)}}{\partial x} \, \varphi_p^{(2)*} \, dz \right]_{-\infty}^{+\infty} \\
& + \mathrm{Im} \int_{S_F} \frac{\partial \varphi_p^{(1)}}{\partial z} \, \varphi_p^{(1)*} \, dx + \frac{1}{\gamma} \, \mathrm{Im} \int_{S_I} \left\{ \frac{\partial \varphi_p^{(2)}}{\partial z} \, \varphi_p^{(2)*} - \gamma \, \frac{\partial \varphi_p^{(1)}}{\partial z} \, \varphi_p^{(1)*} \right\} dx \quad (40)
\end{aligned}
$$

In the above 'Im' means that only the imaginary part is to be taken.

Taking account of the boundary conditions on S_F and S_I as we did in deriving (31) and (32), one can easily prove that the integrals on S_F and S_I have no contributions because the integrands are real quantities. Therefore, with the notations in (37), the result can be written in the form

$$
W_p' = -\frac{1}{\gamma} \, \mathrm{Im}\left[\int_0^{h} w(z) \, \frac{\partial \varphi_p}{\partial x} \, \varphi_p^* \, dz \right]_{-\infty}^{+\infty} \quad (41)
$$

Here it is noteworthy that the work done by a body must be zero when the body is fixed (as in the diffraction problem) or freely oscillating in waves without external oscillation devices supplying the energy.

7. Wave Drift Force

Having prepared all necessary equations, let us derive the formula for the wave drift in a two-layer fluid. The asymptotic expressions of $\varphi_p^{(m)}$, given by (22) and (23), must be substituted in (36). To perform this procedure in general, Eq. (22) for instance can be written as

$$
\varphi_p^{(m)}(x,z) = Z^{(m)}(k_p;z) \Big\{ e^{ik_p x} + R_{pp} \, e^{-ik_p x} \Big\} + Z^{(m)}(k_q;z) \, R_{pq} \, e^{-ik_q x}, \quad (42)
$$

with convention of $p \neq q$; that is, when $p = 1$ (the incident wave is of the surface-wave mode) then $q = 2$, and when $p = 2$ (the incident wave is of the internal-wave mode) we have $q = 1$.

It should also be noted that, owing to the orthogonality in the Appendix, there is no need to consider cross terms between k_p-wave and k_q-wave in evaluating the integrals with respect to z. Therefore, using (42), we may write the integrand at $x=+\infty$ in (36) as follows:

$$\left|\frac{\partial \varphi_p^{(m)}}{\partial x}\right|^2 - \frac{\partial^2 \varphi_p^{(m)}}{\partial x^2}\,\varphi_p^{(m)*}$$
$$= 2\big\{Z^{(m)}(k_p;z)\big\}^2 k_p^2\left(1+\left|R_{pp}\right|^2\right) + 2\big\{Z^{(m)}(k_q;z)\big\}^2 k_q^2 \left|R_{pq}\right|^2. \tag{43}$$

Here the integrals with respect to z can be identified with the normalization integral, whose explicit form is provided in the Appendix as follows:

$$\begin{aligned}\mathcal{F}(k) &\equiv \frac{2k}{\gamma}\int_0^h w(z)\big\{Z(k;z)\big\}^2\,dz \\ &= \frac{K}{k} + kh\,\frac{(K\,\mathrm{ch}\,kh_1 - k\,\mathrm{sh}\,kh_1)^2}{\gamma\,k^2\,\mathrm{sh}^2 kh_2} \\ &\quad + \frac{\varepsilon}{\gamma}\frac{h_1}{k}\left[\left(1-\frac{k^2}{K^2}+\frac{1}{Kh_1}\right)\big(K\,\mathrm{ch}\,kh_1 - k\,\mathrm{sh}\,kh_1\big)^2 + \gamma\frac{(K^2-k^2)^2}{K^2}\,\mathrm{sh}^2 kh_1\right].\end{aligned} \tag{44}$$

With these results, the integral at $x=+\infty$ in (36) takes the following form:

$$\big[\,F'_{Dp}\,\big]_{+\infty} = \frac{1}{2K}\Big\{\,k_p\left(1+\left|R_{pp}\right|^2\right)\mathcal{F}(k_p) + k_q\left|R_{pq}\right|^2\mathcal{F}(k_q)\,\Big\}. \tag{45}$$

In the same manner, the integral at $x=-\infty$ can be performed analytically. Namely, with convention of $p\neq q$, (23) is written as

$$\varphi_p^{(m)}(x,z) = T_{pp}\,Z^{(m)}(k_p;z)\,e^{ik_px} + T_{pq}\,Z^{(m)}(k_q;z)\,e^{ik_qx} \tag{46}$$

and then it follows that

$$\left|\frac{\partial \varphi_p^{(m)}}{\partial x}\right|^2 - \frac{\partial^2 \varphi_p^{(m)}}{\partial x^2}\,\varphi_p^{(m)*} = 2\big\{Z^{(m)}(k_p;z)\big\}^2 k_p^2\left|T_{pp}\right|^2 + 2\big\{Z^{(m)}(k_q;z)\big\}^2 k_q^2\left|T_{pq}\right|^2. \tag{47}$$

Therefore, in terms of (44), the result of the integral at $x=-\infty$ takes the form

$$\big[\,F'_{Dp}\,\big]_{-\infty} = \frac{1}{2K}\Big\{\,k_p\left|T_{pp}\right|^2\mathcal{F}(k_p) + k_q\left|T_{pq}\right|^2\mathcal{F}(k_q)\,\Big\}. \tag{48}$$

The wave drift force must be given by the difference between (45) and (48). Therefore, the result from (36) is expressed as

$$F'_{Dp} = \frac{1}{2K}\left[\,k_p\left(1+\left|R_{pp}\right|^2-\left|T_{pp}\right|^2\right)\mathcal{F}(k_p) + k_q\left(\left|R_{pq}\right|^2-\left|T_{pq}\right|^2\right)\mathcal{F}(k_q)\right]. \tag{49}$$

As the next step, let us consider a relation to be obtained from the energy-conservation principle given by (41). With the same convention for $\varphi_p^{(m)}$ and the orthogonal properties for the integrals with respect to z, the final result of (41) can be expressed as follows:

$$W'_p = -\frac{1}{2}\left\{\left(1-\left|R_{pp}\right|^2-\left|T_{pp}\right|^2\right)\mathcal{F}(k_p) - \left(\left|R_{pq}\right|^2+\left|T_{pq}\right|^2\right)\mathcal{F}(k_q)\right\}. \tag{50}$$

As noted at the end of the preceding section, we have $W_p' = 0$ for the case where a body is fixed or freely oscillating in the incident wave. Therefore, the energy conservation principle takes the form

$$\left(1 - \left|R_{pp}\right|^2 - \left|T_{pp}\right|^2\right) \mathcal{F}(k_p) = \left(\left|R_{pq}\right|^2 + \left|T_{pq}\right|^2\right) \mathcal{F}(k_q). \tag{51}$$

Substitution of this in (49) gives the final form of the calculation formula for the wave drift force in a two-layer fluid:

$$F_{Dp}' = \frac{1}{K}\left[k_p\left|R_{pp}\right|^2 \mathcal{F}(k_p) + \left\{ \frac{k_p + k_q}{2}\left|R_{pq}\right|^2 + \frac{k_p - k_q}{2}\left|T_{pq}\right|^2 \right\} \mathcal{F}(k_q) \right]. \tag{52}$$

By considering the limiting case of $\gamma \to 1$, let us confirm the corresponding formula for a single-layer fluid. For $\gamma = 1$, $k_2 \to \infty$ and the internal wave no longer exists, and hence

$$p = 1,\ \mathcal{F}(k_2) = 0,\ k_1 = k,\ K = k\tanh kh. \tag{53}$$

In this limiting case, $\varepsilon = 0$ in (44); thus, the coefficient associated with the normalization integral can be transformed into

$$\begin{aligned} \mathcal{J} \equiv \frac{k}{K}\,\mathcal{F}(k) &= 1 + \frac{h}{K}\,\frac{(K\,\mathrm{ch}\,kh_1 - k\,\mathrm{sh}\,kh_1)^2}{\mathrm{sh}^2 kh_2} \\ &= 1 + \frac{h}{K}(K\,\mathrm{sh}\,kh - k\,\mathrm{ch}\,kh)^2 = 1 + \frac{2kh}{\mathrm{sh}\,2kh}. \end{aligned} \tag{54}$$

Therefore, it follows from (52) that

$$F_D' = \frac{F_D}{\frac{1}{2}\rho g A^2} = \left|R\right|^2 \left\{ 1 + \frac{2kh}{\mathrm{sh}\,2kh} \right\}, \tag{55}$$

with R being the coefficient of the reflected wave in a single-layer fluid. This result is well known as a formula for the wave drift force in water of finite depth.

Another thing noteworthy aspect of (52) is a possibility that the the wave drift force in a two-layer fluid be negative. The wave drift force to be computed from (52) is mostly positive. In particular for the case of $p = 2$ (i.e., for the incident wave of internal-wave mode), the value of (52) is definitely positive because $k_2 > k_1$. However, for the case of $p = 1$, the value of (52) can be negative if the value of $|T_{12}|$ (the transmitted wave with wavenumber k_2 in the incident wave of the surface-wave mode) is relatively large.

When the energy is not conserved owing to viscous effects such as viscous damping in roll, relation (51) obtained from the energy-conservation principle cannot be used. However, even in this case, the momentum-conservation principle holds and thus the wave-drift force can be computed with (49).

8. Numerical Results and Discussions

Numerical computations were performed for a Lewis-form body as used in the previous study of first-order radiation [1] and diffraction [2] problems. This Lewis-form body can be represented by a conformal mapping with two nondimensional parameters; those are the half-breadth to draft ratio $H_0 = b/d = 0.833$ and the sectional area ratio $\sigma = A/Bd = 0.9$ (in real dimensions, the breadth $B = 2b = 0.2\,\mathrm{m}$ and the draft $d = 0.12\,\mathrm{m}$). Since this body is symmetrical with respect to x, only half of the body surface was discretized into 40 segments for all computations in this article. With this number of segments, satisfaction of the energy-conservation principle given by (51) was virtually perfect with the order of error being 10^{-4} for both cases of body motions fixed and free to oscillate in waves.

8.1 Effects of the density ratio

To see the effects of the density ratio on the second-order wave-drift force, computations were implemented for the same parameters as those in the study of the first-order radiation and diffraction problems; that is, $\gamma = 1.0$, 0.9, 0.7, and 0.2 with the depths of the fluid layers fixed at $h_1 = 1.2d$ and $h = 2.0d$. As $\gamma \to 1$, the fluid reduces to a single-layer fluid of $h = 2.0d$. Conversely as $\gamma \to 0$, the lower fluid behaves more like a rigid block, and the results are expected to approach those for a single-layer fluid with upper-layer depth $h_1 = 1.2d$. To illustrate this behavior, computations were also carried out for single-layer fluids of $h = 1.2d$ and $2.0d$.

Figure 2 shows the nondimensional value of the wave-drift force for the case where all body motions are fixed, in which the left-hand and right-hand sides are for the surface-wave

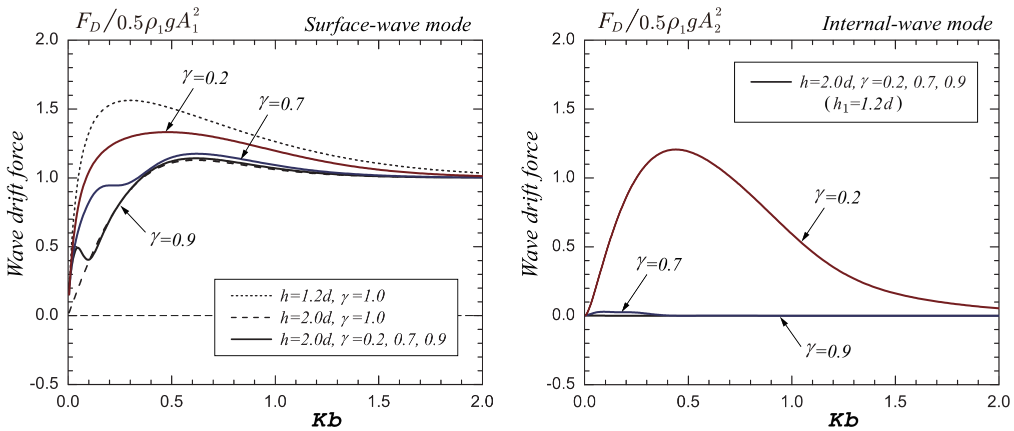

Fig. 2 Wave-drift force on a Lewis-form body ($H_0 = 0.833$, $\sigma = 0.9$) in two-layer fluids: effect of the difference in the fluid density for the case where all body motions are fixed

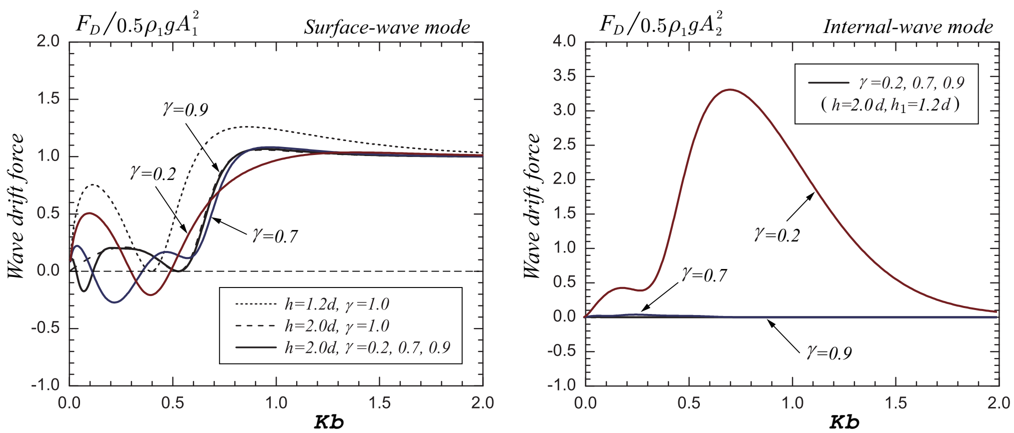

Fig. 3 Wave-drift force on a Lewis-form body ($H_0 = 0.833$, $\sigma = 0.9$) in two-layer fluids: effect of the difference in the fluid density for the case where only the heave motion is free to oscillate

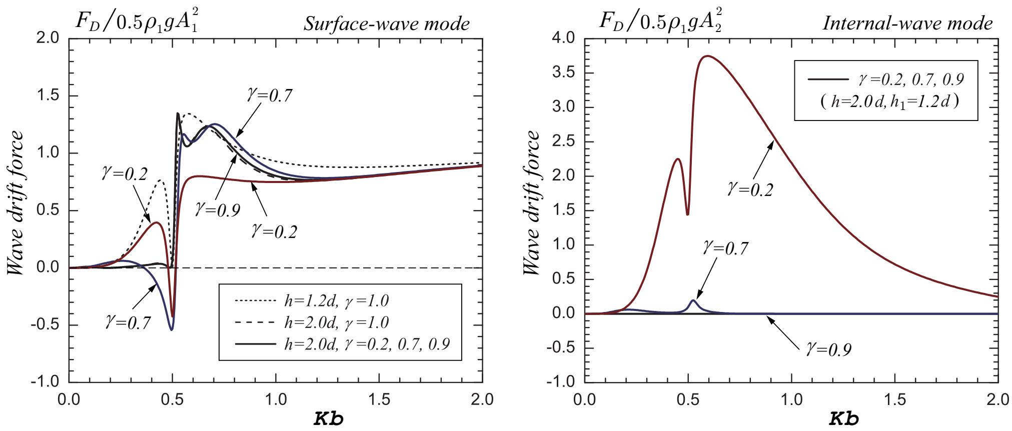

Fig. 4 Wave-drift force on a Lewis-form body ($H_0 = 0.833$, $\sigma = 0.9$) in two-layer fluids: effect of the difference in the fluid density for the case where all body motions are free to oscillate

and internal-wave modes, respectively, of the incident wave.

It should be noted first that the wave drift force shown in Fig. 2 is always positive over the whole range of frequency, although theoretically there is a possibility of negative value in the incident wave of surface-wave mode. The results for $\gamma = 0.9$ are close to those for a single-layer fluid of $h = 2.0d$, except for very low frequencies, and the results for $\gamma = 0.7$ are also almost the same as those for $\gamma = 0.9$ in the frequency range of $Kb > 0.4$. On the other hand, for $\gamma = 0.2$, the results in the incident wave of surface-wave mode tend to approach the results for a single-layer fluid of $h = 1.2d$, and the nondimensional value of the drift force in the incident wave of the internal-wave mode also becomes large. (Note that the amplitude A_2 of the incident wave of the internal-wave mode is taken as that on the interface.)

Figure 3 shows computed results for the same parameters but for the case where only the heave motion is free to oscillate. Compared to Fig. 2, a big difference can be seen in lower frequencies, where the drift force in two-layer fluids becomes negative in the incident wave of the surface-wave mode over a certain frequency range; which can be attributed to a larger value of T_{12} in the calculation formula of (52). It can be said that the results for $\gamma = 0.7$ are almost the same as those for $\gamma = 0.9$ and for a single-layer fluid of $h = 2.0d$ at frequencies of $Kb > 0.6$ which is higher than the resonant frequency in heave. The wave-drift force in the incident wave of the internal-wave mode is always positive but very small for larger values of γ. However, for $\gamma = 0.2$, the nondimensional value becomes larger than double the corresponding value in the diffraction case, owing to the effect of heave motion.

Figure 4 shows the results when all modes (heave, sway, and roll) of body motion are free to oscillate. In the present computations, the gyrational radius in roll is set to $\kappa_{xx} = 0.6b$ and the vertical distance between the center of gravity and the free surface is set to $\overline{\mathrm{OG}} = 0.45b$. A rapid change can be seen around $Kb \simeq 0.5$ both for the surface-wave and internal-wave modes, which is obviously due to the resonance in roll. (It should be noted that the roll amplitude near resonance is unrealistically very large because the viscous damping is not considered in the present theory.) When the incident wave is of surface-wave mode, the wave-drift forces for $\gamma = 0.2$ and 0.7 become negative at frequencies lower than the roll resonant frequency. However, a marked difference when compared to Fig. 3 is that the wave-drift force is almost zero at very low frequencies. Another thing to be noted is that the results for $\gamma = 0.9$ are very close to those for a single-layer fluid over the whole frequency range , including the heave and roll resonant frequencies; which implies that a small difference in the fluid density between the upper and lower layers gives no prominent difference in the wave drift force and motion characteristics.

The results shown above are for the case where a body floats in the upper fluid only and the interface is located at a relatively deeper position. The horizontal force (like the wave drift force) may be affected by the presence of internal waves near a body, which is the case particularly when a body intersects the interface and this will be studied next.

8.2 Effects of the interface position

For the same Lewis-form body ($b = B/2 = 0.1\,\mathrm{m}$ and $d = 0.12\,\mathrm{m}$) and fixed values of $h = 0.4\,\mathrm{m}$ and $\gamma = 0.75$, only the vertical position of the interface was changed from

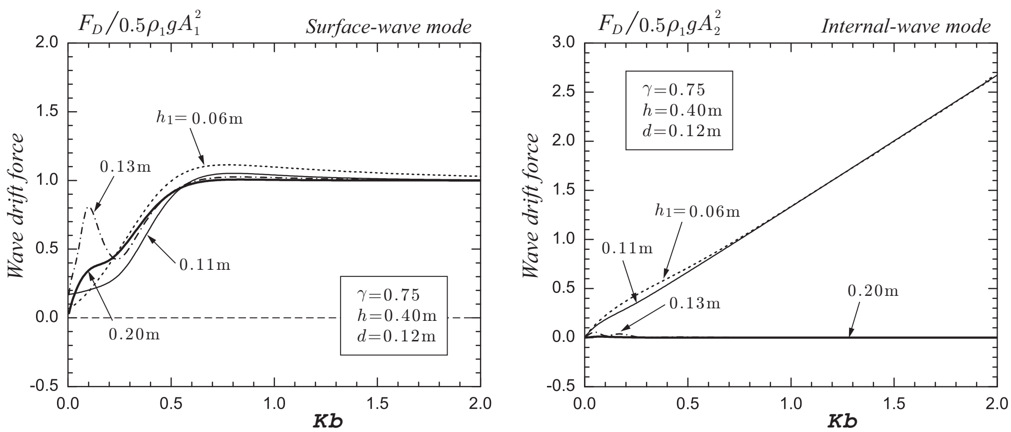

Fig. 5 Wave-drift force on a Lewis-form body ($H_0 = 0.833$, $\sigma = 0.9$) in two-layer fluids: effect of the interface position for the case where all body motions are fixed.

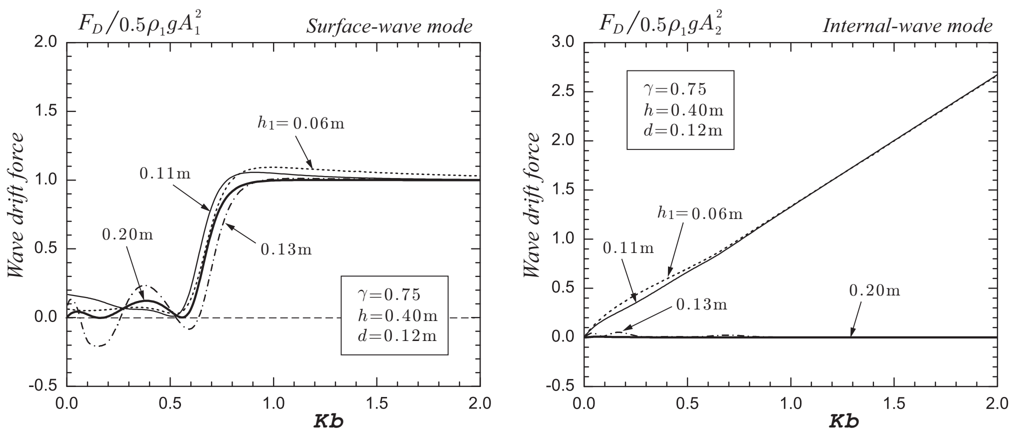

Fig. 6 Wave-drift force on a Lewis-form body ($H_0 = 0.833$, $\sigma = 0.9$) in two-layer fluids: effect of the interface position for the case where only the heave motion is free to oscillate.

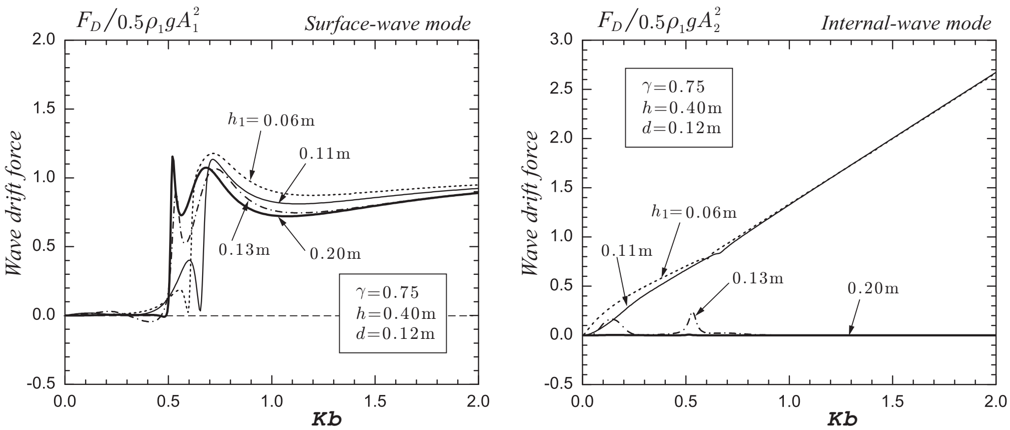

Fig. 7 Wave-drift force on a Lewis-form body ($H_0 = 0.833$, $\sigma = 0.9$) in two-layer fluids: effect of the interface position for the case where all body motions are free to oscillate.

$h_1 = 0.06$ m to 0.20 m, including the case where the body intersects the interface.

Figure 5 shows computed results of the wave-drift force for the case where all body motions are fixed, and like before the left-hand and right-hand sides are for the surface-wave and internal-wave modes, respectively, of the incident wave. In the incident wave of the surface-wave mode, the drift force is always positive, and no prominent difference exists among the results for different interface positions, except that undulatory variation can be seen at $Kb < 0.25$ for the case of $h_1 = 0.13$ m where the interface is located just below the bottom of the body ($d = 0.12$ m). On the other hand, in the incident wave of the internal-wave mode, a remarkable change can be seen depending on whether a body intersects the interface. When the interface position is deeper than the draft of a body, the wave-drift force is negligibly small. However, once a body intersects the interface, the wave-drift force becomes large and increases almost linearly with respect to Kb, for which we may envisage that the internal incident wave will be blocked by a body and almost all waves may be reflected; that is, the coefficient of R_{22} in the calculation formula (52) is largely different depending on whether the body intersects the interface.

Figure 6 shows the results when only the heave motion is free to oscillate. Obviously, owing to the heave motion, the wave-drift force becomes small in frequencies lower than the heave resonant frequency, which implies that longer incident waves transmit because the heave is free to oscillate. It should be noted, however, that the drift force at $h_1 = 0.13$ m fluctuates in lower frequencies and becomes negative in a certain range of frequency, which is due to the effect of waves with internal-wave mode, as can be conjectured from (52).

On the other hand, in the incident wave of the internal-wave mode, no marked difference can be seen as compared to Fig. 5, which implies that the reflection-wave coefficient R_{22} (especially when a body intersects the interface) is not much influenced by the heave motion and the hydrodynamic situation near the cross-point between body and interface may be viewed locally as a diffraction problem regardless of the heave motion.

Lastly, Fig. 7 shows the results for various vertical positions of the interface when all modes of body motion are free to oscillate. As shown [2], the resonant frequency in roll changes slightly depending on the position of the interface, which is due mainly to the change in the roll restoring moment. Therefore, the frequency where rapid variation in the wave-drift force appears is slightly different depending on the vertical position of the interface. It can be seen that the wave-drift force is almost zero at lower frequencies, irrespective of the interface position. Another point to be emphasized is that the wave-drift force looks always positive when a body intersects the interface (at $h_1 = 0.11\,\mathrm{m}$ and $0.06\,\mathrm{m}$), which means that the transmitted wave with internal-wave mode T_{12} in the calculation formula of (52) is relatively small. When the incident wave is of the internal-wave mode, as compared to Figs. 5 and 6, a slight difference can be seen around the roll resonance, but we should note that the roll amplitude near the resonance becomes unrealistically very large for lack of viscous damping in the present study.

9. Conclusions

The wave-drift force in a 2-D two-layer fluid of finite depth has been studied with the potential-flow assumption. Based on the momentum and energy conservation principles, a compact calculation formula for the wave drift force was obtained; the key to success was to use effectively the orthogonality relations for the eigenfunctions in a two-layer fluid. Owing to the presence of the interface, for a prescribed frequency, there can exist two different incident waves with surface-wave mode (longer wavelength) and internal-wave mode (shorter wavelength), and each incident wave will be diffracted by a body into two different wave modes and hence the energy of the incident wave may be transferred from one mode to the other. The wave-drift force in this rather complicated situation was described with only one equation, which includes the coefficients of reflected and transmitted waves in a two-layer fluid. An important feature to be seen from this calculation formula is that the possibility of negative drift force exists in the incident wave of the surface-wave mode; this can be exerted by a large value of the transmitted wave with internal-wave mode.

Numerical computations were performed with the boundary-integral-equation method using the Green function for the two-layer fluid problem. Computed results of the wave-drift force were shown for both incident waves with surface-wave and internal-wave modes and also for three cases where all body motions are completely fixed, only the heave motion being free, and all body motions being free to oscillate. Furthermore, by changing the density ratio and the interface position including the case where a body intersects the interface, those effects on the wave-drift force were discussed.

The main results obtained from the present numerical study may be summarized as follows:

(1) When the body motions are fixed, the wave-drift force seems to be positive for all frequencies, regardless of the density ratio and the interface position. However, when the position of the interface is slightly deeper than the bottom of a body and the body motions are free to respond to the incident wave of a surface-wave mode, the wave-drift force becomes negative at frequencies lower than the resonant frequency of body motion.

(2) When the difference in the fluid density between the upper and lower layers is large (say $\gamma = 0.2$), the wave-drift force becomes large, even in the incident wave of an internal-wave mode. On the other hand, when the difference in the fluid density is small (say $\gamma = 0.9$), the results are very close to those for a single-layer fluid over the whole frequency range, except at very low frequencies when all or some of the body motions are fixed.

(3) When a body intersects the interface, the body reflects most of the incident wave of internal-wave mode, particularly at higher frequencies, and hence the wave-drift force

nondimensionalized in terms of the square of the wave amplitude on the interface, seems to increase linearly in proportional to the square of the frequency.

References

[1] Ten, I and Kashiwagi, M (2004) Hydrodynamics of a body floating in a two-layer fluid of finite depth, Part 1: Radiation problem, J Marine Science and Technology 9 (3): 127–141

[2] Newman, J N (1976) The interaction of stationary vessels with regular waves. In: Proceedings of the 11th Symp on Naval Hydrodynamics, London, pp 491–501

[3] Yeung, R W and Nguyen T (1999) Radiation and diffraction of waves in a two-layer fluid. In: Proceedings of the 22nd Symp on Naval Hydrodynamics, Washington, D.C., pp 875–891

[4] Linton, C M and McIver, M (1995) The interaction of waves with horizontal cylinders in two-layer fluids. J Fluid Mech 304: 213–229

[5] Cadby, J R and Linton, C M (2000) Three dimensional water wave scattering in two-layer fluids. J Fluid Mech 423: 155–173

[6] Sturova, I V (2003) Radiation loads on interface piercing cylinder in a two-layer fluid of finite depth by a coupled element technique. In: Proceedings of the 8th International Conference on Numerical Ship Hydrodynamics, Busan, Vol 2, pp 80–91

Appendix

The orthogonality properties of the eigenfunctions with respect to z in the two-layer fluid problem are explained in [1], a summary of which is given below.

As explicitly given by (10), the z-dependent functions in the upper and lower layers are denoted by $Z^{(1)}(k;z)$ and $Z^{(2)}(k;z)$, respectively. If necessary, the eigenfunctions corresponding to the eigenvalues $k = k_p$ $(p = 1, 2)$ are represented by a subscript; e.g., $Z_p^{(1)}(k_p;z)$ and $Z_p^{(2)}(k_p;z)$.

The orthogonality can be proven in the same way as that in the Sturm-Liouville eigenvalue problem, and the basic equation is given as

$$\begin{aligned}
\mathcal{L} &\equiv \gamma \int_0^{h_1} \left\{ \frac{d^2 Z_1^{(1)}}{dz^2} Z_2^{(1)} - Z_1^{(1)} \frac{d^2 Z_2^{(1)}}{dz^2} \right\} dz + \int_{h_1}^{h} \left\{ \frac{d^2 Z_1^{(2)}}{dz^2} Z_2^{(2)} - Z_1^{(2)} \frac{d^2 Z_2^{(2)}}{dz^2} \right\} dz \\
&= (k_1^2 - k_2^2) \left[\gamma \int_0^{h_1} Z^{(1)}(k_1;z) Z^{(1)}(k_2;z)\, dz + \int_{h_1}^{h} Z^{(2)}(k_1;z) Z^{(2)}(k_2;z)\, dz \right] \\
&\equiv (k_1^2 - k_2^2) \int_0^h w(z) Z(k_1;z) Z(k_2;z)\, dz, \qquad (56)
\end{aligned}$$

where

$$\begin{cases} w(z) = \gamma, \quad Z(k_p;z) = Z^{(1)}(k_p;z) \quad 0 \le z \le h_1 \\ w(z) = 1, \quad Z(k_p;z) = Z^{(2)}(k_p;z) \quad h_1 \le z \le h \end{cases} \qquad (57)$$

Integrating by parts for the first line of (56) and substituting the boundary conditions on $z=0$, $z=h_1$, and $z=h$ (these are the same in form as (6)–(8)), one can easily prove that $\mathcal{L}=0$ for the case of $k_1 \neq k_2$; that is,

$$\int_0^h w(z)\, Z(k_1;z)\, Z(k_2;z)\, dz = 0 \quad \text{for } k_1 \neq k_2 . \tag{58}$$

This means that there is no need to consider the integrals of cross-terms between the k_1-wave and k_2-wave modes.

Next, the normalization integral for the case of $k_1 = k_2 \equiv k$ can be obtained by taking the limit of $k_1 \to k_2$ in (56). Substituting $k_1 = k_2 + \delta k$ in (56), considering the Taylor expansion with respect to k, and retaining only the term of $O(\delta k)$, the desired result for the normalization integral can be derived and expressed in the form

$$\begin{aligned}
\mathcal{F} &\equiv \frac{2k}{\gamma} \int_0^h w(z) \bigl\{ Z(k;z) \bigr\}^2 dz \\
&= \frac{K}{k} \Bigl[\bigl\{ Z^{(1)} \bigr\}^2 \Bigr]_{z=0} + \frac{kh}{\gamma} \Bigl[\bigl\{ Z^{(2)} \bigr\}^2 \Bigr]_{z=h} \\
&\quad + \varepsilon\, kh_1 \Biggl[\bigl\{ Z^{(1)} \bigr\}^2 + \frac{1}{\gamma} \Bigl(1 + \frac{1}{Kh_1} - \varepsilon \frac{k^2}{K^2} \Bigr) \bigl\{ Z^{(1)\prime} \bigr\}^2 + 2\, \frac{k}{K} Z^{(1)} Z^{(1)\prime} \Biggr]_{z=h_1} \\
&= \frac{K}{k} + kh \frac{(K \operatorname{ch} kh_1 - k \operatorname{sh} kh_1)^2}{\gamma\, k^2 \operatorname{sh}^2 kh_2} \\
&\quad + \frac{\varepsilon}{\gamma} \frac{h_1}{k} \Biggl[\Bigl(1 - \frac{k^2}{K^2} + \frac{1}{Kh_1} \Bigr) \bigl(K \operatorname{ch} kh_1 - k \operatorname{sh} kh_1 \bigr)^2 + \gamma \frac{(K^2 - k^2)^2}{K^2} \operatorname{sh}^2 kh_1 \Biggr].
\end{aligned} \tag{59}$$

Wave Drift Forces and Moments on Two Ships Arranged Side by Side in Waves*

Masashi KASHIWAGI†, Kazuaki ENDO† and Hiroshi YAMAGUCHI‡

† Research Institute for Applied Mechanics, Kyushu University
Kasuga, Fukuoka 816-8580, Japan

‡ Akishima Laboratories (Mitsui Zosen), Inc.,
Tsutsujigaoka, Akishima, Tokyo 196-0012, Japan

Abstract

Hydrodynamic interactions are studied between two floating bodies situated side by side and closely as a model of LNG-FPSO system. Main interest is placed on the wave drift forces and moments which are of second order in the wave amplitude and can be computed from quadratic products of the first-order quantities. To solve the first-order radiation and diffraction problems with hydrodynamic interactions taken into account, a higher-order boundary-element method is applied directly to the whole wetted surface of two ships. The second-order wave drift forces on each ship are computed by the near-field method based on the pressure integration, and validity is confirmed by comparing the sum of the forces on each ship with the corresponding value computed by the far-field method. Experiments are also conducted in beam waves for the side-by-side arrangement of a modified Wigley model and a rectangular barge model. Measured results are in favorable agreement with computed results not only for the first-order hydrodynamic forces but also for the second-order steady forces in sway and heave.

Keywords: Hydrodynamic interaction, wave drift force, side-by-side mooring, FPSO, higher-order boundary element method, near-field method, far-field method.

1. Introduction

Since the energy problem is becoming more and more important in a global scale, development of the natural gas in remote offshore locations is drawing attention and put into practice. For transportation, the natural gas must be converted into Liquefied Natural Gas (LNG) at an offshore or onshore plant and shipped by a LNG carrier to customers.

To economically produce and process gas in remote offshore locations, an exploitation system of Floating Production Storage and Offloading (LNG-FPSO) is considered and its performance in a severe natural environment has been studied (e.g. Huijsmans *et al.*, 2001; Buchner *et al.*, 2001; Choi and Hong, 2002). When LNG in storage tanks is offloaded to a LNG carrier, the LNG carrier is usually moored side by side to the FPSO due to relatively easy operation of offloading. However, when two floating bodies are situated side by side with relatively small gap, hydrodynamic interactions between two bodies are expected to be large and complex, which must be taken into account in the design of a mooring system. Owing to hydrodynamic interactions, two ships may collide and large repulsion and drift forces

* *Reprinted from Journal of Ocean Engineering, Vol. 32, pp. 529–555, 2005 (January)*

may be exerted, resulting in damage of the mooring system. To evaluate hydrodynamic-interaction effects on oscillatory and steady forces, accurate numerical computations must be performed not only for hydrodynamic forces and wave-induced motions of the first order in the incident-wave amplitude but also for time-averaged steady forces of the second order. The latter steady forces are called the wave drift forces and can be computed only from quadratic products of the first-order quantities.

It is well known that two different methods are available for computing the wave drift forces: the near-field method based on the direct pressure integration and the far-field method based on the momentum-conservation principle. The near-field method (e.g. Ogilvie, 1983) gives individual forces on each ship but computations are rather complicated because various components must be evaluated, such as the flow velocity on the wetted surface of a ship and the relative wave height along the waterline of a ship. On the other hand, the far-field method (Maruo, 1960; Newman, 1967) is relatively easy to compute but gives only the total force on all ships that are included by a fictitious vertical circular cylinder located far from the ships. Since the prediction of the steady forces on each ship is prerequisite in the present study, the near-field method must be used. To keep good numerical accuracy, the present study adopts a higher-order boundary element method (HOBEM), by which the velocity potential (pressure) on the ship's wetted surface can be obtained directly and spatial derivatives of the velocity potential can be evaluated without numerical differentiation.

Recently, Fang and Chen (2002) proposed a practical far-field method for computing the wave drift forces on each ship separately by considering a control surface surrounding only either ship. However, their analysis is not correct mathematically, as demonstrated in the present paper, and a corrected 'new' method is described. It is shown that the new method gives the same results as those by the near-field method and by the conventional far-field method, if no overlap region exists between fictitious vertical circular cylinders taken as a control surface for the principle of momentum conservation.

Validation of the results is confirmed not only by numerical computations but also by experiments conducted using a modified Wigley model and a rectangular barge model arranged side by side. Measured are the added-mass and damping coefficients by the forced heave oscillation of either of the two models, the first-order wave-exciting forces, and the second-order steady forces on each model when both models are completely fixed in beam waves. Among these, attention is mainly placed on the second-order steady forces in the present paper. Relatively good agreement is found between computed and measured results, and thus the calculation method developed may be applied to actual ships of general geometry.

2. Formulation and Solution Method

We consider two ships which are located in close proximity and oscillate sinusoidally in a plane progressive wave. The geometries of two ships can be arbitrary. The position and bow direction of each ship may also be arbitrary, but for simplicity and engineering importance, it is assumed that two ships are arranged side by side and the bow direction of each ship is the same.

To linearize the boundary-value problem, the incident wave and resultant ship motions are assumed to be of small amplitude. For the analysis of this problem, as shown in Fig. 1, we use not only the global coordinate system o-xyz fixed in space but also the local coordinate system o_k-$x_k y_k z_k$ (where $k = A$ or B) fixed with respect to the mean position of each ship. The origin of each coordinate system is placed on the undisturbed free surface, the x-axis is positive in the direction of ship's bow, and the z-axis is positive vertically downward. Since the ships are considered symmetric with respect to their longitudinal centerplane, the center of gravity is assumed to be at $\boldsymbol{x}_G = (x_{Gk}, 0, z_{Gk})$. Not only the Cartesian coordinate system o-xyz but also the cylindrical coordinate system o-$r\theta z$ will be used, the relations of which are $x = r\cos\theta$ and $y = r\sin\theta$.

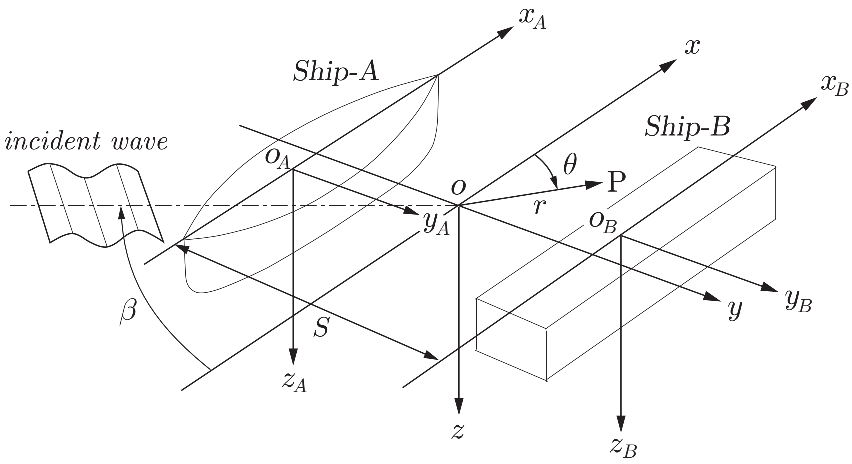

Fig. 1 Coordinate systems and notations

Assuming the incompressible and inviscid flow with irrotational motion, the velocity potential is introduced. Based on the perturbation method, the linearized boundary-value problem (which is of first order in the wave amplitude) must be solved first, and then the wave drift forces and moments (which are of second order in the wave amplitude) can be computed only from quadratic products of the first-order quantities.

In the first-order problem, all unsteady motions are assumed to be sinusoidal in time with circular frequency ω, and by linear decomposition the velocity potential is expressed in the form

$$\Phi(x,y,z;t) = \mathrm{Re}\left[\frac{g\zeta_w}{i\omega}\,\varphi(P)\,e^{i\omega t}\right], \tag{1}$$

$$\varphi(P) = \varphi_D(P) - \frac{\omega^2}{g}\,a\sum_{j=1}^{6}\sum_{\ell=A}^{B}\frac{\xi_{j\ell}\epsilon_j}{\zeta_w}\,\varphi_{j\ell}(P), \tag{2}$$

where

$$\varphi_D(P) = \varphi_I(P) + \varphi_S(P), \tag{3}$$

$$\varphi_I(P) = Z_0(z)e^{-ik_0(x\cos\beta + y\sin\beta)}, \tag{4}$$

$$Z_0(z) = \frac{\cosh k_0(z-h)}{\cosh k_0 h}, \quad \frac{\omega^2}{g} = k_0\tanh k_0 h\,. \tag{5}$$

Here Re in (1) means the real part to be taken; g is the gravitational acceleration; ζ_w is the amplitude of incident wave; $P = (x,y,z)$ denotes a field point in the fluid; a is the characteristic length scale for nondimension (which is taken as half of the ship's length); j

is the mode number of six degrees of freedom in the radiation problem and the suffix $\ell = A$ or B denotes the number of ships; $\epsilon_j = 1$ for $j = 1 \sim 3$ (translational motions) and $\epsilon_j = a$ for $j = 4 \sim 6$ (rotational motions); $\xi_{j\ell}$ is the complex amplitude of the jth mode of motion of the ℓth ship; h is the water depth which is assumed finite and constant.

The diffraction potential φ_D is defined as the sum of the incident-wave potential φ_I plus the scattering potential φ_S. β is the angle of incidence of a plane progressive wave relative to the positive x-axis, with $\beta = 180°$ defined as the head wave.

In what follows, unless otherwise explicitly specified, it should be understood that all physical quantities are written in nondimension. As an example, the total velocity potential $\varphi(P)$ defined by (2) can be written as follows:

$$\varphi(P) = \varphi_I(P) + \psi(P), \tag{6}$$

$$\psi(P) = \varphi_S(P) - K \sum_{j=1}^{6} \sum_{\ell=A}^{B} X_{j\ell}\, \varphi_{j\ell}(P), \tag{7}$$

where

$$X_{j\ell} = \frac{\xi_{j\ell}\, \epsilon_j}{\zeta_w} \tag{8}$$

is the nondimensional amplitude of the jth mode of ship motion, and K is also made nondimensional, equal to $\omega^2 a/g$. It is noteworthy that $\psi(P)$ defined by (7) stands for the disturbance potential due to the presence of ships in an incident wave.

The governing equation and linearized boundary conditions to be satisfied by the diffraction and radiation potentials, $\varphi_m(P)$ ($m = D$ or $j\ell$), are summarized as follows:

$$[L] \qquad \nabla^2 \varphi_m = 0 \qquad \text{for } z \leq 0, \tag{9}$$

$$[F] \qquad \frac{\partial \varphi_m}{\partial z} + K\, \varphi_m = 0 \qquad \text{at } z = 0, \tag{10}$$

$$[B] \qquad \frac{\partial \varphi_m}{\partial z} = 0 \qquad \text{at } z = h, \tag{11}$$

$$[H] \quad \begin{cases} \dfrac{\partial \varphi_D}{\partial n} = 0 \\[2mm] \dfrac{\partial \varphi_{j\ell}}{\partial n} = n_{jk}\, \delta_{k\ell} \qquad \left(\begin{array}{l} j = 1 \sim 6 \\ k,\, \ell = A \,\text{or}\, B \end{array} \right). \end{cases} \tag{12}$$

Here n_{jk} is the jth component of the normal vector on the kth ship and $\delta_{k\ell}$ denotes Kronecker's delta. The normal vector $\boldsymbol{n}$ is defined as positive when directing into the fluid from the boundary surface, n_j for $j = 1 \sim 3$ denotes the components of $\boldsymbol{n}$, and n_j for $j = 4 \sim 6$ is defined as the components of $(\boldsymbol{x} - \boldsymbol{x}_G) \times \boldsymbol{n}$. The incident-wave potential is explicitly given by (4), but the other disturbance potentials must be sought to satisfy the above equations and the radiation condition of generated waves radiating away from a ship.

To solve the above first-order boundary-value problem, the present study adopts the direct boundary element method using the free-surface Green function $G(P;Q)$. This method solves the integral equations for the diffraction and radiation velocity potentials on the wetted surface of two ships directly, which are written as

$$C(P)\,\varphi_m(P) + \sum_{k=A}^{B} \iint_{S_k} \varphi_m(Q) \frac{\partial}{\partial n_Q} G(P;Q)\, dS$$

$$= \begin{cases} \varphi_I(P) & \text{for } m = D \\ \displaystyle\sum_{k=A}^{B} \iint_{S_k} \frac{\partial \varphi_m(Q)}{\partial n_Q} G(P;Q)\, dS & \text{for } m = j\ell \end{cases} \tag{13}$$

where $P = (x, y, z)$ is the field point, $Q = (x', y', z')$ is the source point on the body surface, and $C(P)$ is the solid angle which can be computed numerically by considering the case of zero normal velocity (equi-potential) on all boundary surfaces.

The free-surface Green function $G(P;Q)$, satisfying all of the linearized homogeneous boundary conditions, has been well studied and various expressions are known. In the present study, Seto's calculation method (Seto, 1993) for the case of finite water depth is employed, which combines both expressions of the contour integral and the power series. For a subsequent purpose, only the power-series expression is given below:

$$G(P;Q) = \frac{1}{\pi} \sum_{n=1}^{\infty} C_n\, Z_n(z)\, Z_n(z')\, K_0(k_n R) + \frac{i}{2}\, C_0\, Z_0(z)\, Z_0(z')\, H_0^{(2)}(k_0 R), \tag{14}$$

where

$$C_0 = \frac{k_0^2}{K + (k_0^2 - K^2)h}, \quad C_n = \frac{k_n^2}{K - (k_n^2 + K^2)h}, \tag{15}$$

$$Z_n(z) = \frac{\cos k_n(z-h)}{\cos k_n h}, \quad K = -k_n \tan k_n h, \tag{16}$$

$$\left.\begin{aligned} &R = \sqrt{(x-x')^2 + (y-y')^2} = \sqrt{r^2 + r'^2 - 2rr'\cos(\theta - \theta')} \\ &x + iy = r\, e^{i\theta}, \quad x' + iy' = r'\, e^{i\theta'} \end{aligned}\right\} \tag{17}$$

Here $K_0(k_n R)$ and $H_0^{(2)}(k_0 R)$ in (14) denote the second kind of modified Bessel function and the second kind of Hankel function, respectively, which are associated with the evanescent and progressive waves respectively.

It should be noted that, within the framework of linear potential theory, hydrodynamic interactions are taken into account exactly in the numerical solutions to be obtained from (13).

3. Linear Pressure Forces and Ship Motions

Once the velocity potentials on the body surface are obtained, it is straightforward to compute the first-order hydrodynamic forces. The linearized unsteady pressure on the body surface can be computed directly from the velocity potentials obtained. Integrating this pressure multiplied by the ith component of the normal vector over the kth ship, the hydrodynamic forces acting in the ith direction of the kth ship can be computed. Likewise the restoring forces can be computed from the change of hydrostatic pressure due to the displacement of a ship from its equilibrium position. These results may be expressed in the form

$$F_i^k = E_i^k + K \sum_{j=1}^{6} \sum_{\ell=A}^{B} X_{j\ell}\, \mathcal{F}_{ij}^{k\ell} - \sum_{j=1}^{6} X_{j\ell}\, C_{ij}^k, \tag{18}$$

where

$$E_i^k = \iint_{S_k} \varphi_D \, n_{ik} \, dS, \tag{19}$$

$$\mathcal{F}_{ij}^{k\ell} = A_{ij}^{k\ell} - i\, B_{ij}^{k\ell} = -\iint_{S_k} \varphi_{j\ell} \, n_{ik} \, dS. \tag{20}$$

Here E_i^k is the wave-exciting force in the ith mode of motion of the kth ship, and $A_{ij}^{k\ell}$ and $B_{ij}^{k\ell}$ are the added-mass and damping coefficients respectively in the ith direction of the kth ship due to the jth mode of motion of the ℓth ship. C_{ij}^k in (18) denotes the restoring-force coefficients, which are free from hydrodynamic interactions between two ships and thus almost zero except for C_{jj}^k $(j = 3, 4, 5)$ and $C_{35}^k = -C_{53}^k$.

Denoting the generalized mass matrix of the kth ship with M_{ij}^k and using (18) for the hydrodynamic and hydrostatic forces on the kth ship, the coupled motion equations of two ships are written in the form

$$\sum_{j=1}^{6} \left[X_{jk} \left\{ -K M_{ij}^k \delta_{ij} + C_{ij}^k \right\} - K \sum_{\ell=A}^{B} X_{j\ell} \, \mathcal{F}_{ij}^{k\ell} \right] = E_i^k \tag{21}$$

for $k = A,\, B$; $i = 1 \sim 6$. The complex motion amplitude X_{jk} can be determined by solving these coupled equations; thereby the first-order solution will be completed.

4. Velocity Potentials at Far Field

For computing the wave drift forces by the far-field method, we must obtain the asymptotic expression of the disturbance potential in an analytic form, which is valid at large distances from each ship or both ships.

For this analysis, in addition to the local Cartesian coordinates (x_k, y_k, z), the local cylindrical coordinates (r_k, θ_k, z) are used. The origin of the local coordinate system with respect to the kth ship is located at $(x_{ok}, y_{ok}, 0)$ in the global coordinate system, and thus the relation between the local and global coordinates is given by $(x_k, y_k, z) = (x - x_{ok}, y - y_{ok}, z)$. Therefore, with Graf's addition theorem for Bessel functions, the Hankel function appearing in (14) as the progressive wave term of the free-surface Green function can be written as

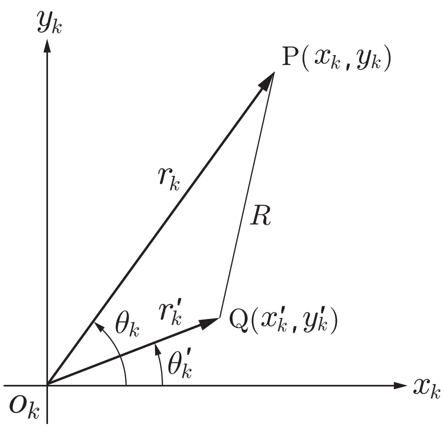

Fig. 2 Field and source points in the local coordinate system

$$H_0^{(2)}(k_0 R) = \sum_{m=-\infty}^{\infty} J_m(k_0 r'_k) \, H_m^{(2)}(k_0 r_k) \, e^{-im(\theta_k - \theta'_k)}, \tag{22}$$

where (r'_k, θ'_k, z') is the source point on the surface of the kth ship, and $r_k > r'_k$ is required for (22) being valid (see Fig. 2).

When $P = (r_k, \theta_k, z)$ is located in the fluid region, the solid angle in (13) must be taken equal to $C(P) = 1$. At a distance from the source of disturbance, the evanescent-wave term,

$K_0(k_n R)$ in (14), will be negligibly small. Taking these into account, substituting (22) in the Green function, and considering the body boundary condition (12) for the diffraction problem, the asymptotic expression of the disturbance potential $\psi(P)$ may be obtained in the form

$$\psi(P) = \varphi(P) - \varphi_I(P) = \sum_{k=A}^{B} \psi^k(P), \tag{23}$$

$$\begin{aligned} \psi^k(P) &= \iint_{S_k} \left\{ \frac{\partial \varphi(Q)}{\partial n_Q} - \varphi(Q) \frac{\partial}{\partial n_Q} \right\} G(P;Q)\, dS \\ &\simeq \sum_{m=-\infty}^{\infty} \mathcal{A}_m^k \, Z_0(z)\, H_m^{(2)}(k_0 r_k)\, e^{-im\theta_k} \quad \text{as } r_k \to \infty, \end{aligned} \tag{24}$$

where the coefficient $\mathcal{A}_m^k$ is related to the amplitude of progressive waves generated by the disturbance of the kth ship, which is given by

$$\mathcal{A}_m^k = \frac{i}{2} C_0 \iint_{S_k} \left\{ \frac{\partial \varphi}{\partial n} - \varphi \frac{\partial}{\partial n} \right\} Z_0(z)\, J_m(k_0 r_k)\, e^{im\theta_k}\, dS. \tag{25}$$

We note that k is taken as A or B and that (24) is valid outside of a fictitious vertical circular cylinder encompassing only the kth ship.

Furthermore, with Graf's addition theorem, the Hankel function $H_m^{(2)}(k_0 r_k)$ in (24) can be expressed with the global cylindrical coordinates (r, θ, z). Referring to Fig. 3 and considering the case of $r > L_{ko}$, the following relation holds:

$$H_m^{(2)}(k_0 r_k)\, e^{-im\theta_k} = \sum_{n=-\infty}^{\infty} J_{m-n}(k_0 L_{ko})\, e^{-i(m-n)\alpha_{ko}} \left\{ H_n^{(2)}(k_0 r)\, e^{-in\theta} \right\}, \tag{26}$$

where L_{ko} and α_{ko} are defined in Fig. 3.

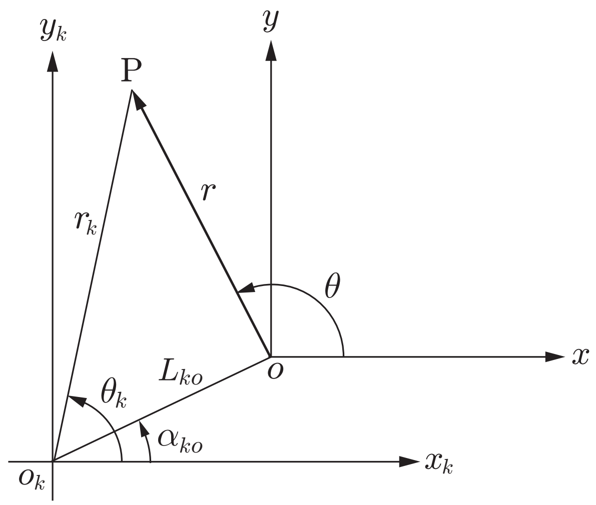

Fig. 3 Relation between the global and local coordinate systems

Substituting (26) in (24) and interchanging the symbols m and n for the order of Bessel functions, the disturbance potential $\psi(P)$ can be expressed in the global coordinate system as follows:

$$\psi(P) = \psi^A(P) + \psi^B(P) \simeq \sum_{m=-\infty}^{\infty} \mathcal{A}_m\, Z_0(z)\, H_m^{(2)}(k_0 r)\, e^{-im\theta} \quad \text{as } r \to \infty, \tag{27}$$

where

$$\mathcal{A}_m = \sum_{\ell=A}^{B} \sum_{n=-\infty}^{\infty} \mathcal{A}_n^{\ell}\, J_{n-m}(k_0 L_{\ell o})\, e^{-i(n-m)\alpha_{\ell o}}. \tag{28}$$

This asymptotic expression (27) is valid at a far field outside of a fictitious vertical circular cylinder encompassing both ships A and B.

Let us rewrite the incident-wave potential (4) with the cylindrical coordinate system. In the global coordinate system, the result can be expressed as

$$\varphi_I(P) = \sum_{m=-\infty}^{\infty} \alpha_m\, Z_0(z)\, J_m(k_0 r)\, e^{-im\theta}, \tag{29}$$

where

$$\alpha_m = e^{im(\beta-\pi/2)}. \tag{30}$$

In the local coordinate system with the origin in the kth ship, the result can be expressed as

$$\varphi_I^k(P) = \sum_{m=-\infty}^{\infty} \alpha_m^k\, Z_0(z)\, J_m(k_0 r_k)\, e^{-im\theta_k}, \tag{31}$$

where

$$\alpha_m^k = \alpha_m\, e^{-ik_0(x_{ok}\cos\beta + y_{ok}\sin\beta)}. \tag{32}$$

For computing the wave drift force on each ship by the far-field method, the disturbance potential must be described with the local coordinates of a ship to be considered. That is,

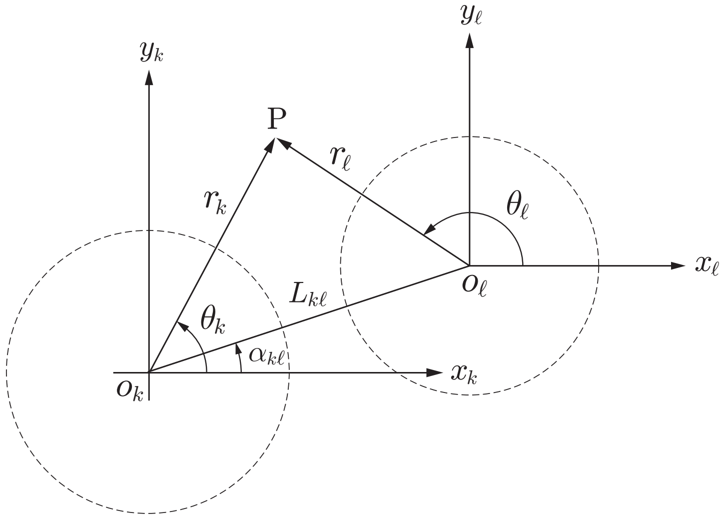

Fig. 4 Relation between local coordinate systems with respect to the kth ship and ℓth ship

the disturbance potential by Ship-A, $\psi^A(P)$, must be expressed with the local coordinates of Ship-B, and vice versa.

Referring to Fig. 4, we consider the disturbance potential by the k-th ship, given by (24), in terms of the local coordinates of the ℓ-th ship; which can be achieved by applying Graf's addition theorem for the Hankel function. For the case of $L_{k\ell} > r_\ell$, the following relation holds:

$$H_m^{(2)}(k_0 r_k)\, e^{-im\theta_k} = \sum_{n=-\infty}^{\infty} H_{m-n}^{(2)}(k_0 L_{k\ell})\, e^{-i(m-n)\alpha_{k\ell}} \Big\{ J_n(k_0 r_\ell)\, e^{-in\theta_\ell} \Big\}, \tag{33}$$

where $L_{k\ell}$ and $\alpha_{k\ell}$ are defined in Fig. 4.

In the same manner as in obtaining (27) and (28), we may obtain an expression of the disturbance potential by the kth ship expressed with the local coordinate system of the ℓth ship. The result takes the form

$$\psi^{k\ell}(P) = \sum_{m=-\infty}^{\infty} \mathcal{A}_m^{k\ell}\, Z_0(z)\, J_m(k_0 r_\ell)\, e^{-im\theta_\ell}, \tag{34}$$

where

$$\mathcal{A}_m^{k\ell} = \sum_{n=-\infty}^{\infty} \mathcal{A}_n^{k}\, H_{n-m}^{(2)}(k_0 L_{k\ell})\, e^{-i(n-m)\alpha_{k\ell}}. \tag{35}$$

As is obvious from (29), $\psi^{k\ell}(P)$ given by (34) can be regarded as a progressive wave incident on the ℓth ship. Therefore the total incident-wave potential on the ℓth ship must be written as

$$\psi_I^{\ell}(P) = \varphi_I^{\ell}(P) + \psi^{k\ell}(P) = \sum_{m=-\infty}^{\infty} \left\{ \alpha_m^{\ell} + \mathcal{A}_m^{k\ell} \right\} Z_0(z)\, J_m(k_0 r_\ell)\, e^{-im\theta_\ell}. \tag{36}$$

Likewise, in the local coordinate system of the kth ship, the disturbance by the ℓth ship may be viewed as an incident wave, and thus the total incident-wave potential on the kth ship must be written as

$$\psi_I^{k}(P) = \varphi_I^{k}(P) + \psi^{\ell k}(P) = \sum_{m=-\infty}^{\infty} \left\{ \alpha_m^{k} + \mathcal{A}_m^{\ell k} \right\} Z_0(z)\, J_m(k_0 r_k)\, e^{-im\theta_k}. \tag{37}$$

To summarize the above, since the velocity potential is given as the sum of the incident-wave and disturbance potentials, the far-field asymptotic expression of the velocity potential can be given in the following form:

$$\varphi(P) = \sum_{m=-\infty}^{\infty} \Big\{ \alpha_m J_m(k_0 r) + \mathcal{A}_m H_m^{(2)}(k_0 r) \Big\} Z_0(z)\, e^{-im\theta}. \tag{38}$$

When considering with the global coordinate system, α_m and $\mathcal{A}_m$ are given by (30) and (28) respectively, and (38) is valid outside of a fictitious vertical circular cylinder encompassing both ships. On the other hand, when considering in a field outside of a fictitious vertical circular cylinder encompassing only the kth ship, α_m in (38) must be $\alpha_m^k + \mathcal{A}_m^{\ell k}$ shown in (37) and $\mathcal{A}_m$ in (38) must be $\mathcal{A}_m^k$ shown in (24). (Of course (r,θ) in (38) must be replaced by (r_k, θ_k) of the kth local coordinates.) It should be stressed that the contributions of $\mathcal{A}_m^{\ell k}$ and $\mathcal{A}_m^{k\ell}$ are entirely neglected in the method of Fang and Chen (2002) for computing the wave drift force and moment on each ship by a practical far-field method.

5. Calculation of Wave Drift Forces

5.1 Far-field method

With the far-field asymptotic representation of (38) for the velocity potential, the calculation formulae for the time-averaged wave drift forces were provided by Kashiwagi and Yoshida (2001), the analyses of which were based on the far-field method, i.e. the principle of linear and angular momenta conservation, initiated by Maruo (1960) and Newman (1967).

Performing the same analytical integrations as in Kashiwagi and Yoshida with respect to z and θ at a certain large distance of r, the calculation formulae for the wave drift forces $(\overline{F}_x - i\overline{F}_y)$ in the horizontal plane and the drift yaw moment $(\overline{M}_z)$ about the vertical axis can be obtained as follows:

$$\frac{\overline{F}_x - i\,\overline{F}_y}{\frac{1}{2}\,\rho g \zeta_w^2\, a} = \frac{i\,k_0}{C_0 K} \sum_{m=-\infty}^{\infty} \Big[\, 2\,\mathcal{A}_m\,\mathcal{A}_{m+1}^* + \alpha_m\,\mathcal{A}_{m+1}^* + \alpha_{m+1}^*\,\mathcal{A}_m \Big], \tag{39}$$

$$\frac{\overline{M}_z}{\frac{1}{2}\,\rho g \zeta_w^2\, a^2} = -\,\frac{2}{C_0 K} \sum_{m=-\infty}^{\infty} m \Big[\, |\mathcal{A}_m|^2 + \mathrm{Re}\big(\alpha_m\,\mathcal{A}_m^*\big) \Big], \tag{40}$$

where the asterisk in the superscript stands for the complex conjugate.

These formulae are for the total wave drift forces and moment on both ships, because we used (38) expressed with the global coordinates valid at a large distance of r encompassing both ships. It should be noted that essentially the same analyses can be done on a control surface encompassing only the kth ship in terms of the local cylindrical coordinates of the kth ship, which gives the wave drift forces and moment acting on only the kth ship. The resultant calculation formulae are of the same form as (39) and (40), except that α_m and $\mathcal{A}_m$ must be replaced by $\alpha_m^k + \mathcal{A}_m^{\ell k}$ and $\mathcal{A}_m^k$, respectively, as noted at the end of the preceding section. We will provide in this paper the results based on the idea of Fang and Chen, which are obtained by neglecting $\mathcal{A}_m^{\ell k}$ (or $\mathcal{A}_m^{k\ell}$) in the coefficients of the total incident wave on the kth (or ℓth) ship.

As a check of numerical accuracy, satisfaction of the energy-conservation principle may be confirmed. The analysis of this energy conservation in the whole domain of fluid is similar to that for $\overline{M}_z$ and the result takes the form

$$\sum_{m=-\infty}^{\infty} \Big[\, \big|\mathcal{A}_m\big|^2 + \mathrm{Re}\big(\alpha_m\,\mathcal{A}_m^*\big) \Big] = 0. \tag{41}$$

5.2 Near-field method

The wave drift forces can also be computed as the second-order steady forces by integrating the pressure on the wetted surface of a ship concerned, which is the so-called near-field method. Derivation of the calculation equation based on the near-field method is somewhat lengthy. Referring to an established second-order theory using consistent perturbation scheme (e.g. Kashiwagi (2002) and the references therein), the time-averaged second-order steady force in the ith direction ($i = 1 \sim 3$) of the mth ship ($m = A$ or B) can be computed by

$$\begin{aligned}\frac{\overline{F}_i^m}{\frac{1}{2}\rho g\zeta_w^2 a} &= \frac{1}{2K}\iint_{S_m}\left|\nabla\varphi\right|^2 n_i\,dS \\ &\quad -\frac{1}{2}\oint_{C_m}\left|\varphi-\Big\{X_3+X_4\,y-X_5(x-x_G)\Big\}\right|^2\frac{n_i}{\sqrt{1-n_3^2}}\,d\ell \\ &\quad +\mathrm{Re}\iint_{S_m}\Big\{X_j+\varepsilon_{jk\ell}\,X_{k+3}(x_\ell-x_{\ell G})\Big\}\frac{\partial\varphi^*}{\partial x_j}\,n_i\,dS \\ &\quad -KM\,\mathrm{Re}\Big[\varepsilon_{ijk}\,X_{j+3}\,X_k^*\Big]-A_W\,\mathrm{Re}\Big[X_6\,X_4^*(x_F-x_G)\Big]\,\delta_{i3}\,, \end{aligned} \tag{42}$$

where x_ℓ $(\ell = 1,2,3)$ is used to mean (x,y,z); ε_{ijk} is the alternating tensor; M and A_W are the nondimensional mass and water-plane area of the mth ship respectively; and x_F and x_G are the x-ordinates of the centers of floatation and gravity respectively. The integration path of the line integral C_m is to be taken along the water line at $z = 0$, which is associated with the relative wave height along the intersection between the body and free surfaces.

Similarly, the time-averaged second-order steady moment about the ith axis of the mth ship can be computed by the following:

$$\begin{aligned}\frac{\overline{M}_i^m}{\frac{1}{2}\rho g\zeta_w^2 a^2} &= \frac{1}{2K}\iint_{S_m}\left|\nabla\varphi\right|^2 n_{i+3}\,dS \\ &\quad -\frac{1}{2}\oint_{C_m}\left|\varphi-\Big\{X_3+X_4\,y-X_5(x-x_G)\Big\}\right|^2\frac{n_{i+3}}{\sqrt{1-n_3^2}}\,d\ell \\ &\quad +\mathrm{Re}\iint_{S_m}\Big\{X_j+\varepsilon_{jk\ell}\,X_{k+3}(x_\ell-x_{\ell G})\Big\}\frac{\partial\varphi^*}{\partial x_j}\,n_{i+3}\,dS \\ &\quad -KM\,\mathrm{Re}\Big[\varepsilon_{ijk}\,X_{j+3}\,X_{k+3}^*\,\kappa_{kk}^2\Big] \\ &\quad -M\,\mathrm{Re}\Big[X_6\Big\{X_5^*\,\overline{GM}\,\delta_{i1}-X_4^*\,\overline{GM}_L\,\delta_{i2}\Big\}\Big], \end{aligned} \tag{43}$$

where n_{i+3} is defined as $n_{i+3} = \varepsilon_{ijk}(x_j - x_{jG})n_k$; κ_{kk} is the radius of gyration about the kth axis; $\overline{GM}$ and $\overline{GM}_L$ are the transverse and longitudinal metacentric heights, respectively.

With the near-field method, we can compute all of the six components of the second-order steady forces and moments on each ship. The total wave drift forces on both ships, corresponding to (39) and (40), can readily be computed by simple summation of the same force components on each ship. This kind of comparison of the results by the far-field and near-field methods may validate the numerical computation method and indicate the degree of numerical accuracy.

6. Validation of Numerical Computation

The integral equation (13) was solved by the higher-order boundary-element method (HOBEM) using 9-point representation for both the geometry of body surface and the velocity potential. The irregular frequencies are removed by considering a few additional field points on the interior free surface of both ships, for which the solid angle $C(P)$ must be zero. The resultant over-constraint simultaneous equations are solved by the least-squares method.

The HOBEM is advantageous in attaining higher accuracy with less number of panels for a solution of the first-order problem, and more importantly advantageous in computing the spatial derivatives of the velocity potential, $\nabla\varphi$, and the relative wave elevation along the body surface at $z = 0$ which are to be evaluated in the near-field method for the second-order steady forces.

To validate the numerical calculation method and to confirm the accuracy of computed results, computations were performed for two identical ellipsoids, each of which is represented by

$$x = a\cos\theta,\ \ y = b\sin\theta\cos\omega,\ \ z = c\sin\theta\sin\omega \tag{44}$$

The relative lengths of a, b and c in (44) are chosen such that $b/a = 0.15$ and $c/a = 0.125$, and both ships are exactly the same in size and geometry. The divided element angle in θ and ω in (44) are even, and their numbers of division over each ship are chosen such that $N_X = 20$ in θ and $N_Y = 16$ in ω. The number of additional field points on the interior free surface is $N_F = 9$ for each ship.

As an example of numerical results of the wave drift forces, Table 1 shows the steady force in the y-direction in an incident wave of $\lambda/L = 1.0$ and $\beta = 45°$ for the case of all modes of the ship motion being fixed. Table 2 shows the results in the same fashion for the case of all six modes of the motion of both ships being free to oscillate. In these Tables, three cases of S/L, the ratio of the separation distance between the longitudinal centerlines of each ship $S = |x_{oA} - x_{oB}|$ and the ship's length $L = 2a$, are tested. For each case, presented are the results by the far-field method, the near-field method, a 'new' method taking account of $\mathcal{A}_m^{k\ell}$ and $\mathcal{A}_m^{\ell k}$ in (36) and (37) in evaluating the incident-wave coefficients on each ship, and Fang and Chen's method ignoring $\mathcal{A}_m^{k\ell}$ and $\mathcal{A}_m^{\ell k}$. $S/L = 1.0$ corresponds to the case that circles encompassing each ship do not overlap (actually they touch just at one point), and the overlap region increases as the value of S/L decreases (which means violating a condition of justifying Graf's addition theorem shown by (33)).

Irrespective of whether the motions of ships are fixed or not, for $S/L = 1.0$, the result of

Table 1 Computed steady sway forces on two identical ellipsoids of $b/a = 0.150$ and $c/a = 0.125$ in incident wave of $\lambda/L = 1.0$ and $\beta = 45°$, when body motions are completely fixed (diffraction problem)

	Far-field	Near-field	New method	Fang and Chen
For $S/L = 1.00$				
$\overline{F}_y$ on Ship-A		0.02743	0.02736	0.27954
$\overline{F}_y$ on Ship-B		0.43381	0.43341	0.42276
Summation	0.46077	0.46124	0.46077	0.70230
For $S/L = 0.75$				
$\overline{F}_y$ on Ship-A		0.58339	0.59374	0.43417
$\overline{F}_y$ on Ship-B		0.30401	0.33292	0.36571
Summation	0.88668	0.88740	0.92666	0.79988
For $S/L = 0.50$				
$\overline{F}_y$ on Ship-A		0.14506	-0.3073×10^4	0.21433
$\overline{F}_y$ on Ship-B		0.27723	0.8826×10^4	0.32735
Summation	0.42194	0.42229	0.5753×10^4	0.54168

Table 2 Computed steady sway forces on two identical ellipsoids of $b/a = 0.150$ and $c/a = 0.125$ in incident wave of $\lambda/L = 1.0$ and $\beta = 45°$, when all modes of motion of two bodies are free to oscillate

	Far-field	Near-field	New method	Fang and Chen
For $S/L = 1.00$				
$\overline{F}_y$ on Ship-A		0.01967	0.01966	0.01972
$\overline{F}_y$ on Ship-B		0.01653	0.01653	0.01821
Summation	0.03619	0.03620	0.03619	0.03794
For $S/L = 0.75$				
$\overline{F}_y$ on Ship-A		0.02175	0.02184	0.01807
$\overline{F}_y$ on Ship-B		0.01571	0.00357	0.01793
Summation	0.03749	0.03746	0.02541	0.03600
For $S/L = 0.50$				
$\overline{F}_y$ on Ship-A		0.00338	0.8715×10^3	0.01116
$\overline{F}_y$ on Ship-B		0.01324	0.3982×10^4	0.01728
Summation	0.01658	0.01662	-0.3111×10^4	0.02845

the total sway force by the new method is identical to that by the far-field method, and also virtually the same as that by the near-field method. Furthermore, the forces on each ship predicted by the near-field and new methods are in good agreement, which demonstrates validity and good accuracy of the present numerical computations. On the other hand, the results by Fang and Chen's method are similar in the order but not correct, which means that the radiated waves from the other ship must be taken into account as a part of the incident wave. (We note that the disturbance potential around each ship is determined exactly by taking account of hydrodynamic interactions between two ships.)

From the results for $S/L = 0.75$ and $S/L = 0.5$, it can be seen that the near-field method gives reasonable results irrespective of the separation distance, whereas the results by the new method tend to diverge as the separation distance decreases. The results by Fang and Chen do not diverge even for a narrow separation distance, because Graf's addition theorem of (33) is not used. However, the results are not correct although the order and variation tendency of the results are rather similar to the ones by the near-field method.

Needless to say, satisfaction of the energy conservation (41) by the far-field method is very good, with the order of absolute error less than 10^{-4} with $M = 31$ terms ($m = -15 \sim +15$) in the Fourier series in the azimuth direction.

7. Experiments

Experiments were carried out for the side-by-side arrangement of a modified Wigley model (which will be referred to as Ship-A) and a rectangular barge model (which will be referred to as Ship-B) at the experimental tank (its length, width, and depth are 65 m, 5 m and 7 m respectively) of the Research Institute for Applied Mechanics of Kyushu University. The modified Wigley model used in experiments is expressed mathematically as

$$\left.\begin{aligned} \eta &= (1-\xi^2)(1-\zeta^2)(1+0.2\xi^2) + \zeta^2(1-\zeta^8)(1-\xi^2)^4 \\ \xi &= 2x/L,\ \eta = 2y/B,\ \zeta = z/d \end{aligned}\right\} \tag{45}$$

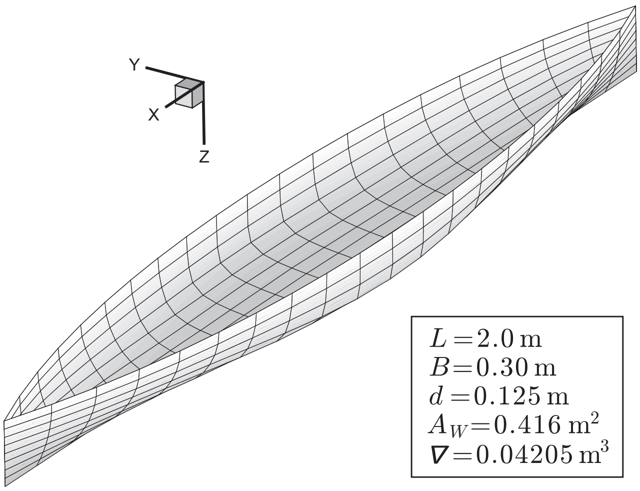

Fig. 5 Perspective view and principal dimensions of a modified Wigley model (referred to as Ship-A)

Both models are $L = 2.0\,\mathrm{m}$ in length, $B = 0.3\,\mathrm{m}$ in breadth, and $d = 0.125\,\mathrm{m}$ in draft. The 3-D perspective view and principal dimensions are shown in Fig. 5 for Ship-A and in Fig. 6 for Ship-B, which also show the panels used for numerical computations. Both ships were set in the beam-wave condition ($\beta = 90°$) with the separation distance between the longitudinal centerlines of each ship set equal to $S = 1.097\,\mathrm{m}$ and $S = 1.797\,\mathrm{m}$.

The experiment conducted first is the forced heave oscillation tests, with Ship-A oscillated and Ship-B fixed, and vice versa. The second experiment is the measurement of the first-order wave-exciting forces and the second-order steady forces in plane progressive waves with both ships completely fixed, corresponding to the diffraction problem. For each of the two separation distances, measurements were carried out for both arrangements of ships; namely, with Ship-A in the upwave side and Ship-B in the downwave side, and vice versa. Therefore,

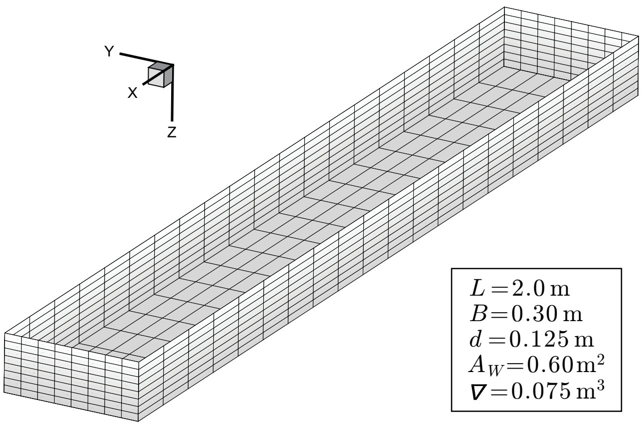

Fig. 6 Perspective view and principal dimensions of a rectangular barge model (referred to as Ship-B)

there were four cases for each of the radiation- and diffraction-problem experiments, among which some typical results will be presented in the next section.

8. Comparison between Experiments and Calculations

8.1 Added-mass and damping coefficients

To demonstrate capability of the HOBEM adopted in the present study, the results are shown for the case of Ship-A forcedly oscillated in heave and Ship-B fixed with separation distance $S = 1.797\,\mathrm{m}$. Fig. 7 shows only four coefficients of the forces acting on Ship-A. Nondimension in Fig. 7 is made using the mass of Ship-A ($\rho\nabla^A$) for the added-mass coefficient and the product of the mass of Ship-A and oscillation frequency ($\rho\nabla^A\omega$) for the damping coefficient. For all cases shown in Fig. 7, hydrodynamic interactions are properly accounted for; especially we note that the sway-force coefficients (A_{23}^{AA} and B_{23}^{AA}) are exerted only by wave interactions between Ship-A and Ship-B. Some discrepancies can be seen in the heave-force coefficients (A_{33}^{AA} and B_{33}^{AA}) at low frequencies, which may be attributed to the effect of reflection waves from parallel side walls of the tank.

8.2 Wave-exciting forces

Hydrodynamic interactions in the first-order wave-exciting forces can also be accounted for by the present calculation method. As an example, Fig. 8 shows the sway exciting forces on Ship-A (E_2^A) and Ship-B (E_2^B) which are situated in the upwave and downwave sides, respectively, in beam waves ($\beta = 90°$) with separation distance $S = 1.097\,\mathrm{m}$. Likewise, Fig. 9 shows the heave exciting forces on Ship-A (E_3^A) and Ship-B (E_3^B) for the same experimental condition. The nondimension for the sway and heave exciting forces is made using $\rho g \zeta_w A_W^k$ ($k = A$ or B), with A_W^k being the water-plane area of the kth ship.

The overall agreement between measured and computed results is good, although slight discrepancies can be seen in a range of long wavelengths (which may be due to reflection-wave effects from side walls of the tank) and near the maximum peak at about $\lambda/L = 0.65$ (which may be due to viscous effects ignored in the present calculation method).

8.3 Wave drift forces

Since the second-order wave drift forces are of main concern in the present paper, their results will be shown for two typical cases:

(1) Ship-A is situated in the upwave side and Ship-B is in the downwave side with separation distance $S = 1.097\,\mathrm{m}$, and

(2) Ship-A is situated in the downwave side and Ship-B is in the upwave side with separation distance $S = 1.797\,\mathrm{m}$.

For the first case, the steady sway forces on Ship-A ($\overline{F}_2^A$) and Ship-B ($\overline{F}_2^B$) are shown in Figs. 10 and 11, respectively, and the total drift force in sway (the sum of steady sway forces on each ship) is shown in Fig. 12. In comparison of the steady force on each ship, computed results of the near-field method and Fang and Chen's method are shown, because the far-field method gives only the total drift force on both ships and the 'new' method cannot be applied for two ships situated abreast with a narrow gap, as demonstrated in Tables 1 and 2. In Fig. 12 for the total drift force, computed results by the far-field method are shown by the broken line.

We can see from these figures that computed results by the near-field method agree well with measured ones and the results by Fang and Chen's method are apparently incorrect,

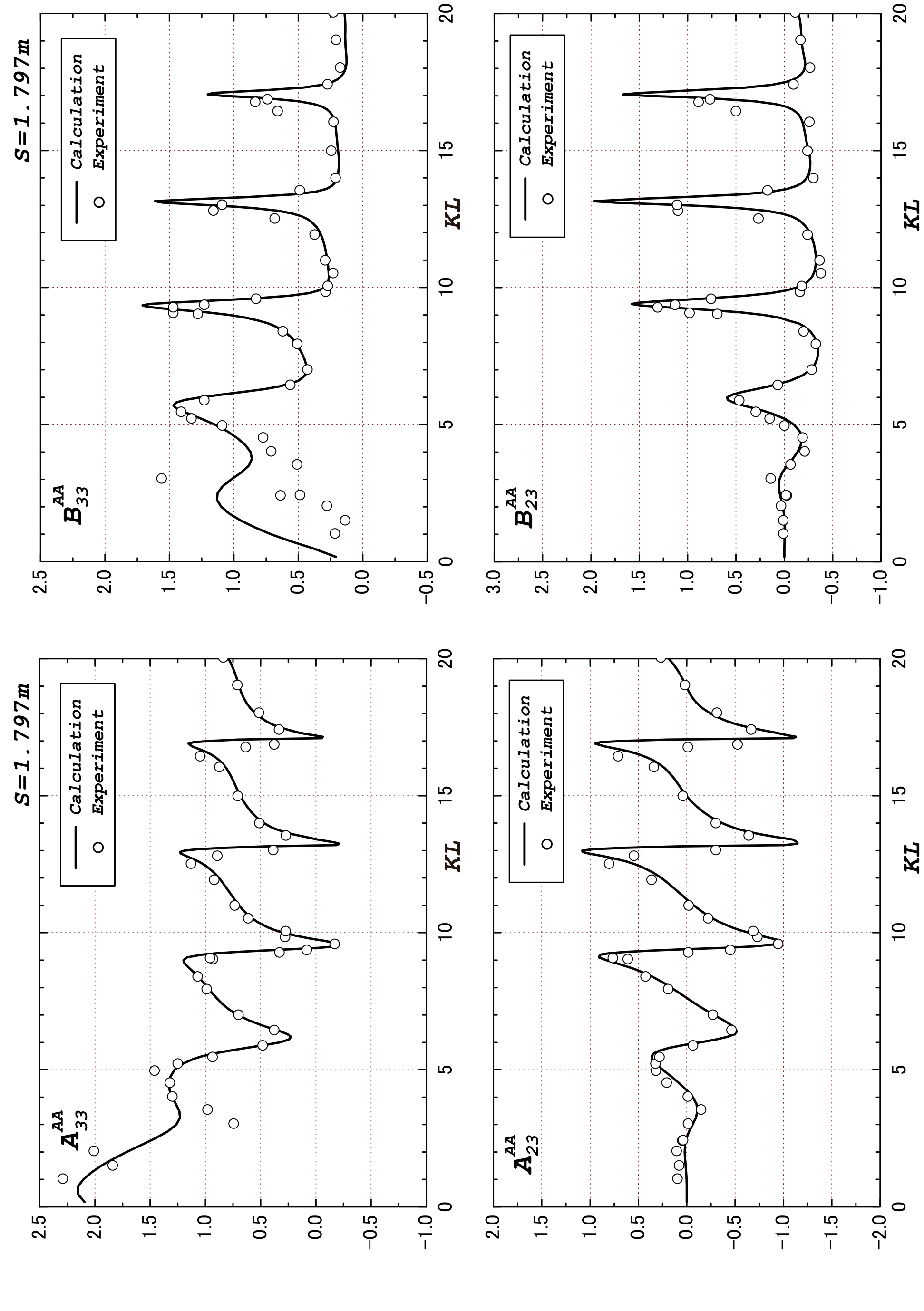

Fig. 7 Added mass and damping coefficients of a modified Wigley model due to heave motion of a modified Wigley model when a rectangular barge is abreast with separation distance of $S = 1.797$ m

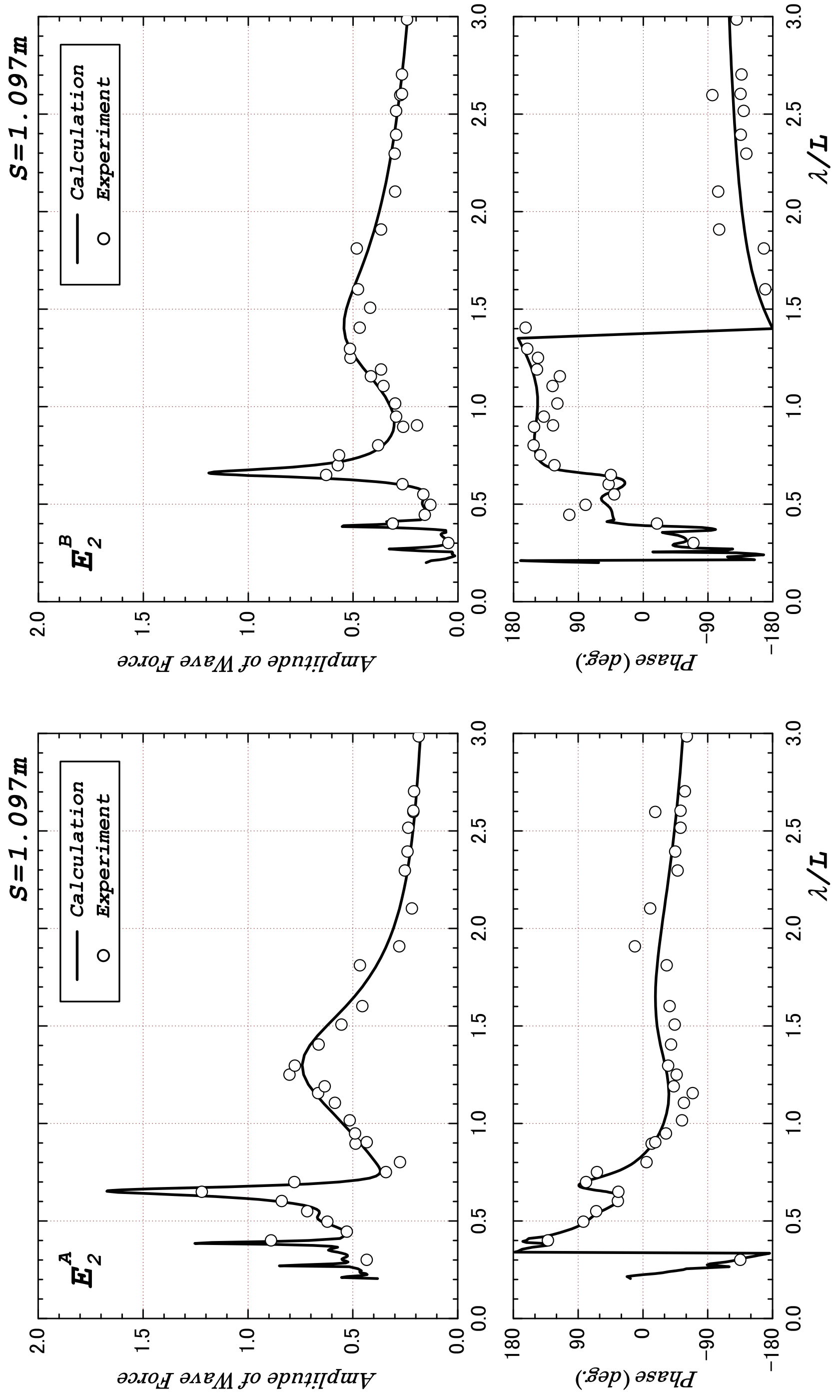

Fig. 8 Wave-exciting force in sway of a modified Wigley model (Ship-A, in the upwave side) and a rectangular barge model (Ship-B, in the downwave side) in beam waves ($\beta = 90°$), arranged side by side with separation distance of $S = 1.097$ m

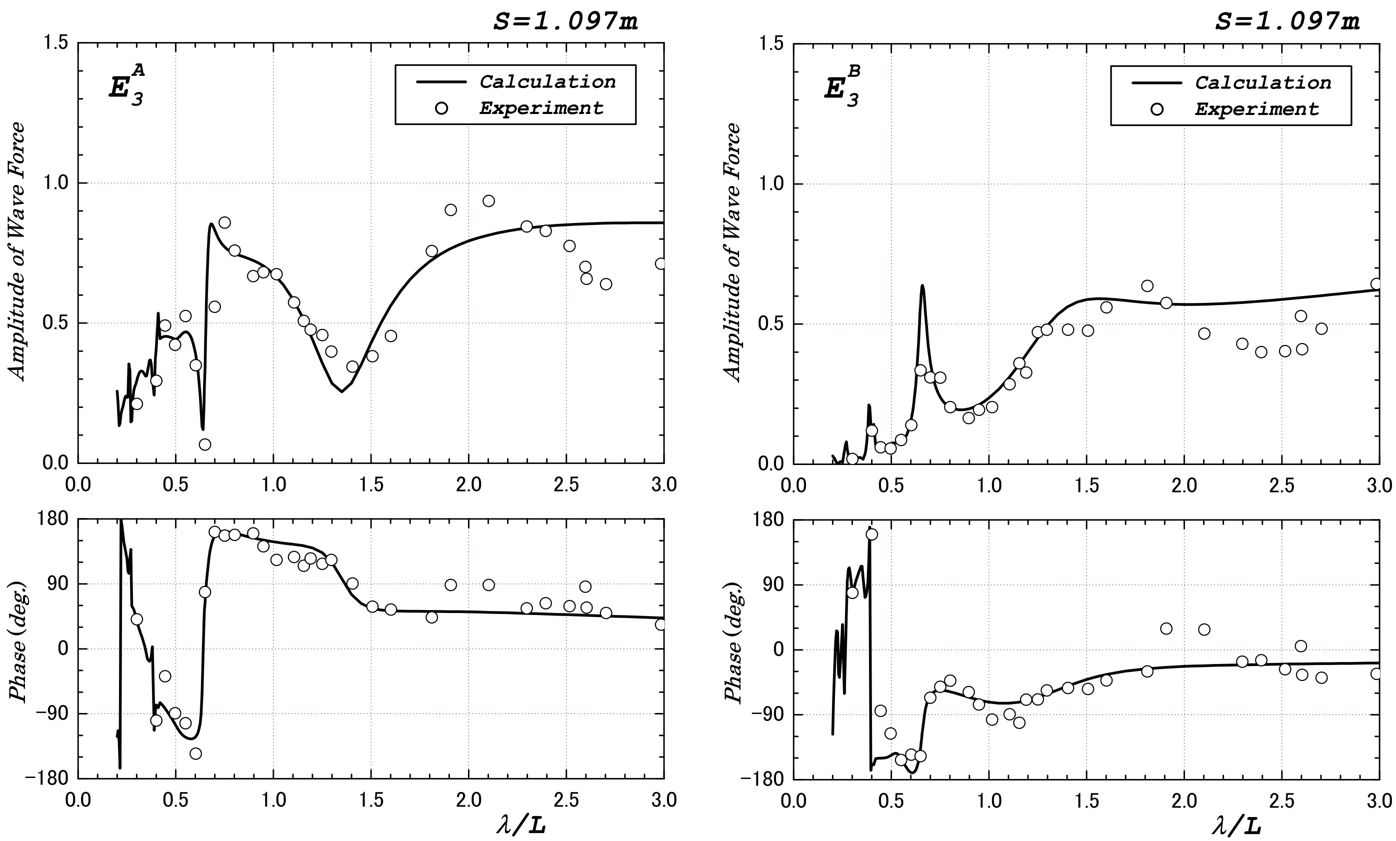

Fig. 9 Wave-exciting force in heave of a modified Wigley model (Ship-A, in the upwave side) and a rectangular barge model (Ship-B, in the downwave side) in beam waves ($\beta = 90°$), arranged side by side with separation distance of $S = 1.097\,\mathrm{m}$

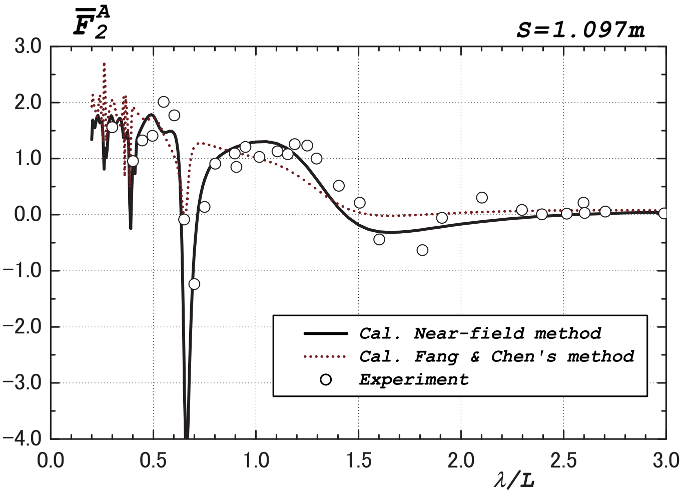

Fig. 10 Sway steady force on Ship-A situated in the upwave side of beam wave ($\beta = 90°$) for the case of $S = 1.097\,\mathrm{m}$

particularly for the force on a ship in the upwave side. It is noteworthy that, around $\lambda/L = 0.67$, the steady sway force becomes large negative on Ship-A in the upwave side and large positive on Ship-B in the downwave side; that is, a large repulsion force is exerted between two ships around this wavelength, but the total force in sway on both ships is positive as seen in Fig. 12.

Computed results by the far-field and near-field methods must be coincident as confirmed for two identical ellipsoids, but a small discrepancy can be seen in Fig. 12. This discrepancy did not diminish even when the number of panels on both ships was increased, from which we conjecture that numerical inaccuracy occurs in evaluating the velocity components around

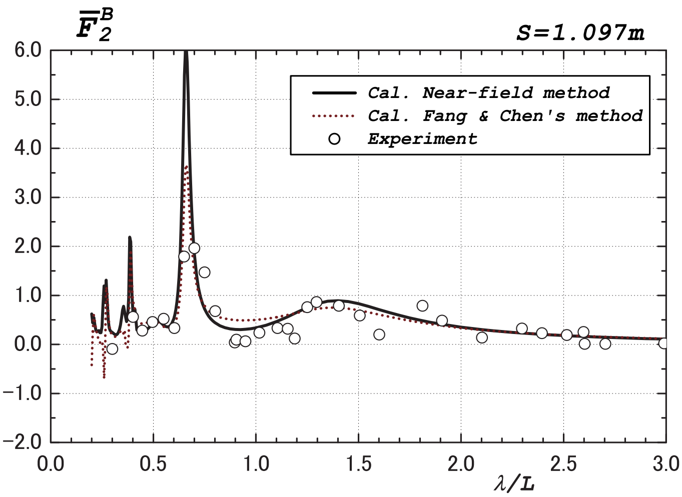

Fig. 11 Sway steady force on Ship-B situated in the downwave side of beam wave ($\beta = 90°$) for the case of $S = 1.097\,\mathrm{m}$

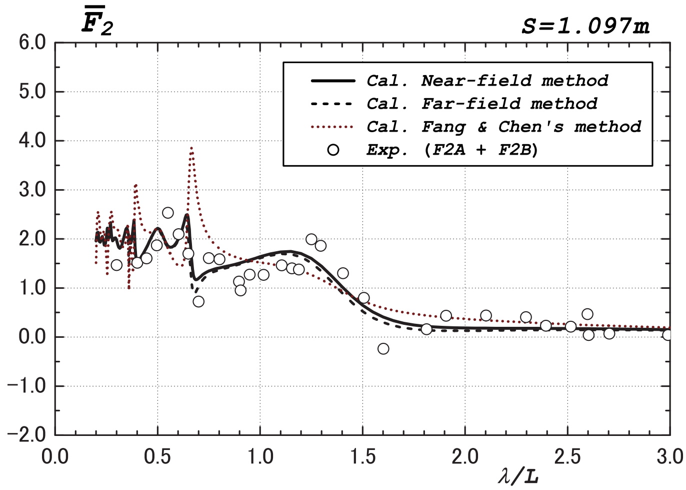

Fig. 12 Sway steady force on two ships in the beam wave ($\beta = 90°$) for the case of Ship-A in the upwave side and $S = 1.097\,\mathrm{m}$

the edge or corner of a rectangular barge model. However, this order of discrepancy may be allowable in practical computations for an engineering purpose.

The near-field method predicts all components of the steady forces on each ship, unlike the far-field method or Fang and Chen's method. To demonstrate this capability, Figs. 13 and 14 show the steady heave forces on Ship-A and Ship-B, respectively, and the sum of these are shown in Fig. 15 with experimental values. Not only the total heave force but also the individual heave force on each ship is positive for all cases, and the heave force becomes large around $\lambda/L = 0.67$ at which a large repulsion force in sway is exerted. The agreement between computed and measured results is favorable except for long wavelengths at which

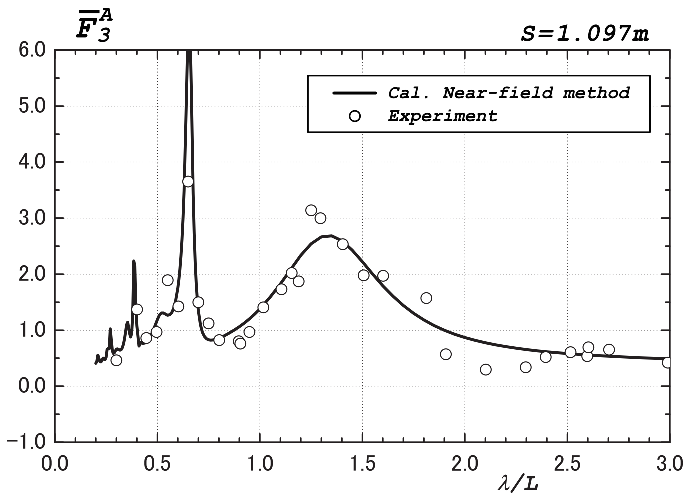

Fig. 13 Heave steady force on Ship-A situated in the upwave side of beam wave ($\beta = 90°$) for the case of $S = 1.097\,\mathrm{m}$

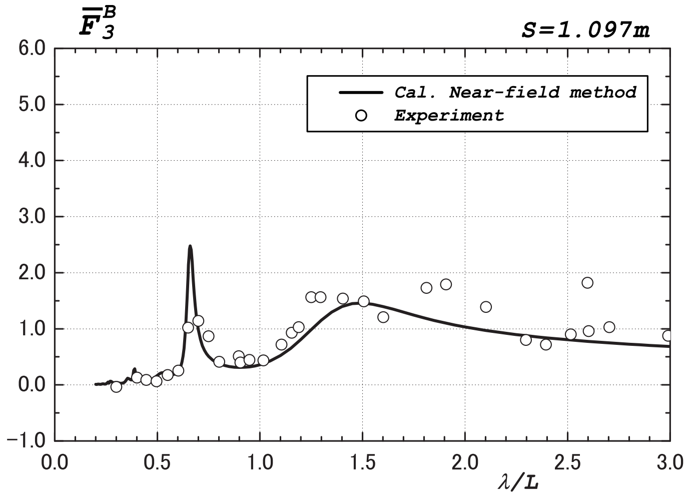

Fig. 14 Heave steady force on Ship-B situated in the downwave side of beam wave ($\beta = 90°$) for the case of $S = 1.097\,\mathrm{m}$

measured results may be contaminated by reflection waves from parallel side walls of the tank.

For the second case, i.e. when Ship-B is situated in the upwave side with larger separation distance of $S = 1.797\,\mathrm{m}$, the results are shown in Figs. 16–21 in the same way. Regarding the steady sway force, as can be seen in Figs. 16 and 17, a larger force is exerted on Ship-B in the upwave side, and when the force on Ship-B is large, the force on Ship-A tends to be small, and vice versa. The steady sway forces on each ship are predicted well by the near-field method but not so well by Fang and Chen's method especially for a ship in the upwave side. Therefore, when summing up individual sway forces on each ship, as shown

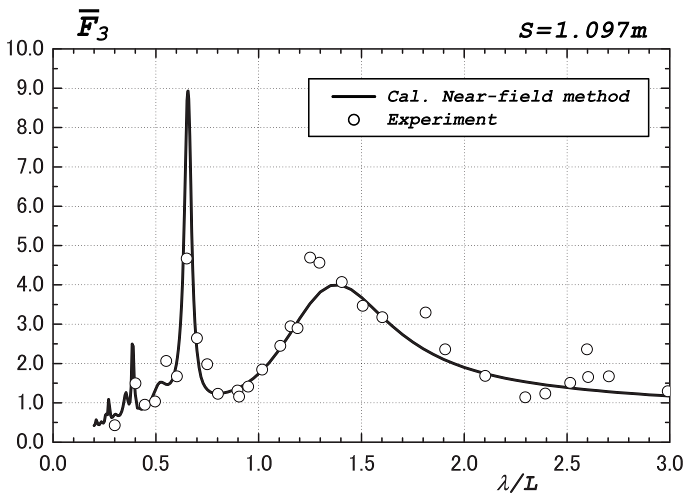

Fig. 15 Heave steady force on two ships in the beam wave ($\beta = 90°$) for the case of Ship-A in the upwave side and $S = 1.097\,\mathrm{m}$

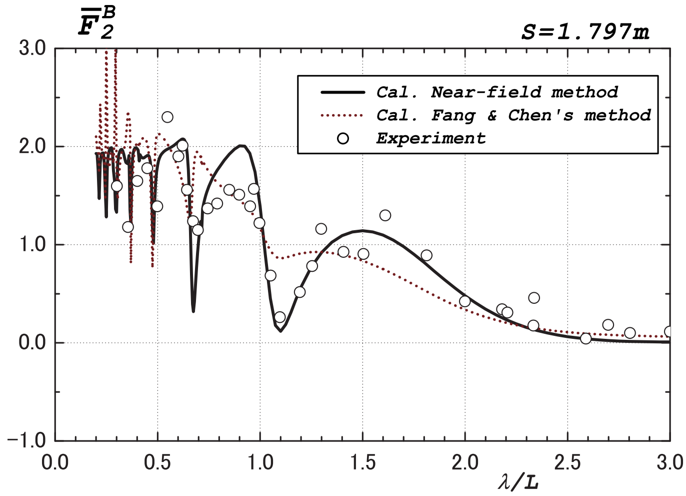

Fig. 16 Sway steady force on Ship-B situated in the upwave side of beam wave ($\beta = 90°$) for the case of $S = 1.797$ m

in Fig. 18, the results by the near-field method are in good agreement with measured ones, but the results by Fang and Chen's method are not.

Noticeable discrepancy can be seen in Fig. 18 between the results by the near-field and far-field methods, and the degree of this discrepancy is larger than that in the first case shown in Fig. 12. Fig. 18 is for the case that a rectangular barge model is situated in the upwave side and receiving a larger force. For a barge model, numerical inaccuracy may occur near rectangular edges or corners. Thus the discrepancy in the results for Ship-B in the upwave side tends to be prominent between the far-field and near-field methods, as compared to the opposite arrangement shown in Fig. 12.

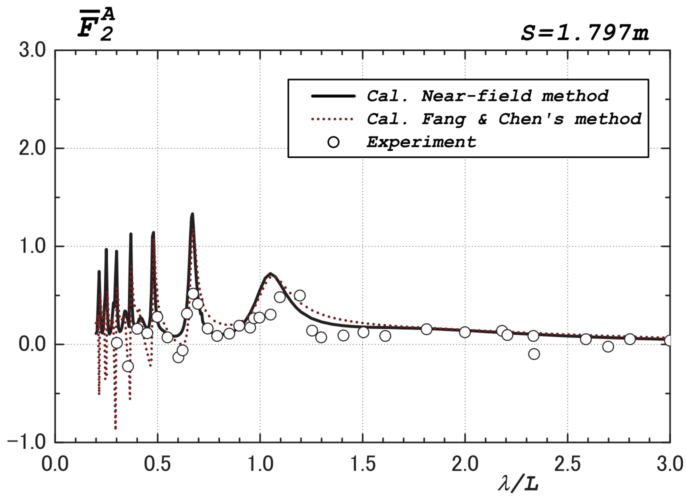

Fig. 17 Sway steady force on Ship-A situated in the downwave side of beam wave ($\beta = 90°$) for the case of $S = 1.797$ m

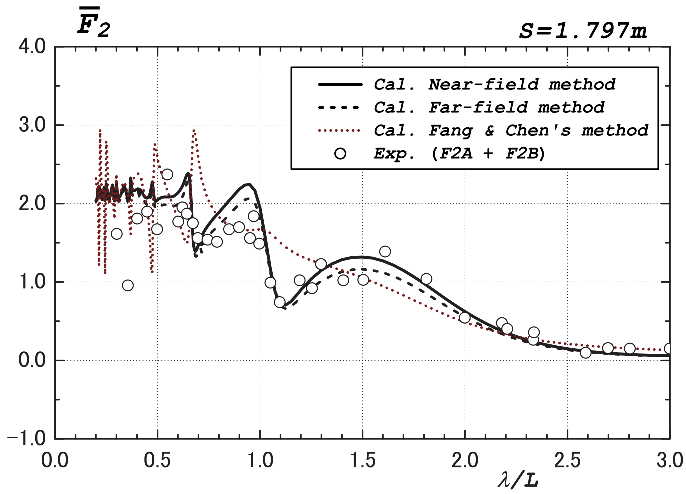

Fig. 18 Sway steady force on two ships in the beam wave ($\beta = 90^\circ$) for the case of Ship-B in the upwave side and $S = 1.797\,\mathrm{m}$

The steady heave forces are compared in Figs. 19–21. We must anticipate the side-wall effects of a tank in the heave force at larger wavelengths, which may be a reason of discrepancy between measured and computed results. Another discrepancy to be noted is the value of wavelength at which the heave force on Ship-A in the downwave side takes a maximum. Since Ship-B with sharp edges is located in the upwave side, we can envisage that vortices are shed in the downstream and the flow is different from the potential flow; which can be considered as a possible reason of discrepancy. Nevertheless, the overall agreement is rather good, confirming validity of the near-field method developed in the present study.

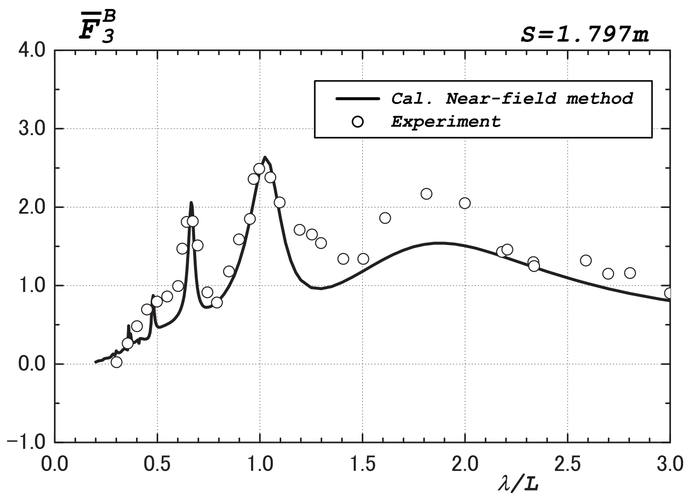

Fig. 19 Heave steady force on Ship-B situated in the upwave side of beam wave ($\beta = 90^\circ$) for the case of $S = 1.797\,\mathrm{m}$

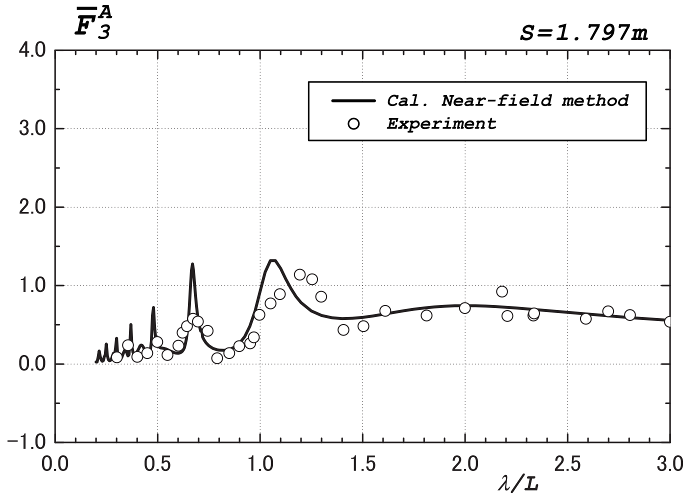

Fig. 20 Heave steady force on Ship-A situated in the downwave side of beam wave ($\beta = 90°$) for the case of $S = 1.797\,\mathrm{m}$

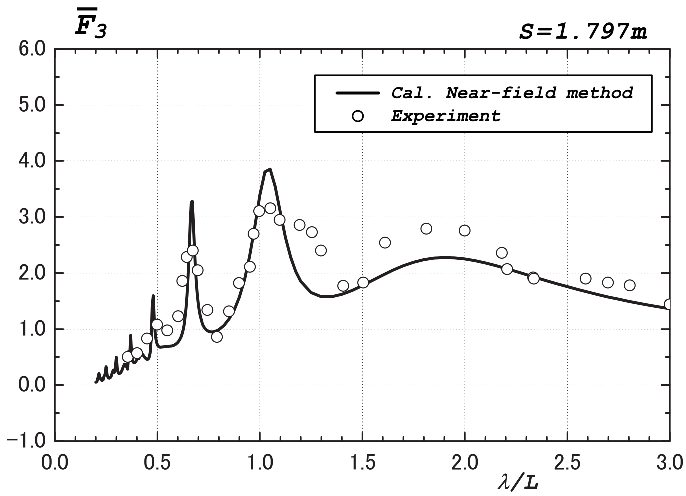

Fig. 21 Heave steady force on two ships in the beam wave ($\beta = 90°$) for the case of Ship-B in the upwave side and $S = 1.797\,\mathrm{m}$

9. Conclusions

With a higher-order boundary-element method, numerical computations were implemented for the first-order oscillatory hydrodynamic forces and the second-order steady forces on each of the two ships arranged side by side. Hydrodynamic interactions were taken into account exactly in the framework of potential theory for the first-order and second-order problems studied in this paper. For the computation of second-order steady forces, in addition to the near-field and far-field methods, a 'new' far-field method was studied, computing the force on each ship by considering a control surface encompassing only either ship and applying the principle of momentum conservation. Experiments were also conducted using two ship models with side-by-side arrangement, and measured results were compared with computed ones.

From the study above, the followings were observed:

(1) Hydrodynamic interactions are well accounted for by the present calculation method, because the agreement between measured and computed results is good as a whole.

(2) When hydrodynamic interactions are severe, the second-order steady forces on each ship become large in both sway and heave. The sway steady forces on each ship are repulsive but the total force on both ships is positive. The heave steady forces on each ship are always positive in the vertically downward direction.

(3) Irrespective of whether the two ships are free to oscillate, the results by the 'new' far-field method are in good agreement with the ones by the near-field method, if no overlap region exists between fictitious vertical circular cylinders surrounding each ship.

(4) When a rectangular barge is located in the upwave side, discrepancy in computed and measured results tends to be prominent especially in the results of a downwave-side ship; which may be attributed to vortices shed in the downstream from sharp edges of a rectangular barge and also to numerical inaccuracy in computing the flow velocity near rectangular edges or corners.

References

1. Buchner, B., Dijk, A. van, Wilde, J. J. de, 2001. Numerical multiple-body simulations of side-by-side mooring to an FPSO. Proc. 11th Int. Offshore & Polar Eng. Conf., ISOPE, Stavanger, Norway, Vol. 1, pp. 343–353.

2. Choi, Y. R., Hong, S. Y., 2002. An analysis of hydrodynamic interaction of floating multi-body using higher-order boundary element method. Proc. 12th Int. Offshore & Polar Eng. Conf., ISOPE, Kitakyushu, Japan, Vol. 3, pp. 303–308.

3. Fang, M. C., Chen, G. R., 2002. On three-dimensional solutions of drift forces and moments between two ships in waves. Journal of Ship Research 46 (4), 280–288.

4. Huijsmans, R. H. M., Pinkster, J. A., Wilde, J. J. de, 2001. Diffraction and radiation of waves around side-by-side moored vessels. Proc. 11th Int. Offshore & Polar Eng. Conf., ISOPE, Stavanger, Norway, Vol. 1, pp. 406–412.

5. Kashiwagi, M., Yoshida, S., 2000. Wave drift force and moment on a VLFS supported by a great number of floating columns. Journal of Offshore and Polar Eng., 11 (3), 176–183.

6. Kashiwagi, M., 2002. Wave-induced local steady forces on a column-supported very large floating structure. Journal of Offshore and Polar Eng., 12 (2), 98–104.

7. Maruo, H., 1960. The drift of a body floating on waves. Journal of Ship Research 4, 1–10.

8. Newman, J. N., 1967. The drift force and moment on ships in waves. Journal of Ship Research 11 (1), 51–60.

9. Ogilvie, T. F., 1983. Second order hydrodynamic effects on ocean platforms. Int. Workshop on Ship and Platform Motion, Berkeley, USA, pp. 205–265.

10. Seto, H., 1993. Some expressions of pulsating source potentials in shallow water and their efficient algorithms. Trans. of the West-Japan Soc. of Nav. Arch., Vol. 85, pp. 25–36.

Development of Floating Body with High Performance in Wave Reflection*

Masashi KASHIWAGI, Hirofumi YAMADA and Makoto YASUNAGA
Research Institute for Applied Mechanics, Kyushu University
Kasuga, Fukuoka 816-8580, Japan

Tomohiro TSUJI
SRI Hybrid Limited, Kobe, Japan

ABSTRACT

A theoretical study is made first on the transmission and reflection waves past 2-dimensional, general, antisymmetric floating bodies which are oscillating in response to regular incident waves. As a result, the reciprocity theorem for the transmission and reflection coefficients and the wave-energy splitting theorem for the symmetric and antisymmetric wave components are derived for a general case of the motions of an antisymmetric body being free. Next, in order to develop floating piers with high performance in wave reflection, numerical computations and corresponding experiments are conducted with emphasis placed on the effects of horizontal fins attached to the original body of the rectangular shape. Depending on the number and location of the fins, there exist one or two frequencies at which zero wave transmission can be realized. With this fact, it is suggested that the transmission wave can be small over the frequency range of our interest by optimizing the number, size, and location of horizontal fins attached to a rectangular-shaped main body.

Keywords: Wave reflection and transmission, reverse theorem, wave-energy splitting theorem, antisymmetric body, perfect reflection, waveless frequency.

1. INTRODUCTION

There is a practical demand that floating breakwaters or piers (hereafter described generically as breakwaters) with high performance in the wave reflection to be developed and installed near the mouth of a marina to protect yachts or other small vessels from waves coming from the open sea or generated by a high-speed boat running in proximity. From a viewpoint of preservation of water by exchanging with fresh water, floating-type breakwaters may be preferable. In fact, there have been many studies so far for the development of floating breakwaters using various ideas, and most of them were moored by slack chains anchored to the sea bottom. However, in this study, it is required that the water depth is relatively shallow, and that floating breakwaters to be developed must not move horizontally to avoid collision with vessels in the marina; that is, the movement of floating breakwaters may be restricted to heave by a number of vertical piles mounted to the sea bottom. In addition, the section shape of a body is required to be relatively simple for easy construction.

* *Reprinted from International Journal of Offshore and Polar Engineering, Vol. 17, No. 1, pp. 39–46, 2007 (March)*

Under these circumstances, experiments in a wave channel and numerical computations based on the potential-flow theory have been conducted for a variety of 2-D models with a rectangular-shaped model used as the original one. To enhance the performance in wave reflection, small horizontal fins are attached to the right and/or left part of the bottom and/or side wall of the original body, and the performance is tested by changing systematically the number, length, and position of the fins.

In connection with antisymmetric bodies (a body with only one fin attached to the right or left lower bottom), a theoretical study is made of transmission and reflection waves past 2-D, general, antisymmetric bodies oscillating freely in response to incident waves. Based on Green's theorem applied to the two different velocity potentials, very useful relations are found. One of these relations is the so-called reciprocity property that both of the transmission and reflection coefficients for an antisymmetric body are independent of the incoming direction of incident waves; this property is valid irrespective of whether the body motions are fixed or free to oscillate in waves. The other is the wave-energy splitting theorem: The energy of the symmetric (antisymmetric) wave component when the incident wave is incoming from the right is equal to that of the antisymmetric (symmetric) wave component when the incident wave is incoming from the left.

Numerical computations indicate that, depending on the number and location of the horizontal fins, there exist one or two frequencies at which zero wave transmission is realized, and these frequencies are different from the so-called waveless frequency at which the wave-exciting force in heave becomes zero. Although the degree of agreement between numerical computations and corresponding experiments is not very good because of viscous effects, particularly around the heave resonance, experimental results seem to support the findings by this paper's theoretical and numerical studies.

2. REFLECTION AND TRANSMISSION WAVES

Under the assumption that the fluid is incompressible and inviscid with irrotational motion, we introduce the velocity potential and consider the flow around a floating body in regular waves. The wave-induced motion of a body and associated fluid motion are assumed to be linear in the incident-wave amplitude and harmonic in time with circular frequency ω of the incident wave. In what follows, all oscillatory quantities will be expressed in complex form, with the time dependence $e^{i\omega t}$ understood.

In order to treat the problem in general, we consider an antisymmetric body; in this case, depending on the incoming direction of the incident wave, the flow field around a body may be different. Accordingly, as shown in Fig. 1, let us first consider the case where the incident wave is incoming from the positive x-axis and write the resulting velocity potential in the form:

$$\phi^+(x,y) = \frac{g\zeta_a}{i\omega}\Big\{ \phi_D^+(x,y) - KX_j^+\phi_j(x,y) \Big\} \equiv \frac{g\zeta_a}{i\omega}\,\varphi^+(x,y), \tag{1}$$

$$\phi_D^+ = \phi_0^+ + \phi_4^+, \tag{2}$$

$$\phi_0^+ = \frac{\cosh k(y-h)}{\cosh kh}\,e^{ikx},\ \ K = \frac{\omega^2}{g} = k\tanh kh, \tag{3}$$

where ζ_a is the amplitude of the incident wave and g is the acceleration of gravity. ϕ_D^+ is the diffraction potential which is the sum of the incident-wave potential ϕ_0^+ and the scattering potential ϕ_4^+ (we note that this definition follows Newman (1977) but may be defined differently by other authors). The water depth is assumed to be finite and constant

h in this paper, and the wavenumber k of a progressive wave satisfies the dispersion relation given by Eq. 3.

X_j^+ denotes the complex amplitude of the body motion in the j-th mode ($j = 1$ for sway, $j = 2$ for heave, and $j = 3$ for roll), and ϕ_j is the radiation potential with unit velocity in the j-th direction (which is independent of the incident wave and hence has no superscript attached). The summation sign with respect to j is deleted throughout this paper with the convention that any term of an equation containing the same index twice should be summed over that index.

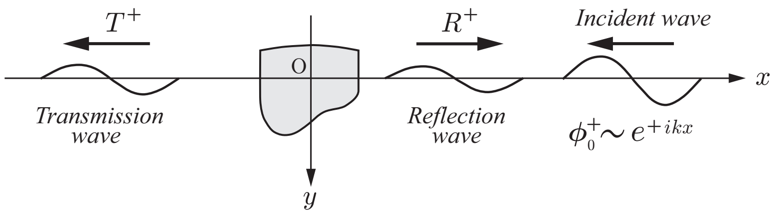

Fig. 1 Reflection and transmission waves for an incident wave incoming from the positive x-axis.

The asymptotic expression of the velocity potential at $x \to \pm\infty$ can be given as follows:

$$\begin{aligned}\varphi^+(x, y) =& \; \phi_D^+(x, y) - KX_j^+\phi_j(x, y)\\ \sim& \; \frac{\cosh k(y-h)}{\cosh kh}\left[e^{ikx} + iH_4^\pm\, e^{\mp ikx} - KX_j^+ iH_j^\pm\, e^{\mp ikx}\right].\end{aligned} \tag{4}$$

Here the upper or lower sign in the double sign is taken according to whether $x \to +\infty$ or $-\infty$, respectively. $H_4^\pm$ and $H_j^\pm$ ($j = 1 \sim 3$) denote the Kochin functions associated with the far-field scattered and radiated waves, respectively. (Their explicit expressions will be given subsequently.)

From Eq. 4, the velocity potential on the free surface ($y = 0$) may be expressed as:

$$\varphi^+(x, 0) \sim \begin{cases} e^{ikx} + R_F^+\, e^{-ikx} & \text{as } x \to +\infty \\ T_F^+\, e^{ikx} & \text{as } x \to -\infty \end{cases} \tag{5}$$

where:

$$\left.\begin{aligned} R_F^+ = R_D^+ - iKX_j^+H_j^+\,, \quad R_D^+ = iH_4^+ \\ T_F^+ = T_D^+ - iKX_j^+H_j^-\,, \quad T_D^+ = 1 + iH_4^- \end{aligned}\right\} \tag{6}$$

R^+ and T^+ are defined as the coefficients of reflection and transmission waves, respectively. Suffix D to these coefficients indicates the quantities for the diffraction problem; likewise suffix F indicates the quantities for the case where the body motions are free to respond to the incident wave. These coefficients and the amplitude of a body's wave-induced motion are nondimensionalized using the incident-wave amplitude.

In a similar manner, we consider the case of Fig. 2 where the incident wave is incoming from the negative x-axis and write the corresponding velocity potential in the form:

$$\phi^-(x, y) = \frac{g\zeta_a}{i\omega}\Big\{\, \phi_D^-(x, y) - KX_j^-\phi_j(x, y)\Big\} \equiv \frac{g\zeta_a}{i\omega}\,\varphi^-(x, y). \tag{7}$$

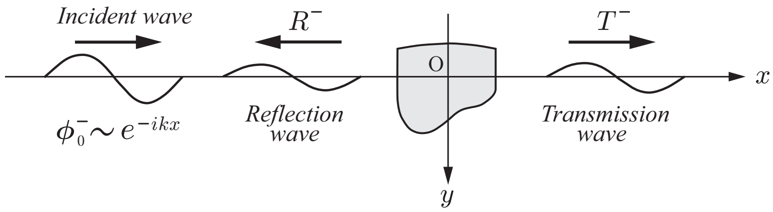

Fig. 2 Reflection and transmission waves for an incident wave incoming from the negative x-axis.

The asymptotic expression of this velocity potential at $x \to \pm\infty$ takes the following form:

$$\begin{aligned}\varphi^-(x,y) &= \phi_D^-(x,y) - KX_j^- \phi_j(x,y) \\ &\sim \frac{\cosh k(y-h)}{\cosh kh}\left[e^{-ikx} + ih_4^{\pm}\, e^{\mp ikx} - KX_j^- iH_j^{\pm}\, e^{\mp ikx} \right]. \end{aligned} \tag{8}$$

Because the scattered wave is different from that in the former case, the associated Kochin function is expressed as $h_4^{\pm}$. (Note that $h_4^{\pm} = H_4^{\mp}$ for a body with horizontal symmetry.)

From Eq. 8, the velocity potential on the free surface can be expressed with the reflection and transmission coefficients as follows:

$$\varphi^-(x,0) \sim \begin{cases} T_F^-\, e^{-ikx} & \text{as } x \to +\infty \\ e^{-ikx} + R_F^-\, e^{ikx} & \text{as } x \to -\infty \end{cases} \tag{9}$$

where:

$$\left.\begin{aligned} R_F^- &= R_D^- - iKX_j^- H_j^-\,, \quad R_D^- = ih_4^- \\ T_F^- &= T_D^- - iKX_j^- H_j^+\,, \quad T_D^- = 1 + ih_4^+ \end{aligned}\right\} \tag{10}$$

For a symmetric body about the y-axis, it is obvious from Eqs. 6 and 10 that $R^+ = R^-$ and $T^+ = T^-$; in this particular case then, the superscript ($+$ or $-$) will be deleted.

In order to compute the reflection and transmission waves, the diffraction and radiation potentials must be determined first. Then the Kochin functions and wave-induced motions must be evaluated; this is described below.

3. NUMERICAL SOLUTION METHOD

In addition to the far-field behavior described above, the velocity potential must satisfy the following linearized boundary conditions:

$$\frac{\partial \phi^{\pm}}{\partial y} + K\phi^{\pm} = 0 \qquad \text{on } y = 0, \tag{11}$$

$$\frac{\partial \phi^{\pm}}{\partial y} = 0 \qquad \text{on } y = h, \tag{12}$$

$$\left.\begin{aligned} \frac{\partial \phi_D^{\pm}}{\partial n} &= 0 \\ \frac{\partial \phi_j}{\partial n} &= n_j \end{aligned}\right\} \quad \text{on } S_H, \tag{13}$$

where S_H denotes the body surface below $y = 0$ and n_j denotes the j-th component ($n_1 = n_x$, $n_2 = n_y$, and $n_3 = xn_2 - yn_1$) of the normal vector, which is defined as positive outward from the body surface.

The diffraction ($\phi_D^{\pm}$) and radiation (ϕ_j) potentials are determined directly by solving an integral equation to be derived from Green's theorem; which may be written in the form:

$$C(\mathrm{P})\psi_j(\mathrm{P}) + \int_{S_H} \psi_j(\mathrm{Q}) \frac{\partial}{\partial n_{\mathrm{Q}}} G(\mathrm{P};\mathrm{Q})\, d\ell(\mathrm{Q}) = \begin{cases} \phi_0^{\pm}(\mathrm{P}) & (j = D) \\ \displaystyle\int_{S_H} n_j(\mathrm{Q}) G(\mathrm{P};\mathrm{Q})\, d\ell(\mathrm{Q}) & (j = 1 \sim 3) \end{cases} \tag{14}$$

where $\mathrm{P} = (x, y)$ and $\mathrm{Q} = (\xi, \eta)$ denote the field and integration points, respectively, located on the body surface, and $C(\mathrm{P})$ denotes the solid angle. $G(\mathrm{P};\mathrm{Q})$ represents the free-surface Green function in water of constant finite depth (Thorne, 1953; Wehausen and Laiton, 1960), and its asymptotic form at a far field is written as:

$$G(\mathrm{P};\mathrm{Q}) \sim iC_0 \frac{\cosh k(y-h)}{\cosh kh} \frac{\cosh k(\eta - h)}{\cosh kh}\, e^{-ik|x-\xi|}, \tag{15}$$

$$C_0 = \frac{k}{K + h(k^2 - K^2)}. \tag{16}$$

Substituting Eq. 15 into Eq. 14 with $C(\mathrm{P}) = 1$, the asymptotic form of the velocity potential at $x \to \pm\infty$ can readily be obtained. Since the results are expressed as Eq. 4 or Eq. 8 depending on the incoming direction of the incident wave, the Kochin functions in the diffraction and radiation problems can be defined explicitly as follows:

$$\left.\begin{aligned} H_4^{\pm} &= -C_0 \int_{S_H} \phi_D^{+} \frac{\partial}{\partial n} \frac{\cosh k(\eta - h)}{\cosh kh}\, e^{\pm ik\xi}\, d\ell, \\ h_4^{\pm} &= -C_0 \int_{S_H} \phi_D^{-} \frac{\partial}{\partial n} \frac{\cosh k(\eta - h)}{\cosh kh}\, e^{\pm ik\xi}\, d\ell, \\ H_j^{\pm} &= C_0 \int_{S_H} \left(n_j - \phi_j \frac{\partial}{\partial n}\right) \frac{\cosh k(\eta - h)}{\cosh kh}\, e^{\pm ik\xi}\, d\ell. \end{aligned}\right\} \tag{17}$$

The integral equation Eq. 14 is solved by the so-called constant-panel collocation method, with a remedy for getting rid of the irregular frequencies proposed by Haraguchi and Ohmatsu (1993). The free-surface Green function is evaluated using a power-series expression for relatively large values of $|x - \xi|$ and integral expressions for other values of $|x - \xi|$. The numerical method adopted for evaluating integral expressions is similar to that proposed by Seto (1991, 1992) for 3-D cases.

Once the velocity potentials on the body surface are determined, it is straightforward to compute the hydrodynamic forces. With the convention that all quantities are written in nondimensional form, the hydrodynamic forces in the diffraction and radiation problems are expressed in the form:

$$\left.\begin{aligned} E_j^{\pm} &= \int_{S_H} \phi_D^{\pm} n_j\, d\ell, \\ f_{jk} &= -\int_{S_H} \phi_k n_j\, d\ell = A_{jk} - iB_{jk}, \end{aligned}\right\} \tag{18}$$

where $E_j^{\pm}$ is called the wave-exciting force in the j-th direction, and A_{jk} and B_{jk} are the added-mass and damping coefficient, respectively, in the j-th direction due to the k-th mode of motion.

In terms of these forces, the equations of motion of a body can be expressed in a matrix form as follows:

$$\Big[-K\big(M_{jk}+f_{jk}\big)+C_{jk}\Big]X_k^{\pm}=E_j^{\pm}\quad (j=1\sim 3), \tag{19}$$

where M_{jk} denotes the mass matrix, and its values in the diagonal ($j=k$) are the body mass (m) for $j=1$ and 2 and the moment of inertia for $j=3$; also nonzero values at off-diagonals are $M_{13}=M_{31}=-my_G$ and $M_{23}=M_{32}=mx_G$, where (x_G, y_G) is the position of the center of gravity, generally unequal to the origin of the coordinate system due to body asymmetry. C_{jk} denotes the restoring force coefficients due to the static pressure. It should be noted that both M_{jk} and C_{jk} are real quantities and the symmetry relation of $M_{jk}=M_{kj}$ and $C_{jk}=C_{kj}$ holds, as is the same for the added mass and damping coefficients.

4. HYDRODYNAMIC RELATIONS

In order to derive some important reciprocity and energy-conservation relations for the reflection and transmission waves, Green's theorem can be applied to the two different velocity potentials. The idea is the same as that proposed by Newman (1975), and we can obtain the following relation:

$$\int_{S_H}\Big(\phi\frac{\partial\psi}{\partial n}-\psi\frac{\partial\phi}{\partial n}\Big)d\ell=\frac{1}{2kC_0}\bigg[\Big(\phi\frac{\partial\psi}{\partial x}-\psi\frac{\partial\phi}{\partial x}\Big)_{y=0}\bigg]_{-\infty}^{+\infty} \tag{20}$$

Here both potentials ϕ and ψ must satisfy the free-surface and water-bottom conditions given by Eqs. 11 and 12, but not necessarily the same boundary conditions on the body surface (S_H) and the radiation surface at $x=\pm\infty$. The square brackets with superscript $+\infty$ and subscript $-\infty$ means the difference between the quantities in the brackets evaluated at $x=+\infty$ and $x=-\infty$.

As the first application of Eq. 20, we consider φ^+ for ϕ and φ^- for ψ. In this case, the left-hand side of Eq. 20, denoted by $\mathcal{L}$, may be evaluated as follows:

$$\begin{aligned}\mathcal{L}&=\int_{S_H}\Big\{\big(\phi_D^+-KX_j^+\phi_j\big)\big(-KX_k^-n_k\big)-\big(\phi_D^--KX_k^-\phi_k\big)\big(-KX_j^+n_j\big)\Big\}d\ell\\&=-KX_k^-\big(E_k^++KX_j^+f_{kj}\big)+KX_j^+\big(E_j^-+KX_k^-f_{jk}\big)\\&=-KX_k^-X_j^+\big(-KM_{kj}+C_{kj}\big)+KX_j^+X_k^-\big(-KM_{jk}+C_{jk}\big)=0,\end{aligned} \tag{21}$$

where the body-boundary condition Eq. 13, the hydrodynamic forces Eq. 18, the equations of body motion Eq. 19, and the symmetry relation of $M_{jk}=M_{kj}$ and $C_{jk}=C_{kj}$ have been used.

The right-hand side of Eq. 20, denoted by $\mathcal{R}$, may be evaluated by using Eqs. 5 and 9, and the result becomes:

$$\mathcal{R}=\frac{i}{C_0}\Big(T_F^+-T_F^-\Big). \tag{22}$$

$\mathcal{L}=\mathcal{R}$ thus gives the following relation:

$$T_F^+=T_F^-. \tag{23}$$

This means that the coefficient of a transmission wave past an antisymmetric body is independent of the incoming direction of incident wave and must be the same in both amplitude and phase; this is the case even when the body motions are free to oscillate in response to the incident wave.

Next we consider $\overline{\varphi^{+}}$ (which is the complex conjugate and physically the reverse-time velocity potential) for ϕ and φ^{-} for ψ. In this case, in the same way as we obtained Eq. 21, the left-hand side of Eq. 20 becomes

$$\begin{aligned}
\mathcal{L} &= \int_{S_H} \Big\{ \big(\overline{\phi_D^{+}} - K\overline{X_j^{+}\phi_j}\big)\big(-KX_k^{-}n_k\big) - \big(\phi_D^{-} - KX_k^{-}\phi_k\big)\big(-K\overline{X_j^{+}}n_j\big) \Big\}\, d\ell \\
&= -KX_k^{-}\big(\overline{E_k^{+}} + K\overline{X_j^{+}f_{kj}}\big) + K\overline{X_j^{+}}\big(E_j^{-} + KX_k^{-}f_{jk}\big) \\
&= -KX_k^{-}\overline{X_j^{+}}\big(-KM_{kj} + C_{kj}\big) + K\overline{X_j^{+}}X_k^{-}\big(-KM_{jk} + C_{jk}\big) = 0,
\end{aligned} \tag{24}$$

where a fact that M_{jk} and C_{kj} are real quantities has been used.

On the other hand, using Eqs. 5 and 9, the right-hand side of Eq. 20 takes the form:

$$\mathcal{R} = -\frac{i}{C_0}\Big(R_F^{-}\overline{T_F^{+}} + \overline{R_F^{+}}T_F^{-}\Big). \tag{25}$$

Thus $\mathcal{L} = \mathcal{R}$ gives the following relation:

$$R_F^{-}\overline{T_F^{+}} + \overline{R_F^{+}}T_F^{-} = 0. \tag{26}$$

Substituting the relation $T_F^{+} = T_F^{-}$ given by Eq. 23 into Eq. 26, we can obtain an important relation for the reflection wave:

$$\big|R_F^{+}\big| = \big|R_F^{-}\big|. \tag{27}$$

Namely, the amplitude of the reflection wave past an oscillating antisymmetric body must be also the same, irrespective of the incoming direction of incident wave.

It is obvious from the above proof that the relations of Eqs. 23 and 27 are also true for the diffraction problem; in fact, these relations for the diffraction problem were proved for the first time by Bessho (1975) with the idea of the reverse-time velocity potential.

By taking φ^{+} for ϕ and $\overline{\varphi^{+}}$ for ψ (or similarly φ^{-} for ϕ and $\overline{\varphi^{-}}$ for ψ) and evaluating Eq. 20 in the same manner, we can easily prove that:

$$\big|R_F^{+}\big|^2 + \big|T_F^{+}\big|^2 = \big|R_F^{-}\big|^2 + \big|T_F^{-}\big|^2 = 1. \tag{28}$$

This is known as the relation of energy conservation for the case where the body motions are free to oscillate in waves.

In passing, let us consider the followings:

$$\left.\begin{aligned}
\big|R^{+} \pm T^{+}\big|^2 &= \big|R^{+}\big|^2 + \big|T^{+}\big|^2 \pm \big(R^{+}\overline{T^{+}} + \overline{R^{+}}T^{+}\big) \\
\big|R^{-} \pm T^{-}\big|^2 &= \big|R^{-}\big|^2 + \big|T^{-}\big|^2 \pm \big(R^{-}\overline{T^{-}} + \overline{R^{-}}T^{-}\big)
\end{aligned}\right\} \tag{29}$$

In terms of Eqs. 23 and 26, we can see that:

$$\overline{R^{+}}T^{+} = \overline{R^{+}}T^{-} = -R^{-}\overline{T^{+}} = -R^{-}\overline{T^{-}}. \tag{30}$$

Accordingly, combining these results, it follows that:

$$\big|R^{+} \pm T^{+}\big| = \big|R^{-} \mp T^{-}\big|. \tag{31}$$

We note that $R+T$ and $R-T$ give the symmetric and antisymmetric wave components, respectively, with respect to $x=0$ and the amplitude is related to the energy of a progressive wave. We can then understand that the energy of the symmetric (antisymmetric) wave component when the incident wave is incoming from the right is equal to the energy of the antisymmetric (symmetric) wave component when the incident wave is incoming from the left. This new finding can be regarded as an extension of the wave-energy splitting theorem to antisymmetric bodies.

For bodies with horizontal symmetry, $R\overline{T} + \overline{R}T = 0$ from Eq. 26 and $|R|^2 + |T|^2 = 1$ from Eq. 28, hence:

$$\left|R + T\right| = \left|R - T\right| = 1. \tag{32}$$

This relation has been known (Kato *et al.*, 1974; Newman, 1975) and implies that the energies of the symmetric and antisymmetric wave components are splitted equally into half of the energy of incident wave.

5. EXPERIMENTS

This study on the development of floating breakwaters started with measurements for the original model shown in Fig. 3, which was proposed by SRI Hybrid Limited. This original model is featured in a simple rectangular shape with small feet projecting vertically downward, which are expected to generate vortices from the tip and thus contribute to dissipation of the energy of incident wave, thus making the transmission wave small.

A floating pier with the section shape of the original model is actually developed, which is restricted to move only in heave by a number of bottom-mounted vertical piles in a real harbor. To simulate this real situation, the experiments in this study were all performed with only the heave motion free, i.e. sway and roll modes are fixed.

To enhance the performance in the wave reflection, horizontal fins are attached to the original model in several styles, as shown in Fig. 3. The dimensions of the original model and attached fins are given in Fig. 4, and Table 1 lists the actual lengths of these dimensions. The incident wave is assumed to be coming from the right, and thus Model-2 in Fig. 3 is equivalent to the case of Model-1 with the incident wave coming from the left. Thus, following the notations above, if the velocity potential for a flow around Model-1 is denoted by ϕ^+, the velocity potential for a flow around Model-2 can be written as ϕ^-.

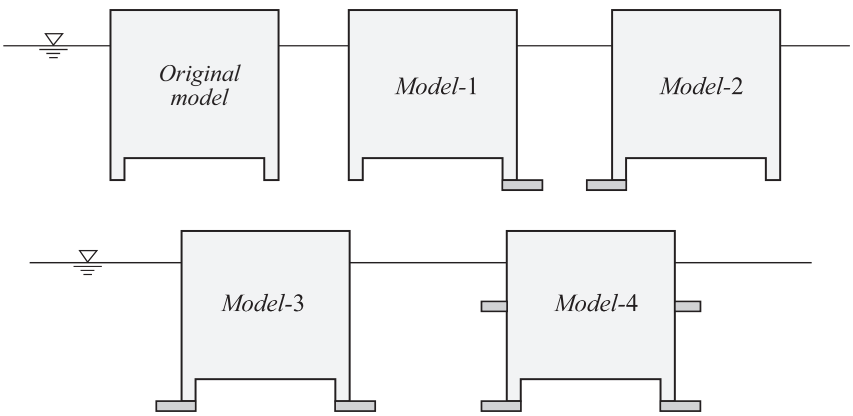

Fig. 3 Shapes of various models of floating breakwaters used in the experiments; incident wave assumed to be from right

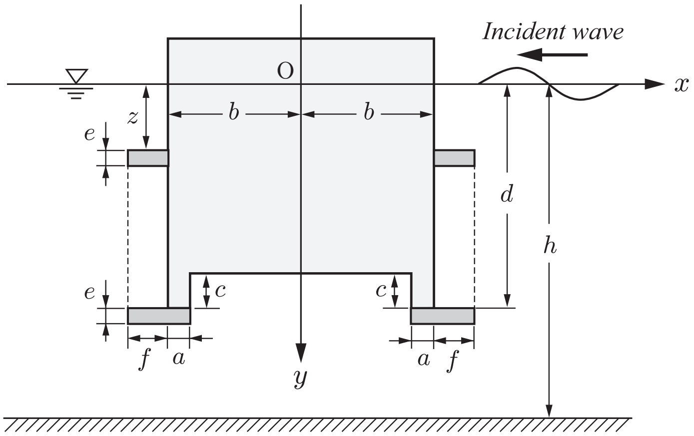

Fig. 4 Coordinate system and notations for various dimensions in the models

The experiments were carried out with the wave channel (10 m long and 0.3 m wide) at the Research Institute for Applied Mechanics of Kyushu University. The heave motion of floating bodies was measured using a potentiometer as the vertical movement of a heaving rod installed in the body, and the transmission wave was measured using a capacitance-type wave probe at a distance from the body. The amplitudes of the heave motion and transmission wave were nondimensionalized with the amplitude of the incident wave, which was measured in advance without a floating body at the position where the models were placed.

Table 1 Dimensions of the tested models and the water depth in the experiments

Notations	Length (mm)
a	22.5
b	150.0
c	37.5
d	247.5
e	10.0
f	30.0, 45.0, 60.0
z	87.5
h	400.0

6. RESULTS AND DISCUSSION

Figure 5 shows the results for the original model; open circles indicate measured results with only the heave motion free, and solid lines show corresponding computed results. For reference, computed values of the transmission coefficients for the cases of all motions (sway, heave, and roll) free and fixed (i.e. diffraction) are indicated by the dotted line and the broken line, respectively. The abscissa is taken as λ_∞/B, where λ_∞ is the wavelength in water of infinite depth, and B is the breadth of the model equal to $2b$ in Fig. 4; thus $\lambda_\infty/B = \pi/Kb$.

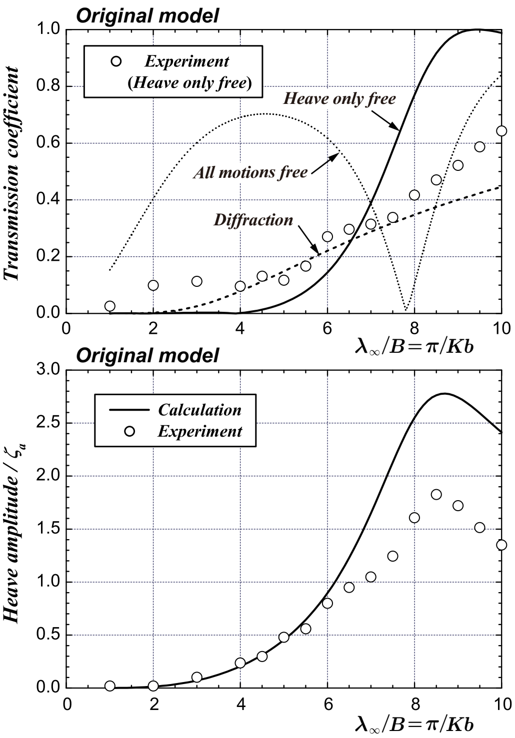

Fig. 5 Nondimensional amplitudes of transmission wave and heave motion of original model

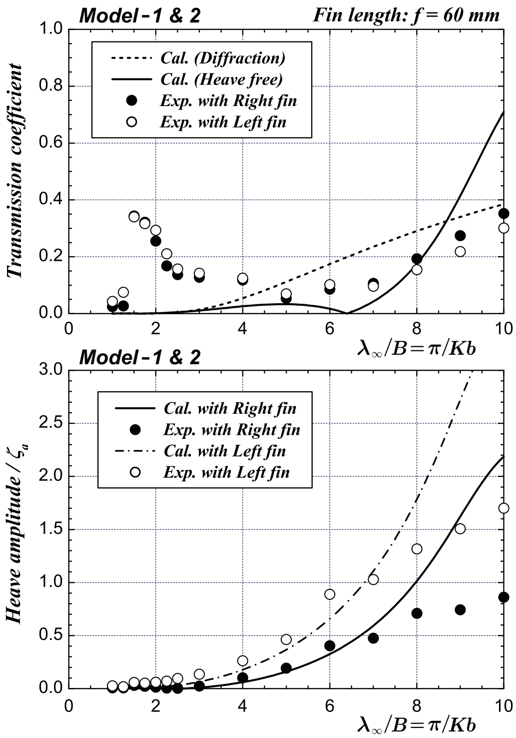

Fig. 6 Nondimensional amplitudes of transmission and heave motion of Model-1 and Model-2 with fin length f = 60 mm

Around the heave resonant frequency, the numerical calculation overpredicts the heave amplitude, which may be attributed to the viscous damping due to vortex shedding from sharp corners. Correspondingly, the transmission coefficient around the heave resonant frequency is overpredicted by the present calculation based on the potential theory. Still, it is obvious from Fig. 5 that the transmission coefficient with the effect of heave motion becomes larger than that for the case of wave diffraction only. We should note that measured values of the transmission coefficient tend to become larger in short wavelengths; this may be due to the effects of little oscillation in sway and roll. (The rigidity of the heaving rod was not enough to completely fix the sway and roll motions, because the heaving rod used was relatively long and flexible.) In fact, this little oscillation in sway and roll was prominent in the measurements in short wavelengths, and as shown by the dotted line, the numerical calculation predicts a larger effect from sway and roll motions on the transmission coefficient. In waves of short wavelength, we can envisage that variation in the pressure may be confined to a fluid layer near the free surface, and thus for a body with the vertical sides, larger motions will be induced in sway and roll rather than in heave.

Figure 6 shows both results of Model-1 and Model-2. As proved theoretically above, the transmission coefficient must be identical even if the left and right shapes of a body are reversed, and this is true for both cases of body motions being fixed and free. Of course, computed results are confirmed to satisfy this so-called reciprocity property, and we can see

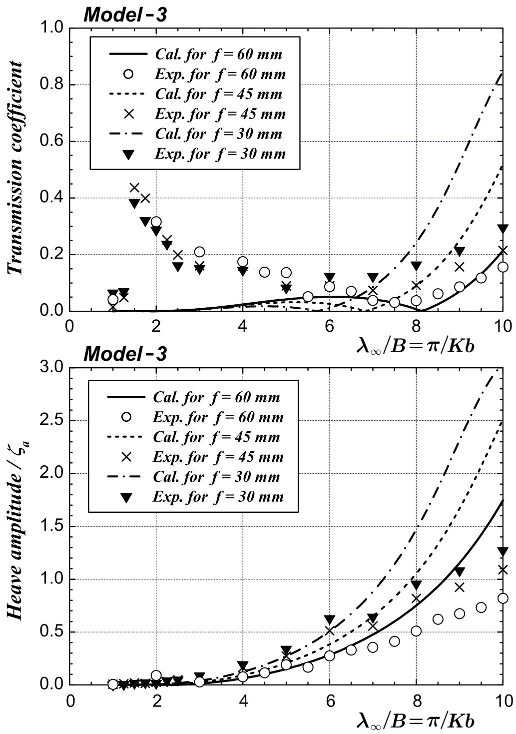

Fig. 7 Nondimensional amplitudes of transmission and heave motion of Model-3 with 3 different fin lengths: $f = 30$, 45 and 60 mm

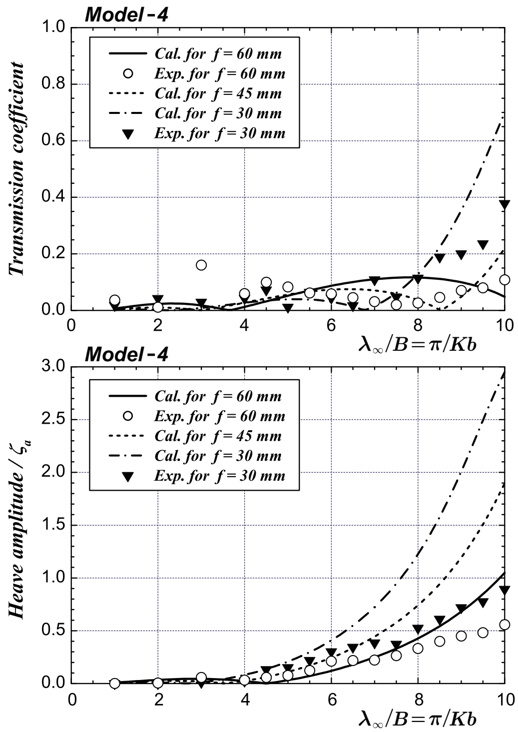

Fig. 8 Nondimensional amplitudes of transmission wave and heave motion of Model-4 with 3 different fin lengths: $f = 30$, 45 and 60 mm

also experimentally from Fig. 6 that the measured results for Model-1 and Model-2 support this reciprocity property. Although the transmission (and reflection) coefficients are the same, Model-1 and Model-2 have different heave amplitudes, and each of the results agrees with the numerical calculation except near the heave-resonant frequency. Large values of the transmission coefficient at shorter wavelengths in Fig. 6 (and Fig. 7 as well) may be attributed to the same reason given for the original body, that is, noticeable oscillation in sway and roll was observed because of a relatively long and thus non-rigid heaving rod.

Another feature to be noted in Fig. 6 is the existence of a frequency at which complete reflection (zero transmission) is realized ($\lambda_\infty/B \simeq 6.4$ for Model-1 and Model-2). Since the transmission coefficient is given by Eq. 6 and only the heave is free in the present case, zero transmission coefficient can be achieved if:

$$1 + iH_4^- = iKX_2^+H_2^- . \tag{33}$$

Physically this means that the radiation wave generated by the heave motion cancels out the diffraction wave at downstream infinity ($x \to -\infty$); that is, both waves are the same in magnitude and opposite in sign. Some authors, e.g. Evans (1975), have studied this subject of complete reflection for symmetric bodies.

As in Fig. 6, if the zero transmission frequency exists in the frequency range of our interest, we can expect reduction of the transmission wave over a wider range of frequencies. It is also interesting to see that the heave motion with a fin attached to the right (weather side) can be smaller than that with the same fin attached to the left (lee side). However, the resonant frequencies in both cases are the same and lower than that of the original model (thus move to the right-hand side in the present figure), because the added mass becomes large, as will be shown later. Fig. 7 shows the result for Model-3 (where the same horizontal fins were attached symmetrically to both sides of small projecting feet), in which 3 fins different in length were tested.

Fundamental features of Model-3 in the transmission coefficient and heave amplitude are the same as those for Model-1 and Model-2, and the wavelength of zero transmission and heave resonance becomes longer with increase in the fin length. Except for large values at shorter wavelengths, numerical computations based on the potential flow account for a tendency in reduction of the wave transmission for different lengths of the attached fin. Among the 3 cases shown in Fig. 7, using twin fins of $f = 60\,\mathrm{mm}$ provides the best overall performance in less wave transmission over the range of wavelengths tested in this study.

In order to see effects of increase in the number of fins, the same 4 horizontal fins were attached to the original model, Model-4 in Fig. 4, and the length of these fins was changed in the same way as for Model-3. Fig. 8 shows the results for this Model-4. (In this case, however, no measured results are available for $f = 45\,\mathrm{mm}$.) In the case of 4 fins, it is apparent from Fig. 8 that there exist 2 different wavelengths at which zero transmission (perfect reflection) is realized. These wavelengths for zero transmission and the wavelength for heave resonance become longer as the fin length increases. From the viewpoint of real construction and installation, a simpler shape and a smaller body size may be preferable, hence an optimal selection seems to exist in the number and size of the fin.

In fact, the transmission coefficient for the case of 4 fins with $f = 60\,\mathrm{mm}$ becomes relatively large near the middle between the 2 frequencies of zero transmission. Thus, among the 3 cases shown in Fig. 8, using 4 fins of $f = 45\,\mathrm{mm}$ appears to be the best on the whole for less wave transmission over the range of wavelengths tested in this study.

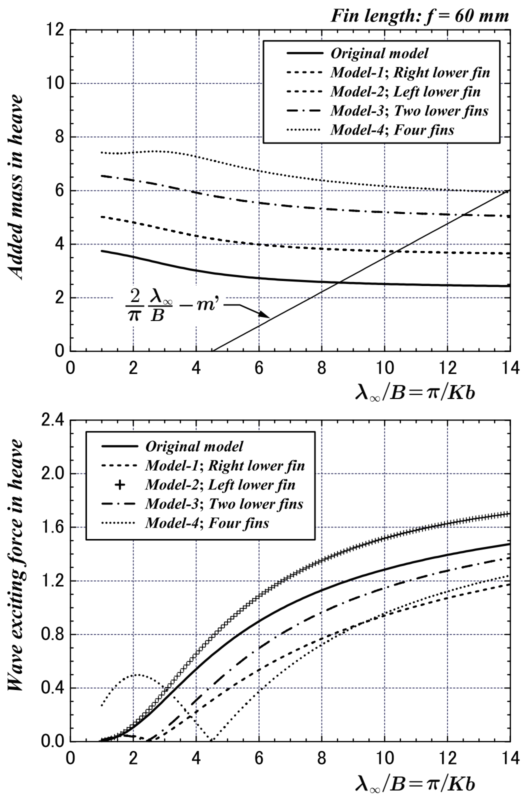

Fig. 9 Added mass and wave-exciting force in heave of various models (fin length: $f = 60\,\mathrm{mm}$)

Figure 9 shows the added mass A_{22} and the wave-exciting force E_2^+ in heave for various models (fin length in Model-1 to Model-4 is $f = 60\,\mathrm{mm}$), for an understanding of a relation between hydrodynamic forces and characteristics in the wave reflection and wave-induced heave motion. A_{22} and E_2^+ are nondimensionalized in terms of ρb^2 and $\rho g \zeta_a b$, respectively. We can see that A_{22} becomes large with an increased number of horizontal fins. A thin solid line with linear increase indicates the value of:

$$\frac{2}{\pi}\frac{\lambda_\infty}{B} - m', \tag{34}$$

where m' is the nondimensional mass of body, hence the cross-point between the thin solid line and each line of A_{22} gives the wavelength of heave resonance for the corresponding model. (To be exact, the value of m' is slightly different depending on the number of fins, but its difference is negligible in the figure.) The wavelength of heave resonance becomes obviously longer with the number of fins, which is a reason of reduction in heave amplitude in the range of $\lambda_\infty/B < 10$.

Another reason for reduction in heave amplitude is the decrease in magnitude of the heave-exciting force shown in the lower figure of Fig. 9. It is noteworthy that the so-called waveless frequency (at which the wave-exciting force becomes zero) exists for bodies with at least one fin attached on the weather side (Model-1, Model-3 and Model-4). At the waveless frequency, Haskind-Newman's relation tells us that:

$$E_2^+ = H_2^+ = 0 \tag{35}$$

is realized, where H_2^+ is the Kochin function associated with the radiated wave at $x = +\infty$ by the forced heave motion. According to Fig. 9, the value of the waveless frequency is different depending on the number of fins, and this value is much different from the heave resonant frequency for the bodies studied in this paper.

As mentioned earlier, zero transmission can be realized if Eq. 33 is satisfied; this is true at one particular frequency for Model-1 to Model-3, in which at least one horizontal fin is attached irrespective of weather or lee location, and at 2 particular frequencies for Model-4, in which twin horizontal fins are attached on the same vertical side. However, these frequencies of zero transmission are generally different from the waveless and heave-resonant frequencies.

Finally, the effect on the transmission coefficient of the vertical position of side fins in Model-4 was numerically investigated by changing the value of z of both side fins; Fig. 10 shows the result. We can see that the value of the zero transmission frequency is not so sensitive to the vertical position of side fins, and the transmission coefficients are very similar for different vertical positions of the side fins. Although the present computations are only for $f = 30$ mm, a conclusion obtained from Fig. 10 is the same for other fin lengths.

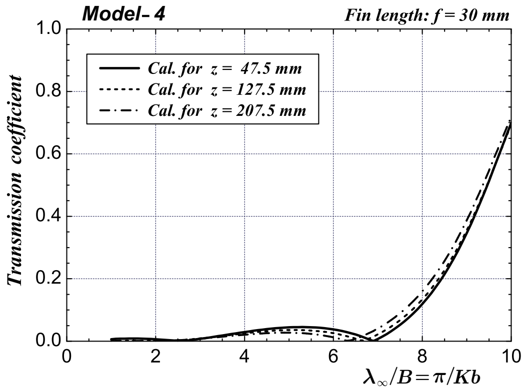

Fig. 10 Effect of the vertical position of side fins in Model-4 on the transmission coefficient (fin length: $f = 30$ mm)

7. CONCLUSIONS

In order to develop floating piers with high performance in the wave reflection, theoretical, numerical, and experimental studies have been carried out for the hydrodynamic characteristics of a flow around 2-D floating bodies heaving in regular waves. Main results obtained in this paper may be summarized as follows:

1) A theoretical proof was provided for the so-called reciprocity property that both of the transmission and reflection coefficients for an antisymmetric body are independent of the incoming direction of the incident wave; this is true irrespective of whether the body motions are fixed or free to oscillate in incident waves. In addition, it was also proved that the energy of the symmetric (antisymmetric) wave component when the incident wave is coming from the right is equal to that of the antisymmetric (symmetric) wave component when the incident wave is coming from the left.

2) With one horizontal fin attached to the right or left bottom part (or twin horizontal fins to both sides of the bottom) of a rectangular body, zero wave transmission can be realized at a certain frequency. By changing the length of a fin, this frequency can be adjusted and thus set to almost the middle in the frequency range of our interest. In this manner, it may be possible to make the transmission wave small over a wide range of frequencies.

3) With 2 horizontal fins attached to upper and lower parts on the same vertical side (or 2 pairs of 2 horizontal fins to both of the vertical sides) of a rectangular body, there exist 2 different frequencies at which zero wave transmission is realized. Thus we can optimize the number, size, and location of horizontal fins with which the wave transmission becomes small over the frequency range of our interest.

4) The heave amplitude can be reduced in the frequency range of our interest by increasing the number of horizontal fins, mainly because the added mass increases, hence the resonant frequency shifts to a lower frequency (longer wavelength).

5) The vertical position of horizontal side fins in Model-4 is not influential in reducing the transmission coefficient, and the length of the fins is more important in changing the frequency of zero transmission.

REFERENCES

1 Bessho, M (1975). “On Time-Reversed Velocity Potentials in the Theory of Water Waves,” *J Kansai Soc of Nav Arch*, No. 159, pp. 75–84.

2 Evans, D V (1975). “A Note on the Total Reflexion or Transmission of Surface Waves in the Presence of Parallel Obstacles,” *J Fluid Mech*, Vol 67, pp 465–462.

3 Haraguchi, T, and Ohmatsu, S (1993). “On an Improved Solution of the Oscillation Problem on Non-wall Sided Floating Bodies and a New Method for Eliminating the Irregular Frequencies,” *Trans West-Japan Soc Nav Arch*, Vol 66, pp 9–23.

4 Kato, N, Kudo, K, Sugita, M, and Motora, S (1974). “A Fundamental Study on the Wave Absorber,” *J Soc of Nav Arch Japan*, Vol. 136, pp. 93–106.

5 Newman, J N (1975). “Interaction of Waves with Two-Dimensional Obstacles: A Relation Between the Radiation and Scattering Problems,” *J Fluid Mech*, Vol. 71, pp. 273–282.

6 Newman, J N (1977). *Marine Hydrodynamics*, The MIT Press, p. 288.

7 Seto, H (1991). “Efficient Evaluation of Some Singular Integrals Appearing in Multipole Expansions in Water of Finite Depth,” *Trans of West-Japan Soc of Nav Arch*, No. 83, pp. 103–113.

8 Seto, H (1992). "Some Expressions of Pulsating Source Potentials in Shallow Water and Their Efficient Algorithm," *Trans of West-Japan Soc of Nav Arch*, No. 85, pp. 25–36.

9 Thorne, R C (1953). "Multipole Expansions in the Theory of Surface Waves," *Proc Cambridge Phil Soc*, Vol 49, pp 707–715.

10 Wehausen, J V, and Laiton, E V (1960). "Surface Waves," *Handbuch der Physik*, Springer-Verlag, Vol 9, p 483.

3-D Effects on Measured Results Using a 2D Model in a Narrow Wave Channel*

Masashi KASHIWAGI
Department of Naval Architecture & Ocean Engineering, Osaka University
2-1 Yamada-oka, Suita, Osaka 565-0871, Japan

Changhong HU
Research Institute for Applied Mechanics, Kyushu University
6-1 Kasuga-koen, Kasuga, Fukuoka 816-8580, Japan

ABSTRACT

The forced oscillation test in heave using a box-shaped floating body was conducted in a narrow wave channel to obtain the added-mass and damping coefficients. When the gap between the sidewalls of the model and the wave channel was 5 mm, measured results showed unnatural variation at higher frequencies, and there was a large discrepancy from computed results by a 2D BEM based on the potential-flow theory. Measured results after lessening the gap from 5 mm to 1 mm became reasonable, but we could still observe noticeable discrepancy and dependency on the oscillation amplitude in the damping coefficient. To understand the hydrodynamic reasons in these observations, numerical computations were performed using a 3D BEM for potential flows and an in-house 2D computer code for nonlinear viscous fluids. We confirmed through comparisons that the unnatural variation observed at higher frequencies for the gap equal to 5 mm was associated with trapped waves generated in the gap, and that the discrepancy in the damping coefficient between the experiment and the computation by BEM was associated with the effect of vortex shedding.

Keywords: Added mass and damping coefficient, 3D effects, viscous effects, forced oscillation test.

1. INTRODUCTION

We are currently concerned with strongly nonlinear wave-body interactions such as a local, green-water impact on deck and its effects on the global motion of a floating body in large-amplitude waves. Numerical calculation methods applicable to such strongly nonlinear problems are being developed at the RIAM (Research Institute for Applied Mechanics) of Kyushu University (e.g. Hu and Kashiwagi, 2006). In particular, the method based on the CIP scheme (Yabe *et al.*, 2001) in a Cartesian grid is named RIAM-CMEN (Computation Method for Extremely Nonlinear hydrodynamics). This computer code has been validated through comparisons with 2D experiments for wave-induced motions of a body including the water-on-deck phenomenon. Although RIAM-CMEN has now been extended to 3D problems and is being validated by comparison with 3D experiments measuring the pressure on

∗ *Reprinted from International Journal of Offshore and Polar Engineering, Vol. 20, No. 1, pp. 1–7, 2010 (March)*

deck and ship motions in waves (Hu and Kashiwagi, 2007), we realized that validation of the code should be made for fundamental components of the hydrodynamic force appearing in the motion equations of a floating body.

The model prepared for 2D experiments was box-shaped under the still-water surface, with a rather small freeboard and a box-shaped upstructure installed on the deck, because we planned to measure a phenomenon of water on deck and its effect on body motions. Using this model, we conducted the forced heave oscillation test to measure the added-mass and damping coefficients in heave. First the experiment was carried out with amplitude of forced heave oscillation set to 10 mm, and the obtained results were unnatural in variation particularly at the higher frequencies of $Ka > 2.0$ (where a is the half-length of a model and $K = \omega^2/g$). Although we did the same experiment with amplitude of forced oscillation lowered to 5 mm, the variation tendency was virtually the same and the results were much different from those computed by a 2D BEM (Boundary Element Method) based on the linear potential theory. Then, before proceeding to a comparison with computation by the 2D version of RIAM-CMEN, we were obliged to study the reasons for the unnatural results obtained in the experiment. Through observation of the wave field around the model, we noticed large-amplitude waves in the gap between the sidewalls of the model and the wave channel, which seemed to be not propagating away from the body. From this observation, we conjectured that the unnatural variation and values in the measured results, particularly at higher frequencies, must be associated with a flow in the gap.

After several trials, the model was modified, attaching a thin plate to both sides of the model, which lessened the gap between the model and wave channel from 5 mm to 1 mm. With this modification of the model, the obtained results were found to be reasonable and close to the computed results by a 2D BEM. In order to understand more clearly the hydrodynamic reasons in this drastic change, we performed numerical computations using a 3D BEM with the method of mirror images to see 3D effects, and the 2D RIAM-CMEN to see viscous effects. A comparison of these results with corresponding experiments seems to be convincing and provides us with a suggestion for carrying out 2D experiments in a wave channel.

This paper is organized as follows. First, the experiment and obtained results are shown in the next section, including a comparison with results computed by a 2D BEM. Next, a brief description is given for the numerical computation methods adopted; that is, a 3D BEM combined with the method of images and the 2D RIAM-CMEN solving the Navier-Stokes equations. Then, the comparison is shown between measured and computed results, and discussions are undertaken on 3D effects related to trapped waves in the gap and viscous effects associated with vortex shedding. Conclusions are summarized last.

2. EXPERIMENT

The forced oscillation test for measuring the heave added-mass and damping coefficients was conducted in a narrow and long wave channel (18 m in length, 0.3 m in width, and 0.4 m in water depth) at the Research Institute for Applied Mechanics of Kyushu University. The model used in the experiment was box-shaped under the still water level, as shown in Fig. 1, and its length and draft are $L = 0.5$ m and $d = 0.1$ m. The model was originally made as the width being $B = 0.29$ m in width, which means that the gap between the sidewalls of the channel and the box-shaped model is $s = 5$ mm on both sides.

In the forced heave oscillation test, the harmonic heave motion $z(t)$ is given, for example, as $z(t) = z_a \cos \omega t$ by a forced oscillation apparatus, where z_a is the amplitude of heave

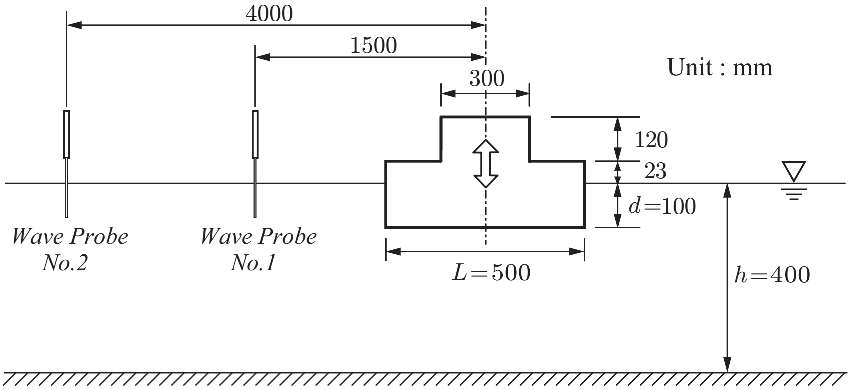

Fig. 1 Dimensions of a tested box-shaped model in a wave channel and the location of wave probes.

and ω the angular frequency of harmonic oscillation. Then the reaction force, say $F(t)$, is measured by a dynamometer and analyzed with the Fourier-series expansion. From the linearized motion equation in heave, the measured reaction force $F(t)$ may be expressed as:

$$F(t) = -\Big\{(m + A_{33})\ddot{z}(t) + B_{33}\dot{z}(t) + C_{33}z(t)\Big\}, \tag{1}$$

where m is the mass of a body and A_{33}, B_{33}, and C_{33} are the added mass, damping coefficient, and restoring-force coefficient, respectively. Since m and $C_{33} = \rho gLB$ are known in advance, the added mass A_{33} and the damping coefficient B_{33} can be obtained by equating the cosine and sine components, respectively, on both sides of Eq. 1.

In addition to the force measurement by a dynamometer, the amplitude of a progressive wave was also measured by a capacitance-type wave probe at 2 different positions shown in Fig. 1. Denoting the amplitude ratio between progressive wave (ζ_a) and heave oscillation (z_a) as $\bar{A} = \zeta_a/z_a$, the principle of energy conservation in the potential-flow theory relates the damping coefficient B_{33} with the progressive-wave ratio $\bar{A}$ in the form:

$$B_{33} = \frac{\rho g^2}{\omega^3}\,\bar{A}^2. \tag{2}$$

A comparison (difference) between 2 different values of B_{33}, one obtained from the direct measurement of the force, and the other from Eq. 2, may provide information on viscous effects.

Obtained results of the added-mass and damping coefficients are shown in nondimensional form in Figs. 2 and 3; these are for the amplitude of forced heave motion equal to $z_a = 5$ mm and 10 mm, respectively. The nondimensional forms of the coefficients are such that:

$$A_{33}/\rho a^2, \quad B_{33}/\rho a^2\sqrt{g/a},$$

where $a = L/2$ is half breadth, and the abscissa is taken as $Ka = \omega^2 a/g$. The solid and broken lines indicate computed results by a 2D BEM using the free-surface Green function which satisfies the linearized boundary conditions on the free surface and bottom of constant finite water depth and also the radiation condition of outgoing waves. Note that the measured results in Figs. 2 and 3 are for the case where the gap between the sidewall of the wave channel and that of box-shaped model is $s = 5$ mm.

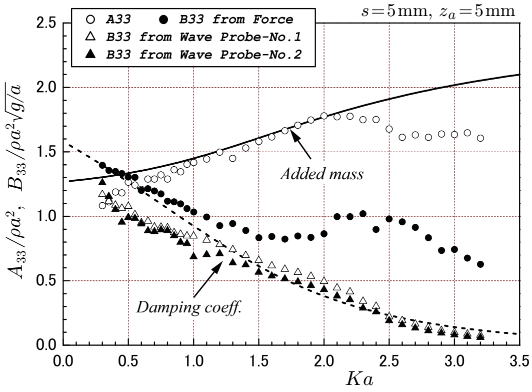

Fig. 2 Heave added-mass and damping coefficients for the case of gap equal to $s = 5$ mm and oscillation amplitude equal to $z_a = 5$ mm. Solid and broken lines are computed results by 2D BEM

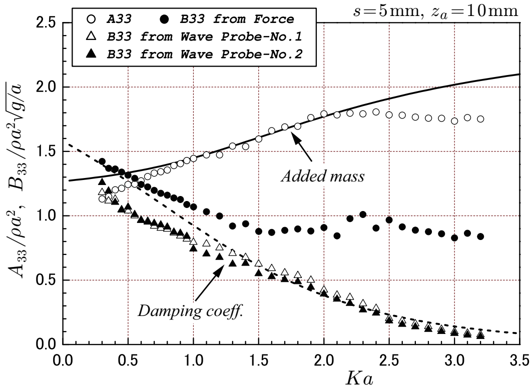

Fig. 3 Heave added-mass and damping coefficients for the case of gap equal to $s = 5$ mm and oscillation amplitude equal to $z_a = 10$ mm. Solid and broken lines are computed results by 2D BEM

We can see that the variation tendency in measured results is the same irrespective of the amplitude of forced heave motion. (Exactly speaking, the damping coefficients obtained by the direct force measurement at $z_a = 10$ mm are larger than those measured at $z_a = 5$ mm at higher frequencies.) More importantly, variation in the added mass and the damping coefficient obtained by the direct force measurement looks unnatural in the frequency range of $Ka > 2.0$. This unnatural variation may not be attributed to viscous effects only. In fact, a tendency to become apart from predicted values by the BEM in the added mass for $Ka > 2.0$ should have nothing to do with viscous effects. In addition, the difference between the damping coefficient obtained by the force measurement and that obtained from the

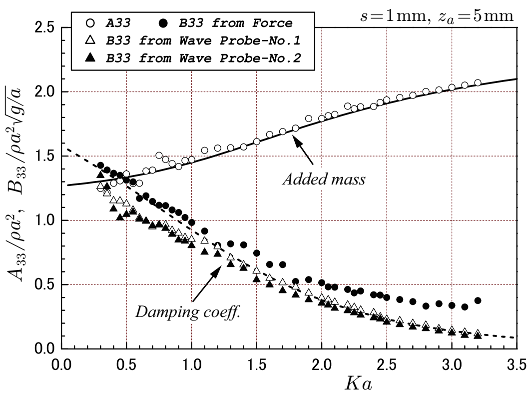

Fig. 4 Heave added-mass and damping coefficients for the case of gap equal to $s = 1$ mm and oscillation amplitude equal to $z_a = 5$ mm. Solid and broken lines are computed results by 2D BEM

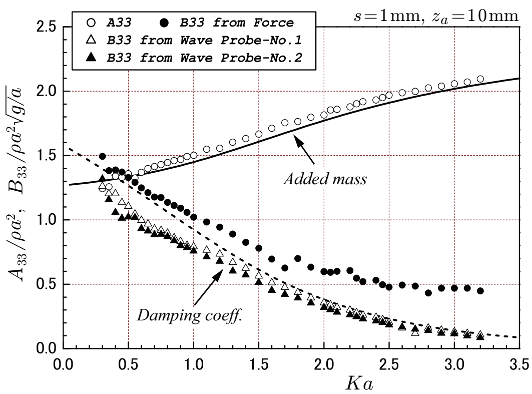

Fig. 5 Heave added-mass and damping coefficients for the case of gap equal to $s = 1$ mm and oscillation amplitude equal to $z_a = 10$ mm. Solid and broken lines are computed results by 2D BEM

energy-conservation principle is too large to explain only with the effect of vortex shedding.

From these results, we envisaged that 3D effects associated with a flow in the gap between the sidewalls of the wave channel and the tested model exist in the results shown in Figs. 2 and 3. In order to confirm this conjecture, the model was modified by attaching to both sides of the model a thin plate 4 mm in thickness and the same in form and size as the side of the model, resulting in the gap being $s = 1\,\mathrm{mm}$. Then the same experiment and analysis were carried out after the modification, and obtained results are shown in Figs. 4 and 5 in the same manner as before. We can see that the added mass agrees with the predicted value by a 2D BEM, and that there is no unnatural tendency at higher frequencies as compared to the case where the gap equals $s = 5\,\mathrm{mm}$. Further, variation in the damping coefficient also looks plausible in that the measured values by a dynamometer are closer to but still larger than the predicted line by a 2D BEM and measured values from the energy-conservation principle.

Comparing the results of $z_a = 5\,\mathrm{mm}$ with those of $z_a = 10\,\mathrm{mm}$, we can see that the damping coefficient by the force measurement becomes larger as the amplitude of forced oscillation increases; this is also plausible when considering that the amount of vortex shedding and its effect on the force depend on the oscillation amplitude (Keulegan-Carpenter number).

In order to understand 3D effects due to a flow in the gap between the model and wave channel and viscous effects due to vortex shedding, we performed numerical computations using a 3D BEM based on the method of mirror images and a 2D CFD method solving the Navier-Stokes equations. Those computation methods are summarized directly below.

3. NUMERICAL COMPUTATIONS

3.1 3-D Higher-Order BEM

As usual in the BEM, the flow is assumed to be incompressible and inviscid with irrotational motion, and then the velocity potential is introduced, satisfying Laplace's equation. The boundary conditions are linearized, and all oscillatory quantities are assumed to be time-harmonic with angular frequency ω.

Since the corresponding experiment is the so-called radiation problem, the velocity potential is expressed in the form:

$$\Phi = \mathrm{Re}\Big[\, i\omega X_j\, \phi_j(x,y,z)\, e^{i\omega t} \Big]. \tag{3}$$

Here X_j denotes the amplitude of forced motion in the j-th mode ($j = 3$ only in the present paper) and ϕ_j the radiation potential due to unit velocity in the j-th mode.

A right-hand Cartesian coordinate system is considered, with the x-y plane taken on the undisturbed free surface, and the positive z-axis taken vertically downward. The origin of the coordinate system is placed at the center of a floating body, and the water depth is assumed constant as in the experiment. Then the boundary conditions to be satisfied are

$$[F] \quad \frac{\partial \phi_j}{\partial z} + K\phi_j = 0 \quad \text{on } z = 0, \tag{4}$$

$$[B] \quad \frac{\partial \phi_j}{\partial z} = 0 \qquad \text{on } z = h, \tag{5}$$

$$[H] \quad \frac{\partial \phi_j}{\partial n} = n_j \qquad \text{on } S_H, \tag{6}$$

$$[W] \quad \frac{\partial \phi_j}{\partial y} = 0 \qquad \text{on } y = \pm(b+s), \tag{7}$$

and the radiation condition of outgoing waves at longitudinal infinity of the wave channel ($x \to \pm\infty$). Here $K = \omega^2/g$ with g the gravitational acceleration, and n_j in Eq. 6 denotes the j-th component of the normal vector, defined as positive when directing out of the body surface (S_H) and into the fluid.

Eq. 7 is the condition of zero normal velocity on the vertical sidewall of a wave channel located at $y = \pm(b+s)$, where $b = B/2$ and s is the gap between the model and the wave channel. In order to satisfy this boundary condition, the method of mirror images is adopted in the present study (see Fig. 6). Since there are vertical sidewalls of the wave channel on both sides of an actual floating body, an infinite number of mirror images must be considered to satisfy exactly the condition of Eq. 7. However, if we will use an ordinary free-surface Green-function method with multiple bodies viewed as a large single body, the number of mirror images must be truncated due to limitation in the number of unknowns and accordingly in the computation time. As shown in Fig. 6, we consider $2M+1$ bodies in total, where $m = 0$ corresponds to the actual body and $m = \pm1, \pm2, \cdots, \pm M$ correspond to mirror-image bodies.

Then from Green's theorem, an integral equation for the velocity potential on the surface of bodies can be obtained in the form:

$$C(\mathrm{P})\phi_j(\mathrm{P}) + \sum_{m=-M}^{M} \iint_{S_m} \phi_j(\mathrm{Q}) \frac{\partial}{\partial n_{\mathrm{Q}}} G(\mathrm{P};\mathrm{Q})\, dS = \sum_{m=-M}^{M} \iint_{S_m} \frac{\partial \phi_j(\mathrm{Q})}{\partial n_{\mathrm{Q}}} G(\mathrm{P};\mathrm{Q})\, dS, \tag{8}$$

where $C(\mathrm{P})$ is the solid angle; $\mathrm{P} = (x, y, z)$ the field point; $\mathrm{Q} = (x', y', z')$ the integration point on the surface of each body denoted as S_m; $G(\mathrm{P};\mathrm{Q})$ is the free-surface Green function

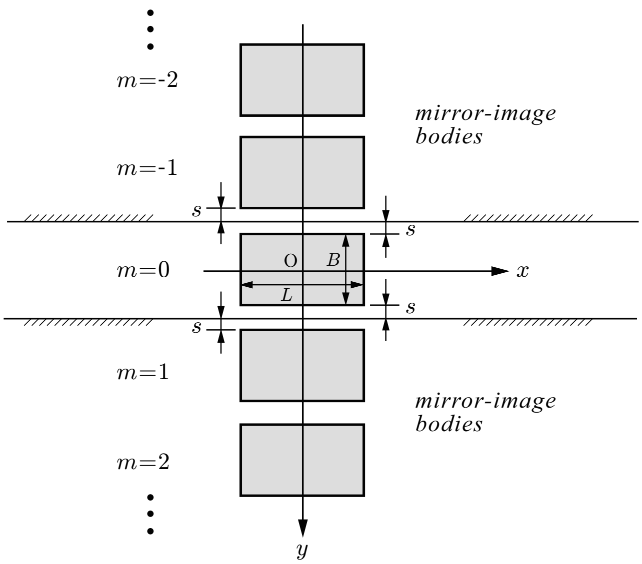

Fig. 6 Notations in the method of mirror images and coordinate system adopted in 3D BEM.

satisfying Eqs. 4 and 5, and the radiation condition for the case of no wave channel. Numerical computations of this Green function for finite water depth were performed using both the power-series expansion and integral expressions, depending on the horizontal distance between P and Q.

The integral equation (Eq. 8) was solved by means of a HOBEM (higher-order boundary-element method), described in Kashiwagi (1995), discretizing the body surface into a large number of quadrilateral panels and representing both body surface and velocity potential on each panel with 9-point quadratic shape functions.

Once the velocity potential ϕ_j on the body surface is determined by solving Eq. 8, the added-mass and damping coefficients in heave of the actual body located in the middle of a wave channel can be computed by:

$$A_{33} - i\,\frac{B_{33}}{\omega} = -\rho \iint_{S_0} \phi_3\, n_3\, dS. \tag{9}$$

Here we should note that the area of integration is just on the surface of the actual body.

In order to reduce the number of unknowns in numerical computations, the so-called

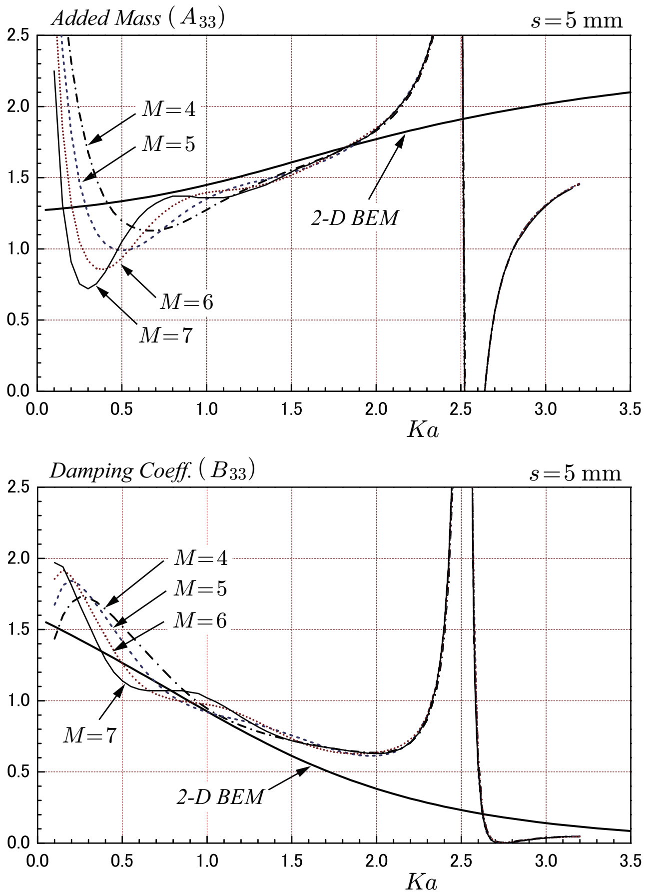

Fig. 7 Convergence check in heave added-mass and damping coefficients computed by 3D BEM with the method of mirror images for the case of gap equal to $s = 5$ mm

double symmetry relations with respect to the x- and y-axes were employed, and thus only a quarter of the total bodies was considered in the panel discretization. Suppose that the numbers of panels in the x-, y-, and z-axes over a quarter of an actual body are Nx, Ny, and Nz, respectively, and the number of mirror images in the positive y-axis is M; then the total number of unknowns are:

$$\left.\begin{aligned} N_T &= N_0 + M \times N_m \\ N_0 &= (Nx+1) \times (Ny+Nz+1) + Ny \times Nz \\ N_m &= N_0 + (Nx+1) \times (Ny+Nz) + (Ny-1) \times Nz \end{aligned}\right\} \tag{10}$$

For the case of $Nx = 10$, $Ny = 6$, $Nz = 4$, and $M = 7$, the total number of unknowns from Eq. 10 will be $N_T = 2070$. In fact, after a convergence check, the number of panels over a quarter of the actual body was fixed to $Nx = 10$, $Ny = 6$, and $Nz = 4$, and then the convergence in the added-mass and damping coefficients, Eq. 9, with increasing the number of mirror images was studied numerically. The results are shown in Fig. 7 for the case of a gap equal to $s = 5$ mm and in Fig. 8 for the case of $s = 1$ mm. We can see from these figures that the results can be regarded as almost converged for the frequency range of $Ka > 1.0$ by

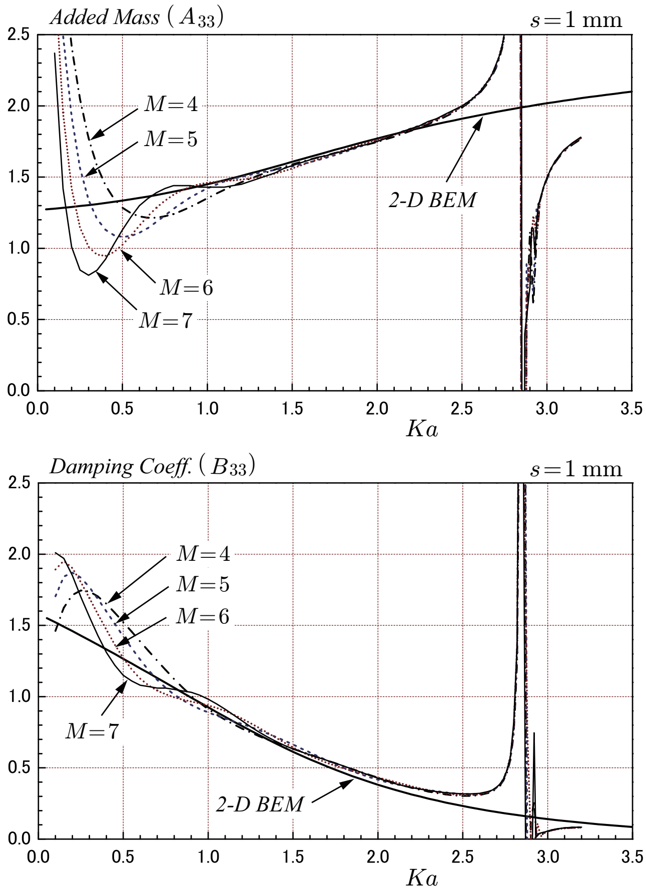

Fig. 8 Convergence check in heave added-mass and damping coefficient computed by 3-D BEM with the method of mirror images for the case of gap equal to $s = 1$ mm.

taking $M = 7$. (In this case the total number of bodies is $2M + 1 = 15$). It should be noted however that the results around $Ka = 2.9$ in Fig. 8 are somewhat sensitive to the frequency and not accurate, because the damping coefficients at those frequencies sometimes become negative. (The value on the entire bodies including mirror images must be positive from consideration of energy conservation principle). Apart from this limited range of frequency for the case of $s = 1\,\mathrm{mm}$, computed results with $M = 7$ will be used in this paper as the results of 3D BEM in comparison with measured results.

3.2 2D CFD Code: RIAM-CMEN

At RIAM (Research Institute for Applied Mechanics) of Kyushu University, efforts have been devoted to develop an in-house computer code which can be applied to strongly nonlinear problems in wave-body interactions. The main feature of this code is that the wave-body interaction is treated as a multi-phase problem with a stationary Cartesian grid. In this kind of method, the free surface must be detected by an interface-capturing scheme, for which the CIP method, initiated by Yabe *et al.* (2001) using a density function is basically adopted. The CFD code developed in this framework is given the code name RIAM-CMEN (Computation Method for Extremely Nonlinear hydrodynamics). Although RIAM-CMEN is extended to 3D problems, the 2D version will be used in the present study for a comparison with results measured in the forced oscillation test.

In this code, an unsteady, viscous and incompressible flow is considered. Then the governing equations for the fluid velocity u_i in the i-th direction and the pressure p are as follows:

$$\frac{\partial u_i}{\partial x_i} = 0, \tag{11}$$

$$\frac{\partial u_i}{\partial t} + u_j \frac{\partial u_i}{\partial x_j} = -\frac{1}{\rho}\frac{\partial p}{\partial x_i} + \frac{1}{\rho}\frac{\partial}{\partial x_j}\left(\mu S_{ij}\right) + f_i, \tag{12}$$

where $S_{ij} = \partial u_i/\partial x_j + \partial u_j/\partial x_i$ is the viscous stress; ρ is the fluid density; μ is the viscosity coefficient; and f_i denotes a body force such as the gravity force, etc. The surface tension is neglected, and no turbulence models are introduced.

To solve Eqs. 11 and 12 with a finite difference method, a Cartesian grid with staggered arrangement of the variables is employed. The calculation of time evolution in Eq. 12 is performed by a fractional step method, with the equation divided into 3 steps:

- advection phase ($q^n \to q^*$);
- first non-advection phase ($q^* \to q^{**}$);
- and second non-advection phase ($q^{**} \to q^{n+1}$),

where q represents the variables to be computed, and $t^{n+1} - t^n = \Delta t$ is the size of one time step.

In the advection phase, only the advection equation is solved with the CIP scheme (Yabe *et al.*, 2001), constructing an interpolation function for the profile of a quantity concerned within a computational cell in terms of a cubic polynomial and using it during the advection with a semi-Lagrangian concept.

In the first nonadvection phase, all terms on the right-hand side of Eq. 12 except for the pressure-related terms are evaluated using an Euler explicit scheme with a central finite difference algorithm. In the second nonadvection phase, coupling between the velocity and the pressure is treated by an implicit scheme. Taking account of the continuity equation, Eq. 11, the following Poisson-type equation can be obtained:

$$\frac{\partial}{\partial x_i}\left(\frac{1}{\rho}\frac{\partial p^{n+1}}{\partial x_i}\right) = \frac{1}{\Delta t}\frac{\partial u_i^{**}}{\partial x_i}. \tag{13}$$

Equation 13 is assumed valid for liquid, gas and solid phases, thus giving the pressure distribution in the whole computation domain.

The interface between water and air is the free surface, which is determined by an interface capturing method. To recognize different phases in a multi-phase flow, we define density functions ϕ_m for liquid ($m = 1$), gas ($m = 2$), and solid ($m = 3$) phases. The density function for a solid body ϕ_3 will be computed first by integrating in time the equations of body motions, thus determining the exact position of the rigid-body surface. Next, the density function for liquid ϕ_1 will be determined by solving the advection equation. Finally, the remaining density function for gas ϕ_2 can be determined from a simple identity $\phi_1 + \phi_2 + \phi_3 = 1$.

The advection equation for ϕ_1 may be solved by using some version of CIP-based schemes. In the present paper, THINC (Tangent of Hyperbola for INterface Capturing) scheme, originally proposed by Xiao *et al.* (2005), is adopted. This scheme is based on a conservative form of the advection equation:

$$\frac{\partial \phi_1}{\partial t} + \frac{\partial (u_j \phi_1)}{\partial x_j} = 0. \tag{14}$$

Hence the conservation of mass may be guaranteed.

The main concept for solution is the same as that in the CIP method, but unlike a higher-order polynomial in the CIP method, a hyperbolic tangent function is used to reproduce a step-like sharp change of ϕ_1 near the free surface. Thus, no spurious oscillation appears in the results. Hu and Kashiwagi (2007) provide more details.

As already described, a floating body is treated as a rigid body. The body surface is approximated using virtual particles, which have the geometrical information of the local area and the normal vector to the body surface. The pressure at a particle can be evaluated by interpolation in terms of the pressures at surrounding grid points. Using the pressure thus obtained and the geometrical information at particles, hydrodynamic forces on the body can be calculated as:

$$F_j = -\iint_{S_H} p\, n_j \, dS, \tag{15}$$

where S_H denotes the wetted portion of the body surface, and n_j is the j-th component of the normal vector.

Once the time history of the hydrodynamic force due to forced heave oscillation is obtained, the added-mass and damping coefficients can be determined by the Fourier-series analysis as in the experiment.

Numerical computations by RIAM-CMEN were performed with a grid of 400×183 (in the horizontal and vertical directions, respectively), in which the minimum grid spacing was 3 mm around the body. The time step size was $\Delta t/T = 1/1000$; T is the oscillation period. The total simulation time was $15T$ and the time history for the last $10T$ was used for the Fourier analysis to calculate the added-mass and damping coefficients.

4. COMPARISON AND DISCUSSIONS

Results computed by a 3D BEM based on the method of mirror images and by the 2D version of RIAM-CMEN are compared with results measured by the experiment. The results for

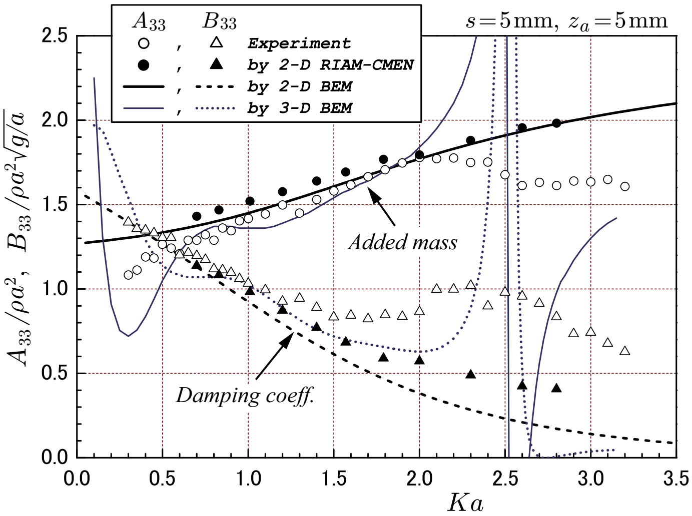

Fig. 9 Comparison of heave added-mass and damping coefficients for the case of gap equal to $s = 5$ mm and oscillation amplitude equal to $z_a = 5$ mm

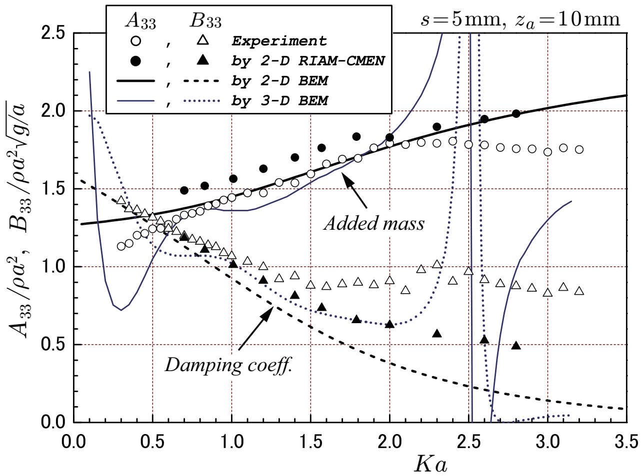

Fig. 10 Comparison of heave added-mass and damping coefficients for the case of gap equal to $s = 5$ mm and oscillation amplitude equal to $z_a = 10$ mm

the gap of $s = 5$ mm are shown in Fig. 9 for the case of oscillation amplitude of $z_a = 5$ mm, and in Fig. 10 for the case of oscillation amplitude of $z_a = 10$ mm. In the same way, the results for the gap of $s = 1$ mm are shown in Figs. 11 and 12 for $z_a = 5$ mm and 10 mm, respectively. Results computed by the 2D and 3D BEMs are the same irrespective of the amplitude of forced oscillation, because they are based on the linear theory. The damping coefficients shown in these comparisons are only the values obtained by the direct force measurement, and they are indicated by open triangles. On the other hand, measured values of the added mass are indicated by open circles.

Results computed by the 3D BEM show a sharp variation around $Ka = 2.5$ for the case of $s = 5$ mm and $Ka = 2.8$ for the case of $s = 1$ mm. This may be attributed to the presence

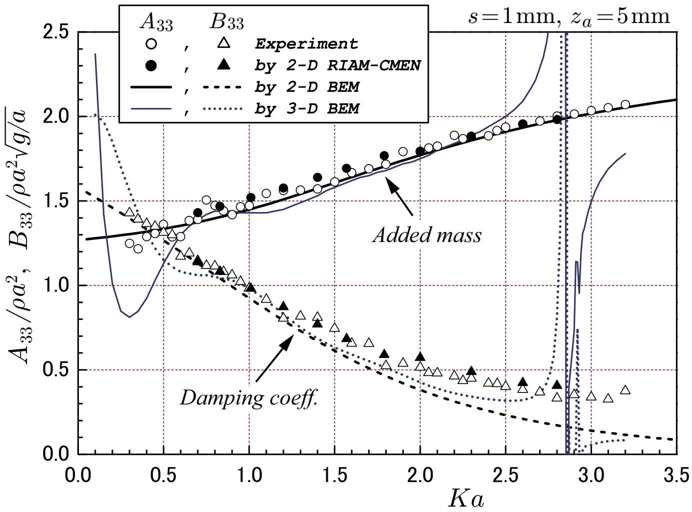

Fig. 11 Comparison of heave added-mass and damping coefficients for the case of gap equal to $s = 1$ mm and oscillation amplitude equal to $z_a = 5$ mm

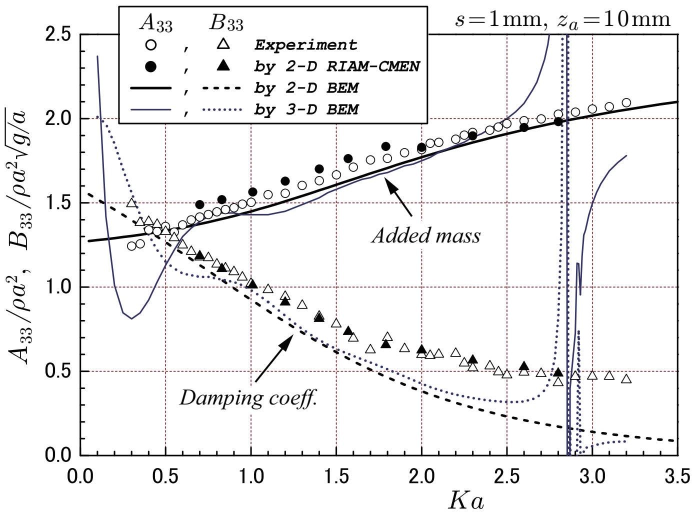

Fig. 12 Comparison of heave added-mass and damping coefficients for the case of gap equal to $s = 1$ mm and oscillation amplitude equal to $z_a = 10$ mm

of trapped wave generated in the gap between the body and the sidewall of the wave channel (Linton and Evans, 1992; Maniar and Newman, 1997). The cut-off frequency to be used for a rough estimation of trapped waves is given by $KB_T = \pi$, where B_T is the width of a channel. In the present case, this estimation gives $Ka = KB_T(a/B_T) = \pi(0.25/0.3) \simeq 2.62$, which seems to correspond to the frequency where a sharp variation is observed in the computed results.

First, looking at Fig. 9, we can see that unnatural variation in the measured results for $Ka > 2.0$ may be explained by the presence of a trapped wave. Of course there is a quantitative difference around the trapped-mode frequency, and the variation in measured results is much milder than that in the results of 3D BEM results. This is partly because the BEM assumes an inviscid fluid with irrotational motion, and viscous effects are ignored. Another reason is that the measurement duration in the experiment was finite to take only a part of the measured data, which was seemingly constant in amplitude, and thus the trapped wave was not fully developed.

At any rate, we may conclude that a large difference between results measured and computed by a 2D BEM can be partly explained by 3D effects due to the existence of the gap between the sidewalls of the model and the wave channel.

A comparison of Figs. 9 and 10 reveals that the damping coefficient at $z_a = 10$ mm shown in Fig. 10 is larger than that at $z_a = 5$ mm shown in Fig. 9, especially for $Ka > 1.0$. This difference can be attributed to the viscous effect due to vortex shedding from sharp corners of the model. In fact, computed results by the 2D RIAM-CMEN include such viscous effects, and the difference from the results of 2D BEM may be regarded as a contribution from viscous effects. Obviously the results computed by the 2D RIAM-CMEN for $z_a = 10$ mm are larger than those for $z_a = 5$ mm, which is an important nonlinear effect. It is interesting to see that the sum of the value by the 3D BEM and the difference between the 2D BEM and RIAM-CMEN becomes almost the same in magnitude as the measured results.

Looking at Figs. 11 and 12 for the case of gap equal to $s = 1$ mm, the difference between results computed computed by 2D BEM and 3D BEM is small except for $Ka < 1.0$ and around the trapped-mode frequency. We note, as described before, that the results of 3D BEM for $Ka < 1.0$ are not converged as the number of mirror images increases up to $M = 7$. No unnatural variation can be seen in measured results around the trapped-mode frequency. This implies that 3D effects are remarkably decreased by lessening the gap from $s = 5$ mm to $s = 1$ mm. In particular, in Fig. 11 for $z_a = 5$ mm, results measured and computed by 2D BEM are in good agreement, and the difference in the damping coefficient can be explained as viscous effects, because results computed by the 2D RIAM-CMEN solving the Navier-Stokes equations agree with measured results.

In Fig. 12 for $z_a = 10$ mm, the measured values of the added mass are slightly larger than the computed values by the BEM, yet relatively in good agreement with the results computed by the 2D RIAM-CMEN. Looking at the damping coefficient shown in Fig. 12, the measured results are obviously larger than those computed by the BEM, and this difference seems to be explained successfully by the 2D RIAM-CMEN, implying that the viscous effects due to vortex shedding are crucial for a box-shaped body and for a case of large amplitude in body motion.

5. CONCLUSIONS

With a model of a box-shaped floating body, we carried out the forced heave oscillation test in a narrow and long wave channel to obtain the data of the heave added-mass and damping coefficients for validating an in-house computer code (RIAM-CMEN) based on CFD techniques. In the original experiment, the gap between the sidewalls of the model and the wave channel was 5 mm. In this case, an unnatural variation was observed in the added mass at higher frequencies, and correspondingly the damping coefficient was too large to attribute only to the effect of vortex shedding. After modifying the model by lessening the gap from 5 mm to 1 mm, we did the same experiment. In this case, the obtained results became reasonable and close to computed results by a 2D BEM. In order to understand hydrodynamic reasons in this drastic change, numerical computations were performed using a 3D BEM with the method of images to see 3D effects, and the 2D RIAM-CMEN to see viscous effects. We found that the unnatural variation at higher frequencies (around $Ka = 2.5$) was associated with the generation of a trapped wave in the gap between the sidewalls of the model and the wave channel (that is, the effect of 3D flow), and that the difference in the damping coefficient between the values obtained by the force measurement and computed by the BEM was associated with the effect of vortex shedding.

From this study, we realized that the gap between the sidewalls of a model and a wave channel must be made small as much as possible in carrying out 2-D experiments using a wave channel, within the extent that the friction and surface tension does not affect the results.

REFERENCES

1 Hu, C and Kashiwagi, M (2006). "Validation of CIP-Based method for Strongly Nonlinear Wave-Body Interactions," *Proc 26th Symposium on Naval Hydrodynamics* (Rome), Vol. 4, pp. 247–258.

2 Hu, C and Kashiwagi, M (2007). "Numerical and Experimental Studies on Three-Dimensional Water on Deck with a Modified Wigley Model," *Proc 9th Numerical Ship Hydrodynamics* (Ann Arbor), Vol. 1, pp. 159–169.

3 Kashiwagi, M (1995). "A Calculation Method for Steady Drift Force and Moment on Multiple Bodies (in Japanese)," *Bulletin of Res Inst for Appl Mech*, Vol. 170, pp. 83–98.

4 Linton, C M and Evans, D V (1992). "Integral Equations for a Class of Problems Concerning Obstacles in Waveguides," *J Fluid Mech*, Vol. 245, pp. 349–365.

5 Maniar, H D and Newman, J N (1997). "Wave Diffraction by a Long Array of Cylinders," *J Fluid Mech*, Vol. 339, pp. 309–330.

6 Xiao, F, Honma, Y and Kono, T (2005). "A Simple Algebraic Interface Capturing Scheme Using Hyperbolic Tangent Function," *Int J Numerical Methods in Fluids*, Vol. 48, pp. 1023–1040.

7 Yabe, Y, Xiao, F and Utsumi, T (2001). "The Constrained Interpolation Profile Method for Multiphase Analysis," *J Comp Physics*, Vol. 169, pp. 556–569.

Effects of Forward Speed of a Ship on Added Resistance in Waves*

Masashi KASHIWAGI†, Takehiro IKEDA‡ and Takuma SASAKAWA†

† Department of Naval Architecture & Ocean Engineering, Osaka University
2-1 Yamada-oka, Suita, Osaka 565-0871, Japan

‡ Akishima Laboratories (Mitsui Zosen), Inc.,
Tsutsujiga-oka, Akishima, Tokyo 196-0012, Japan

ABSTRACT

Despite a large amount of work so far, it is said that the prediction accuracy in the area of added resistance is not enough, particularly in a range of short waves. For engineering purposes, application of the enhanced unified theory (EUT) seems promising for evaluating the ware-amplitude function, which is the most important term in Maruo's formula for the added resistance. To confirm the applicability of the EUT, measurements of the wave-induced ship motions and added resistance are carried out using a modified Wigley model at several Froude numbers, and obtained results are compared with computed ones. Discrepancy in the added resistance is observed at short wavelengths when forward speed is present, and the amount of this discrepancy tends to increase and then become constant as forward speed increases. This discrepancy may be attributed to hydrodynamic nonlinear effects in the wave diffraction at the bow, which may be intensified in the presence of forward speed. A practical factor for correcting this discrepancy, which is to be applied only to the component due to diffraction of an incident wave, is proposed in a form of mathematical function in the Froude number and the ratio of wavelength to ship length.

Keywords: Added resistance, forward-speed effect, enhanced unified theory, wave diffraction, short wavelength.

1. INTRODUCTION

When a ship navigates in waves, the ship's forward speed decreases compared to that in a calm sea because the resistance increases in waves. This increase in resistance is called the added resistance, which is due mainly to unsteady wave making, specifically the wave radiation by ship oscillations and the diffraction of an incident wave on the ship hull. The added resistance caused by the unsteady wave-making phenomenon can be exactly estimated by Maruo's formula (1960) which is based on the principle of momentum and energy conservation. The wave-amplitude function (which is referred to as Kochin function) included in this formula influences greatly the prediction accuracy of the added resistance. The Kochin function consists of 2 wave components: the radiation wave and the scattering wave.

According to various studies so far, the strip-theory method seems to provide sufficient engineering accuracy in a frequency range where the effect of the radiation wave is dominant. On the other hand, the scattering wave generated mainly near the ship bow cannot be

∗ *Reprinted from International Journal of Offshore and Polar Engineering, Vol. 20, No. 3, pp. 196–203, 2010 (September)*

evaluated by the strip theory. Accordingly some practical formulae have been proposed (Fujii and Takahashi, 1975; Faltinsen, 1980) for the component of the added resistance due to bow wave diffraction in short waves. In contrast, the enhanced unified theory (EUT) developed by Kashiwagi (1995a) takes account of the effect of wave reflection at the bow through the body boundary condition in the diffraction problem in the framework of linearized slender-ship theories. In addition, 3D and forward-speed effects ignored in the strip theory are incorporated in the EUT through matching between the inner and outer solutions. Thus we can expect that the EUT can predict the added resistance at least with engineering accuracy over the whole range of wavelengths including short waves. In fact, for the case of zero forward speed, it was confirmed (Kashiwagi, 1995a) that computed results for the wave drift force by the EUT and a 3D panel method agree very well, not only for the diffraction problem but also for the case of all modes of ship motion being free.

However, when the forward speed of a ship exists, the wave diffraction near the ship bow becomes intensified, and hydrodynamic nonlinear effects which are not taken into account in the EUT and Maruo's formula may become prominent, resulting in a relatively large difference between the results of EUT and measurement, especially in short waves.

In order to confirm the degree of agreement in the prediction by EUT and the amount of discrepancy due to the effect of forward speed, we conducted measurements of the added resistance and ship motions using a modified Wigley model at several Froude numbers, including zero speed. Numerical computations are implemented with EUT and NSM (New Strip Method), and also with a 3D HOBEM (Higher-Order Boundary Element Method) for the zero-speed case. Their results are compared with measured ones, from which forward-speed effects on the added resistance are investigated. It is found that the agreement at zero speed between the EUT and the experiment is very good, but when the forward speed of a ship exists, the discrepancy at shorter wavelengths is observed, which tends to increase and then become constant in quantity as the forward speed increases. In order to correct this discrepancy from a practical viewpoint, a correction factor to be applied only to the added-resistance component due to wave diffraction is newly proposed as a function of the Froude number and the ratio of wavelength to ship length.

2. CALCULATION METHOD

2.1 Formulation

Let us consider a ship advancing with constant speed U and oscillating with circular frequency ω in deep water. As shown in Fig. 1, a Cartesian coordinate system moving with the ship is taken, where the x-axis is directed to the ship's bow and the z-axis is directed downward.

With the assumption of linearized potential flow, the velocity potential is introduced and expressed as:

$$\Phi = U\big[-x + \phi_S(x,y,z)\big] + \mathrm{Re}\big[\phi(x,y,z)\,e^{i\omega t}\big], \tag{1}$$

$$\phi = \frac{g\zeta_w}{i\omega_0}\Big\{\phi_0(x,y,z) + \phi_7(x,y,z)\Big\} + \sum_{j=1}^{6} i\omega X_j\,\phi_j(x,y,z), \tag{2}$$

$$\phi_0 = \exp\big\{-k_0 z - ik_0(x\cos\beta + y\sin\beta)\big\} \equiv \psi_0(y,z)\,e^{i\ell x}, \tag{3}$$

$$\omega = \omega_0 - k_0 U\cos\beta,\ \ k_0 = \omega_0^2/g,\ \ \ell = -k_0\cos\beta. \tag{4}$$

Here ϕ_0 denotes the incident-wave potential; ζ_w, ω_0, k_0, β are the amplitude, circular frequency, wavenumber, and incident angle of an incoming regular wave, respectively; g is the gravitational acceleration. ϕ_7 in (2) denotes the scattering potential, and ϕ_j the radiation potential of the j-th mode of motion with complex amplitude X_j ($j = 1$ for surge, $j = 3$ for heave, and $j = 5$ for pitch). ϕ_S in Eq. 1 denotes the steady disturbance potential due to the forward motion of a ship in otherwise calm water.

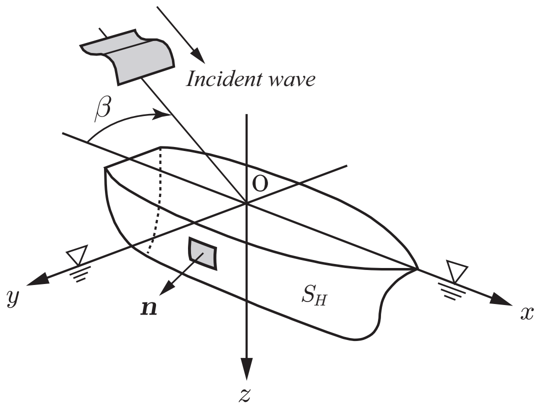

Fig. 1 Coordinate system and notations

In order to obtain numerical solutions for the unsteady velocity potentials represented by ϕ_j ($j = 1 \sim 7$), the EUT is applied in this study. The EUT was developed by Kashiwagi (1995a), extending the unified theory initiated by Newman (1978) and Sclavounos (1984) to include various important terms for the prediction of the added resistance. Related theories are reviewed by Kashiwagi (1997, 2000). Below, we will describe only some important equations for computing the added resistance together with comments which may help the readers.

2.2 Added Resistance by EUT

Once the linearized boundary-value problem for the unsteady velocity potentials have been solved, the added resistance in waves, which is a time-averaged quantity of second order with respect to the amplitude of incident wave, can be computed with Maruo's formula (1960):

$$\frac{R_{AW}}{\rho g \zeta_w^2} = \frac{1}{4\pi k_0}\left[-\int_{-\infty}^{k_1} + \int_{k_2}^{k_3} + \int_{k_4}^{\infty}\right] \times \left\{ \left|H_C(k)\right|^2 + \left|H_S(k)\right|^2 \right\} \frac{\kappa(k)\{k - k_0\cos\beta\}}{\sqrt{\kappa^2(k) - k^2}}\, dk\,, \tag{5}$$

where

$$\left.\begin{aligned} \kappa(k) &= \frac{1}{g}(\omega + kU)^2 = K + 2k\tau + \frac{k^2}{K_0} \\ K &= \frac{\omega^2}{g}\,,\ \tau = \frac{U\omega}{g}\,,\ K_0 = \frac{g}{U^2} \end{aligned}\right\} \tag{6}$$

$$\left.\begin{aligned} k_1 \\ k_2 \end{aligned}\right\} = -\frac{K_0}{2}\left(1 + 2\tau \pm \sqrt{1 + 4\tau}\right) \tag{7}$$

$$\left.\begin{aligned} k_3 \\ k_4 \end{aligned}\right\} = \frac{K_0}{2}\left(1 - 2\tau \mp \sqrt{1 - 4\tau}\right) \tag{8}$$

Here it should be understood that $k_3 = k_4$ for $\tau > 1/4$ and the integration range from k_2 to ∞ in Eq. 5 becomes continuous.

The wave-amplitude functions in Eq. 5, $H_C(k)$ and $H_S(k)$, are given as a superposition of all components of ship-generated progressive waves, where $H_C(k)$ and $H_S(k)$ denote the symmetric and antisymmetric components of the wave, respectively, with respect to the centerplane ($y = 0$) of a ship. Thus, specifically the symmetric component, for example, can be given in the form:

$$H_C(k) = H_7(k) - \frac{\omega\omega_0}{g} \sum_{j=1,3,5} \frac{X_j}{\zeta_w} H_j(k), \tag{9}$$

where $H_j(k)$ is called the Kochin function for the radiation ($j = 1 \sim 6$) and diffraction ($j = 7$) problems. In the slender-ship theory, the symmetric component of the Kochin function can be computed as follows:

$$H_j(k) = \int_L Q_j(x)\, e^{ikx}\, dx \quad (\text{for } j = 1, 3, 5, 7). \tag{10}$$

Here $Q_j(x)$ denotes the strength of the source distribution along the x-axis in the expression of outer solution in the EUT.

This source strength is determined as a solution of an integral equation to be obtained through matching between the inner and outer solutions. The integral equation thus obtained can be expressed as:

$$Q_j(x) + \frac{i}{2\pi}\Big(\frac{\sigma_3}{\sigma_3^*} - 1\Big) \int_L Q_j(\xi)\, f(x-\xi)\, d\xi = \sigma_j(x) + \frac{U}{i\omega}\widehat{\sigma}_j(x) \quad \text{for } j = 1, 3, 5 \tag{11}$$

for the radiation problem (where the asterisk in superscript means the complex conjugate) and:

$$Q_7(x) + \frac{1}{\pi}\sigma_7(x)\Big\{Q_7(x)\, h_C(\beta) - \int_L Q_7(\xi)\, f(x-\xi)\, d\xi\Big\} = \sigma_7(x)\, e^{i\ell x} \tag{12}$$

$$h_C(\beta) = \csc(\beta)\cosh^{-1}(|\sec\beta|) - \ln(2|\sec\beta|)$$

for the symmetric part of the diffraction problem.

The kernel function $f(x-\xi)$ in Eqs. 11 and 12 includes 3D corrections and forward-speed effects, whose detailed expression for $f(x-\xi)$ may be found in Newman and Sclavounos (1980). $\sigma_j(x)$ and $\widehat{\sigma}_j(x)$ in Eq. 11 represent 2D Kochin functions computed from the particular solution of the inner problem, which are essentially identical to the Kochin functions used in the strip-theory method.

The inner solution in the EUT can be given in the form:

$$\begin{aligned} \phi_j(x; y, z) =& \varphi_j(y, z) + \frac{U}{i\omega}\widehat{\varphi}_j(y, z) \\ &+ C_j(x)\big\{\varphi_3(y, z) - \varphi_3^*(y, z)\big\} \quad \text{for } j = 1, 3, 5 \end{aligned} \tag{13}$$

for the radiation problem and

$$\begin{aligned} \phi_7(x; y, z) =& -e^{-k_0 z + i\ell x}\cos(k_0 y \sin\beta) \\ &+ C_7(x)\big\{\psi_{2D}(y, z) + e^{-k_0 z}\cos(k_0 y\sin\beta)\big\}\, e^{i\ell x} \end{aligned} \tag{14}$$

for the symmetric part of the diffraction problem.

The first line on the right-hand side of Eqs. 13 and 14 represents the particular solution, and the second line represents a homogeneous solution with coefficient $C_j(x)$ to be determined through matching between the inner and outer solutions.

We note that the particular solution in the radiation problem is identical to the solution in the strip theory, and ψ_{2D} in the homogeneous component in the diffraction problem is sought to satisfy the body boundary condition of the form:

$$\frac{\partial \psi_{2D}}{\partial n} = k_0\, e^{-k_0 z}\big\{ (n_3 + i n_1 \cos\beta)\cos(k_0 y \sin\beta) + n_2 \sin\beta \sin(k_0 y \sin\beta)\big\} \quad \text{on } S_H(x) \tag{15}$$

where n_j denotes the j-th component of the unit normal vector, and $S_H(x)$ is the sectional contour at station x.

Here it should be emphasized that a contribution of the n_1-term is retained in Eq. 15, with which the wave diffraction from the bow in the ship's longitudinal direction is taken into account in an approximate manner. Retaining this term in the body boundary condition provides a big difference in the pressure distribution near the bow and the resulting wave-exciting force in surge and the added resistance in waves.

The 2D Kochin function $\sigma_7(x)$ appearing in Eq. 12 is computed in terms of ψ_{2D}. Hence, the effect of bow wave diffraction as well as 3D and forward-speed effects are incorporated in the source distribution $Q_7(x)$ as a solution of integral equation Eq. 12 for the diffraction problem. In terms of the source distribution thus obtained, the Kochin function and then the added resistance are computed as shown by Eqs. 10, 9 and 5.

The complex amplitude of the j-th mode of motion X_j, which is needed in computing Eq. 9, is a solution of the coupled motion equations among surge, heave and pitch for the symmetric component. In the EUT, the solution for surge is also given in a form of Eq. 13, including 3D and forward-speed effects through the coefficient of homogeneous component. The hydrodynamic forces (added mass, damping force and exciting force) needed in the motion equations are computed with the inner solution, and thus various effects ignored in the strip theory are also included implicitly through the complex amplitude of ship motion. From these calculation procedures, it may be understood that the added resistance to be computed by EUT is markedly different (at least theoretically) from that to be computed by the strip-theory method.

Unlike a conventional method based on the strip theory, the source distribution is placed just on $z = 0$ as explicitly written by Eq. 10. In this case, it has been believed that the semi-infinite integral with respect to k in Eq. 5 causes a problem in numerical convergence. However, no difficulty arises by using a semi-analytical calculation method proposed by Kashiwagi (1992), and in fact that calculation method is adopted in this study for evaluating the integrals in Eq. 5.

Lastly, for convenience in subsequent discussions, the added resistance to be computed from Eq. 5 is written as a summation of 2 components as follows:

$$R_{AW} = R_{AW}^{(d)} + R_{AW}^{(m)}, \tag{16}$$

where $R_{AW}^{(d)}$ denotes the added resistance computed only with the diffraction solution (namely, the ship motions are completely fixed), and $R_{AW}^{(m)}$ denotes all other contributions concerned with ship motions. We note that $R_{AW}^{(m)}$ involves terms which are quadratic in the radiation wave and cross terms between the radiation and scattering waves.

3. EXPERIMENT

In the experiment which measures the wave-induced ship motions and added resistance, we employed a modified Wigley model which is represented mathematically by the following equation:

$$\eta = (1-\zeta^2)(1-\xi^2)(1+a_2\xi^2+a_4\xi^4)+\zeta^2(1-\zeta^8)(1-\xi^2)^4, \tag{17}$$

where $\xi = x/(L/2)$, $\eta = y/(B/2)$, and $\zeta = z/d$, with L, B, and d the length, breadth, and draft, respectively. a_2 and a_4 are bluntness coefficients, which are taken as $a_2 = 0.6$ and $a_4 = 1.0$ in the tested model. Table 1 shows other principal particulars of the model.

Table 1 Principal particulars of modified Wigley model and values used in the experiment

Length: L (m)	2.500
Breadth: B (m)	0.500
Draft: d (m)	0.175
Displacement: ∇ (m^3)	0.13877
Gyrational radius: κ_{yy}/L	0.236
Center of gravity: $\overline{\mathrm{OG}}$ (m)	0.031
Froude number: Fn	0.0, 0.1, 0.15, 0.2
Wavelength: λ/L	$0.3 \sim 2.0$

We note that this modified Wigley model is rather blunt ($L/B = 5$) and of realistic ship geometry, although it has longitudinal symmetry and no bulbous bow. The experiment was conducted at the towing tank (100 m long, 7.8 m wide, and 4.35 m deep) of Osaka University.

In order to investigate the effect of forward speed, measurements were carried out at several Froude numbers; $Fn = 0.0$, 0.1, 0.15 and 0.2. In the measurements, ship motions were free in surge, heave and pitch, while the model was towed with constant torque exerted by a servomotor so as to keep the model at a time-averaged constant location. The force acting on the model was measured by a dynamometer mounted on the lowest part of the heaving rod. In addition, the heave and pitch motions were measured by a potentiometer, the surge motion was measured by a laser displacement meter, and the incident wave was measured by an ultrasonic wave sensor installed far ahead of the ship model in the towing carriage.

Generated waves were all regular head waves (i.e. $\beta = 180$ deg). Accordingly the encounter circular frequency is given by $\omega = \omega_0 + k_0 U$ with $k_0 = \omega_0^2/g = 2\pi/\lambda$. The wavelength was varied in the range of $0.3 \le \lambda/L \le 2.0$. The amplitude of the incident wave was chosen such that ζ_w/λ is about 1/60 for $\lambda/L \le 0.7$ and ζ_w is about 0.03 m for $\lambda > 0.7$.

Measured data were Fourier-analyzed, and the first-harmonic quantities of the wave frequency were expressed in terms of the amplitude and the phase difference with time reference $t = 0$ taken when the trough of the incident wave was midship. The added resistance in measurement (R_{AW}) is defined as the difference between the time-averaged steady component of the wave-induced unsteady force expressed with Fourier-series expansion (F_0) and the resistance measured in still water (R_S), that is:

$$R_{AW} = F_0 - R_S\,. \tag{18}$$

4. RESULTS AND DISCUSSIONS

4.1 Case of Zero Forward Speed

In the preceding study on the added resistance based on the strip-theory method, the added resistance (referred to as the drift force for the zero-speed case) due to wave reflection from the bow part has been evaluated by a practical formula such as

$$R_{AW}^{(d)} = \frac{1}{2}\rho g \zeta_w^2 \,\alpha_1 B \mathcal{B}_f, \tag{19}$$

which was proposed by Fujii and Takahashi (1975) as a modification of the result of Havelock (1940) for the drift force on a bottom-mounted vertical cylinder in very short waves. $\mathcal{B}_f$ in Eq. 19 is called the bluntness factor, which can be computed only with the shape of the water plane of a body concerned. Coefficient α_1 is the so-called finite-draft effect, and it is given from the reflection-wave coefficient (Ursell, 1947) by a vertical plate of draft d in the form:

$$\alpha_1 = \frac{\pi^2 I_1^2(k_0 d)}{\pi^2 I_1^2(k_0 d) + K_1^2(k_0 d)}\,. \tag{20}$$

where $I_1(k_0 d)$ and $K_1(k_0 d)$ denote the first kind and second kind of modified Bessel functions of order one, respectively.

Today, at least for the case of zero forward speed, 3D panel methods can be applied with high reliability to predict the drift force irrespective of the wavelength and body geometry. Furthermore, it is relatively easy to compute not only the component of the drift force due to wave diffraction but also other components related to a ship's wave-induced motions.

On the other hand, numerical computations in this paper are based on the EUT and thus it is informative to check to what extent the drift force predicted by the EUT, agrees with that by a 3D panel method. If good agreement exists, there is no need to use a classical formula like Eq. 19, and no need to introduce a correction factor like Eq. 20, at least for the zero-speed case.

In this paper, to maintain good accuracy, the HOBEM described in Kashiwagi (1995b) was employed as a 3D panel method. In this HOBEM, the body surface is discretized into a large number of quadrilateral panels, and both the body surface and velocity potential on each panel are represented with 9-point quadratic shape functions. The normal vector is computed by using differentiation of the shape function and the coordinates of a panel under consideration, and the velocity potential on the body surface is determined directly by solving an integral equation for that. The irregular frequencies are removed by considering a few additional field points on the interior free surface of a floating body. The Kochin function needed in applying Maruo's formula is evaluated in terms of the velocity potential and its normal derivative on the body surface.

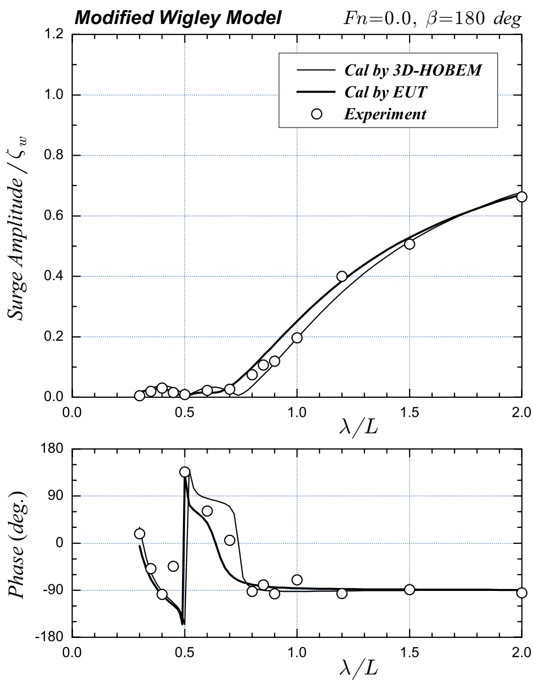

Fig. 2 Surge motion of modified Wigley model in head waves at zero forward speed

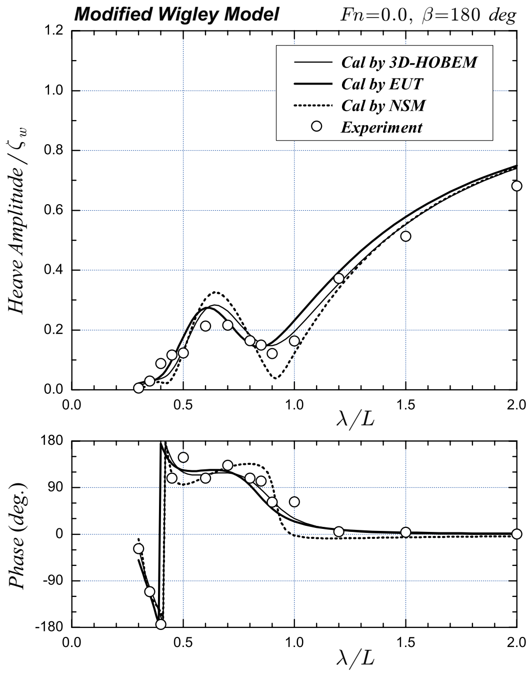

Fig. 3 Heave motion of modified Wigley model in head waves at zero forward speed

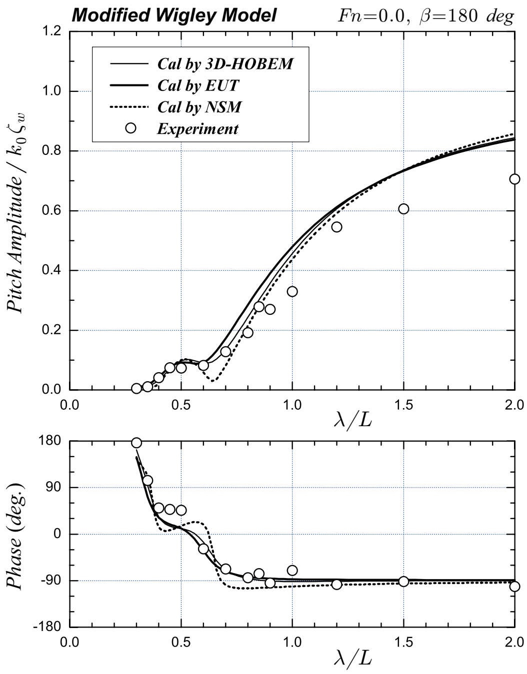

Fig. 4 Pitch motion of modified Wigley model in head waves at zero forward speed

Comparisons of surge, heave, and pitch motions are shown in Figs. 2, 3 and 4, respectively, for the nondimensional amplitude and the phase lead with reference to the incident wave. The results of the 3D HOBEM and the EUT are indicated by thin and thick solid lines, respectively. For reference, the results by the NSM (New Strip Method) for heave and pitch are indicated by a broken line. By comparison, we can see favorable agreement between the EUT and 3D HOBEM and also with measured values shown by open circles.

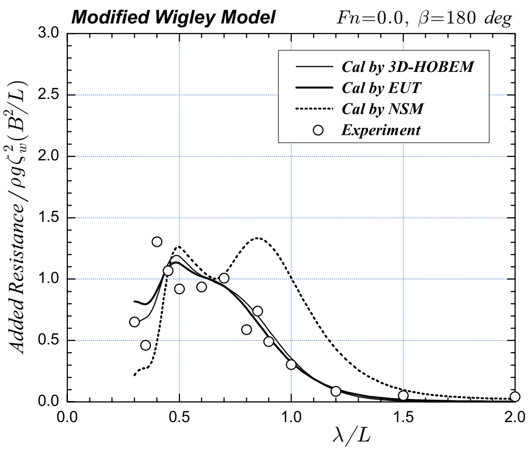

Fig. 5 Wave drift force on modified Wigley model in head waves at zero forward speed

Figure 5 shows the result of comparison for the drift force (the added resistance at $Fn = 0.0$). Although the drift force is a 2nd-order quantity with respect to the incident-wave amplitude, the agreement between the EUT and 3D HOBEM and also with measured results is good from a practical point of view.

From these comparisons, we can confirm that the EUT provides almost the same degree of accuracy as the 3D HOBEM in the prediction of not only 1st-order but also 2nd-order quantities for the zero-speed case.

4.2 Case of Nonzero Forward Speed

Because 3D panel methods for the case of nonzero forward speed are generally time-consuming and still not reliable, in this paper computed results by EUT are compared with measured results in the experiment.

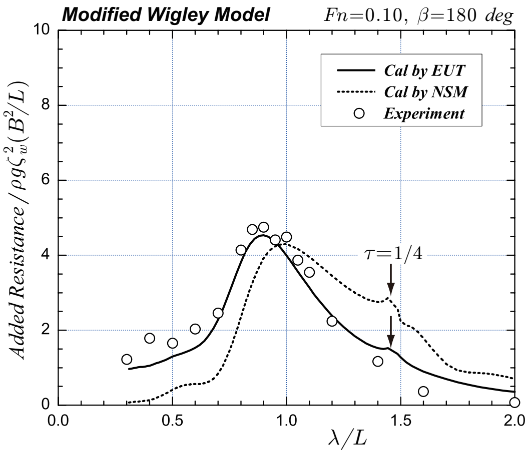

Fig. 6 Added resistance on modified Wigley model in head waves at $Fn = 0.10$

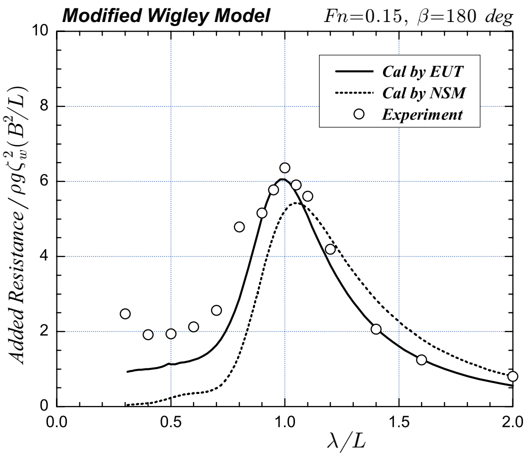

Fig. 7 Added resistance on modified Wigley model in head waves at $Fn = 0.15$

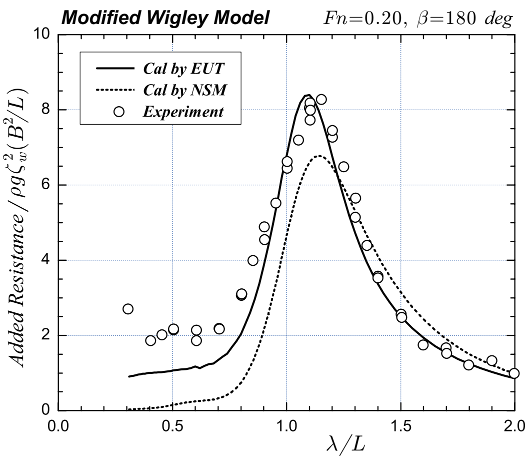

Fig. 8 Added resistance on modified Wigley model in head waves at $Fn = 0.20$

The results of comparison at $Fn = 0.1$, 0.15, and 0.2 are shown in Figs. 6, 7 and 8, respectively. For reference, computed results by the NSM are also shown with a broken line in each figure. Note that for the case of $Fn = 0.1$, a special wavelength corresponding to $\tau = U\omega/g = 1/4$ exists within the range of the wavelength tested, specifically at $\lambda/L = 1.465$.

We can see that the maximum value of the added resistance increases with increasing forward speed of a ship and the wavelength at which the added resistance takes a maximum becomes longer as the forward speed of a ship increases. (This is because the resonance frequency in ship motions shifts to a longer wavelength as the forward speed increases on account of a Doppler effect.) These characteristics are well accounted for by the EUT, and the degree of agreement with measured values looks good except in the range of short wavelengths. It should be noted that the amount of discrepancy in this short-wavelength range is not so large for the case of $Fn = 0.1$ but tends to increase as the Froude number increases.

Considering that the agreement of the results of the EUT with those of 3D HOBEM and experiment is favorable for the zero-speed case, this discrepancy at short wavelengths must be attributed to some forward-speed effects associated with diffraction of an incident wave near the bow, such as the energy dissipation due to wave breaking which is not taken into account in Maruo's theory for the added resistance and cannot be accounted for by a linear theory like the EUT.

Notwithstanding a discrepancy mentioned above, it is obvious from a comparison with computed results by NSM that the results of the EUT can partially account for the effect of wave reflection at the bow simply by retaining a contribution of the x-component of the normal vector in the body boundary condition for the diffraction problem.

4.3 Correction of Forward-Speed Effect

In the Fujii-Takahashi formula for the component of added resistance due to wave diffraction, a correction for the forward-speed effect is incorporated with coefficient α_2 in the form:

$$\left.\begin{aligned} &R_{AW}^{(d)} = \frac{1}{2}\rho g \zeta_w^2\, \alpha_1 \big(1+\alpha_2\big) B \mathcal{B}_f \\ &\alpha_2 = 5.0\sqrt{Fn} \end{aligned}\right\} \tag{21}$$

This coefficient α_2 represents the effect of forward speed, but the dependency on Fn (function form and its coefficient) may change depending on ship-hull forms. In fact, Takahashi (1987) modified slightly the coefficients in α_1 and α_2 after checking existing experimental data, and some other data (e.g. Kuroda *et al.*, 2008) seem to support a linear dependency in Fn, that is, $\alpha_2 \propto Fn$ at least at smaller Froude numbers.

A close look at the present results (Figs. 6–8) for a modified Wigley model reveals that, as already described, discrepancy can be seen only in a shorter-wavelength region where ship motions are small. The amount of discrepancy is small at a lower Froude number and tends

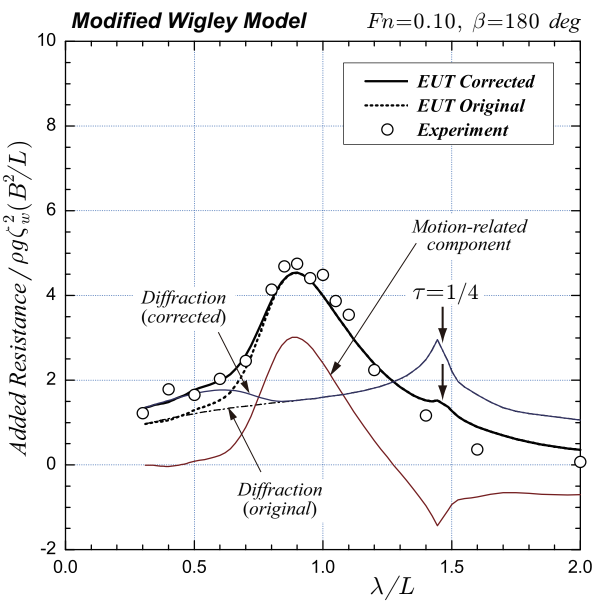

Fig. 9 Components in the added resistance and comparison between computed results by EUT with correction and measured results for modified Wigley model in head waves at $Fn = 0.10$

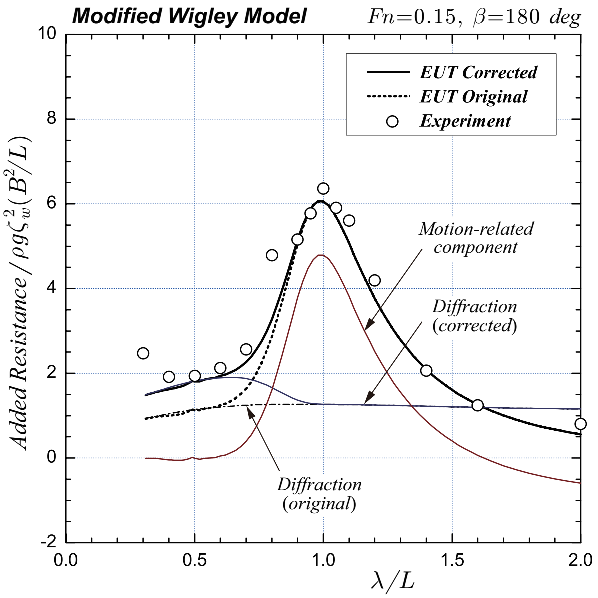

Fig. 10 Components in the added resistance and comparison between computed results by EUT with correction and measured results for modified Wigley model in head waves at $Fn = 0.15$.

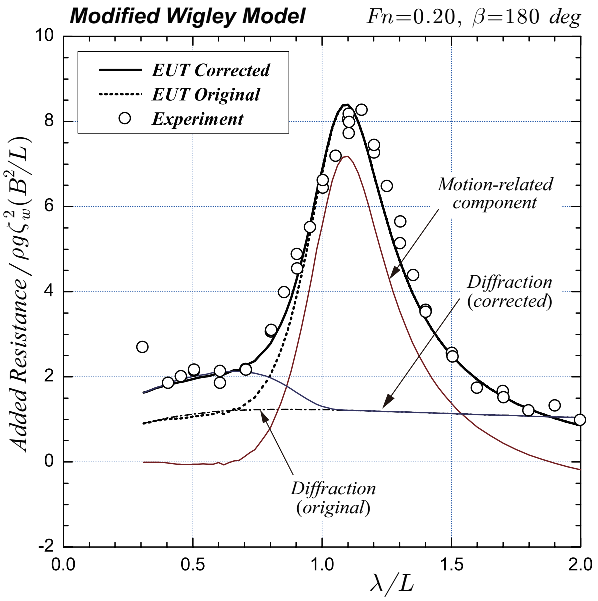

Fig. 11 Components in the added resistance and comparison between computed results by EUT with correction and measured results for modified Wigley model in head waves at $Fn = 0.20$.

to increase and then approach a constant value with increasing the forward speed. Further, this discrepancy attenuates rapidly as the effects of ship motions become dominant.

Taking account of these tendencies, we consider a correction only for the component of added resistance due to wave diffraction $R_{AW}^{(d)}$ and propose the following correction formula:

$$R_{AW} = \big(1+f\big)R_{AW}^{(d)} + R_{AW}^{(m)} \tag{22}$$

where

$$f = 4\tanh(Fn)\exp\left\{-0.02\,\frac{(\lambda/L)^{10}}{Fn^3}\right\} \tag{23}$$

The coefficients and the order of polynomials appearing in Eq. 23 are determined by trial and error such that the result of Eq. 22 matches the measured results in this study.

The results obtained by Eq. 22 are shown by thick, solid lines in Figs. 9, 10 and 11 for $Fn = 0.1$, 0.15 and 0.2, respectively. The original results by EUT are indicated by a broken line. For reference, the original component due to wave diffraction $R_{AW}^{(d)}$ is indicated by a dash-dotted line, and the sum of all contributions related to ship motions $R_{AW}^{(m)}$ is indicated by thin solid line.

We can see from Figs. 9∼11 that corrected values according to Eq. 22 agree very well with measured ones. (This is natural, because the correction factor in Eq, 23 is determined in that fashion.) However, it should be pointed out that the coefficients in Eq. 23 are determined only from the experimental data for a modified Wigley model and basic computations for the components in Eq. 22, $R_{AW}^{(d)}$ and $R_{AW}^{(m)}$, are performed using the EUT. Therefore, if a correction is considered on the basis of computations by the NSM or equivalent methods like the Fujii-Takahashi formula, the resulting correction factor will be obviously different from Eq. 23. However, it may be worth noting that, as seen in Figs 5∼8, computed results by the NSM for a modified Wigley model are different from the measured ones not only at short wavelengths but also at longer wavelengths. This implies that the Fujii-Takahashi formula combined with the strip-theory method may not conform to the experimental results presented in this paper.

5. CONCLUSIONS

In order to investigate applicability of the EUT to the prediction of the added resistance, particularly for short waves, we have conducted experiments using a modified Wigley model at a number of forward speeds (including zero speed), and the measured results were compared with computed ones by the EUT. For the zero-speed case, a 3D HOBEM which can give an exact solution in the framework of linearized potential theory has also been applied, and its computed results were compared with corresponding ones by the EUT. The results obtained in this study may be summarized as follows:

- For the zero-speed case, good agreement was confirmed between the EUT and 3D HOBEM and also with measured results not only for the 1st-order ship motions but also for the 2nd-order wave drift force (the added resistance at zero forward speed). No correction is then needed for the prediction of the added resistance by the EUT.
- As the forward speed of a ship increases, the maximum value of the added resistance increases, and the wavelength at which the added resistance takes a maximum becomes longer on account of a Doppler effect.
- At shorter wavelengths where ship motions are small, discrepancy in the added resistance could be observed between computed results by the EUT and measured results. The amount of this discrepancy is small at a lower speed and tends to increase and then approach a constant value with increase of the forward speed. As the ship-motion

effects become dominant, the discrepancy observed at shorter wavelengths becomes small rapidly.

- A correction factor for this discrepancy was proposed as a function of Fn and λ/L and applied to the diffraction component computed by the EUT for the case of fixed ship motions. The results corrected with this correction factor are naturally in good agreement with measured results in this study.

The applicability of the correction formula presented in this paper to other hull forms must be confirmed and modified if necessary, which is left to future work.

REFERENCES

1 Faltinsen, O M, Minsaas, K J, Liapis, N and Skjordal, S O (1980). "Prediction of Resistance and Propulsion of a Ship in a Seaway," *Proc 13th Symp on Naval Hydrodyn, Tokyo*, pp 505–529.

2 Fujii, H and Takahashi, T (1975). "Experimental Study on the Resistance Increase of a Large Full Ship in Regular Oblique Waves (in Japanese)," *J Soc Nav Arch Japan*, Vol 137, pp 132–137.

3 Havelock, T H (1940). "The Pressure of Water Waves upon a Fixed Obstacle," *Proc Royal Soc London*, Series A, No 963, Vol 175, pp 409–421.

4 Kashiwagi, M (1992). "Added Resistance, Wave-Induced Steady Sway Force and Yaw Moment on an Advancing Ship," *Ship tech Res*, Vol 39, No 1, pp 3–16.

5 Kashiwagi, M (1995a). "Prediction of Surge and Its Effect on Added Resistance by Means of the Enhanced Unified Theory," *Trans West-Japan Soc Nav Arch*, No 89, pp 77–89.

6 Kashiwagi, M (1995b). "A Calculation Method for Steady Drift Force and Moment on Multiple Bodies (in Japanese)," *Bulletin Res Inst Appl Mech, Kyushu Univ*, Vol 170, pp 83–98.

7 Kashiwagi, M (1997). "Numerical Seakeeping Calculations Based on the Slender Ship Theory," *Ship Tech Res*, Vol 44, No 4, pp 167–192.

8 Kashiwagi, M (2000). "The State of the Art on Slender-Ship Theories of Seakeeping," *Proc 4th Osaka Colloquium on Seakeeping Performance of Ships*, pp 11–25.

9 Maruo, H (1960). "Wave resistance of a ship in regular head seas," *Bulletin of the Faculty of Eng, Yokohama National Univ*, Vol 9, pp 73–91.

10 Newman, J N (1978). "The theory of ship motions," *Advances in Applied Mechanics*, Vol 18, pp 221–283.

11 Newman, J N and Sclavounos, P D (1980). "The Unified Theory of Ship Motions," *Proc 13th Symp on Naval Hydrodyn, Tokyo*, pp 373–394.

12 Sclavounos, P D (1985). "The diffraction of free-surface waves by a slender ship," *J Ship Res*, Vol 28, No 1, pp 29–47.

13 Takahashi, T (1988). "A Practical Prediction Method of Added Resistance of a Ship in Waves and the Direction of Its Application to Hull Form Design (in Japanese)," *Trans West-Japan Soc Nav Arch*, No 75, pp 75–95.

14 Ursell, F (1947). "The Effect of a Fixed Vertical Barrier on Surface Waves in Deep Water," *Proc Phil Soc*, Vol 42, pp 374–382.

Hydrodynamic Study on Added Resistance Using Unsteady Wave Analysis*

Masashi KASHIWAGI
Department of Naval Architecture & Ocean Engineering, Osaka University
2-1 Yamada-oka, Suita, Osaka 565-0871, Japan

Abstract

It is known that the added resistance in waves can be computed from ship-generated unsteady waves through the unsteady wave analysis method. To investigate the effects of nonlinear ship-generated unsteady waves and bluntness of the ship geometry on the added resistance, measurements of unsteady waves, wave-induced ship motions, and added resistance were carried out using two different (blunt and slender) modified Wigley models. The ship-generated unsteady waves are also produced by the linear superposition using the waves measured for the diffraction and radiation problems and the complex amplitudes of ship motions measured for the motion-free problem in waves. Then a comparison is made among the values of the added resistance by the direct measurement using a dynamometer and by the wave analysis method using the Fourier transform of measured and superposed waves. It is found that near the peak of the added resistance where ship motions become large, the degree of nonlinearity in the unsteady wave becomes prominent, especially at the forefront part of the wave. Thus, the added resistance evaluated with measured waves at larger amplitudes of incident wave becomes much smaller than the values by the direct measurement and by the wave analysis with superposed waves or measured waves at smaller amplitude of incident wave. Discussion is also made on the characteristics of the added resistance in the range of short incident waves.

Keywords: Added resistance, unsteady wave analysis, Fourier transform, linear superposition, nonlinear effects.

1. Introduction

When a ship navigates in waves, the resistance on the ship increases compared with that in calm water. This increase of resistance is called added resistance. Because accurate estimation of the added resistance is important and essential for evaluating the ship performance in actual seas, a large number of work has been made so far on this topic. It is well known by virtue of Maruo's (1960) work that the dominant component in the added resistance is the one resulting from unsteady disturbance waves generated by a ship and their interaction with incident waves. Maruo's theory is based on what we call the far-field method considering the energy and momentum flux of diffracted and radiated waves at a large distance from the ship. With the same approach, Gerritsma and Beukelman (1972) proposed a simpler calculation method in terms of strip-theory results, which has been applied by many other researchers using different versions of the strip-theory method; e.g., by Salvesen (1974) using the STF strip theory (Salvesen *et al.* 1970). The added resistance can also be

* *Reprinted from Journal of Ship Research, Vol. 57, No. 4, pp. 220–240, 2013 (December)*

computed by the near-field method as the time-averaged second-order force in the incident-wave amplitude by direct pressure integration on the wetted surface of a ship. For instance, Faltinsen *et al.* (1980) introduced the near-field method together with a simplified formula for the added resistance to be applied in a short-wave length region. Theoretically, computed results by the near- and far-field methods must be identical as long as the potential-flow formulation is used assuming the inviscid flow with irrotational motion. However, generally some discrepancies may exist between the two methods because of numerical inaccuracy and approximations in each method. In an actual fluid, there must be a difference, because the results by the near-field method based on the direct pressure integration must include other components related to the energy loss resulting from fluid viscosity and wave breaking. However, it has not been made clear how much in the added resistance is associated with the energy loss resulting from fluid viscosity and wave breaking. Furthermore, even for the wave-making component, details in the hydrodynamic relation between the added resistance and ship-generated unsteady waves seem to be still unclear, because in most of the past work, e.g., Kashiwagi *et al.* (2010), computed values by the potential-flow theory for the wave-making component in the added resistance have been compared with the total value of the added resistance measured directly by a dynamometer.

On the other hand, Ohkusu (1977, 1980, 1984) proposed a method for measuring ship-generated unsteady waves and then evaluating the wave amplitude function (known as the Kochin function) and the added resistance. This analysis method enables us to compare the wave profile and to take out only the wave-making component from the total added resistance and thus may provide us with deeper understanding on hydrodynamic relations. However, accurate measurement of unsteady waves including higher-order nonlinear components is not so easy and subsequent analyses for the Fourier transform of the wave elevation and for the added resistance have not been made in an accurate and convincing manner.

The present study is intended to evaluate the magnitude of unsteady wave-making component in the added resistance, to understand hydrodynamic relations of the added resistance with ship disturbance waves (for instance, which component or which part of unsteady waves is dominant in the added resistance), to elucidate nonlinear effects in ship-generated unsteady waves on the added resistance, to investigate the effect of bluntness in the ship geometry, and so on. For that purpose, experiments are conducted for measuring ship-generated unsteady waves (including second-order second-harmonic components) for three canonical cases of the diffraction problem (where all modes of ship motions are fixed except for the steady translation) in regular head waves, the forced oscillation problem in heave and pitch (where surge is fixed) in otherwise calm water, and the motion-free problem (where surge, heave, and pitch are free) in regular head waves. The added resistance is measured directly using a dynamometer for all three cases and also measured are the wave-exciting forces in the diffraction problem and wave-induced ship motions in the motion-free problem. To see the degree of nonlinearity, measurements related to the incident wave are performed with two different incident-wave amplitudes. Furthermore, two different (relatively blunt and slender) modified Wigley models are adopted in the experiments, and all of the measurements mentioned are implemented for both modified Wigley models. In fact, it was revealed in our preliminary experiment (Kashiwagi 2010; Wakabayashi *et al.* 2010) that a large discrepancy exists between the results of added resistance by the direct measurement and by the unsteady wave analysis method, particularly near the peak of the added resistance where wave-induced ship motions become large.

To study possible reasons of this discrepancy, the linear superposition in ship-generated unsteady waves is made using measured waves in the diffraction and radiation problems and the complex amplitudes of heave and pitch motions measured in the motion-free problem. Through comparisons of superposed waves with directly measured waves in the motion-free condition in incident waves of two different amplitudes, the amount of nonlinearity on the added resistance is investigated. A comparison of the values of the added resistance measured for the diffraction and motion-free problems provides information on the characteristics of added resistance in short incident waves and on the importance of steady sinkage and trim on the added resistance.

In this article, Section 2 outlines the theory on the unsteady wave analysis and its relation with the added resistance. In Section 3, an analytical investigation is made on the fundamental feature of the Fourier transform of wave components and then which component of progressive waves is dominant in the added resistance. Experiments, analysis methods for unsteady waves, and tested ship models are described in Section 4. Obtained results are shown in Section 5, and discussions are made on nonlinear effects in the unsteady wave and bluntness effects of ship geometry on the added resistance by comparing the results for two different modified Wigley models. Conclusions are summarized in Section 6.

2. Theory for Unsteady Wave Analysis

We consider a ship advancing at constant forward speed, U, into a regular incident wave of amplitude, A, circular frequency ω_0. The depth of water is assumed infinite; thus the wave number of incident wave is given by $k_0 = \omega_0^2/g$, with g the acceleration resulting from gravity. Corresponding to the experiment, only the head wave is considered, and the analysis is made with a right-handed Cartesian coordinate system O-xyz with the origin placed at the center of a ship and on the undisturbed free surface, which translates with the same constant speed as that of a ship along the positive x-axis. The positive z-axis is taken upward. The unsteady responses of ship and associated ambient flow of fluid are assumed to be periodic with circular frequency of encounter $\omega = \omega_0 + k_0 U$.

By assuming the flow inviscid with irrotational motion, the velocity potential is introduced and written in the form

$$\varPhi(\boldsymbol{x}, t) = U\big\{ -x + \phi_S(\boldsymbol{x})\big\} + \mathrm{Re}\Big[\big\{\phi_0(\boldsymbol{x}) + \phi(\boldsymbol{x})\big\}\, e^{i\omega t}\Big]\,, \tag{1}$$

where $\boldsymbol{x} = (x, y, z)$ and $\phi_S(\boldsymbol{x})$ denotes the steady disturbance potential; $\phi_0(\boldsymbol{x})$ and $\phi(\boldsymbol{x})$ are the spatial part of the incident wave and unsteady disturbance potentials, respectively. By linear assumption, the disturbance potential $\phi(\boldsymbol{x})$ is decomposed as follows:

$$\phi(\boldsymbol{x}) = \frac{igA}{\omega_0}\varphi_7(\boldsymbol{x}) + \sum_{j=1,3,5} i\omega X_j \ell_j \varphi_j(\boldsymbol{x})\,. \tag{2}$$

Here $\varphi_7(\boldsymbol{x})$ denotes the scattering potential and $\varphi_j(\boldsymbol{x})$ the radiation potential due to the j-th mode of motion (j = 1, 3, 5 for surge, heave, and pitch, respectively) with X_j its

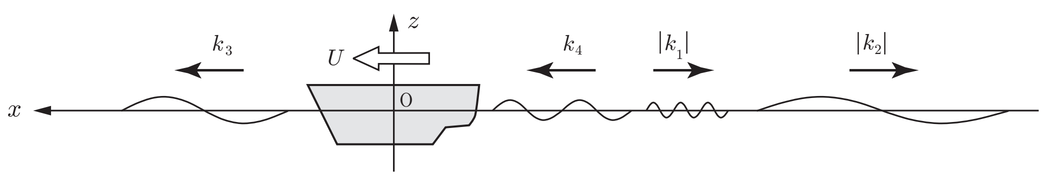

Fig. 1 Coordinate system and schematic illustration of wave components

complex amplitude. Symbol ℓ_j is adopted to express the length dimension for pitch; that is, $\ell_5 = L/2$ and $\ell_j = 1$ for surge and heave.

At a distance from a ship, the elevation of ship-generated unsteady wave may be computed by neglecting the contribution from the steady disturbance in the form

$$\zeta(x,y) = -\frac{1}{g}\left(i\omega - U\frac{\partial}{\partial x}\right)\phi(x,y,0) \tag{3}$$

and each component of the unsteady disturbance potentials in Eq. (2) can be expressed by the far-field representation in the slender-ship theory as follows:

$$\varphi_j(x,y,0) = \int_L Q_j(\xi)\, G(x-\xi,y,0)\, d\xi\,, \tag{4}$$

where $Q_j(x)$ denotes the source strength along the x-axis and $G(x,y,z)$ is the Green function, equivalent to the velocity potential resulting from an oscillating and translating source with unit strength. By substituting Eq. (2) and Eq. (4) into Eq. (3) and neglecting the local wave term in the Green function, the elevation of progressive wave can be computed from

$$\zeta(x,y) = \frac{i}{2\pi}\left[-\int_{-\infty}^{k_1} + \int_{k_2}^{k_3} + \int_{k_4}^{\infty}\right] C(k)\frac{(\omega+kU)}{\omega_0}\frac{\kappa}{\sqrt{\kappa^2-k^2}}\, e^{-ikx-i\epsilon_k|y|\sqrt{\kappa^2-k^2}}\, dk, \tag{5}$$

where

$$\left.\begin{aligned} \kappa &= \frac{1}{g}\big(\omega+kU\big)^2 = K + 2k\tau + \frac{k^2}{K_0} \\ K &= \frac{\omega^2}{g},\ \tau = \frac{U\omega}{g},\ K_0 = \frac{g}{U^2},\ \epsilon_k = \mathrm{sgn}(\omega+kU) \end{aligned}\right\} \tag{6}$$

$$\left.\begin{matrix} k_1 \\ k_2 \end{matrix}\right\} = -\frac{K_0}{2}\big(1+2\tau \pm \sqrt{1+4\tau}\big), \tag{7}$$

$$\left.\begin{matrix} k_3 \\ k_4 \end{matrix}\right\} = \frac{K_0}{2}\big(1-2\tau \mp \sqrt{1-4\tau}\big), \tag{8}$$

$$C(k) = A\left[C_7(k) + \frac{\omega\omega_0}{g}\sum_{j=1,3,5}\frac{X_j\ell_j}{A}C_j(k)\right], \tag{9}$$

$$C_j(k) = \int_L Q_j(\xi)\, e^{ik\xi}\, d\xi. \tag{10}$$

Here $C_j(k)$ is known as the Kochin function (wave amplitude function) resulting from each component in the disturbance potential, and $C(k)$ in Eq. (9) is the total Kochin function for the motion-free case. The complex amplitude of the j-th mode of ship motion, X_j $(j = 1,3,5)$, must be determined from the coupled motion equations.

In accordance with Eq. (9) for the Kochin function, the spatial part of ship-generated progressive wave $\zeta(x,y)$ can be written as the linear superposition of scattering wave $\zeta_7(x,y)$ and radiation waves $\zeta_j(x,y)$ by surge $(j=1)$, heave $(j=3)$, and pitch $(j=5)$ motions in the form

$$\zeta(x,y) = A\left[\zeta_7(x,y) + \sum_{j=1,3,5}\frac{X_j\ell_j}{A}\zeta_j(x,y)\right]. \tag{11}$$

Noting that the wave numbers k_j $(j = 1 \sim 4)$ appearing as the limits of integration in Eq. (5) are the roots of $\kappa^2 = k^2$ and $\epsilon_k = \mathrm{sgn}(\omega + kU) = -1$ for $-\infty < k < k_1$ and $\epsilon_k = 1$ for $k_2 < k < \infty$, we can write the elevation of progressive wave, Eq. (5), in the form

$$\zeta(x,y) = \frac{i}{2\pi}\int_{-\infty}^{\infty} u(\kappa^2 - k^2)\, C(k)\sqrt{\frac{\kappa}{k_0}}\,\frac{\kappa}{\sqrt{\kappa^2 - k^2}}\, e^{-ikx - i\epsilon_k|y|\sqrt{\kappa^2 - k^2}}\, dk, \tag{12}$$

where $u(\kappa^2 - k^2)$ is the unit step function, equal to 1 for $\kappa^2 > k^2$ and zero otherwise.

Let us consider the Fourier transform of $\zeta(x,y)$ with respect to x, defined by the following integral:

$$\zeta^*(\ell, y) = \int_{-\infty}^{\infty} \zeta(x,y)\, e^{i\ell x}\, dx. \tag{13}$$

Substituting Eq. (12) in Eq. (13) and using an integral representation of Dirac's delta function

$$\frac{1}{2\pi}\int_{-\infty}^{\infty} e^{i(\ell - k)x}\, dx = \delta(\ell - k), \tag{14}$$

we can obtain with relative ease the following relation:

$$\zeta^*(k, y) = i\, C(k)\sqrt{\frac{\kappa}{k_0}}\,\frac{\kappa}{\sqrt{\kappa^2 - k^2}}\, e^{-i\epsilon_k|y|\sqrt{\kappa^2 - k^2}}. \tag{15}$$

According to Maruo's (1960) theory, the added resistance in head waves can be computed in terms of the Kochin function by the following formula:

$$R_{AW} = \frac{\rho g}{4\pi k_0}\left[-\int_{-\infty}^{k_1} + \int_{k_2}^{k_3} + \int_{k_4}^{\infty}\right] \big|\, C(k)\big|^2 \frac{\kappa}{\sqrt{\kappa^2 - k^2}}(k + k_0)\, dk. \tag{16}$$

Therefore, substituting Eq. (15) in Eq. (16) provides a formula for computing the added resistance with the Fourier transform of ship-generated unsteady waves in the form

$$R_{AW} = \frac{\rho g}{4\pi}\left[-\int_{-\infty}^{k_1} + \int_{k_2}^{k_3} + \int_{k_4}^{\infty}\right] \big|\, \zeta^*(k,y)\big|^2 \frac{\sqrt{\kappa^2 - k^2}}{\kappa^2}(k + k_0)\, dk. \tag{17}$$

Here we should note a few things regarding the wave numbers k_j $(j = 1 \sim 4)$ appearing in Eq. (17). First, for $\tau > 1/4$, k_3 and k_4 become complex as is obvious from Eq. (8), and the integration range in Eq. (17) must be treated as continuous for $k_2 < k$. Next, $\omega = \omega_0 + k_0 U$ holds in head waves, which gives the following relations:

$$\left.\begin{aligned} \omega_0 &= \frac{g}{2U}\big(-1 + \sqrt{1 + 4\tau}\big) \\ k_0 &= \frac{\omega_0^2}{g} = \frac{K_0}{2}\big(1 + 2\tau - \sqrt{1 + 4\tau}\big) = -k_2 = |k_2| \end{aligned}\right\} \tag{18}$$

On the other hand, it can be proven that the relation between the ship's speed U and the phase velocity c of a wave with wave number k_j $(j = 1, 3, 4)$ along the x-axis is given by

$$\left.\begin{aligned} &0 < U < \frac{c}{2} && \text{for } k_3\text{-wave} \\ &\frac{c}{2} < U < c && \text{for } k_4\text{-wave} \\ &c < U && \text{for } k_1\text{-wave} \end{aligned}\right\} \tag{19}$$

Because $c/2$ is equal to the group velocity with which the energy of progressive wave is transported, we can understand the location of existence, the relative wavelength, and the propagation direction when viewed from a ship moving at forward speed U for each of the k_j-waves ($j = 1 \sim 4$); these are schematically shown in Fig. 1. It is noteworthy that at $\tau = 1/4$, k_3 becomes equal to k_4 and U becomes equal to the group velocity of progressive wave. For $\tau > 1/4$, no wave exists ahead of the ship.

3. Weight Function in Added Resistance

In reality, there are various progressive-wave components with different wave numbers over the integration range with respect to k shown in Eq. (17). To see which component of progressive waves contributes predominantly to the added resistance, we will investigate the values of the integrand of Eq. (17), by rewriting Eq. (17) in the form

$$R_{AW} = \frac{\rho g}{4\pi}\left[\int_{-\infty}^{k_1} + \int_{k_2}^{k_3} + \int_{k_4}^{\infty}\right] W_1(k)\, W_2(k)\, dk, \tag{20}$$

where

$$W_1(k) = \left|\, \zeta^*(k,y)\right|^2, \tag{21}$$

$$W_2(k) = \frac{\sqrt{\kappa^2 - k^2}}{\kappa^2}\, \epsilon_k \left(k + k_0 \right). \tag{22}$$

It should be noted again that $W_2(k) = 0$ at $k = k_j$ ($j = 1 \sim 4$) because of $\kappa^2 = k^2$, and $W_2 \geq 0$ over the integration range because $k + k_0 = k - k_2 > 0$ for $k > k_2$ by Eq. (18) and $\epsilon_k < 0$ and $(k + k_0) < 0$ for $k < k_1$. Needless to say, $W_1 \geq 0$ but its value strongly depends on the wave number k of progressive wave as will be analytically shown below.

To see qualitatively dominant wave components and general characteristics in the Fourier transform of progressive waves, it may be informative to consider a simplified wave profile. For that purpose, let us consider a wave component, propagating in the positive x-axis with wave number k_ℓ and amplitude of the following form:

$$\zeta(x,y) = \alpha\, \frac{u(x_s - x)}{\sqrt{|x - x_s|}}\, e^{-ik_\ell x}, \tag{23}$$

where α denotes the amplitude coefficient, x_s the starting point of wave existence along a line parallel to the x-axis (thus may depend on y), and $u(x_s - x)$ the unit step function which is nonzero at the downstream side from $x = x_s$.

The Fourier transform of this wave may be expressed as

$$\zeta^*(k,y) = \int_{-\infty}^{\infty} \zeta(x,y)\, e^{ikx}\, dx = \alpha \sqrt{\frac{\pi}{|k - k_\ell|}}\, e^{i(k-k_\ell)x_s}\, e^{i\frac{\pi}{4}\mathrm{sgn}(k-k_\ell)}. \tag{24}$$

Therefore, it is obvious that the value of $W_1(k)$ becomes very large at $k = k_\ell$ and decays in proportion to $1/|k - k_\ell|$.

For larger values of k (i.e. shorter waves), $W_2(k)$ becomes small with order of $O(1/k)$ and the amplitude coefficient α must be small in reality. As already noted, k_j ($j = 1 \sim 4$) is a root of $\kappa^2 - k^2 = 0$, and $k + k_0 = k - k_2$. Hence, dominant wave components in the added resistance may be relatively longer waves with smaller value of k satisfying $k_2 < k$. We note that if $k_2 < k < 0$, the wave propagates in the negative x-axis like k_2-wave in Fig. 1, and if $0 < k$, the wave propagates in the positive x-axis like k_3- and k_4-waves in Fig. 1.

4. Experiments

4.1 Wave measurement and analysis

Experiments were carried out, measuring the added resistance in head waves by a dynamometer, ship-generated unsteady waves using a larger number of wave probes of capacitance type and also wave-induced ship motions in the motion-free case. The measurement of unsteady waves was performed with the multifold method developed by Ohkusu (1977). In this method, as shown in Fig. 2, N wave probes ($N = 12$ in the present study) were fixed in space and positioned with almost equal interval over the distance of ship's movement in one period of encounter along a longitudinal line parallel to the x-axis (at constant y).

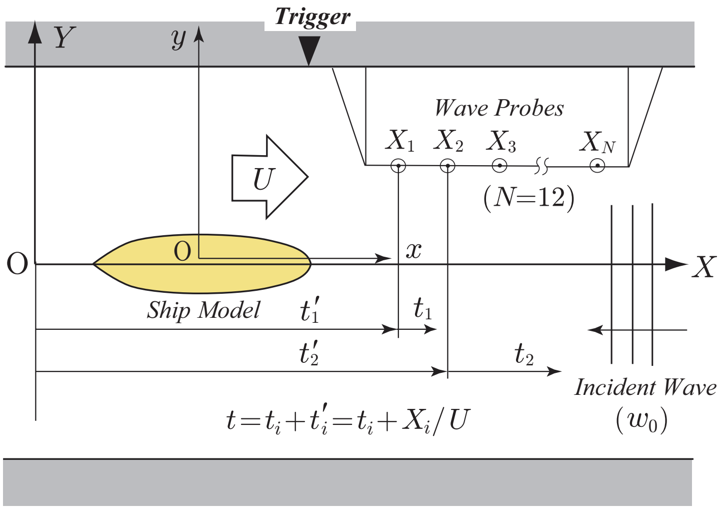

Fig. 2 Schematic illustration for arrangement of wave probes in the unsteady-wave measurement

In the coordinate system O-xy moving at constant speed U with a ship, the ship-generated wave is expressed as the sum of steady and unsteady waves in the form

$$\begin{aligned}\zeta_w(x,y;t) = {} & \zeta_0(x,y) + \zeta_c(x,y)\cos\omega t + \zeta_s(x,y)\sin\omega t \\ & + \zeta_c^{(2)}(x,y)\cos 2\omega t + \zeta_s^{(2)}(x,y)\sin 2\omega t + \cdots \end{aligned} \tag{25}$$

For brevity in the explanation subsequently, higher harmonic components will be omitted (although the second-order second-harmonic components, $\zeta_c^{(2)}(x,y)$ and $\zeta_s^{(2)}(x,y)$, are included in actual analyses).

Rewriting Eq. (25) with the space-fixed coordinate system O-XY in terms of the relation

$$X = x + Ut, \ Y = y, \tag{26}$$

it follows that

$$\zeta_w(X-Ut,y) = \zeta_0(X-Ut,y) + \zeta_c(X-Ut,y)\cos\omega t + \zeta_s(X-Ut,y)\sin\omega t. \tag{27}$$

Like in Fig. 2, let us denote the location of i-th wave probe as $X = X_i$ ($i = 1 \sim N$), the time instant when the ship's bow reaches the i-th wave probe as $t = t_i' = X_i/U$, and the time from this moment as t_i. Then we can write

$$t = t_i + t_i' = t_i + X_i/U\,. \tag{28}$$

Substituting this relation into Eq. (27) gives

$$\begin{aligned}\zeta_w(-Ut_i, y) = \zeta_0(-Ut_i, y) + \zeta_c(-Ut_i, y)\cos\omega\big(t_i + X_i/U\big)\\ +\zeta_s(-Ut_i, y)\sin\omega\big(t_i + X_i/U\big)\,.\end{aligned} \tag{29}$$

Because $x = -Ut$, the wave record in time by the i-th wave probe, which will be denoted as $\zeta_w^i(t, y)$, can be written as

$$\zeta_w^i(t, y) = \zeta_0(x, y) + \zeta_c(x, y)\cos\omega\big(t + X_i/U\big) + \zeta_s(x, y)\sin\omega\big(t + X_i/U\big), \tag{30}$$

where t_i is rewritten as t and $x = -Ut$.

This equation implies that three unknowns (steady component $\zeta_0(x, y)$ and unsteady cosine and sine components $\zeta_c(x, y)$ and $\zeta_s(x, y)$) can be determined from the wave data ζ_w^i measured at different time instants with phase difference of $\omega X_i/U$ ($i = 1 \sim N$) using N wave probes. In the present experiment, $N = 12$ wave probes were used and thus the unknowns can be determined with the least squares method (which is true even for the case where second-order second-harmonic components are included in the analysis).

The Fourier transform of the measured unsteady wave written as a complex form of $\zeta(x, y) = \zeta_c(x, y) - i\,\zeta_s(x, y)$ was computed as follows. Suppose that the range of x in actual measurement is from b to a and the number of total data points is $M+1$. Then by assuming linear variation between adjacent data points ($\zeta_n \sim \zeta_{n+1}$), we integrate analytically with respect to x over each segment of data points. The result of this analytical integration can be expressed as

$$\zeta^*(k, y) \simeq \int_b^a \zeta(x, y)\, e^{ikx}\, dx = \sum_{n=2}^{M} \mathit{\Gamma}_n(k)\, \zeta_n(y), \tag{31}$$

where

$$\begin{aligned}\mathit{\Gamma}_n(k) &= \frac{1}{k^2}\left[\frac{e^{ikx_n} - e^{ikx_{n-1}}}{x_n - x_{n-1}} - \frac{e^{ikx_n} - e^{ikx_{n+1}}}{x_n - x_{n+1}}\right]\\ &= \frac{1}{2}\big(x_{n+1} - x_{n-1}\big) \quad \text{as } k \to 0\end{aligned} \tag{32}$$

4.2 Tested ship models

To see the effect of bluntness of the ship model, two modified Wigley models with different bluntness were used in the experiments: one is a blunt model with wider breadth ($L/B = 5.0$) and the other is a slender model with $L/B = 6.67$. For convenience, these ship models are called "blunt" and "slender" modified Wigley models, respectively, in the present study. These modified Wigley models can be expressed mathematically as

(1) Blunt modified Wigley model:

$$\eta = (1 - \zeta^2)(1 - \xi^2)(1 + 0.6\xi^2 + \xi^4) + \zeta^2(1 - \zeta^8)(1 - \xi^2)^4 \tag{33}$$

(2) Slender modified Wigley model:

$$\eta = (1 - \zeta^2)(1 - \xi^2)(1 + 0.2\xi^2) + \zeta^2(1 - \zeta^8)(1 - \xi^2)^4 \tag{34}$$

Table 1 Principal dimensions of ‘blunt’ and ‘slender’ modified Wigley models

Item	Blunt	Slender
Length L(m)	2.5	2.0
Breath B(m)	0.5	0.3
Draft d(m)	0.175	0.125
Displacement ∇ (m^3)	0.13877	0.04205
Water-plane area A_w (m^2)	1.005	0.416
Gyrational radius κ_{yy}/L	0.236	0.248
Center of gravity KG (m)	0.145	0.0846

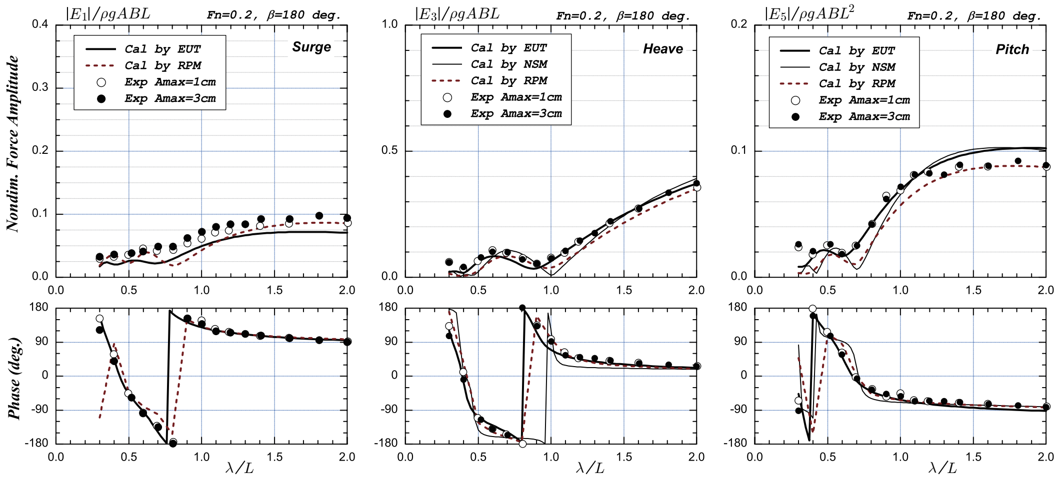

Fig. 3 Wave-exciting surge force, heave force and pitch moment on the blunt modified Wigley model at $Fn = 0.2$

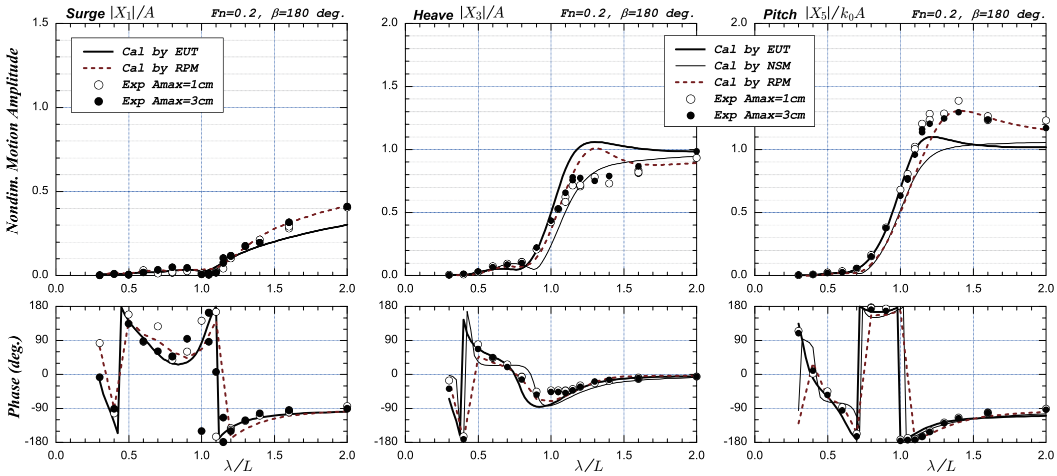

Fig. 4 Wave-induced surge, heave and pitch motions of the blunt modified Wigley model at $Fn = 0.2$

where $\xi = x/(L/2)$, $\eta = y/(B/2)$, and $\zeta = z/d$. The principal dimensions of these two models are shown in Table 1.

To see also the degree of contribution of each component wave $\zeta_j(x, y)$ defined in Eq. (11) in the linear superposition of ship-generated unsteady waves to the added resistance, the experiments were conducted for the cases of wave diffraction (where ship motions are completely fixed), forced oscillations in heave and pitch (where incident waves are absent), and free response in waves (where surge, heave, and pitch are free to respond to waves). These experiments were implemented for the two modified Wigley models in the same way.

The lateral distance of a longitudinal line used for the wave measurement from the centerline of a ship (x-axis) was set equal to $y = B/2+$ 0.1 m. The Froude number was $Fn = 0.2$ in all measurements in the present study.

The incident waves were generated basically with target amplitude set equal to $A = 3.0$ cm for the blunt modified Wigley model and $A = 2.5$ cm for the slender modified Wigley model (because the model size is different as shown in Table 1). When the wave steepness $2A/\lambda$ becomes larger than 1/30, the target value of incident wave amplitude was determined to satisfy $2A/\lambda = 1/30$.

In the present study, it is important to see the validity of linear superposition in the unsteady wave and associated nonlinear effects on the added resistance. Thus, all experiments in waves were performed for $A = 1.0$ cm as well. In the forced oscillation tests, the oscillation amplitude was set equal to $X_3 = 1.0$ cm for heave and $X_5 = 1.364°$ for pitch to ensure satisfaction of the linear assumption in the wave generation.

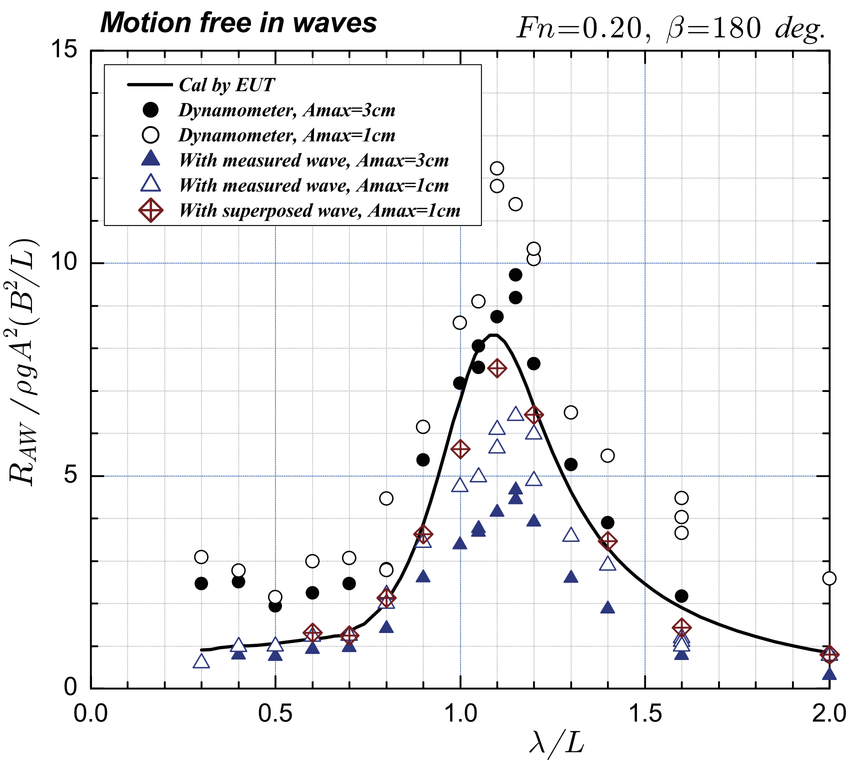

Fig. 5 Added resistance on the blunt modified Wigley model at $Fn = 0.2$ in the motion-free case

5. Results and Discussions

5.1 Blunt modified Wigley model

First, the results of linear quantities of the wave-exciting forces and wave-induced motions in surge, heave, and pitch are shown in Figs. 3 and 4. In these results, the phase lead is defined as positive with reference to the time instant when the crest of incident wave is at midship. Computed results by Enhanced Unified Theory (EUT), New Strip Method (NSM), and Rankine Panel Method (RPM) are also included in these figures for comparison. The readers are referred to Kashiwagi (1995, 1997) and Iwashita and Ito (1998) for the details of EUT and RPM, respectively, both of which are frequency-domain linear calculation methods, and the steady disturbance potential $\phi_S(\boldsymbol{x})$ is simply ignored in EUT, whereas it is computed numerically as double-body flow in RPM and its effects on the body and free-surface boundary conditions are properly taken into account. We can see from Figs. 3 and 4 that the linearity is well preserved in the first-order quantities of wave-exciting forces and wave-induced motions; that is, the difference in nondimensional results measured at $A = 1.0$ cm and $A = 3.0$ cm is small.

Next, various results on the added resistance are shown in Fig. 5. The results of direct measurement by a dynamometer are shown with closed circle for $A = 3.0$ cm and open circle for $A = 1.0$ cm. Corresponding results obtained by the unsteady wave analysis using measured waves at $A = 3.0$ cm and $A = 1.0$ cm are shown with a closed triangle and open

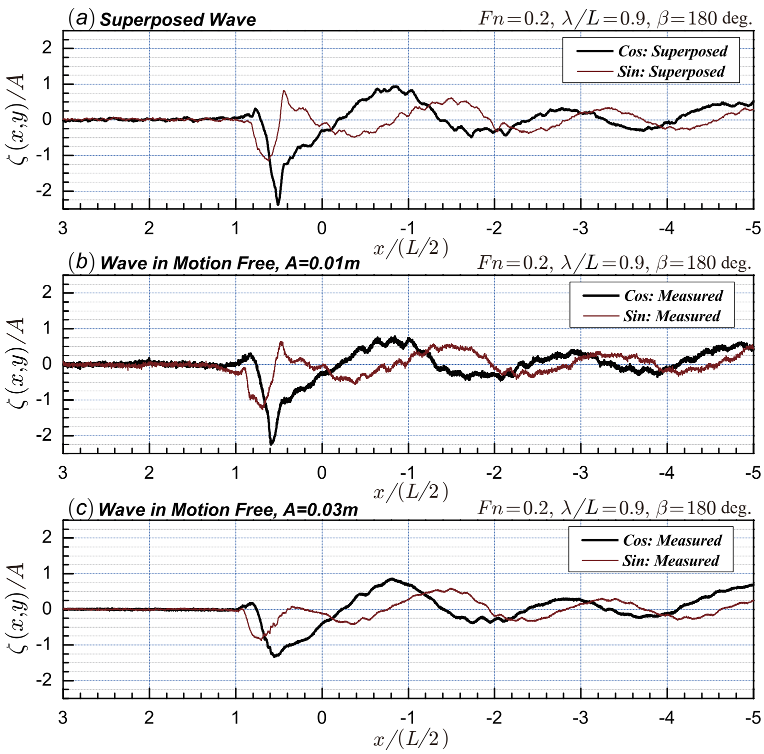

Fig. 6 Wave profiles generated by the blunt modified Wigley model at $Fn = 0.2$ in a regular wave of $\lambda/L = 0.9$. (a) Superposed wave, (b) Measured wave at $A = 1.0$ cm, (c) Measured wave at $A = 3.0$ cm

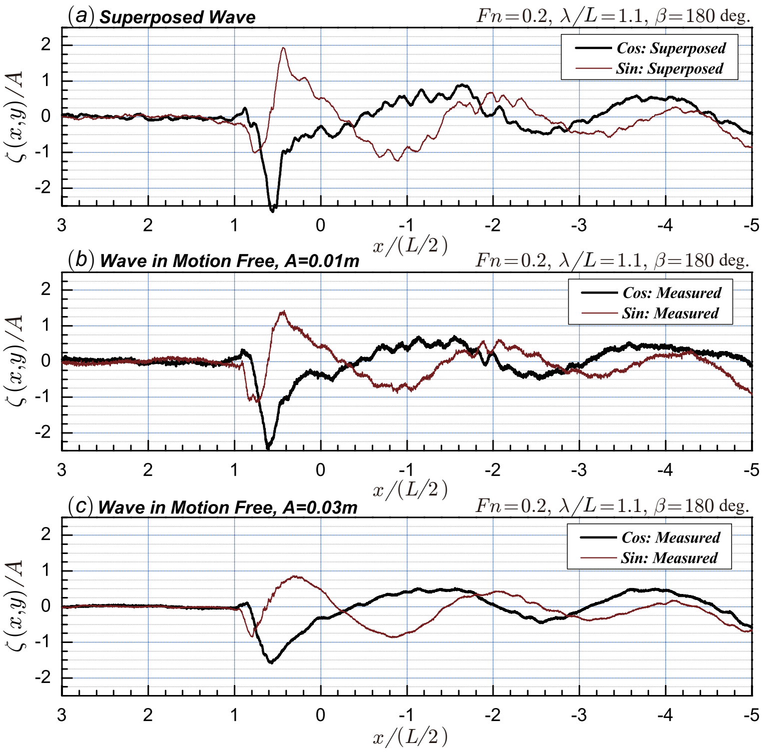

Fig. 7 Wave profiles generated by the blunt modified Wigley model at $Fn = 0.2$ in a regular wave of $\lambda/L = 1.1$. (a) Superposed wave, (b) Measured wave at $A = 1.0$ cm, (c) Measured wave at $A = 3.0$ cm

triangle, respectively. In addition, computed results by EUT are shown with a solid line. We can see a large discrepancy between the results by the direct measurement and the unsteady wave analysis, particularly near the peak, but the results by the wave analysis at $A = 1.0$ cm are obviously larger than those by the wave analysis at $A = 3.0$ cm and approach the values of direct measurement and potential-flow computation by EUT.

To see and confirm the linearity in the unsteady wave, the wave profile was computed by the linear superposition according to Eq. (11), using the component waves obtained by the experiments of wave diffraction ($j = 7$), forced heave ($j = 3$), and forced pitch ($j = 5$), together with complex amplitudes of heave and pitch motions (shown in Fig. 4) measured in the motion-free experiment. (The surge mode is not included, because the forced oscillation test in surge could not be conducted.) For the scattering wave and complex motion amplitudes in the linear superposition, the results measured at $A = 1.0$ cm are used. The superposed wave profile was Fourier-transformed and the added resistance was computed from Eq. (17). Obtained results from this linear superposition using component waves and complex amplitudes are also shown in Fig. 5 with diamond symbol. It is remarkable that these results are much closer to the results of direct measurement (especially at $A = 3.0$ cm) and computed ones by EUT. Furthermore, except near the peak, the results with superposed wave are very close to the ones with measured wave at $A = 1.0$ cm.

To see the difference at the level of wave profile, a comparison is shown among the superposed wave, measured wave at $A = 1.0$ cm and measured wave at $A = 3.0$ cm in Fig. 6

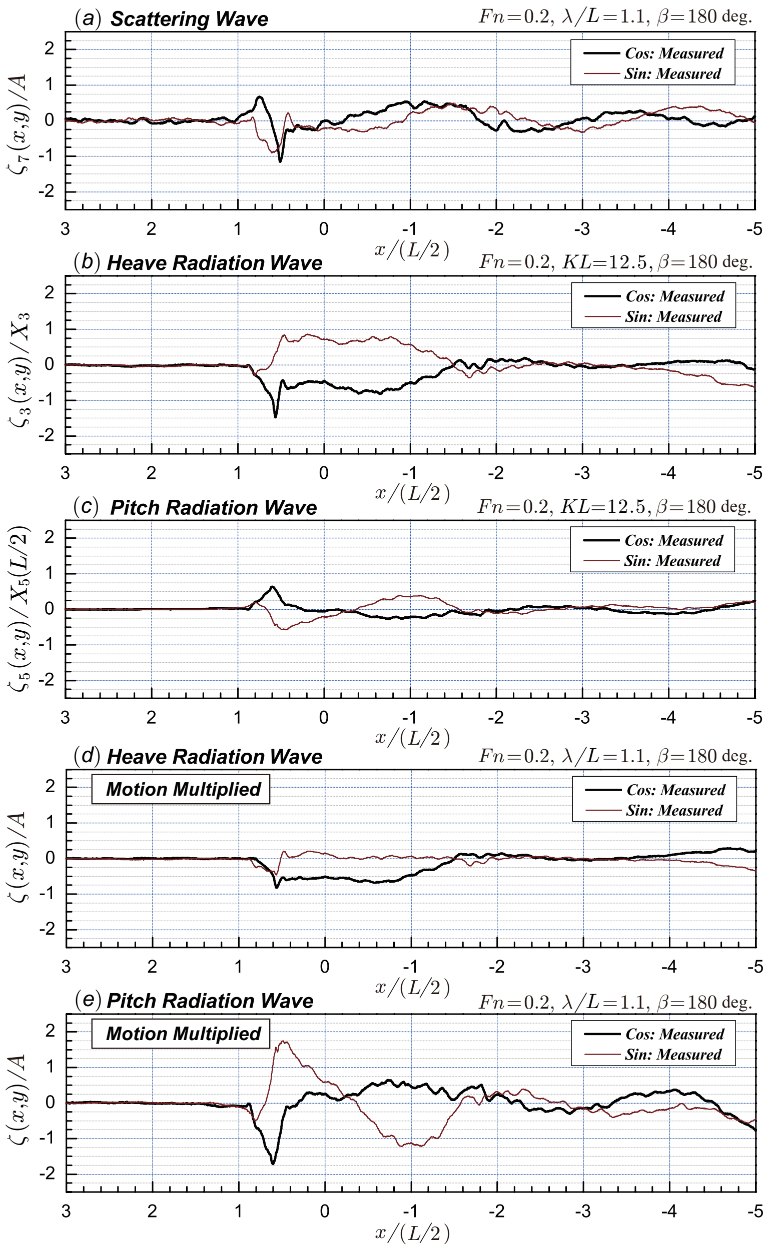

Fig. 8 Component waves in the linear superposition generated by the blunt modified Wigley model at $Fn = 0.2$ in a regular wave of $\lambda/L = 1.1$. (a) Scattering wave, (b) Heave radiation wave, (c) Pitch radiation wave, (d) Heave radiation wave with motion complex amplitude multiplied, (e) Pitch radiation wave with motion complex amplitude multiplied.

for $\lambda/L = 0.9$ and in Fig. 7 for $\lambda/L = 1.1$ as two typical examples. From these comparisons, we can see that the overall appearance of the wave profile is very similar between superposed and directly measured waves. However a prominent difference exists near the forefront part

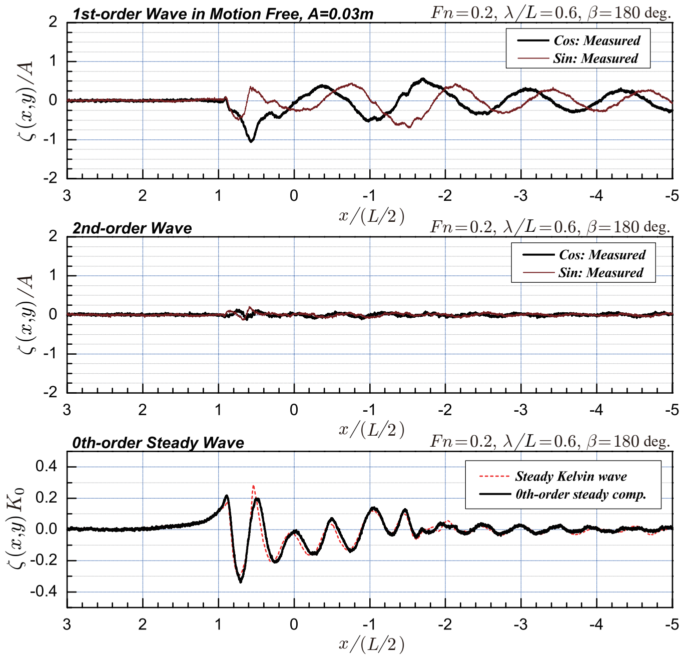

Fig. 9 Wave profiles of the 0th-, first-, and second-order components generated by the blunt modified Wigley model at $Fn = 0.2$ and in a regular wave of $\lambda/L = 0.6$ and $A = 3.0$ cm.

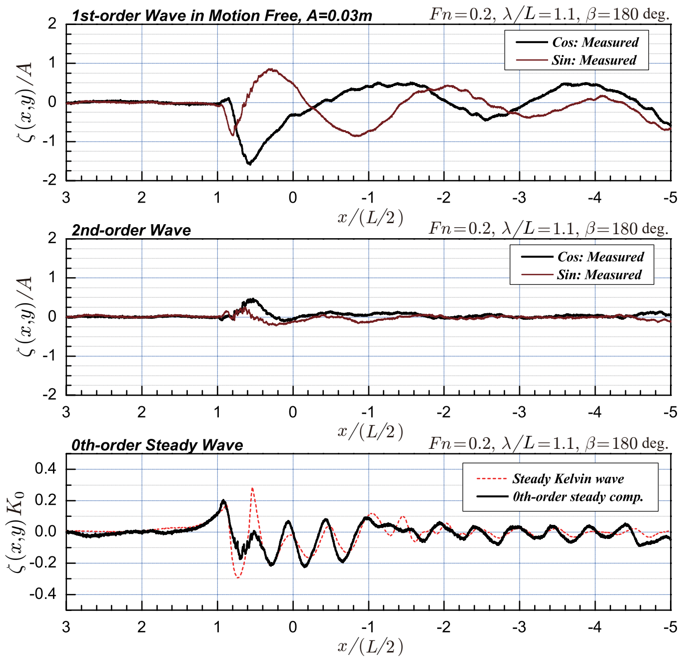

Fig. 10 Wave profiles of the 0th-, first-, and second-order components generated by the blunt modified Wigley model at $Fn = 0.2$ and in a regular wave of $\lambda/L = 1.1$ and $A = 3.0$ cm.

of the wave; particularly in the wave measured at $A = 3.0$ cm, the forefront part looks collapsed (or probably the wave-breaking occurs) and the amplitude becomes small. At $\lambda/L = 0.9$ the superposed wave and measured wave at $A = 1.0$ cm are very similar and thus the resultant added resistances are almost the same. On the other hand, at $\lambda/L = 1.1$, the superposed wave is still larger than the measured wave at $A = 1.0$ cm in the forefront part and the component of short wave length is more conspicuous; these differences are reflected in the results of the added resistance shown in Fig. 5.

The main source of difference in the forefront part seems to come from the wave by the pitch motion. To show this fact visually, each wave profile of the component waves in the linear superposition is shown in Fig. 8 for the case of $\lambda/L = 1.1$ corresponding to the top figure in Fig. 7. From the top, (a), (b), and (c) are the scattering wave, heave radiation

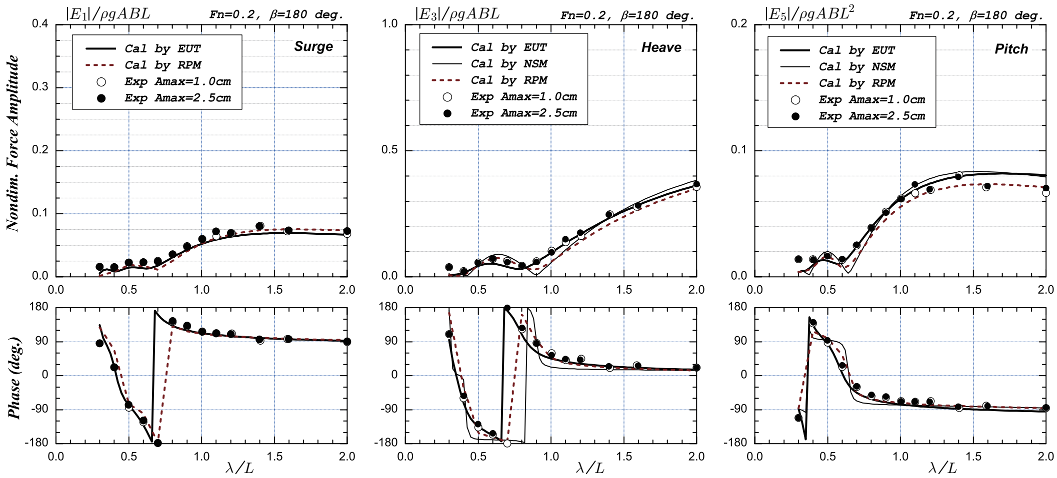

Fig. 11 Wave-exciting surge force, heave force and pitch moment on the slender modified Wigley model at $Fn = 0.2$.

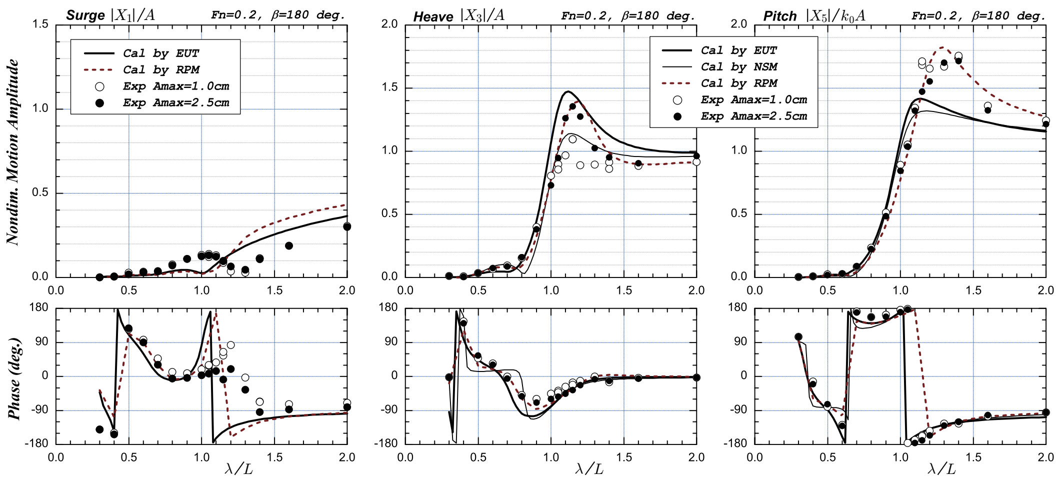

Fig. 12 Wave-induced surge, heave and pitch motions of the slender modified Wigley model at $Fn = 0.2$.

wave, and pitch radiation wave, respectively; these are normalized with unit amplitude. Furthermore, (d) and (e) are the heave and pitch component waves obtained after the measured complex amplitude of each mode is multiplied. Therefore, the summation of (a), (d) and (e) provides the result of superposed wave shown as the top figure in Fig. 7. From these figures we can see that each component wave contributes to a large amplitude in the forefront part but the most dominant component is the pitch radiation wave. We should note that the forced oscillation tests were performed with relatively small amplitude ($X_3 = 1.0$ cm and $X_5 = 1.36°$) within the range of linear theory being valid. Therefore, when the amplitude of ship motions becomes large, linearity in the amplitude of generated wave near the ship's bow or shoulder part is violated as a result of large pitch motion. Consequently, some nonlinear higher-order local waves with energy dissipation may be generated.

To provide some information on the nonlinear wave effects, the 0th-, first-, and second-order terms in the Fourier-series expansion are shown in Fig. 9 and Fig. 10 for $\lambda/L = 0.6$ and $\lambda/L = 1.1$, respectively; these were measured at incident-wave amplitude A =3.0 cm. A comparison with steady Kelvin wave for the 0th-order term is also included in these figures. It is obvious that the relative magnitude of the second-order nonlinear terms is small at $\lambda/L = 0.6$ even for the case of $A = 3.0$ cm but it is large at $\lambda = 1.1$. It is noteworthy that the 0th-order component in the measured wave at $\lambda/L = 1.1$ and $A = 3.0$ cm is largely different from the steady Kelvin wave, especially near the forefront part, implying the possibility of wave-breaking and nonlinear interaction between steady and unsteady waves.

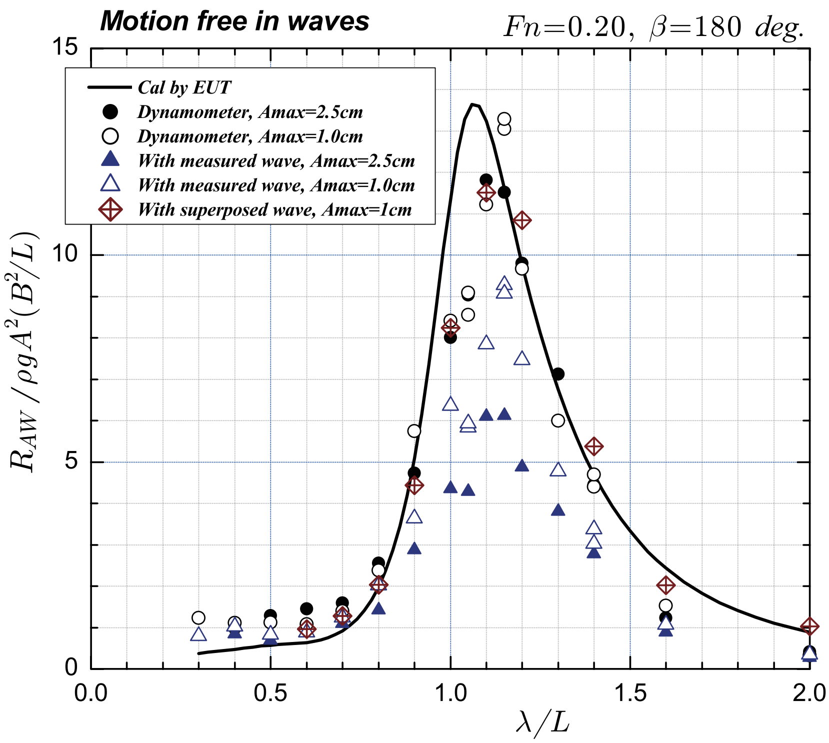

Fig. 13 Added resistance on the slender modified Wigley model at $Fn = 0.2$ in the motion-free case.

5.2 Slender modified Wigley model

In the same order as for the blunt modified Wigley model, the results of linear quantities are shown first in Fig. 11 for the wave-exciting forces and in Fig. 12 for the wave-induced ship motions. We can see that the linearity holds well in these linear quantities except near the resonant peak in the heave motion; it is shown in Kashiwagi *et al.* (2000) that this peak value is sensitive to the cross-coupling radiation forces between heave and pitch.

The results of the added resistance are shown in Fig. 13, where the results of direct measurement by a dynamometer are indicated with a closed circle for $A = 2.5$ cm and an open circle for $A = 1.0$ cm; the results by the unsteady wave analysis using measured waves are indicated with a closed triangle for $A = 2.5$ cm and an open triangle for $A = 1.0$ cm; the results obtained from superposed waves are indicated with a diamond symbol. The linear superposition of unsteady wave has been made exactly in the same manner as that for the blunt modified Wigley model using the scattering wave and heave and pitch motions measured at $A = 1.0$ cm and the radiation waves obtained by the forced heave ($X_3 = 1.0$ cm) and pitch ($X_5 = 1.364$ deg) oscillations. For reference, computed results by EUT are also shown by a solid line.

We can see a prominent discrepancy in the results obtained by the unsteady wave analysis between at $A = 2.5$ cm and at $A = 1.0$ cm near the peak, which is the same tendency as that in the blunt modified Wigley model. The values of the added resistance obtained from

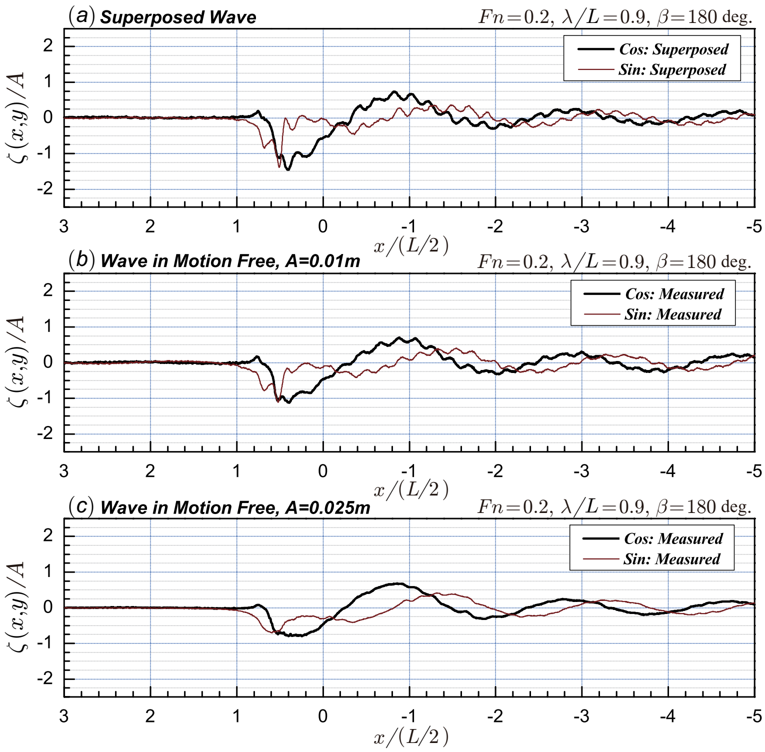

Fig. 14 Wave profiles generated by the slender modified Wigley model at $Fn = 0.2$ in a regular wave of $\lambda/L = 0.9$. (a) Superposed wave, (b) Measured wave at $A = 1.0$ cm, (c) Measured wave at $A = 2.5$ cm

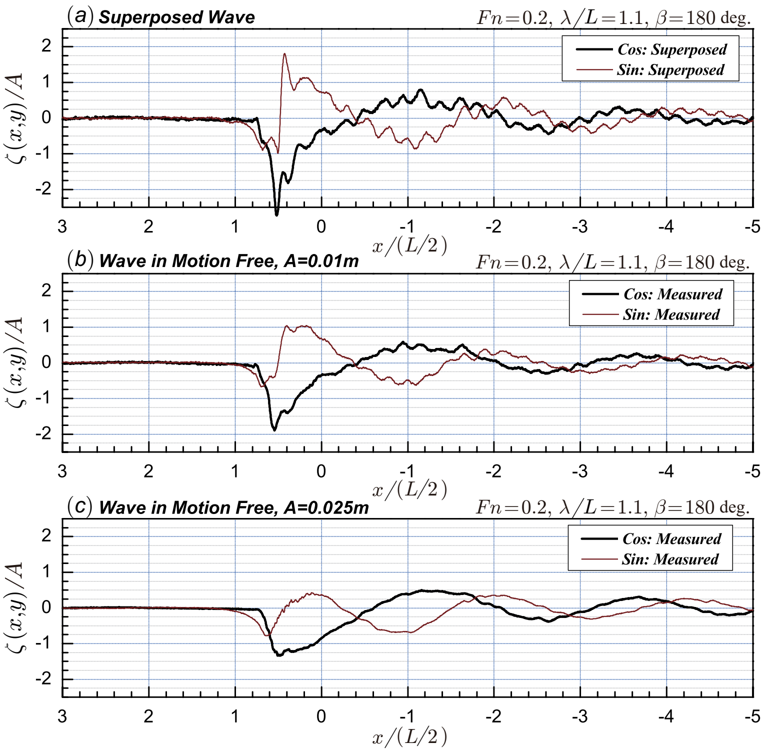

Fig. 15 Wave profiles generated by the slender modified Wigley model at $Fn = 0.2$ in a regular wave of $\lambda/L = 1.1$. (a) Superposed wave, (b) Measured wave at $A = 1.0$ cm, (c) Measured wave at $A = 2.5$ cm

superposed waves are further larger and almost the same as directly measured values and in good agreement with computed results by EUT (except for a slight shift in the peak wavelength).

To see the difference in the wave profile, two examples are shown at $\lambda/L = 0.9$ and $\lambda/L = 1.1$ in Figs. 14 and 15, respectively, for a superposed wave, measured waves at $A = 1.0$ cm and $A = 2.5$ cm. Obviously the wave measured at $A = 2.5$ cm is different from the others in the profile, especially near the forefront part of the wave and in the magnitude of short-wave length component. We can see also a difference in the amplitude of the forefront part even between the superposed wave and measured wave at $A = 1.0$ cm. These differences in the wave profile are reflected in the result of the added resistance shown in Fig. 13. This fact implies that higher-order nonlinear waves or nonlinear interactions with steady disturbance may exist and ship-generated waves actually break when the ship motions are large.

To support this conjecture, the 0th-, first-, and second-order terms in the Fourier-series expansion at $\lambda/L = 1.1$ are shown in Fig. 16 for $A = 1.0$ cm and in Fig. 17 for $A = 2.5$ cm. Noticeable magnitude in the second-order second-harmonic terms (about 25 % of the 1st-order term) can be seen, and the unsteady wave at $A = 2.5$ cm breaks near the forefront part as can be seen from a comparison between the 0th-order term and the steady Kelvin wave. (It should be noted, however, that in most cases, the 0th-order wave obtained in the unsteady wave analysis is confirmed to be very much similar to the steady Kelvin wave.)

By the way, the wave profile $\zeta(x, y)$ can be reproduced by the inverse Fourier transform

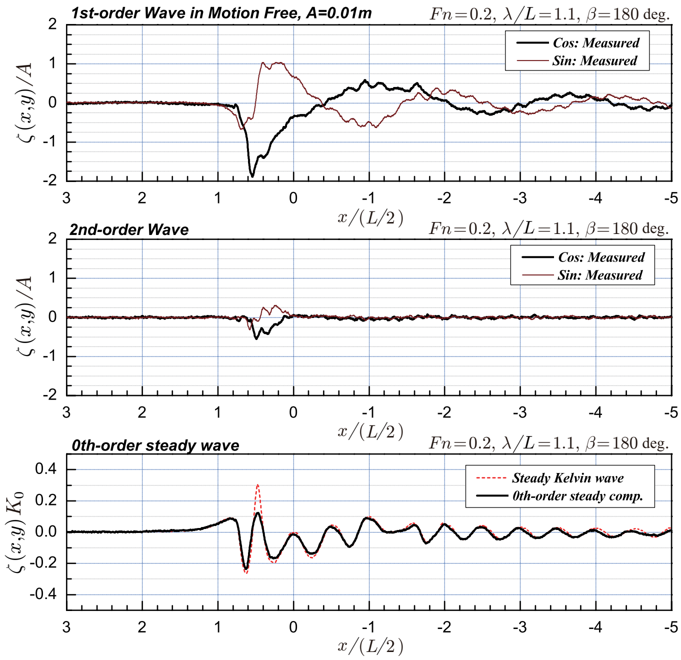

Fig. 16 Wave profiles of the 0th-, first-, and second-order components generated by the slender modified Wigley model at $Fn = 0.2$ and in a regular wave of $\lambda/L = 1.1$ and $A = 1.0$ cm

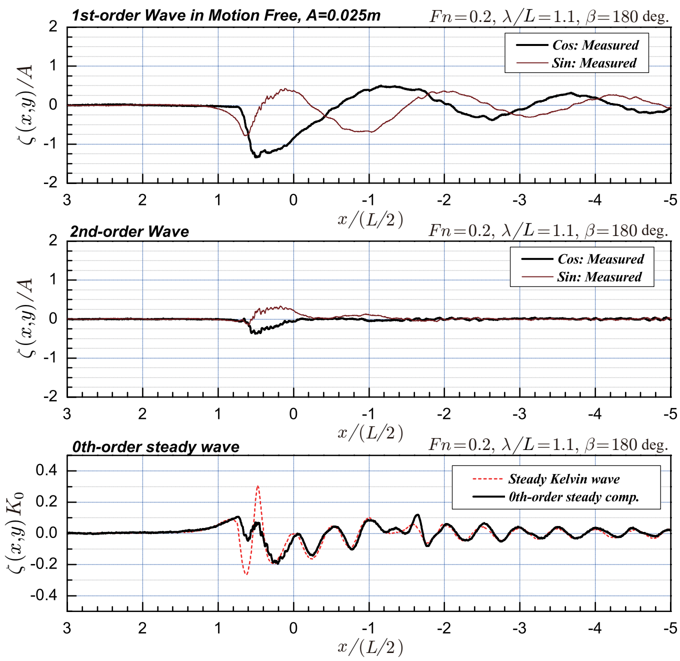

Fig. 17 Wave profiles of the 0th-, first-, and second-order components generated by the slender modified Wigley model at $Fn = 0.2$ and in a regular wave of $\lambda/L = 1.1$ and $A = 2.5$ cm

with respect to k of the Fourier-transformed wave data $\zeta^*(k, y)$. In this computation, we can extract the wave in a specified wavenumber range (say, $\beta < k < \alpha$) from the following calculation:

$$\zeta_{\beta<k<\alpha}(x, y) = \frac{1}{2\pi} \int_{\beta}^{\alpha} \zeta^*(k, y)\, e^{-ikx}\, dk \tag{35}$$

In the present study, the superposed or measured wave is decomposed into the wave groups in the following four different wavenumber ranges:

$$\left.\begin{array}{ll} \text{Range-1}: & -50 < k < k_1\,, \\ \text{Range-2}: & k_1 < k < 0\,, \\ \text{Range-3}: & 0 < k < k_C\,, \\ \text{Range-4}: & k_C < k < 50 \end{array}\right\} \tag{36}$$

where $k_C = \omega/U = K_0\tau$ and k_1 is given by Eq. (7). It should be noted here that the wave groups in Range-1 and Range-4 have been neglected conventionally in computation of the added resistance (e.g. Ohkusu 1980) as short-wave length components giving less contribution.

In the case of $\lambda/L = 1.1$ and slender modified Wigley model shown in Fig. 15, computed results from the superposed wave are shown in Fig. 18 and corresponding ones from the

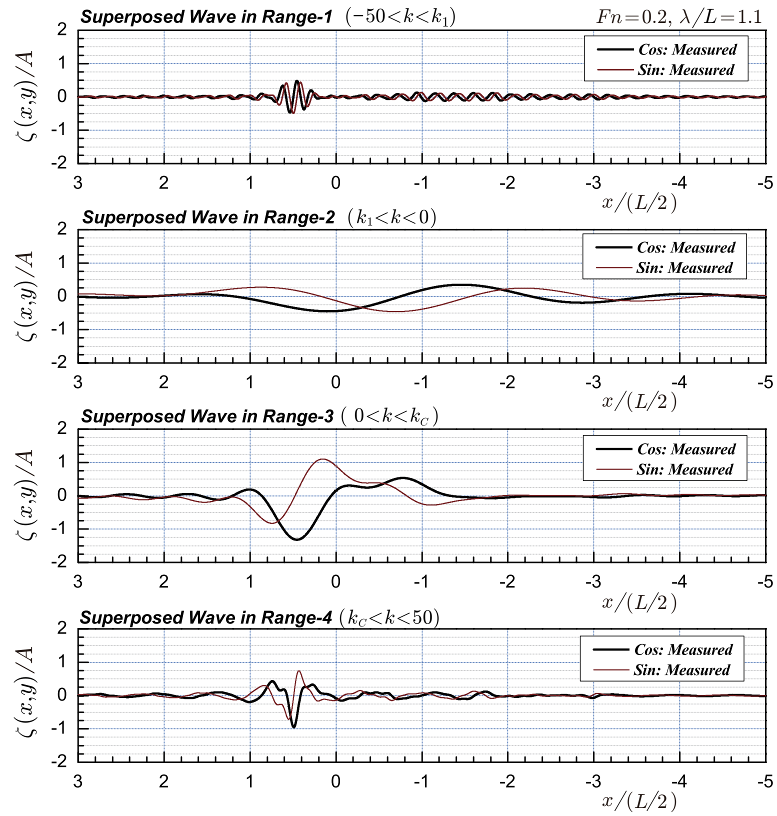

Fig. 18 Wave components extracted from superposed wave for the slender modified Wigley model at $Fn = 0.2$ and $\lambda/L = 1.1$

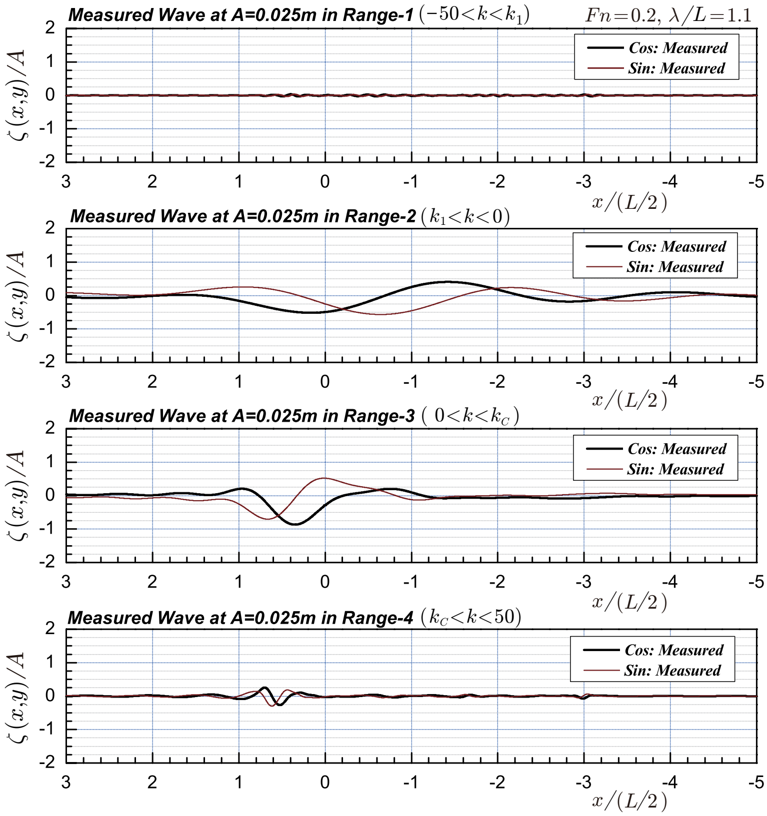

Fig. 19 Wave components extracted from measured wave for the slender modified Wigley model at $Fn = 0.2$ and in a regular wave of $\lambda/L = 1.1$ and $A = 2.5$ cm

measured wave at $A = 2.5$ cm are shown in Fig. 19. It can be seen from Fig. 18 that the wave around the forefront part includes various wave components and especially short-wave length components are not necessarily small. On the contrary, Fig. 19 obtained from the measured wave at $A = 2.5$ cm tells us that short-wave length components are very small even at the forefront part and longer-wave length components are almost the same as those in Fig. 18. These results suggest that a difference in prediction of the added resistance originates from relatively short wave length components around the forefront part and thus higher resolution for those wave components in the numerical computation is a key for enhancement in the prediction of the added resistance.

5.3 Added resistance at short incident waves

Up to the preceding subsection, attention has been focused on the difference near the peak of the added resistance. However, as seen in Fig. 5, directly measured results of added resistance on the blunt modified Wigley model in the short-wave length region are obviously larger than those obtained from the unsteady wave analysis. In this region, the dominant component in the added resistance is the result of wave diffraction, because wave-induced unsteady ship motions are generally negligible.

To see the magnitude and trend of the added resistance in the diffraction problem (where ship motions are completely fixed), the results of the added resistance in this case are plotted and compared in the same manner as in the motion-free case. Fig. 20 shows the result for the blunt modified Wigley model, and Fig. 21 shows the corresponding result for the slender modified Wigley model. (The results at $A = 3.0$ cm for the blunt modified Wigley model

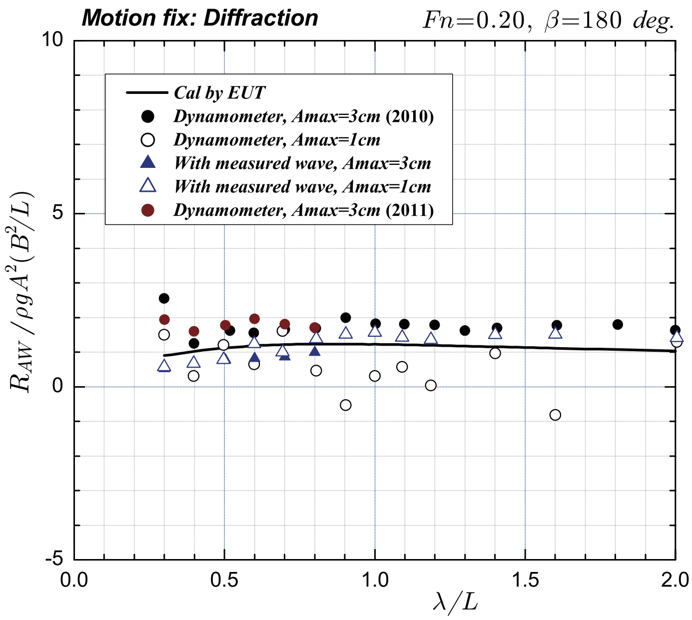

Fig. 20 Added resistance on the blunt modified Wigley model at $Fn = 0.2$ in the diffraction problem

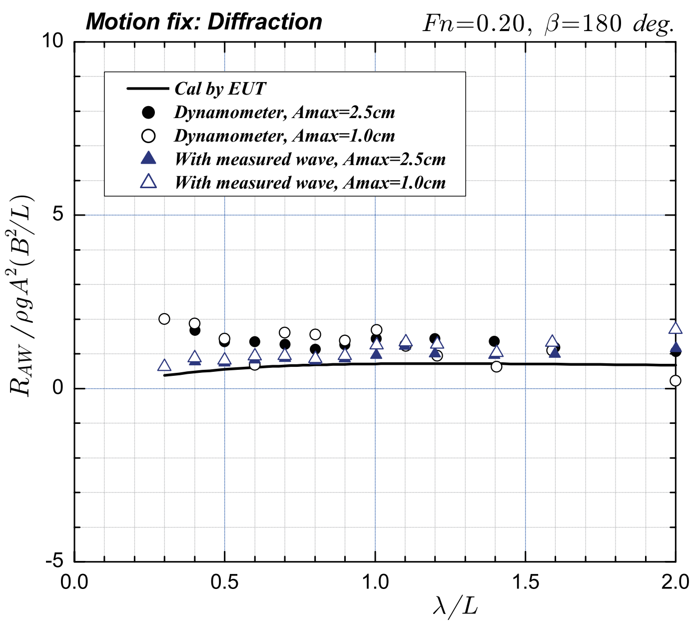

Fig. 21 Added resistance on the slender modified Wigley model at $Fn = 0.2$ in the diffraction problem

were confirmed to be essentially the same as those obtained in the previous experiment, Kashiwagi *et al.* 2011.) From these figures we can see that: 1) the added resistance is almost constant irrespective of the incident-wave length; 2) the results obtained from the wave analysis are in acceptable agreement with computed values by EUT; and 3) directly measured values by a dynamometer are slightly larger than those by the wave analysis, especially in the short-wave length region.

More importantly, from a comparison with the results of motion-free case (specifically a comparison between Figs. 5 and 20), we can see that the added resistance in the motion-free case is obviously larger than that in the diffraction case at short incident waves; this tendency is prominent for the blunt modified Wigley model. In the range of short incident waves, although wave-induced motions are negligibly small, the steady sinkage and trim in the motion-free case are naturally nonzero. Because this is only the difference between the motion-free and diffraction cases in short incident waves, this difference can be a reason of the fact that the added resistance in the motion-free case is slightly larger than that in the diffraction case. This means that there must be interactions between steady and unsteady flows, and the effect of steady sinkage and trim should be taken into account in the prediction of the added resistance, which may become more important for blunt ships.

6. Conclusions

To study the contribution of an unsteady wave-making component in the added resistance and nonlinear effects in ship-generated waves on the added resistance, experiments were conducted for measuring ship-generated unsteady waves, wave-induced ship motions, and the added resistance by using two different modified Wigley models and two different incident-wave amplitudes. The wave measurement was carried out for three canonical problems of wave diffraction with ship motions fixed, forced oscillations in heave and pitch, and free response of ship motions in waves. Then by using measured waves in the diffraction and radiation problems, the ship-generated unsteady wave was produced by the linear superposition.

Through comparisons of superposed waves with directly measured waves in the motion-free condition at two different incident-wave amplitudes, nonlinearity in the wave elevation was studied and the effect of that nonlinearity on the added resistance has been investigated by means of the unsteady wave-analysis method. The results obtained in this study can be summarized as follows:

1) When ship motions become large near the peak of the added resistance, linearity in the unsteady wave elevation is not satisfied especially at the forefront part of the wave. Consequently, the added resistance obtained from the waves measured at larger amplitude of incident wave becomes much smaller near the peak than those obtained from superposed linear waves and measured directly by a dynamometer.
2) The added resistance evaluated using superposed waves is in fairly good agreement with the result computed by the potential flow theory (EUT in the present paper) over the range of wave length tested.
3) The unsteady wave around the forefront part consists of various wave components. In fact, short-wave length components are not negligible in the linear waves and important in precise prediction of the wave profile at the forefront part and hence of the added resistance.
4) At short incident waves, there was prominent difference in the added resistance on the

blunt modified Wigley model between the values by the direct measurement and by the unsteady wave analysis. However, this difference is reduced in the diffraction problem where ship motions are completely fixed. This fact implies that the steady sinkage and trim should be taken into account in the prediction of the added resistance.

5) The added resistance in the diffraction problem is almost constant irrespective of the wave length of incident wave, and the values of direct measurement by a dynamometer are almost the same as those obtained from the wave analysis. However, as the incident wave becomes short, directly measured values tend to be larger than the results of the wave analysis. This difference should be attributed to nonlinear effects, which are not accounted for in the potential flow theory.

Acknowledgments

The experiments for the unsteady wave analysis in the present study have been carried out at the towing tank of Research Institute for Applied Mechanics (RIAM), Kyushu University, as a joint experiment with Hiroshima University. We thank Prof. Changhong Hu of Kyushu University for his permission of using the towing tank of RIAM and Prof. Hidetsugu Iwashita of Hiroshima University for his great help in the measurement and subsequent analyses for unsteady waves. Acknowledgment should also be extended to Mr. Takuma Sasakawa, Mr. Tomoki Wakabayashi, and Mr. Kenta Yamamoto who participated in the experiments in the course of master study and contributed to the analysis of measured data.

References

1. Faltinsen, O M, Minsaas, K J, Liapis, N and Skjørdal, S O (1980). "Prediction of resistance and propulsion of a ship in a seaway," *Proc of 13th Symposium on Naval Hydrodynamics*, Tokyo, pp 505–529.

2. Gerritsma, J and Beukelman, W (1972). "Analysis of the resistance increase in waves of a fast cargo ship," *International Shipbuilding Progress*, Vol 19, No 217.

3. Iwashita, H and Ito, A (1998). "Seakeeping Computations of a Blunt Ship Capturing the Influence of the Steady Flow," *Journal of Ship Technology Research*, Vol 45, No 4, pp 159–171.

4. Kashiwagi, M (1995). "Prediction of Surge and Its Effect on Added Resistance by Means of the Enhanced Unified Theory," *Trans West-Japan Society of Naval Architects*, No 89, pp 77–89.

5. Kashiwagi, M (1997). "Numerical Seakeeping Calculations Based on the Slender Ship Theory," *Ship Technology Research* (*Schiffstechnik*), Vol.44, No.4, pp 167–192.

6. Kashiwagi, M (2010). "Prediction of Added Resistance by Means of Unsteady Wave-Pattern Analysis," *Proc 25th Intl Workshop on Water Waves and Floating Bodies*, Harbin, pp 69–72.

7. Kashiwagi, M, Ikeda, T and Sasakawa, T (2010). "Effects of Forward Speed of a Ship on Added Resistance in Waves," *Intl Journal of Offshore & Polar Engineering*, Vol 20, No 3, pp 196–203.

8. Kashiwagi, M, Kawasoe, K and Inada, M (2000). "A Study on Ship Motion and Added Resistance in Waves (in Japanese)," *Journal of Kansai Society of Naval Architects, Japan*, No 234, pp 85–94.

9. Kashiwagi, M, Sasakawa, T and Wakabayashi, T (2011). "Hydrodynamic Consideration on Added Resistance and Ship-generated Unsteady Waves," *Proc 26th Intl Workshop on Water Waves and Floating Bodies*, Athens, pp 69–72.

10. Maruo, H (1960). "Wave resistance of a ship in regular head seas," *Bulletin of the Faculty of Engineering, Yokohama National University*, Vol 9, pp 73–91.

11. Ohkusu, M (1977). "Analysis of Waves Generated by a Ship Oscillating and Running on Calm Water with Forward Velocity (in Japanese)," *Journal of the Society of Naval Architects of Japan*, Vol 142, pp 36–44.

12. Ohkusu, M (1980). "Added Resistance in Waves in the Light of Unsteady Wave Pattern Analysis," *Proc of 13th Symposium on Naval Hydrodynamics*, Tokyo, pp 413–425.

13. Ohkusu, M (1984). "Added Resistance in Waves of Hull Forms with Blunt Bow," *Proc of 15th Symposium on Naval Hydrodynamics*, Humburg, pp 135–147.

14. Salvesen, N (1974). "Second-order steady state forces and moments on surface ships in oblique regular waves," *Proc of Intl Symp on Dynamics of Marine Vehicles and Structures in Waves*, Univ College London, pp 212–226.

15. Salvesen, N, Tuck, E O and Faltinsen, O M (1970). "Ship motions and sea loads," *Trans of Society Naval Architects and Marine Engineers*, Vol 78, pp 250–287.

16. Wakabayashi, T, Sasakawa, T and Kashiwagi, M (2010). "Study on Added Resistance with Unsteady Wave-Pattern Analysis," *Proc 5th Asia-Pacific Workshop on Marine Hydrodynamics - APHydro2010*, Osaka, pp 1–4.

Wave-Induced Steady Forces and Yaw Moment of a Ship Advancing in Oblique Waves*

Ardhana WICAKSONO and Masashi KASHIWAGI
Department of Naval Architecture & Ocean Engineering, Osaka University
2-1 Yamada-oka, Suita, Osaka 565-0871, Japan

Abstract

Wave-induced added resistance, steady sway force, and steady yaw moment, which are of second order in the incident-wave amplitude, are studied for the forward-speed case using the far-field method based on the principles of momentum and energy conservation. The Kochin functions representing ship-disturbance waves, important input data in the far-field method, are evaluated by means of both enhanced unified theory (EUT) and new strip method (NSM) to see the difference due to bow wave diffraction, 3D and forward-speed effects in the final results of second-order steady forces and moment. Special attention is paid on the precise integration method to ensure convergence in semi-infinite integrals in the calculation formulae, introducing no artificial decaying factor unlike conventional strip-theory methods. Validation of the present calculation method is made through comparison with the experiment conducted with a bulk-carrier model advancing in regular oblique waves and motion-free condition. Good agreement between computed and measured results and also superiority of EUT to NSM are confirmed for all modes of ship motion and the steady forces and yaw moment in a wide range of wave frequency.

Keywords: Added resistance, Steady sway force, Steady yaw moment, Far-field method, Kochin function, Oblique waves, Forward-speed effect, Enhanced unified theory.

1. Introduction

It is well known that the resistance of a ship will increase when the ship is advancing in waves at constant forward speed. This increment is called the added resistance, which is the longitudinal component of the wave-induced steady force of second order in the wave amplitude. Since the prediction of ship resistance is crucial for the economic operation in actual seas, many studies on the added resistance have been conducted so far.

In actual seaways, owing to the nature of the ocean, ships must sail obliquely to the direction of wave propagation. In oblique waves, not only the added resistance but also the same kind of steady sway force and yaw moment may be exerted. As an effect of these steady sway force and yaw moment, the check helm and drift angle of the ship may be exerted to attain equilibrium, which will induce another kind of resistance increase. Therefore, accurate prediction of wave-induced steady force and moment becomes important in considering the maneuvering motion of a ship in waves.

Early development of the theoretical formulation for the added resistance was provided by Maruo [2] by means of the principles of momentum and energy conservation. In the calculation formula derived, the Kochin function, equivalent to the amplitude of ship-generated

∗ *Reprinted from Journal of Marine Science and Technology, Vol. 23, No. 4, pp. 767–781, 2018 (December), https://doi.org/10.1007/s00773-017-0510-6*

disturbance waves far from the ship, is needed as the input. Newman [3] studied the wave-induced steady yaw moment on a floating body at zero speed, and derived a formula by using the angular momentum conservation principle. Their analyses were based on the stationary-phase method, which is expedient for the zero-speed problem, but becomes messy for the case of forward speed present. In fact, Lin and Reed [4] succeeded in obtaining a formula for the steady sway force using the stationary-phase method, but they found it difficult to derive a formula for the steady yaw moment when the forward speed exists.

Kashiwagi [?] proposed an analysis method utilizing the Fourier-transform theory to tackle the difficulty of stationary-phase method, and consequently derived the formulae for the steady forces and yaw moment at forward speed. Kashiwagi [6] computed further the Kochin function and then the added resistance, steady sway force, and steady yaw moment for the forward-speed but motion-fixed cases by means of the unified theory of Sclavounos [8]. Later Kashiwagi [9] proposed Enhanced Unified Theory (EUT) as an extension from the unified theory of Newman [10] and Sclavounos [8], and analyzed surge-related problems by retaining the x-component of the normal vector in the body boundary condition and also lateral motion modes in the same fashion as that for heave and pitch, with 3D and forward-speed effects taken into account.

Compared to a large amount of work on the added resistance, few studies have been made on the steady sway force and yaw moment. Naito *et al.* [11] measured the wave-induced steady forces on a tanker model for motion-fixed cases. Iwashita *et al.* [12] compared computed results by the 3D Green function method with measured results for the steady sway force and yaw moment only for the diffraction problem, but agreement was not good in shorter waves when the forward speed is present. Another measurement of wave-induced steady forces was conducted by Ueno *et al.* [13] using a VLCC model at Froude number $Fn = 0.069$ in a very short wave. Utilizing a time-domain 3D higher-order boundary element method, Joncquez [14] evaluated the second-order forces and moments for all motion modes at zero speed, but the ship was free to heave and pitch. When the forward speed is considered, evaluation of forces and moment was done only for head-wave case.

For the ship maneuvering problem in waves, Skejic and Faltinsen [15] investigated the time-averaged second-order wave loads utilizing several theories, and compared their computed results for the sway force and yaw moment with available measured data for oblique incident waves. Later Seo and Kim [16] incorporated computed results of wave-induced horizontal forces (added resistance and sway force) and yaw moment into the equations of maneuvering motion of a ship. In beam-sea case, the agreement between simulated and observed results was found to be relatively poor due to considerable drift effects on the turning direction. The discrepancy in the prediction of steady yaw moment was understood to be a significant cause of the difference. Recently Zhang *et al.* [17] stressed the importance of the wave-induced second-order quantities in the maneuvering motion through the time-domain Rankine panel method, where the trailing vortex sheet is introduced to the double-body flow.

In this paper, study is made on the wave-induced added resistance, steady sway force, and steady yaw moment using the calculation formulae derived by Kashiwagi [5] for the general forward-speed case. The Kochin functions for symmetric and antisymmetric components of ship-disturbance waves are important input in those calculation formulae, and they are computed by EUT and NSM. Special attention is paid on the precise integration method to remove square-root singularities at the limits of integration range and to ensure the convergence in semi-infinite integrals appearing in the calculation formulae not only for the added resistance, but also for the steady sway force and yaw moment. Therefore, the calculation method in this paper is markedly different from conventional ones based on the strip-theory methods in that the numerical integration in the formulae is exactly implemented without introducing any artificial convergence factor and that the computation method for the Kochin function is exact in the framework of the linear slender-ship theory and applicable to all frequencies. In the effort to validate this computation scheme, numerical computations are made for comparison with the experiment conducted by Yasukawa *et al.* [18] using a bulk carrier model advancing in regular oblique waves with forward speed and six-degree-of-freedom motions.

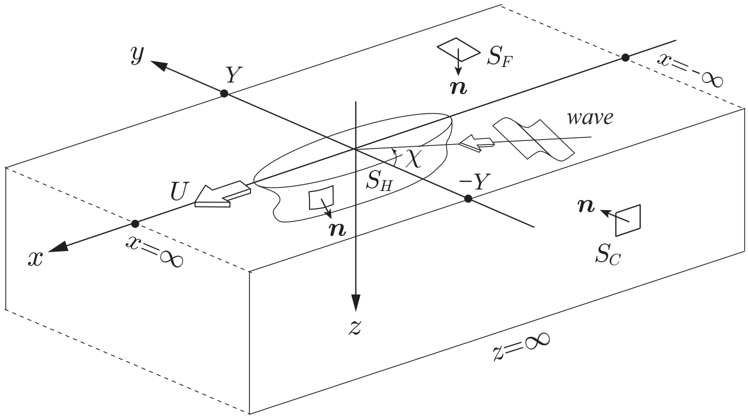

Fig. 1 Coordinate system and notations

2. Linearized Theory of a Ship in Waves

2.1 Formulation of boundary-value problem

For applying the principles of momentum and energy conservation, we need an expression of the body-disturbance velocity potential valid at a distance from a ship, which advances at constant forward speed U and oscillates with circular frequency ω in regular waves. For subsequent analyses, a Cartesian coordinate system O-xyz is taken, with the origin placed at the center of a ship and on the undisturbed free surface. As shown in Fig. 1, the x-axis is directed to the ship's bow and the z-axis is positive downward. The depth of water is assumed infinite. A plane progressive incident wave incoming with angle χ relative to the x-axis is considered, which has amplitude ζ_a and circular frequency ω_0. In this case, the oscillation of a ship occurs with the circular frequency of encounter given by $\omega = \omega_0 - k_0 U \cos\chi$, where k_0 is the wave number of incident wave and equal to ω_0^2/g, with g the acceleration due to gravity.

Under the assumption that the fluid is inviscid with irrotational motion and that the amplitudes of incident wave and ship's oscillation are small, the velocity potential can be introduced and written as

$$\Phi(x,y,z,t) = U\big[-x + \phi_s(x,y,z)\big] + \Re\big[\phi(x,y,z)\, e^{i\omega t}\big], \tag{1}$$

where ϕ_s represents the steady disturbance potential due to forward motion of a ship, which will be ignored eventually in this paper with assumption of slenderness of a ship. The spatial part of the unsteady velocity potential $\phi(x,y,z)$ is given as a sum of the incident-wave potential ϕ_0 and the body-disturbance velocity potential ϕ_B. The latter component consists of the scattering and radiation potentials. These are expressed in the form

$$\phi(x,y,z)=\frac{g\zeta_a}{i\omega_0}\Big\{\phi_0(x,y,z)+\phi_B(x,y,z)\Big\}, \tag{2}$$

$$\phi_0(x,y,z)=\exp\big\{-k_0z-ik_0(x\cos\chi+y\sin\chi)\big\}, \tag{3}$$

$$\phi_B(x,y,z)=\phi_7(x,y,z)-\frac{\omega\omega_0}{g}\sum_{j=1}^{6}\frac{X_j}{\zeta_a}\phi_j(x,y,z). \tag{4}$$

The first term ϕ_7 in Eq. 4 is the scattering potential and the last term ϕ_j is the radiation potential due to ship oscillation in six degrees of freedom ($j=1\sim6$) with complex amplitude X_j in the j-th mode of motion. Symbol $\Re$ in Eq. 1 means the real part to be taken (likewise $\Im$ will be used later to mean the imaginary part).

All of the velocity potentials are governed by Laplace's equation and subject to the free-surface boundary condition given by

$$[F]\quad\left(i\omega-U\frac{\partial}{\partial x}\right)^2\phi-g\frac{\partial\phi}{\partial z}=0\quad\text{on } z=0 \tag{5}$$

and the condition of vanishing velocity as $z\to\infty$. In addition, the disturbance potential ϕ_B must satisfy the radiation condition in the far field, and each velocity potential in ϕ_B can be characterized by the body boundary condition

$$\frac{\partial\phi_j}{\partial n}=n_j+\frac{U}{i\omega}m_j\quad(j=1\sim6) \tag{6}$$

$$=-\frac{\partial\phi_0}{\partial n}\qquad(j=7), \tag{7}$$

where

$$\left.\begin{aligned}&(n_1,n_2,n_3)=\boldsymbol{n},\ (n_4,n_5,n_6)=\boldsymbol{r}\times\boldsymbol{n}\\&(m_1,m_2,m_3)=-(\boldsymbol{n}\cdot\nabla)\,\boldsymbol{V}\\&(m_4,m_5,m_6)=-(\boldsymbol{n}\cdot\nabla)\,(\boldsymbol{r}\times\boldsymbol{V})\\&\boldsymbol{r}=(x,y,z),\ \boldsymbol{V}=\nabla\big[-x+\phi_s(x,y,z)\big]\end{aligned}\right\}. \tag{8}$$

Here n_j denotes the j-th component of the unit normal vector directing into the fluid and m_j is the so-called m-term representing interactions between the unsteady and steady flows. In the case of uniform-flow approximation for the steady flow field, it follows from Eq. 8 that $m_j=0$ for $j=1\sim4$, $m_5=-n_3$, and $m_6=n_2$.

2.2 Far-field expression of the velocity potential

With Green's theorem, the body-disturbance potential can be given by

$$\phi_B(P)=\iint_{S_H}\left(\frac{\partial\phi_B}{\partial n}-\phi_B\frac{\partial}{\partial n}\right)G_{3D}(P;Q)\,dS(Q), \tag{9}$$

where $P=(x,y,z)$ is the field point and $Q=(\xi,\eta,\zeta)$ is the integration point on the wetted ship hull surface S_H; $\partial/\partial n$ is the normal differentiation with respect to Q; $G_{3D}(P;Q)$ denotes the Green function satisfying all homogeneous boundary conditions except for the body boundary condition.

At a large distance far from the ship, the local-wave components decay and thus, we may consider only the progressive wave terms in the Green function, which can be expressed as

$$G_{3D}(P;Q) \sim \frac{i}{2\pi}\left[-\int_{-\infty}^{k_1} + \int_{k_2}^{k_3} + \int_{k_4}^{\infty}\right] \frac{\kappa}{\sqrt{\kappa^2-k^2}} \times e^{-\kappa(z+\zeta)-i\epsilon_k|y-\eta|\sqrt{\kappa^2-k^2}-ik(x-\xi)}\,dk, \tag{10}$$

where

$$\left.\begin{aligned} &\kappa = \frac{1}{g}(\omega+kU)^2 = K + 2k\tau + \frac{k^2}{K_0} \\ &K = \frac{\omega^2}{g},\ \ \tau = \frac{U\omega}{g},\ \ K_0 = \frac{g}{U^2},\ \ \epsilon_k = \operatorname{sgn}(\omega+kU) \end{aligned}\right\}, \tag{11}$$

$$\left.\begin{aligned} k_1 \\ k_2 \end{aligned}\right\} = -\frac{K_0}{2}\left(1+2\tau\pm\sqrt{1+4\tau}\right), \tag{12}$$

$$\left.\begin{aligned} k_3 \\ k_4 \end{aligned}\right\} = +\frac{K_0}{2}\left(1-2\tau\mp\sqrt{1-4\tau}\right). \tag{13}$$

Note that k_j $(j = 1 \sim 4)$ are the limits of integration range, given from $\kappa^2 = k^2$, and the integration range corresponds to the values satisfying $\kappa^2 \geq k^2$. In the case of $\tau > 1/4$, k_3 and k_4 become complex and thus the limits of integration should be interpreted as continuous for $k_2 < k$. We also note that $\epsilon_k = -1$ for $k < k_1$ and $\epsilon_k = 1$ for $k_2 < k$. Therefore, the integration range with respect to k may be written in terms of the unit step function $u(\kappa^2 - k^2)$ as follows:

$$\left[-\int_{-\infty}^{k_1} + \int_{k_2}^{k_3} + \int_{k_4}^{\infty}\right] \longrightarrow \int_{-\infty}^{\infty} \epsilon_k\, u(\kappa^2-k^2)$$

Substituting Eq. 10 into Eq. 9, the far-field expression of the disturbance potential can be obtained in the form

$$\phi_B(P) \sim \frac{i}{2\pi}\int_{-\infty}^{\infty} \epsilon_k\, u(\kappa^2-k^2)\, H^{\pm}(k) \frac{\kappa}{\sqrt{\kappa^2-k^2}}\, e^{-\kappa z \mp i\epsilon_k y\sqrt{\kappa^2-k^2}-ikx}\,dk, \tag{14}$$

where the upper or lower of the complex signs is to be taken according as the sign of y is positive or negative, respectively. $H^{\pm}(k)$ is the Kochin function equivalent to the complex amplitude of the far-field disturbance wave and expressed as

$$H^{\pm}(k) = C(k) \pm i\epsilon_k\, S(k), \tag{15}$$

$$\left.\begin{aligned} C(k) \\ S(k) \end{aligned}\right\} = \iint_{S_H}\left(\frac{\partial\phi_B(Q)}{\partial n} - \phi_B(Q)\frac{\partial}{\partial n}\right) e^{-\kappa\zeta+ik\xi} \left\{\begin{aligned} \cos\left(\eta\sqrt{\kappa^2-k^2}\right) \\ \sin\left(\eta\sqrt{\kappa^2-k^2}\right) \end{aligned}\right\} dS(Q). \tag{16}$$

$C(k)$ and $S(k)$ stand for the symmetric and antisymmetric wave components, respectively, with respect to the center plane of a symmetric ship about $y = 0$.

Since the disturbance potential is given in a linear superposition as in Eq. 4, the Kochin functions can be written in the same way as follows:

$$C(k) = C_7(k) - \frac{\omega\omega_0}{g}\sum_{j=1,3,5}\frac{X_j}{\zeta_a}\, C_j(k), \tag{17}$$

$$S(k) = S_7(k) - \frac{\omega\omega_0}{g} \sum_{j=2,4,6} \frac{X_j}{\zeta_a} S_j(k), \tag{18}$$

where $j = 1, 3, 5$ denote the longitudinal ship motions (surge, heave and pitch) and $j = 2, 4, 6$ the lateral ship motions (sway, roll, and yaw). X_j/ζ_a denotes the normalized complex amplitude of jth mode of ship motion, which must be given by solving the ship-motion equations.

3. Calculation Formulae for Wave-Induced Steady Forces and Yaw Moment

It is well known that the calculation formulae for wave-induced steady force and moment can be obtained from the principles of momentum and energy conservation, and associated analyses can be done on the control surface far from the ship using the far-field expression of the velocity potential, shown in the previous section.

Maruo [2] derived the formula for the added resistance ($\overline{R}$) but the analysis using the stationary-phase method was complicated. Kashiwagi [5] showed a simpler analysis by use of Parseval's theorem in the Fourier transform, and by extending the analysis, he also derived the formulae for the steady sway force ($\overline{Y}$) and yaw moment ($\overline{N}$). Those formulae can be summarized as follows:

$$\frac{\overline{R}}{\rho g \zeta_a^2} = \frac{1}{4\pi k_0} \int_{-\infty}^{\infty} \epsilon_k u(\kappa^2 - k^2) \left\{ \left|C(k)\right|^2 + \left|S(k)\right|^2 \right\} \frac{\kappa\,(k - k_0\cos\chi)}{\sqrt{\kappa^2 - k^2}}\, dk, \tag{19}$$

$$\begin{aligned} \frac{\overline{Y}}{\rho g \zeta_a^2} = &- \frac{1}{4\pi k_0} \int_{-\infty}^{\infty} \epsilon_k u(\kappa^2 - k^2) \Big[\Im\Big\{ 2C(k)\, S^*(k) \Big\} \\ &- \Big\{ \left|C(k)\right|^2 + \left|S(k)\right|^2 \Big\} \frac{k_0 \sin\chi}{\sqrt{\kappa^2 - k^2}} \Big] \kappa\, dk, \end{aligned} \tag{20}$$

$$\begin{aligned} \frac{\overline{N}}{\rho g \zeta_a^2} = &\frac{1}{4\pi k_0} \int_{-\infty}^{\infty} \epsilon_k u(\kappa^2 - k^2)\, \Re\Big\{ C'(k)\, S^*(k) - S'(k)\, C^*(k) \Big\} \kappa\, dk \\ &- \frac{\sin\chi}{2}\, \Re\Big[H'(k_0,\chi) + \frac{1}{k_0}\left(\tau + \frac{k_0\cos\chi}{K_0}\right) H(k_0,\chi) \Big]. \end{aligned} \tag{21}$$

Here $C'(k)$ and $S'(k)$ in Eq. 21 denote differentiation with respect to k and the asterisk in the superscript stands for the complex conjugate. $H(k_0,\chi)$ are the values of the Kochin function evaluated at $k = k_0\cos\chi$ and $\pm\epsilon_k\sqrt{\kappa^2 - k^2} = k_0\sin\chi$. Thus, from Eqs. 15 and 16, we can write as

$$\begin{aligned} H(k_0,\chi) &= \iint_{S_H} \left(\frac{\partial \phi_B(Q)}{\partial n} - \phi_B(Q) \frac{\partial}{\partial n} \right) e^{-k_0\zeta + ik_0(\xi\cos\chi + \eta\sin\chi)}\, dS(Q) \\ &= C(k_0,\chi) + i\, S(k_0,\chi). \end{aligned} \tag{22}$$

We must realize from these formulae that the Kochin function is an important input and the numerical integration with respect to k must be performed accurately.

4. Overview of Enhanced Unified Theory

In the present study, the EUT is used to provide the body-disturbance velocity potential valid at a distance from the ship and consequently an expression of the Kochin function. The

EUT and its results have been explained by Kashiwagi [9, 19] and thus only the overview and some key equations will be given in this section.

The EUT for the radiation problem is basically the same as the unified theory developed by Newman [10]. However, the surge mode ($j = 1$) is analyzed in the same fashion as that for heave and pitch and its motion is computed from the coupled motion equations among surge, heave, and pitch. Furthermore, unlike the original unified theory, similar analyses are also made for lateral-motion modes ($j = 2, 4, 6$), which can be found in Kashiwagi [20] and Appendix-1 of Kashiwagi [21].

The diffraction problem in EUT is basically the same as the unified theory described in Sclavounos [8], but the effects of wave diffraction near the bow are taken into account by retaining the x-component (n_1) of normal vector in the body boundary condition for the inner problem. These bow diffraction effects are incorporated together with 3D and forward-speed effects in the outer solution through matching between the inner and outer solutions. In fact, the effect of n_1 term in the body boundary condition is crucial near the ship ends, giving an important contribution to the surge exciting force and the added resistance. Analyses for the antisymmetric component of the scattering potential are also made, as shown in Appendix-1 of Kashiwagi [21].

In the slender-ship theory, the outer solution valid far from the ship can be expressed with line distributions of 3D sources for the symmetric flow and of 3D doublets for the antisymmetric flow along the x-axis. Thus the disturbance velocity potential may be written in the form

$$\phi_j^{(o)}(x,y,z) = \int_L Q_j(\xi)\, G_{3D}^C(x-\xi,y,z)\, d\xi + \int_L D_j(\xi)\, G_{3D}^S(x-\xi,y,z)\, d\xi. \tag{23}$$

Here G_{3D}^C is the 3D Green function considered in Eq. 9 with $\eta = \zeta = 0$, physically equivalent to the velocity potential due to the source with unit strength. Q_j denotes its strength, which is unknown but can be determined through matching with the inner solution. Likewise, G_{3D}^S is the velocity potential due to the doublet with unit strength and axis parallel to the y-axis, which is given by

$$G_{3D}^S(x,y,z) \equiv -\frac{\partial}{\kappa \partial y} G_{3D}(x,y,z). \tag{24}$$

D_j in Eq. 23 is the unknown strength of the doublet and can be determined through the matching procedure. The range of integration in Eq. 23 is assumed to be from the stern end to the bow end of a ship along the x-axis.

By substituting the asymptotic expression of the Green function Eq. 10 into Eq. 23, we can obtain the expressions for the symmetric and antisymmetric Kochin functions in the following form:

$$C_j(k) = \int_L Q_j(\xi)\, e^{ik\xi}\, d\xi, \tag{25}$$

$$S_j(k) = \frac{\sqrt{\kappa^2 - k^2}}{\kappa} \int_L D_j(\xi)\, e^{ik\xi}\, d\xi \equiv \frac{\sqrt{\kappa^2 - k^2}}{\kappa}\, \widehat{S}_j(k). \tag{26}$$

In the EUT, as a result of matching between the inner and outer solutions, Q_j and D_j are determined by solving the integral equations, whose kernel functions include 3D and forward-speed effects. For instance, for the radiation problem ($j = 1 \sim 6$), the integral equations are given in the form

$$Q_j(x) + \frac{i}{2\pi}\Big(1 - \sigma_3/\sigma_3^*\Big) \int_L Q_j(\xi)\, f(x-\xi)\, d\xi = \sigma_j(x) + \frac{U}{i\omega}\,\widehat{\sigma}_j(x) \quad \text{for } j = 1, 3, 5, \tag{27}$$

$$D_j(x) + \frac{i}{2\pi}\Big(1 - \sigma_2/\sigma_2^*\Big) \int_L D_j(\xi)\, h(x-\xi)\, d\xi = \sigma_j(x) + \frac{U}{i\omega}\,\widehat{\sigma}_j(x) \quad \text{for } j = 2, 4, 6. \tag{28}$$

Here $\sigma_j(x)$ and $\widehat{\sigma}_j(x)$ on the right-hand side of Eqs. 27 and 28 are 2D Kochin functions which can be computed with the particular solutions in the inner problem considered in the transverse y-z plane at station x.

The solution in the inner problem is sought to satisfy the 2D Laplace equation, the free-surface boundary condition of Eq. 5 with $U = 0$, and the body boundary condition of Eqs. 6 and 7 on the contour of transverse section at station x, which will be denoted as $\mathcal{B}(x)$. Its solution for the radiation problem can be written in the form

$$\phi_j^{(i)}(x; y, z) = \varphi_j(y, z) + \frac{U}{i\omega}\widehat{\varphi}_j(y, z) + C_j^H(x)\, \varphi^H(y, z), \tag{29}$$

where φ_j and $\widehat{\varphi}_j$ are the particular solutions satisfying the following body boundary conditions:

$$\frac{\partial \varphi_j}{\partial n} = n_j, \quad \frac{\partial \widehat{\varphi}_j}{\partial n} = m_j. \tag{30}$$

Namely the particular solution in Eq. 29 is exactly the same as the solution in the strip theories. The last term in Eq. 29 stands for a homogeneous solution, which can be given by $\varphi^H = \varphi_j - \varphi_j^*$ ($j = 3$ for symmetric problems and $j = 2$ for antisymmetric problems), and its coefficient $C_j^H(x)$ can be determined by the matching with outer solution.

In terms of φ_j, the Kochin function σ_j is computed from

$$\sigma_j(x) = \int_{\mathcal{B}(x)} \left(\frac{\partial \varphi_j}{\partial n} - \varphi_j \frac{\partial}{\partial n} \right) e^{-Kz} \left\{ \begin{array}{c} \cos Ky \\ \sin Ky \end{array} \right\} d\ell(y, z), \tag{31}$$

where the upper term ($\cos Ky$) in braces should be taken for $j = 1, 3, 5$ and the lower term for $j = 2, 4, 6$. Likewise $\widehat{\sigma}_j(x)$ is computed in terms of $\widehat{\varphi}_j$ in place of φ_j in Eq. 31.

The kernel functions $f(x-\xi)$ and $h(x-\xi)$ in the integral equations of Eqs. 27 and 28 represent the 3D and forward-speed effects. Their explicit expressions are given in Newman and Sclavounos [22] for $f(x-\xi)$ and in Kashiwagi [20] for $h(x-\xi)$. We can see from Eqs. 27 and 28 that if the 3D and forward-speed effects become small, the strengths of source Q_j and doublet D_j may approach the 2D values on the right-side side; which is the case for higher frequencies.

Corresponding expressions for the diffraction problem are provided in Kashiwagi [21]. Expressions for the symmetric and antisymmetric Kochin functions are formally the same as those in Eq. 25 and Eq. 26, respectively, although the integral equations corresponding to Eqs. 27 and 28 are different in form. However, the numerical solutions method for the integral equations can be the same.

5. Numerical Integration Methods

Once the Kochin function has been obtained as a function of k, the accuracy in computed values of the wave-induced steady forces ($\overline{R}$ and $\overline{Y}$) and yaw moment ($\overline{N}$) depends on the numerical integration with respect to k. To be considered for correct numerical integration are the following two issues: (1) Removal of square-root singularity at the limit of integration range k_j $(j = 1 - 4)$, and (2) precise treatment of semi-infinite integrals to ensure the convergence.

5.1 Removal of singularity at integration limits

We will have to consider two types of integral:

$$\mathcal{J}_{23} \equiv \int_{k_2}^{k_3} \frac{F(k)}{\sqrt{\kappa^2 - k^2}}\,dk, \quad \mathcal{J}_4 \equiv \int_{k_4}^{\infty} \frac{F(k)}{\sqrt{\kappa^2 - k^2}}\,dk. \tag{32}$$

The square-root singularity exists in these integrals because of $\sqrt{\kappa^2 - k^2} = 0$ at k_j $(j = 2, 3, 4)$. To explain the variable transformation method for this issue, let us consider the following two integrals in general:

$$\left.\begin{aligned} \mathcal{A} &= \int_a^b \frac{f(x)}{\sqrt{(x-a)(b-x)}}\,dx \\ \mathcal{B} &= \int_b^{\infty} \frac{f(x)}{\sqrt{(x-a)(x-b)}}\,dx \end{aligned}\right\}. \tag{33}$$

For integral $\mathcal{A}$, we will use the following transformation of variable:

$$x = \frac{b+a}{2} + \frac{b-a}{2}\,\xi, \quad \xi = \sin\theta. \tag{34}$$

Then $\mathcal{A}$ can be transformed into the following form:

$$\mathcal{A} = \int_{-1}^{1} \frac{f(x)}{\sqrt{1-\xi^2}}\,d\xi = \int_{-\pi/2}^{\pi/2} f(x)\,d\theta, \tag{35}$$

where x is given by Eq. 34 with θ. We can see no singularity in the last integral with respect to θ, hence the numerical integration can be done in a straightforward manner.

Next, for integral $\mathcal{B}$, similar idea can be applied and the following variable transformation is used

$$x = \frac{b+a}{2} + \frac{b-a}{2}\,\xi, \quad \xi = \sqrt{u^2+1}. \tag{36}$$

Then we can obtain the result as follows:

$$\mathcal{B} = \int_1^{\infty} \frac{f(x)}{\sqrt{\xi^2 - 1}}\,d\xi = \int_0^{\infty} \frac{f(x)}{\sqrt{u^2+1}}\,du, \tag{37}$$

which contains again no singularity at the integration limit $(u = 0)$ so that the numerical integration can be performed with conventional schemes. In the present study, the Gauss quadrature has been used to successive integrals with finite integration range.

5.2 Semi-Infinite Integral

Many studies using the strip theory have been made so far for computing the Kochin function and then the added resistance based on Eq. 19. Most of those studies usually multiply the integrand by an artificial convergence factor, like $\exp(-\kappa z_s)$, to ensure the convergence as $k \to \infty$, and the value of z_s is tuned to see reasonably fast convergence and relatively good agreement with experiments. However, this treatment implies that the depthwise position of the line distribution of singularities in the outer solution is not on $z = 0$ and hence inconsistent in the context of slender-ship theory. Kashiwagi [6, 7] settled this problem by showing no difficulty in convergence of the integral in Eq. 19 for the added resistance, even if the sources are placed exactly on $z = 0$. In this paper, the calculation method in Kashiwagi [6, 7] is extended to the integrals for $\overline{Y}$ and $\overline{N}$, and an analytical mistake in Kashiwagi [6, 7] is corrected.

As an example for explaining the calculation method, let us consider the following semi-infinite integral:

$$\int_{k_4}^{\infty} \left|C(k)\right|^2 \frac{\kappa\,(k - k_0\cos\chi)}{\sqrt{\kappa^2 - k^2}}\,dk = \int_{k_4}^{\infty} \left|C(k)\right|^2 \frac{\left(1 - \sqrt{1 - k^2/\kappa^2}\right)(k - k_0\cos\chi)}{\sqrt{\kappa^2 - k^2}}\,dk$$
$$+\mathcal{R}_4 - \mathcal{T}_4\, k_0\cos\chi, \tag{38}$$

where

$$\mathcal{R}_4 \equiv \int_{k_4}^{\infty} \left|C(k)\right|^2 k\,dk, \quad \mathcal{T}_4 \equiv \int_{k_4}^{\infty} \left|C(k)\right|^2 dk. \tag{39}$$

Note that the first term on the right-hand side of Eq. 38 arises no problem in convergence, because $1 - \sqrt{1 - k^2/\kappa^2}$ in the numerator becomes rapidly zero as k increases. Therefore, our attention will be focused on how to evaluate the integrals denoted as $\mathcal{R}_4$ and $\mathcal{T}_4$.

At first, with the assumption that k and x are non-dimensionalized with half the ship length $L/2$, the Kochin function $C(k)$ is written in the form

$$C(k) = \int_{-1}^{1} Q(x)\,e^{ikx}\,dx. \tag{40}$$

After partial integration, it follows that

$$C(k) = \frac{i}{k}\int_{-1}^{1} Q'(x)\,e^{ikx}\,dx, \tag{41}$$

where we have used the assumption of $Q(\pm 1) = 0$, that is, both ship ends are closed, which is plausible in the potential-flow problem. Substituting these into Eq. 39, we have

$$\left.\begin{aligned} \mathcal{R}_4 &= i\int_{-1}^{1} Q'(x)\,dx \int_{-1}^{1} Q^*(\xi)\; I_4(\xi - x)\,d\xi \\ \mathcal{T}_4 &= \int_{-1}^{1} Q(x)\,dx \int_{-1}^{1} Q^*(\xi)\; I_4(\xi - x)\,d\xi \end{aligned}\right\}, \tag{42}$$

where

$$I_4(\xi - x) \equiv \int_{k_4}^{\infty} e^{ik(x-\xi)}\,dk = \pi\delta(\xi - x) - i\frac{e^{-ik_4(\xi - x)}}{\xi - x}, \tag{43}$$

and $\delta(\xi - x)$ denotes Dirac's delta function, which is obtained from the following relations:

$$\lim_{k\to\infty} \frac{\cos k(\xi - x)}{\xi - x} = 0, \quad \lim_{k\to\infty} \frac{\sin k(\xi - x)}{\xi - x} = \pi\,\delta(\xi - x) \tag{44}$$

Substituting Eq. 43 in Eq. 42 gives the following results:

$$\mathcal{R}_4 = i\pi \int_{-1}^{1} Q'(x)Q^*(x)\,dx + \int_{-1}^{1} Q'(x)\,e^{ik_4x}\,dx \int_{-1}^{1} \frac{Q^*(\xi)\,e^{-ik_4\xi}}{\xi - x}\,d\xi, \tag{45}$$

$$\mathcal{T}_4 = \pi \int_{-1}^{1} \big|Q(x)\big|^2\,dx - i \int_{-1}^{1} Q(x)\,e^{ik_4x}\,dx \int_{-1}^{1} \frac{Q^*(\xi)\,e^{-ik_4\xi}}{\xi - x}\,d\xi. \tag{46}$$

The first terms on the right-hand side of Eqs. 45 and 46 are missing in the analysis of Kashiwagi [6, 7]. However, we note that these terms have nothing to do with k_4, and they will cancel out with corresponding terms to be obtained from the integral for $-\infty < k < k_1$. In order to show this, let us consider the integral for $-\infty < k < k_1$ in the same way. Namely

$$\begin{aligned} -\int_{-\infty}^{k_1} \big|C(k)\big|^2 \,\frac{\kappa\,(k - k_0\cos\chi)}{\sqrt{\kappa^2 - k^2}}\,dk & \\ = \int_{k_1}^{-\infty} \big|C(k)\big|^2 \,\frac{\big(1 - \sqrt{1 - k^2/\kappa^2}\big)(k - k_0\cos\chi)}{\sqrt{\kappa^2 - k^2}}\,dk & \\ + \mathcal{R}_1 - \mathcal{T}_1\,k_0\cos\chi, & \end{aligned} \tag{47}$$

where

$$\mathcal{R}_1 \equiv \int_{k_1}^{-\infty} \big|C(k)\big|^2\,k\,dk, \quad \mathcal{T}_1 \equiv \int_{k_1}^{-\infty} \big|C(k)\big|^2\,dk. \tag{48}$$

Following the same procedure as that for $\mathcal{R}_4$ and $\mathcal{T}_4$, we come across an integral corresponding to Eq. 43, which can be written by use of Eq. 44 in the form

$$I_1(\xi - x) \equiv \int_{k_1}^{-\infty} e^{ik(x-\xi)}\,dk = -\pi\delta(\xi - x) - i\frac{e^{-ik_1(\xi - x)}}{\xi - x}. \tag{49}$$

It can be seen that the first term on the right-hand side of Eq. 49 is opposite in sign to that of Eq. 43. Thus, in the end after summing up, there is no contribution from the first terms in Eqs. 45 and 46.

Regarding the singular integral with respect to ξ in Eqs. 45 and 46, the analytical integration method shown in Kashiwagi [6, 7] can be applied, using the Fourier-series representation for the line distribution of sources. The resulting singular integral is the same in form as Glauert's integral popular in the wing theory and thus can be evaluated analytically. Specifically, introducing the variable transformation of $x = \cos\theta$ and $\xi = \cos\varphi$, we have the following:

$$\int_{-1}^{1} \frac{Q^*(\xi)\,e^{-i\nu\xi}}{\xi - x}\,d\xi = \sum_{n=1}^{\infty} c_n^* \int_0^{\pi} \frac{\sin n\varphi \sin\varphi}{\cos\varphi - \cos\theta}\,d\varphi = -\pi \sum_{n=1}^{\infty} c_n^* \cos n\theta, \tag{50}$$

where

$$\left.\begin{aligned} Q(x)\,e^{i\nu x} &= \sum_{n=1}^{\infty} c_n \sin n\theta \\ c_n &= \frac{2}{\pi}\int_0^{\pi} Q(\cos\theta)\,e^{i\nu\cos\theta}\sin n\theta\,d\theta \end{aligned}\right\} \tag{51}$$

and ν must be understood as k_4 or k_1.

Using these results and performing resultant integrals with respect to θ, $\mathcal{R}_j$ and $\mathcal{T}_j$ $(j=4$ or 1) defined in Eq. 39 and Eq. 48 can be expressed as

$$\mathcal{R}_j = (-1)^j\, i\pi \int_{-1}^{1} Q'(x)Q^*(x)\,dx + \frac{\pi^2}{2}\sum_{n=1}^{\infty}\Big[\,k_j\,\Im\big(c_n\,c_{n+1}^*\big) + n\,|c_n|^2\Big], \tag{52}$$

$$\mathcal{T}_j = (-1)^j \pi \int_{-1}^{1} \big|Q(x)\big|^2\,dx + \frac{\pi^2}{2}\sum_{n=1}^{\infty}\Im\big(c_n\,c_{n+1}^*\big). \tag{53}$$

As already mentioned, the first terms on the right-hand side of Eqs. 52 and 53 do not contribute to the final result because of cancellation after summing up the terms of $j=1$ and $j=4$. Needless to say, the same calculation method will be used to the integrals related to the antisymmetric component of the Kochin function $S(k)$ in Eq. 19.

The same technique can be applied to the integrals for the steady sway force $\overline{Y}$ in Eq. 20 and for the steady yaw moment $\overline{N}$ in Eq. 21. Let us start with the steady sway force. We will have to consider the following integral:

$$\begin{aligned}\int_{\nu}^{\infty} \kappa\,\Im\Big\{C(k)S^*(k)\Big\}\,dk = \int_{\nu}^{\infty} \kappa\Big(\sqrt{1-k^2/\kappa^2}-1\Big)\,\Im\Big\{C(k)\widehat{S}^*(k)\Big\}\,dk \\ + \int_{\nu}^{\infty} \kappa\,\Im\Big\{C(k)\widehat{S}^*(k)\Big\}\,dk,\end{aligned} \tag{54}$$

where $\widehat{S}(k)$ is defined in Eq. 26.

It should be noted again that no problem exists in convergence for the first term on the right-hand side of Eq. 54, because $\sqrt{1-k^2/\kappa^2} \to 1$ rapidly as $k\to\infty$. Thus we consider the last integral.

Since $\kappa = K + 2k\tau + k^2/K_0$, we should evaluate analytically the following integrals:

$$\mathcal{Y}_n \equiv \int_{\nu}^{\infty} k^n\,\Im\Big\{C(k)\widehat{S}^*(k)\Big\}\,dk, \quad n=0,1,2. \tag{55}$$

With these results, the last term in Eq. 54 can be computed from

$$\int_{\nu}^{\infty} \kappa\,\Im\Big\{C(k)\widehat{S}^*(k)\Big\}\,dk = K\,\mathcal{Y}_0 + 2\tau\,\mathcal{Y}_1 + \frac{1}{K_0}\mathcal{Y}_2. \tag{56}$$

The analysis for Eq. 55, using the Fourier-series representation for the line distribution of sources and doublets, are rather lengthy and thus, their transformation and results are shown in Appendix of this paper.

Likewise, the semi-infinite integral in the steady yaw moment can be written as follows:

$$\begin{aligned}&\int_{\nu}^{\infty} \kappa\,\Re\Big\{C'(k)S^*(k) - S'(k)C^*(k)\Big\}\,dk \\ &\quad = \int_{\nu}^{\infty} \kappa\Big(\sqrt{1-k^2/\kappa^2}-1\Big)\,\Re\Big\{C'(k)\widehat{S}^*(k) - \widehat{S}'(k)C^*(k)\Big\}\,dk \\ &\quad + \int_{\nu}^{\infty} \kappa\,\Re\Big\{C'(k)\widehat{S}^*(k) - \widehat{S}'(k)C^*(k)\Big\}\,dk.\end{aligned} \tag{57}$$

The first term on the right-hand side of Eq. 57 can be numerically integrated without any difficulty. For evaluating the last term in Eq. 57, we consider analytically the following integrals:

$$\mathcal{N}_n \equiv \int_\nu^\infty k^n \,\Re\Big\{ C'(k)\widehat{S}^*(k) \Big\}\, dk, \quad n = 0, 1, 2, \tag{58}$$

$$\tilde{\mathcal{N}}_n \equiv \int_\nu^\infty k^n \,\Re\Big\{ \widehat{S}'(k)C^*(k) \Big\}\, dk, \quad n = 0, 1, 2. \tag{59}$$

With the results of these integrals, we can readily evaluate the last integral in Eq. 57 from

$$\begin{aligned} &\int_\nu^\infty \kappa\,\Re\Big\{ C'(k)\widehat{S}^*(k) - \widehat{S}'(k)C^*(k) \Big\}\, dk \\ &= K(\mathcal{N}_0 - \tilde{\mathcal{N}}_0) + 2\tau\,(\mathcal{N}_1 - \tilde{\mathcal{N}}_1) + \frac{1}{K_0}(\mathcal{N}_2 - \tilde{\mathcal{N}}_2). \end{aligned} \tag{60}$$

The analytical procedure for computing Eqs. 58 and 59 is essentially the same as that for $\mathcal{Y}_n$ $(n = 0, 1, 2)$, and we note that the calculation of $\tilde{\mathcal{N}}_n$ can be done easily from the result of $\mathcal{N}_n$ simply by exchanging $C(k)$ and $\widehat{S}(k)$. The final expressions for $\mathcal{N}_n$ and $\tilde{\mathcal{N}}_n$ $(n = 0, 1, 2)$ are summarized in Appendix of this paper.

6. Experiment and Tested Ship Model

Experiments measuring the wave-induced steady forces (added resistance and sway force) and yaw moment have been conducted at the seakeeping and maneuvering model basin of Nagasaki R&D Center, Mitsubishi Heavy Industries, and some of the results are reported by Yasukawa *et al.* [18]. These experimental data are used for comparison with computations in the present paper.

The ship model used in the experiment is a bulk carrier named JASNAOE-BC084 in full-load condition, which is a modified version from KVLCC2 and its body plan and principal particulars are shown in Yasukawa *et al.* [23]. Some of the important values in the principal particulars are listed in Table 1, and the length-wise projection of the body is illustrated in Fig. 2.

In this experiment conducted by Yasukawa *et al.* [18], wave-induced ship motions and steady forces were measured at 4 different forward speeds; they are 0, 4, 8, and 13.5 knots in real-ship scale. For each speed, measurements were carried out at 4 different incident-wave

Table 1 Principal particulars of JASNAOE-BC084 hull

Item	Value	Unit
Length between perpendiculars (L)	320.00	m
Breadth (B)	58.00	m
Draft (d)	20.80	m
Block coefficient (C_B)	0.84	–
Midship coefficient (C_M)	0.99	–
Waterplane coefficient (C_W)	0.93	–
Center of gravity (OG)	9.80	m
Roll gyrational radius (κ_{xx}/B)	0.35	–
Pitch gyrational radius (κ_{yy}/L)	0.25	–
Yaw gyrational radius (κ_{zz}/L)	0.25	–

angles (χ) as shown in Fig. 3. In the highest speed case (13.5 knot), the measurement was done only in head waves ($\chi = 180$ deg). The range of wavelengths (the ratio of wavelength to ship length λ/L) is $\lambda/L = 0.4-1.5$, but the wavelength $\lambda/L = 0.4$ was not used in oblique waves of $\chi = 30°$ and $90°$.

In all cases, the ship model was set to be free in all modes of ship motion, but coil springs were used to constrain loosely the surge, sway, and yaw motions. According to the report, the incident-wave amplitude was measured by two different wave probes; one is near-field probe installed on the running carriage, upstream of the ship model, and the other is far-field probe fixed spatially near the side wall of the towing tank. At the wavelengths where interaction is intense, for instance where the peaks of forces are measured ($\lambda/L = 1.0 \sim 1.2$), a large difference was observed in the incident-wave amplitude measured by these two different probes. This phenomenon can be understood, since the record by the near-field probe may include the ship disturbance waves. On the other hand, the record by the far-field probe must contain only negligibly small, or not at all, waves generated by the ship. For this physical reason, the non-dimensional values in terms of the far-field incident-wave amplitudes will be used as the experimental data in this paper.

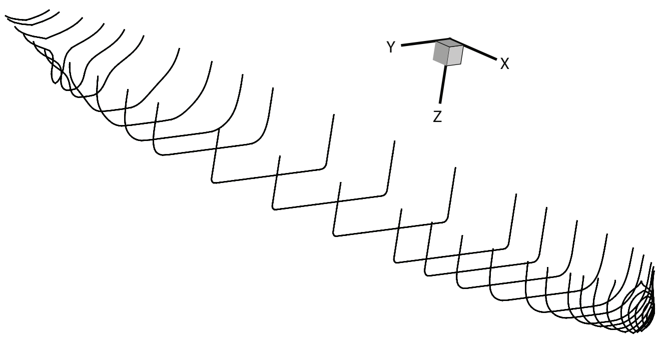

Fig. 2 Length-wise projection of body plan

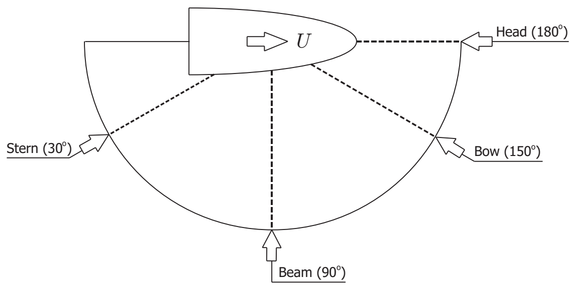

Fig. 3 Ship-waves encountering angles

The amplitude ζ_a and maximum slope $k_0\zeta_a$ of the incident wave are used for non-dimensional values of the translational and rotational motions, respectively. Time-averaged wave-induced steady forces (added resistance $\overline{R}$ and sway force $\overline{Y}$) and yaw moment $\overline{N}$ are non-dimensionalized with $\rho g\zeta_a^2(B^2/L)$ and $\rho g\zeta_a^2 LB$, respectively, where ρ is the density of water; g the acceleration of gravity; L the ship length; and B the ship breadth.

7. Results and Discussion

Precise prediction of the Kochin functions is of vital importance for computations of the wave-induced steady forces and moment. As shown in Eqs. 17 and 18, the complex amplitude of ship motions, X_j/ζ_a ($j = 1-6$) must be given for the motion-free case. Therefore, a comparison is made first for the amplitude of ship motions. In oblique waves where antisymmetric motions arises, we observed that the linear computation (considering only the wave-making component for the damping) gives overpredicted roll motion and its coupling,

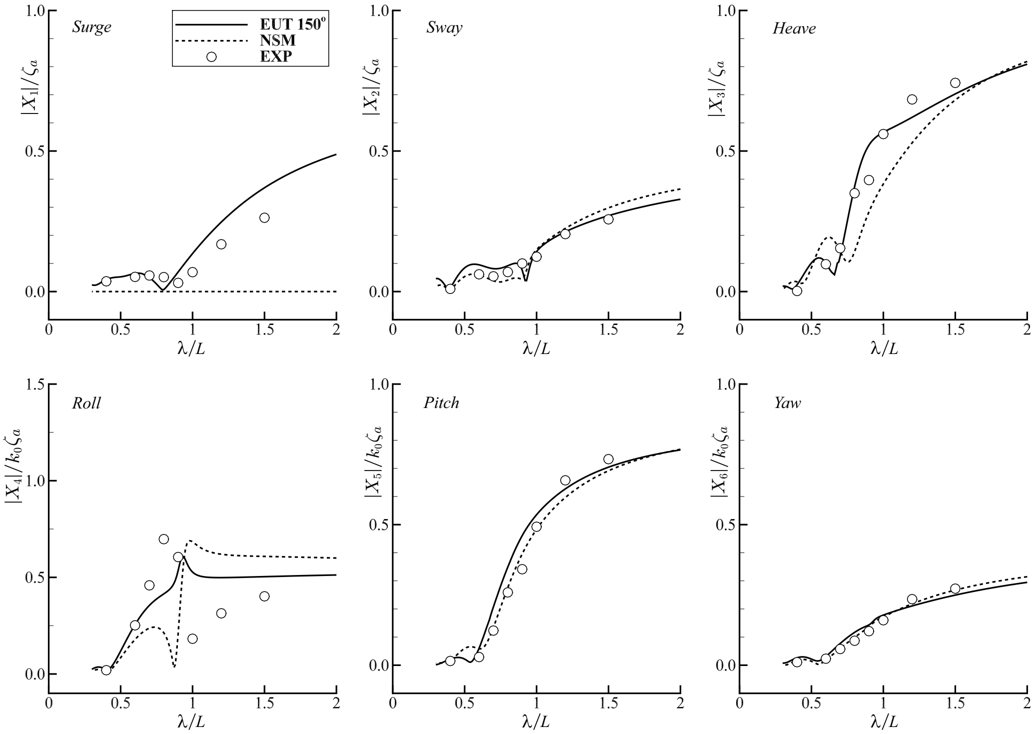

Fig. 4 Ship motions in bow oblique waves ($\chi = 150$ deg) at 4 knots ($Fn = 0.037$)

particularly near the resonant peak in roll. Therefore, we introduced an equivalent damping coefficient taking account of viscous effects, based on the component analysis method as formulated by Himeno [23].

Figure 4 shows the non-dimensional amplitudes of wave-induced motions of bulk carrier advancing at 4 knot ($Fn = 0.037$) in bow oblique waves ($\chi = 150$ deg). Computed results by EUT and NSM are compared with the experimental data non-dimensionalized by the incident-wave amplitude measured with far-field wave probe (which are denoted as EXP). We can observe remarkable agreement between computed and measured results as well as the superiority of EUT to NSM on certain modes of motion, like heave and roll. Nevertheless, the computed wavelength where the roll motion takes a peak due to its resonance is slightly different from the measured one, which may be attributed to an error in the measurement of roll moment of inertia and vertical position of the center of gravity, although the uncertainty level in the measurement cannot be described explicitly.

As representative examples, the wave-induced added resistance, sway force, and yaw moment at 4 knot ($Fn = 0.037$) are presented in Fig. 5 (for $\chi = 150°$ and $180°$) and in Fig. 6 (for $\chi = 30°$ and $90°$). Overall, computed values are in favorable agreement with measured data. EUT is in general better than NSM due to inclusion of 3D and forward-speed effects. In shorter waves, EUT is also prominently superior to NSM, mainly because the effect of n_1 term is retained in the body boundary condition for the diffraction problem. It should be noted that the values of $\overline{Y}$ and $\overline{N}$ must be zero in head waves, but as shown in Fig. 5, nonzero values can be observed, which indicates a possible degree of experimental error or noise.

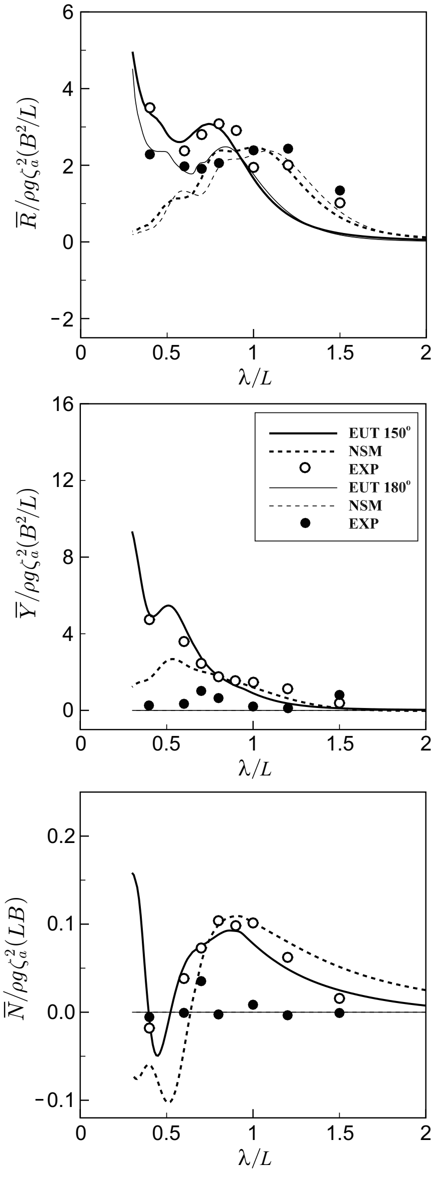

Fig. 5 $\overline{R}$, $\overline{Y}$ and $\overline{N}$ in bow ($\chi = 150$ deg) and head ($\chi = 180$ deg) waves at 4 knot ($Fn = 0.037$)

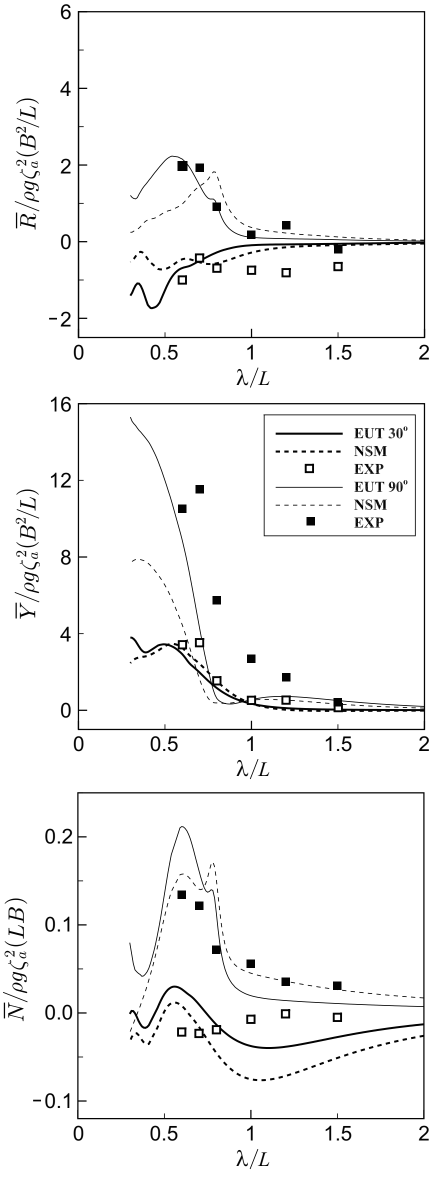

Fig. 6 $\overline{R}$, $\overline{Y}$ and $\overline{N}$ in stern ($\chi = 30$ deg) and beam ($\chi = 90$ deg) waves at 4 knot ($Fn = 0.037$)

At higher forward speed of 13.5 knot ($Fn = 0.124$), the measurement was done only for head waves, in which obviously the steady sway force ($\overline{Y}$) and yaw moment ($\overline{N}$) are very small, hence only the added resistance ($\overline{R}$) is depicted in Fig. 7. We note that the peak value of the added resistance tends to be sensitive to the accuracy in the incident-wave amplitude and also to nonlinear effects in ship motion.

As examined previously by Skejic and Faltinsen [15] and Seo and Kim [16], the horizontal steady forces and moment show its large influence on the ship maneuvering trajectory, with

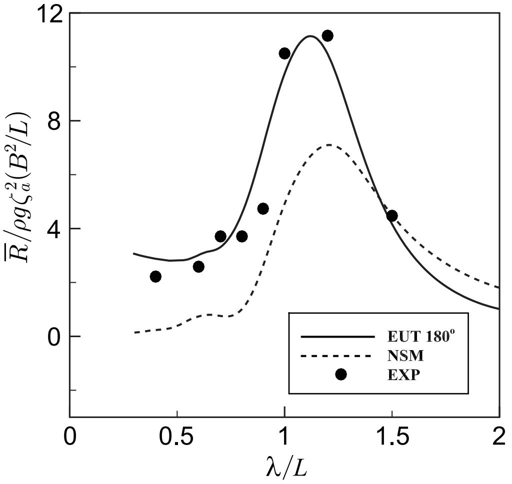

Fig. 7 Added resistance in head waves at 13.5 knot ($Fn = 0.124$)

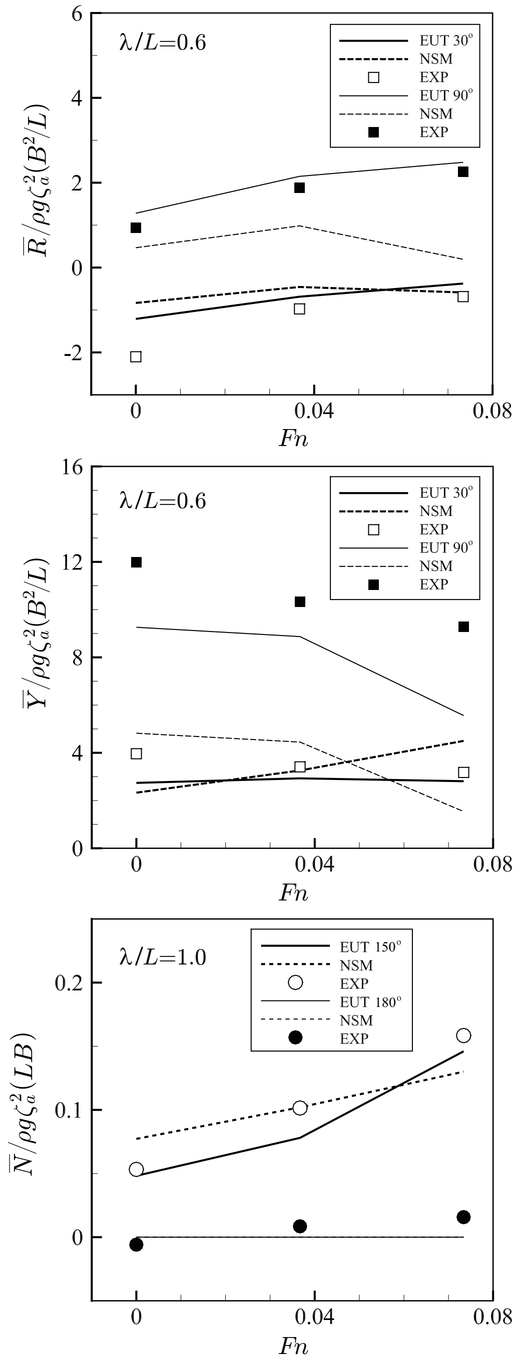

Fig. 8 Forward-speed effect to steady horizontal forces and moment

emphasis put on the difficulty in computation of steady yaw moment. In maneuvering motions, the amplitude of these second-order quantities in wave amplitude changes at every time step in numerical simulations, depending on varying values of U and χ. Therefore, we checked the steady forces and moment in increasing the forward speed at crucial frequencies in oblique wave condition, and the results of which are shown in Fig. 8.

In relatively short waves ($\lambda/L = 0.6$), the superiority of EUT to NSM is evident in the prediction of $\overline{R}$ and $\overline{Y}$. One of the noteworthy points is a significant value of the added resistance even in zero speed due to realistic ship geometry. In contrast, for a fore-aft symmetric ship (e.g. Wigley hull), it is clear that this quantity will be essentially zero.

On the other hand, for the steady yaw moment ($\overline{N}$), we suspect potential difficulty in the computation due to its sensitivity to several parameters. However, relatively good agreement can be confirmed between computed and measured results at $\lambda/L = 1.0$.

After all, more validation and improvement of the computation method should be made for higher Froude numbers and other distinct ship geometries.

8. Conclusions

Investigation on the wave-induced steady forces (added resistance and sway force) and yaw moment acting on an advancing ship in oblique waves has been made. We employed enhanced unified theory (EUT) and new strip method (NSM) for solving the radiation and diffraction problems, computing the ship motions in waves and the symmetric and antisymmetric components of the Kochin function equivalent to the complex amplitude of ship-generated disturbance waves at a distance from the ship. These Kochin functions are important input data in the formulae for computing the steady forces and moment based on the principles of momentum and energy conservation. Special attention was paid on the precise computation method ensuring convergence in the semi-infinite integrals appearing in those formulae not only for the added resistance, but also for the steady sway force and yaw moment. The analytical integration method shown in this paper is exact and distinctly different from conventional ones which introduce an artificial convergence factor. For validation of the computation method, we used the experimental data conducted by Yasukawa *et al.* [18] with a bulk carrier model in the motion-free case with forward speed under several incident-wave angles.

Through a comparison between computed and measured results, we observed that EUT can predict the steady horizontal forces and yaw moment better than NSM. When the wavelength is much small compared to the ship length, the wave diffraction near the ship ends becomes dominant and important for accurate computations of wave-induced steady forces, especially for the added resistance and sway force. The EUT is superior in accounting for the effect of bow wave diffraction, because the x-component of the normal vector is retained in the body boundary condition.

For wavelengths longer than $\lambda/L \approx 1.0$, contribution of the radiation Kochin function becomes important and the radiation Kochin function was found to be rather sensitive to the ship's forward speed. Therefore, forward-speed effects must be taken into account in a reasonable way for the wave-induced steady horizontal forces and yaw moment.

Acknowledgments

The authors acknowledge Prof. Hironori Yasukawa of Hiroshima University for his permission to use the experimental data shown in this paper and associated discussions at the JASNAOE Strategy Research Committee on IMO Guideline of Minimum Engine Power. The authors are also indebted to the discussion with Dr. Hiroshi Isshiki on the analytical treatment of semi-infinite integrals. A part of this study was supported by JSPS Grant-in-Aid for Scientific Research (Grant number 17H01357) and also the subsidy for International Collaboration Promotion Program at Osaka University.

References

[1] Maruo H (1960) Wave resistance of a ship in regular head seas. Bulletin Faculty of Eng Yokohama National University 9:73-91

[2] Newman JN (1967) The drift force and moment on ships in waves. J Ship Res 11(1):51-60

[3] Lin WC, Reed AM (1976) The second order steady force and moment on a ship moving in an oblique seaway. In: Proceedings of the 11th Symposium on Naval Hydrodynamics. London, pp 333-345

[4] Kashiwagi M (1991) Calculation formulas for the wave-induced steady horizontal force and yaw moment on a ship with forward speed. Reports of RIAM 37(107):1-18, Kyushu University

[5] Kashiwagi M (1992) Added resistance, wave-induced steady sway force and yaw moment on an advancing ship. Schiffstechnik 39(1):3-16

[6] Kashiwagi M, Ohkusu M (1993) Study on the wave-induced steady force and moment. J Soc Naval Archit Jpn 173:185-194

[7] Sclavounos PD (1984) The diffraction of free-surface waves by a slender ship. J Ship Res 28(1):29-47

[8] Kashiwagi M (1995) Prediction of surge and its effect on added resistance by means of the enhanced unified theory. Trans West-Jpn Soc Naval Archit 89:77-89

[9] Newman JN (1978) The theory of ship motions. Advances in Appl Mech 18:221-283

[10] Naito S, Mizoguchi S, Kagawa K (1991) Steady forces acting on ships with advance velocity in oblique waves. J Kansai Soc Nav Archit Jpn 213:45-50

[11] Iwashita H, Ito A, Okada T, Ohkusu M, Mizoguchi S (1992) Wave forces acting on a blunt ship with forward speed in oblique sea. J Soc Nav Archit Jpn 171:109-123

[12] Ueno M, Nimura T, Miyazaki H, Nonaka K, Haraguchi T (2001) Steady wave forces and moment acting on ships in manoeuvring motion in short waves. J Soc Nav Archit Jpn 188:163-172

[13] Joncquez SAG (2009) Second-order forces and moments acting on ships in waves. PhD thesis. Technical University of Denmark, Copenhagen

[14] Skejic R, Faltinsen OM (2008) A unified seakeeping and maneuvering analysis of ships in regular waves. J Mar Sci Technol 13:371-394

[15] Seo M, Kim Y (2011) Numerical analysis on ship maneuvering coupled with ship motion in waves. Ocean Eng 38:1934-1945

[16] Zhang W, Zou Z, Deng D (2017) A study on prediction of ship maneuvering in regular waves. Ocean Eng 137:367-381

[17] Yasukawa H, Hirata N, Matsumoto A, Kuroiwa R, Mizokami S (2017) Evaluation of wave-induced steady forces and turning motion of a full hull ship in waves. J Mar Sci Technol (to be published)

[18] Yasukawa H, Sano M, Hirata N, Yonemasu I, Kayama Y, Hashizume Y (2015) Maneuverability of C_b-series full hull ships (1st report: tank tests). J Jpn Soc Nav Archit Ocean Eng 21:11-22

[19] Kashiwagi M, Ikeda T, Sasakawa T (2010) Effects of forward speed of a ship on added resistance in waves. Intl J Offshore Polar Eng 20(3):196-203

[20] Kashiwagi M (1985) The unified slender ship theory for lateral motions of ships with forward speed. J Kansai Soc Nav Archit Jpn 197:21-30

[21] Kashiwagi M (1997) Numerical seakeeping calculations based on the slender ship theory. Schiffstechnik 44:167-192

[22] Newman JN, Sclavounos PD (1980) The unified theory of ship motions. In: Proceedings of the 13th Symposium on Naval Hydrodynamics. Tokyo, pp 373-394

[23] Himeno Y (1981) Prediction of ship roll damping - a state of the art. Rep No 239. Nav Arch Mar Eng, University of Michigan

Appendix

A1. Analytical Integration for $\mathcal{Y}_n$, $\mathcal{N}_n$, and $\tilde{\mathcal{N}}_n$

For computing the wave-induced steady sway force and yaw moment, the following integrals are needed to integrate analytically:

$$\mathcal{Y}_n \equiv \int_\nu^\infty k^n \,\Im\Big\{C(k)\widehat{S}^*(k)\Big\}\,dk, \quad n = 0, 1, 2, \tag{61}$$

$$\mathcal{N}_n \equiv \int_\nu^\infty k^n \,\Re\Big\{C'(k)\widehat{S}^*(k)\Big\}\,dk, \quad n = 0, 1, 2, \tag{62}$$

$$\tilde{\mathcal{N}}_n \equiv \int_\nu^\infty k^n \,\Re\Big\{\widehat{S}'(k)C^*(k)\Big\}\,dk, \quad n = 0, 1, 2, \tag{63}$$

where ν must be understood as a value equal to or larger than k_4 or $|k_1|$.

We consider $\mathcal{Y}_n$ first. By substituting the definition of the Kochin functions $C(k)$ and $\widehat{S}(k)$ shown in Eqs. 25 and 26 and performing partial integration with assumption of $Q(\pm 1) = 0$ and $D(\pm 1) = 0$, we have

$$\mathcal{Y}_0 = \Im\left[\int_{-1}^1 Q(x)\,dx \int_{-1}^1 D^*(\xi)\,d\xi \int_\nu^\infty e^{ik(x-\xi)}\,dk\right], \tag{64}$$

$$\mathcal{Y}_1 = \Im\left[i\int_{-1}^1 Q'(x)\,dx \int_{-1}^1 D^*(\xi)\,d\xi \int_\nu^\infty e^{ik(x-\xi)}\,dk\right], \tag{65}$$

$$\mathcal{Y}_2 = \Im\left[\int_{-1}^1 Q'(x)\,dx \int_{-1}^1 D^{*\prime}(\xi)\,d\xi \int_\nu^\infty e^{ik(x-\xi)}\,dk\right]. \tag{66}$$

The semi-infinite integral with respect to k can be given by the formula of Eq. 43, but as explained in the analysis for the added resistance, there is no need to consider the contribution from Dirac's delta function in the final result for the steady sway force as well. To evaluate singular integrals with respect to ξ to be obtained from the last term in Eq. 43, we prepare the following Fourier series:

$$\left.\begin{aligned} D^*(\xi)\,e^{-i\nu\xi} &= \sum_{n=1}^\infty s_n^* \sin n\varphi \\ D^{*\prime}(\xi)\,e^{-i\nu\xi} &= -\frac{1}{\sin\varphi}\sum_{n=1}^\infty s_n^*\big\{-i\nu\sin\varphi\sin n\varphi + n\cos n\varphi\big\} \\ s_n^* &= \frac{2}{\pi}\int_0^\pi D^*(\cos\varphi)\,e^{-i\nu\cos\varphi}\sin n\varphi\,d\varphi \end{aligned}\right\}. \tag{67}$$

Then the singular integrals with respect to ξ can be analytically integrated like Eq. 50, and the results are written as

$$\int_{-1}^{1} \frac{D^*(\xi)\, e^{-i\nu\xi}}{\xi - x}\, d\xi = -\pi \sum_{n=1}^{\infty} s_n^* \cos n\theta, \tag{68}$$

$$\int_{-1}^{1} \frac{D^{*\prime}(\xi)\, e^{-i\nu\xi}}{\xi - x}\, d\xi = -\pi \sum_{n=1}^{\infty} s_n^* \Big\{ i\nu \cos n\theta + n\, \frac{\sin n\theta}{\sin\theta} \Big\}, \tag{69}$$

where $x = \cos\theta$ has been used. Then after substituting Eq. 51, resulting integrals with respect to x can be evaluated as the integrals with respect to θ, for which the following formulae will be used:

$$\int_0^{\pi} \cos m\theta \sin n\theta \sin\theta\, d\theta = \frac{\pi}{4} \{\, \delta_{m+1,n} - \delta_{m,n+1} \,\} \tag{70}$$

$$\int_0^{\pi} \cos m\theta \cos n\theta\, d\theta = \int_0^{\pi} \sin m\theta \sin n\theta\, d\theta = \frac{\pi}{2}\, \delta_{m,n} \tag{71}$$

$$\int_0^{\pi} \frac{\sin m\theta \cos n\theta}{\sin\theta}\, d\theta = \begin{cases} \pi & \text{for } m > n \\ 0 & \text{otherwise} \end{cases} \tag{72}$$

where $\delta_{m,n}$ denotes Kroenecker's delta symbol, equal to 1 when $m = n$ and zero otherwise.

Performing integration by using these formulae, we can obtain the following results:

$$\begin{aligned} \mathcal{Y}_0 &= \Im\Big[-i \int_{-1}^{1} Q(x)\, e^{i\nu x}\, dx \int_{-1}^{1} \frac{D^*(\xi)\, e^{-i\nu\xi}}{\xi - x}\, d\xi \Big] \\ &= \frac{\pi^2}{4} \Re \sum_{n=1}^{\infty} \{\, c_{n+1}\, s_n^* - c_n\, s_{n+1}^* \,\}, \end{aligned} \tag{73}$$

$$\begin{aligned} \mathcal{Y}_1 &= \Im\Big[\int_{-1}^{1} Q'(x)\, e^{i\nu x}\, dx \int_{-1}^{1} \frac{D^*(\xi)\, e^{-i\nu\xi}}{\xi - x}\, d\xi \Big] \\ &= \frac{\pi^2}{4} \Re \sum_{n=1}^{\infty} \Big[\nu \{\, c_{n+1}\, s_n^* - c_n\, s_{n+1}^* \,\} - i\big(2n\, c_n\, s_n^*\big) \Big], \end{aligned} \tag{74}$$

$$\begin{aligned} \mathcal{Y}_2 &= \Im\Big[-i \int_{-1}^{1} Q'(x)\, e^{i\nu x}\, dx \int_{-1}^{1} \frac{D^{*\prime}(\xi)\, e^{-i\nu\xi}}{\xi - x}\, d\xi \Big] \\ &= \frac{\pi^2}{4} \Re \sum_{n=1}^{\infty} \Big[\nu^2 \{ c_{n+1}\, s_n^* - c_n\, s_{n+1}^* \,\} - i\nu\big(4n\, c_n\, s_n^*\big) \\ &\quad + 2n \sum_{\ell=1}^{\infty} (n + 2\ell - 1) \{\, c_{n+2\ell-1}\, s_n^* - s_{n+2\ell-1}\, c_n^* \} \Big] \end{aligned} \tag{75}$$

where the Fourier-series coefficient c_n is given in Eq. 51.

Next we consider $\mathcal{N}_n$ and $\tilde{\mathcal{N}}_n$. We note that $\tilde{\mathcal{N}}_n$ can be computed from the results of $\mathcal{N}_n$, simply by replacing c_n and s_n^* with s_n and c_n^*, respectively, in the Fourier-series coefficients.

In the calculation for $\mathcal{N}_n$ and $\tilde{\mathcal{N}}_n$, the derivatives of the Kochin functions with respect to k are needed, which can be given simply as

$$C'(k) = \int_{-1}^{1} ix\, Q(x)\, e^{ikx}\, dx, \quad \widehat{S}'(k) = \int_{-1}^{1} ix\, D(x)\, e^{ikx}\, dx \tag{76}$$

Since the analytical procedure is almost the same as that for $\mathcal{Y}_n$ $(n=0,1,2)$, only the final results for $\mathcal{N}_n$ $(n=0,1,2)$ are written below.

$$\mathcal{N}_0 = -\frac{\pi^2}{8}\Re\sum_{n=1}^{\infty}\big(c_{n+2}\,s_n^* - c_n\,s_{n+2}^*\big), \tag{77}$$

$$\mathcal{N}_1 = -\frac{\pi^2}{8}\Re\sum_{n=1}^{\infty}\Big[\nu\big(c_{n+2}\,s_n^* - c_n\,s_{n+2}^*\big) - i\,2\big\{n\,c_{n+1}\,s_n^* + (n+1)\,c_n\,s_{n+1}^*\big\}\Big], \tag{78}$$

$$\begin{aligned}\mathcal{N}_2 = -\frac{\pi^2}{8}\Re\sum_{n=1}^{\infty}\Bigg[&\nu^2\big(c_{n+2}\,s_n^* - c_n\,s_{n+2}^*\big) - i\,\nu 4\big\{n\,c_{n+1}\,s_n^* + (n+1)\,c_n\,s_{n+1}^*\big\}\\ &-4\,n\,c_n\sum_{\ell=1}^{\infty}\Big\{(n+2\ell)\,s_{n+2\ell}^* + (n+2\ell-2)\,s_{n+2\ell-2}^*\Big\}\Bigg].\end{aligned} \tag{79}$$

Enhanced Unified Theory with Forward-Speed Effect Taken into Account in the Inner Free-Surface Condition*

Masashi KASHIWAGI
Department of Naval Architecture & Ocean Engineering, Osaka University
2-1 Yamada-oka, Suita, Osaka 565-0871, Japan

Abstract

The enhanced unified theory (EUT) has been used as a core theory in the integrated system developed at RIOS (Research Initiative on Oceangoing Ships) of Osaka University for predicting the propulsion and seakeeping performance of a ship in actual seas. In this study, the EUT is modified by adopting partially the solution method in the rational strip theory of Ogilvie and Tuck as a particular solution in the inner problem, thereby a forward-speed effect in the convection term of the free-surface condition is incorporated in the inner solution. This forward-speed effect is analytically shown to contribute only to the cross-coupling radiation forces. Some other forward-speed and 3D effects important in a low-frequency range are also included in the homogeneous component of the inner solution through matching with the outer solution in a similar manner to the unified theory of Newman. Numerical computations are implemented for a slender modified Wigley model and the RIOS bulk carrier model. Good agreement is confirmed in a comparison with experimental data for the cross-coupling added mass and damping coefficients between heave and pitch and also for the resulting ship motions, particularly in heave near the resonant frequency. The added resistance around the motion-resonant wavelength is found to be improved but sensitive to a slight change in heave and pitch motions. Thus, it is stressed that accurate prediction of the ship motions and resultant Kochin function is critical for more accurate prediction of the added resistance in waves.

Keywords: Enhanced unified theory, rational strip theory, cross-coupling radiation force, ship motion, added resistance, forward-speed effect, seakeeping.

1. Introduction

Although the design of the ship hull form has been based mainly on the propulsion performance in still water, recently, prediction and onboard data analysis for the propulsion and seakeeping performance of a ship in actual irregular waves have been attracting attention of the researchers (Orihara & Tsujimoto 2018; Minoura *et al.* 2019). In fact, real ships navigate mostly in rough seas, and thus, the so-called short-term and long-term predictions of ship response in actual seas must be made to guarantee the performance and safety of a ship. This trend to study the seakeeping performance of a ship is partly because the Energy Efficiency Design Index regulation was introduced by International Maritime Organization (IMO) to reduce greenhouse gas emission from the ships in operation. Thus, it becomes

* *Reprinted from Journal of Ship Research, Published on 11 December, 2020, Paper Number: SNAME-JSR-04200028, https://doi.org/10.5957/JOSR.04200028*

important to predict with sufficient accuracy the wave-induced ship motions, the added resistance, and the resultant speed loss of a ship in irregular waves represented by a directional wave spectrum (Kashiwagi 2009; Kim *et al.* 2017) even in the initial stage of ship design, necessitating computations for various profiles of a candidate ship.

However, in the ship-building community, strip methods have been used for a quick initial prediction of the seakeeping performance with recognition that several shortcomings exist in the theory used. On the other hand, some advanced calculation methods like Computational Fluid Dynamics (CFD) are available at present (ITTC 2017), but practically, CFD methods are time-consuming despite a fact that they allow studying all nonlinear effects related to large-amplitude motions and fluid viscosity. Moreover, because all physical phenomena are included altogether, it may be hard to understand which components are influential and how and why they are important. El Moctar *et al.* (2017) studied the added resistance using CFD methods, but they conclude that predicting the wave-induced resistance of ships in waves remains challenging. In the framework of linear potential flow with forward speed, Rankine Panel Methods (RPM) are popular these days (Kim & Kim 2011; Shao & Faltinsen 2012; Söding *et al.* 2014 to name a few), but most studies using RPM have been made for regular head waves, and they are still unreliable for low-frequency stern quartering waves and time-consuming if we would compute for all wave directions and frequencies needed for predicting ship responses to irregular waves. Particularly, for the short-term prediction in irregular waves in terms of the spectrum method, the frequency response functions for hydrodynamic quantities concerned must be obtained over a wide range of frequencies and incident-wave angles at various ship speeds. Therefore, the calculation method to be used must be fast in computation, reliable in accuracy, and able to deal with practical geometries such as the bulbous bow. These requirements may be satisfied by the enhanced unified theory (EUT) developed by Kashiwagi (1995). With this background, the Research Initiative on Oceangoing Ships (RIOS) at Osaka University has adopted the EUT as a core theory in the integrated prediction and analysis system, in which almost all physical quantities relevant to the seakeeping performance of ships can be computed.

What is important in this prediction system is not only fast computation for various conditions but also we must be able to understand semianalytically whether obtained results are reasonable and which components in the boundary conditions or governing equations are essential for further improvement in the results obtained. This kind of understanding is of critical importance from an academic viewpoint. In that sense, slender-ship theories are still valuable and worth revisiting for understanding a relationship particularly between forward-speed term in the free-surface condition and hydrodynamic-force components in the ship-motion equations.

The EUT is based on the slender ship theory and is enhanced from the original unified theory (UT) initiated by Newman (1978) which has brought in 3D effects important for lower frequencies and some forward-speed effects to the 2D strip-theory solution. Sclavounos (1984) extended Newman's UT for the radiation problem to the diffraction problem, but the effect of bow-wave diffraction was not taken into account. The EUT can analyze the surge-mode radiation problem in the same fashion as that for heave and pitch and also the wave-scattering problem near the ship bow at short waves by retaining the n_x term in the body boundary condition. Consequently, the added resistance can be computed with reasonable accuracy using this EUT. However, notwithstanding relatively good agreement with measured results, it is known as one of the deficiencies that the forward-speed effects in cross-coupling added mass and damping coefficients (particularly between heave and pitch) are not properly accounted for in the EUT (Kashiwagi *et al.* 2000).

Regarding this deficiency, Ogilvie and Tuck (1969) developed a rational strip theory (RST) in which the free-surface boundary condition in the inner problem close to the ship hull retains not only the zero-speed leading term but also the second leading term that is speed-dependent and proportional to the parameter $\tau = U\omega/g$ (where U and ω are the forward speed and oscillation circular frequency, respectively, and g is the gravitational acceleration). After comprehensive analysis, it was proven that the solution representing the forward-speed effect linearly proportional to U in the inner free-surface condition contributes eventually only to the cross-coupling added mass and damping coefficients. Numerical computations based on this RST had been implemented by Faltinsen (1974) and very impressive agreement with measured results was found in the cross-coupling terms between heave and pitch. These findings and proof could be achieved for the first time with analytical study, and they are useful information for understanding the physics in computed results to be obtained with large-scale time-consuming computations.

Recalling these results, we recognized that the analysis in the RST of Ogilvie and Tuck (1969) must be adopted as the particular solution in the UT in place of the conventional strip theory solution, and then 3D effects in a low-frequency range must be incorporated through the homogeneous solution as in the original UT. With this idea, the present paper proposes a new slender ship theory while keeping the basic theoretical framework of the EUT, and its validity is confirmed by comparison with experiments for the cross-coupling added mass and damping coefficients in heave and pitch; the resulting ship motions in surge, heave, and pitch; and the added resistance in the motion-free condition in head waves. The ship models used for numerical computations and comparison with experiments are a slender modified Wigley model with longitudinal symmetry and the RIOS bulk carrier model with block coefficient $C_b = 0.8$.

In this article, Section 2 outlines the formulation, the concept of slender ship theory, resulting outer and inner solutions, and their matching to take account of the forward-speed effect in the inner free-surface boundary condition. In Section 3, the calculation method is described for the cross-coupling radiation forces originating from the forward-speed term in the inner free-surface condition and also briefly for the ship motions and added resistance. Computed results are compared in Section 4 with measured results in the experiment, and discussion is made on the degree of improvement in the ship motions and added resistance by taking account of the forward-speed effect in the inner free-surface condition. Conclusions are written in Section 5.

2. Theory

2.1 Formulation

A ship is assumed to advance at constant forward speed U and oscillate with circular frequency ω in deep water. The right-handed Cartesian coordinate system moving with the ship is chosen, with the x-axis pointing in the direction of forward motion and the z-axis downward. Because there is no outstanding deficiency in the EUT for the diffraction problem, only the radiation problem is considered in this study under the assumption of inviscid fluid with irrotational motion. Then, the velocity potential is introduced and expressed as follows:

$$\Phi(x,y,z,t) = U\Phi_B(x,y,z) + \Re\sum_{j=1}^{6} i\omega X_j\,\phi_j(x,y,z)\,e^{i\omega t}. \tag{1}$$

Here $\Phi_B = -x + \phi_S(x, y, z)$ denotes the steady component of the velocity potential due to ship's steady forward motion at U (thus ϕ_S is the steady perturbation potential). In this article, Φ_B is taken as the double-body velocity potential, satisfying the rigid-wall condition on $z = 0$. The spatial part $\phi_j(x, y, z)$ in the unsteady component in Eq. (1) is the radiation potential due to oscillatory motion in the j-th mode with unit velocity, thus X_j denotes the complex amplitude, where in particular $j = 1$ for surge, $j = 3$ for heave, and $j = 5$ for pitch. Symbol $\Re$ in Eq. (1) means the real part to be taken.

Assuming small amplitude in the oscillatory motion of a ship, the linearized theory can be used. Then, the body boundary condition to be satisfied by the radiation potential ϕ_j is expressed in the form given as follows:

$$\frac{\partial \phi_j}{\partial n} = n_j + \frac{U}{i\omega} m_j \quad \text{on } S_H, \tag{2}$$

where

$$\left.\begin{aligned} &(n_1, n_2, n_3) = \boldsymbol{n},\ (n_4, n_5, n_6) = \boldsymbol{r} \times \boldsymbol{n} \\ &(m_1, m_2, m_3) = -(\boldsymbol{n} \cdot \nabla)\, \boldsymbol{V} \\ &(m_4, m_5, m_6) = -(\boldsymbol{n} \cdot \nabla)\, (\boldsymbol{r} \times \boldsymbol{V}) \\ &\boldsymbol{r} = (x, y, z),\ \boldsymbol{V} = \nabla \Phi_B = \nabla\big[-x + \phi_S(x, y, z)\big] \end{aligned}\right\} . \tag{3}$$

Here S_H denotes the mean wetted surface of ship hull, $\boldsymbol{n}$ is the normal vector defined as positive when pointing into fluid region from the boundary surface, $\boldsymbol{r}$ is the position vector, and $\boldsymbol{V}$ is the velocity vector of steady flow induced by the double-body velocity potential Φ_B.

The linearized free-surface boundary condition to be satisfied by the radiation potential ϕ_j is written as follows:

$$\begin{aligned} &-g\frac{\partial \phi_j}{\partial z} + (i\omega)^2 \phi_j + 2i\omega\, U \overline{\nabla} \Phi_B \cdot \overline{\nabla} \phi_j \\ &+U^2 \overline{\nabla} \Phi_B \cdot \overline{\nabla}\left(\overline{\nabla}\Phi_B \cdot \overline{\nabla}\phi_j\right) + \frac{1}{2} U^2 \overline{\nabla}\left(\overline{\nabla}\Phi_B \cdot \overline{\nabla}\Phi_B\right) \cdot \overline{\nabla}\phi_j \\ &+\Big(U\overline{\nabla}^2 \Phi_B + \mu\Big)\left(i\omega + U\overline{\nabla}\Phi_B \cdot \overline{\nabla}\right)\phi_j = 0 \quad \text{on } z = 0, \end{aligned} \tag{4}$$

where g is the acceleration due to gravity, $\overline{\nabla}$ denotes the gradient operator only in the horizontal plane (x, y), and μ is Rayleigh's artificial viscosity coefficient ensuring the radiation condition be satisfied at infinity.

2.2 Note on the slender ship theory

The aforementioned 3D boundary-value problem may be solved with a sophisticated numerical solution method like RPM. However, it is of engineering importance to consider a simplified and fast computation method while keeping sufficient accuracy and making it easier to understand hydrodynamic implication and importance of each term in the boundary conditions. It may be possible for slender ships by introducing the slenderness parameter ϵ as a guide, which is usually taken as B/L or d/L, with B, d, L being ship's breadth, draft, and length, respectively. In the limit of $\epsilon \to 0$, the ship will be viewed as a segment in the x-axis, and then the body boundary condition cannot be imposed, but the 3D wave pattern is important on the free surface (which is called the outer problem). On the other hand, in the near field close to the body surface, the y- and z-axes may be stretched by the variable transformation of $y = \epsilon Y$ and $z = \epsilon Z$. Then, the body boundary condition can be satisfied in the magnified Y-Z plane. On the contrary, however, a proper behavior of outgoing waves cannot be detected in the inner problem, and hence, no radiation condition is imposed. In this inner problem, the free-surface boundary condition may be simplified depending on the order of oscillation frequency ω and forward speed U relative to the rate of change of the velocity potential in the transverse and longitudinal directions. To assume the orders of ω and U are equivalent to consider the relative length of the waves generated by the harmonic oscillation $2\pi g/\omega^2$ and the steady translation $2\pi U^2/g$, respectively, although the entire wave pattern of real 3D waves changes with ω and U (Becker 1958).

In both outer and inner problems, a unique solution cannot be obtained because of the lack of certain boundary condition, and hence, a homogeneous solution may be allowed in each problem. The unknown coefficients of these homogeneous components will be determined later through matching between outer and inner solutions in an overlap region.

Before describing details of the outer and inner solutions, let us focus our attention on the free-surface condition by assuming the relative orders of ω and U in terms of the slenderness parameter ϵ. For brevity of explanation, we adopt the uniform-flow approximation for the steady velocity potential $\varPhi_B \simeq -x$ and omit Rayleigh's artificial viscosity μ in Eq. (4). Then, the free-surface boundary condition takes the following form:

$$\frac{\partial \phi_j}{\partial z} - \frac{1}{g}\left(i\omega - U\frac{\partial}{\partial x}\right)^2 \phi_j = 0 \quad \text{on } z = 0. \tag{5}$$

This is valid in the outer filed far from the ship and represents 3D wave systems changing with ω and U.

For convenience in subsequent analyses, the Fourier transform with respect to x will be used with the following definition:

$$\left.\begin{aligned} F^*(k) &= \int_{-\infty}^{\infty} F(x)\, e^{ikx}\, dx \\ F(x) &= \frac{1}{2\pi}\int_{-\infty}^{\infty} F^*(k)\, e^{-ikx}\, dk \end{aligned}\right\}. \tag{6}$$

Because the Fourier transform of $\partial\phi_j/\partial x$ is given by $-ik\phi_j^*$, the Fourier transform of Eq. (5) with respect to x can be expressed as follows:

$$\frac{\partial \phi_j^*}{\partial z} + \kappa(k)\,\phi_j^* = 0 \quad \text{on } z = 0, \tag{7}$$

where

$$\kappa(k) = \frac{1}{g}\big(\omega + kU\big)^2 = K + 2\tau k + \frac{k^2}{K_0}, \tag{8}$$

$$K = \frac{\omega^2}{g},\ \tau = \frac{U\omega}{g},\ K_0 = \frac{g}{U^2}. \tag{9}$$

We note that $\kappa(k)$ defined by Eq. (8) is the 3D wave number including both ω and U and that appearance of the Fourier-transform variable k implies the 3D effect and at the same time, the forward-speed effect related to differentiation with respect to x multiplied by U.

Like conventional strip theories, by assuming the orders of ω and U as $\omega = O(\epsilon^{-1/2})$ and $U = O(1)$, the relative order of each term in Eq. (7) can be evaluated in the inner region of $z = O(\epsilon)$ given as follows:

$$\underset{O(1)}{\frac{\partial \phi_j^*}{\partial z}} + \underset{O(1)}{K\,\phi_j^*} + \underset{O(\sqrt{\epsilon})}{2\tau k\,\phi_j^*} + \underset{O(\epsilon)}{\frac{k^2}{K_0}\phi_j^*} = 0 \quad \text{on } z = 0. \tag{10}$$

Therefore, we can see that the leading-term equation comprises the first two terms and can be written as follows:

$$\frac{\partial \phi_j^*}{\partial z} + K\,\phi_j^* = 0 \quad \text{on } z = 0, \tag{11}$$

which is the boundary condition for $k = 0$, namely for the 2D and zero-speed case.

It has been argued that the strip theory satisfying Eq. (11) is valid only in a high-frequency range of $\omega = O(\epsilon^{-1/2})$, which is not true. As long as $U = 0$, Eq. (11) is valid even for low frequencies including the limit of $\omega \to 0$. However, because the third and fourth terms in Eq. (10) are neglected as higher orders from the outset, the forward-speed effect in the free-surface condition cannot be incorporated in the strip theory solution, no matter how we manipulate. In fact, for the forward-speed case, if we would consider $\omega = O(1)$ or $O(\epsilon)$, the third and fourth terms become more dominant than the second term, and hence, not only the second term but also the third and fourth terms should be taken into account in some way. We should emphasize that the difference in the order of the third term from the leading term is simply $O(\sqrt{\epsilon})$ even in the high-frequency regime.

One smart method for taking account of 3D and forward-speed effects (i.e. the terms including variable k) in Eq. (10) in the framework of 2D solution is the UT by Newman (1978). As will be shown later, those effects included in the outer solution typically expressed with 3D wave number $\kappa(k)$ are incorporated into the inner solution through the coefficient of homogeneous component, which could be realized by matching with the outer solution at lower frequencies. Hence, the homogeneous coefficient is given as a function of k and 3D wave number $\kappa(k)$. However the free-surface condition satisfied by the particular and homogeneous solutions remains Eq. (11). Probably, because of this treatment for the forward-speed effects, computed results by the UT for cross-coupling radiation forces between heave and pitch are not in good agreement with measured results (Kashiwagi *et al.* 2000). Nevertheless, effectiveness of including a homogeneous component in the inner solution to account for 3D effects prominent at low frequencies can be well recognized from an article of Kashiwagi & Ohkusu (1991) on tank-wall interference effects on an oscillating ship with forward speed.

Another smart method for taking account of the forward-speed effect in the free-surface condition under the assumption of $\omega = O(\epsilon^{-1/2})$ and $U = O(1)$ is the RST by Oglivie and Tuck (1969). To incorporate the third term proportional to τ in Eq. (10) into the particular solution of the inner problem, they adopted a systematic perturbation analysis and expressed the unsteady velocity potential in a power series of increasing order $\sqrt{\epsilon}$ as follows:

$$\phi_j^* = \phi_j^{(1)} + \sqrt{\epsilon}\,\phi_j^{(2)} + \cdots. \tag{12}$$

Then, the leading-order forward-speed correction in Eq. (10) was considered in the following perturbation procedure:

$$\left.\begin{aligned} &\frac{\partial \phi_j^{(1)}}{\partial z} + K\,\phi_j^{(1)} = 0 \quad \text{on } z = 0 \\ &\frac{\partial \phi_j^{(2)}}{\partial z} + K\,\phi_j^{(2)} = -2\tau k\,\phi_j^{(1)} \quad \text{on } z = 0 \end{aligned}\right\}. \tag{13}$$

Exactly speaking, as will be shown later, there exist some other nonhomogeneous terms to be included on the right-hand side for $\phi_j^{(2)}$ which are contributions from interactions between the steady perturbation and unsteady flows and are the same order proportional to τ in a systematic analysis with slender ship assumption.

Because the left-hand side of Eq. (13) is the same as Eq. (11), the solution method for satisfying Eq. (13) can be essentially the same as that for the 2D problems. Although the analysis for $\phi_j^{(2)}$ in the RST is rather complicated, the final results for computing hydrodynamic forces are simple, contributing only to the cross-coupling terms in proportion to τ, and can be computed only with information of the leading term $\phi_j^{(1)}$ in Eq. (13). However, unlike UT, no homogeneous component is allowed in the inner solution. Thus, in a low-frequency range where the second and third terms become smaller in order than the 4th term in Eq. (10), the analysis of RST may be invalid, despite a fact that there are no numerical difficulties even when ω and U become small.

To circumvent aforementioned deficiencies in UT and RST, we should consider a hybrid method combining important ideas in both UT and RST. Namely the RST analysis will be used to incorporate the forward-speed effect (proportional to τ) of the free-surface condition into the particular inner solution, and the idea of UT will be used to incorporate 3D and forward-speed effects (which become important in a low-frequency range) into the coefficient of homogeneous inner solution through matching with the outer solution. This hybrid analysis method in the framework of slender ship theory is newly proposed in this article and notable in that the free-surface forward-speed effect proportional to τ can be taken into account in the inner particular solution, and other 3D and forward-speed effects can be incorporated in the inner homogeneous solution.

One may say that satisfaction of the free-surface condition with 3D wavenumber $\kappa(k)$ kept in Eq. (7) is possible within the 2D Laplace equation by using a numerical solution method like 2D+T theory (Chapman 1976, Yeung & Kim 1981, Faltinsen & Zhao 1991, to name a few). However, computation methods for that formulation are much more complicated and time-consuming than the strip theory-type solution method. Hence, if we would seek a solution satisfying the 3D forward-speed free-surface condition, it may be better to use a fully 3D numerical solution method like RPM, rather than 2D+T theory. The method newly proposed in this study keeps the framework of 2D strip theory for an engineering purpose and improves the EUT, particularly in the accuracy of cross-coupling radiation forces due to the free-surface forward-speed effect proportional to $\tau = U\omega/g$.

2.3 Outer solution and its expansion

In the outer region far from the ship, the steady disturbance described by ϕ_S decays, and thus an approximation of $\Phi_B \simeq -x$ is acceptable. In this case, the free-surface boundary condition, Eq. (4), can be simplified as Eq. (5). The velocity potential of hydrodynamic point source with unit strength satisfying Eq. (5) together with a proper radiation condition and 3D Laplace's equation is known as the 3D Green function (which will be subsequently denoted as G_{3D}). Because the ship may be viewed as a segment along the x-axis in the outer region, the outer solution can be described by a line distribution of 3D sources, in the form given as follows:

$$\begin{aligned}\phi_j^{(o)}(x,y,z) &= \int_{-\infty}^{\infty} Q_j(\xi) G_{3D}(x-\xi,y,z)\,d\xi \\ &= \frac{1}{2\pi}\int_{-\infty}^{\infty} Q_j^*(k) G_{3D}^*(k;y,z)\,e^{-ikx}\,dk, \end{aligned} \tag{14}$$

where Q_j is the unknown source strength along the x-axis, and thus, the outer solution expressed by Eq. (14) is a so-called homogeneous solution. The asterisk in superscript in Eq. (14) stands for the Fourier transform with respect to x, defined by Eq. (6).

The Fourier transform of the 3D Green function has been well studied. Referring to the result in Kashiwagi (1997), its expansions at higher and lower frequencies may be expressed as follows:

$$\begin{aligned} G_{3D}^*(k;y,z) &\sim i\epsilon_k\, e^{-\kappa(k)(z+i\epsilon_k|y|)} \\ &\simeq i\, e^{-K(z+i|y|)}\Big\{1-2\tau k(z+i|y|)\Big\} \\ &\qquad + O\big((\kappa R)^{-1},\, k^2/\kappa^2\big) \quad \text{for } KR \gg 1, \end{aligned} \tag{15}$$

$$\begin{aligned} G_{3D}^*(k;y,z) &\sim G_{2D}(y,z) - \frac{1}{\pi}\big(1-Kz\big)f^*(k) \\ &\qquad + O\big(K^2R^2,\, (\kappa-K)R,\, k^2R^2\big) \quad \text{for } KR \ll 1, \end{aligned} \tag{16}$$

where $R=\sqrt{y^2+z^2}$ and the 3D wave number $\kappa(k)$ is defined in Eq. (8). Symbol ϵ_k is defined as $\epsilon_k = \mathrm{sgn}(\omega+kU)$, which is equal to 1.0 at higher frequencies. Function $f^*(k)$ in Eq. (16) accounts for 3D and forward-speed effects in a low frequency range, which is given by the following equation:

$$f^*(k) = \ln\frac{2K}{|k|} + \pi i - \left[\begin{array}{c} \dfrac{\kappa}{\sqrt{\kappa^2-k^2}}\Big\{\pi i\,\epsilon_k + \cosh^{-1}\Big(\dfrac{\kappa}{|k|}\Big)\Big\} \\ \dfrac{\kappa}{\sqrt{k^2-\kappa^2}}\Big\{-\pi + \cos^{-1}\Big(\dfrac{\kappa}{|k|}\Big)\Big\} \end{array}\right], \tag{17}$$

where the upper and lower expressions in the brackets apply to $\kappa > |k|$ and $\kappa < |k|$, respectively.

We note that Eq. (15) includes the leading two different orders under the assumption of $\omega = O(\epsilon^{-1/2})$ and $U=O(1)$, adopted in the RST, which is obtained by taking the first two terms in the expansion of $\kappa(k)$ shown in Eq. (8). In the original EUT, an approximation of $\kappa(k)\simeq K$ is used in Eq. (15). We also note that $G_{2D}(y,z) = G_{3D}^*(0;y,z)$ in Eq. (16). All terms containing valuable k are related to the x-dependency (i.e. 3D effects) through the Fourier transform. It is worth mentioning that the 3D wave number $\kappa(k)$ is kept in Eq. (17) without any simplification.

Substituting these results in Eq. (14) and using some formulae in the inverse Fourier transform, we can obtain the expansion of the outer solution, necessary for matching with the inner solution in an overlap region, in the form given as follows:

$$\begin{aligned} \phi_j^{(o)}(x,y,z) &\simeq i\, e^{-K(z+i|y|)}\Big\{Q_j(x) - i2\tau(z+i|y|)Q_j'(x)\Big\} \\ &\qquad \text{for } KR \gg 1, \end{aligned} \tag{18}$$

$$\begin{aligned} \phi_j^{(o)}(x,y,z) &\simeq Q_j(x)G_{2D}(y,z) - \frac{1}{\pi}\big(1-Kz\big)\int_{-\infty}^{\infty} Q_j(\xi)f(x-\xi)\,d\xi \\ &\qquad \text{for } KR \ll 1. \end{aligned} \tag{19}$$

Detailed expression for the kernel function $f(x-\xi)$ in Eq. (19), used in numerical computations, can be found in Newman and Sclavounos (1980).

2.4 Inner solution and its expansion

In the inner region close to the ship hull, the governing equation for the velocity potential can be the 2D Laplace equation because of variable stretching in the y- and z-axes with the slenderness parameter ϵ. Furthermore, from the body boundary condition, the order of ϕ_S for the steady disturbance flow can be estimated as ϵ^2. Then, under the assumption of $\omega = O(\epsilon^{-1/2})$ and $U = O(1)$ as in the RST, the two-term expansion of the body and free-surface boundary conditions given by Eqs. (2)–(4) may take the following form:

$$[H] \quad \frac{\partial \phi_j}{\partial n} = N_j + \frac{U}{i\omega} M_j \quad \text{on } S_H(x), \tag{20}$$

$$[F] \quad \frac{\partial \phi_j}{\partial z} + K\,\phi_j = -\frac{i\omega\, U}{g} \left\{ 2\frac{\partial \phi_j}{\partial x} - 2\frac{\partial \phi_S}{\partial y}\frac{\partial \phi_j}{\partial y} - \frac{\partial^2 \phi_S}{\partial y^2}\phi_j \right\} \text{ on } z = 0, \tag{21}$$

where N_j and M_j are slender-body approximations of n_j and m_j defined in Eq. (3), and the order of magnitude of both terms is the same and $O(\epsilon)$ for $j = 1$ and $O(1)$ for $j = 3$ and 5. Therefore, with assumption of $\omega = O(\epsilon^{-1/2})$ and $U = O(1)$, the speed-dependent terms proportional to U in both Eqs. (20) and (21) are smaller than the zero-speed leading terms, with relative difference in the order of $\sqrt{\epsilon}$, namely, the radiation potential ϕ_j is expected to be a power series of increasing order $\sqrt{\epsilon}$, with the leading term being of zero-speed case and its order being $\phi_1 = O(\epsilon^2)$, $\phi_3 = O(\epsilon)$ and $\phi_5 = O(\epsilon)$.

By taking account of this order estimation and the knowledge learned from the UT (Newman 1978) regarding the existence of a homogeneous solution in the case of no radiation condition, we can construct the inner solution in the following form:

$$\phi_j^{(i)}(x; y, z) = \varphi_j(y, z) + C_j(x)\varphi_H(y, z) + \frac{U}{i\omega}\left\{ \widehat{\varphi}_j(y, z) + (i\omega)^2 \psi_j(y, z) \right\}, \tag{22}$$

where φ_j and $\widehat{\varphi}_j$ are the particular solutions satisfying the following boundary conditions:

$$\left. \begin{aligned} \frac{\partial \varphi_j}{\partial n} &= N_j \quad \text{on } S_H(x) \\ \frac{\partial \varphi_j}{\partial z} + K\varphi_j &= 0 \quad \text{on } z = 0 \end{aligned} \right\}, \tag{23}$$

$$\left. \begin{aligned} \frac{\partial \widehat{\varphi}_j}{\partial n} &= M_j \quad \text{on } S_H(x) \\ \frac{\partial \widehat{\varphi}_j}{\partial z} + K\widehat{\varphi}_j &= 0 \quad \text{on } z = 0 \end{aligned} \right\}. \tag{24}$$

$\varphi_H(y, z)$ in Eq. (22) is a homogeneous solution which is permitted in the inner problem because of no radiation condition. The solution satisfying homogeneous body and free-surface boundary conditions can be obtained as $\varphi_H(y, z) = \varphi_3(y, z) - \overline{\varphi_3(y, z)}$, where the overbar denotes the complex conjugate, and $C_j(x)$ in Eq. (22) is the coefficient of homogeneous solution which is unknown at this stage and to be determined from matching. The last term $\psi_j(y, z)$ in Eq. (22) is supplemented to account for the forward-speed effect on the right-hand side of the free-surface condition given by Eq. (21).

Taking the same order terms after substituting Eq. (22) into Eqs. (20) and (21), the body and free-surface conditions for the supplementary term ψ_j can be of the following form:

$$\left. \begin{aligned} \frac{\partial \psi_j}{\partial n} &= 0 \quad \text{on } S_H(x) \\ \frac{\partial \psi_j}{\partial z} + K\psi_j &= -\frac{1}{g}\left\{ 2\frac{\partial \varphi_j}{\partial x} - 2\frac{\partial \phi_S}{\partial y}\frac{\partial \varphi_j}{\partial y} - \frac{\partial^2 \phi_S}{\partial y^2}\varphi_j \right\} \text{ on } z = 0 \end{aligned} \right\}. \tag{25}$$

We note that the order of ψ_j must be the same as $\epsilon \times O(\varphi_j)$ i.e. $\psi_j = O(\epsilon^2)$ for $j = 3$ and 5; thus, $(i\omega)^2 \psi_j$ in Eq. (22) is of $O(\epsilon)$, which is the same as that of $\widehat{\varphi}_j$.

For matching with the outer solution in an overlap region, let us consider an asymptotic expression of Eq. (22) at a far field for larger values of KR. Because evanescent waves may be neglected, the following results can be readily obtained:

$$\left.\begin{aligned} \varphi_j &\sim i\sigma_j(x)\, e^{-K(z+i|y|)} \\ \widehat{\varphi}_j &\sim i\,\widehat{\sigma}_j(x)\, e^{-K(z+i|y|)} \end{aligned}\right\}, \tag{26}$$

where $\sigma_j(x)$ and $\widehat{\sigma}_j(x)$ are the 2D Kochin functions computed from φ_j and $\widehat{\varphi}_j$, respectively. Specifically, they can be computed as follows:

$$\sigma_j(x) = \int_{S_H(x)} \left(\frac{\partial \varphi_j}{\partial n} - \varphi_j \frac{\partial}{\partial n} \right) e^{-Kz+iKy}\, d\ell \tag{27}$$

$$\widehat{\sigma}_j(x) = \int_{S_H(x)} \left(\frac{\partial \widehat{\varphi}_j}{\partial n} - \widehat{\varphi}_j \frac{\partial}{\partial n} \right) e^{-Kz+iKy}\, d\ell \tag{28}$$

The inhomogeneous free-surface condition for ψ_j shown in Eq. (25) implies that the flow is the same as that induced by the following pressure distribution on the free surface

$$\begin{aligned} P(x;y) &= -\frac{\rho}{i\omega} \left\{ 2\frac{\partial \varphi_j}{\partial x} - 2\frac{\partial \phi_S}{\partial y}\frac{\partial \varphi_j}{\partial y} - \frac{\partial^2 \phi_S}{\partial y^2}\, \varphi_j \right\}_{z=0} \\ &\sim -\frac{2\rho}{\omega}\sigma_j'(x)\, e^{-iK|y|} + p_F(x;y), \end{aligned} \tag{29}$$

where $p_F(x;y)$ represents a regular pressure distribution due to decaying behavior of ϕ_S as $|y| \to \infty$.

Using the analysis in terms of the Fourier transform and neglecting evanescent-wave terms, the asymptotic expression for ψ_j originating from the first term on the right-hand side of Eq. (29) takes the form as follows:

$$\begin{aligned} \psi_j(y,z) &= -\frac{2}{g\pi}\sigma_j'(x) \lim_{\mu\to 0} \int_{-\infty}^{\infty} \frac{K\, e^{-|m|z+imy}}{(m^2-K^2)(|m|-K+i\mu)}\, dm \\ &\sim -\frac{2}{g} i\sigma_j'(x)\big(z+i|y|\big)\, e^{-K(z+i|y|)}. \end{aligned} \tag{30}$$

Therefore, by collecting the results shown previously, the expansion of the inner solution valid for $KR \gg 1$ can be obtained, which is essentially the same as that in the RST. On the other hand, the expansion for $KR \ll 1$ can be the same as that in the UT. To sum up, the results of the inner solution expansion can be written as follows:

$$\phi_j^{(i)}(x;y,z) \simeq i\, e^{-K(z+i|y|)} \Big\{ \sigma_j(x) + \frac{U}{i\omega}\widehat{\sigma}_j(x) - i2\tau\big(z+i|y|\big)\sigma_j'(x) \Big\} \quad \text{for } KR \gg 1, \tag{31}$$

$$\begin{aligned} \phi_j^{(i)}(x;y,z) \simeq & \Big[\sigma_j(x) + \frac{U}{i\omega}\widehat{\sigma}_j(x) + C_j(x) \Big\{ \sigma_3(x) - \overline{\sigma_3(x)} \Big\} \Big]\, G_{2D}(y,z) \\ & + i2C_j(x)\overline{\sigma_3(x)}\, e^{-Kz}\cos Ky \quad \text{for } KR \ll 1. \end{aligned} \tag{32}$$

By comparing these results with Eqs. (18) and (19), we can realize that the matching for determining two unknowns, $Q_j(x)$ and $C_j(x)$, is possible, and the results are essentially the same as those in the UT (Kashiwagi 1997). The only difference is that the inner solution contains a new supplementary component $\psi_j(y,z)$ which represents a contribution from the speed-dependent convection term in the inner free-surface condition and is physically of critical importance as a correction to the UT. This term eventually contributes only to the cross-coupling added mass and damping coefficients as will be shown in the following section.

3. Hydrodynamic Forces

3.1 Added mass and damping coefficients

Once the inner solution has been determined, the analyses for computing the hydrodynamic force can be a merger of both RST and UT. For the radiation problem, after applying the so-called Tuck's theorem (Ogilvie & Tuck 1969) to the integral of linearized pressure on the ship hull surface, the result can be expressed with the added mass (A_{jk}) and damping coefficient (B_{jk}) in the j-th direction due to the k-th mode of motion, in the form given as follows:

$$\begin{aligned} A_{jk} + \frac{1}{i\omega} B_{jk} = &- \rho \int_L ds \int_{S_H(x)} \Big(N_j - \frac{U}{i\omega} M_j \Big) \Big\{ \varphi_k + \frac{U}{i\omega} \widehat{\varphi}_k \Big\} \, d\ell \\ &- \rho \int_L dx \, C_k(x) \int_{S_H(x)} \Big(N_j - \frac{U}{i\omega} M_j \Big) \Big\{ \varphi_3 - \overline{\varphi_3} \Big\} \, d\ell - \rho \, i 2\tau \, \mathcal{Z}_{jk} . \end{aligned} \tag{33}$$

Here $\mathcal{Z}_{jk}$ represents the additional term accounting for the forward-speed effect proportional to τ, to be computed from the new term $\psi_j(y,z)$ in the inner solution. Although the analytical transformation for this term is the same as shown in the study of Ogilvie and Tuck (1969), it is summarized in Appendix of this article for self-confirmation. From this transformation, we can see that $\mathcal{Z}_{jk} = 0$ for the case of $j = k$, and hence, the forward-speed effect in the free-surface condition contributes only to the cross-coupling terms of $j \neq k$. Specifically, the final result for the case of $j = 3$ and $k = 5$ (or $j = 5$ and $k = 3$) can be expressed as follows:

$$\left. \begin{aligned} \mathcal{Z}_{35} = - \mathcal{Z}_{53} = \int_L I(x) \, dx \\ I(x) = \int_{y_0(x)}^{\infty} \big\{ \varphi_3^2(y,0) + \sigma_3^2 \, e^{-i2Ky} \big\} \, dy + \frac{i}{2K} \sigma_3^2 \, e^{-i2Ky_0(x)} \end{aligned} \right\} , \tag{34}$$

where $y_0(x)$ denotes the half breadth of the transverse section $S_H(x)$ at station x.

Once the solution of φ_3 for heave has been obtained, the 2D Kochin function σ_3 and the value of $\varphi_3(y,0)$ on the free surface necessary for computing Eq. (34) can be computed from the following expressions:

$$\sigma_3 = \int_{S_H(x)} \left(\frac{\partial \varphi_3}{\partial n} - \varphi_3 \frac{\partial}{\partial n} \right) e^{-K\zeta + iK\eta} \, d\ell, \tag{35}$$

$$\varphi_3(y,0) = \int_{S_H(x)} \left(\frac{\partial \varphi_3}{\partial n} - \varphi_3 \frac{\partial}{\partial n} \right) G_{2D}(y,0;\eta,\zeta) \, d\ell, \tag{36}$$

where $G_{2D}(y,z;\eta,\zeta)$ denotes the 2D free-surface Green function used in Eqs. (16) and (32) and its computation method is well established.

It is noteworthy that the relation of $\mathcal{Z}_{35} = -\mathcal{Z}_{53}$ means that the Timman-Newman relation for the forward-speed effect (Timman & Newman 1962) is also satisfied in this additional term and that the analysis for the cross-coupling between sway ($j = 2$) and yaw ($j = 6$) can be performed in a similar manner.

In the slender ship analysis for the heave and pitch modes, we may approximate as $N_5 = -xN_3$, $M_5 = N_3$ for pitch. Thus, we have relations of $\varphi_5 = -x\varphi_3$, $\widehat{\varphi}_5 = \varphi_3$ for the particular solutions and $\sigma_5 = -x\sigma_3$, $\widehat{\sigma}_5 = \sigma_3$ for the 2D Kochin functions. The particular solution of the radiation potential φ_3 for an arbitrary 2D body shape can be obtained using the boundary element (or Green function) method.

3.2 Ship motions and added resistance

After computing hydrodynamic forces (not only in the radiation problem but also in the diffraction problem), the complex motion amplitude X_j ($j = 1, 3, 5$) can be obtained by solving the coupled motion equations of the form given as follows:

$$\sum_{k=1,3,5} \Big[(i\omega)^2 \left\{ m_{jk}\delta_{jk} + A_{jk} \right\} + i\omega B_{jk} + C_{jk} \Big] X_k = \zeta_a E_j \tag{37}$$

among the modes of surge ($j = 1$), heave ($j = 3$), and pitch ($j = 5$), where ζ_a denotes the amplitude of regular incident wave with circular frequency ω_0 (which is related to ω with $\omega = \omega_0 + U\omega_0^2/g$ in head wave), and E_j denotes the wave-exciting force in the j-th mode by the unit amplitude of incident wave. m_{jk} and δ_{jk} are the mass matrix coefficient and Kroenecker's delta function, respectively; hence, m_{jk} is the ship's mass for $j = k = 1$ or 3, and the moment of inertia for $j = k = 5$. C_{jk} denotes the restoring force coefficient.

In terms of the complex motion amplitude computed, the 3D Kochin function for the term symmetric in the port and starboard sides can be computed from the linear superposition of the following form:

$$\left. \begin{aligned} H(k) &= H_7(k) - \frac{\omega\omega_0}{g} \sum_{j=1,3,5} \frac{X_j}{\zeta_a} H_j(k) \\ H_j(k) &= \int_L Q_j(\xi)\, e^{ik\xi}\, d\xi \end{aligned} \right\}, \tag{38}$$

where $Q_j(x)$ is the strength of source distribution along the x-axis in the outer solution.

Once the 3D Kochin function could be computed, as well known as Maruo's formula (Maruo 1960), the added resistance in head waves can be computed from

$$\frac{R_{AW}}{\rho g \zeta_a^2} = \frac{1}{4\pi k_0} \left[-\int_{-\infty}^{k_1} + \int_{k_2}^{k_3} + \int_{k_4}^{\infty} \right] \left| H(k) \right|^2 \frac{\kappa}{\sqrt{\kappa^2 - k^2}} (k + k_0)\, dk\,. \tag{39}$$

where

$$\left. \begin{matrix} k_1 \\ k_2 \end{matrix} \right\} = -\frac{K_0}{2} \big(1 + 2\tau \pm \sqrt{1 + 4\tau} \big), \tag{40}$$

$$\left. \begin{matrix} k_3 \\ k_4 \end{matrix} \right\} = \frac{K_0}{2} \big(1 - 2\tau \mp \sqrt{1 - 4\tau} \big). \tag{41}$$

We note that the wave numbers k_j ($j = 1 \sim 4$) are given as the roots of $\kappa^2 = k^2$; for $\tau > 1/4$, k_3 and k_4 become complex and the integration range in Eq. (39) must be continuous for $k_2 < k$; $k_0 = \omega_0^2/g$ is the wave number of incident wave in deep water; $\kappa(k)$ and $K_0 = g/U^2$

are defined in Eqs. (8) and (9). There are a couple of points to be cautious in the numerical integration of Eq. (39), for which the readers are referred to Wicaksono and Kashiwagi (2018).

4. Results and Discussions

To validate the present theory taking account of the forward-speed effect in the free-surface condition of the inner problem, computed results for the added mass and damping coefficients, particularly cross-coupling terms between heave and pitch, and also for the wave-induced ship motions (surge, heave, and pitch) in head waves are compared with corresponding values measured in the experiment.

The values to be computed by Eq. (33) may be divided into three components: the first term on the right-hand side is the same as the result of the strip method (which is referred to as New Strip Method (NSM) in subsequent comparisons), the second term on the right-hand side is the contribution from the homogeneous solution in the enhanced unified theory (Kashiwagi 1997) and thus, the sum of the first and second terms is referred to as the EUT, and the third term is a newly added correction accounting for the forward-speed effect in the free-surface boundary condition in the inner problem. Therefore, the results including this correction term in the NSM and EUT are denoted as modified NSM (which is essentially the same as the RST) and modified EUT, respectively.

4.1 Slender modified Wigley model

The first comparison is made for a slender modified Wigley model, the geometry of which is expressed mathematically as follows:

$$y = \frac{B}{2}\Big\{(1-\zeta^2)(1-\xi^2)(1+0.2\xi^2) + \zeta^2(1-\zeta^8)(1-\xi^2)^4\Big\}, \tag{42}$$

where $\xi = 2x/L$ and $\zeta = z/d$. The principal dimensions of this model used in the experiment by Kashiwagi *et al.* (2000) are shown in Table 1.

Table 1 Principal dimensions of a slender modified Wigley model

Length: L (m)	2.000
Breadth: B (m)	0.300
Draft: d (m)	0.125
Block coefficient: C_b	0.5607
Displacement volume: $\nabla = C_b LBd\,(\mathrm{m}^3)$	0.04205
Midship coefficient: C_m	0.9091
Water-plane Area: $A_w\,(\mathrm{m}^2)$	0.4160
Center of gravity: $\overline{OG}$ (m)	0.0404
Gyrational radius: κ_{yy}/L	0.248

The cross-coupling added mass coefficients A_{53} and A_{35} (nondimensionalized with $\rho\nabla L$) and damping coefficients B_{53} and B_{35} (nondimensionalized with $\rho\nabla L\sqrt{g/L}$) are shown in Fig. 1 for $Fn = 0.2$, with abscissa taken as KL. As indicated in the legend, thin solid and dotted lines are original EUT and NSM, respectively; thick solid and broken lines are modified EUT and modified NSM, respectively, which contain the forward-speed correction term. We note that all these values in the cross-coupling terms are induced by the forward-

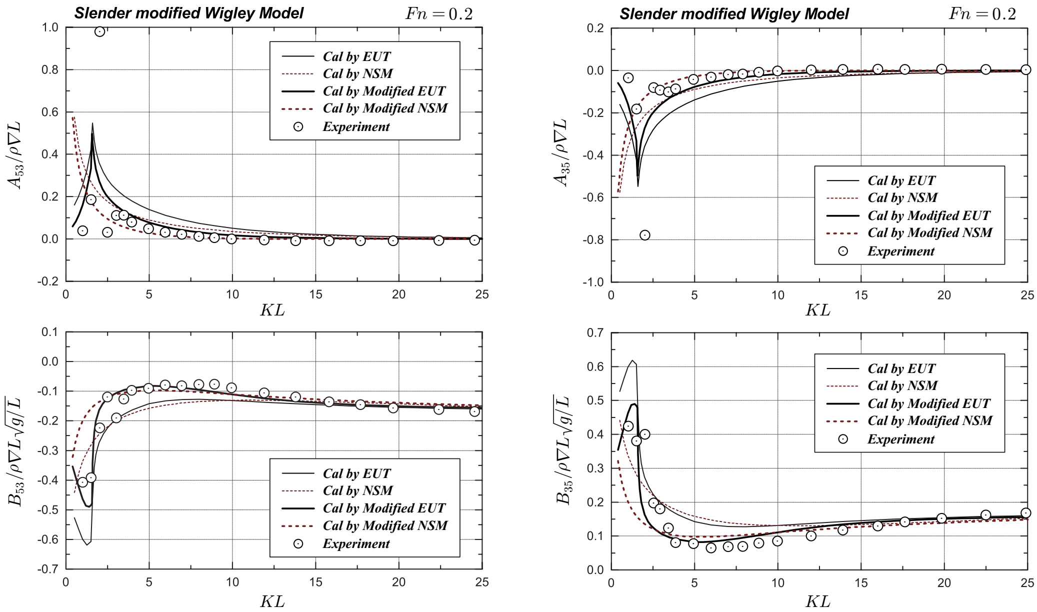

Fig. 1 Cross-coupling added mass and damping coefficients between heave and pitch for a slender modified Wigley model, at $Fn = 0.2$

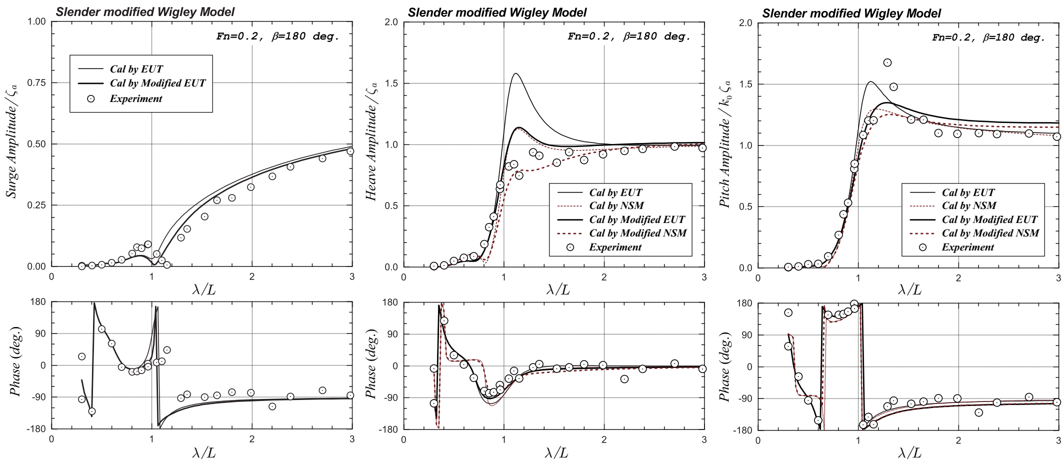

Fig. 2 Wave-induced ship motions (surge, heave, and pitch) of a slender modified Wigley model at $Fn = 0.2$ in head waves

speed effect only because the modified Wigley model considered is longitudinally symmetric, and hence, the values at zero forward speed must be exactly zero.

The agreement between experiment and modified EUT is good enough over the range where experimental data are available, including the critical frequency $\tau = Fn\sqrt{KL} = 0.25$ (which corresponds to $KL = 1.56$ at $Fn = 0.2$). The modified NSM is also good in agreement except in the very low-frequency range less than $\tau < 0.25$. We can see from these results that the additional term in the cross-coupling radiation forces, linearly proportional to

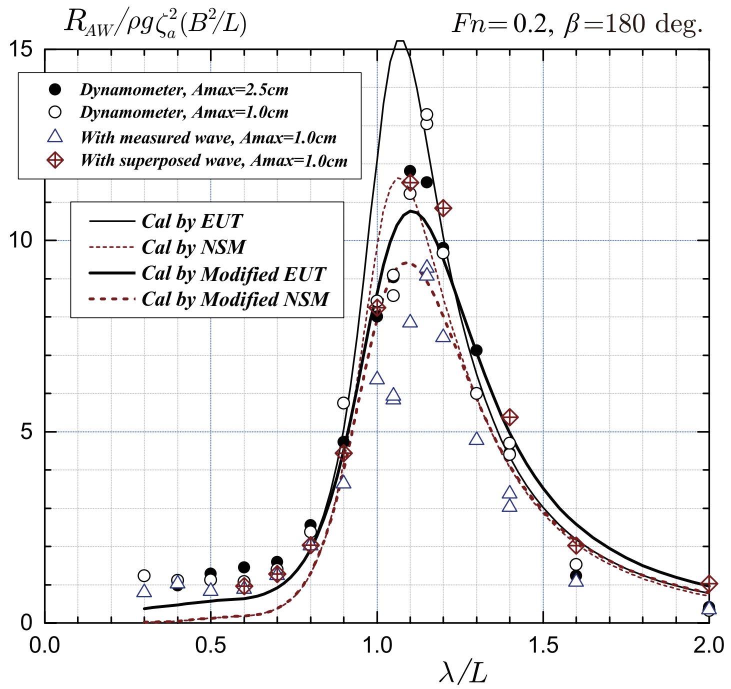

Fig. 3 Added resistance on a slender modified Wigley model at $Fn = 0.2$ in the motion-free condition in head waves

the forward speed U and originating from the inner free-surface condition, is of critical importance for better agreement with experimental data in a low frequency range. Although the additional term $\psi_j(y,z)$ in the inner solution of Eq. (22) is regarded as the second leading term under the assumption of $\omega = O(\epsilon^{-1/2})$ and $U = O(1)$, this term is the same in order as a particular solution $\widehat{\varphi}_j(y,z)$ and computed with the leading-order solution $\varphi_j(y,z)$, as shown in Eq. (25) and Eq. (34). Thus, as inferred from Eqs. (22) and (33), the contribution from this additional term becomes practically important even in lower frequencies as a forward-speed effect proportional to τ originating from the free-surface condition. In a low-frequency range, other forward-speed and 3D effects may become more important, which are taken into account through the homogeneous component of the inner solution.

Figure 2 shows the nondimensional amplitude and phase in surge, heave, and pitch motions. In the surge motion, only the results by the EUT are shown, and slight improvement can be observed by virtue of forward-speed correction in the heave-pitch coupling terms which is because the surge is computed from coupled motion equations among surge, heave, and pitch. More prominent improvement in agreement with the experiment can be observed in heave around the resonant frequency of $\lambda/L \simeq 1.1$. This prominent improvement indicates that the accuracy of cross-coupling added mass and damping coefficients between heave and pitch is of critical importance for predicting accurately the ship motions, particularly in heave, around the resonant frequency, because the diagonal components in the inertial force and restoring force coefficients almost cancel at the resonant frequency. In this case, the off-diagonal components become important, despite the magnitude of cross-coupling coefficients itself is relatively small as shown in Fig. 1. Similar observation regarding the importance of cross-coupling radiation forces around the motion-resonant wavelength was demonstrated experimentally in Kashiwagi *et al.* (2000).

The added resistance computed with these complex motion amplitudes in surge, heave, and pitch is shown in Fig. 3, in which the experimental data for comparison are taken from Kashiwagi (2013). It can be seen that the prediction of added resistance, especially near its peak, is sensitive to a change in the complex motion amplitude, which is also the case in the experiment. By incorporating the linear forward-speed effect term in the heave-pitch cross-coupling radiation forces, the peak wavelength in the added resistance tends to shift slightly to a longer wavelength, agreeing with the experiment. However, the predicted values at longer wavelength region are obviously larger than the measured values, which may be attributed to overprediction of the pitch motion amplitude as observed in Fig. 2. A possible reason of this overprediction of the pitch motion is a slight discrepancy in the pitch damping coefficient and the pitch exciting moment as indicated in Kashiwagi *et al.* (2000), but more careful check should be made for confirming this conjecture.

4.2 RIOS bulk carrier

The RIOS at Osaka University provided a bulk carrier model which can be open to the public for experiments and numerical computations with research purpose. The principal dimensions of this model are shown in Table 2, and its body plan is also shown in Fig. 4.

Table 2 Principal dimensions of RIOS bulk carrier model

Length between perpendiculars: L_{pp} (m)	2.400
Breadth: B (m)	0.400
Draft: d (m)	0.128
Block coefficient: C_b	0.800
Displacement volume: $\nabla = C_b LBd$ (m^3)	0.09830
Midship coefficient: C_m	0.9950
Water-plane Area: A_w (m^2)	0.8354
Center of gravity: $\overline{OG}$ (m)	0.0205
Gyrational radius: κ_{yy}/L	0.256

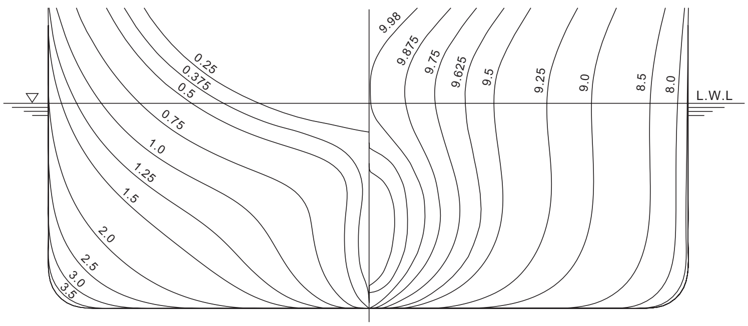

Fig. 4 Body plan of RIOS bulk carrier

Measured and computed results for the cross-coupling added mass and damping coefficients between heave and pitch are shown in Fig. 5 in the same fashion as that for the slender modified Wigley model, but the Froude number in this comparison is $Fn = 0.18$. Clearly

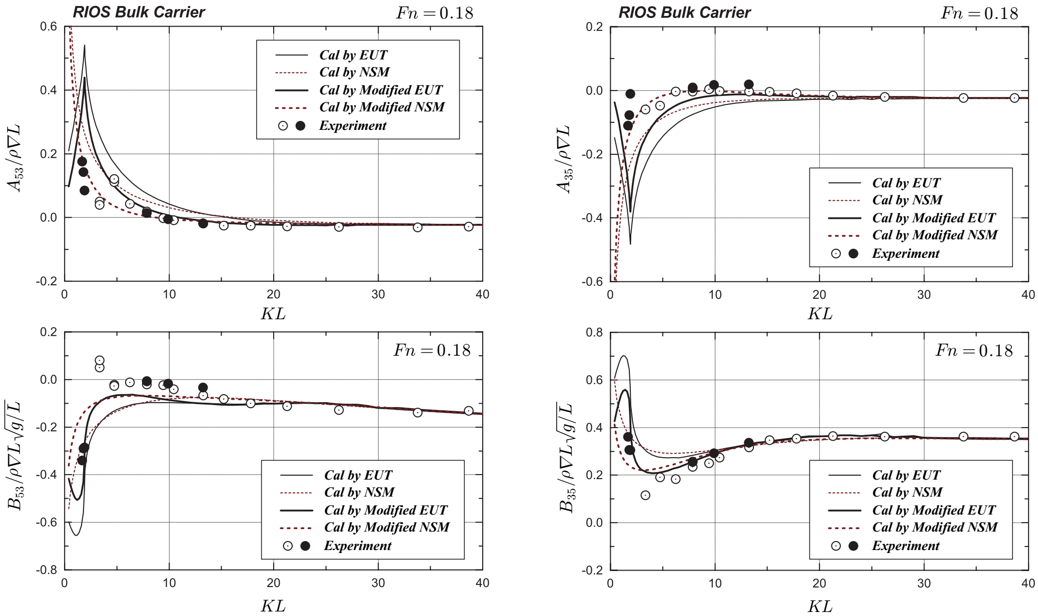

Fig. 5 Cross-coupling added-mass and damping coefficients between heave and pitch for RIOS bulk-carrier model, at $Fn = 0.18$

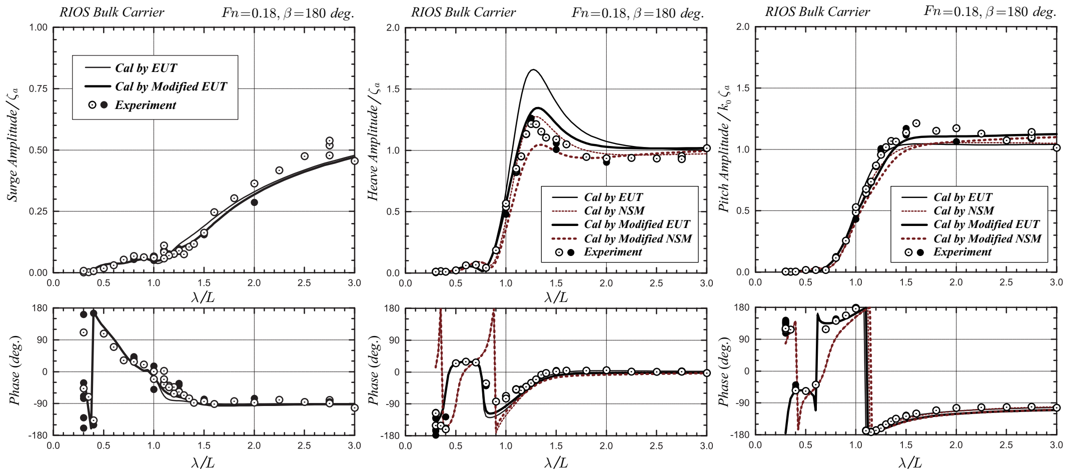

Fig. 6 Wave-induced ship motions (surge, heave, and pitch) of RIOS bulk-carrier model at $Fn = 0.18$ in head waves

the degree of agreement is improved by adding the linear forward-speed correction term originating from the forward-speed effect in the inner free-surface condition. Around the critical frequency equal to $\tau = Fn\sqrt{KL} = 0.25$ ($KL = 1.93$ at $Fn = 0.18$), computed results show rapid change, which looks also observed in the experiment but a little exaggerated in the computation based on the linear potential flow theory.

Figure 6 shows the nondimensional amplitude and phase of wave-induced ship motions. We can see prominent improvement in the peak value of heave motion by the modified EUT

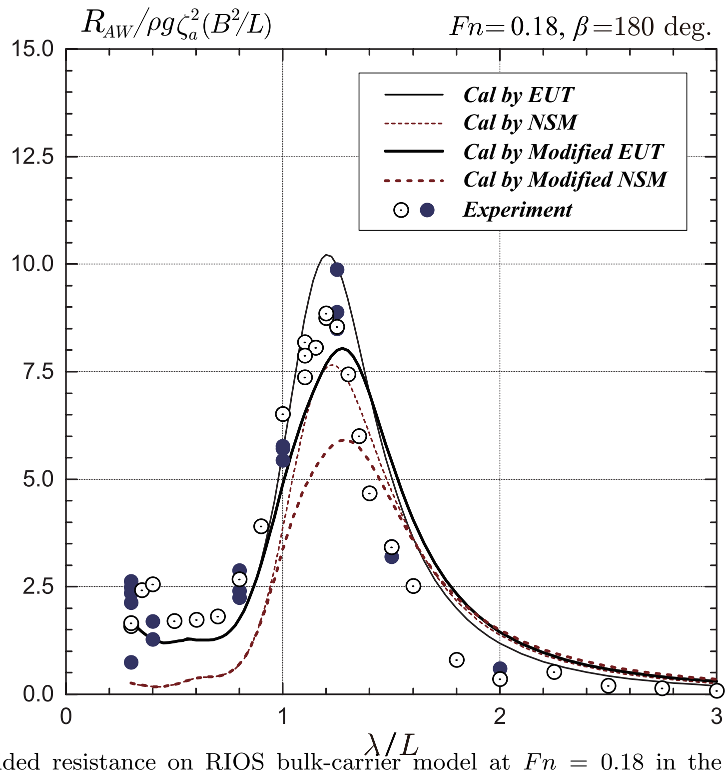

Fig. 7 Added resistance on RIOS bulk-carrier model at $Fn = 0.18$ in the motion-free condition in head waves

taking account of the linear forward-speed effect term in the inner free-surface condition. We note that $\lambda/L = 1.25$ near the peak corresponds to $KL = 9.902$ at $Fn = 0.18$, where the improvement from the original EUT can be observed mainly in the added mass coefficients A_{53} and A_{35} rather than in the damping coefficients B_{53} and B_{35}. Therefore, we can say that the accuracy in the cross-coupling added mass coefficients is important for accurate prediction of the peak amplitude, especially in heave.

A comparison for the added resistance on the RIOS bulk carrier model is shown in Fig. 7. The degree of agreement between computed results by the modified EUT and measured results is unexpectedly not so good, and we can see again that the prediction of added resistance is sensitive to the complex amplitude of ship motions. The wavelength at which the added resistance takes the maximum looks slightly different in the modified EUT. (Note that $\lambda/L = 1.1$ and 1.2 correspond to $KL = 11.684$ and 10.437, respectively.) Looking at the pitch motion RAO in Fig. 6 and the added resistance in Fig. 7, we can conjecture that slight underprediction of pitch motion around $\lambda/L = 1.1 \sim 1.2$ may be a reason of the difference in the added resistance and slight overprediction of heave motion in the range of $\lambda/L > 1.25$ may be a reason of overprediction in the added resistance.

As we have seen, obviously the prediction accuracy is improved in the cross-coupling radiation forces and the resultant ship motions especially, in heave, but the prediction accuracy in the added resistance is not necessarily improved, especially for RIOS bulk carrier model, which suggests that the total balance in computing the Kochin function would be important for accurate prediction of the added resistance.

5. Conclusions

Within the framework of the EUT, a study has been conducted on the effect of forward speed proportional to the parameter $\tau = U\omega/g$ in the inner free-surface condition on hydrodynamic radiation forces, wave-induced ship motions, and resultant added resistance. To compute the additional radiation forces originating from the term proportional to the forward speed of a ship in the inner free-surface condition, the solution method developed in Ogilvie and Tuck's RST has been adopted for the particular inner solution. The resultant contribution from this forward-speed effect exists only in the cross-coupling added mass and damping coefficients, specifically between heave and pitch in the present study, which satisfies the Timman-Newman relation.

Numerical computations and comparison with measured results have been made for a slender modified Wigley model with longitudinal symmetry and a real ship of the RIOS bulk carrier with block coefficient $C_b = 0.8$. For both cases, prominent improvement in the cross-coupling added mass and damping coefficients between heave and pitch could be confirmed. Furthermore, it was confirmed that the improvement in these cross-coupling terms contributes to better agreement with measured results in the amplitude of ship motions (particularly in heave) near the resonant frequency. This is because the diagonal components in the inertial and restoring forces cancel, and hence, off-diagonal components become important at the resonant frequency.

However, the degree of improvement in the added resistance was found to be not so much as expected, and we realized that the prediction of added resistance is sensitive to slight change in the cross-coupling radiation forces and resultant ship motions, especially around the motion-resonant wavelength, because the added resistance takes the maximum near the motion-resonant wavelength. For more accurate prediction of the wave-making component in the added resistance, we should consider a computation method that is balanced in the degree of accuracy for computing the ship-generated wave-amplitude function known as the Kochin function over a wider range of wavelength.

Acknowledgment

A part of this study was supported by JSPS Grant-in-Aid for Scientific Research (Grant number 17H01357) and also the subsidy for International Collaboration Promotion Program at Osaka University, for which the author is thankful.

References

1. Becker, E. 1958: Das Wellenbild einer unter der Oberfläche eines Stromes Schwerer Flüssigkeit pulsierender Quelle, *Z. Angewandte Mathematik and Mechanik*, Vol. 38, pp. 391–399.

2. Chapman, R. B. 1976: Free-surface effects for yawed surface-piercing plates, *Journal of Ship Research*, Vol. 20, No. 3, pp. 125–136.

3. el Moctar, B. O., Sigmund, S., Ley, J., and Schellin, T. 2017: Numerical and Experimental Analysis of Added Resistance of Ships in Waves, *Journal of Offshore Mechanics and Arctic Engineering*, Vol. 139 (1): 001301.

4. Faltinsen, O. M. 1974: A numerical investigation of the Ogilvie-Tuck formulae for added-mass and damping coefficients, *Journal of Ship Research*, Vol. 18 (2), pp. 73–84.

5. Faltinsen, O. M. and Zhao, R. 1991: Numerical predictions of ship motions at high forward speed, *Philosophical Transactions, Royal Society*, Series A, Vol. 334, No. 1634, pp. 241–252.
6. ITTC Report of the Seakeeping Committee, 2017: *Proceedings of the 28th ITTC*, Wuxi, Vol. 1.
7. Kashiwagi, M. and Ohkusu, M. 1991: A New Theory for Side-Wall Interference Effects on Forward-Speed Radiation and Diffraction Forces, *Ship Technology Research (Schiffstechnik)*, Vol. 38, No. 1, pp. 17–47.
8. Kashiwagi, M. 1995: Prediction of surge and its effect on added resistance by means of the enhanced unified theory, *Transactions of the West-Japan Society of Naval Architects*, Vol. 89, pp. 77–89.
9. Kashiwagi, M. 1997: Numerical seakeeping calculations based on the slender ship theory, *Ship Technology Research (Schiffstechnik)*, Vol. 44, pp. 167–192.
10. Kashiwagi, M., Kawasoe, K., and Inada, M. 2000: A Study on Ship Motion and Added Resistance in Waves, *Journal of Kansai Society of Naval Architects, Japan*, No. 234, pp. 85-94.
11. Kashiwagi, M. 2009: Impact on Hull Design on the Added Resistance in Waves – Application of the Enhanced Unified Theory, *Proceedings of 10th International Marine Design Conference (IMDC)*, Trondheim, Norway, Vol. 1, pp. 521-535.
12. Kashiwagi, M. 2013: Hydrodynamic study on added resistance using unsteady wave analysis, *Journal of Ship Research*, Vol. 57 (4), pp. 220–240.
13. Kim, K. H., and Kim, Y. 2011: Numerical study on added resistance of ships by using a time-domain Rankine panel method, *Ocean Engineering*, Vol. 38, pp. 1357-1367.
14. Kim, M., Hizir, O., Turan, O., Day, S., and Incecik, A. 2017: Estimation of added resistance and ship speed loss in a seaway, *Ocean Engineering*, Vol. 141, pp. 465-476.
15. Maruo, H. 1960: Wave resistance of a ship in regular head seas, *Bulletin of the Faculty of Engineering, Yokohama National University*, Vol. 9, pp. 73-91.
16. Minoura, M., Hanaki, T. and Nanjo, T. 2019: Improvement of Statistical Estimation of Ship Performance in Actual Seas by Normalization of Data Unevenness using Cluster Analysis, *Proceedings of 14th International Symposium on Practical Design of Ships and Other Floating Structures (Yokohama, Japan)*, PRADS2019-W4-C-1.
17. Newman, J. N. 1978: The theory of ship motions, *Advances in Applied Mechanics*, Vol. 18, pp. 221–283.
18. Newman, J. N., and Sclavounos, P. D. 1980: The Unified Theory of Ship Motions, *Proceedings of 13th Symposium on Naval Hydrodynamics*, Tokyo, pp. 373–394.
19. Ogilvie, T. F., Tuck, E. O. 1969: A rational strip theory of ship motions: Part 1, *Report No. 13. Naval Architecture and Marine Engineering, University of Michigan.*
20. Orihara, H., and Tsujimoto, M. 2018: Performance prediction of full-scale ship and analysis by means of on-board monitoring. Part 2: Validation of full-scale performance, predictions in actual seas, *Journal of Marine Science and Technology*, Vol. 23, No. 4, pp. 782-801.

21. Sclavounos, P. D. 1984: The diffraction of free-surface waves by a slender ship, *Journal of Ship Research*, Vol. 28 (1), pp. 29–47.

22. Shao, Y. L., and Faltinsen, O. M. 2012: Linear seakeeping and added resistance analysis by means of body-fixed coordinate system, *Journal of Marine Science and Technology*, Vol. 17 (4), pp. 493–510.

23. Söding, H., Shigunov, V., Schellin, T. E., and el Moctar, O. 2014: A Rankine panel method for added resistance of ships in waves, *Journal of Offshore Mechanics and Arctic Engineering*, Vol. 136 (3): 031601.

24. Timman, R., Newman, J. N. 1962: The coupled damping coefficients of a symmetric ship, *Journal of Ship Research*, Vol. 5 (4), pp. 34–55.

25. Wicaksono, A., and Kashiwagi, M. 2018: Wave-induced steady forces and yaw moment of a ship advancing in oblique waves, *Journal of Marine Science and Technology*, Vol. 23, pp. 767–781.

26. Yeung, R. W. and Kim, S. H. 1981: Radiation Forces on Ships with Forward Speed, *Proceedings of 3rd Intl. Conf. on Numerical Ship Hydrodynamics*, Paris, pp. 499–515.

Appendix

A1. Analytical Transformation for $\mathcal{Z}_{jk}$

In terms of linearized Bernoulli's pressure equation, the hydrodynamic force can be computed and expressed as follows:

$$F_j = \sum_{k=1}^{6} T_{jk} X_k = \sum_{k=1}^{6} \left[-(i\omega)^2 \left\{ A_{jk} + \frac{1}{i\omega} B_{jk} \right\} \right] X_k . \tag{A1}$$

Here T_{jk} is referred to as the transfer function for the force acting in the j-th direction due to the k-th mode of motion, and the contribution from the velocity potential ψ_k in Eq. (22) to the transfer function may be computed from the following equation:

$$T_{jk}^{(2)} \equiv \rho (i\omega)^3 U \int_L dx \int_{S_H(x)} \psi_k \, N_j \, d\ell . \tag{A2}$$

Thus, we will consider the following integral along the sectional contour at station x.

$$I_{jk}(x) \equiv \int_{S_H(x)} \psi_k \, N_j \, d\ell . \tag{A3}$$

Taking account of the body boundary conditions for ψ_k and φ_j and applying Green's theorem, we have the following equation:

$$I_{jk} = \int_{S_H(x)} \left\{ \psi_k \frac{\partial \varphi_j}{\partial n} - \varphi_j \frac{\partial \psi_k}{\partial n} \right\} d\ell = - \left[\int_{C_F} + \int_{C_\infty} \right] \left\{ \psi_k \frac{\partial \varphi_j}{\partial n} - \varphi_j \frac{\partial \psi_k}{\partial n} \right\} d\ell . \tag{A4}$$

On the free surface (C_F), $d\ell = -dy$ and $\frac{\partial}{\partial n} = \frac{\partial}{\partial z}$. Hence, from the free-surface boundary conditions for ψ_k and φ_j, it follows that

$$\begin{aligned}\mathcal{J}_F &\equiv -\int_{C_F} \left\{ \psi_k \frac{\partial \varphi_j}{\partial n} - \varphi_j \frac{\partial \psi_k}{\partial n} \right\} d\ell \\ &= -\frac{2}{g} \int_{y_0(x)}^{\infty} \varphi_j \Big\{ 2\frac{\partial \varphi_k}{\partial x} - 2\frac{\partial \phi_S}{\partial y}\frac{\partial \varphi_k}{\partial y} - \frac{\partial^2 \phi_S}{\partial y^2}\varphi_k \Big\}\, dy, \end{aligned} \tag{A5}$$

where $y_0(x)$ denotes the half breadth of the transverse section $S_H(x)$ at station x.

Performing the partial integration for the last terms gives the following equation:

$$\begin{aligned}\mathcal{J}_F = &-\frac{4}{g}\int_{y_0(x)}^{\infty} \varphi_j \frac{\partial \varphi_k}{\partial x}\, dy \\ &+ \frac{2}{g}\int_{y_0(x)}^{\infty} \frac{\partial \phi_S}{\partial y}\left(\frac{\partial \varphi_k}{\partial y}\varphi_j - \varphi_k \frac{\partial \varphi_j}{\partial y}\right) dy + \frac{2}{g}\left[\frac{\partial \phi_S}{\partial y}\,\varphi_j\,\varphi_k \right]_{y_0(x)}^{\infty} \end{aligned} \tag{A6}$$

Here we note that the second term in Eq. (A6) becomes zero for $j = k$. Even for the case of $j \neq k$, this term can be found equal to zero for the coupling between heave ($j = 3$) and pitch ($j = 5$), because $\varphi_5 = -x\varphi_3$ holds in the slender ship approximation.

To ensure the convergence in the integral with respect to y in the first term of Eq. (A6), the asymptotic expression of $\varphi_j\, \partial \varphi_k/\partial x$ will be subtracted from the integrand and added after analytical integration. Then, because the asymptotic expression of φ_j is given by Eq. (26), the result takes the following form:

$$\begin{aligned}\mathcal{J}_F = &-\frac{4}{g}\int_{y_0(x)}^{\infty} \left\{ \varphi_j \frac{\partial \varphi_k}{\partial x} + \sigma_j \sigma_k'\, e^{-i2Ky} \right\} dy \\ &-\frac{2}{g}\left[\frac{\partial \phi_S}{\partial y}\,\varphi_j\,\varphi_k + \frac{i}{K}\sigma_j\sigma_k'\, e^{-i2Ky} \right]_{y=y_0(x)} + \frac{2i}{gK}\,\sigma_j\sigma_k' \lim_{R\to\infty} e^{-i2KR}. \end{aligned} \tag{A7}$$

On the other hand, the line integral along C_∞ in Eq. (A4) (denoted as $\mathcal{J}_\infty$) can be evaluated analytically only with the asymptotic expressions given by Eq. (26) and Eq. (30). The result with this transformation can be written as follows:

$$\begin{aligned}\mathcal{J}_\infty &= 2\int_0^{\infty} \left\{ \psi_k \frac{\partial \varphi_j}{\partial y} - \varphi_j \frac{\partial \psi_k}{\partial y} \right\}_{y=\infty} dz \\ &= -\frac{4i}{g}\,\sigma_j\sigma_k' \lim_{y\to\infty} e^{-i2Ky} \int_0^{\infty} e^{-2Kz}\, dz. \end{aligned} \tag{A8}$$

We can see that this result exactly cancels out the last term in Eq. (A7), because the result of the integral with respect to z in Eq. (A8) is $1/2K$.

Because $I_{jk}(x)$ in Eq. (A4) is given by the sum of $\mathcal{J}_F$ and $\mathcal{J}_\infty$, it follows that

$$\begin{aligned}I_{jk}(x) = &-\frac{4}{g}\int_{y_0(x)}^{\infty} \left\{ \varphi_j \frac{\partial \varphi_k}{\partial x} + \sigma_j \sigma_k'\, e^{-i2Ky} \right\} dy \\ &-\frac{2}{g}\left[\frac{\partial \phi_S}{\partial y}\,\varphi_j\,\varphi_k + \frac{i}{K}\,\sigma_j\sigma_k'\, e^{-i2Ky} \right]_{y=y_0(x)}. \end{aligned} \tag{A9}$$

For further transformation, we will use the body boundary condition for the steady disturbance potential ϕ_S on $z = 0$ given by the following equation:

$$\frac{\partial \phi_S}{\partial y} = -y_0'(x) \quad \text{on } z = 0 \tag{A10}$$

and the following identity:

$$\frac{d}{dx}\int_{y_0(x)}^{\infty}\left\{\varphi_j\varphi_k+\sigma_j\sigma_k\,e^{-i2Ky}\right\}dy=\int_{y_0(x)}^{\infty}\left\{\varphi_j\frac{\partial\varphi_k}{\partial x}+\sigma_j\sigma_k'\,e^{-i2Ky}\right\}dy$$
$$+\int_{y_0(x)}^{\infty}\left\{\varphi_k\frac{\partial\varphi_j}{\partial x}+\sigma_k\sigma_j'\,e^{-i2Ky}\right\}dy-y_0'(x)\left\{\varphi_j\varphi_k+\sigma_j\sigma_k\,e^{-i2Ky_0(x)}\right\}. \tag{A11}$$

In the above, we note that the left-hand side becomes zero after integrating it with respect to x over the ship's length, under the assumption that both ends of a ship smoothly close. With these equations, first we consider the case of $j=k$.

In this case, from Eq. (A11), we have the following equation:

$$2\int_{y_0(x)}^{\infty}\left\{\varphi_j\frac{\partial\varphi_j}{\partial x}+\sigma_j\sigma_j'\,e^{-i2Ky}\right\}dy=y_0'(x)\left\{\varphi_j^2+\sigma_j^2\,e^{-i2Ky_0(x)}\right\}. \tag{A12}$$

Substituting this relation and Eq. (A10) into Eq. (A9), it follows the following equation:

$$\begin{aligned}I_{jj}(x)&=-\frac{2}{g}\left[y_0'(x)\left\{\varphi_j^2+\sigma_j^2\,e^{-i2Ky_0(x)}\right\}-y_0'(x)\varphi_j^2+\frac{i}{K}\sigma_j\sigma_j'\,e^{-i2Ky_0(x)}\right]\\&=-\frac{2}{g}\frac{d}{dx}\left[\frac{i}{2K}\sigma_j^2\,e^{-i2Ky_0(x)}\right].\end{aligned} \tag{A13}$$

Thus, this term becomes zero after integrating over the ship's length, with the same reason as for obtaining Eq. (A12). Therefore, we could prove that there is no component proportional to the forward speed in the diagonal added mass and damping coefficients.

Next, we consider the case of $j\neq k$, particularly the coupling between heave and pitch. In this case, approximations of $\varphi_5=-x\varphi_3$ and hence $\sigma_5=-x\sigma_3$ can be used in the slender ship theory. Thus, we can derive the following relation:

$$\varphi_3\frac{\partial\varphi_5}{\partial x}+\sigma_3\sigma_5'\,e^{-i2Ky}=\varphi_5\frac{\partial\varphi_3}{\partial x}+\sigma_5\sigma_3'\,e^{-i2Ky}-\left\{\varphi_3^2+\sigma_3^2\,e^{-i2Ky}\right\}. \tag{A14}$$

By applying this relation to Eq. (A11) for $(j,k)=(3,5)$ and $(j,k)=(5,3)$, we can obtain the following equation:

$$\begin{aligned}&\frac{d}{dx}\int_{y_0(x)}^{\infty}\left\{\varphi_j\varphi_k+\sigma_j\sigma_k\,e^{-i2Ky}\right\}dy\\&\quad=2\int_{y_0(x)}^{\infty}\left\{\varphi_j\frac{\partial\varphi_k}{\partial x}+\sigma_j\sigma_k'\,e^{-i2Ky}\right\}dy\\&\quad\quad\pm\int_{y_0(x)}^{\infty}\left\{\varphi_3^2+\sigma_3^2\,e^{-i2Ky}\right\}dy-y_0'(x)\left\{\varphi_j\varphi_k+\sigma_j\sigma_k\,e^{-i2Ky_0(x)}\right\},\end{aligned} \tag{A15}$$

where the upper $(+)$ and lower $(-)$ signs in the second line on the right-hand side of Eq. (A15) must apply to $(j,k)=(3,5)$ and $(j,k)=(5,3)$, respectively.

As before, the left-hand side of Eq. (A15) becomes zero after integration over the ship's length. With this kept in mind, we substitute Eq. (A15) and Eq. (A10) into Eq. (A9), then the result can be expressed as follows:

$$I_{jk}(x)=\pm\frac{2}{g}\int_{y_0(x)}^{\infty}\left\{\varphi_3^2+\sigma_3^2\,e^{-i2Ky}\right\}dy-\frac{2}{g}\,e^{-i2Ky_0(x)}\left\{\frac{i}{K}\sigma_j\sigma_k'+y_0'(x)\,\sigma_j\sigma_k\right\}. \tag{A16}$$

Furthermore, we can prove the following relations:

$$\frac{d}{dx}\left[\frac{i}{2K}\sigma_j\sigma_k\,e^{-i2Ky_0(x)}\right] = e^{-i2Ky_0(x)}\left\{\frac{i}{K}\sigma_j\sigma_k' + y_0'(x)\,\sigma_j\sigma_k\right\} + e^{-i2Ky_0(x)}\frac{i}{2K}\Big(\sigma_j'\sigma_k - \sigma_j\sigma_k'\Big), \tag{A17}$$

$$\sigma_j'\sigma_k - \sigma_j\sigma_k' = \pm\sigma_3^2, \tag{A18}$$

where the meaning of the complex sign given earlier is the same as in Eq. (A15) and Eq. (A16). Substituting Eq. (A17) and Eq. (A18) in Eq. (A16), it follows the following equation:

$$I_{jk}(x) = \pm\frac{2}{g}\left[\int_{y_0(x)}^{\infty}\left\{\varphi_3^2 + \sigma_3^2\,e^{-i2Ky}\right\}dy + \frac{i}{2K}\,\sigma_3^2\,e^{-i2Ky_0(x)}\right]. \tag{A19}$$

Because this is the result after transformation of Eq. (A3), we can obtain from Eqs. (A1) and (A2) the expression for an additional contribution to the added mass and damping coefficients for the case of $(j,k)=(3,5)$ and $(j,k)=(5,3)$ in the form given as follows:

$$A_{jk} + \frac{1}{i\omega}B_{jk} = -\rho i\omega U\int_L I_{jk}(x)\,dx = \mp\rho i2\frac{U\omega}{g}\int_L I(x)\,dx, \tag{A20}$$

where

$$I(x) \equiv \int_{y_0(x)}^{\infty}\left\{\varphi_3^2(y,0) + \sigma_3^2\,e^{-i2Ky}\right\}dy + \frac{i}{2K}\sigma_3^2\,e^{-i2Ky_0(x)}. \tag{A21}$$

This result is the expression given as Eq. (34) in the present article.

Prediction of Nonlinear Vertical Bending Moment Using Measured Pressure Distribution on Ship Hull*

Kurniawan T. WASKITO†, Masashi KASHIWAGI†,
Hidetsugu IWASHITA‡ and Munehiko HINATSU†

† Department of Naval Architecture & Ocean Engineering, Osaka University
2-1 Yamada-oka, Suita, Osaka 565-0871, Japan

‡ Department of Transportation & Environmental Systems, Hiroshima University
1-4-1 Kagamiyama, Higashi-Hiroshima 739-8527, Japan

Abstract

Accurate prediction of wave loads on ships and floating structures is paramount in the structural design stage. Use of a segmented ship model is a common method to quantify the wave loads. Nevertheless, the value could be measured only at segmented sections. To obtain the wave loads at any longitudinal position and to account for nonlinear features in the wave loads more precisely, local quantities of the pressure on the whole ship-hull surface need to be measured along with ship motions in waves. In this paper, an unprecedented experiment using a bulk carrier model has been carried out to measure the spatial distribution of wave-induced unsteady pressure by means of a large number of Fiber Bragg Gratings (FBG) pressure sensors affixed on the whole ship-hull surface, and at the same time the wave-induced ship motions and ship-side wave profile have been measured. In order to see hydrodynamic characteristics in nonlinear and forward-speed effects on measured and analyzed results, some computations with the linear frequency-domain Rankine Panel Method (RPM) and the nonlinear Computational Fluid Dynamics (CFD) method solving the Reynolds-Averaged Navier-Stokes (RANS) equations are made. Favorable agreement is found for the pressure distribution and resulting vertical bending moment between the results of the experiment and corresponding numerical computations. Validation of the measured pressure distribution has also been made through a comparison of the wave-exciting force and moment between the two independent results obtained by integration of the measured pressure over the entire wetted surface of a ship and by direct measurement using a dynamometer. Very good agreement is confirmed in this case, too. As another validation for the wave loads, a comparative study is made with the benchmark test data of a 6750-TEU container ship used for the ITTC-ISSC joint workshop in 2014; which also demonstrates remarkable agreement. The present study may provide a new research technique, especially in the experiment, for predicting the waveload distribution and for studying local hydrodynamic features in wave-related unsteady phenomena.

Keywords: Wave loads, Vertical bending moment, Nonlinearity, Pressure distribution, Fiber bragg grating, Rankine panel method, CFD.

---

* *Reprinted from Applied Ocean Research, Vol. 101, No. 102261 (pp. 1–20), 2020 (August), DOI: https://doi.org/10.1016/j.apor.2020.102261*

1. Introduction

Prediction of wave-induced shearing force and bending moment as the wave loads on a ship is of vital importance for evaluating the ship's structural strength in waves, and hence accurate prediction of wave loads on ships is required. In the analysis of fluid-structure interactions especially for large ships, the so-called two-way coupling in the analysis is prerequisite to account for the influence of flexible deformation of a ship. In fact, much work has been made on ship hydroelasticity problems so far, thereby various methods have been developed for both frequency- and time-domain problems [1–4]. However, the quasi-static response analysis is still deemed as the practical method particularly in the early stage of structural design rather than the direct calculation method involving the dynamic response analysis which is more time-consuming. For that reason, evaluation of the bending moment taking account of primarily rigid-body motions is a dominant part in the study on the wave loads.

Comprehensive reviews on the progress in the assessment of wave loads for ships and offshore structures have been presented by the Loads Committee in the ISSC [5, 6] and also by the Seakeeping Committee in the ITTC [7]. For instance, Hirdaris *et al.* [5] summarized related papers published basically in the past three years up to 2011, and Temarel *et al.* [6] reviewed the progress made in the next three years up to 2014 in the area of wave-induced loads; in which the advantages and disadvantages of various computation methods including relatively simpler potential-flow approaches and time-consuming CFD methods are discussed with reference to accuracy, modeling nonlinear effects, ease of modeling and coupling with structural assessment procedures, and so on. In particular, CFD methods making use of RANS equations are promising for solving complicated seakeeping problems which include various nonlinearities related to large-amplitude waves, resultant ship motions and ship's actual wetted surface, and also forward-speed effects on wave loads and other motion-related hydrodynamic quantities. A good survey of the history in the application of CFD methods to seakeeping problems at least up to 2012 is provided by Guo *et al.* [8]. Not only survey but also computation was made of the wave-induced ship motions of and added resistance on KVLCC2 tanker model especially in short waves by using the ISIS-CFD flow solver, FINE/Marine V 2.2, and they also did careful grid-convergence and uncertainty analyses for numerical results. Thanks to dramatic advances of computer technology and science, the number of papers on seakeeping nonlinear problems with CFD methods is increasing over the last decade. Among them, we can see recent work in Niklas *et al.* [9] computing the added resistance using STAR-CCM+ and in Judge *et al.* [10] computing the slamming pressure using CFDShip-Iowa V 4.5. Use of OpenFOAM for seakeeping problems is also increasing recently, such as Wang *et al.* [11] and Xu *et al.* [12] to name a few. However, most of them are concerned with pressure-integrated global quantities like wave-induced ship motions and added resistance, and few papers treat the unsteady spatial pressure distribution and resultant wave loads.

Looking back at the work on the wave loads done in the 1980s in Japan [13–16], it was already noted principally with experimental work that the nonlinearity in the sagging and hogging moments must be taken into account for sufficiently accurate prediction of the vertical bending moment. However, in order to assess this kind of nonlinear effects on the wave loads by numerical computations, the time-domain analysis methods must be used [17, 18, 19]. Recently some of the methods using nonlinear potential-flow approaches [20] or CFD methods employing RANS or even URANS models [21, 22] have been investigated. Nevertheless, the examples of studies using CFD methods on the wave loads or local pressure histories are fewer in number, e.g. [23, 24, 25]. Among them, it should be noted that Hänninen *et* *al.* [26] computed local pressure histories at ten locations around the still water line in the bow area of a passenger ship using an interface-capturing CFD method ISIS-CFD. Then as a validation, computed results were compared with measured results in the experiment conducted by themselves. Notwithstanding advancement of computer performance, computation efficiency is still needed to consider from the practical viewpoint [27, 28] in the study of wave loads and seakeeping problems.

On the other hand, to date, the wave loads computed by the potential-flow approaches or CFD methods have been validated through comparisons with experiments featuring various ship hulls with different level of nonlinearities at extreme seas [29–33]. Nonetheless, most of the work focused only on integrated values such as hydrodynamic forces acting on the entire ship hull and ship motions in waves. To attain more thorough understanding of hydrodynamic features, local hydrodynamic quantities like spatial distribution of the pressure on the hull surface of a ship should be checked. From a viewpoint of wave-load measurement conducted so far in a towing tank, segmented ship models have been commonly used [34, 35] in which the wave loads could be measured only at segmented sections with load cell installed. However, we need to obtain the distribution of wave loads at any longitudinal position of a ship with higher accuracy and to account for the nonlinearity in the wave loads; which could be realized by measuring the spatial distribution of unsteady pressure on the whole ship-hull surface and by properly integrating it in conjunction with the measurement of ship motions and time-variant wetted surface of a ship in waves.

For that purpose, we have conducted an unprecedented experiment at Research Institute for Applied Mechanics (RIAM), Kyushu University in 2018 using a bulk carrier ship model. Measured in that experiment were the unsteady pressure distribution by means of a large number of Fiber Bragg Gratings (FBG) pressure sensors [36, 37, 38] and simultaneously the wave-induced ship motions and ship-side wave profile. As a matter of fact, the experiment for measuring the unsteady pressure on a ship in head waves started in 2015, and the measurement has been repeated with FBG pressure sensor improved year by year through collaboration with the company manufacturing this sensor, CMIWS Co., Ltd, and then repeatability and reliability in measured results have been confirmed [39, 40, 41]. Although the number of FBG sensors used in 2015 was only 28, the total number of sensors affixed to the ship model has been increased year by year to enhance the density of measurement and to resolve the nonlinearity in the pressure above still waterline. In the experiment in 2018, we used version 6.0 of the FBG sensor and 333 FBG pressure sensors were affixed only on the port side of a ship considering the symmetrical pressure field in head waves, among which 70 sensors were placed above the still waterline to see nonlinearities. Using these measured data, a study is made in this paper on the wave-load distribution. To figure out nonlinear effects on the pressure distribution and resultant wave loads in a precise manner, the analysis is commenced from the zero-speed case in which the responses of the pressure and ship motions can be regarded as linear. Meanwhile, nonlinear responses of wave loads are studied for a forward-speed case, where an asymmetric and hence nonlinear feature in sagging and hogging moments is demonstrated by using the pressure distribution and wave-induced ship motions measured at synchronized time instants. Some comparisons are made by means of the linear potential theory of RPM developed by Iwashita *et al.* [42] as well as a commercial CFD software FINE/Marine V 8.2 [48] solving the RANS equations to see nonlinear effects and features in the vertical bending moment. A comparative study with the benchmark data on wave-induced motions and loads of a 6750-TEU container ship adopted for the ITTC-ISSC joint workshop in 2014 [43] is also made for further validation.

Although comparisons are made between measured and computed results, the main objective of the present study is not the validation of the computation methods used but the acquisition of the spatial distribution of wave-induced unsteady pressure only with experimental measurement. The obtained data can be used for hydrodynamic study on the local quantities like the distribution of wave loads and added resistance, particularly the longitudinal distribution of the vertical bending moment in this paper. The obtained data can also be used as the validation data for CFD methods, but more importantly, with CFD methods used as a guide in the analysis of measured data, we can establish a new experimental technique to see the details in the wave-load distribution and consequently enhance the level of our understanding of nonlinear and forward-speed effects on wave loads in terms of the experimental data obtained.

2. Experimental Set-up

The experiment was conducted in the towing tank (its length, breadth, and depth are 65 m, 5 m, and 7 m, respectively) of RIAM, Kyushu University. The tank has a plunger-type wave maker with wedge inclination angle of 40 deg at one end and a wave-absorbing beach at the other end. The wave maker can be activated remotely with the signal from a computer specifying the amplitude and frequency of the driving motor. In the experiment in 2018, we used the RIOS (Research Initiative on Oceangoing Ships) bulk carrier [42, 44, 45] whose principal particulars are shown in Table 1. Fig. 1 shows the body plan and also the position of pressure sensors, in which 333 FBG pressure sensors in total (including 70 sensors above the still waterline) were affixed on the port side (see Fig. 1) and 19 strain-type pressure sensors were embedded in the starboard side (only at ordinate numbers 5.0, 9.0 and 9.5, indicated by green-color square symbol in Fig. 1) to check the measurement accuracy of the FBG pressure sensors. Since the experiment was performed in regular head waves, the pressures at the same symmetric points on both sides of a ship must take the same value; with this principle, measured values by the FBG and strain-type pressure sensors can be compared and the accuracy can be confirmed. The FBG pressure sensor used is ps1000A-V6 manufactured by CMIWS Co., Ltd and the strain-type pressure sensor used is P306V-05S manufactured by SSK Co., Ltd.

Table 1 Principal particulars of RIOS bulk carrier model

Item	Value
Length: L_{pp} (m)	2.400
Breadth: B (m)	0.400
Draft: d (m)	0.128
Block coefficient: C_b	0.800
Waterline coefficient: C_w	0.870
Horizontal center of gravity: x_G (m)	0.0510
Vertical center of gravity: z_G (m)	−0.0200
Vertical center of buoyancy: z_B (m)	−0.0618
Gyrational radius in pitch: κ_{yy}/L	0.250

The ship model was free to surge, heave, and pitch. When the model was towed by the carriage at a constant speed, the mean position of the model was controlled by pulling the model (in fact the fore heaving rod mentioned later) with an adjusted force induced by a

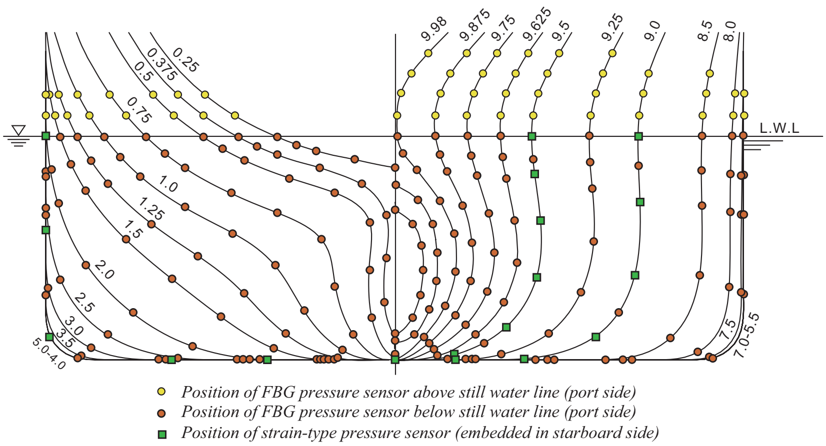

(a) Body plan and position of pressure sensors

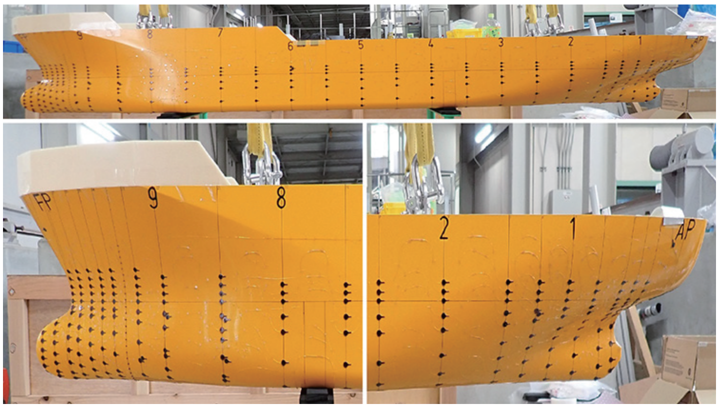

(b) Photo of ship model and position of pressure sensors

Fig. 1 RIOS bulk carrier model; (a) Body plan, (b) Position of pressure sensors

servo motor, which was realized by adjusting manually the electric current to a servo motor while monitoring the mean position of the model even in a wave that the ship model would be oscillating in surge. Then the wave-induced ship motions in surge, heave, and pitch were measured by potentiometers and the resistance was measured by strain gauges installed at the bottom of fore and rear heaving rods (see Figs. 3 and 5). These measurements can be done at the same time with measurement of the pressure (which will be explained below) but these are independent and there is no interference with each other.

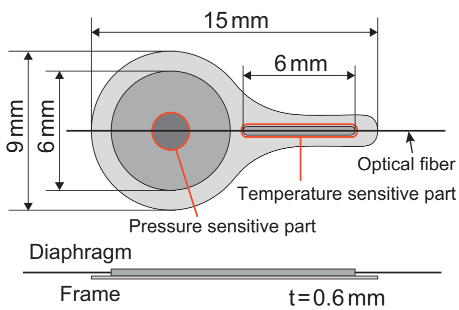

Fig. 2 FBG sensor used in the experiment [38]

The mechanism and measurement principle of the FBG pressure sensor are explained by Wakahara *et al.* [36] and Iwashita *et al.* [37]. The FBG is a type of distributed diffraction grating etched into the optical fiber core that reflects a particular wavelength of light, called Bragg wavelength, and transmits the remainder. If the spacing between reflectors changes due to variation of pressure load or temperature, the Bragg wavelength also changes. Thus by identifying a change in the Bragg wavelength in terms of the calibration coefficient obtained beforehand, the pressure can be measured.

Reliability of the sensor has been improved year by year since 2015 by minimizing the effect of temperature variation on the pressure to be measured and the size of the sensor itself. Fig. 2 shows a schematic diagram of the FBG sensor Version 6.0 [38] used in the experiment in 2018, with 9 mm in diameter, 15 mm in length, and 0.6 mm in thickness. One sensor can measure the pressure and temperature at the same time, because two FBGs with different spacings of Bragg grating are contained in one sensor and fixed in order not to interfere with each other. Therefore, the effect of temperature variation on the pressure measurement can be compensated in principle. It is also possible to arrange many (in the order of 10 – 15) FBG sensors with different spacing of Bragg grating along one optical fiber, so that the simultaneous multipoint measurement can be made.

The calibration curve for FBG sensors can be written as

$$P(x, y, z; t) = C_p(\mathit{\Delta}\lambda_p - S_t \mathit{\Delta}\lambda_t)C_f \tag{1}$$

where $\mathit{\Delta}\lambda_p$ and $\mathit{\Delta}\lambda_t$ denote the amount of change in the Bragg wavelength due to variation of the pressure and temperature, respectively. S_t is the compensation factor to account for the effect of temperature variation and its value is around 0.6 and less than 1.0. C_p denotes the calibration coefficient proportional to a change in the Bragg wavelength. The calibrated values of C_p and S_t are provided for each FBG sensor by CMIWS Co., Ltd based on a laboratory test, but they tend to change and differ in actual measurement. Thus the correction coefficient C_f must be obtained from the calibration measurement in situ, which was done by providing several different hydrostatic pressures on the pressure sensors. In order to alter the hydrostatic pressure, the vertical position of the ship model was changed

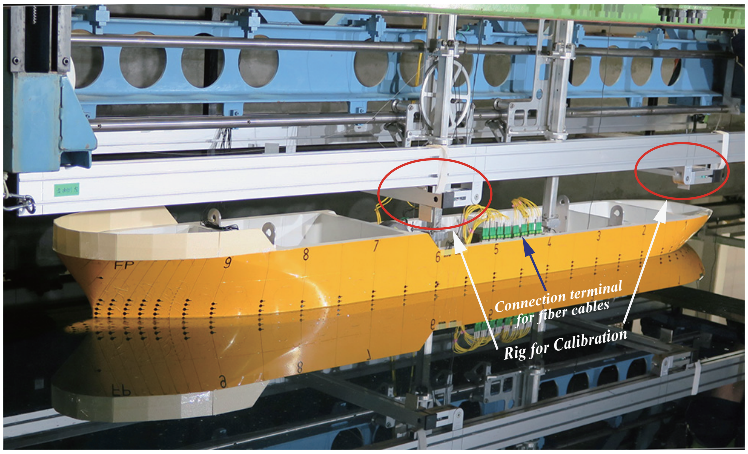

Fig. 3 Overview of ship model set to the towing carriage and measurement system, showing connection terminal of optical fiber cables

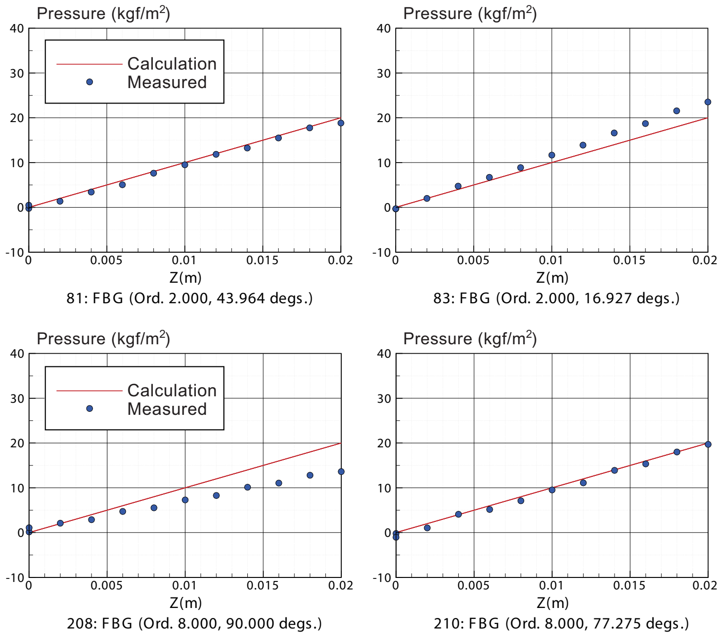

Fig. 4 Samples of calibration results for FBG pressure sensor

with the adjustable lifting and lowering rig attached to the ship model (see Fig. 3). Before a calibration measurement, the ship model was pressed downward so that all the sensors were in water. Then the ship model was lifted up and stopped step by step with 2.0 mm each and up to 2 cm in the end. The measurement in the inverse direction was also performed by pressing down the model with 2.0 mm each to confirm linearity and no hysteresis.

Figure 4 shows some samples of the calibration response at 4 typical positions taken among 333 sensors. We could see a linear response at all positions and the values are

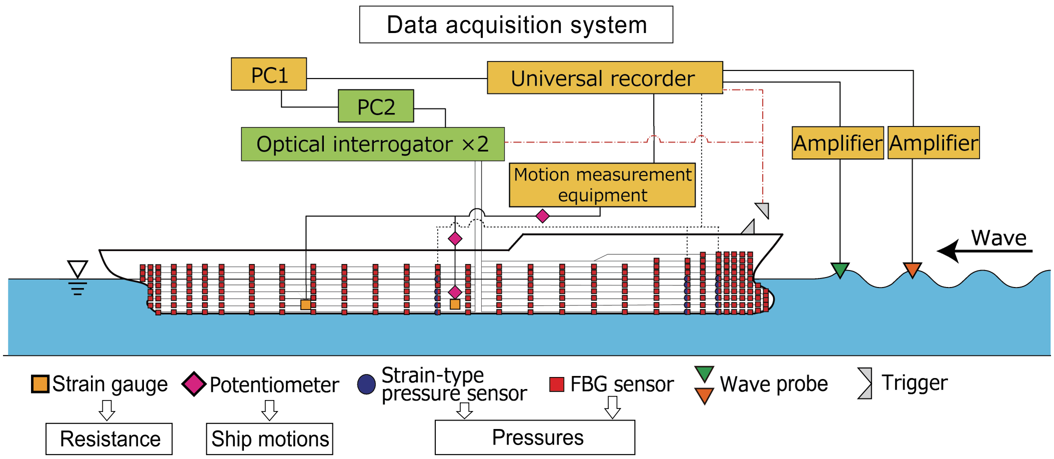

Fig. 5 Data acquisition system in the RIOS bulk carrier experiment

Table 2 Measurement channels of the experiment

Channel	Item
Ch. 1	Trigger signal
Ch. 2	Wave-0 (carriage-fixed wave probe)
Ch. 3	Surge
Ch. 4	Heave
Ch. 5	Pitch
Ch. 6	Longitudinal force, $F_{x(f)}$ (fore)
Ch. 7	Longitudinal force, $F_{x(a)}$ (aft)
Ch. 8	Wave-1 (space-fixed wave probe)
Ch. 9-27	Strain-type pressure sensors
Ch. 28-360	FBG pressure sensors

virtually the same both when pressing down and lifting up the model (i.e. no hysteresis). However, a difference from the theoretical value of hydrostatic pressure can be observed at some positions, from which the correction coefficient C_f in Eq. (1) was determined in terms of a least-squares method for all 333 sensors automatically with a personal computer (PC) used in the in-situ analysis. This calibration measurement has been carried out, whenever necessary, without removing any instrument in the experimental set-up.

The schematic arrangement of the data measurement and acquisition system is depicted in Fig. 5 and the cannel number of each item is presented in Table 2. The pressure was measured simultaneously by all FBG sensors connected to the optical interrogators. The green-color part is the recording system for FBG pressure sensors and the orange-color part for other electric equipments like wave probes, potentiometers, strain-type sensors and so on. Data recorded on different computers (indicated as PC1 and PC2 in Fig. 5) were synchronized with a trigger signal which came up when the fore perpendicular of the ship went through the position of space-fixed wave probe. Because of large amount of data, the data sampling frequency was set to 200 Hz, which implies that 133,200 data of the pressure and temperature were transferred to a PC per second. Recorded data were A/D converted and Fourier-analyzed. More details for the Fourier analysis will be described in the subsequent section.

The experiment was conducted at $Fn = 0.0$ and 0.18 in regular head waves at the wavelength range of 0.3$\sim$3.0 with motion-free condition, measuring not only the pressure distribution but also hydrodynamic forces and wave-induced ship motions (surge, heave, and pitch). In addition, the ship-side wave, i.e. the wave profile on the ship-hull surface, was measured in advance using capacitance-type wave gauges which were installed on another ship model made of urethane with the same geometry and dimensions. Since these wave gauges were set along the girth with small separation gap from the hull surface and at the same transverse sections as those for measuring the pressure, we can detect the correct wetted surface of ship hull at each time instant, which is of critical importance for the pressure integration over the ship-hull surface and for computing resultant hydrodynamic forces.

The amplitude of incident wave in the motion-free test was set within the range of linear theory ($2\zeta_a/\lambda \leq 1/30$). Furthermore, for a fundamental check whether the linear superposition is satisfied, the measurement of pressure distribution has been performed for the diffraction (with motion fixed in waves) and radiation (with prescribed motions in calm water) problems, together with direct measurement of the total force by a dynamometer. The experiments for the diffraction and radiation problems were carried out by setting the ship model to another equipment for the forced oscillation test.

One serious problem we realized during the experiment conducted in September of 2018 was that the repeatability in measured results tends to be influenced by the temperature difference between water and air, especially when its value of the difference becomes larger than 1.0 °C. Therefore we decided to perform the measurement during the midnight while confirming the temperature difference, Δt, satisfies an experience-based condition of $\Delta t <$ 1.0°C. This issue on the effect of temperature variation on the accuracy of measured results is now being improved by the sensor company and will be provided as version 7.0 of the FBG pressure sensor.

3. Formulation and Computation Methods

The following subsections outline the potential flow theory and the CFD method used for the purpose of comparison with measured results, and then present the analysis methods of ship-side wave and pressure for evaluating the vertical bending moment by pressure integration over the wetted surface of a ship.

3.1 Potential flow theory

For a comparison with measured results in the experiment, numerical computations based on the linear potential-flow theory were implemented using the 3D frequency-domain Rankine panel method (RPM) with the formulation as described in [42, 44] and [46]. Although this RPM was basically developed for the forward-speed problems, we have applied RPM for the zero-speed case in the present study by modifying a numerical method to satisfy the radiation condition, as will be described below.

Because of zero forward speed, the velocity potential for harmonic oscillation problems can be written as

$$\Phi(x,y,z;t) = \mathrm{Re}\left[\,\phi(x,y,z)\,e^{i\omega t}\,\right] \tag{2}$$

where the time-dependent part is written with circular frequency ω, and $\phi(x,y,z)$ is the spatial part of the velocity potential which is given in a form of linear superposition as

$$\phi(x,y,z) = \frac{ig\zeta_a}{\omega}\left(\,\phi_0 + \phi_7\,\right) + i\omega \sum_{j=1}^{6} X_j\,\phi_j \tag{3}$$

where ζ_a denotes the amplitude of incident wave, g the gravitational acceleration, X_j the complex amplitude in j-th mode of six degree-of-freedom ship motions. Re in Eq. (2) means only the real part of the expression must be taken. The velocity potential of incident wave is denoted as ϕ_0 which is given explicitly as

$$\phi_0 = e^{Kz - iK(x\cos\chi + y\sin\chi)} \tag{4}$$

Here the coordinate system in the present analysis is taken such that the positive x- and y-axes are in the bow and port directions of a ship, respectively, and the z-axis is positive vertically upward with the origin taken on the undisturbed free surface $z = 0$ and at the midship. The wavenumber of incident wave is given as $K = \omega^2/g$, and χ denotes the incident angle of an incoming regular wave relative to the x-axis and hence $\chi = \pi$ means the head wave.

The unsteady velocity potential ϕ_j in Eq. (3) denotes the radiation ($j = 1 \sim 6$) and scattering ($j = 7$) velocity potentials; which is governed by the Laplace equation and expressed by a source distribution over the body surface S_H and the free surface S_F, with Rankine source used as the kernel function. Namely

$$\phi_j(P) = \iint_{S_H+S_F} \sigma_j(Q)\, G(P,Q)\, dS(Q) \tag{5}$$

where $P = (x, y, z)$ denotes a field point in the fluid and $Q = (x', y', z')$ the integration point on the boundary surface, and

$$G(P,Q) = \begin{cases} G_0(P,Q) + G_0'(P,Q) & \text{when } \ Q \text{ on } S_H \\ G_0(P,Q) & \text{when } \ Q \text{ on } S_F \end{cases} \tag{6}$$

$$G_0(P,Q) = -\frac{1}{4\pi r}, \quad G_0'(P,Q) = -\frac{1}{4\pi r'} \tag{7}$$

$$\left.\begin{array}{l} r \\ r' \end{array}\right\} = \sqrt{(x-x')^2 + (y-y')^2 + (z \mp z')^2} \tag{8}$$

Here $\sigma_j(Q)$ in Eq. (5) denotes the strength of sources which is unknown. $G_0'(P,Q)$ is the mirror image of $G_0(P,Q)$ reflected in the undisturbed free surface ($z = 0$) and hence $G_0(P,Q) + G_0'(P,Q)$ satisfies the rigid-wall boundary condition on $z = 0$.

In case of zero forward speed, the linearized free-surface boundary condition is given in the form

$$\frac{\partial \phi_j}{\partial z} - K\phi_j = 0 \quad \text{on } z = 0 \tag{9}$$

and the linearized body boundary condition on the wetted hull surface of a ship can be expressed in the form

$$\left.\begin{array}{ll} \dfrac{\partial \phi_j}{\partial n} = n_j & (j = 1 \sim 6) \\ \dfrac{\partial \phi_7}{\partial n} = -\dfrac{\partial \phi_0}{\partial n} & (j = 7) \end{array}\right\} \text{ on } \ S_H \tag{10}$$

where $(n_1, n_2, n_3) = \boldsymbol{n}$ denotes the normal vector pointing into the fluid from the boundary surface and $(n_4, n_5, n_6) = \boldsymbol{r} \times \boldsymbol{n}$, with $\boldsymbol{r} = (x, y, z)$ the position vector. The unknown source strength $\sigma_j(Q)$ must be determined such that the boundary conditions, Eqs. (9) and (10), are satisfied. The procedure for obtaining an integral equation for the source strength is as follows.

When the field point P is located on the boundary (S_H or S_F), the normal derivative of Eq. (5) can be written in the form

$$\frac{1}{2}\sigma_j(P) + \iint_{S_H+S_F} \sigma_j(Q)\, \frac{\partial G(P,Q)}{\partial n_P}\, dS(Q) = \frac{\partial \phi_j(P)}{\partial n_P} \tag{11}$$

Specifically when P is on S_H, the body boundary condition Eq. (10) must be specified as the forcing term on the right-hand side, and when P is on S_F (note that $z = 0$), the free-surface boundary condition can be satisfied by substituting the following equation into the right-hand of Eq. (11)

$$\frac{\partial \phi_j(P)}{\partial n} = -\frac{\partial \phi_j(P)}{\partial z} = -K\phi_j(P) \tag{12}$$

This free-surface boundary condition gives the following homogeneous form of integral equation:

$$\frac{1}{2}\sigma_j(P) + \iint_{S_H+S_F} \sigma_j(Q) \left\{ \frac{\partial G(P,Q)}{\partial z} - KG(P,Q) \right\} dS(Q) = 0 \tag{13}$$

The resulting equations on S_H and S_F can be expressed as a series of algebraic equations by discretizing the boundary surfaces with appropriate smaller panels and assuming the source strength $\sigma_j(Q)$ to be constant on each panel. Integrations of the Rankine source and its normal dipole over each panel are necessary, which are performed with analytical formulae established by Newman [47]. Then we can obtain a solution by solving a linear system of simultaneous equations for the source strength on S_H and S_F. Once the source strength is determined, the velocity potential can be computed from Eq. (5), then the hydrodynamic forces in the radiation and diffraction problems can be computed.

The wave radiation condition is satisfied numerically by the so-called panel shift technique [42], shifting the collocation points by one panel upstream on the free surface. In order to avoid wave reflection from the outward boundary which can disturb the flow around a ship, we use Rayleigh's artificial friction which is equivalent to introducing a numerical damping beach on the free surface. In this case, we can transform the wavenumber K in Eq. (9) into a complex quantity with small negative imaginary part. Namely Eq. (9) is transformed as

$$\frac{\partial \phi_J}{\partial z} - \big(K - i\epsilon\big)\phi_j = 0 \quad \text{on } z = 0 \tag{14}$$

Here ϵ is a function of (x, y) on the free surface that may be specified as [31]

$$\epsilon = \frac{\omega}{g}\,\alpha \left\{ 1 - e^{-\beta(R-1)} \right\} \quad \text{for } R \geq 1 \tag{15}$$

where $R = \sqrt{x^2 + y^2}$ is the distance from the origin of the coordinate system and all length dimensions are normalized with half length of a ship $L/2$. The values of α and β must be tuned and are taken as $\alpha = 0.5$ and $\beta = 1.5$ in the present study.

A computation mesh with quadrilateral-type panels of total number 5,032 on the ship hull and 5,320 on the free surface is shown in Fig. 6. The number of panels on the free surface was set with longitudinal and lateral lengths equal to $-2L \leq x \leq 0.5L$ and $2L$, respectively, which was confirmed to be sufficient to prevent disturbance waves from the outward boundary and to provide reasonable and converged results of hydrodynamic forces.

3.2 Computational fluid dynamics method

In order to discuss nonlinear and forward-speed effects to be seen in the wave-induced unsteady pressure on the ship-hull surface, we have used a commercial CFD software, FINE/Marine V 8.2 [48], which is based on the ISIS-CFD flow solver developed at Ecole Centrale de Nantes (ECN), solving the incompressible RANS equations with an unstructured finite volume method and Volume-of-Fluid (VOF) type interface capturing method for detecting the free surface between air and water. Mathematical details in the development of ISIS-CFD are described by Queutey and Visonneau [49].

For simulating free-surface flows and their interactions with an advancing ship, the use of interface capturing methods is effective. In order to enhance the sharpness of the interface, many studies have been made. For a review of the development of various interface capturing techniques, we can refer to Wackers *et al.* [50], which also describes the details of ISIS-CFD flow solver together with validation results. Application of ISIS-CFD flow solver to

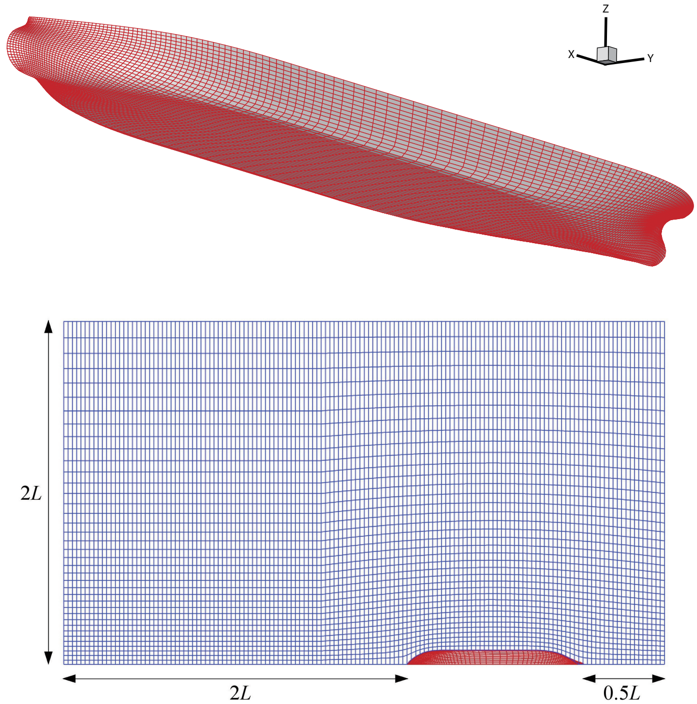

Fig. 6 Computational mesh of RPM for RIOS bulk carrier, Upper: ship-hull surface mesh, Lower: free-surface mesh

unsteady seakeeping problems was shown by Guo *et al.* [8], and careful and systematic study on uncertainty and convergence using 4 different meshes was performed, which shows the reliability and accuracy of computed results for the prediction of ship motions and added resistance. Hänninen *et al.* [26] also applied ISIS-CFD solver to compute the time histories of local pressure at 10 locations around the still waterline in the bow area of a passenger ship. By using 3 different meshes, they have checked the dependency of numerical results on the mesh resolution, the time step per wave period, and the iteration number within a time step, thereby confirming reliability of the method, although the computational cost is still very high.

Judging from these results obtained so far regarding the reliability of the ISIS-CFD flow solver for seakeeping problems, it may be appropriate to use FINE/Marine as an analysis tool for hydrodynamic discussion on the experimental results to be obtained in the present study.

This CFD code solves the incompressible unsteady RANS equations using the finite volume method to generate the spatial discretization of the equations. The governing equations for an incompressible flow are the Navier-Stokes and continuity equations. In treating turbulent flows, it is common to separate the velocity vector into mean and fluctuating parts as follows:

$$u_i = \overline{u}_i + u_i' \tag{16}$$

where an overbar denotes the average value and u_i' the fluctuating component. Then the averaged Navier-Stokes and continuity equations can be written as

$$\frac{\partial \overline{u}_i}{\partial t} + \overline{u}_j \frac{\partial \overline{u}_i}{\partial x_j} = -\frac{1}{\rho}\frac{\partial \overline{p}}{\partial x_i} + \nu \nabla^2 \overline{u}_i + g\delta_{i3} - \frac{\partial}{\partial x_j}\overline{u_i' u_j'} \tag{17}$$

$$\frac{\partial \overline{u}_j}{\partial x_j} = 0 \tag{18}$$

where ρ and ν denote the density and kinematic viscosity coefficient of the fluid, respectively, and δ_{i3} is the Kronecker's delta, equal to 1 only for $i = 3$.

Because of existence of the last term in Eq. (17), which is due to the Reynolds stress $-\rho\overline{u_i' u_j'}$, some kinds of turbulence modeling must be normally introduced. The k-ω SST model [51, 52] is adopted for the simulation with FINE/Marine.

Table 3 Summary of schemes used in the CFD simulations by FINE/Marine [48]

Item	Scheme used
Grid system	Unstructured, non-conformal, fully hexahedral grid
Spatial discretization	Finite volume method
Advection term	QUICK 3rd-order upwind difference
Viscous diffusion term	2nd-order central difference
Time marching	Backward difference, sub-iteration with virtual time
Coupling between pressure and velocity	Projection method solving Poisson's equation
Free-surface capturing	VOF method (BRICS scheme)
Turbulence model	k-ω SST
Body-surface boundary condition	Logarithmic function as wall function

Table 3 shows a summary of the schemes used in the present CFD simulation. Details refer to FINE/Marine V 8.2 [48]. In Fig. 7, only half of the ship hull is used in the calculations, thus a symmetry boundary condition is adopted at the center plane boundary. Box 1 represents the domain of the incident wave, ship-hull, and vortex. Thus, the mesh density of this domain was set to be relatively fine to prevent the numerical attenuation of the wave. Boxes 2, 3 and 4 represent the downstream domain. In these domains, the mesh density was relatively coarse to prevent the wave reflection from the external boundary as shown in Figs. 7 and 8. L_{ref} in Fig. 7 takes a larger value between ship length L and wavelength λ. H_w is the wave height equal to $2\zeta_a$. At wavelength of $\lambda/L = 1.25$, the total number of elements was 2,907,979, as shown on the left side of Fig. 8, and the time step was taken equal to 1/250 of the encounter period, with the incident-wave amplitude equal to 0.0240 m in accordance with the experiment. On the right side of Fig. 8, close-up views of the mesh for the bow and stern parts are shown.

In fact, there are recommended values in the user manual of FINE/Marine for the number of mesh and time step, which were used for the computations in this paper. Furthermore, before implementing the present study, we have studied independently for a simpler problem of incident-wave propagation to check the dependency of numerical results on the number of mesh and time step, and we have confirmed appropriate selection of the parameters; with which we confirmed that virtually no decaying phenomenon exists in an important computational domain around a ship. Therefore we believe that computed results by the CFD method shown in this paper are reliable enough for the purpose of observing underlying physics to be seen in the measured results, although detailed convergence study is not performed by ourselves.

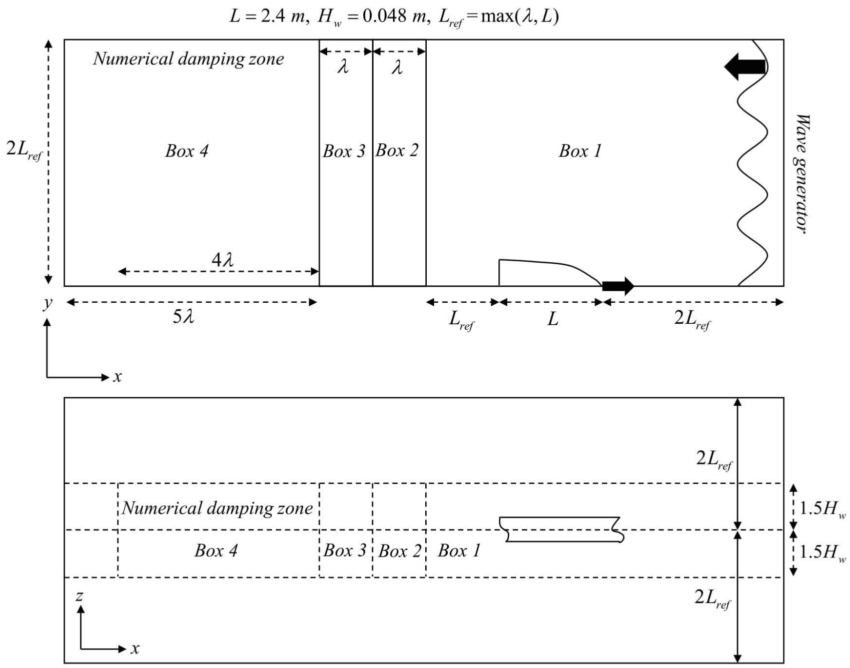

Fig. 7 Calculation domain of CFD computation for RIOS bulk carrier

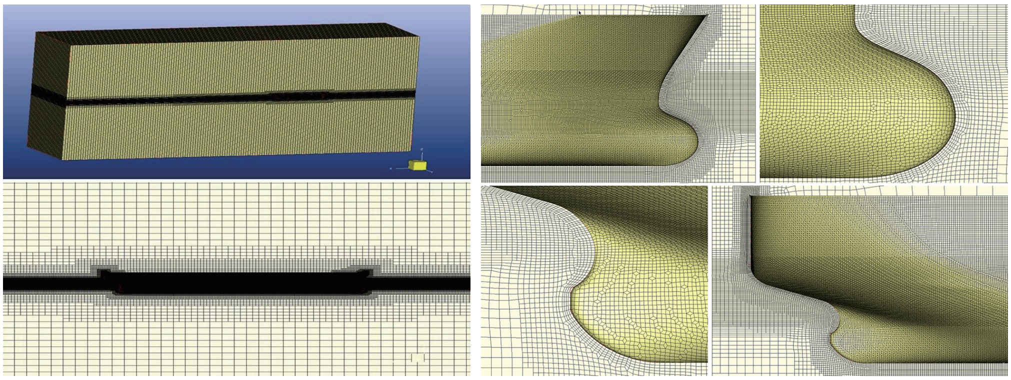

Fig. 8 Computational mesh of CFD for bulk carrier, Left: calculation domain mesh, Right: close-up view of bow and stern part mesh

3.3 Analysis of ship-side wave

In order to synchronize the time histories of unsteady physical quantities measured in the experiment, the origin of time should be taken equal to the time instant when the crest of incident wave arrives at the origin of the coordinate system. In what follows, we consider a general case that the forward speed U of a ship exists; hence the circular frequency of encounter $\omega_e\,(= \omega - KU\cos\chi)$ must be used for harmonic oscillation problems.

Suppose that a regular head wave with amplitude ζ_a and wavenumber $K\,(= \omega^2/g)$ was measured at $x = \ell$ and its first-harmonic component in the Fourier series was obtained in the form

$$\zeta(\ell,t) = \mathrm{Re}\big[\,(\zeta_{\ell c} - i\zeta_{\ell s})\,e^{i\omega_e t}\,\big] = \mathrm{Re}\big[\,(\zeta_{0c} - i\zeta_{0s})\,e^{i(\omega_e t + K\ell)}\,\big] \tag{19}$$

Here the complex amplitude at the origin ($x = 0$) is denoted as $\zeta_{0c} - i\zeta_{0s}$, which can be obtained from Eq. (19) as

$$\zeta_{0c} - i\zeta_{0s} = \big(\zeta_{\ell c} - i\zeta_{\ell s}\big)\,e^{-iK\ell} \equiv \zeta_0 \equiv \zeta_a\,e^{i\varphi} \tag{20}$$

Therefore the amplitude ζ_a and phase φ can be calculated as

$$\zeta_a = \big|\zeta_0\big| = \sqrt{\zeta_{\ell c}^2 + \zeta_{\ell s}^2}\,, \quad \varphi = -K\ell - \tan^{-1}\big(\zeta_{\ell s}/\zeta_{\ell c}\big) \tag{21}$$

Meanwhile, suppose that the ship-side wave at an arbitrary point $\zeta(t)$ was recorded and its Fourier-series expansion is written as

$$\zeta(t) = \zeta^{(0)} + \sum_{n=1}^{N} \mathrm{Re}\Big[\,(\zeta_c^{(n)} - i\zeta_s^{(n)})\,e^{in\omega_e t}\,\Big] \tag{22}$$

In order to synchronize the phase of this time record with the incident wave measured at the origin, the time-dependent part should be divided by the complex amplitude ζ_0 given by Eq. (20). For instance, the first-harmonic component of Eq. (22) can be transformed as

$$\mathrm{Re}\left[\,\frac{\zeta_c^{(1)} - i\zeta_s^{(1)}}{\zeta_0}\,e^{i\omega_e t}\,\right] = \mathrm{Re}\left[\,\frac{\zeta_c^{(1)} - i\zeta_s^{(1)}}{\zeta_a}\,e^{i\omega_e(t-\varphi/\omega_e)}\,\right] \tag{23}$$

Therefore, the time histories of all ship-side waves measured should be shifted in time with $\Delta t = \varphi/\omega_e$.

In the same way for higher-harmonic components in Eq. (22), we can shift the time with $\Delta t = \varphi/\omega_e$ and hence write the ship-side wave record in the form

$$\left.\begin{aligned} \zeta(t) &= \frac{U^2}{2g}\,c_0 + \zeta_a \sum_{n=1}^{N} \mathrm{Re}\big[\,c_n\,e^{in\omega_e t}\,\big] \\ c_0 = 2K_0\zeta^{(0)}, \quad c_n &= \frac{(\zeta_c^{(n)} - i\zeta_s^{(n)})}{\zeta_0^n}\,\big|\zeta_0\big|^{n-1} \end{aligned}\right\} \tag{24}$$

where the steady-wave component has been normalized with $U^2/2g = 1/2K_0$ and the unsteady-wave component normalized with ζ_a. In the present study, we used up to the 5th harmonic component ($N = 5$) and the coefficients c_n ($n = 0 \sim 5$) for each ship-side wave were saved for subsequent use.

The same transformation must be implemented to all harmonic oscillatory quantities such as wave-induced ship motions and hydrodynamic pressures on the ship hull; thereby we can synchronize all the data, even if the measurement had been carried out at different times.

3.4 Analysis of pressure

In the experiment measuring the pressure, the static pressure when the ship does not move in still water was taken as the zero base. Thus the time histories of measured pressure fluctuate around zero. However, the data obtained by pressure sensors affixed around the still waterline must be of rectified pulse-type signals, because the sensor positions repeat coming out and plunging into water.

Typical examples of the pressure time history are shown in Fig. 9, which were obtained from the measurement with FBG sensors at the transverse section of ordinate number 9.5 and at 4 different locations along the girth, i.e. $\theta = 30$, 60, 90, and 93 degs from the lowest figure (where θ is the polar angle with $\theta = 0$ taken at the bottom center and $\theta = 90$ the still waterline). We note here that the hydrostatic pressure is set as the zero base in this measurement of the pressure. We can see that the time histories at $\theta = 90$ and 93 degs show half-rectified pulse-type variation because the location of the pressure sensor is repeatedly coming out of water and plunging into water. However, looking at closely these nonlinear time histories, it can be seen that the pressure is not exactly zero when the sensor is obviously in air (e.g. in the case of $\theta = 93$ deg shown in the uppermost figure). These data must be analyzed and modified if necessary, with the information of ship-side wave.

The procedure for rectifying physically unreasonable time histories of the pressure is as follows. (1) In order to decide the time instant and duration for the analysis, the trigger signal will be searched in the time record. This is because the Fourier analysis for all the measured quantities has been made with the trigger signal used as a reference time instant every time, so that we can use the time record measured at the same location in the towing tank for every measurement. Then the time duration for the analysis was decided to be $\pm T$ (encounter wave period) from the trigger signal. (2) From the incident-wave record, the origin of the time history will be adjusted as explained with regard to Eqs. (23) and (24), and thereby synchronized with the record of the ship-side wave. (3) The time instant when the ship-side wave intersects the position of the pressure sensor in question will be searched, so that the time instant and duration when the sensor is in air can be determined. If the measured value of the pressure is nonzero during that time span, the value at intersecting time will be set equal to zero and at the same time the profile of measured pressure will be shifted to satisfy the physical condition that the pressure is exactly zero when the sensor is in air.

Fig. 9 Examples of the time history of measured pressure in motion-free condition

Once the time history of the pressure has been rectified, the Fourier-series analysis incorporating higher-order terms will be made for the pressure time histories, as will be explained later. For that analysis, however, the constituents of the total pressure should be correctly understood, which can be made as explained in what follows. The total pressure $P(\boldsymbol{x}, t)$ at a certain sensor can be written, with the atmospheric pressure taken as the base, in the form

$$P(\boldsymbol{x}, t) = -\rho g z + p(\boldsymbol{x}, t) \tag{25}$$

The first term on the right-hand side is the hydrostatic pressure, and the second term is the steady and unsteady hydrodynamic pressures to be measured in the experiment.

When the amplitude of ship motions is small, the relationship between the inertial coordinate system $\boldsymbol{x}$ moving at constant speed of a ship (which is called the space-fixed coordinate system) and the body-fixed coordinate system $\overline{\boldsymbol{x}}$ is given as

$$\boldsymbol{x} = \overline{\boldsymbol{x}} + \boldsymbol{\alpha}_{Ts} + \boldsymbol{\alpha}_T(t) + \big[\, \boldsymbol{\alpha}_{Rs} + \boldsymbol{\alpha}_R(t) \big] \times \overline{\boldsymbol{x}} \tag{26}$$

$$\left.\begin{array}{c} \boldsymbol{\alpha}_{Ts} = (0, 0, \xi_{3s}), \;\; \boldsymbol{\alpha}_{Rs} = (0, \xi_{5s}, 0) \\ \boldsymbol{\alpha}_T(t) = (\xi_1(t), 0, \xi_3(t)), \;\; \boldsymbol{\alpha}_R(t) = (0, \xi_5(t), 0) \end{array}\right\} \tag{27}$$

where $\boldsymbol{\alpha}_T$ and $\boldsymbol{\alpha}_R$ denote the translational and rotational motion vectors, respectively, and these are given in head waves as shown above. Suffix s implies the steady components.

Substituting the z-component of Eq. (26) into Eq. (25), it follows that

$$P(\boldsymbol{x}, t) = -\rho g \overline{z} - \rho g \big(\xi_{3s} - \overline{x} \xi_{5s} \big) - \rho g \big\{ \xi_3(t) - \overline{x} \xi_5(t) \big\} + p(\boldsymbol{x}, t) \tag{28}$$

Since the value of $-\rho g \overline{z}$ is taken as the zero base in the actual measurement, the pressure on the right-hand side of Eq. (28) except for $-\rho g \overline{z}$ is the measured pressure at sensor positions on the ship hull; let this measured pressure be denoted as $p_M(\overline{\boldsymbol{x}}, t)$. Then the total pressure can be retrieved from the following relation:

$$p_T(\overline{\boldsymbol{x}}, t) = \left\{ \begin{array}{ll} p_M(\overline{\boldsymbol{x}}, t) & \text{for } \overline{z} > 0 \\ p_M(\overline{\boldsymbol{x}}, t) - \rho g \overline{z} & \text{for } \overline{z} < 0 \end{array} \right. \tag{29}$$

The total pressure thus obtained was expanded with the Fourier series as follows:

$$\begin{aligned} p_T(\overline{\boldsymbol{x}}, t) &= p^{(0)}(\overline{\boldsymbol{x}}) + \sum_{n=1}^{N} \mathrm{Re}\Big[\big\{ p_c^{(n)}(\overline{\boldsymbol{x}}) - i p_s^{(n)}(\overline{\boldsymbol{x}}) \big\} \, e^{in\omega_e t} \Big] \\ &\equiv p^{(0)}(\overline{\boldsymbol{x}}) + p_u(\overline{\boldsymbol{x}}, t) \end{aligned} \tag{30}$$

where $p_u(\overline{\boldsymbol{x}}, t)$ is meant to denote only the time-variant term, and it is found that $N = 10$ is sufficient to represent even highly nonlinear rectified pulse-type signals. This time-variant unsteady pressure $p_u(\overline{\boldsymbol{x}}, t)$ will be used to compute the wave loads in the next section.

However, we note that the unsteady pressure obtained above is just the value only at the location of the pressure sensor. In order to compute the unsteady pressure at any point on the ship-hull surface (which will be needed in the pressure integration), we will have to use a spline interpolation in terms of the values at sensor positions. The interpolation has been done firstly along the girth (θ direction) at each transverse section where the measurement was made. Then in terms of the values along the girth, the secondary interpolation was made in the longitudinal direction. Convergence of the results was confirmed by computing integrated forces with increasing the number of panels on the ship hull.

4. Vertical Bending Moment

The wave loads normally refer to the shear force and bending moment, but in this paper, attention is focused on the vertical bending moment (VBM hereafter). There are two components in VBM owing to the integration of unsteady pressure and the inertia force [53]. These are time-variant and basically nonlinear, thus the VBM acting on the transverse section at $x = x_0$ in the ship's longitudinal direction may be computed from

$$\begin{aligned} M_v(x_0, t) = &\int_{x_A}^{x_0} dx \int_{C_H(x)} p_u(\overline{\boldsymbol{x}}, t)\, n_5(\boldsymbol{x}, t)\, d\ell \\ &- \int_{x_A}^{x_0} \frac{w(x)}{g} \big(x - \ell_x - x_0\big) \Big\{ \ddot{\xi}_3(t) - \big(x - \ell_x\big) \ddot{\xi}_5(t) \Big\}\, dx \end{aligned} \tag{31}$$

where
$$n_5(\boldsymbol{x}, t) = \big(z - \ell_z\big) n_1(\boldsymbol{x}, t) - \big(x - \ell_x - x_0\big) n_3(\boldsymbol{x}, t) \tag{32}$$

is the extended normal vector for computing the VBM at $x = x_0$, and the hogging moment is defined to be positive in Eq. (31). The origin of the coordinates in Eq. (31) is shifted to the center of gravity, denoted as $(\ell_x, 0, \ell_z)$. The x- and z-components of the normal vector, $n_1(\boldsymbol{x}, t)$ and $n_3(\boldsymbol{x}, t)$, are expressed in the space-fixed coordinate system, which are changing in time due to wave-induced ship motions, although the corresponding terms in the body-fixed coordinate system, denotes as $\tilde{n}_1(\overline{\boldsymbol{x}})$ and $\tilde{n}_3(\overline{\boldsymbol{x}})$, are time-invariant. The relationship between these terms is given as follows:

$$\left\{ \begin{array}{c} n_1(\boldsymbol{x}, t) \\ n_3(\boldsymbol{x}, t) \end{array} \right\} = \left[\begin{array}{cc} \cos\xi_5(t) & \sin\xi_5(t) \\ -\sin\xi_5(t) & \cos\xi_5(t) \end{array} \right] \left\{ \begin{array}{c} \tilde{n}_1(\overline{\boldsymbol{x}}) \\ \tilde{n}_3(\overline{\boldsymbol{x}}) \end{array} \right\} \tag{33}$$

where $\xi_5(t)$ is the wave-induced pitch motion of a ship. The lower limit x_A in the integral with respect to x in Eq. (31) is the longitudinal position of aft end of a ship and $C_H(x)$ the contour of transverse section at station x.

We note that the wetted surface of ship hull can be computed with a spline interpolation from the information of ship-side wave given by Eq. (24) and the unsteady pressure $p_u(\overline{\boldsymbol{x}}, t)$ from Eq. (30) at each time step; both of these are given in the body-fixed coordinate system. Furthermore, as shown by Eq. (33), the normal-vector components in the space-fixed coordinate system can be computed from the information of body-fixed coordinates. In the present case, the unsteady pressure $p_u(\overline{\boldsymbol{x}}, t)$ includes nonlinear components as indicated by Eq. (30), but in the linear problem consisting of only the first-harmonic components, the unsteady pressure may be given as a linear superposition of the diffraction pressure p_D, the radiation pressure p_R, and the variation of hydrostatic pressure p_S; which is the case in the linear potential-flow theory like RPM.

The second line in Eq. (31) indicates the inertia-force term, where $\ddot{\xi}_3(t)$ and $\ddot{\xi}_5(t)$ are the acceleration in heave and pitch, respectively, and $w(x)$ is the weight-distribution function related to the ship's mass m and the gyrational radius in pitch κ_{yy} as follows:

$$\left. \begin{array}{l} \displaystyle\int_{x_A}^{x_F} \frac{w(x)}{g}\, dx = m, \quad \int_{x_A}^{x_F} \frac{w(x)}{g} x\, dx = m\ell_x \\ \displaystyle\int_{x_A}^{x_F} \frac{w(x)}{g} (x - \ell_x)^2 dx = m\kappa_{yy}^2 \end{array} \right\} \tag{34}$$

where x_F in the upper limit of integration range denotes the fore end of a ship.

In calculating the VBM according to Eq. (31), the integrated result up to $x_0 = x_F$ must be consistent to the equations of coupled motion equations in surge, heave, and pitch. Namely the integrated value of Eq. (31) up to $x_0 = x_F$ must be equal to zero. In order to ensure this condition of zero VBM at the fore end of a ship and the correct computation of VBM in the time domain, the origin in time histories (i.e. the phase with respect to an incident wave) of all harmonic oscillatory quantities, particularly both unsteady pressure and ship motions, must be synchronized as explained in Section 3.3.

Normally the weight distribution should be provided as an input data in actual problems. However, in the present study, since the weight distribution was not measured and unknown, the VBM due to the inertia force is computed under the assumption of uniform structural density; that is, the weight distribution is assumed equal to the distribution of volume displacement, which may be computed from the state of equilibrium in the zero-speed static condition or in the steady translation of a ship including the steady hydrodynamic-pressure force.

5. Results and Discussion

This section is divided into four subsections. Each of which shows different aspects of our findings. Section 5.1 will outline the reliability of measured unsteady pressure distribution and its comparison with computed results by RPM and CFD methods. Then the VBM evaluated from the unsteady pressure distribution at zero speed (Section 5.2) and forward speed (Section 5.3) are discussed. Lastly, in Section 5.4 a comparison is made with the benchmark data for the VBM measured directly at a specified transverse section by a segmented ship of a 6750-TEU container ship.

5.1 Validation of unsteady pressure distribution

Comparison of the spatial distribution of first-harmonic pressure has been done by Iwashita *et al.* [37, 39, 41, 42] and Kashiwagi *et al.* [38, 40] along the girth at some transverse sections between the results measured in the motion-free case in head waves and computed with some

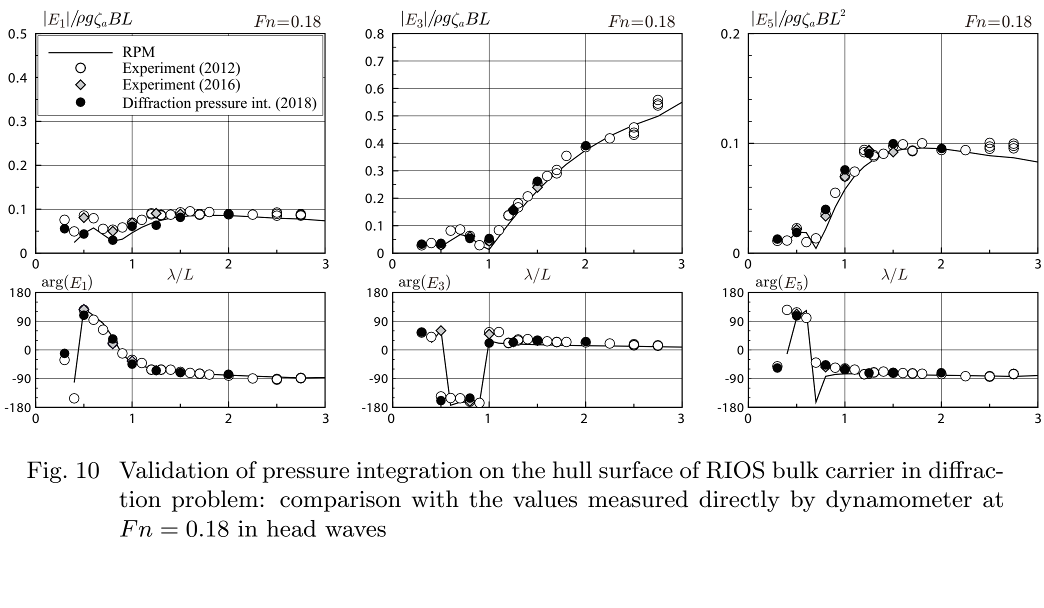

Fig. 10 Validation of pressure integration on the hull surface of RIOS bulk carrier in diffraction problem: comparison with the values measured directly by dynamometer at $Fn = 0.18$ in head waves

Table 4 Relative errors in the comparison between the values of direct measurement by dynamometer $\overline{Exp}$ and diffraction pressure integration DPI

λ/L	$\lvert E_1\rvert/\rho g\zeta_a BL$			$\lvert E_3\rvert/\rho g\zeta_a BL$			$\lvert E_5\rvert/\rho g\zeta_a BL^2$		
	$\overline{Exp}$	DPI	$E(\%)$	$\overline{Exp}$	DPI	$E(\%)$	$\overline{Exp}$	DPI	$E(\%)$
0.8	0.051	0.030	−41.18	0.064	0.054	−15.63	0.034	0.040	17.65
1.0	0.069	0.061	−11.59	0.044	0.054	22.73	0.070	0.076	11.43
1.25	0.090	0.064	−28.49	0.160	0.156	−2.50	0.093	0.091	−2.15
1.5	0.091	0.082	−9.89	0.247	0.262	6.07	0.095	0.100	5.26
2.0	0.087	0.091	4.60	0.381	0.392	3.02	0.095	0.095	0.53

methods based on the linear potential-flow theory in the frequency domain, through which repeatability and reliability of the experimental data has been confirmed.

As another validation of measured results, we have computed the first-harmonic wave-exciting forces from the integration of unsteady pressure distribution measured for the diffraction problem and compared the result with the corresponding forces measured directly with dynamometer. The results are shown in Fig. 10, where the values obtained by the integration of measured unsteady diffraction pressure are indicated with black circle symbol and the values directly measured with dynamometer are indicated with white circle and gray diamond symbols (which are the results in the experiments conducted in 2012 and 2016, respectively). Computed results by the RPM of the forward-speed version are provided with solid line for comparison. Overall, good agreement can be observed in figures. In order to quantify the errors, Table 4 presents the relative errors between the results by the direct measurement and pressure integration at the range of wavelength $0.8 < \lambda/L < 2.0$. In this table, the values of direct measurement denoted as $\overline{Exp}$ are the average of the experiments in 2012 and 2016 and the results of diffraction pressure integration are indicated as DPI. The relative error is computed from $(DPI - \overline{Exp})/\overline{Exp}$. We note that the wave-exciting forces at shorter wavelengths are relatively small and slight discrepancy between the two small values provides a large value in the error percentage. For instance, at $\lambda/L = 1.0$ the largest relative error occurs in the heave exciting force with 22.73 % error, but the value itself is very small and thus this difference is not conspicuous in the figure. Looking at Table 4 with this fact kept in mind, we can see fairly good agreement for the heave force and pitch moment at all wavelengths, which indicates reliability of the unsteady pressure measured with FBG pressure sensors. We note however that there exist slight discrepancies in the surge exciting force at some shorter wavelengths, typically prominent underestimation with 41.18% error at $\lambda/L = 0.8$. This order of error is visible even in the figure. A possible reason of this difference may be attributed to the scarcity of FBG pressure sensors in the bow upper region above the still waterline, because the pressure on that region contributes to the surge force. On the other hand, the dominant pressures for the heave and pitch forces act on the bottom of a ship because of the direction of normal vector and the pressures near or above still waterline contribute little especially for a wall-sided ship.

As another demonstration of the results, a side view of the spatial distribution of unsteady pressure is shown in Fig. 11 for the case of $\lambda/L = 1.0$ in head wave and $Fn = 0.0$, where the pressure is shown in the nondimensional form of $p/\rho g\zeta_a$ and $\zeta_a = 0.0106$ m in accordance with the experiment in this particular example. Note that the color scale in the contour display is taken from −2.0 to +2.0, and that the phase of variation θ is taken such that $\theta = 0$

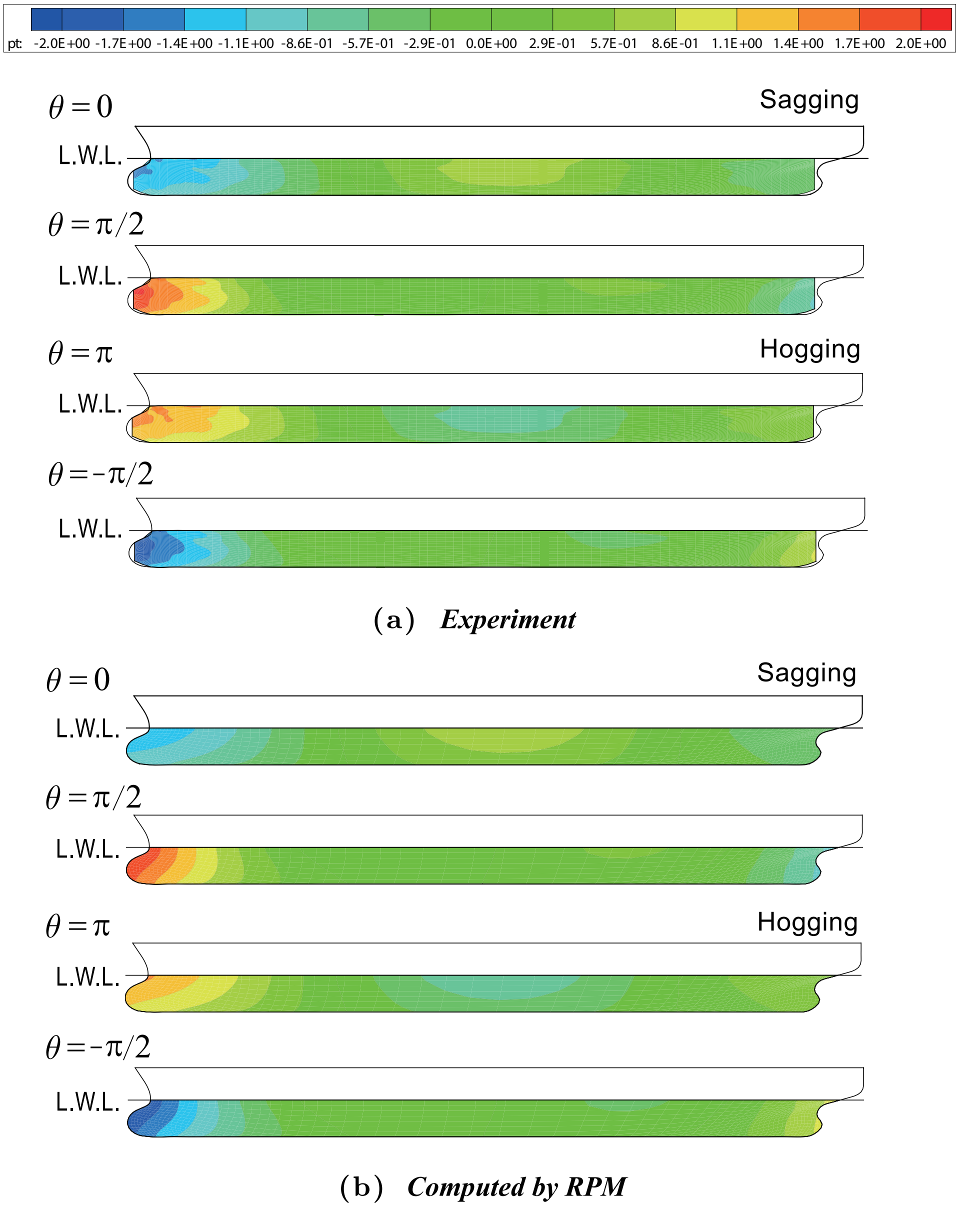

Fig. 11 Unsteady pressure distribution at $\lambda/L = 1.0$ and $Fn = 0.0$ in head wave; (a) Experiment, (b) Computation by RPM. Values are shown with $p/\rho g \zeta_a$ and $\zeta_a = 0.0106$ m

corresponds to the time instant of maximum sagging moment. Overall, favorable agreement can be seen between experimental data and computed results by the linear RPM explained in Section 3.1, although we can see slight discrepancy in the magnitude at the bow region particularly at time instants of $\theta = 0$ and $\theta = \pi$. Namely the phase in the pressure variation looks a little different between the experiment and the computation by RPM in this paper, but it is confirmed by Iwashita *et al.* [42] using the free-surface Green-function method that

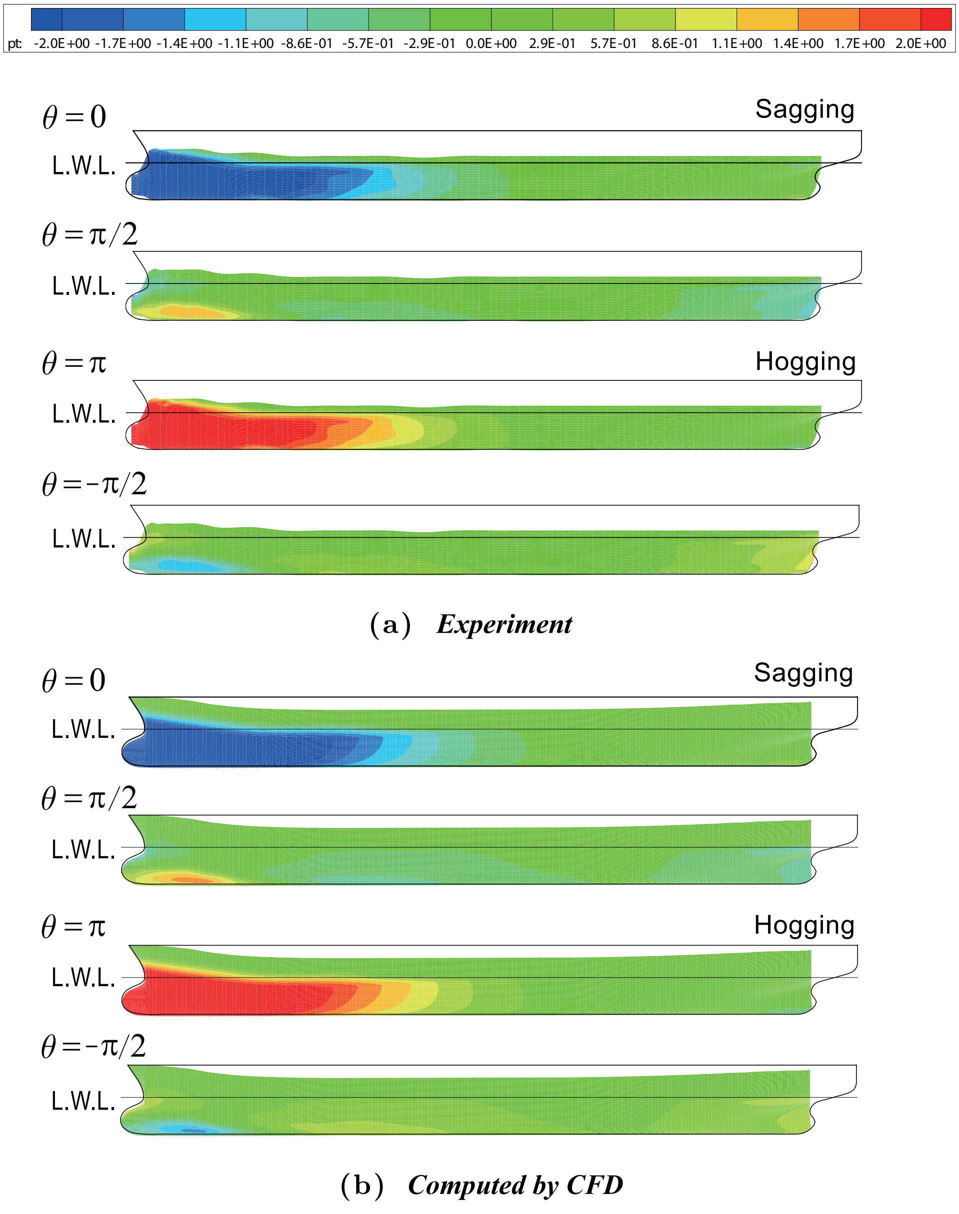

Fig. 12 Unsteady pressure distribution at $\lambda/L = 1.25$ and $Fn = 0.18$ in head wave; (a) Experiment, (b) Computation by CFD. Values are shown with $p/\rho g\zeta_a$ and $\zeta_a = 0.0240$ m

the amplitude of the first harmonic component in the unsteady pressure at $Fn = 0.0$ agrees well along the girth at each of the transverse sections where the measurement was conducted.

Likewise, a side view of the unsteady pressure distribution at $\lambda/L = 1.25$ in head wave and $Fn = 0.18$ is shown in Fig. 12 in the nondimensional form of $p/\rho g\zeta_a$ with $\zeta_a = 0.0240$ m, where a comparison is made between experiment and nonlinear computation by CFD using FINE/Marine. It should be noted that the maximum nondimensional value of unsteady pressure becomes a little larger than 4.0 near the bow and free surface in this particular case, but the color scale in the contour display is kept the same as that in Fig. 11 to see the relative magnitude and to show overall good agreement even for the forward-speed case. We also note that $\lambda/L = 1.25$ is close to the resonant frequency in ship motions at $Fn = 0.18$ (as will be shown later) and the degree of agreement for this unsteady pressure distribution was not so good when compared to computed results by the forward-speed version of RPM [42], which may be due to large ship motions and hence strong nonlinear effects.

5.2 Vertical bending moment at zero speed

We start with an easier case, i.e. at zero forward speed ($Fn = 0.0$) in head waves. Since the wave steepness H/λ (the ratio of wave height H with wavelength λ) in the experiment was set

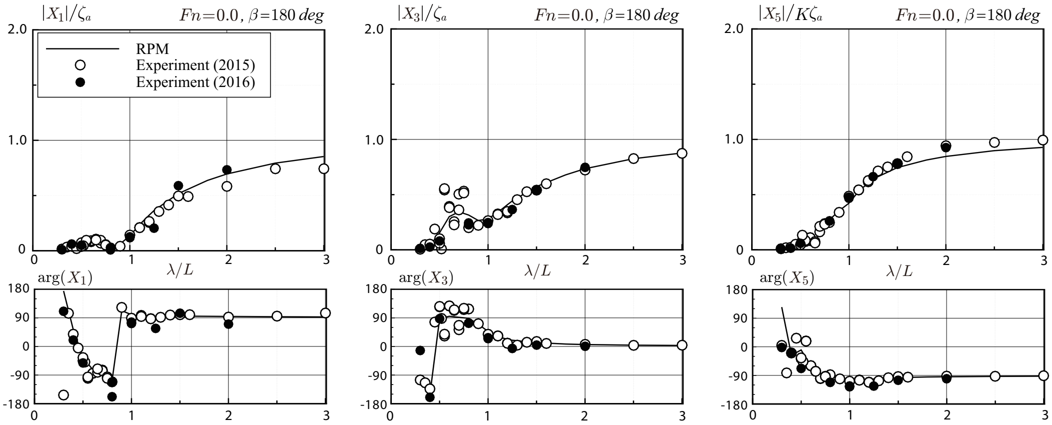

Fig. 13 Surge, heave, and pitch RAOs of RIOS bulk carrier at $Fn = 0.0$ in head waves

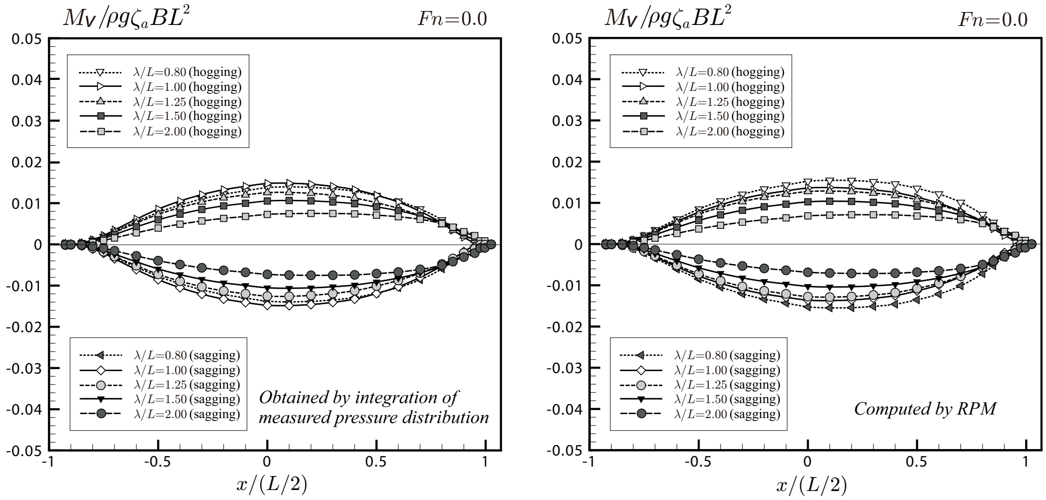

Fig. 14 Longitudinal distribution of vertical bending moment (VBM) on RIOS bulk carrier at $Fn = 0.0$ in head waves. Left: integration of measured pressure distribution, Right: computed by RPM

to about 1/50, measured phenomena must be in the framework of linear theory. Therefore the linear potential theory, typically RPM, can be used for the numerical computation. For computing the VBM from Eq. (31), the motion RAOs are necessary, the results of which are presented in Fig. 13 for surge, heave, and pitch motions, and good agreement can be seen between measured and computed results (the results shown with white and black circle symbols were obtained by the experiments conducted in 2015 and 2016, respectively). We have already confirmed in Fig. 11 that the unsteady pressure distribution at $Fn = 0.0$ was also in good agreement between measured and computed results. Thus we can expect good agreement in the VBM as well. In fact, the VBM was evaluated from Eq. (31) using only the measured data and also only the computed values by RPM. A comparison of the longitudinal distribution of VBM thus evaluated is shown in Fig. 14 at wavelengths of $\lambda/L = 0.8$, 1.0, 1.25, 1.5, and 2.0 for the maximum values in the hogging (plus) and sagging (minus) moments. As expected, very good agreement can be confirmed for the sectional values of VBM between the values evaluated with experimental data and computed with RPM; which proves that the unsteady pressure distribution on the ship-hull surface has been successfully measured and the procedure for the data analysis and evaluation of VBM is consistent.

5.3 Vertical bending moment at forward speed

Next comparison is for the case of forward speed of $Fn = 0.18$, in which nonlinearity in the VBM must be observed especially when the ship motions are resonant around $\lambda/L = 1.25$; that is, as pointed out by some scholars [13–16], the magnitude in the sagging moment may be larger than that in the hogging moment, although the wave steepness is the same as that at $Fn = 0.0$. To see visually the degree of nonlinearity at $\lambda/L = 1.25$, two snapshots for the wave profile at sagging and hogging conditions in the experiment are shown in Fig. 15. Since the degree of nonlinearity looks conspicuous from these snapshots, numerical computations at $Fn = 0.18$ were implemented using CFD software, FINE/Marine V 8.2.

As a preliminary check for computing the VBM, the motion RAOs are computed by CFD and compared with measured values (the experiments plotted with white and black circles were conducted in September 2017 and 2018, respectively). In CFD computations, the amplitude of ship motion was taken equal to half of the peak-to-peak mean value in the computed time histories. Obtained results are shown in Fig. 16 at 6 wavelengths in the range of $\lambda/L = 0.5 \sim 2.0$ for comparison. However, CFD results under $\lambda/L = 0.5$ are not presented because of large computation time due to necessity of increasing the number of meshes and time steps for obtaining converged results in short wave simulation. It should be noticed that the surge is fixed in the CFD computation whereas it was free in the experiment. The pitch

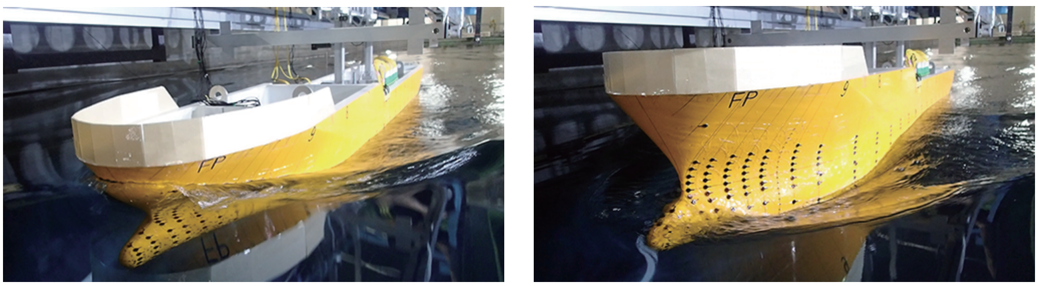

Fig. 15 Snap shots of wave profile at $\lambda/L = 1.25$ of head wave and $Fn = 0.18$. Left: sagging, Right: hogging

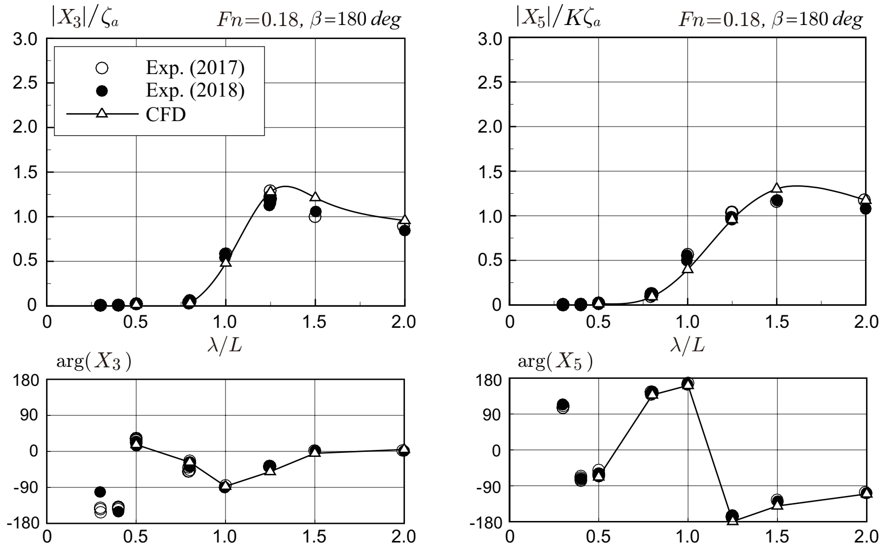

Fig. 16 Heave and pitch RAOs of RIOS bulk carrier at $Fn = 0.18$ in head waves

is naturally coupled with surge even for a longitudinally symmetric body at zero speed. Thus there must be a difference in the physical situation between computation and experiment in the present comparison; which may affect particularly the pitch-motion results, although at forward speed the heave would also be affected by surge through the coupling among surge, heave, and pitch motions.

Table 5 shows the values in digits and the relative standard deviation (SD) representing the uncertainty of the experiment conducted in 2017 and 2018. The repeatability can be seen with relatively small deviation particularly in heave at $\lambda/L = 1.25$ and in pitch at $\lambda/L = 1.5$ with 0.18% and 0.73%, respectively. It is noted that the heave motion becomes resonant around $\lambda/L = 1.25$ at $Fn = 0.18$. Comparing the CFD results with the average value of the experiment, a good agreement can be seen at heave-resonant $\lambda/L = 1.25$ only with 7.80% overestimation and 4.01% underestimation for heave and pitch, respectively, although the surge is fixed in the CFD computations. We can conclude from these comparisons that overall computed results by CFD are in good agreement with measured values, despite slight discrepancies at some other wavelengths.

Table 5 Results and relative errors of heave and pitch motions between CFD and experiment

λ/L	$\lvert X_3\rvert/\zeta_a$					$\lvert X_5\rvert/K\zeta_a$				
	Ex2017	Ex2018	SD(%)	CFD	E(%)	Ex2017	Ex2018	SD(%)	CFD	E(%)
0.5	0.023	0.019	13.47	0.015	−28.57	0.018	0.018	0.00	0.014	−22.22
0.8	0.039	0.040	1.79	0.032	−18.99	0.097	0.097	0.00	0.093	−4.12
1.0	0.586	0.503	10.78	0.480	−11.85	0.565	0.501	8.49	0.398	−25.33
1.25	1.187	1.184	0.18	1.278	7.80	1.036	0.960	5.38	0.958	−4.01
1.5	1.001	1.059	3.98	1.213	17.77	1.162	1.174	0.73	1.300	11.30
2.0	0.897	0.845	4.22	0.957	9.87	1.176	1.080	6.02	1.174	4.08

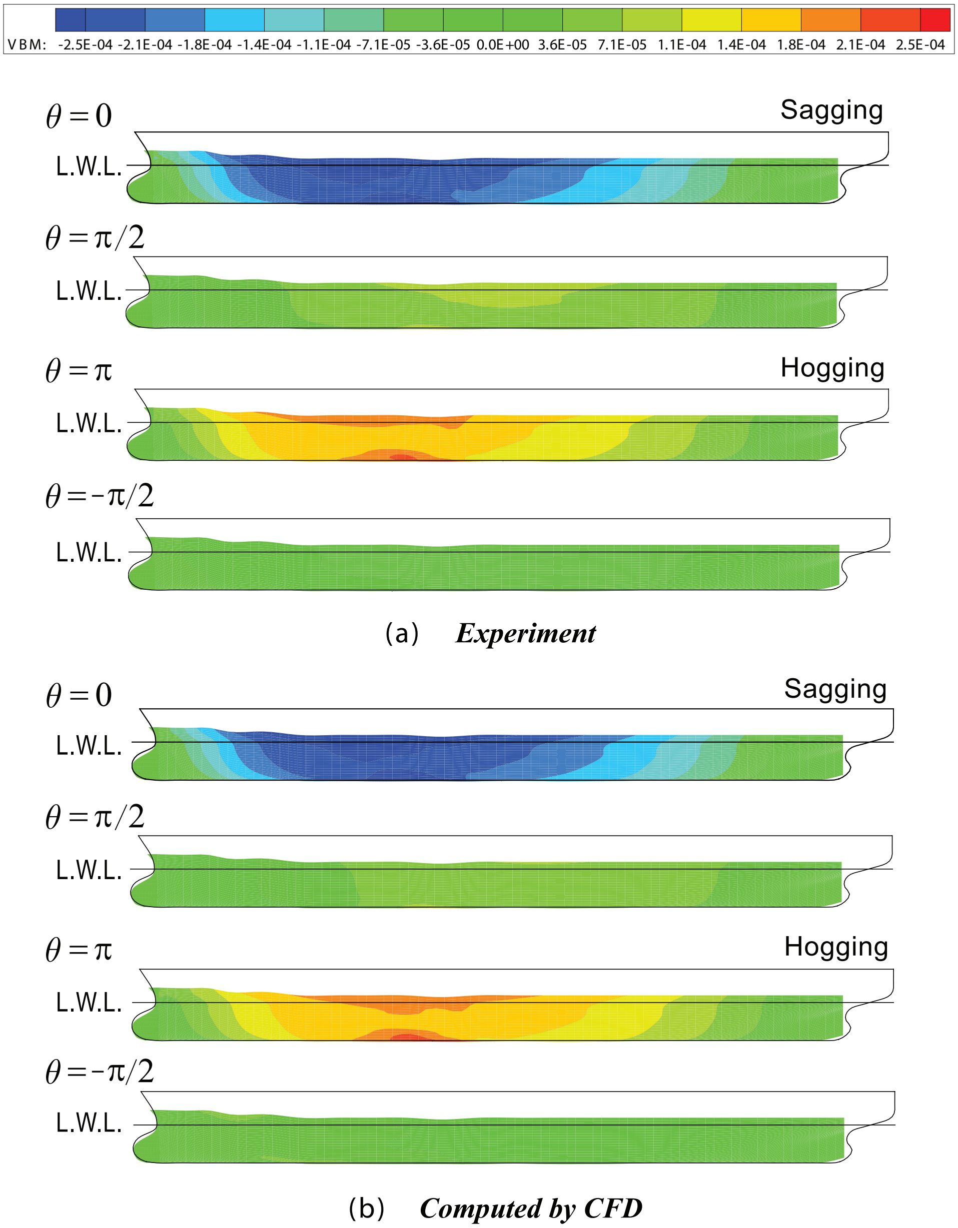

Fig. 17 VBM distribution at $\lambda/L = 1.25$ of head wave and $Fn = 0.18$; (a) Experiment, (b) Computation by CFD

The spatial distribution of unsteady pressure at $\lambda/L = 1.25$ and $Fn = 0.18$ was already compared in Fig. 11, as a validation of the measured results. Even in this motion-resonant nonlinear condition, we could see favorable agreement in the pressure distribution on almost the whole ship-hull surface.

As is obvious from Eq. (31), once the value of $n_5(\boldsymbol{x}, t)$ defined by Eq. (32) is multiplied by the pressure distribution, we can obtain the integrand function for the first term of VBM to

Table 6 Results and relative errors of VBM between CFD and experiment around motion-resonant wavelengths.

λ/L	$x/(L/2)$	$M_V/\rho g\zeta_a BL^2$ (Hogging)			$M_V/\rho g\zeta_a BL^2$ (Sagging)		
		Exp	CFD	$E(\%)$	Exp	CFD	$E(\%)$
1.0	−0.2	0.014	0.016	14.3	−0.016	−0.019	18.8
	0.1	0.015	0.018	20.0	−0.019	−0.022	15.8
	0.4	0.012	0.015	25.0	−0.019	−0.022	15.8
	0.7	0.006	0.007	16.7	−0.016	−0.017	6.3
1.25	−0.2	0.020	0.022	10.0	−0.023	−0.024	4.3
	0.1	0.023	0.025	8.7	−0.027	−0.029	7.4
	0.4	0.022	0.024	9.1	−0.028	−0.030	7.1
	0.7	0.016	0.018	12.5	−0.023	−0.024	4.3
1.5	−0.2	0.014	0.016	14.3	−0.016	−0.018	12.5
	0.1	0.016	0.018	12.5	−0.019	−0.021	10.5
	0.4	0.015	0.017	13.3	−0.020	−0.022	10.0
	0.7	0.010	0.012	20.0	−0.016	−0.018	12.5

be computed by the pressure integration. For the second inertia term of VBM in Eq. (31), the weight distribution is initially treated as the Bonjean volume distribution along the girth at each transverse section. Then, once the sum of these two terms is integrated with respect to x up to a desired position $x = x_0$, we can provide the spatial distribution of VBM, which is depicted in Fig. 17 for the case of $\lambda/L = 1.25$ and $Fn = 0.18$ in a nondimensional form divided by $\rho g\zeta_a L^2$. Overall, good agreement can be seen also in this VBM distribution. It should be pointed out that the maximum values in both sagging and hogging moments

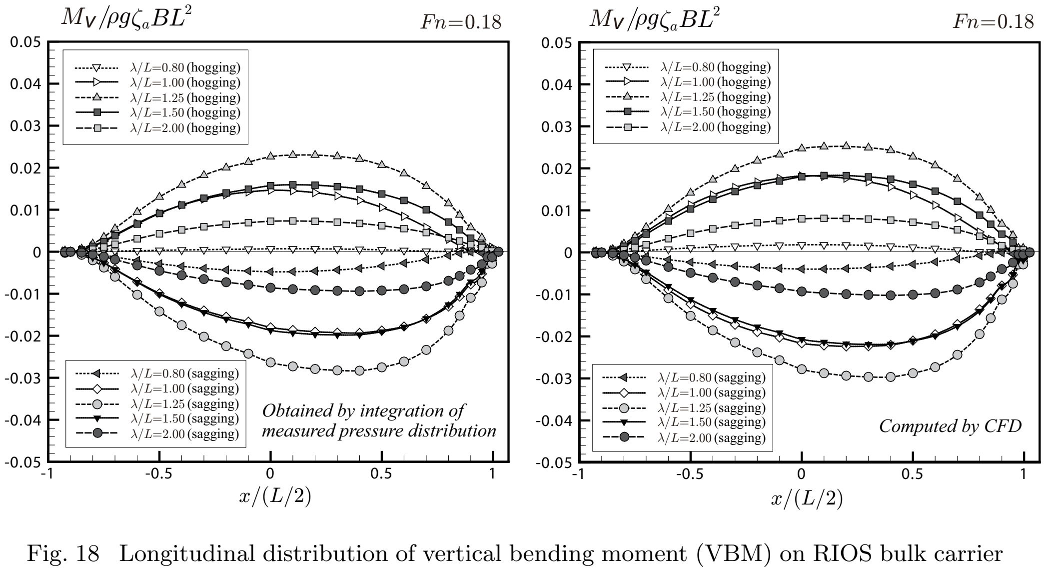

Fig. 18 Longitudinal distribution of vertical bending moment (VBM) on RIOS bulk carrier at $Fn = 0.18$ in head waves. Left: integration of measured pressure distribution, Right: computed by CFD

occur at a slightly forward position from the midship.

According to Eq. (31), by integrating this kind of distribution of VBM along the girth direction at each transverse section in the ship's longitudinal direction, we can obtain the longitudinal distribution of VBM, as already done and shown in Fig. 14 for the zero-speed case. For the forward-speed case of $Fn = 0.18$, obtained results are shown in Fig. 18 for several wavelengths ($\lambda/L = 0.8 \sim 2.0$) of head waves. Computations are performed only with experimental data of the pressure distribution and ship motion and in the same way only with CFD. It should be noted that Fig. 18 are plotted for the maximum value in the hogging moment and the minimum value in the sagging moment in the time histories of the VBM generated according to Eq. (31). We also note that, in the forward-speed case, the steady hydrodynamic pressure due to forward translation of a ship is incorporated in the VBM computation in terms of satisfying the steady-state equilibrium condition.

From the comparison in Fig. 18, we can see very good overall agreement between the experiment and CFD computation, although the CFD computation tends to overestimate slightly for some wavelengths. For instance, at motion-resonant wavelength $\lambda/L = 1.25$, from a comparison between left and right figures in Fig. 18 we can observe overprediction in the magnitude of hogging moment and also slightly in the sagging moment. Looking at relative magnitude between $\lambda/L = 1.0$ and 1.5, we can see a slight difference in the rear half of a ship. Nevertheless, the agreement in the overall variation tendency is very good, confirming the validity of experimental and CFD results. Table 6 shows the values in digits and relative errors of VBM at several sections of $x/(L/2) = -0.2, 0.1, 0.4, 0.7$; which indicate relatively small difference even at around motion-resonant wavelengths, with maximum error 25%. More importantly, the asymmetric property in the VBM can be clearly observed by both experiment and CFD, with larger sagging moment for all wavelengths (although the degree of asymmetry is different depending on the wavelength), and the position where the cross-sectional VBM becomes maximal is shifted a little forward from the corresponding position observed at $Fn = 0.0$ (Fig. 14); which is anticipated also from Fig. 17 and must be understood as an important forward-speed effect. In fact, as shown in Fig. 11 for $Fn = 0.18$, the magnitude of unsteady pressure becomes very large in the bow region (particularly at resonant wavelength $\lambda/L = 1.25$) due to existence of the forward speed of a ship, and consequently the VBM tends to take maximal values at a position forward from the midship.

5.4 Validation of VBM with benchmark test data

The VBM has been computed in this study by integrating the unsteady pressure distribution obtained by the experiment or computation over the ship hull and the results were compared, but this kind of comparison is essentially the same as the comparison of the spatial distribution of unsteady pressure. Thus, if possible, a comparison should be made for the VBM measured directly at a specified transverse section by a segmented ship model for a wide range of wavelength.

For that purpose, the analysis method in this paper was further validated through comparison with the benchmark data of a 6750-TEU container ship whose principal particulars are shown in Table 7. This benchmark test was conducted to assess the performance of seakeeping analysis codes and the results were disclosed at the ITTC-ISSC joint workshop in 2014. The experimental results were provided by KRISO and summarized by Kim *et al.* [43].

Since the tested container ship model was constructed using a flexible backbone and segmented hulls, hydroelastic responses may be prominent in waves especially for the forward-speed case. Thus for a comparison with the present method, the zero-speed test condition

Table 7 Principal particulars of 6750-TEU container ship used for bench-mark test, Kim *et al.* [43]

Item	Prototype	Model
Scale	1/1	1/70
L_{OA} (m)	300.891	4.298
L_{BP} (m)	286.6	4.094
B (m)	40.0	0.571
d (m)	11.98	0.171
C_b	0.624	0.624
KM (m)	18.662	0.267
GM (m)	2.100	0.030
KG (m)	16.562	0.237
L_{CG} from AP (m)	138.395	1.977
κ_{xx} (m)	14.4	0.206
$\kappa_{yy}(=\kappa_{zz})$ (m)	70.144	1.002
Natural period of roll (sec)	20.5	2.450
Neutral axis from keel (m)	7.35	0.105

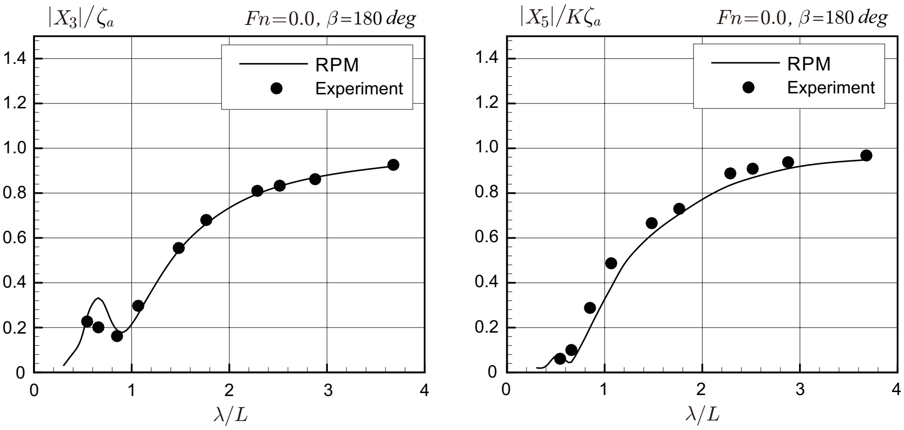

Fig. 19 Comparison of heave and pitch RAOs of 6750-TEU container ship, at $Fn = 0.0$ and $H/\lambda < 1/100$ in head waves (experiment data by Kim *et al.* [43])

is chosen, which may satisfy the quasi-static assumption and the results are mostly linear. The tested ship model consists of eight segmented hulls. The mass at each segmented hull approaches a uniform distribution and thus the total mass distribution is assumed equal to the distribution of volume displacement. Sectional forces were measured at seven sections by strain gauges installed on the backbone. Since the results are expected to be linear, comparison with the benchmark test data is made with the computation by RPM.

First, the RAOs of heave and pitch motions are presented in Fig. 19. Then the resulting VBM is shown in Fig. 20, where the RAO of VBM at Section 4 is compared on the left-hand side, whilst the longitudinal distribution of VBM is shown on the right-hand side for wave-lengths of $\lambda/L = 0.6$, 1.07 and 1.48. The values in digits and relative errors of the Fig. 19 and the left-hand side of the Fig. 20 are presented in Table 8. The amplitude of heave and

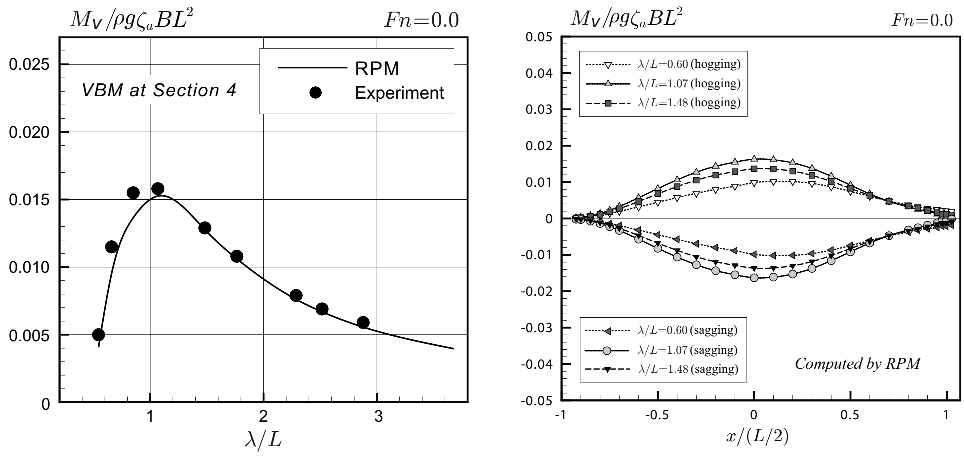

Fig. 20 Validation of vertical bending moment (VBM) on 6750-TEU container ship, Left: comparison of VBM at Section 4, Right: longitudinal distribution of VBM computed by RPM (experiment data by Kim *et al.* [43])

Table 8 Results and relative errors of heave, pitch, and VBM at Section 4 of 6750-TEU container ship, Kim *et al.* [43].

Case	λ/L	$\lvert X_3\rvert/\zeta_a$			$\lvert X_5\rvert/\zeta_a$			$\lvert M_V\rvert/\rho g\zeta_a BL^2$		
		Exp	RPM	$E(\%)$	Exp	RPM	$E(\%)$	Exp	RPM	$E(\%)$
1	0.54	0.227	0.249	9.7	0.061	0.073	19.7	0.0050	0.0040	−20.0
2	0.67	0.201	0.332	65.2	0.100	0.046	−54.0	0.0115	0.0100	−13.0
3	0.85	0.162	0.189	16.7	0.288	0.199	−30.9	0.0155	0.0136	−12.3
4	1.07	0.297	0.260	−12.5	0.487	0.380	−22.0	0.0158	0.0153	−3.2
5	1.48	0.555	0.544	−2.0	0.666	0.615	−7.7	0.0129	0.0128	−0.8
6	1.76	0.680	0.663	−2.5	0.730	0.706	−3.3	0.0108	0.0106	−1.9
7	2.28	0.810	0.796	−1.7	0.888	0.836	−5.9	0.0079	0.0076	−3.8
8	2.52	0.833	0.831	−0.2	0.909	0.869	−4.4	0.0069	0.0067	−2.9
9	2.88	0.862	0.870	0.9	0.938	0.909	−3.1	0.0059	0.0056	−5.1
10	3.68	0.926	0.920	−0.6	0.968	0.948	−2.1	–	0.0040	–

pitch represents favorable agreement at wavelengths larger than $\lambda/L = 1.07$ despite slight underestimation in pitch. Looking at the amplitude of VBM explained at Section 4, it is noted that the maximum value of VBM is observed at $\lambda/L = 1.07$ but this maximum value is slightly underestimated with 3.2% by RPM; which may be attributed to a slight underestimation of heave and pitch motions as indicated at $\lambda/L = 1.07$. Slight underestimation of ship motions results in some underestimation of VBM for the corresponding wavelengths. Nonetheless, in general, the VBM computed by RPM is in good agreement with the results directly measured using a ship model with backbone and segmented hulls.

6. Conclusions

In order to provide world's first experimental data of the spatial distribution of wave-induced unsteady pressure on the whole hull surface of a ship oscillating in waves, an unprecedented experiment was conducted, measuring the pressures at a large number of locations on the ship hull simultaneously in terms of 333 FBG pressure sensors affixed with double-sided tape on almost whole ship-hull surface. To detect the time-variant wetted surface of the ship hull, the measurement of incident head wave, wave-induced ship motions and ship-side wave profile was also carried out, and all the data were synchronized by adjusting the phase of all data in terms of the complex amplitude of incident wave obtained after the Fourier-series analysis. The time history of the spatial distribution of unsteady pressure was obtained with a spline-interpolation technique using point-wise pressures measured at 333 points which include a bow area above the still waterline. Since the pressure distribution is the base for computing almost all hydrodynamic quantities like total hydrodynamic forces, the VBM distribution, the added resistance, ship motions and so on, the experimental data obtained in this study can be effectively used for deepening our understanding of local physical phenomena; for example, which part of the ship hull provides dominant pressures to the physical quantity concerned, what kind of nonlinearities or hydrodynamic cancellation are essential in understanding the phenomenon in question.

Validation of obtained data of unsteady pressure has been made by confirming the repeatability, namely the standard deviation, of the measured results and by comparing the measured and computed values along the girth at some of the transverse sections where the pressure measurement has been done. The pressure distribution obtained with interpolation was compared to the results computed by RPM for the zero-speed linear case and by CFD for the forward-speed nonlinear case. Remarkable agreement for both cases could be confirmed. In addition, in this paper, the first-harmonic wave-exciting forces were computed by integrating the unsteady pressure distribution over the wetted surface of a motion-fixed ship model and compared with the values directly measured with dynamometer. Good agreement was also confirmed in this validation, but at the same time small discrepancy in the surge exciting force was pointed out, a reason of which should be attributed to the scarcity of FBG pressure sensors in the bow upper region, suggesting a necessity of increasing the sensors in that region for more precise study.

In terms of measured and computed spatial distribution of unsteady pressure and wave-induced ship motions, the longitudinal distribution of the VBM along the ship's length was computed and shown in a form of maximum values in the hogging and sagging moments. Obtained results by using only the measured data agreed well with computed results not only for the zero-speed linear case but also for the forward-speed nonlinear case. Especially for the latter case of $Fn = 0.18$, asymmetric and hence nonlinear property in the VBM was clearly observed with larger value in the sagging moment by both experiment and CFD computation. The error values in the nonlinear VBM were presented at several longitudinal positions and it could be seen from these values that the degree of agreement between measured and computed results is good especially at around the motion-resonant wavelengths. As an important forward-speed effect, it was also observed that the longitudinal position where the sectional VBM takes maximum is shifted forward from the midship due to large increase in the unsteady pressure in the bow region and also increase in the ship motions particularly near the motion-resonant frequency. This finding on the forward-speed effect on the VBM is a world first to the best of our knowledge.

As further validation, a comparison was also made with the benchmark data used in the ITTC-ISSC joint workshop for the frequency-response function of the VBM measured at a specified longitudinal position using a segmented model of 6750-TEU container ship. Favorable agreement was confirmed also in this comparison. From these favorable results, the method proposed in this study may provide a new paradigm for obtaining experimentally the VBM distribution at any position, and obtained results could be useful as the validation data for other numerical computation methods.

Acknowledgments

The experiment for measuring the spatial distribution of unsteady pressure on the ship-hull surface was conducted as a collaboration work between Osaka University and Hiroshima University. Several students from both universities have been involved over a couple of years in this experiment and contributed to accurate measurement and analysis of large amount of data, for which the authors are grateful. This experimental work was supported in part by the Collaborative Research Program of Research Institute for Applied Mechanics (RIAM), Kyushu University, and in fact the measurement was carried out in the towing tank of RIAM. The authors are thankful to this support and help provided by Prof. Changhong Hu of RIAM and his colleagues. The present work was also partially supported with JSPS Grant-in-Aid for Scientific Research (A), Grant Number 17H01357 at Osaka University and also Grant-in-Aid for Scientific Research (B), Grant Number 18H01639 at Hiroshima University.

References

[1] R. E. D. Bishop, W. G. Price, Y. Wu, A general linear hydroelasticity theory of floating structures moving in a seaway, Philosophical Transactions of the Royal Society of London, Series A, Mathematical and Physical Sciences, Vol. 316, (1986) pp. 375-426.

[2] I. Senjanović, Š. Malenica, S. Tomašević, Hydroelasticity of large container ships, Marine Structures, Vol. 22, (2009) pp. 287-314.

[3] K. H. Kim, Y. Kim, Numerical analysis of springing and whipping using fully-coupled FSI models, Ocean Engineering, Vol. 91, (2014) pp. 28-50

[4] M. Kashiwagi, S. Kuga, S. Chimoto, Time- and Frequency-Domain Calculation Methods for Ship Hydroelasticity with Forward Speed, Proc. of Hydroelasticity in Marine Technology (Split, Croatia), (2015) pp. 477-492.

[5] S. E. Hidaris,W. Bai, D. Dessi, A. Ergin, X. Gu, O. A. Hermundstad, R. Huijsmans, K. Iijima, U. D. Nielsen, J. Parunov, N. Fonseca, A. Papanikolaou, K. Argyriadis, Loads for use in the design of ships and offshore structures, Ocean Engineering, Vol. 78, (2014) pp. 131-174.

[6] P. Temarel, W. Bai, A. Bruns, Q. Derbanne, D. Dessi, S. Dhavalikar, N. Fonseca, T. Fukasawa, X. Gu, A. Nestegård, A. Papanikolaou, J. Parunov, K. H. Song, S. Wang, Prediction of wave-induced loads on ships: Progress and Challenges, Ocean Engineering, Vol. 119, (2016) pp. 274-308.

[7] ITTC, The seakeeping committee final report and recommendations, Proceedings of the 27th ITTC, Copenhagen, 2017.

[8] B. J. Guo, S. Steen, G. B. Deng, Seakeeping prediction of KVLCC2 in head waves with RANS, Applied Ocean Research, Vol. 35, (2012) pp. 56-67.

[9] K. Niklas, H. Pruszko, Full scale CFD seakeeping simulations for case study ship redesigned from V-shaped bulbous bow to X-bow hull form, Applied Ocean Research, Vol. 89, (2019) pp. 188-201.

[10] C. Judge, M. Mousaviraad, F. Stern, E. Lee, A. Fullerton, J. Geiser, C. Schleicher, C. Merrill, C. Weil, J. Morin, M. Jiang, C. Ikeda, Experiments and CFD of a high-speed deep-V planing hull – part II: Slamming in waves, Applied Ocean Research, Vol. 97, (2020) 102059.

[11] J. Wang, W. Zhao, D. C. Wan, Development of naoe-FOAM-SJTU solver based on OpenFOAM for marine hydrodynamics, Journal of Hydrodynamics, Vol. 31, No. 1, (2019) pp. 1-20.

[12] W. Xu, G. Filip, K. J. Maki, A Method for the Prediction of Extreme Ship Responses using Design-Event Theory and Computational Fluid Dynamics, Journal of Ship Research, Vol. 64, No. 1, (2019) pp. 48-60.

[13] N. Toki, K. Hatakenaka, T. Takahashi, Experimental and theoretical approach to the estimation of non-linear vertical wave loads, Journal of the Society of Naval Architects of Japan, Vol. 154, (1983) pp. 141-150.

[14] T. Kuroiwa, H. Ohtsubo, Nonlinearity of Sagging Moment of Fine Ships (in Japanese), Journal of the Society of Naval Architects of Japan, Vol. 161, (1987) pp. 234-241.

[15] M. Ueno, I. Watanabe, On Asymmetry of Vertical Bending Moment on Ships (in Japanese), Journal of the Society of Naval Architects of Japan, Vol. 162, (1987) pp. 175-182.

[16] I. Watanabe, M. Ueno, Effects of bow flare shape to the wave loads of a container ship, Journal of the Society of Naval Architects of Japan, Vol. 166, (1989) pp. 259-266.

[17] I. Watanabe, C. Guedes Soares, Comparative study on the time-domain analysis of non-linear ship motions and loads, Marine Structures, Vol. 12, (1999) pp. 153-170.

[18] M.K. Wu, O.A. Hermundstad, Time-domain simulation of wave-induced nonlinear motions and loads and its applications in ship design, Marine Structures Vol 15, (2002) pp. 561-597.

[19] Y. Kim, K.H. Kim, J.H. Kim, T. Kim, M.G. Seo, Y. Kim, Time-domain analysis of nonlinear motion responses and structural loads on ships and offshore structures: development of WISH programs, International Journal of Naval Architecture and Ocean Engineering, Vol. 3 (1), 2011, pp. 37-52.

[20] S.E. Hirdaris, Y. Lee, G. Mortola, A. Incecik, O. Turan, S.Y. Hong, B.W. Kim, K.H. Kim, S. Bennett, S.H. Miao, P. Temarel, The influence of nonlinearities on the symmetric hydrodynamic response of a 10,000 TEU container ship, Ocean Engineering, Vol.,111, (2016) pp. 166-178.

[21] Y. Jin, S. Chai, J. Duffy, C. Chin, N. Bose, URANS predictions of wave induced loads and motions on ships in regular head and oblique waves at zero forward speed, Journal of Fluids and Structures, Vol. 74, (2017) pp. 178-204.

[22] P. A. Lakshmynarayanana, P. Temarel, Application of a two-way partitioned method for predicting the wave-induced loads of a flexible containership, Applied Ocean Research, Vol. 96, (2020) 102052.

[23] J. Oberhagemann, O. el Moctar, T. E. Schellin, Fluid-structure coupling to assess whipping effects on global loads of a large containership, Proceedings of 27th Symposium on Naval Hydrodynamics, Seoul, Korea, (2008).

[24] J. Oberhagemann, M. Holtmann, O. el Moctar, T. E. Schellin, D. Kim, Stern slamming of a LNG carrier, Journal of Offshore Mechanics and Arctic Engineering, Vol. 131(3) (2009) 031103.

[25] H. Orihara, Comparison of CFD simulations with experimental data for a tanker model advancing in waves, International Journal of Naval Architecture and Ocean Engineering, Vol. 3, No. 1 (2011) pp. 1-8.

[26] S. K. Hänninen, T. Mikkola, J. Matusiak, Computational and experimental study on local ship loads in short and steep waves, Journal of Marine Science and Technology, Vol. 19 (2014) pp. 103-115.

[27] M. K. Wu, T. Moan, Efficient calculation of wave-induced ship responses considering structural dynamic effects, Applied Ocean Research, Vol. 27, (2005) pp. 81-96.

[28] S. P. Singh, D. Sen, D., A comparative study on 3D wave load and pressure computations for different level of modelling of nonlinearities, Marine Structures, Vol. 20, (2007) pp. 1-24.

[29] I. Drummen, M. K. Wu, T. Moan, Experimental and numerical study of containership responses in severe head seas, Marine Structures, Vol. 22, (2009) pp. 172-193.

[30] N. Fonseca, R. Pascoal, C. Guedes Soares, G. Clauss, C. Schmittner, Numerical and experimental analysis of extreme wave induced vertical bending moments on a FPSO, Applied Ocean Research, Vol. 32, (2010) pp. 374-390.

[31] G. F. Clauss, M. Klein, Experimental investigation on the vertical bending moment in extreme sea states for different hulls, Ocean Engineering, Vol. 119, (2016) pp. 181-192.

[32] S. Rajendran, N. Fonseca, C. Guedes Soares, Prediction of extreme motions and vertical bending moments on a cruise ship and comparison with experimental data, Ocean Engineering, Vol. 127, (2016) pp. 368-386.

[33] G. Vasquez, N. Fonseca, C. Guedes Soares, Experimental and numerical vertical bending moment of a bulk carrier and a roll-on/roll-off ship in extreme waves, Ocean Engineering, Vol. 124, (2016) pp. 404-418.

[34] S. Mizokami, H. Yasukawa, T. Kuroiwa, H. Sueoka, S. Nishimura, S. Miyazaki, Wave Load on a Container Ship in Rough Seas, Journal of the Society of Naval Architects of Japan, Vol. 189, (2001) pp. 181-192.

[35] R. Miyake, T. Zhu, H. Kagemoto, On the estimation of wave-induced loads acting on practical merchant ships by a Rankine source method, Journal of the Society of Naval Architects of Japan, Vol. 190, (2001) pp. 107-119.

[36] M. Wakahara, A. Tanigami, S. Shingo, M. Nakajima, T. Fukasawa, K. Kanai, Development of an Affix-type Multipoint Pressure Sensor by Use of FBG – 2nd Report: Multipoint pressure measurements on the surface of model ship in resistance test (in Japanese), Journal of the Japan Society of Naval Architects, Vol. 7, (2008) pp. 9-14.

[37] H. Iwashita, M. Kashiwagi, An Innovative EFD for Studying Ship Seakeeping, Proceedings of the 33rd IWWWFB (Guidel-Plages, France), (2018) pp. 85-88.

[38] M. Kashiwagi, H. Iwashita, S. Miura, M. Hinatsu, Study on Added Resistance with Measured Unsteady Pressure Distribution on Ship-Hull Surface, Proceedings of the 34th IWWWFB (Newcastle, Australia), (2019) pp. 81-84.

[39] H. Iwashita, M. Kashiwagi, Y. Ito, Y. Seki, S. Yoshida, M. Wakahara, Measurement of unsteady pressure distributions of a ship advancing in waves (in Japanese), Conf Proc of the Japan Soci of Naval Archi and Ocean Eng, Vol. 22 (2016) pp. 235-238.

[40] M. Kashiwagi, H. Iwashita, Y. Seki, S. Yoshida, Y. Ito, A. Katano, H. Ohnishi, M. Wakahara, Measurement of unsteady pressure distributions of a ship advancing in waves (in Japanese), Conf Proc of the Japan Soci of Naval Archi and Ocean Eng, Vol. 24 (2017) pp. 613-616.

[41] H. Ohnishi, H. Iwashita, M. Kashiwagi, T. Hara, Y. Ito, M. Wakahara, An Innovative EFD for Ship Seakeeping, Proc of Workshop on Environmental Technologies in Naval Archi and Ocean Eng, Hiroshima, (2017) pp. 97-101.

[42] H. Iwashita, M. Kashiwagi, Y. Ito, Y. Seki, J. Yoshida, M. Wakahara, Calculation of Ship Seakeeping in Low Speed / Low-Frequency Range by Frequency-Domain Rankine Panel Methods (in Japanese), Journal of The Japan Society of Naval Architects and Ocean Engineers, Vol. 24, (2017) pp. 129-146.

[43] Y. Kim, J. H. Kim, Benchmark study on motions and loads of a 6750-TEU containership, Ocean Engineering, Vol. 119, (2016) pp. 262-273.

[44] E. Yasuda, H. Iwashita, M. Kashiwagi, Improvement of Rankine Panel Method for Seakeeping Prediction of a Ship in Low Frequency Region, Proceedings of the 35th International Conference on Ocean, Offshore and Arctic Engineering (Busan, Korea), Paper Number: OMAE2016-54163, 2016.

[45] Y. Seki, M. Kashiwagi, H. Iwashita, Experimental study on added resistance and unsteady pressure distribution in following waves, Proceedings of the 13th Practical Design of Ships and Other Floating Structures, Copenhagen, ID-147, 2016.

[46] P. D. Sclavounos, D. Nakos, Ship motion by a three dimensional Rankine panel method, Proceedings of the 18th Symposium on Naval Hydrodynamics, National Academy Press, Washington, DC, (1990) pp. 21-40.

[47] J. N. Newman, Distributions of sources and normal dipoles over a quadrilateral panel, Journal of Engineering Mathematics, Vol. 20, (1986) pp. 113-126.

[48] NUMECA, Theoretical Manual FINE/Marine, https://www.numeca.com/product/finemarine

[49] P. Queutey, M. Visonneau, An interface capturing method for free-surface hydrodynamic flows, Comput. Fluids, Vol. 36 (9) (2007) pp. 1481-1510.

[50] J. Wackers, B. Koren, H. C. Raven, A. van der Ploeg, A. R. Starke, G. B. Deng, P. Queutey, M. Visonneau, T. Hino, K. Ohashi, Free-Surface Viscous Flow Solution Methods for Ship Hydrodynamics, Archives of Computational Methods in Engineering, Vol. 18 (2011) pp. 1-41.

[51] F. R. Menter, Two-equation eddy-viscosity turbulence models for engineering applications, AIAA Journal, Vol. 32, (8) (1994) pp. 1598-1605.

[52] F. R. Menter, M. Kuntz, R. Langtry, Ten years of industrial experience with the SST turbulence model, Turbul. Heat. Mass Transf., Vol. 4, (4) (2003) pp. 625-632.

[53] M. Kashiwagi, S. Mizokami, H. Yasukawa, Y. Fukushima, Prediction of wave loads on actual ships by the Enhanced Unified Theory, Proceedings of the 23rd International Symposium on Naval Hydrodynamics, France, (2000) pp. 95-109.

List of Publications by Professor Masashi Kashiwagi

(A) Peer-Reviewed Journal Papers

1. Kashiwagi, M. : On the Stability Derivatives of High Speed Ships Oscillating in Low Frequency (in Japanese), *Journal of Kansai Society of Naval Architects*, Japan, 1983 (June), Vol. 189, pp. 53–64.

2. Kashiwagi, M. : Wave Exciting Forces Acting on a Ship Travelling in Following Seas (in Japanese), *Journal of Society of Naval Architects of Japan*, 1983 (December), Vol. 154, pp. 129–140.

3. Kashiwagi, M. and Hatta, K. : On the Hydrodynamic Forces on High Speed Ships Oscillating in Sway and Yaw (in Japanese), *Journal of Kansai Society of Naval Architects, Japan*, 1984 (September), Vol. 194, pp. 65–74.

4. Kashiwagi, M. : On the Hydrodynamic Forces on High Speed Ships Oscillating in Sway and Yaw (2nd Report) (in Japanese), *Journal of Kansai Society of Naval Architects, Japan*, 1984 (December), Vol. 195, pp. 17–27.

5. Kashiwagi, M. : The Unified Slender Body Theory for Lateral Motions of Ships with Forward Speed (in Japanese), *Journal of Kansai Society of Naval Architects, Japan*, 1985 (June), Vol. 197, pp. 21–30.

6. Kashiwagi, M. : A New Method for Calculating the Maneuvering Motion of a Ship in Nonuniform Current and Its Application in Naruto Kaikyou (in Japanese), *Journal of Japan Institute of Navigation*, 1986 (September), Vol. 75, pp. 55–67.

7. Kashiwagi, M., Varyani, K. and Ohkusu, M. : Hydrodynamic Forces Acting on a Submerged Elliptic Cylinder Translating and Oscillating in Waves, *Transactions of the West-Japan Society of Naval Architects*, 1987 (August), No. 74, pp. 64–78.

8. Ohkusu, M., Kashiwagi, M. and Koterayama, W. : Hydrodynamics of a Depth Controlled Towed Vehicle (in Japanese), *Journal of Society of Naval Architects of Japan*, 1987 (December), Vol. 162, pp. 99–109.

9. Kashiwagi, M. and Varyani, K. : Interaction Forces on Oscillating and Translating Two Cylinders Submerged under a Free Surface, *Journal of the Society of Naval Architects of Japan*, 1987 (December), Vol. 162, pp. 211–-221.

10. Koterayama, W., Kyozuka, Y., Nakamura, M., Ohkusu, M. and Kashiwagi, M. : A Preliminary Design of a Depth- and Roll-Controllable Towed Vehicle for Ocean Measurements (in Japanese), *Journal of the Society of Naval Architects of Japan*, 1988 (June), Vol. 163, pp. 130–140.

11. Kashiwagi, M. and Ohkusu, M. : The Effects of Forward Speed in the Radiation Problem of a Surface-Piercing Body, *Journal of the Society of Naval Architects of Japan*, 1988 (December), Vol. 164, pp. 92–104.

12. Kashiwagi, M. and Ohkusu, M. : Study on the Effects of Side-Wall Interference on Added-Mass and Damping Coefficients by Means of Slender-Ship Theory (in Japanese), *Journal of Society of Naval Architects of Japan*, 1989 (June), Vol. 165, pp. 153–162.

13. Kashiwagi, M. : 3-D Integral-Equation Method for Calculating the Effects of Tank-Wall Interference on Hydrodynamic Forces Acting on a Ship, *Journal of Kansai Society of Naval Architects, Japan*, 1989 (September), Vol. 212, pp. 89–101.

14. Koterayama, W., Nakamura, M., Kaneko, A., Kyozuka, Y., Kashiwagi, M., Inada, M., Ishidera, H. and Ito Y. : Towed Vehicle "DRAKE" for Ocean Measurements and Its In-Situ Experiments in the Kuroshio (in Japanese), *Journal of the Society of Naval Architects of Japan*, 1989 (December), Vol. 166, pp. 485–495.

15. Kashiwagi, M., Ohkusu, M. and Inada, M. : Side-Wall Effects on Radiation and Diffraction Forces on a Ship Advancing in Waves (in Japanese), *Journal of the Society of Naval Architects of Japan*, 1990 (December), Vol. 168, pp. 229–244.

16. Kashiwagi, M. and Ohkusu, M. : A New Theory for Side-Wall Interference Effects on Forward-Speed Radiation and Diffraction Forces, *Ship Technology Research (Schiffstechnik)*, 1991 (March), Vol. 38, No. 1, pp. 17–47.

17. Ohkusu, M., Kashiwagi, M., Ikegami, K., Ozaki, M. and Isozaki, Y. : Study on Performance of Floating Breakwater Utilizing the Relative Motion of Inside Water (in Japanese), *Journal of the Society of Naval Architects of Japan*, 1991 (June), Vol. 169, pp. 215–222

18. Kashiwagi, M. : Radiation and Diffraction Forces Acting on an Offshore-Structure Model in a Towing Tank, *International Journal of Offshore and Polar Engineering*, 1991 (June), Vol. 1, No. 2, pp. 101–107.

19. Kashiwagi, M. : Added Resistance, Wave-Induced Steady Sway Force and Yaw Moment on an Advancing Ship, *Ship Technology Research (Schiffstechnik)*, 1992 (February), Vol. 39, No. 1, pp. 3–16.

20. Kashiwagi, M., Ohkusu, M. and Inada, M. : Side-Wall Effects on Hydrodynamic Forces and Motions of a Ship Advancing in Waves, *Selected Papers in Naval Architecture and Ocean Engineering*, 1992 (December), pp. 31–48.

21. Kashiwagi, M. : Interaction Forces between Twin Hulls of a Catamaran Advancing in Waves (Part1: Radiation Problem) (in Japanese), *Journal of the Society of Naval Architects of Japan*, 1993 (June), Vol. 173, pp. 119–131.

22. Kashiwagi, M. : Interaction Forces between Twin Hulls of a Catamaran Advancing in Waves (Part1: Radiation Problem) (in Japanese), *Journal of the Society of Naval Architects of Japan*, 1993 (June), Vol. 173, pp. 119–131.

23. Kashiwagi, M. : Interaction Forces between Twin Hulls of a Catamaran Advancing in Waves (Part2: Wave-Exciting Forces and Motions in Waves) (in Japanese), *Journal of the Society of Naval Architects of Japan*, 1993 (December), Vol. 174, pp. 181–191.

24. Kashiwagi, M. : Prediction of Surge and its Effects on Added Resistance by Means of the Enhanced Unified Theory, *Transactions of West-Japan Society of Naval Architects*, 1995 (March), No. 89, pp. 77–89.

25. Kashiwagi, M. : A New Theory for Oscillating and Translating Slender Ships (in Japanese), *Journal of the Society of Naval Architects of Japan*, 1995 (December), Vol. 178, pp. 169–177.

26. Kashiwagi, M. : Full-Nonlinear Simulations of Hydrodynamic Forces on a Heaving Two-Dimensional Body, *Journal of the Society of Naval Architects of Japan*, 1996 (December), Vol. 180, pp. 373–381.

27. Kashiwagi, M. : Numerical Seakeeping Calculations Based on Slender Ship Theory, *Ship Technology Research (Schiffstechnik)*, 1997 (October), Vol. 4, No. 4, pp. 167–192.

28. Kashiwagi, M.: A B-Spline Galerkin Scheme for Calculating the Hydroelastic Response of a Very Large Floating Structure in Waves, *Journal of Marine Science and Technology*, 1998 (May), Vol. 3, No. 1, pp. 37–49.

29. Kashiwagi, M., Momoda, T. and Inada, M.: A Time-Domain Nonlinear Simulation Method for Wave- Induced Motions of a Floating Body, *Journal of the Society of Naval Architects of Japan*, 1998 (December), Vol. 184, pp. 139–148.

30. Kashiwagi, M.: Research on Hydroelastic Responses of VLFS: Recent Progress and Future Work, *International Journal of Offshore and Polar Engineering*, 2000 (June), Vol. 10, No. 2, pp. 81–90.

31. Kashiwagi, M.: Nonlinear Simulations of Wave-Induced Motions of a Floating Body by Means of the Mixed Eulerian-Lagrangian Method, *Journal of Mechanical Engineering Science, The Institution of Mechanical Engineers Part C*, 2000 (July), Vol. 214, pp. 841–855.

32. Kashiwagi, M., Kawasoe, K. and Inada, M.: A Study on Ship Motion and Added Resistance in Waves (in Japanese), *Journal of Kansai Society of Naval Architects, Japan*, 2000 (September), No. 234, pp. 85–94.

33. Kashiwagi, M.: Hydrodynamic Interactions among a Great Number of Columns Supporting a Very Large Flexible Structure, *Journal of Fluids and Structures*, 2000 (October), Vol. 14, No. 7, pp. 1013–1034.

34. Kashiwagi, M.: A Time-Domain Mode-Expansion Method for Calculating Transient Elastic Responses of a Pontoon-Type VLFS, *Journal of Marine Science and Technology*, 2000 (December), Vol. 5, No. 2, pp. 89–100.

35. Kashiwagi, M. and Yoshida, S.: Wave Drift Force and Moment on VLFS Supported by a Great Number of Floating Columns, *International Journal of Offshore and Polar Engineering*, 2001 (September), Vol. 11, No. 3, pp. 176–183.

36. Kashiwagi, M.: Wave-Induced Local Steady Forces on a Column-Supported Very Large Floating Structure, *International Journal of Offshore and Polar Engineering*, 2002 (June), Vol. 12, No. 2, pp. 98–104.

37. Momoki, T., Kashiwagi, M. and Hu, C-H.: Numerical Simulations of Highly Nonlinear Interactions of Water Waves with an Offshore Structure (in Japanese), *Transactions of the West-Japan Society of Naval Architects*, 2003 (March), Vol. 105, pp. 65–74.

38. Kashiwagi, M., Sugimoto, K., Ueda, T., Yamazaki, K., Arihama, K., Kimura, K., Yamashita, R., Itoh, A. and Mizokami, S.: An Analysis System for Propulsive Performance in Waves (in Japanese), *Journal of Kansai Society of Naval Architects, Japan*, 2004 (March), No. 241, pp. 67–82.

39. Kashiwagi, M.: Transient Responses of a VLFS during Landing and Take-off of an Airplane, *Journal of Marine Science and Technology*, 2004 (April), Vol. 9, No. 1, pp. 14–23.

40. Kashiwagi, M.: Asymptotic Values of Heave and Pitch Motions in a Very Long Wave (in Japanese), *Journal of Kansai Society of Naval Architects, Japan*, 2004 (September), No. 242, pp. 45–51.

41. Ten, I. and Kashiwagi, M.: Hydrodynamics of a Body Floating in a Two-Layer Fluid of Finite Depth (Part 1: Radiation Problem), *Journal of Marine Science and Technology*, 2004 (October), Vol. 9, No. 3, pp. 127–141.

42. Hu, C-H. and Kashiwagi, M. : A CIP Method for Numerical Simulations of Violent Free Surface Flows, *Journal of Marine Science and Technology*, 2004 (December), Vol. 9, No. 4, pp. 143–157.

43. Kashiwagi, M., Endo, K. and Yamaguchi, H. : Wave Drift Forces and Moments on Two Ships Arranged Side by Side in Waves, *Journal of Ocean Engineering*, 2005 (January), Vol. 32, pp. 529–555.

44. Kashiwagi, M. : Wave Scattering Among a Large Number of Floating Cylinders, *Journal of Structural Engineering and Mechanics*, 2005 (September), Vol. 21, No. 1, pp. 53–66.

45. Kashiwagi, M. : Wave-Induced Motions of a Body Floating in a Two-Layer Fluid, *International Journal of Offshore and Polar Engineering*, 2005 (September), Vol. 15, No. 3, pp. 175–182.

46. Hu, C-H., Kishev, Z., Kashiwagi, M., Sueyoshi, M. and Faltinsen, O.M. : Application of CIP Method for Strongly Nonlinear Marine Hydrodynamics, *Ship Technology Research (Shiffstechnik)*, 2006 (April), Vol. 53, No. 2, pp. 74–87.

47. Kishev, Z., Hu, C-H. and Kashiwagi, M. : Numerical Simulation of Violent Sloshing by a CIP-Based Method, *Journal of Marine Science and Technology*, 2006 (June), Vol. 11, No. 2, pp. 111–122.

48. Kashiwagi, M., Ten, I. and Yasunaga, M. : Hydrodynamics of a Body Floating in a Two-Layer Fluid of Finite Depth (Part 2: Diffraction Problem and Wave-Induced Motions), *Journal of Marine Science and Technology*, 2006 (September), Vol. 11, No. 3, pp. 150–164.

49. Nishi, Y., Hu, C-H. and Kashiwagi, M. : Multigrid Technique for Numerical Simulations of Water Impact Phenomena, *International Journal of Offshore and Polar Engineering*, 2006 (December), Vol. 16, No. 4, pp. 283–289.

50. Kashiwagi, M., Yamada, H., Yasunaga, M. and Tsuji, T. : Development of Floating Body with High Performance in Wave Reflection, *International Journal of Offshore and Polar Engineering*, 2007 (March), Vol. 17, No. 1, pp. 39–46.

51. Kashiwagi, M. and Hu, C-H. : Numerical Calculation Method on Extremely Nonlinear Wave-Body Interactions and Experimental Validation (in Japanese), *Progress in Multiphase Flow Research Part-2*, 2007 (March), pp. 189–196.

52. Kashiwagi, M. : Wave Drift Force in a Two-Layer Fluid of Finite Depth, *Journal of Engineering Mathematics*, 2007 (August), Vol. 58, pp. 51–66.

53. Kashiwagi, M. : 3-D Calculation for Multiple Floating Bodies in Proximity Using Wave Interaction Theory, International Journal of Offshore and Polar Engineering, 2008 (March), Vol. 18, No. 1, pp. 14–20.

54. Sueyoshi, M., Kashiwagi, M. and Naito, S. : Numerical Simulations of Wave-Induced Nonlinear Motions of a Two-Dimensional Floating Body by Moving Particle Semi-Implicit Method, *Journal of Marine Science and Technology*, 2008 (May), Vol. 13, No. 2, pp. 85–94.

55. Mori, K., Imanishi, H., Tsuji, Y., Hattori, T., Matsubara, M., Mochizuki, S., Inada, M. and Kashiwagi, M. : Direct Total Skin-Friction Measurement of a Flat Plate in Zero-Pressure-Gradient Boundary Layers, *Fluid Dynamics Research*, 2009 (March), Vol. 41, pp. 1–19.

56. Mikami, T. and Kashiwagi, M. : Time-Domain Strip Method with Memory-Effect Function Considering Body Nonlinearity of Ships in Large Waves (2nd report), *Journal of Marine Science and Technology*, 2009 (June), Vol. 14, No. 2, pp. 185–199.

57. Hu, C-H. and Kashiwagi, M. : Two Dimensional Numerical Simulation and Experiment on Strongly Nonlinear Wave-Body Interactions, *Journal of Marine Science and Technology*, 2009 (June), Vol. 14, No. 2, pp. 200–213.

58. He, G-H. and Kashiwagi, M. : Nonlinear Solution for Vibration of a Vertical Plate and Transient Waves, Generated by Wave Impact, *International Journal of Offshore and Polar Engineering*, 2009 (September), Vol. 19, No. 3, pp. 189–197.

59. He, G-H., Kashiwagi, M. and Hu, C-H. : Nonlinear Solution for Vibration of Vertical Elastic Plate by Initial Elevation of Free Surface, *International Journal of Offshore and Polar Engineering*, 2010 (March), Vol. 20, No. 1, pp. 34–40.

60. Hu, C-H., Sueyoshi, M. and Kashiwagi, M. : Numerical Simulation of Strongly Nonlinear Wave-Ship Interaction by CIP based Cartesian Grid Method, *International Journal of Offshore and Polar Engineering*, 2010 (June), Vol. 20, No. 2, pp. 81–87.

61. Kashiwagi, M. and Hu, C-H. : 3-D Effects on Measured Results Using a 2-D Model in a Narrow Wave Channel, *International Journal of Offshore and Polar Engineering*, 2010 (June), Vol. 20, No. 2, pp. 88–-94.

62. Kagemoto, H., Murai, M. and Kashiwagi, M. : Can a Single Floating Body be Expressed as the Sum of Two Bodies?, *Journal of Engineering Mathematics*, 2010 (July), Vol. 68, pp. 153–164.

63. Kashiwagi, M., Ikeda, T. and Sasakawa, T. : Effects of Forward Speed of a Ship on Added Resistance in Waves, *International Journal of Offshore and Polar Engineering*, 2010 (September), Vol. 20, No. 3, pp. 196–203.

64. Bondarenko, O. and Kashiwagi, M. : Dynamic Behavior of Ship Propulsion Plant in Actual Seas, *Journal of Japan Institute of Marine Engineers*, 2010 (September), Vol. 45, pp. 76–80.

65. Kashiwagi, M. and Shi, Q. : Pressure Distribution Computed by Wave-Interaction Theory for Adjacent Multiple Bodies, *Journal of Hydrodynamics, Series B*, 2010 (October), Vol. 22, pp. 526–531.

66. Iwashita, H., Elangovan, M., Kashiwagi, M. and Sasakawa, T. : On an Unsteady Wave Pattern Analysis of Ships Advancing in Waves (in Japanese), *Journal of the Japan Society of Naval Architects and Ocean Engineers*, 2011 (June), Vol. 13, pp. 95–106.

67. Bondarenko, O. and Kashiwagi, M. : Statistical Consideration of Propeller Load Fluctuation at Racing Condition in Irregular Waves, *Journal of Marine Science and Technology*, 2011 (December), Vol. 6, No. 4, pp. 402–410.

68. He, G-H. and Kashiwagi, M. : Nonlinear Analysis on Hydroelastic Behavior of Vertical Plate due to Solitary Waves, it Journal of Marine Science and Technology, 2012 (June), Vol. 17, No. 2, pp. 154–167.

69. Kashiwagi, M. : Hydrodynamic Study on Added Resistance Using Unsteady Wave Analysis, *Journal of Ship Research*, 2013 (December), Vol. 57, No. 4, pp. 220–240.

70. He, G-H. and Kashiwagi, M. : Time-Domain Analysis of Steady Ship-Wave Problem Using Higher-Order BEM, *International Journal of Offshore and Polar Engineering*, 2014 (March), Vol. 24, No. 1, pp. 1–10.

71. He, G-H. and Kashiwagi, M. : A Time-Domain Higher-Order Boundary Element Method for 3D Forward-Speed Radiation and Diffraction Problems, *Journal of Marine Science and Technology*, 2014 (June), Vol. 19, No. 2, pp. 228–244.

72. He, G-H. and Kashiwagi, M.: Radiation-problem Solutions Using a Time-domain Iterative HOBEM, *International Journal of Offshore and Polar Engineering*, 2014 (June), Vol. 24, No. 2, pp. 81–89.

73. Tasrief, M. and Kashiwagi, M.: Development of Practical Integrated Optimization Method for Ship Geometry with High Performance in Waves, *Journal of Japan Society of Naval Architects and Ocean Engineers*, 2014 (June), Vol. 19, pp. 89–100.

74. Sakai, K., Kashiwagi, M. and Takaramoto, R.: Wave-energy Absorption by a Rotating Electric-power Generator Set inside an Asymmetric Floating Body, *Journal of Japan Society of Naval Architects and Ocean Engineers*, 2014 (June), Vol. 19, pp. 205–211.

75. Takaramoto, R., Kashiwagi, M. and Sakai, K.: Wave Energy Absorption in Irregular Waves by a Floating Body Equipped with Interior Rotating Electric-Power Generator, *Journal of Ocean and Wind Energy*, 2014 (August), Vol. 1, No. 3, pp. 129–134.

76. Iida, T., Kashiwagi, M. and He, G-H.: Numerical Confirmation of Cloaking Phenomenon on an Array of Floating Bodies and Reduction of Wave Drift Force, *International Journal of Offshore and Polar Engineering*, 2014 (December), Vol. 24, No. 4, pp. 241–246.

77. Iida, T., Kashiwagi, M. and Miki, M.: Wave Pattern in Cloaking Phenomenon around a Body Surrounded by Multiple Vertical Circular Cylinders, *International Journal of Offshore and Polar Engineering*, 2016 (March), Vol. 26, No. 1, pp. 13–19.

78. Liu, Y., Hu, C-H., Sueyoshi, M., Iwashita, H. and Kashiwagi, M.: Motion Response Prediction by Hybrid Panel-Stick Models for a Semi-Submersible with Bracings, *Journal of Marine Science and Technology*, 2016 (December), Vol. 21, No. 4, pp. 742–757.

79. Iwashita, H., Kashiwagi, M., Ito, Y. and Seki, Y.: Calculations of Ship Seakeeping in Low-Speed /Low-Frequency Range by Frequency-Domain Rankine Panel Methods (in Japanese), *Journal of the Japan Society of Naval Architects and Ocean Engineers*, 2016 (December), Vol. 24, pp. 129–146.

80. Kashiwagi, M.: Hydrodynamic Interactions of Multiple Bodies with Water Waves, *International Journal of Offshore and Polar Engineering*, 2017 (June), Vol. 27, No. 2, pp. 113–122.

81. Sasa, K., Faltinsen, O.M., Lu L-F., Sasaki W., Prpic-Orsic, J., Kashiwagi, M. and Ikebuchi, T.: Development and validation of speed loss for a blunt-shaped ship in two rough sea voyages in the Southern Hemisphere, *Ocean Engineering*, 2017 (July), Vol. 142, pp. 577–596.

82. Zhang, J. and Kashiwagi, M.: Application of ALE to Nonlinear Wave Radiation by a Non-wall-sided Structure, *Journal of Japan Society of Naval Architects and Ocean Engineers*, 2017 (June), Vol. 25, pp. 109–121.

83. Iida, T. and Kashiwagi, M.: Water Wave Focusing Using Coordinate Transformation, *Journal of Energy and Power Engineering*, 2017 (October), Vol. 11, No. 10, pp. 631–636.

84. Zhang, Z., He, G-H., Kashiwagi, M. and Wang, Z.: A quasi-cloaking phenomenon to reduce the wave drift force on an array of adjacent floating bodies, *Applied Ocean Research*, 2018 (February) Vol. 71, pp. 1–10, https://doi.org/10.1016/j.apor.2017.11.011

85. Iida, T. and Kashiwagi, M.: Small Water Channel Network for Designing Wave Fields in Shallow Water, *Journal of Fluid Mechanics*, 2018 (April), Vol. 849, pp. 90–110, http://dx.doi.org/10.1017/ jfm.2018.355

86. Wicaksono, A. and Kashiwagi, M. : Wave-induced steady forces and yaw moment of a ship advancing in oblique waves, *Journal of Marine Science and Technology*, 2018 (December), Vol. 23, pp. 767–781, https://doi.org/10.1007/s00773-017-0510-6

87. Iida, T. and Kashiwagi, M. : Negative Refraction of Deep Water Waves through Water Channel Network, *Journal of Hydrodynamics*, 2019 (January), Vol. 31, pp. 840–847, https://doi.org/10.1007/ s42241-019-0021-5

88. Loukogeorgaki, E. and Kashiwagi, M. : Minimization of Drift Force on a Floating Cylinder by Optimizing the Flexural Rigidity of a Concentric Annular Plate, *Applied Ocean Research*, 2019 (April), Vol. 85, pp. 136–150, https://doi.org/10.1016/j.apor.2019.02.001

89. Kitagawa, Y. and Kashiwagi, M. : A Strip-Theory Method Including nx-Related Terms and Its Effects on Propeller Inflow Velocity in Waves, *Journal of Japan Society of Naval Architects and Ocean Engineers*, 2019 (June), Vol. 29, pp. 39–50.

90. Heo, K. and Kashiwagi, M. : A Numerical Study of Second-order Springing of an Elastic Ship Using Higher-order Boundary Element Method (HOBEM), *Applied Ocean Research*, 2019 (December), Vol. 93, No. 101903 (pp. 1–16) https://doi.org/10.1016/j.apor.2019.101903

91. Liu, Y., Cong, P., Yoshida, S., Gou, Y. and Kashiwagi, M. : Enhanced Endo's approach for evaluating free-surface Green's function with application to wave-structure interactions, *Ocean Engineering*, 2020 (July), Vol. 207, No. 107377 (pp. 1–18), https://doi.org/10.1016/ j.oceaneng.2020.107377

92. Chen, C., Sasa, K., Ohsawa, T., Kashiwagi, M., Prpic-Orsic, J. and Mizojiri, T. : Comparative assessment of NCEP and ECMWF global datasets and numerical approaches on rough sea generation for ship navigation based on numerical simulation and shipboard measurements, *Applied Ocean Research*, 2020 (August), Vol. 101, No. 102219.

93. Waskito, K.T., Kashiwagi, M., Iwashita, H. and Hinatsu, M. : Prediction of Nonlinear Vertical Bending Moment Using Measured Pressure Distribution on Ship Hull, *Applied Ocean Research*, 2020 (August), Vol. 101, No. 102261.

94. Yang, K-K., Kashiwagi, M. and Kim, Y. : Numerical Study on Ship-Generated Unsteady Waves Based on a Cartesian-Grid Method, *Journal of Hydrodynamics*, 2020 (October), Vol. 32, No. 5, pp. 953–968.

95. Heo, K. and Kashiwagi, M. : Numerical study on the second-order hydrodynamic force and response of an elastic body –in bichromatic waves, *Ocean Engineering*, 2020 (December), Vol. 217, Paper No. 107870.

96. Kashiwagi, M. : Enhanced Unified Theory with Forward-Speed Effect Taken into Account in the Inner Free-Surface Condition, *Journal of Ship Research*, 2020 (December), Paper Number: SNAME-JSR-04200028, https://doi.org/10.5957/JOSR.04200028

97. Yang, K-K., Kim, B-S., Kim, Y., Kashiwagi, M. and Iwashita, H. : Numerical Study on Unsteady Pressure Distribution on Bulk Carrier in Head Waves with Forward Speed, *Processes (Open Access Journal) by MDPI*, 2021 (January), https://doi.org/10.3390/pr9010171

98. Hong, Y., Heo, K. and Kashiwagi, M. : Hydroelastic Analysis of a Ship with Forward Speed Using Orthogonal Polynomials as Mode Functions of Timoshenko Beam, *Applied Ocean Research* (submitted)

99. Zhang, J., Duan, W., Kashiwagi, M. and Ma, S. : A short note on computation of nonlinear wave-structure interaction without solving acceleration potential, *Applied Ocean Research* (submitted)

(B) Proceedings of International Conferences

1. Koterayama, W., Kyozuka, Y., Nakamura, M., Ohkusu, M. and Kashiwagi, M.: Motions of Depth Controllable Towed Vehicle, Proc. of 7th International Symposium on Offshore Mechanics and Arctic Eng., 1988 (February), Vol. 1, pp. 423–430.

2. Kashiwagi, M. and Ohkusu, M.: Radiation Problem of a Two-Dimensional Surface-Piercing Body With Forward Speed, Proc. of 3rd International Workshop on Water Waves and Floating Bodies (Woods Hole, USA), 1988 (April), pp. 91–95.

3. Ohkusu, M., Kashiwagi, M. and Varyani, K.: Theoretical Prediction of Wave Forces on Offshore Structure in Current and Waves, Proc. of Techno-Ocean '88 International Symposium (Kobe), 1988 (November), Vol. 2, pp.214–222.

4. Kashiwagi, M.: Theoretical Prediction of Tank-Wall Effects on Hydrodynamic Forces Acting on an Oscillating and Translating Slender Ship, Proc. of 4th International Workshop on Water Waves and Floating Bodies (Bergen, Norway), 1989 (May), pp. 105–109.

5. Kashiwagi, M. and Ohkusu, M.: Side-Wall Effects on Hydrodynamic Forces Acting on a Ship with Forward and Oscillatory Motions, Proc. of 5th International Conference on Numerical Ship Hydrodynamics (Hiroshima), 1989 (September), pp. 499–511.

6. Kashiwagi, M.: Radiation and Diffraction Forces Acting on an Offshore-Structure Model in a Towing Tank, Proc. of 1st Pacific/Asia Offshore Mechanics Symposium (Seoul, Korea), 1990 (June), Vol. 2, pp. 95–102.

7. Koterayama,W., Nakamura, M., Kyozuka, Y., Kashiwagi, M. and Ohkusu, M.: Depth and Roll Controllable Towed Vehicle "DRAKE" for Ocean Measurements, Proc. of 1st Pacific/Asia Offshore Mechanics Symposium (Seoul), 1990 (June), pp. 257–264.

8. Koterayama, W., Kaneko, A., Kashiwagi, M. and Nakamura, M.: A New Ocean Measurement System Using ADCP on a Towed Vehicle, Proc. of 4th Pacific Congress on Marine Science and Technology (Tokyo), 1990 (July), pp. 325–332.

9. Kashiwagi, M. and Ohkusu, M.: Second-Order Steady Force and Yaw Moment on a Ship Advancing in Waves, Proc. of 6th International Workshop on Water Waves and Floating Bodies (Woods Hole, USA), 1991 (April), pp. 109–113.

10. Kashiwagi, M. and Ohkusu, M.: Forward-Speed Effects on Hydrodynamic Interactions between Twin Hulls of a Catamaran in Waves, Proc. of 8th International Workshop on Water Waves and Floating Bodies (Newfoundland, Canada), 1993 (May), pp. 49–52.

11. Kashiwagi, M. and Bessho, M.: A New Flow Model for a 2-D Shallow-Draft Ship Advancing at High Speed in Waves, Proc. of 2nd Japan-Korea Joint Workshop on Ship and Marine Hydrodynamics (Osaka), 1993 (June), pp. 45–52.

12. Kashiwagi, M.: A New Development in the Theory for 3-D Unsteady Problem of a Ship Advancing in Waves, Proc. of 2nd Symposium on Nonlinear and Free-Surface Flows (Hiroshima), 1993 (November), pp. 23–27.

13. Kashiwagi, M.: Heave and Pitch Motions of a Catamaran Advancing in Waves, Proc. of 2nd International Conference on Fast Sea Transportation (Yokohama), 1993 (December), pp. 643–655.

14. Kashiwagi, M.: A New Green-Function Method for the 3-D Unsteady Problem of a Ship with Forward Speed, Proc. of 9th International Workshop on Water Waves and Floating Bodies (Oita, Japan), 1994 (April), pp. 99–104.

15. Kashiwagi, M. : A New Forward-Speed Slender-Ship Theory Incorporating 3-D Interactions among Transverse Sections, Proc. of 3rd Symposium on Nonlinear and Free-Surface Flows (Hiroshima), 1994 (December), pp. 27–31.

16. Kashiwagi, M. : A New Slender-Ship Theory with Arbitrary Forward Speed and Oscillation Frequency, Proc. of 10th International Workshop on Water Waves and Floating Bodies (Oxford, UK), 1995 (April), pp. 109–114.

17. Kashiwagi, M. : Time-Domain Full-Nonlinear Wave Radiation by a 2-D Floating Body, Proc. of 4th Symposium on Nonlinear and Free-Surface Flows (Hiroshima), 1995 (October), pp. 17–20.

18. Kashiwagi, M. : A Precise Calculation Method for Hydroelastic Behaviors of Very Large Floating Structures, Proc. of 11th International Workshop on Water Waves and Floating Bodies (Hamburg, Germany), 1996 (March), pp. 99–103.

19. Kashiwagi, M. : A Calculation Method of Hydrodynamic Forces on a Shallow-Draft and Very Large Floating Structure, Proc. of Techno-Ocean '96 International Conference (Kobe), 1996 (October), pp. 627–632.

20. Kashiwagi, M. : A B-Spline Galerkin Method for Computing Hydroelastic Behaviors of a Very Large Floating Structure, International Workshop on Very Large Floating Structures (in Yokosuka), 1996 (November), pp. 149–156.

21. Kashiwagi, M. : Time-Domain Full-Nonlinear Computations of an Oscillating 2-D Floating Body, 2nd International Conference on Hydrodynamics (ICHD-96), (in Hong Kong), 1996 (December), pp. 177–182.

22. Kashiwagi, M. and Furukawa, C. : A Mode-Expansion Method for Predicting Hydroelastic Behavior of a Shallow Draft VLFS, International Conference on Offshore Mechanics and Arctic Engineering (in Yokohama), 1997 (April), Vol. 6, pp. 179–186.

23. Kashiwagi, M. : A B-Spline Galerkin Scheme for Computing Wave Forces on a Floating Very Large Elastic Plate, Proc. of the 7th International Offshore and Polar Engineering Conference (Honolulu), 1997 (May), Vol. 1, pp. 229–236.

24. Kashiwagi, M. : A Full-Nonlinear Simulation Method for Motions of a Floating Body in Waves, Proc. of 5th Symposium on Nonlinear and Free-Surface Flows (Hiroshima), 1997 (October), pp. 49–52.

25. Kashiwagi, M. : A New Direct Method for Calculating Hydroelastic Deflection of a Very Large Floating Structure in Waves, Proc. of 13th International Workshop on Water Waves and Floating Bodies (Alphen aan den Rijn, The Netherlands), 1998 (March), pp. 63–66.

26. Kashiwagi, M. : A Direct Method versus a Mode-Expansion Method for Calculating Hydroelastic Response of a VLFS in Waves, Proc. of the 8th International Offshore and Polar Engineering Conference (Montreal), 1998 (May), Vol. 1, pp. 215–222.

27. Kashiwagi, M. : A New Solution Method for Hydroelastic Problems of a Very Large Floating Structure in Waves, Proc. of 17th International Conf. on Offshore Mechanics and Arctic Eng. (Lisbon, Portugal), 1998 (July), Paper No. OMAE98-4332 (CD-ROM).

28. Kashiwagi, M. : Nonlinear Simulations of Wave-Induced Motions of a Floating Body by Means of MEL Method, Proc. of 3rd International Conference on Hydrodynamics (Seoul, Korea), 1998 (October), pp. 185–190.

29. Kashiwagi, M. : Nonlinear Motions of a Floating Body in Time Domain, Proc. of 6th Symposium on Nonlinear and Free-Surface Flows (Hiroshima), 1998 (November), pp. 43–47.

30. Kashiwagi, M. : Hydrodynamic Interactions among a Great Number of Columns Supporting a Very Large Flexible Structure, Proc. of 2nd International Conference on Hydroelasticity in Marine Technology (Fukuoka), 1998 (December), pp. 165–176.

31. Mikami, T., Kobayashi, M., Shimada, K., Miyajima, S., Kashiwagi, M. and Ohkusu, M. : The Response of VLFS with Anisotropic Rigidity in Waves, Proc. of 2nd International Conference on Hydroelasticity in Marine Technology (Fukuoka), 1998 (December), pp. 247–254.

32. Kashiwagi, M. : A Hierarchical Interaction Theory for Wave Forces on a Great Number of Buoyancy Bodies, Proc. of 14th International Workshop on Water Waves and Floating Bodies (Port Huron, USA), 1999 (April), pp. 68–71.

33. Kashiwagi, M. : Research on Hydroelastic Responses of VLFS: Recent Progress and Future Work, Proc. of 9th International Offshore and Polar Engineering Conference (Brest, France), 1999 (May), Vol. 1, pp. 17–26.

34. Kashiwagi, M., Mizokami, S. and Yasukawa, H. : Application of the Enhanced Unified Theory to Seakeeping Calculations of Actual Ships, Proc. of 4th Japan-Korea Joint Workshop on Ship & Marine Hydrodynamics (Fukuoka), 1999 (July), pp. 59–66.

35. Kashiwagi, M. : A Time-Domain Green Function Method for Transient Problems of a Pontoon-Type VLFS, Proc. of 3rd International Workshop on Very Large Floating Structures (VLFS'99) (Honolulu, USA), 1999 (September), Vol. 1, pp. 97–104.

36. Mizokami, S. and Kashiwagi, M. : Wave Pressure Calculation of a VLCC by Enhanced Unified Theory, Proc. of 7th Symposium on Nonlinear and Free-Surface Flows (Hiroshima), 1999 (October), pp. 33–36.

37. Kashiwagi, M. : Wave Interactions with a Multitude of Floating Cylinders, Proc. of 15th International Workshop on Water Waves and Floating Bodies (Caesarea, Israel), 2000 (February), pp. 99–102.

38. Kashiwagi, M. : Wave Drift Force and Moment on a VLFS Supported by a Great Number of Floating Columns, Proc. of the 10th International Offshore and Polar Engineering Conference (Seattle), 2000 (May), Vol. 1, pp. 49–56.

39. Kashiwagi, M. : Transient Elastic Motions of a Pontoon-Type Very Large Floating Structure, Proc. of 4th International Conference on Hydrodynamics: ICHD2000 (Yokohama), 2000 (September), Vol. 1, pp. 211–216.

40. Kashiwagi, M., Mizokami, S., Yasukawa, H. and Fukushima, Y. : Prediction of Wave Pressure and Loads on Actual Ships by the Enhanced Unified Theory, Proc. of 23rd Symposium on Naval Hydrodynamics (Val de Reuil, France), 2000 (September), Tuesday Sessions, pp. 95–109.

41. Kashiwagi, M. : The State of the Art on Slender-Ship Theories of Seakeeping, Proc. of 4th Osaka Colloquium on Seakeeping Performance of Ships (Osaka), 2000 (October), pp. 11–25.

42. Kashiwagi, M. : A Near-Field Method for Calculating the Wave Drift Force on a Column-Supported Large Floating Structure, Proc. of Techno-Ocean 2000 International Symposium (Kobe), 2000 (November), Vol. 2, pp. 539–542.

43. Kashiwagi, M. : Second-Order Steady Forces on Multiple Cylinders in a Rectangular Periodic Array, Proc. of 16th International Workshop on Water Waves and Floating Bodies (Hiroshima), 2001 (April), pp. 69–72.

44. Kashiwagi, M. : Wave-Induced Local Steady Forces on a Column-Supported Very Large Floating Structure, Proc. of 11th International Offshore and Polar Engineering Conference (Stavanger, Norway), 2001 (June), Vol. 1, pp. 264–271.

45. Kashiwagi, M. : A New Flow Model of a Shallow-Draft Ship Oscillating in Waves at Forward Speed, Proc. of 22nd International Conference on Hydrodynamics and Aerodynamics in Marine Engineering (Varna, Bulgaria), 2001 (October), pp. 185–194.

46. Kashiwagi, M. : First- and Second-Order Water Waves Around an Array of Floating Vertical Cylinders, Proc. of 17th International Workshop on Water Waves and Floating Bodies (Cambridge, UK), 2002 (April), pp. 73–76.

47. Kashiwagi, M. : Spatial Distribution of the Waves among a Great Number of Cylinders at Near Trapped-Mode Frequency, Proc. of 10th Congress of the International Maritime Association of the Mediterranean (Crete, Greece), 2002 (May), CD-ROM.

48. Kashiwagi, M. and Ohwatari, Y. : Spatial Distribution of the Wave Around Multiple Floating Bodies, Proc. of 12th International Offshore and Polar Engineering Conference (Kitakyushu), 2002 (May), Vol. 3, pp. 479–486.

49. Kashiwagi, M. : A Flow Model for a Displacement-Type Fast Ship with Shallow Draft in Regular Waves, Proc. of 24th International Symposium on Naval Hydrodynamics (Fukuoka), 2002 (July), Vol. 2, pp. 181–191.

50. Momoki, T., Kashiwagi, M. and Hu, C-H. : CFD Simulations of Nonlinear Waves and Interactions with a Structure, Proc. of Techno-Ocean 2002 International Conference (Kobe), 2002 (November), CD-ROM (Paper No. T-H-2).

51. Hu, C-H. and Kashiwagi, M. : 2-D Numerical Simulation of Extreme Wave-Body Interactions, Proc. of 8th Symposium on Nonlinear and Free-Surface Flows (Hiroshima), 2002 (December), pp. 1–4.

52. Kashiwagi, M. and Higashimachi, N. : Numerical Simulations of Transient Responses of VLFS during Landing and Take-off of an Airplane, Proc. of 4th International Workshop on Very Large Floating Structure (Tokyo), 2003 (January), pp. 75–83.

53. Hu, C-H. and Kashiwagi, M. : A CIP Based Numerical Simulation Method for Extreme Wave-Body Interactions, Proc. of 17th International Workshop on Water Waves and Floating Bodies (Le Croisic, France), 2003 (April), pp. 81–84.

54. Hu, C-H., Kashiwagi, M. and Momoki, T. : Numerical Simulation of Non-Linear Free Surface Wave Generation by CIP Method and Its Applications, Proc. of 13th International Offshore and Polar Engineering Conference (Honolulu, USA), 2003 (May), Vol. 3, pp. 294–299.

55. Kashiwagi, M. and Higashimachi, N. : Transient Responses of a VLFS during Landing and Take-off of an Airplane, Proc. of 3rd International Conference on Hydroelasticity in Marine Technology (Oxford, UK), 2003 (September), pp. 259–269.

56. Hu, C-H. and Kashiwagi, M. : Development of CFD Simulation Method for Extreme Wave-Body Interactions, Proc. of 8th International Conference on Numerical Ship Hydrodynamics (Busan, Korea), 2003 (September), Vol. 2, pp. 50–57.

57. Kashiwagi, M. and Endo, K.: Wave-Induced Steady Force on Two Ships with Side-by-Side Arrangement, Proc. of 9th Symposium on Nonlinear and Free-Surface Flows (Hiroshima), 2003 (December), pp. 21–24.

58. Hu, C-H., Kashiwagi, M. and Kishev, Z.: Numerical Simulation of Violent Sloshing by CIP Method, Proc. of 19th International Workshop on Water Waves and Floating Bodies (Cortona, Italy), 2004 (March), pp. 67–70.

59. Kagemoto, H., Murai, M. and Kashiwagi, M.: Can a single floating body be expressed as the sum of two bodies?, Proc. of 19th International Workshop on Water Waves and Floating Bodies (Cortona, Italy), 2004 (March), pp. 79–82.

60. Kashiwagi, M.: Wave Drift Forces and Moments on Two Ships with Side-by-Side Arrangement, Proc. of 19th International Workshop on Water Waves and Floating Bodies (Cortona, Italy), 2004 (March), pp. 83–86.

61. Kashiwagi, M., Ten, I.: Radiation and Diffraction Problems of a Floating Body in a Two-Layer Fluid of Finite Depth, Proc. of the 14th International Offshore and Polar Engineering Conference (Toulon), 2004 (May), Vol. 3, pp. 366–373.

62. Kishev, Z., Hu, C-H. and Kashiwagi, M.: Experimental Simulation of Violent Sloshing and Numerical Computations, Proc. of 2nd Asia-Pacific Workshop on Marine Hydrodynamics (Busan, Korea), 2004 (June), pp. 311–314.

63. Kashiwagi, M.: Wave Scattering Among a Large Number of Floating Cylinders, Proc. of 3rd International Conference on Advances in Structural Engineering and Mechanics (ASEM'04) (Seoul, Korea), 2004 (September), pp. 559–571.

64. Hu, C-H., Faltinsen, O.M. and Kashiwagi, M.: Development and Validation of CIP-Based Cartesian Grid Method for Nonlinear Wave-Body Interactions, Proc. of 7th Numerical Towing Tank Symposium (Hamburg, Germany), 2004 (October).

65. Kashiwagi, M.: Recent Research on Seakeeping Problems at RIAM, Kyushu University, Proc. of 1st MARIN-NMRI Workshop (Tokyo, Japan), 2004 (October), pp. 22–35.

66. Kashiwagi, M.: Wave Drift Forces on Two Ships in Close Proximity, Proc. of International Conference of TECHNO-OCEAN'04, 2004 (November), pp. 578–584.

67. Kashiwagi, M. and Ten, I.: Wave Radiation and Diffraction by a Floating Body in a Two-Layer Fluid, Proc. of 6th International Conference on Hydrodynamics (ICHD'04), VI - Theory and Applications - (Perth, West Australia), 2004 (November), pp. 383–389.

68. Kashiwagi, M.: Wave Drift Forces on Two Ships of Side-by-Side Arrangement, Proc. of International Symposium on Technology of Ultra Deep Ocean Eng. (Tokyo), 2005 (January), pp. 141–148.

69. Hu, C-H., Faltinsen, O.M. and Kashiwagi, M.: 3-D Numerical Simulation of Water-Entry Problem by CIP based Cartesian Grid Method, Proc. of 20th International Workshop on Water Waves and Floating Bodies (Spitsbergen, Norway), 2005 (May), pp. 95–98.

70. Kashiwagi, M.: Wave-Body Interactions in a Two-Layer Fluid of Finite Water Depth, Proc. of 20th International Workshop on Water Waves and Floating Bodies (Spitsbergen, Norway), 2005 (May), pp. 111–114.

71. Sueyoshi, M., Kishev, Z. and Kashiwagi, M.: A Particle Method for Impulsive Loads Caused by Violent Sloshing, Proc. of 20th International Workshop on Water Waves and Floating Bodies (Spitsbergen, Norway), 2005 (May), pp. 239–242.

72. Kishev, Z., Hu, C-H. and Kashiwagi, M.: Numerical Simulation of Violent Sloshing by CIP Method with Experimental Validation, Proc. of 15th International Offshore and Polar Engineering Conference (Seoul, Korea), 2005 (June), Vol. 3, pp. 274–281.

73. Kashiwagi, M.: Wave-Induced Motions of a Body Floating in a Two-Layer Fluid, Proc. of 15th International Offshore and Polar Engineering Conference (Seoul, Korea), 2005 (June), Vol. 3, pp. 358–365.

74. Hu, C-H., Faltinsen, O.M. and Kashiwagi, M.: 3-D Numerical Simulation of Freely Moving Floating Body by CIP Method, Proc. of 15th International Offshore and Polar Engineering Conference (Seoul, Korea), 2005 (June), Vol. 3, pp. 674–679.

75. Kashiwagi, M. and Sumi, K.: Development of Hull Form of a Ship with High Performance in Waves, Proc. of International Conf. on Fast Sea Transportation FAST-2005 (St. Petersburg, Russia), 2005 (June), CD-ROM.

76. Hu, C-H., Kashiwagi, M. and Faltinsen, O.M.: Recent Progress in CIP Method for Strongly Nonlinear Ship-Wave Interactions, Proc. of 4th International Workshop on Ship Hydrodynamics (IWASH '05) (Shanghai, China), 2005 (September), pp. 41–47.

77. Hu, C-H., Kashiwagi, M. and Faltinsen, O.M.: 3-D Computation of Ship-Wave Interaction by CIP/ Cartesian Grid Method, Proc. of 8th Numerical Towing Tank Symposium (NuTTS '05) (Varna, Bulgaria), 2005 (October), pp. 13.1–13.6.

78. Hu, C-H. and Kashiwagi, M.: Experimental Validation of the Computation Method for Strongly Nonlinear Wave-Body Interactions, Proc. of 21st International Workshop on Water Waves and Floating Bodies (Loughborough, UK), 2006 (April), pp. 73–76.

79. Kashiwagi, M.: Wave Drift Force on a Floating Body in Two-Layer Fluids, Proc. of 21st Inter- national Workshop on Water Waves and Floating Bodies (Loughborough, UK), 2006 (April), pp. 85–88.

80. Nishi, Y., Hu, C-H. and Kashiwagi, M.: A Numerical Simulation of Water Impact Phenomena by the CIP-based CFD Combined with the Multigrid Method, Proc. of 16th International Offshore and Polar Engineering Conference (San Francisco, USA), 2006 (June), Vol. 3, pp. 420–427.

81. Hu, C-H., Kashiwagi, M. and Kitadai, A.: Numerical Simulation of Strongly Nonlinear Wave-Body Interactions with Experimental Validation, Proc. of 16th International Offshore and Polar Engineering Conference (San Francisco, USA), 2006 (June), Vol. 3, pp. 467–472.

82. Kashiwagi, M., Yamada, H., Yasunaga, M. and Tsuji, T.: Development of a Floating Body with High Performance in Wave Reflection, Proc. of 16th International Offshore and Polar Engineering Conference (San Francisco, USA), 2006 (June), Vol. 3, pp. 641–648.

83. Kashiwagi, M., Oda, S. and Mikami, T.: Added Resistance in Regular Waves of a Blunt Ship in Ballast Condition, Proc. of 3rd Asia-Pacific Workshop on Marine Hydrodynamics (Shanghai, China), 2006 (June), pp. 93–99.

84. Hu, C-H., Kashiwagi, M. and Kitadai, A.: CFD Simulation and Laboratory Experiment on 2-D Strongly Nonlinear Wave-Body Interactions, Proc. of 3rd Asia-Pacific Workshop on Marine Hydrodynamics (Shanghai, China), 2006 (June), pp. 232–236.

85. Hu, C-H. and Kashiwagi, M.: Validation of CIP-based Method for Strongly Nonlinear Wave-Body Interactions, Proc. of 26th International Symposium on Naval Hydrodynamics (Rome, Italy), 2006 (September), Vol. 4, pp. 247–258.

86. Hu, C-H. and Kashiwagi, M.: Wave-Body Interaction Experiments for Validation of CFD method on Strongly Nonlinear Problems, Proc. of 9th Numerical Towing Tank Symposium (NuTTS'06) (Le Croisic, France), 2006 (October), pp. 59–64.

87. Kashiwagi, M.: Wave Reflection and Transmission by an Asymmetric Floating Body in Regular Waves, Proceedings of 2nd PAAMES and AMEC2006 (Cheju, Korea), 2006 (October), pp. 50–60.

88. Kashiwagi, M.: Reciprocity Relations of Waves Generated by an Asymmetric Floating Body, Proc. of 22nd International Workshop on Water Waves and Floating Bodies (Plitvice, Croatia), 2007 (April), pp. 117–120.

89. Nishi, Y., Kashiwagi, M., Koterayama, W., Nakamura, M., Samnuel, S.Z.H., Yamamoto, I. and Hyakudome, T.: Resistance and Propulsion Performance of an Underwater Vehicle Estimated by a CFD Method and Experiment, Proc. of 17th International Offshore and Polar Engineering Conference (Lisbon, Portugal), 2007 (July), Vol. 3, pp. 2045–2052.

90. Kashiwagi, M.: 3-D Calculation for Multiple Floating Bodies in Proximity Using Wave Interaction Theory, Proc. of 17th International Offshore and Polar Engineering Conference (Lisbon, Portugal), 2007 (July), Vol. 3, pp. 2246–2252.

91. Hu, C-H. and Kashiwagi, M.: A CFD Approach for Extremely Nonlinear Wave-Body Interactions: Development and Validation, Proc. of IUTAM Symposium on Fluid-Structure Interaction in Ocean Engineering (Hamburg, Germany), 2007 (July).

92. Hu, C-H. and Kashiwagi, M.: Numerical and Experimental Studies on Three-Dimensional Water on Deck with a Modified Wigley Model, Proc. of 9th Numerical Ship Hydrodynamics (Ann Arbor, Michigan), 2007 (August), Vol. 1, pp. 159–169.

93. Sueyoshi, M., Kihara, H. and Kashiwagi, M.: A Hybrid Technique Using Particle and Boundary- Element Methods for Wave-Body Interaction Problems, Proc. of 9th Numerical Ship Hydrodynamics (Ann Arbor, Michigan), 2007 (August), Vol. 1, pp. 241–252.

94. Mikami, T. and Kashiwagi, M.: A Time-Domain Nonlinear Strip Method with Whipping Taken into Account, Proc. of 9th Numerical Ship Hydrodynamics (Ann Arbor, Michigan), 2007 (August), Vol. 3, pp. 186–197.

95. Kashiwagi, M., Hu, C-H., Miyake, R. and Zhu, T.: A CIP-Based Cartesian Grid Method for Nonlinear Wave-Body Interactions, Proc. of 10th Intl. Symposium on Practical Design of Ships and Other Floating Structures (PRADS), (Houston, USA), 2007 (September), Vol. 2, pp. 894–902.

96. Kihara, H., Sueyoshi, M. and Kashiwagi, M.: A Hybrid Computation Method for Nonlinear Free Surface problems, Proc. of International Conference on Violent Flows (VF-2007) (Fukuoka, Japan), 2007 (November), pp. 305–314.

97. Hu, C-H., Kashiwagi, M. and Xiao, F.: 3D Numerical Simulation of Violent Sloshing by Conservative CIP Method, Proc. of International Conference on Violent Flows (VF-2007) (Fukuoka, Japan), 2007 (November), pp. 373–377.

98. Mikami, T. and Kashiwagi, M.: A Time-Domain Nonlinear Strip Method in View of Elasticity of Ship Hull and Green Water on Deck, Proc. of International Conference on Violent Flows (VF-2007) (Fukuoka, Japan), 2007 (November), pp. 413–420.

99. Hu, C-H., Kashiwagi, M. and Ma, N.: 2-D Numerical Simulation of Water Entry Using CIP Based Method, Proc. of 3rd Asian-Pacific Congress on Computational Mechanics (APCOM'07), (Kyoto, Japan), 2007 (December), CD-ROM MS7-1-1.

100. He, G-H. and Kashiwagi, M. : A Full Nonlinear Solution for Vibration of Vertical Wall by an Initial Elevation of Free Surface, Proceedings of 6th Osaka Colloquium on Seakeeping and Stability of Ships (OC-2008) (Osaka, Japan), 2008 (March), pp. 67–72.

101. Kashiwagi, M., Hu, C-H. and Sueyoshi, M. : CFD Computation of Strongly Nonlinear Wave-Body Interactions on the Free Surface, Proceedings of 6th Osaka Colloquium on Seakeeping and Stability of Ships (OC-2008) (Osaka, Japan), 2008 (March), pp. 83–92.

102. Sueyoshi, M., Kihara, H. and Kashiwagi, M. : Numerical Simulation Using Particle and Boundary Element Method for Highly Nonlinear Interaction Problems between Waves and Floating Body, Proc. of 6th Osaka Colloquium on Seakeeping and Stability of Ships (OC-2008) (Osaka, Japan), 2008 (March), pp. 93–100.

103. Hu, C-H. and Kashiwagi, M. : A Conservative CIP Method for Violent Free Surface Flows, Proc. of 23rd International Workshop on Water Waves and Floating Bodies (Jeju, Korea), 2008 (April), pp. 81–84.

104. Kashiwagi, M. and Hayashi, T. : Experimental Confirmation of Reciprocity Relations of Waves around an Asymmetric Floating Body, Proc. of 23rd International Workshop on Water Waves and Floating Bodies (Jeju, Korea), 2008 (April), pp. 96–99.

105. Sueyoshi, M., Kihara, H. and Kashiwagi, M. : Numerical Simulation of Deck Wetness for a 2D Pontoon-type Floating Structure, Proc. of Oceans'08 / Techno-Ocean'08 (OTO'08) (Kobe, Japan), 2008 (April), CDR (ISBN: 978-1-4244-2126-8).

106. Kashiwagi, M., Hu, C-H., Hashimoto, T. and Yasunaga, M. : Consideration on 3-D Effects on results of Forced Oscillation Test in a 2-D Wave Channel, Proc. of 18th International Offshore and Polar Engineering Conference (Vancouver, Canada), 2008 (July), Vol. 3, pp. 39–46.

107. Hu, C-H., Kashiwagi, M., Sueyoshi, M. and Nakagiri, I. : Numerical Simulation of Strongly Nonlinear Wave-Ship Interaction by CIP/Cartesian Grid Method, Proc. of 18th International Offshore and Polar Engineering Conference (Vancouver, Canada), 2008 (July), Vol. 3, pp. 143–147.

108. Hu, C-H., Kashiwagi, M. and Sueyoshi, M. : Improvement towards High-Resolution Computation on Strongly Nonlinear Wave-Induced Motions of an Actual Ship, Proc. of 27th Symposium on Naval Hydrodynamics (Seoul, Korea), 2008 (October), pp. 525–534.

109. Kashiwagi, M. : Impact on Hull Design on the Added Resistance in Waves – Application of the Enhanced Unified Theory, Proceedings of the 10th International Marine Design Conference (IMDC) Trondheim, Norway, 2009 (May), Vol. 1, pp. 521–535.

110. He, G-H., Kashiwagi, M. and Hu, C-H. : Nonlinear Solution for Vibration of Vertical Elastic Plate by Initial Elevation of Free Surface, Proc. of 19th International Offshore and Polar Engineering Conference (Osaka, Japan), 2009 (June), Vol. 3, pp. 406–413.

111. Kashiwagi, M., Ikeda, T. and Sasakawa, T. : Effects of Forward Speed of a Ship on Added Resistance in Waves, Proc. of 19th International Offshore and Polar Engineering Conference (Osaka, Japan), 2009 (June), Vol. 4, pp. 818–825.

112. He, G-H. and Kashiwagi, M. : Full-Nonlinear Solution for Vibration of Vertical Elastic Plate Due to Wave Impact, Proc. of 5th Hydroelasticity in Marine Technology (Southampton, UK), 2009 (September), Vol. 3, pp. 131–140.

113. Bondarenko, O. and Kashiwagi, M. : Dynamic Behavior of Ship Propulsion in Actual Seas, Proc. of International Symposium on Marine Engineering (Busan, Korea), 2009 (September), CD-ROM.

114. Bondarenko, O., Kashiwagi, M., Lanchukovsky, V. and Miusov, M. : Simulation of Automated Propulsion Plant in Actual Sea, Proc. of International Conference on Engine Room Simulators (ICERS) (New York, USA), 2009 (November), CD-ROM.

115. Kashiwagi, M. : Prediction of Added Resistance by Means of Unsteady Wave-Pattern Analysis, Proc. of 25th International Workshop on Water Waves and Floating Bodies (Harbin, China), 2010 (May), pp. 69–72.

116. Huijsmans, R. H. M., Veer, R. V. and Kashiwagi, M. : Ship Motion Predictions: A Comparison between a CFD Based Method, A Panel Method and Measurements, Proc. of 29th International Conference on Ocean, Offshore and Arctic Engineering (Shanghai, China), 2010 (June)

117. Wakabayashi, T. and Kashiwagi, M. : Study on Added Resistance with Unsteady Wave-Pattern Analysis, Proc. of 5th Asia-Pacific Workshop on Marine Hydrodynamics - APHydro2010 (Osaka, Japan), 2010 (July), pp. 1–4.

118. Kubo, H., Kashiwagi, M. and Hu, C-H. : Numerical Study on Ship Motions and Added Resistance in Waves by Strongly Nonlinear Three-Dimensional Code, Proc. of 5th Asia-Pacific Workshop on Marine Hydrodynamics - APHydro2010 (Osaka, Japan), 2010 (July), pp. 5–8.

119. Mahmuddin, F. and Kashiwagi, M. : Numerical Analysis on 3D Wave Effect, Proc. of 5th Asia-Pacific Workshop on Marine Hydrodynamics - APHydro2010 (Osaka, Japan), 2010 (July), pp. 233–236.

120. He, G-H., Kashiwagi, M. and Yamada, Y. : Hydroelastic Analysis on Interaction of Vertical Plate with Soliton-like Wave, Proc. of 5th Asia-Pacific Workshop on Marine Hydrodynamics - APHydro2010 (Osaka, Japan), 2010 (July), pp. 391–396.

121. Kashiwagi, M. and Kagotani, T. : Development of a Practical Unified Theory, Proc. of 5th Asia-Pacific Workshop on Marine Hydrodynamics - APHydro2010 (Osaka, Japan), 2010 (July), pp. 405–410.

122. Kashiwagi, M. and Hu, C-H. : Strongly Nonlinear Computations for Seakeeping of Ships, Proc. of 28th Symposium on Naval Hydrodynamics (Pasadena, USA), 2010 (September), Invited Lecture on Tuesday.

123. He, G-H. and Kashiwagi, M. : Nonlinear Analysis on Wave-Plate Interaction due to Disturbed Vertical Elastic Plate, Proc. of 9th International Conference on Hydrodynamics (ICHD) (Shanghai, China), 2010 (October), pp. 507–512.

124. Kashiwagi, M. and Shi, Q. : Pressure Distribution Computed by Wave-Interaction Theory for Adjacent Multiple Bodies, Proc. of 9th International Conference on Hydrodynamics (ICHD) (Shanghai, China), 2010 (October), pp. 526–531.

125. He, G-H. and Kashiwagi, M. : Response of Vertical Elastic Plate due to Solitary Wave, Proc. of 4th PAAMES and AMEC2010 (Singapore), 2010 (December), pp. 34–35.

126. Kashiwagi, M., Sasakawa, T. and Wakabayashi, T. : Hydrodynamic Consideration on Added Resistance and Ship-generated Unsteady Waves, Proc. of 26th International Workshop on Water Waves and Floating Bodies (Athens, Greece), 2011 (April), pp. 69–72.

127. Kashiwagi, M., Sasakawa, T. and Wakabayashi, T. : Hydrodynamic Study on Added Resistance by Means of Unsteady Wave Analysis Method, Proc. of 21st International Offshore and Polar Engineering Conference (Maui, USA), 2011 (June), Vol. 3, pp. 581–587.

128. He, G-H., Isshiki, T. and Kashiwagi, M.: Prediction of Radiation Forces by Means of a CIP-based Cartesian Grid Method, Proc. of 21st International Offshore and Polar Engineering Conference (Maui, USA), 2011 (June), Vol. 3, pp. 633–638.

129. Wakabayashi, T. and Kashiwagi, M.: Study on Added Resistance with Unsteady Wave-Pattern Analysis, Proc. of 7th International Workshop on Ship Hydrodynamics (Shanghai, China), 2011 (September), pp. 28–32.

130. Mahmuddin, F. and Kashiwagi, M.: Design Optimization of a 2D Floating Breakwater by Genetic Algorithm, Proc. of 7th International Workshop on Ship Hydrodynamics (Shanghai, China), 2011 (September), pp. 316–321.

131. Kashiwagi, M. and Nishimatsu, S.: Fundamental Research on the Energy Transmission Efficiency of a Rotating Pendulum-type Wave-power Generator, Proc. of 11th International Conference on Fluid Control, Measurements and Visualization (FLUCOME 2011) (Keelung, Taiwan), 2011 (December), CD-ROM.

132. He, G-H. and Kashiwagi, M.: Wave Pattern Analysis by a Higher-order Boundary Element Method, Proc. of 27th International Workshop on Water Waves and Floating Bodies (Copenhagen, Denmark), 2012 (April), pp. 73–76.

133. Kashiwagi, M., Nishimatsu, S. and Sakai, K.: Wave-energy Absorption Efficiency by a Rotating Pendulum-type Electric-power Generator Installed inside a Floating Body, Proc. of 27th International Workshop on Water Waves and Floating Bodies (Copenhagen, Denmark), 2012 (April), pp. 81–84.

134. Bondarenko, O. and Kashiwagi, M.: Ensuring Safe Operation of Ship Propulsion Plant in Extreme Sea Condition, Proc. of the 11th International Marine Design Conference (IMDC), Glasgow, UK, 2012 (June), Vol. 3, pp. 83–96.

135. Mahmuddin, F. and Kashiwagi, M.: Design Optimization of a 2D Asymmetric Floating Breakwater by Genetic Algorithm, Proc. of 22nd International Offshore and Polar Engineering Conference (Rhodes, Greece), 2012 (June), Vol. 3, pp. 1263–1270.

136. Kashiwagi, M. and Mahmuddin, F.: Numerical Analysis of a 3D Floating Breakwater Performance, Proc. of 22nd International Offshore and Polar Engineering Conference (Rhodes, Greece), 2012 (June), Vol. 3, pp. 1271–1278.

137. He, G-H. and Kashiwagi, M.: Time Domain Simulation of Steady Ship Wave Problem by a Higher-Order Boundary Element Method, Proc. of 22nd International Offshore and Polar Engineering Conference (Rhodes, Greece), 2012 (June), Vol. 3, pp. 1149–1155.

138. Kashiwagi, M. and Hara, T.: A Method for Ship Hydroelastic Analysis by Means of Rankine Panel Method, Proc. of Hydroelasticity in Marine Technology 2012 (Tokyo, Japan), 2012 (September), pp. 41–50.

139. Sakai, K., Nishimatsu, S. and Kashiwagi, M.: Study on Wave-Energy Absorption by a Floating Body Equipped with Interior Pendulum-Type Rotating Cylinder, Proc. of 6th Asia-Pacific Workshop on Marine Hydrodynamics - APHydro2012 (Malaysia), 2012 (September), pp. 11–16.

140. Tasrief, M. and Kashiwagi, M.: Improvement of Ship Geometry in Light of Ship Performance in Actual Sea, Proc. of 6th Asia-Pacific Workshop on Marine Hydrodynamics - APHydro2012 (Malaysia), 2012 (September), pp. 83–88.

141. Kim, S. and Kashiwagi, M. : Numerical Computations of Strongly Nonlinear Slamming and Resultant Wave Loads, Proc. of 6th Asia-Pacific Workshop on Marine Hydrodynamics - APHydro2012 (Malaysia), 2012 (September), pp. 175–178.

142. Nakagawa, D., Yamamoto, K. and Kashiwagi, M. : Investigation of Nonlinear Effects on Ship-Generated Unsteady Waves and Added Resistance Using CFD Simulations, Proc. of 6th Asia-Pacific Workshop on Marine Hydrodynamics - APHydro2012 (Malaysia), 2012 (September), pp. 263–268.

143. Yamamoto, K., Wakabayashi, T. and Kashiwagi, M. : Experimental Study on Ship-generated Unsteady Waves and Added Resistance, Proc. of 6th Asia-Pacific Workshop on Marine Hydrodynamics - APHydro2012 (Malaysia), 2012 (September), pp. 501–506.

144. Hu, C-H., Liu, C. and Kashiwagi, M. : Parallel Simulation of RIAM-CMEN for Strongly Nonlinear Wave-Ship Interaction, Proc. of 2nd International Conference on Violent Flows (Nantes, France), 2012 (September), pp. 112–117.

145. Kashiwagi, M., Nakagawa, D. and Yamamoto, K. : Analysis of Unsteady Waves and Added Resistance Using CIP-based Cartesian Grid Method, Proc. of 2nd International Conference on Violent Flows (Nantes, France), 2012 (September), pp. 238–245.

146. He, G-H. and Kashiwagi, M. : Time Domain Calculations for the Forward Speed Diffraction and Radiation Problems of a Wigley Hull, Proc. of 10th International Conference on Hydrodynamics (St. Petersburg, Russia), 2012 (October), Vol. 2, pp. 201–206.

147. Minoura, M., Hirao, C., Miyazaki, Y. and Kashiwagi, M. : External Dynamics System of Twin Floating Bodies for Perfect Wave Absorption, Proc. of 28th International Workshop on Water Waves and Floating Bodies (Avignon, France), 2013 (April), pp. 145–148.

148. Kashiwagi, M. and Wang, X. : A New Slender-Ship Theory Valid for All Oscillatory Frequencies and Forward Speeds, Proc. of 32nd International Conference on Ocean, Offshore and Arctic Engineering OMAE-2013 (Nantes, France), 2013 (June), Paper Number: OMAE2013-11564, pp. 1–8.

149. Kashiwagi, M., Nishimatsu, S. and Sakai, K. : Wave-Energy Absorption by Electric-Power Generator Rotating on Interior Circular Surface of an Asymmetric Floating Body, Proc. of 23rd International Offshore and Polar Engineering Conference (Anchorage, USA), 2013 (July), Vol. 1, pp. 584–590.

150. He, G-H. and Kashiwagi, M. : Higher-Order BEM for Radiation Forces of a Modified Wigley Hull with Forward Speed, Proc. of 23rd International Offshore and Polar Engineering Conference (Anchorage, USA), 2013 (July), Vol. 3, pp. 792–798.

151. Tasrief, M. and Kashiwagi, M. : Improvement of Ship Geometry by Optimizing the Sectional Area Curve with Binary-Coded Genetic Algorithms (BCGAs), Proc. of 23rd International Offshore and Polar Engineering Conference (Anchorage, USA), 2013 (July), Vol. 4, pp. 869–875.

152. Kashiwagi, M. and Yamamoto, K. : Ship-generated Unsteady Waves and Its Importance in Predicting Added Resistance, Proc. of 8th International Workshop on Ship Hydrodynamics (Seoul, Korea), 2013 (September), IWSH2013-O3-1.pdf.

153. Tasrief, M. and Kashiwagi, M. : Optimization of Sectional Area Curve of a Ship, Proc. of 8th International Workshop on Ship Hydrodynamics (Seoul, Korea), 2013 (September), IWSH2013-P7A-2.pdf.

154. Kashiwagi, M., Ishigami, Y., Ishigami, K., Iwashita, H., Higo, Y. and Ikeda, H. : Motion Characteristics in Waves of a Floating Platform of Complex Geometry for Renewable Energy Utilization, Proc. of International Symposium on Marine and Offshore Renewable Energy (Tokyo, Japan), 2013 (October), CD-ROM S7-1.pdf.

155. Sakai, K. and Kashiwagi, M. : Wave-Energy Absorption by an Asymmetric Floating Body Equipped with Rotating Pendulum-Type Electric-Power Generator, Proc. of International Symposium on Marine and Offshore Renewable Energy (Tokyo, Japan), 2013 (October), CD-ROM S7-2.pdf.

156. He, G-H. and Kashiwagi, M. : Numerical Simulation of Fluid-Structure Interaction by an Adaptive Cartesian-Grid CIP Method, Proc. of 29th International Workshop on Water Waves and Floating Bodies (Osaka, Japan), 2014 (April), pp. 73–76.

157. Sasa, K. and Kashiwagi, M. : Improvement of Rankine Panel Method by Theoretical Consideration of Panel Forces on Ship Hull, Proc. of 29th International Workshop on Water Waves and Floating Bodies (Osaka, Japan), 2014 (April), pp. 177–180.

158. Tasrief, M. and Kashiwagi, M. : Improvement of Ship Performance Based on Sensitivity Study to the Added Resistance, Proc. of 24th International Offshore and Polar Engineering Conference (Busan, Korea), 2014 (June), Vol. 3, pp. 978–985.

159. Takaramoto, R., Kashiwagi, M. and Sakai, K. : Wave Energy Absorption in Irregular Waves by a Floating Body Equipped with Interior Rotating Electric-Power Generator, Proc. of 24th International Offshore and Polar Engineering Conference (Busan, Korea), 2014 (June), Vol. 1, pp. 528–533.

160. Iida, T., Kashiwagi, M. and He, G-H. : Numerical Confirmation of Cloaking Phenomenon on an Array of Floating Bodies and Reduction of Wave Drift Force, Proc. of 24th International Offshore and Polar Engineering Conference (Busan, Korea), 2014 (June), Vol. 3, pp. 661–665.

161. Kashiwagi, M., Iida, T. and Miki, M. : Wave Drift Force on Floating Bodies of Cloaking Configuration and Associated Wave Patterns, Proc. of 30th International Workshop on Water Waves and Floating Bodies (Bristol, UK), 2015 (April), pp. 101–104.

162. Tasrief, M. and Kashiwagi, M. : Design of a Ship with High Performance in Waves with Optimized Form Parameters, Proc. of the 12th International Marine Design Conference (IMDC), (Tokyo, Japan), 2015 (May), Vol. 2, pp. 547–554.

163. Iida, T., Kashiwagi, M. and Miki, M. : Wave Pattern in Cloaking Phenomenon around a Body Surrounded by Multiple Vertical Circular Cylinders, Proc. of 25th International Offshore and Polar Engineering Conference (Kona, Hawaii, USA), 2015 (June), Vol. 3, pp. 635–641.

164. Kashiwagi, M., Kuga, S. and Chimoto, S. : Time- and Frequency-Domain Calculation Methods for Ship Hydroelasticity with Forward Speed, Proc. of Hydroelasticity in Marine Technology 2015 (Split, Croatia), 2015 (September), pp. 477–492.

165. Yoshida, J., Wang, X., Ohtaki, M. and Kashiwagi, M. : Nonlinear Effects on Ship Motions and Added Resistance in Large-Amplitude Waves, Proc. of 3rd International Conference on Violent Flows (VF-2016, Osaka, Japan), 2016 (March), CD-ROM.

166. Zhang, J. and Kashiwagi, M. : An Explicit Time-stepping Scheme for Nonlinear Water Waves Computation, Proc. of 3rd International Conference on Violent Flows (VF-2016, Osaka, Japan), 2016 (March), CD-ROM.

167. Iida, T. and Kashiwagi, M. : Shallow Water Cloaking with Anisotropic Fluid, Proc. of 31st International Workshop on Water Waves and Floating Bodies (Michigan, USA), 2016 (April), pp. 65–68.

168. Yasuda, E., Iwashita, H. and Kashiwagi, M. : Improvement of Rankine Panel Method for Seakeeping Prediction of a Ship in Low Frequency Region, Proc. of 35th International Conference on Ocean, Offshore and Arctic Engineering OMAE-2016 (Busan, Korea), 2016 (June), Paper Number: OMAE2016-54163.

169. Miki, M. Iida, T., Kashiwagi, M. and Asaumi, T. : Optimization of Motions of Surrounding Multiple Cylinders to Cloak a Central Body Oscillating in Regular Waves, Proc. of 26th International Offshore and Polar Engineering Conference (Rhodes, Greece), 2016 (June), Vol. 3, pp. 62–67.

170. Kashiwagi, M. : Some Attempts for Internationalization at Maritime and Urban Engineering Program in Graduate School of Osaka University, Proc. of 64th Annual Conference, International Session of Japanese Society for Engineering Education, 2016 (September), pp. 12–15.

171. Wang X. and Kashiwagi, M. : A Practical Method for Ship Motions Prediction in Large Waves, Proc. of 13th International Symposium on Practical Design of Ships and Other Floating Structures - PRADS' 2016 (Copenhagen, Denmark), 2016 (September), ID-110.

172. Seki, Y., Kashiwagi, M. and Iwashita, H. : Experimental Study on Added Resistance and Unsteady Pressure Distribution in Following Waves, Proc. of 13th International Symposium on Practical Design of Ships and Other Floating Structures - PRADS' 2016 (Copenhagen, Denmark), 2016 (September), ID-147.

173. Ashida, Y., Hara, T., Taniguchi, T. and Kashiwagi, M. : Time-Domain Computation Methods for a Floating Platform of Complicated Geometry with Multiple wave interactions, Proc. of 12th International Conference on Hydrodynamics (ICHD) (Egmond aan Zee, Netherlands), 2016 (September), Tracking Number-42.

174. Kashiwagi, M. and Zhu, J. : A Practical Calculation Method for Forward-Speed Effect on Cross-Coupling Radiation Forces in Enhanced Unified Theory, Proc. of 12th International Conference on Hydrodynamics (ICHD) (Egmond aan Zee, Netherlands), 2016 (September), Tracking Number-47.

175. Iida, T. and Kashiwagi, M. : Design of Small Water Channel Network for Shallow Water Cloaking, Proc. of 32nd International Workshop on Water Waves and Floating Bodies (Dalian, China), 2017 (April), pp. 89–92.

176. Kashiwagi, M.: Enhanced Unified Theory with Forward-speed Effect in the Inner Free-surface Condition, Proc. of 32nd International Workshop on Water Waves and Floating Bodies (Dalian, China), 2017 (April), pp. 93–96.

177. Zhang, J. and Kashiwagi, M. : Application of ALE to Nonlinear Wave Diffraction by a Non-wall-sided Structure, Proc. of 27th International Ocean and Polar Engineering Conference (San Francisco, USA), 2017 (June), Vol. 3, pp. 461–468.

178. Chen, C. and Kashiwagi, M. : Ship Routing Based on the Kuroshio Current, Proc. of 36th International Conference on Ocean, Offshore and Arctic Engineering (Trondheim, Norway), 2017 (June), OMAE2017-61606.

179. Tanaka, R., Taniguchi, T. and Kashiwagi, M. : Nonlinear Effects on Ship Hydroelastic Responses with Forward Speed in Large-amplitude Waves, Proc. of 10th International Workshop on Ship Hydrodynamics (Keelung, Taiwan), 2017 (November), IWSH2017-460.pdf.

180. Yang, K-K. and Kashiwagi, M. : Proc. of 10th International Workshop on Ship Hydrodynamics (Keelung, Taiwan), 2017 (November), IWSH2017-461.pdf.

181. Iida, T. and Kashiwagi, M. : Backward Waves through Array of Rectangular Columns, Proc. of 33rd International Workshop on Water Waves and Floating Bodies (Guidel-Plages, France), 2018 (April), pp. 81–84.

182. Iwashita, H. and Kashiwagi, M. : An Innovative EFD for Studying Ship Seakeeping, Proc. of 33rd International Workshop on Water Waves and Floating Bodies (Guidel-Plages, France), 2018 (April), pp. 85–88.

183. Loukogeorgaki, E. and Kashiwagi, M. : Hydroelastic Analysis of an Annular Flexible Floating Plate, Proc. of 28th International Ocean and Polar Engineering Conference (Sapporo, Japan), 2018 (June), Vol. 3, pp. 61–68.

184. Heo, K. and Kashiwagi, M. : Numerical Investigation of Second-order Hydroelastic Response for the Flexible Floating Body, Proc. of 28th International Ocean and Polar Engineering Conference (Sapporo, Japan), 2018 (June), Vol. 3, pp. 69–76.

185. Hara, T. and Kashiwagi, M. : Analytical Integration of Time-Domain Green Function over a Panel on Ship Hull Close to the Free Surface, Proc. of 13th International Conference on Hydrodynamics (ICHD) (Inchon, Korea), 2018 (September), pp. 20–29.

186. Ohtaki, M. and Kashiwagi, M. : Wave Loads Evaluated from Measured Unsteady Pressure Distribution, Proc. of 13th International Conference on Hydrodynamics (ICHD) (Inchon, Korea), 2018 (September), pp. 222–231.

187. Ito, Y. and Kashiwagi, M. : Study on Added Resistance Using Measured and Computed Pressure Distributions on a Ship Hull, Proc. of 13th International Conference on Hydrodynamics (ICHD) (Inchon, Korea), 2018 (September), pp. 251–260.

188. Higaki, T., Khayyer, A., Kashiwagi, M. and Park, J-C. : Hydroelastic Slamming Simulations by a Fully-Lagrangian coupled MPS Method, Proc. of 8th International Conference on Hydroelasticity in Marine Technology (Seoul, Korea), 2018 (September), pp. 115–124.

189. Heo, K. and Kashiwagi, M. : Numerical Analysis for the Second-order Springing of Flexible Body in Head Waves, Proc. of 8th International Conference on Hydroelasticity in Marine Technology (Seoul, Korea), 2018 (September), pp. 157–166.

190. Miura, S. and Kashiwagi, M. : Unsteady Pressure Distribution on Ship-Hull Surface Measured by FBG Pressure Sensors and Computed by Rankine Panel Method, Proc. of 8th PAAMES and AMEC 2018 (Busan, Korea), 2018 (October), pp. 441–447.

191. Umazume, K. and Kashiwagi, M. : Capture Width and Directivity of Maximum Wave Energy Extracted by an Array of Vertical Cylinders, Proc. of 8th PAAMES and AMEC 2018 (Busan, Korea), 2018 (October), pp. 488–493.

192. Kashiwagi, M., Iwashita, H. Miura, S. and Hinatsu, M. : Study on Added Resistance with Measured Unsteady Pressure Distribution on Ship-hull Surface, Proc. of 34th International Workshop on Water Waves and Floating Bodies (Newcastle, Australia), 2019 (April), pp. 81–84.

193. Waskito, K.T. and Kashiwagi, M. : Improvement of Wave Loads Estimation Using Spatial Pressure Distribution on Ship Hull, Proc. of 38th International Conference on Ocean, Offshore and Arctic Engineering (Glasgow, UK), 2019 (June), OMAE2019-95273.

194. Taguchi, M. and Kashiwagi, M.: Experimental Study on a Relation between Nonlinear Hydrodynamic Forces and Wave-induced Ship Motions, Proc. of 38th International Conference on Ocean, Offshore and Arctic Engineering (Glasgow, UK), 2019 (June), OMAE2019-95555.

195. Wicaksono, A. and Kashiwagi, M.: Efficient Coupling of Slender Ship Theory and Modular Maneuvering Model to Estimate the Ship Turning Motion in Waves, Proc. of 29th International Ocean and Polar Engineering Conference (Hawaii, USA), 2019 (June), Vol. 3, pp. 4632–4639.

196. Kashiwagi, M., Iwashita, H., Waskito, K.T. and Hinatsu, M.: Prediction of Wave Loads with Measured Unsteady Pressure Distribution on Ship-Hull Surface, Proc. of 35th International Workshop on Water Waves and Floating Bodies (Seoul, Korea), 2020 (August), pp. 77–80.

197. Hong, Y., Kashiwagi, M. and Heo, K.: Numerical Calculations of Wave-Induced Hydroelastic Response of a Ship with Forward Speed Using Legendre Polynomials as Mode Functions, Proc. of 30th International Ocean and Polar Engineering Conference (Shanghai, China), 2020 (October), Vol. 4, pp. 3537–3543.

198. Kashiwagi, M., Hong, Y. and Heo, K.: Ship Hydroelasticity Analysis with Timoshenko-Beam Approximation Using Legendre and Chebyshev Polynomials, Proc. of 36th International Workshop on Water Waves and Floating Bodies (Seoul, Korea), 2021 (April), (submitted)

199. Liu, Y., Liang, H., Kashiwagi, M. and Cong, P.: Computational Accuracy and Efficiency for Diffraction Transfer Matrix Using Hybrid Source-Dipole Formulations, Proc. of 36th International Workshop on Water Waves and Floating Bodies (Seoul, Korea), 2021 (April), (submitted)

200. Yang, K-K., Kim, B-S., Kim, Y., Kashiwagi, M. and Iwashita, H.: Numerical Analysis of Wave-Induced Unsteady Pressure on Ship-Hull Surface, Proc. of 36th International Workshop on Water Waves and Floating Bodies (Seoul, Korea), 2021 (April), (submitted)

(C) Proceedings of Symposia in Japan and Bulletin of Universities (*Excluding presentation papers at JASNAOE annual meetings*)

1. Kashiwagi, M.: The Unified Slender Body Theory for Swaying and Yawing Ships, Bulletin of Kobe University of Mercantile Marine, 1985 (July), Vol. 33, pp. 1–14.

2. Kashiwagi, M.: Calculation Method for Ship Maneuvering Motion in Non-Uniform Current and Its application to Naruto Strait (in Japanese), Bulletin of Research Institute for Applied Mechanics, 1987 (January), Vol. 63, pp. 163–178.

3. Kashiwagi, M., Varyani, K. and Ohkusu, M.: Forward-Speed Effects on Hydrodynamic Forces Acting on a Submerged Cylinder in Waves, Reports of Research Institute for Applied Mechanics, Kyushu Univ., 1987 (September) Vol. XXXIV, No. 102, pp. 1–26.

4. Kashiwagi, M.: Some Issues in Ship Hydrodynamics with Forward Speed and Harmonic Oscillation (in Japanese), Bulletin of Research Institute for Applied Mechanics, 1987 (December), Vol. 65, pp. 133–150.

5. Kashiwagi, M.: Hydrodynamic Forces on a Submerged Cylinder with Forward and Oscillatory Motions (in Japanese), Proc. of Computational Fluid Dynamics Forum in Naval Architecture, 1987 (December), pp. 140–148.

6. Kashiwagi, M., Inada, M., Yasunaga, M. : A 3-D Calculation Method for Predicting Side-Wall Effects on Hydrodynamic Forces Acting on a Ship Model (in Japanese), Bulletin of Research Institute for Applied Mechanics, 1989 (October), Vol. 68, pp. 123–139.

7. Kashiwagi, M. : Calculation Formulas for the Wave-Induced Steady Horizontal Force and Yaw Moment on a Ship with Forward Speed, Reports of Research Institute for Applied Mechanics, Kyushu University, 1991 (February), Vol. 37, No. 107, pp. 1–18.

8. Kashiwagi, M. : A Consistent Theory for Oscillating Slender Ships at Arbitrary Forward Speed, Reports of Research Institute for Applied Mechanics, Kyushu University, 1995 (March), Vol. 40, No. 111, pp. 1–10.

9. Kashiwagi, M., Kohjo, T. : A Calculation Method for Hydrodynamic Interactions of Multiple Bodies Supporting a Huge Floating Body (in Japanese), Proc. of 13th Symposium of Ocean Engineering, Society of Naval Architects of Japan, 1995 (July), pp. 247–254.

10. Kashiwagi, M. : A Calculation Method for Steady Drift Force and Moment on Multiple Bodies (in Japanese), Bulletin of Research Institute for Applied Mechanics, Vol.78, 1995 (October), pp. 83–98.

11. Kashiwagi, M. : Hydroelastic Responses of a Very Large Floating Structure in Waves, (in Japanese), Bulletin of Research Institute for Applied Mechanics, 1997 (November), Vol. 82, pp. 31–52.

12. Kashiwagi, M. : A Hierarchical Interaction Theory for Wave Forces on a Large Number of Elementary Bodies of a Semisub-Type VLFS (in Japanese), Proc. of 14th Symposium of Ocean Engineering, Society of Naval Architects of Japan, 1998 (July), pp. 425–431.

13. Ikeda, Y., Ohtuka, K., Kagemoto, H., Kashiwagi, M., Kyozuka, Y., Takagi, K., Mikami, T. and Yamashita, S. : Concepts on a Megafloat (in Japanese), Proc. of 14th Symposium of Ocean Engineering, Society of Naval Architects of Japan, 1998 (July), pp. 67–74.

14. Kashiwagi, M. : A Hierarchical Calculation Method for Hydrodynamic Interactions among a Great Number of Floating Bodies (in Japanese), Proc. of 48th Conference on Theoretical Applied Mechanics, 1999 (January), pp. 401–402.

15. Kashiwagi, M. and Yoshida, S. : Hydrodynamic Interactions among Multiple Floating Cylinders in a Regular Arrangement (in Japanese), Proc. of 15th Ocean Engineering Symposium, 2000 (January), pp. 231–238.

16. Kashiwagi, M. : Wave Drift Force and Moment on a Column-Supported Type Very Large Floating Structure (in Japanese), Proc. of 15th Ocean Engineering Symposium, 2000 (January), pp. 239–246.

17. Kashiwagi, M. : Transient Elastic Response of a Very Large Floating Structure (in Japanese), Proc. of 49th Conference on Theoretical Applied Mechanics, 2000 (January), pp. 303–304.

18. Kashiwagi, M. : Wave-Induced Motions of an Elastic Floating Structure Supported by Multiple Cylinders (in Japanese), Proc. of Annual Meeting of the Society of Fluid Mechanics of Japan, 2000 (July), Kyoto, pp. 275–276.

19. Kashiwagi, M., Ohwatari, Y. : Hydrodynamic Nonlinear Interactions among Multiple Floating Bodies (in Japanese), Proc. of 16th Ocean Engineering Symposium, Society of Naval Architects of Japan, 2001 (July), pp. 297–304.

20. Kashiwagi, M. : State of the Art and Future Work in Numerical Marine Hydrodynamics (in Japanese), Proc. of 2001 Annual Meeting of Japan Society of Fluid Mechanics, 2001 (August), pp. 291–292.

21. Hu, C-H., Kashiwagi, M. and Momoki, T. : Numerical Study on Interaction of Waves with Structures by CIP Method (in Japanese), Proc. of 15th Computational Mechanics Conference (Kagoshima), 2002 (November), pp. 433–434.

22. Momoki, T., Kashiwagi, M. and Hu, C-H. : Numerical Simulations of Interactions of Water Waves with an Offshore Structure using CIP Method (in Japanese), Engineering Sciences Reports, Kyushu University, Vol. 25, No. 1, 2003 (June), pp. 17–24.

23. Kashiwagi, M., Ten, I. and Nagao, T. : The Radiation Problem of a Floating Body in a Two-Layer Fluid of Finite Depth, Proc. of 17th Ocean Engineering Symposium, Society of Naval Architects of Japan, 2003 (July), pp. 297–304.

24. Hu, C-H. and Kashiwagi, M. : 2-D and 3-D Numerical Simulations of Dam Breaking by CIP Method, Proc. of 17th Ocean Engineering Symposium, Society of Naval Architects of Japan, 2003 (July), pp. 321–325.

25. Hu, C-H. and Kashiwagi, M. : Numerical Simulation of Strongly-Nonlinear Wave-Body Interactions by CIP Method (in Japanese), Proc. of 2003 Annual Meeting of the Japan Society of Mechanical Engineers (Tokushima Univ.), 2003 (August), Vol. 1, pp. 5–6.

26. Hu, C-H. and Kashiwagi, M. : Numerical Accuracy in Computations of Wave-Impact Phenomena by CIP Method (in Japanese), Proc. of 16th Computational Mechanics Conference (Kobe Univ.), 2003 (November), pp. 219–220.

27. Hu, C-H. and Kashiwagi, M. : Application of CIP Method to Numerical Simulations of Extreme Wave-Body Interactions (in Japanese), Proc. of 53rd Conference on Theoretical Applied Mechanics, 2004 (January), pp. 133–134.

28. Kashiwagi, M. and Wada, K. : Wave-Induced Motions of a Floating Body in a Two-Layer Fluid (in Japanese), Proc. of 18th Ocean Engineering Symposium, Society of Naval Architects of Japan, 2005 (January), CD-ROM.

29. Hu, C-H. and Kashiwagi, M. : 3-D Numerical Simulation of Strongly Nonlinear Wave-Body Interactions by the CIP Method (in Japanese), Proc. of 18th Computational Mechanics Conference (Kobe Univ.), 2005 (November), pp. 627–628.

30. Hu, C-H. and Kashiwagi, M. : Numerical Simulation of Strongly Nonlinear Free Surface Problems by CIP Method (in Japanese), Proc. of 55th Conference on Theoretical Applied Mechanics, 2006 (January), pp. 285–286.

31. Mikami, T. and Kashiwagi, M. : A Calculation Method for Nonlinear Wave Loads Acting on a Ship (in Japanese), Proc. of 55th Conference on Theoretical Applied Mechanics, 2006 (January), pp. 551–552.

32. Kashiwagi, M. and Hu, C-H. : Numerical Calculation Method on Extremely Nonlinear Wave-Body Interactions and Experimental Validation (in Japanese), Proc. of Annual Meeting of the Japanese Society of Multiphase Flow in 2006 (Kanazawa), 2006 (September), pp. 354–355.

33. Hu, C-H. and Kashiwagi, M. : Numerical Simulation of Strongly Nonlinear Ship-Wave Interactions (in Japanese), Proc. of Annual Meeting of the Society of Fluid Mechanics of Japan (Kyushu University), 2006 (September), pp. AM-06-05-002.

34. Hu, C-H. and Kashiwagi, M. : 3D Numerical Simulation of Sloshing by THINC Scheme (in Japanese), Proc. of 2006 Annual Meeting of the Japan Soc. of Mech. Engineers (Kumamoto Univ.), 2006 (September), pp. 97–98.

35. Hayashi, T. and Kashiwagi, M. : Reflection and Transmission Waves by an Asymmetric Body Oscillating in Waves (in Japanese), Reports of Research Institute for Applied Mechanics, Kyushu University, No. 133, 2007 (September), pp. 125–134.

36. Hu, C-H. and Kashiwagi, M. : Development of CFD Code for Strongly Nonlinear Free Surface Flows (in Japanese), Reports of Research Institute for Applied Mechanics, Kyushu University, No. 133, 2007 (September), pp. 139–146.

37. Hu, C-H., Sueyoshi, M. and Kashiwagi, M. : 3-D Computation of Strongly Nonlinear Wave-Ship Interaction by CIP/Cartesian Grid Method (in Japanese), Proc. of 21st Symposium on Computational Fluid Dynamics, 2007 (December), CDROM F5-1.

38. Kashiwagi, M., Sasakawa, T., Wakabayashi, T., Iwashita, H. : Added Resistance and Unsteady Waves Generated by a Ship Advancing and Oscillating in Waves (in Japanese), Annual Meeting of the Japanese Society of Fluid Mechanics (Hokkaido Univ.), 2010 (September), CD-ROM, 26.pdf.

39. Kashiwagi, M., Nishimatsu, S., Hamamoto, M. : Fundamental Research on the Energy Transmission Efficiency of a Rotating Pendulum-type Wave-power Generator (in Japanese), Proc. of 22nd Ocean Engineering Symposium (JASNAOE), 2011 (March), CD-ROM, OES22-045, pp. 1–8.

40. Kashiwagi, M., Nishimatsu, S. and Sakai, K. : Wave-energy Absorption by a Rotating Pendulum- type Electric-power Generator Installed inside an Asymmetric Floating Body (in Japanese), Proc. of 23rd Ocean Engineering Symposium, 2012 (August), CD-ROM, OES23-051.

41. Kashiwagi, M. and Mahmuddin, F. : 3D Effects on Wave Reflection Performance of a Floating Breakwater (in Japanese), Proc. of 23rd Ocean Engineering Symposium, 2012 (August), CD-ROM, OES23-052.

42. Iida, T., Kashiwagi, M. and He, G-H. : Optimization of the position of the floating bodies to reduce the drift force (in Japanese), Proc. of 24th Ocean Engineering Symposium, 2014 (March), CD-ROM, OES24-087.

43. Miki, M., Iida, T., Kashiwagi, M. : The Measurement of Scattering Wave and Wave Drift Force around the Multiple Floating Bodies (in Japanese), Proc. of 25th Ocean Engineering Symposium (JFOES and JASNAOE), 2015 (August), CD-ROM, OES25-067.

(D) Text Books

1. Kashiwagi, M.: Mega-Float Offshore Structure (in charge of Chapter 3), Edited by Performance Division of Ocean Engineering Committee, Japan Society of Naval Architects, Published by Seizando-shoten Co., Ltd. (ISBN: 4-425-71241-2), 1995 (August).

2. Kashiwagi, M.: Fluid Dynamics for Global Environmental Studies (in charge of Chapters 2 and 3), Supervised by Department of Earth System Science and Technology, Interdisciplinary Graduate School of Engineering Sciences, Kyushu University, Published by Seizando-shoten Co., Ltd. (ISBN: 4-425-71301-X), 2001 (March).

3. Kashiwagi, M. (Editor): Hydrodynamics in Ship and Ocean Engineering, Published by RIAM, Kyushu University, ISBN: 4-87780-014-X, 2001 (April).

4. Kashiwagi, M.: Practical Hydrodynamics of Floating Bodies, Volume 1: Numerical Computation Methods for Body-Oscillation Problems (in charge of Chapters 1, 2, 4, 5, 6, 7), Edited by Ocean Engineering Committee of Japan Society of Naval Architects, Published by Seizando-shoten Co., Ltd. (ISBN: 4-425-71321-4), 2003 (April).

5. Kashiwagi, M.: Practical Hydrodynamics of Floating Bodies, Volume 2: Experiments and Analyses, (in charge of Chapter 5), Edited by Ocean Engineering Committee of Japan Society of Naval Architects, Published by Seizando-shoten Co., Ltd. (ISBN: 4-425-71331-1), 2003 (April).

6. Kashiwagi, M., Hu, C-H. and Sueyoshi, M.: Advances in Numerical Simulation on Nonlinear Water Waves (Editor: Qingwei Ma), Volume 11: Advances in Coastal and Ocean Engineering, Chapter 12: Numerical Computation Methods for Strongly Nonlinear Wave-Body Interactions, Published by World Scientific Publishing Co., Ltd. (ISBN-13 978-981-283-649-6), 2010.

7. Kashiwagi, M. and Iwashita, H.: Ship Motions (Seakeeping) - Volume 4 in the Series of Ship and Ocean Engineering -, Supervised by Japan Society of Naval Architects and Ocean Engineers, Published by Seizando-shoten Co., Ltd. (ISBN: 978-4-425-71461-2), 2012 (September).

On the occasion of my retirement from Osaka University in March 2021, I prepared this book containing some selected papers from the publications made over the past 35 years of my research career. These selected papers were reproduced using a template of LaTeX and their original manuscripts kept in my computer, although no digital data exist for the manuscripts and figures before 1995. These selected papers are expected to be informative to those researchers who are interested in hydrodynamic interactions of water waves with floating bodies including ships with forward speed.

Some papers are co-authored with my former students who finished master's or doctoral courses under my supervision at both Kyushu University and Osaka University. I can recall the pleasant times spent with students whose names appear in the complete list of all publications at the end of this book.

ISBN 978-4-907621-02-5